CERN-THESIS-2016-142

# EuCARD-2

Enhanced European Coordination for Accelerator Research & Development

## Academic Dissertation

# High Temperature Superconductor Accelerator Magnets

Van Nugteren, Jeroen (Twente U., Enschede)


The EuCARD-2 Enhanced European Coordination for Accelerator Research & Development project is co-funded by the partners and the European Commission under Capacities 7th Framework Programme, Grant Agreement 312453.

This work is part of EuCARD-2 Work Package **10: Future Magnets (MAG)**.

The electronic version of this EuCARD-2 Publication is available via the EuCARD-2 web site <http://eucard2.web.cern.ch/> or on the CERN Document Server at the following URL: <http://cds.cern.ch/search?p=CERN-THESIS-2016-142>

CERN-THESIS-2016-142

# HIGH
# TEMPERATURE
# SUPERCONDUCTOR
# ACCELERATOR
# MAGNETS

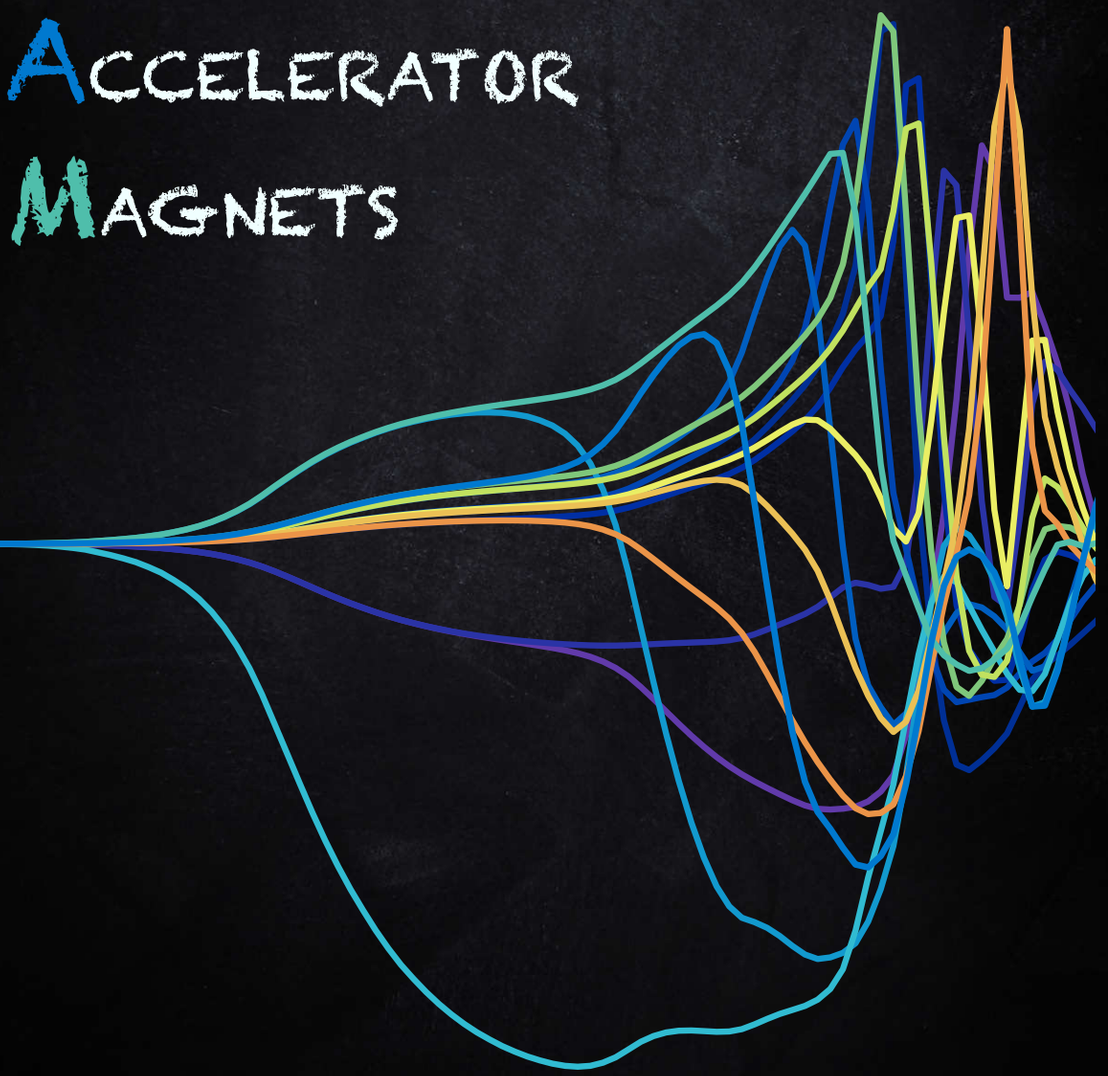

High Temperature Superconductor Accelerator Magnets

JvN
2016

Jeroen van Nugteren

# High Temperature Superconductor Accelerator Magnets

Jeroen van Nugteren

November 10, 2016

PhD Graduation Committee:

| | | | |
|---|---|---|---|
| Chairman | : | prof. dr. ir. J.W.M. Hilgenkamp | University of Twente |
| PhD supervisor | : | prof. dr. ir. H.H.J. ten Kate | University of Twente |
| Co-supervisors | : | dr. G. de Rijk | CERN |
| | | dr. M.M.J. Dhallé | University of Twente |
| Members | : | prof. dr. ir. H.J.M. ter Brake | University of Twente |
| | | prof. dr. ir. A.H. van den Boogaard | University of Twente |
| | | prof. dr. L. Rossi | University of Milan |
| | | prof. dr. J.J. Engelen | University of Amsterdam |
| | | prof. dr. D.C. Larbalestier | Florida State University |
| | | dr. J.A.A.J. Perenboom | Radboud University |

The research described in this thesis was carried out at:
CERN, Geneva, Switzerland,
Technology Department (TE),
Magnets, Superconductors and Cryostats Group (MSC),
Superconducting Magnet Design and Technology Section (MDT).

High Temperature Superconductor Accelerator Magnets
Jeroen van Nugteren
PhD thesis, University of Twente, The Netherlands
ISBN: 978-94-028-0403-4
Printed by: Ipskamp Printing
Cover by: Jeroen van Nugteren and Nikkie Deelen

# High Temperature Superconductor Accelerator Magnets

DISSERTATION

to obtain
the degree of doctor at the University of Twente,
on the authority of the rector magnificus,
prof. dr. H. Brinksma,
on account of the decision of the graduation committee,
to be publicly defended
on Thursday November 10, 2016 at 16:45

by

**Jeroen van Nugteren**

born on October 23, 1986
at Ubbergen, The Netherlands

This thesis has been approved by the PhD supervisor:
prof. dr. ir. H.H.J. ten Kate

# ABSTRACT

For future particle accelerators bending dipoles are considered with magnetic fields exceeding 20 T. This can only be achieved using high temperature superconductors (HTS). These exhibit different properties from classical low temperature superconductors and still require significant research and development before they can be applied in a practical accelerator magnet.

In order to study HTS in detail, a five tesla demonstrator magnet named Feather-M2 is designed and constructed. The magnet is based on ReBCO coated conductor, which is assembled into a 10 kA class Roebel cable. A new and optimized Aligned Block layout is used, which takes advantage of the anisotropy of the conductor. This is achieved by providing local alignment of the Roebel cable in the coil windings with the magnetic field lines.

A new Network Model capable of analyzing transient electro-magnetic and thermal phenomena in coated conductor cables and coils is developed. This model is necessary to solve critical issues in coated conductor accelerator magnets, such as thermal stability, quench propagation and field quality.

The electrical part of the Network Model is validated using a series of benchmark simulation tests and measurements. The model is then used to calculate the dynamic field quality in coil structures. It is concluded that dynamic compensation of the field quality is needed. This can be achieved by a series of persistent current shim coils that are inserted inside the aperture, which is a novel concept introduced in this thesis.

The thermal part of the Network Model is validated by comparing it to an earlier experimentally validated one-dimensional single tape model. Using this a quench is modeled in a section of Roebel cable and later in the full Feather-M2 coil. It is shown that the initialization of the quench consists of three phases: Thermal Drift, Pre-Quench and Quench. The Drift phase can be detected using temperature sensors and the Pre-Quench phase using an array of pick-up coils. These quench detection techniques, provided sufficient margin is maintained, could allow for safe operation of HTS coils up to very high current densities.

An iterative layout optimization algorithm is implemented and used to study layouts at the magnetic field limit of $Nb_3Sn$. It is shown that grading of the $Nb_3Sn$ is essential for reaching magnetic fields beyond 14 T with 20% margin and that operation at 1.9 K and improving the critical current density of the $Nb_3Sn$ conductor are highly recommended. Additionally, preliminary results are shown for layouts using HTS in the high magnetic field region of the coil in 20 T magnets.

# SAMENVATTING (ABSTRACT IN DUTCH)

Om deeltjes af te buigen in toekomstige versnellers zal er gebruik gemaakt worden van dipool magneten. Veldsterktes van hoger dan 20 T worden hiervoor overwogen. Dit kan alleen worden bereikt met Hoge Temperatuur Supergeleiders (HTS). Deze hebben echter andere fysische eigenschappen dan de klassieke Lage Temperatuur Supergeleiders (LTS). Het is daarom noodzakelijk voor de practische toepassing in een versneller om hier onderzoek naar te verichten en dit is het onderwerp van deze thesis.

Allereerst is er een demonstratiemagneet met de naam Feather-M2 ontworpen en gebouwd. Deze magneet is gebaseerd op een ReBCO geleider, die samengesteld in een Roebel kabel, stromen van de orde grootte 10 kA kan dragen. Een nieuw type ontwerp met de naam 'uitgelijnd blok' is toegepast. Hierin wordt optimaal gebruik gemaakt van de anisotropie van de geleider door deze uit te lijnen met het mageetveld.

Een nieuw computermodel is ontwikkeld waarin de kabel wordt benaderd met een netwerk van lijnelementen en knooppunten. Met dit model is het mogelijk om tijdsafhankelijke elektro-magnetische en thermische fenomenen in ReBCO kabels en magneten te bestuderen. Dit model is noodzakelijk om kritieke problemen zoals thermische stabiliteit, thermische drift en veldkwaliteit te bestuderen.

Om het elektrische deel van het netwerkmodel te valideren is een serie tests uitgevoerd. De resultaten hiervan zijn vergeleken met het model. Hierna is het model toegepast op het berekenen van de tijdsafhankelijke veldkwaliteit in verschillende magneetgeometrieën. Hieruit is geconcludeerd dat het noodzakelijk is om het veld dynamisch te corrigeren. Dit kan bereikt worden met behulp van correctiespoelen, die een weerstandsloze stroom geleiden, geplaatst in de boring.

Het thermische gedeelte van het netwerkmodel is gevalideerd aan de hand van een één-dimensionaal model dat eerder experimenteel gevalideerd is. Door gebruik te maken van dit model is het mogelijk om thermische drift te simuleren in Roebel kabels en later ook in de volledige geometrie van Feather-M2. Uit de simulaties volgt dat thermische drift uit drie verschillende fases bestaat: de niet resistieve fase, de enkele tape fase en de kabel fase. De eerste fase kan gedetecteerd worden met temperatuur sensoren en de tweede fase met inductief gekoppelde spoelen. Deze detectietechnieken maken het in principe mogelijk HTS veilig te gebruiken bij zeer hoge stroomdichtheden, mits er voldoende marge met het kritieke oppervlak aangehouden wordt.

Om tweedimensionale magneetontwerpen te bestuderen is er een optimalisatie algoritme geïmplementeerd. Dit algoritme is vervolgens gebruikt om spoelontwerpen dichtbij de magneetveld limiet van de $Nb_3Sn$ geleider te bestuderen. Voor magneten met magneetvelden hoger dan 14 T en een marge van 20% is het noodzakelijk de lagen van de magneet te graderen. Daarbij is het ook bijzonder nuttig om de magneet te bedrijven bij 1.9 K en om de toegepaste stroomdichtheid van de $Nb_3Sn$ geleider te verhogen.

# ACKNOWLEDGEMENTS

Although a thesis is viewed to be the work of an individual it could be seen as raising a child: it takes a village. I this case it takes a well-known university and a world wide renowned research institute to help me become a researcher.

I would like to start by thanking Herman ten Kate and Gijs de Rijk for supervising me. This automatically brings me to Lucio Rossi, Marc Dhallé and Glyn Kirby who I would like to thank for being great day-to-day supervisors. I have enjoyed discussing my research problems with all five and I hope I can continue those in the future.

When I think of other great discussions I had with people during the past few years immediately a few others come to my mind. First and foremost: Jaakko Murtomäki. Because of his creative and chaotic mind many times we came to great ideas together. One of these ideas is the persistent current shim coils described in Chapter 4. Also Felix Wolf and Matthias Mentink were always up for a discussion, for which I thank them. In addition I would like to thank Stefanie Langeslag for her help with taking microscopic images of some of our tapes.

A great part of being a good researcher comes with staying motivated. Luckily there were always people to cheer me up. This is especially true for my girlfriend Nikkie Deelen, who has always supported me during the research and throughout the writing process. Also I wish to thank Tim Mulder, Helder Silva and Valentina Venturi for making my lunches at CERN memorable.

The ideas for developing the Electro-Magnetic and Thermal Network Model, which I present in this thesis, already started to develop when I was still a master student. During that period I was involved in the JackPot project and since then I have always remained in contact with the team involved, therefore I wish to thank Arend Nijhuis, Ezra van Lanen and Gabriella Rolando for providing fertile ground to start from. Another person with whom I could discuss numerical modeling in detail was Antti Stenvall from the University of Tampere. Special thanks to him and his team for their input.

In the beginning I already mentioned it took a whole lot of people to help turning me into a researcher. Since there are so many that I could fill a separate book with names I will default to thanking groups of people. Let me start by thanking the Magnet group (MSC) at CERN led by Luca Bottura where I was allowed to perform my research. The EuCARD2 collaboration played a big role during my PhD too, many thanks to them. I would like to make a special remark on the EuCARD2 workshops: they were the best. Finally I was always allowed to fall back on the Energy Materials and Systems (EMS) group of Twente University and I am very grateful for this.

As many of you may have noticed, this thesis is written in English. Sadly my mother tongue is not English but luckily I found a good friend willing to help me out by checking what I have written word for word, thanks Cissy Li! Last but not least, without my family and friends I probably would not have made it this far. So a special thanks goes to them.

# Table of Contents

# Introduction and Outline

1

> "I am Locutus of Borg. Resistance is futile."
>
> Jean-Luc Picard, Star Trek: TNG, S03E26, 1990

*This thesis concerns the research and development of High Temperature Superconductors (HTS) and their application in high field accelerator dipole magnets for future particle accelerators. It includes a design study for two HTS insert-magnets, named Feather-M0 and Feather-M2, currently being constructed and tested at CERN. These magnets have a very unusual coil layout named Aligned Block, following a novel concept for the optimum use of the so-called ReBCO tape superconductor. As an appetizer, the winding layouts of Feather-M0 and Feather-M2 are shown in Figure 1.1. In this chapter an introduction is given to the quirks and features of ReBCO HTS compared to classical Low Temperature Superconductor (LTS), while providing a brief overview of superconductivity[1] and particle accelerators[2] in general. In addition the Chapters and their structural relationship in this thesis are outlined.*

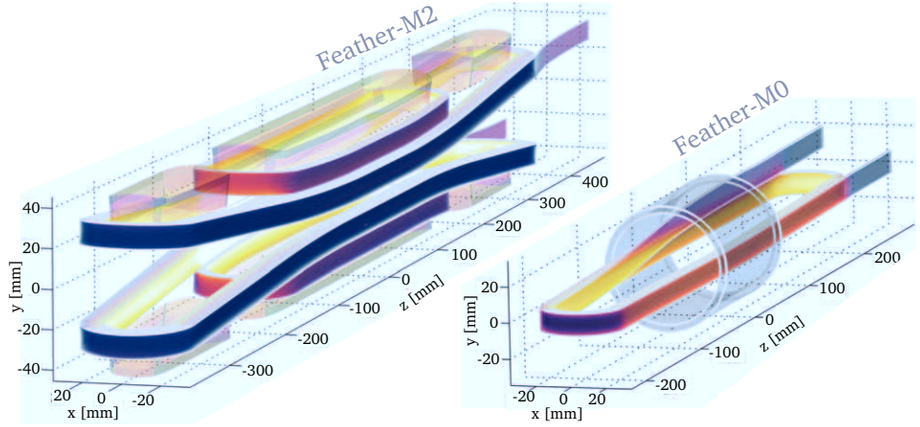


**Figure 1.1.** *Illustration showing dimensions and winding layout of the demonstration High Temperature Superconducting dipole magnet named Feather-M2 and its sub-scale counterpart named Feather-M0.*

[1] An in-depth introduction to superconductivity lies outside the scope of this thesis. Readers interested in the fundamentals of superconductivity are referred to Tinkham [1] and Cyrot et al. [2]. Readers interested in superconducting magnet design are referred to Wilson [3], Iwasa [4], Mess [5] and Russenschuck [6].

[2] A detailed description of the many aspects of particle accelerators lies outside the scope of this thesis. Interested readers are referred to Wiedemann [7].

## 1.1 Particle Accelerators and Colliders

The purpose of a particle accelerator is to accelerate charged particles to near light speed. During the acceleration a gradual transition takes place causing relativistic effects to become dominant. The acceleration is provided by a series of RF cavities, in which an alternating electro-magnetic field exerts a driving force on the particles, that are grouped in bunches. A common strategy is to run the particles through the same set of cavities (in the LHC) some 11 thousand times per second in a storage ring. In order to keep the particle beams inside the storage ring they need to be constantly bend towards its center, which is achieved using a Lorentz force provided by the magnetic field generated by the main bending dipole magnets. In addition, groups of bending dipoles are alternated with quadrupole magnets, which are required to prevent the beams from diverging.

In a circular collider, a specific type of particle accelerator, bunches of particles in the beams are accelerated in opposite directions in two adjacent circular beams, which cross over at an even number of so-called interaction points. At these points the bunches intersect causing some of their particles to collide. Following mass–energy equivalence $E = mc^2$ the kinetic energy of the collision is transformed into a shower of particles including those to be discovered. By analyzing the trajectories physicists are eventually able to discover the existence of new fundamental particles and can de-

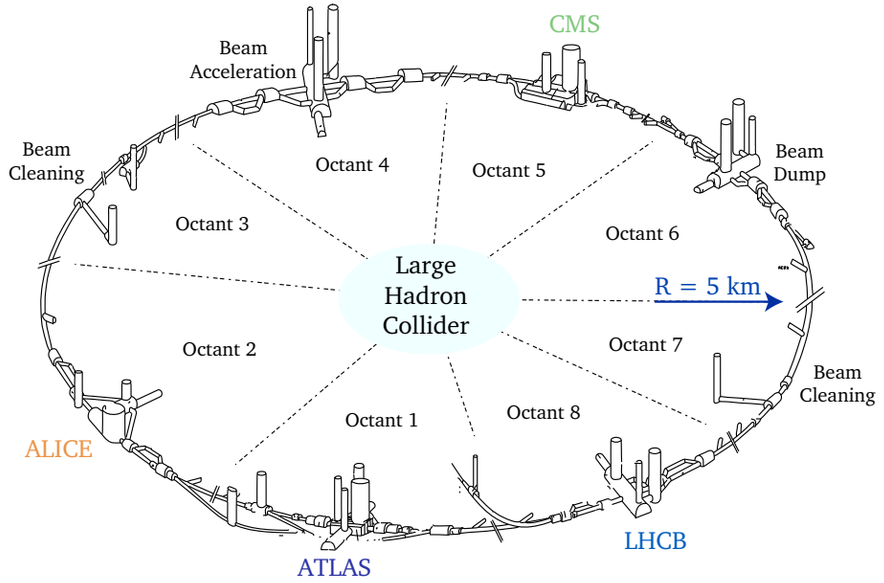


**Figure 1.2.** *Illustration showing the tunnel complex and layout of the Large Hadron Collider (LHC) at CERN (heavily adapted from [8]). Note that for visual clarity the tunnel is interrupted between each octant.*

termine their properties. Presently the most performing is the Large Hadron Collider (LHC) at CERN near Geneva, Switzerland, which is illustrated in Figure 1.2. The circumference of the LHC ring, which is located in a tunnel complex some 100 m under the surface, is about 27 km. The two circulating proton beams intersect in four interactions points, around which large detectors, named ATLAS, ALICE, CMS and LHCb, were built. These detectors are designed and optimized for tracking the debris resulting from the collisions.

The LHC is constructed with superconducting magnets that have a nominal magnetic dipole field of 8.33 T when finally operating at its maximum collision energy of 14 TeV. A photograph of a demonstration model and the cross-section of the coil and surrounding structure are presented in Figure 1.3. In this so-called twin-aperture design, both high vacuum beam tubes and the dipole coil-windings surrounding these beam tubes are accommodated in a single mechanical structure and cryostat [9]. The dipole magnetic field of 8.33 T for beam bending is generated in the two beam pipes across a magnet length of 15 m.

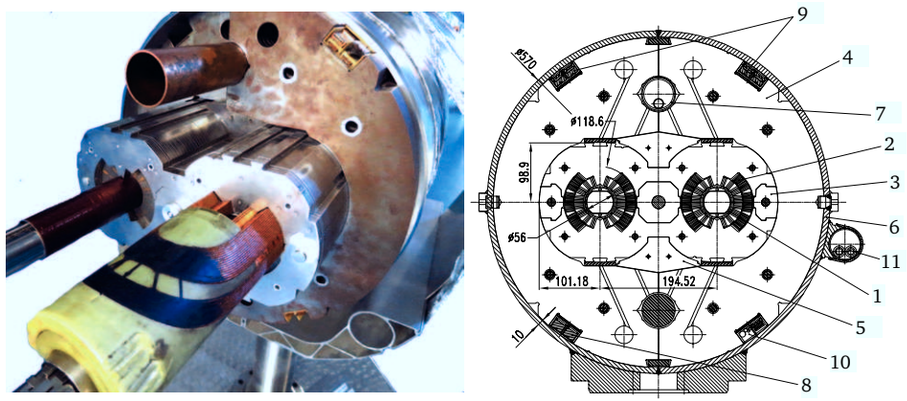


**Figure 1.3.** *Photograph of a cut-away demonstration model (left) and the cross-section of the cold mass of an LHC main bending dipole magnet [9]. The numbers in the cross-section denote: 1. beam tube, 2. coil-windings, 3. collars, 4. iron yoke, 5. iron yoke insert, 6. helium vessel, 7. heat exchanger, 8. dipole bus-bars, 9. arc quadrupole bus-bars, 10. instrumentation wires, 11. bus bars for auxiliary magnets.*

The energy of the particles and thus the collision energy scales directly with the diameter of the ring and the magnetic field strength of the main bending dipoles, i.e. the beam energy can be calculated as $E_{\text{beam}} \simeq 0.3BR_r$ [10], where $B$ is the dipole magnetic field in tesla and $R_r$ is the radius of curvature in kilometers. Note that not all magnets are dipoles and thus only a fraction of the ring is used for bending. With a nominal magnetic field of 8.33 T in the main bending dipoles, the LHC has a beam energy of 7.0 TeV, resulting in a center of mass collision energy of 14 TeV. This energy is important because it determines which particles are able to form and thus which

particles can be discovered and explored. Therefore physicists and engineers are already considering the next generation machine, named the Future Circular Collider (FCC), aiming at a proton-proton collision energy of 100 TeV [11, 12, 13] somewhere between 2040-2050.

In order to reach higher collision energies in a particle accelerator there are two parameters of interest

1. *Circumference* - The diameter increases the bending radius and thus higher collision energies can be achieved with the same magnetic field. In order to reach 100 TeV with the existing 8.33 T LHC dipoles, the ring would be about 200 km long.

2. *Dipole Magnetic Field* - By increasing the bending power higher collision energies can be achieved using the same circumference. The magnetic field required to reach 100 TeV in the existing tunnel is about 60 T, far out of reach for present-day accelerator magnet technology.

For FCC studies both parameters are altered for a machine circumference of 80 to 100 km [14] and main bending dipoles with magnetic fields of 16 T or 20 T. The first lies within the limit of what can ultimately be achieved with triniobium-tin superconductor and the second requires the use of expensive and challenging High Temperature Superconductor (as explained in Section 1.2). For the two to three times higher magnetic field, the radial extent or thickness of the layers of coil-windings around the aperture has to be increased as well. This implies that the classical Cosine Theta coil layout, used for the LHC, eventually may no longer be an optimal configuration. Therefore other coil layout options such as Block, Canted Cosine Theta, Common Coil and other more exotic types, need to be reconsidered.

## 1.2 Superconductors in Magnets

Superconductivity was discovered in 1911 [15] and is a phenomenon that causes the electrical resistance in certain materials to reduce to zero, below a certain critical temperature $T_c$. This allows for a high density of resistanceless current to flow inside the coil-windings, making it feasible to reach much higher magnetic fields than possible with a conventional copper magnet with iron yoke, because the latter is limited to about 2.0 T. Superconductors can be divided into two groups: type-I and type-II. The first typically contains elements, such as mercury, lead and aluminum. The second group comprises alloys and compounds such as Nb-Ti, $Nb_3Sn$ and ReBCO.

The two groups distinguish themselves in their behavior in magnetic field. When a magnetic field is applied to a type-I superconductor below the critical temperature it generates a current on its surface to fully shield the magnetic field. This phenomenon is called the Meissner-Ochsenveld effect [16, 17]. When the magnetic field is increased further, beyond the critical field $B_c$ the currents are no longer able to shield the magnetic field causing the material to lose superconductivity. In a type-II superconductor, however, beyond the first critical field $B_{c1}$ (much lower than $B_c$ in type-I) the magnetic

field is allowed to penetrate the material through so-called vortices, each containing a single flux quantum $\Phi_0$. The vortices comprise of circulating electrical shielding currents, which allow the normal state at their centers to exist (see Figure 1.4). This phenomenon is called the Abrikosov effect. The resulting mixed state, with normal conductivity inside the vortices surrounded by material in the superconducting state, is stable and thus allows superconductivity to be maintained up to very high upper critical magnetic fields, making type-II superconductors crucial for practical applications.

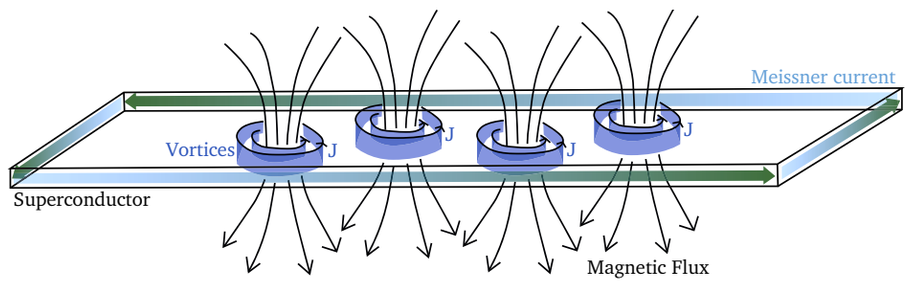


**Figure 1.4.** *Illustration showing a strip of superconductor in the Abrikosov state. The magnetic field is able to penetrate the material through so-called vortices.*

It is energetically favorable for the vortices in a type-II superconductor to be located on micro-structural defects in the material, an effect called flux pinning. Optimizing pinning in practical superconductors is the main challenge for conductor research. Defects are sometimes artificially introduced to maximize the number of pinning centers, for example, the addition of $\alpha$Ti particles in the Nb-Ti superconductor (introduced below). The force required to detach a vortex from its pinning center, is the so-called pinning force. When a transport current is present in the material it applies a Lorentz force to the vortices. When the force exceeds the pinning force, the vortices start to move resulting in dissipation, causing the material to become effectively resistive. This places an upper limit on the superconducting current density, called the critical current density $J_c$.

The critical current density is interdependent with both magnetic field and temperature. Superconductivity can therefore only occur below the so-called critical surface, which is unique to each material. The critical surfaces of the three most relevant superconductors for application in this thesis work are shown in Figure 1.5. The maximum temperature and magnetic field at which superconductivity can still occur are called the critical temperature $T_c$ and the upper critical field $B_{c2}$, respectively. The type-II superconductors are subdivided further into LTS and HTS, based on whether or not their critical temperature exceeds the boiling point of liquid nitrogen temperature. In magnet applications superconductors are always paired with a good resistive conductor that can temporarily take over the current under fault conditions. Due to their low free charge density, superconductors are very poor normal conductors, this is a consequence of the electrons being in a low energy state to accommodate superconductivity.

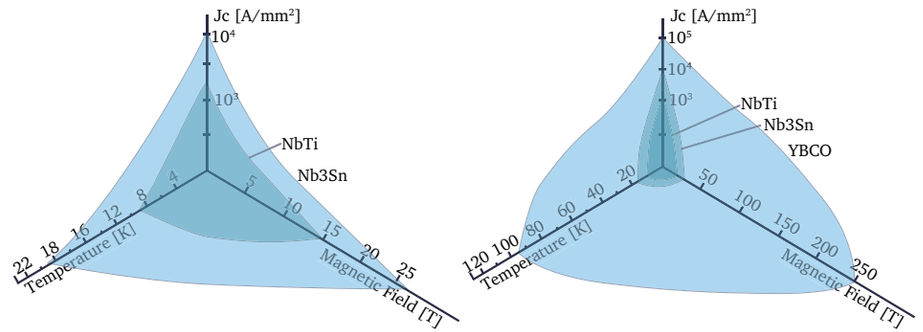


**Figure 1.5.** *Comparison of the critical surfaces of Nb-Ti and $Nb_3Sn$, both LTS conductors, and ReBCO an HTS conductor.*

The most common LTS conductor is the alloy Niobium-Titanium (Nb-Ti), which is the only ductile type-II superconductor that is available in long lengths of wire. Therefore, it is used for practically all applications, such as laboratory magnets for research, MRI scanners, magnetic levitation trains and particle accelerators. The critical temperature of Nb-Ti is 9.2 K and the upper critical field is 14.2 T at absolute zero temperature. To cool Nb-Ti magnets commonly liquid helium is used at a temperature of 4.5 K, which is its boiling point at 1.26 bar. In the LHC the magnets are wound with a Nb-Ti so-called Rutherford cable. To enhance the critical current further the magnets in the LHC are operated at 1.9 K at which point helium is in the superfluid [18] state, making it a very effective coolant and thermal stabilizer.

The nominal magnetic field in the main dipoles of LHC is 8.33 T, at which point the beam energy is 7 TeV [9]. This magnetic field is reached, at 1.9 K, with a margin of 14% to the short sample limit of 9.65 T. This margin is necessary to ensure sufficient thermal stability of the coil and to avoid excessive so-called training behavior, during which the coil needs to be quenched (see Section 1.8) a number of times before it reaches nominal field.

At the short sample limit the operating current equals the critical current, at some point in the coil, thereby determining the absolute but not practical limit. The short sample limit can be calculated from the intersection of the so-called load-line with the critical surface, defined at the operating temperature, as is demonstrated in Figure 1.6. The load-line represents the peak magnetic field on the conductor for a certain operating current. The slope of the load-line depends on the position of the conductors in the coil-windings as well as contribution to the field of magnetic iron used around the coil.

In order to achieve higher magnetic fields, it is possible to add more conductor to the coil, thereby decreasing the slope of the load-line. However, for Nb-Ti the critical surface limits the magnetic field in a practical accelerator coil to about 9 T. To exceed these magnetic fields the next generation superconductor triniobium-tin ($Nb_3Sn$), discovered in 1954, is used. This conductor has an upper critical magnetic field of about

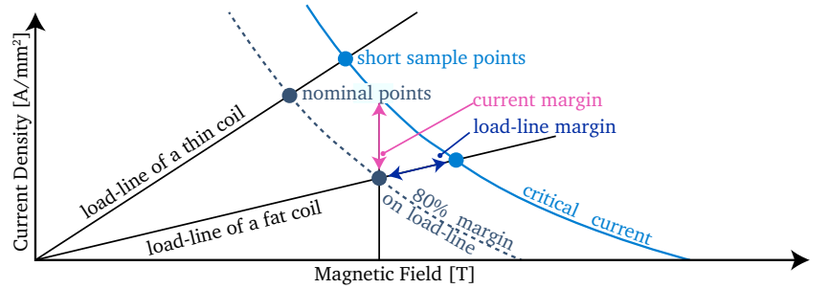


**Figure 1.6.** *Illustration showing the determination of the nominal,* 80% *load-line margin, and short sample operating points through the intersection of the load-line with the critical surface.*

30 T at absolute zero temperature and a critical temperature of 18.3 K. Because the $Nb_3Sn$ compound is brittle, it is necessary to wind the magnet first, after which the tin and the niobium, stored separately in the wire, are reacted in a furnace at temperatures between 625 and 675 °C, a technique called wind-and-react. After the heat treatment the coil-windings are usually impregnated using an epoxy resin to protect the brittle wires. Using $Nb_3Sn$ technology magnetic fields have been demonstrated in short dipole coils (with aperture) up to 15 T [19]. At present in the context of the FCC the possibility is researched of using main bending dipoles constructed with $Nb_3Sn$ that have a magnetic field of 16 T [20, 21], thereby pushing the technology beyond its present limit. In the proposed 100 km tunnel this would allow the center of mass collision energy to reach the target of 100 TeV. Alternatively later on in the project the present 16 T requirement may be adjusted. A 106 km tunnel, for example, would allow use of 15 T magnets, without compromising the collision energy.

## High Temperature Superconductors 1.3

To venture beyond the limit of $Nb_3Sn$ it is necessary to use High Temperature Superconductor (HTS) a relatively new material that exhibits properties that are very different from classical Low Temperature Superconductors (LTS). Because the upper critical magnetic field in HTS is an order of magnitude higher than for LTS, these new conductors can potentially be used in superconducting magnets to boost the magnetic field well beyond 20 T, far above the limits of LTS. Therefore, in view of possible future accelerator projects including FCC, the possibility of using HTS to achieve such very high magnetic fields in accelerator type dipole magnets is explored. As a first target, in order to align with the FCC study, a magnetic field of 20 T is considered. At present there are two HTS conductors available that are sufficiently mature for application in demonstration magnets [22]:

1. *Bismuth Strontium Calcium Copper Oxide* - The compound $Bi_2Sr_2Ca_{n-1}Cu_nO_{2n+4+x}$ (BSCCO) was discovered in 1988 [23]. The variant that is of interest is with $n = 2$ (BSCCO 2212), which has a critical temperature of 95 K and upper critical field

of $200 \pm 25$ T [24, 25]. At present, BSCCO 2212 is available as round wire using a powder-in-tube approach, which makes it possible to use classical Rutherford type cables, nowadays standard in accelerator magnets, allowing the use of many existing coil-winding and manufacturing techniques. However the use of BSCCO 2212 requires a complex and very challenging heat treatment at various stages and at high temperatures up to 900 °C and pressures between 20 and 100 bar in a partial $O_2$ atmosphere, in order to achieve a consistently high critical current density [26]. In addition, the matrix that holds the filaments is made from Silver to allow $O_2$ to penetrate, as it is required to form the optimal composition of the compound. The silver covers about 80% of the wire section, which imposes a lower limit on the conductor cost, in essence the price of silver.

2. *Rare Earth Barium Copper Oxide* - The compound $YBa_2Cu_3O_{7-x}$ (YBCO), discovered in 1987 [27], has a critical temperature of 93 K and an upper critical field of $168 \pm 26$ T [24]. Because the Rare Earth Element (REE) Yttrium (Y) can be interchanged with Gadolinium (Gd) and others, without significant effect on the superconducting properties, this conductor is generally referred to as ReBCO, where Re stands here for a mix of Gd and Y. At present ReBCO is only available in the form of a thin film deposited on a carrier inside a tape (coated conductor). Because the superconducting phase itself is already present in the tape, it does not require any heat treatment. The 1 to 5 $\mu$m superconducting film is flexible enough to allow the tapes to bend in the easy-way direction, making coil-winding possible. In contrast to the BSCCO, the raw material cost is not the dominant factor in the cost of the conductor, allowing it potentially to become less expensive, when the manufacturing cost using thin film deposition technology in large quantities can be drastically reduced. However, the wide tapes require novel approaches when it comes to cabling, coil-winding and magnetic field quality, requiring significant research and development in these areas before application in an accelerator becomes feasible.

Application of ReBCO coated conductors is more widely spread and they are generally considered for power applications. In addition it does not require any heat treatment, is more resistant to mechanical stress and thermal cycling and at present has a higher engineering critical current density than BSCCO. Therefore, in this thesis the focus is on understanding and solving the issues related to the use of ReBCO coated conductor tapes in accelerator type coil-windings for achieving magnetic fields of 20 T.

A ReBCO coated conductor tape comprises multiple layers as illustrated in Figure 1.7. The substrate, usually stainless steel or Hastelloy, which has a high strength and is heat resistant, provides the mechanical stability and is polished to a mirror finish to allow the growth of thin films on its surface. The thicker the substrate the easier it is to handle during the manufacturing process, allowing for a more consistent and higher critical current density. However, it reduces the fraction of superconductor inside the cross-section of the tape, thereby reducing the engineering current density $J_e$, the critical current divided by the total cross-section, which is an important parameter in magnet design. Onto the substrate a series of buffer layers are applied, which prepare the

surface for the deposition of the superonducting ReBCO layer. The buffer and ReBCO layers together are usually on the order of 10 $\mu$m thick, thereby comprising only a small fraction (compared to LTS) of the tape cross-section. Increasing the ReBCO layer thickness or applying multiple layers is a difficult task. The ReBCO layer is protected by a one or two micron thick layer of silver, necessary to prevent the surrounding copper stabilizer from reacting with the superconducting layer.

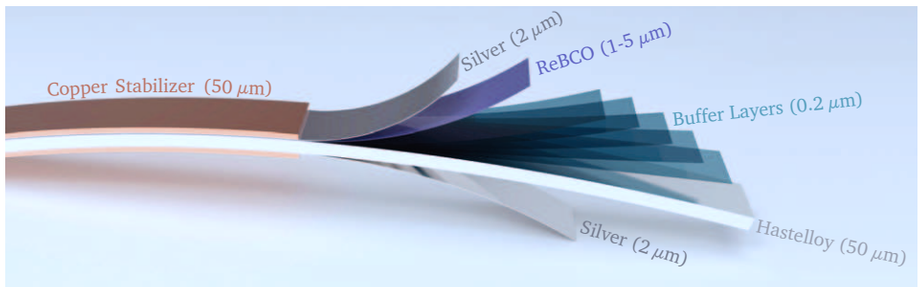


**Figure 1.7.** *Material composition of ReBCO coated conductor. For visual clearness the tape is cut in half along its length such that the inside becomes visible. In reality the copper and the silver layers fully surround the hastelloy substrate carrier.*

The in-field behavior of ReBCO is essentially different from LTS conductor. The superconducting state is primarily present in the $CuO_2$ planes inside the ReBCO layer. When a magnetic field is perpendicular to these planes the Abrikosov mixed state occurs, causing circulating currents on each of these planes. Between the planes the currents are not present, resulting in relatively weak flux line pinning. However when the field is applied in the parallel direction, the size of a vortex is much larger than the thickness of the superconducting layers. Therefore the field can penetrate between the layers, without destroying the superconducting state [2]. This implies that the superconductor is nearly unaffected by magnetic field applied in this direction. Because the crystallographic planes inside a ReBCO coated conductor all have the same orientation, the critical current in applied magnetic field is strongly dependent on the magnetic field angle with respect to the face normal of the planes. This anisotropy is presented in Figure 1.8, which shows the critical current of a Fujikura (one of the ReBCO manufacturers) coated conductor as function of magnetic field $B$, temperature $T$ and magnetic field angle $\alpha$. The scaling of the Fujikura coated conductor was selected as a baseline because sufficient in-field angular data at variable temperature was available to produce the fit and because Fujikura does not use doping, altering the angular dependence. It can be seen that the anisotropy becomes more pronounced in high magnetic fields, at which the difference in critical current, between the good parallel and bad perpendicular magnetic field directions, can be more than a factor five.

The scaling relation used to describe the critical current depends on three variables $J_c(B, T, \alpha)$, where $\alpha$ is the magnetic field angle with respect to the face-normal of the crystallographic planes. The scaling relation used throughout this thesis is described

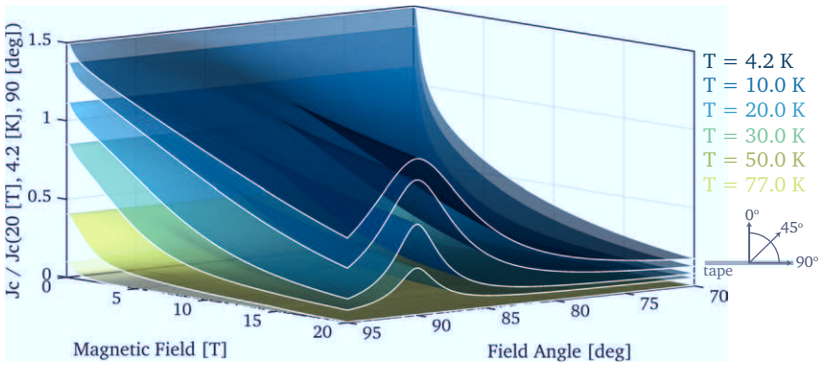


**Figure 1.8.** *Normalized critical current as function of magnetic field, temperature, and field angle of state of the art ReBCO coated conductor source data [28].*

in Appendix A. In order to take into account future performance and the differences between the manufacturers, the critical surface can be scaled. To provide reference, where relevant the engineering current density is provided in a parallel and perpendicular magnetic fields of 20 T at 4.5 K, together with the ReBCO tape thickness.

At present there are seven manufacturers producing ReBCO coated conductor (see Table 1.1) each with their own specific techniques and preferences, based on their customer base. In order to achieve high transport currents the ReBCO layer must be deposited in an epitaxial growth, with a misalignment of only a few degree. To achieve this, the crystallographic alignment of the substrate, which forms a template for the alignment of the ReBCO layer, must be bi-axially controlled. This can be accomplished through three different methods:

1. *Ion Beam Assisted Deposition* - IBAD - The buffer layer is bi-axially aligned using an ion beam during the deposition process. The substrate is often a MgO alloy [29].

2. *Alternating Beam Assisted Deposition* - ABAD - This is a special variant of IBAD, where the beam is alternating. The buffer layer is usually $Y_2O_3$-stabilized $ZrO_2$ (YSZ) [29].

3. *Rolling-Assisted Bi-axial Textured Substrates* - RABITS - The buffer layer is bi-axially aligned through rolling and annealing [30]. The substrate is a $Ni$- or $Cu$-based alloy.

The deposition of the ReBCO layer and the buffer layers, in the case of IBAD, can be performed using various methods, such as pulsed laser deposition (PLD), reactive combination of elements (RCE), inclined substrate deposition (ISD), and metal-organic chemical vapor deposition (MOD). The crystals can be grown in plane with the tape in-situ or out of plane ex-situ. Also for applying the copper stabilizer to the tape there are different techniques, such as electroplating or laminating. With all these variations

the characteristics of the conductor vary significantly from manufacturer to manufacturer. Note that all manufacturers, except for Bruker, have optimized their material for best transport properties and lowest cost for use in energy applications at around 77 K. Optimization of the transport properties for use at 4.5 K and high magnetic field has only just started. Moreover a good performance at liquid nitrogen temperature and self field, does not necessarily scale into a good in field performance at lower temperatures [31]. This means that the conductor can be optimized towards a specific application.

TABLE 1.1.
COMPARISON OF THE METHODS PRESENTLY USED BY DIFFERENT REBCO MANUFACTURERS.

| Manufacturer | Technology | Deposition | Process | Substrate | Stabilizer* |
|---|---|---|---|---|---|
| AMSC | Rabits/MOD | chemical | ex-situ | NiW 75 $\mu$m | lam. 50 $\mu$m per side |
| Bruker HTS | IBAD/PLD | physical | in-situ | Stainless 100 $\mu$m | e.p. 25 $\mu$m per side |
| Fujikura | IBAD/PLD | physical | in-situ | Hastelloy 75 $\mu$m | lam. 75 $\mu$m on one side |
| SuNAM | IBAD/RCE | physical | ex-situ | Hastelloy 60 $\mu$m | e.p. 20 $\mu$m per side |
| SuperOx | IBAD/PLD | physical | in-situ | Hastelloy 60 $\mu$m | e.p. 10 $\mu$m per side |
| SuperPower | IBAD/MOCVD | chemical | in-situ | Hastelloy 50 $\mu$m | e.p. 20 $\mu$m per side |
| Theva | ISD/RCE | physical | ex-situ | Hastelloy 50 $\mu$m | e.p. 20 $\mu$m per side |

*e.p. = electroplated, lam. = laminated

To demonstrate the variety of conductors a comparative overview, showing a selection of material properties, is provided in Figure 1.9. The critical current is given at 77 K in self field and at 4.5 K in a perpendicular applied magnetic field of 19 T. The critical current reflects the quality of the ReBCO layer. It can be seen that the critical current of Bruker is lowest of all manufacturers in 77 K in self field, but highest at 4.5 K in 19 T perpendicular applied magnetic field. This is likely because the Bruker tape is optimized for in-field operation and therefore contains artificial pinning. The most important parameter for magnet design is the in-field engineering current density $J_{e,4.5\,\mathrm{K},19\,\mathrm{T},\perp}$. Commonly the copper stabilizer thickness is included in comparisons. The copper thickness, however, is a choice that depends on the application and therefore obscures the true performance, which is better presented by the non-cu current density $J_{\text{non-cu},4.5\,\mathrm{K},19\,\mathrm{T},\perp}$. The two best conductors, at present, are SuperPower and Bruker. Note that for the Aligned Block, the layout type used for Feather magnets, the performance at 4.5 K in parallel applied magnetic field is perhaps more important. Unfortunately this type of data was not available for all manufacturers. It is expected that the inclusion of artificial pinning centers may actually reduce the performance in the parallel case. The RRR represents the purity of the copper, which should be as high as possible. The mechanical stress $\sigma_{\text{irr}}$ and strain $\epsilon_{\text{irr}}$ limits of the tape are about the same for the different manufacturers. This because the mechanical properties of the tapes are mostly determined by the substrate.

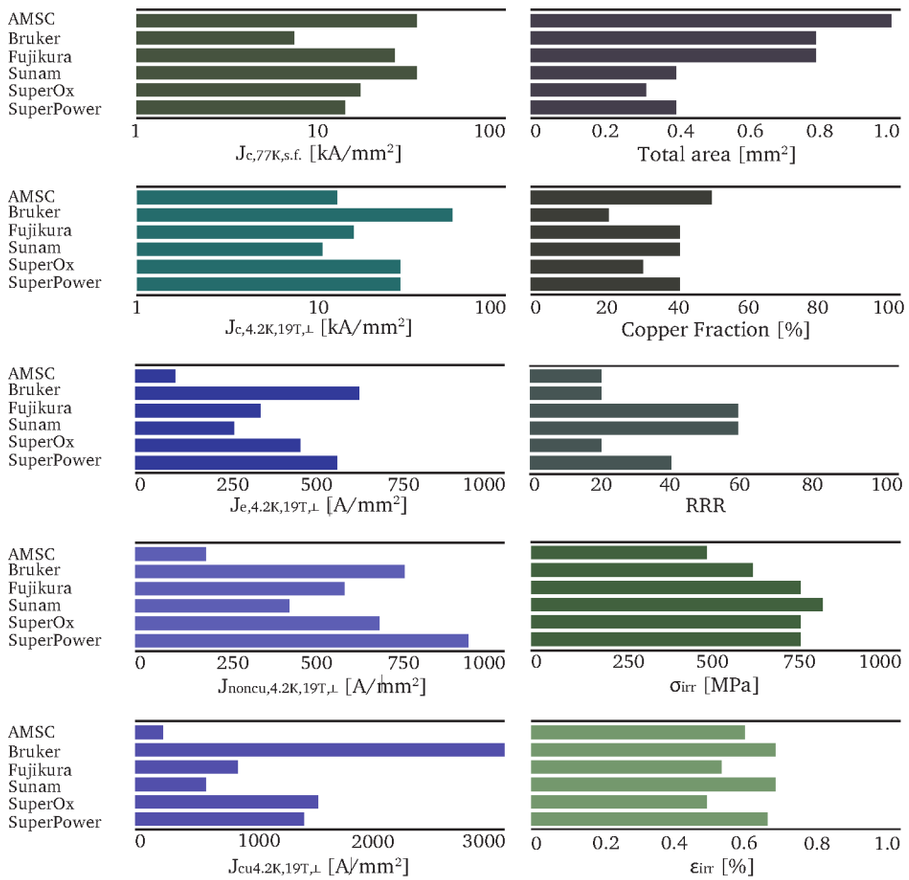


**Figure 1.9.** *Comparison of of* 12 mm *wide ReBCO coated conductors from different manufacturers (data from the University of Geneva [31]). Shown are the critical current at* 77 K *in self field; the critical current density, the engineering current density, the non-copper current density and the copper current density, all given at* 4.2 K *in* 19 T *perpendicular applied magnetic field; the total area of the tapes; the fraction of copper in the tapes; the RRR of the copper and the maximum allowable stress and strain. Note that the conductors are constantly under development and that the shown parameters are prone to change.*

## 1.4 Coated Conductor Cables

One of the requirements for the conductor in an accelerator magnet is that the operating current is in the range of 10 kA, usually corresponding to a cable. This in order to keep the magnet inductance low such that it can be ramped to operating field in about 20 min and to allow for fast ramp-down when the magnet quenches (see Section 1.8). Unfortunately tape conductor is not suitable for a standard Rutherford cable and a dif-

ferent cable technology has to be developed. Three possible cable candidates, Roebel, CORC and Twisted Stack, are compared in Table 1.2.

The CORC cable [32, 33, 34, 35, 36] consists of a copper core, which also acts as stabilizer, on which the tapes are wound in layers (each consisting of three tapes). However the core reduces the filling fraction of the cable with tapes significantly. This results in a lower engineering current density than other cable options, at present around $150\,A/mm^2$ in a 20 T applied magnetic field. This makes it impossible to reach the required stand-alone magnetic field of 5 T (as introduced in Section 1.5), within the given constraints. In addition the tapes in the cable are not aligned, making it infeasible to test it in the Aligned Block coil layout. This shortcoming is likely to become less apparent in the future when Zirconium (Zr) doping reduces the angular dependence of the tapes [37]. The tapes in the cable are transposed per layer, but not between the layers. At present it is not clear what the effect of this is on the current distribution and requires study. The minimum bend radius of the CORC is relatively high making it necessary to perform either a dog bone [38] or freeway overpass/underpass coil-end (see Section 2.3.4) [39, 40]. Another possibility is to use a Canted Cosine Theta coil layout [41], with suitable radius. CORC wires featuring much higher engineering current density and diameters down to 2.5 to 3.0 mm are under development [42]. The use of such CORC wires can then be reconsidered.

TABLE 1.2.
COMPARISON OF RELEVANT PROPERTIES OF THREE DIFFERENT REBCO CABLE GEOMETRIES, THAT ARE ILLUSTRATED IN FIGURE 1.10.

| Name<br>references | CORC<br>[32, 33, 34, 35, 36] | Stacked<br>[43, 44] | Roebel<br>[45, 46] |
|---|---|---|---|
| filling factor | 30 – 40%† | 80% | 70% |
| tape transposition | partially | no | fully |
| tape twist | yes | yes with twist | no |
| tapes aligned | no | yes without twist | yes |
| number of tapes range | 50 – 100 | 10 – 50 | 9 – 50* |
| twist pitch range | 30-60 mm | n.a. (coil end) | 50 – 300 mm |
| soft bending radius | 30-60 mm† | 11 mm | 11 mm |
| hard bending radius | 30-60 mm† | > 2 m | 2 m |

* number of tapes limited by twist pitch.
† depends on cable diameter and thus number of tapes.

The Twisted Stack [43, 44] cable has a high packing fraction, which exceeds that of the Roebel cable. The tapes in the cable are not punched, resulting in less loss of material and thus a more cost-efficient conductor than Roebel. The cable can be twisted to provide transposition, however it thereby sacrifices the tape alignment, required for the Aligned Block. The effect of not having the transposition in a coil has to be studied. The tape stack can easily bend in the soft-way direction, but is very difficult to bend in the hard-way direction. This implies that it is not possible to use flared coil-ends. A

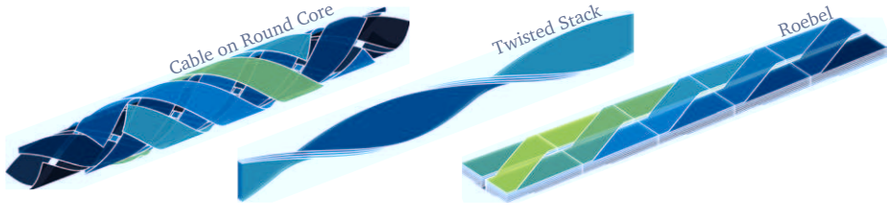


**Figure 1.10.** *Three different geometries for assembling a cable with ReBCO coated conductor. Also refer to Table 1.2.*

solution can again be found in the freeway overpass/underpass coil-end, which consists only of soft-way bending. It is also possible to use a twist in the coil-end to introduce transposition and to allow for easy way bending. This type of design is pursued by the University of Grenoble [47].

Presently the most suitable candidate conductor for use in ReBCO accelerator magnets is the Roebel cable, a geometry originally invented to reduce AC loss in copper power bus-bars in 1913 [48]. Much later in 2005 the concept was found to be applicable for coated conductors as well [49]. A photograph of a Roebel cable is presented in Figure 1.11. In the Roebel cable meandering flat tapes are folded together as illustrated in detail in Figure 1.12. This process can be performed by hand or using an automated cabling machine [50]. The Roebel cable is currently under development at General Cable (GC) in New Zealand [51] and Karlsrühe Institute of Technology (KIT) in Germany [45]. Roebel cables from both KIT and GC were measured up to very high currents well exceeding 10 kA in magnetic fields of 10 T at 4.5 K at CERN [46], proving its potential. Because the tapes in the cable have the same orientation, it is possible to achieve almost perfect alignment with the magnetic field, as is required for the Aligned Block layout. In addition it has a sufficiently small soft-way bending radius to fit inside the 99 mm diameter, making it possible to make the coil-end inside the Fresca2 aperture. Therefore, for the moment, it is the only cable that meets the requirements and was thus selected for the Feather-M2 demonstrator. It is, however, the first time that such an HTS cable is used in a low temperature and high magnetic field accelerator dipole.

## 1.5 Optimized Coil-Windings

The anisotropy in the critical current density of ReBCO coated conductor tapes is a disadvantage. However, when the tapes are used in a parallel magnetic field, the crystallographic planes are also oriented parallel with the field, resulting in optimum use of a very high in-field engineering current density of a few thousand amperes per square millimeter at 20 T and 4.5 K. This sparked the idea of a magnet windings layout in which the coated conductor tapes, or cables made with these tapes, are aligned with the magnetic field everywhere. For a ReBCO magnet in stand-alone mode this is a

**Figure 1.11.** *Photograph of a coiled Roebel cable (by Henry Barnard at CERN). This demonstrator cable was manufactured, using stainless steel tapes, at Karlsruhe Institute of Technology (KIT).*

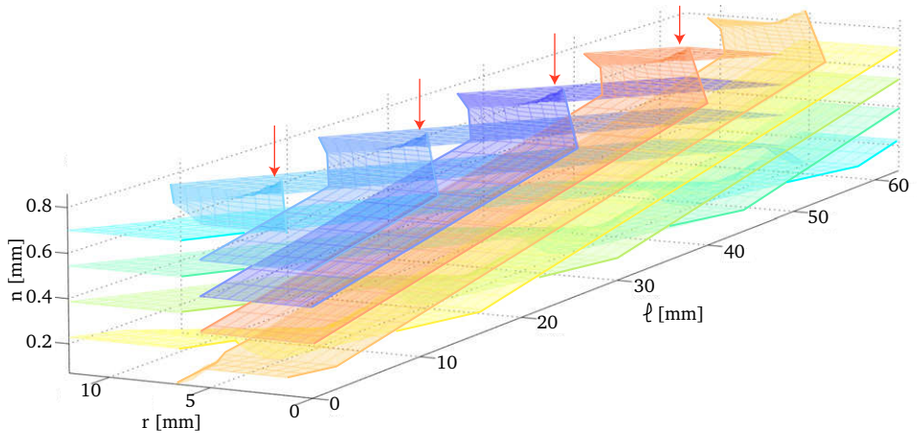


**Figure 1.12.** *Tape trajectories in a Roebel cable with the original KIT layout using 9 strands (only superconducting tapes are shown). Tapes are represented by flat surfaces. Each color represents one of the tapes. At the crossovers, denoted with the red arrows, the tape reorients itself. Note that the vertical axis is not plotted to scale. Slightly more than half a twist pitch (five unit cells) is shown.*

difficult task, because the magnetic field inside the coil-windings varies strongly. This makes the three-dimensional design of the coil-end, within the mechanical constraints of the tapes nearly impossible.

Because the cost ratio between Nb-Ti, $Nb_3Sn$ and ReBCO is approximately 1-10-100 per volume, respectively, a common strategy is to use a graded hybrid coil layout [52, 53]. In such a layout the ReBCO is only used in the high magnetic field region, located at the center of the coil, where Nb-Ti is not superconducting and $Nb_3Sn$ has a too low critical

current density. The $Nb_3Sn$ and optionally Nb-Ti are then used in the intermediate and low field regions respectively, located in the outer sections of the system of coils. Because in the case of a 20 T magnet the Lorentz forces generated by the inner part of the coil, pushing outward, accumulate to pressures exceeding 200 MPa in the outer layers, which are too high for the $Nb_3Sn$ to sustain [54], it is necessary to mechanically separate the inner HTS part of the coil from the LTS outer part, called the insert and outsert, respectively.

In a hybrid magnet where the LTS outsert coil supplies a significant portion of the magnetic field, the field lines in the insert region are more-or-less parallel, making alignment of the coated conductors much easier. This has led to the novel so-called Aligned Block layout applicable to ReBCO insert-magnets. As an example a layout of a hybrid so-called insert-outsert magnet, designed for a 20 T nominal magnetic field, with an Aligned Block insert is presented in Figure 1.13. In the enlargement of the insert, bottom left, it can be seen that the ReBCO conductor blocks are rhombus like shaped to accommodate magnetic field alignment of the cables inside.

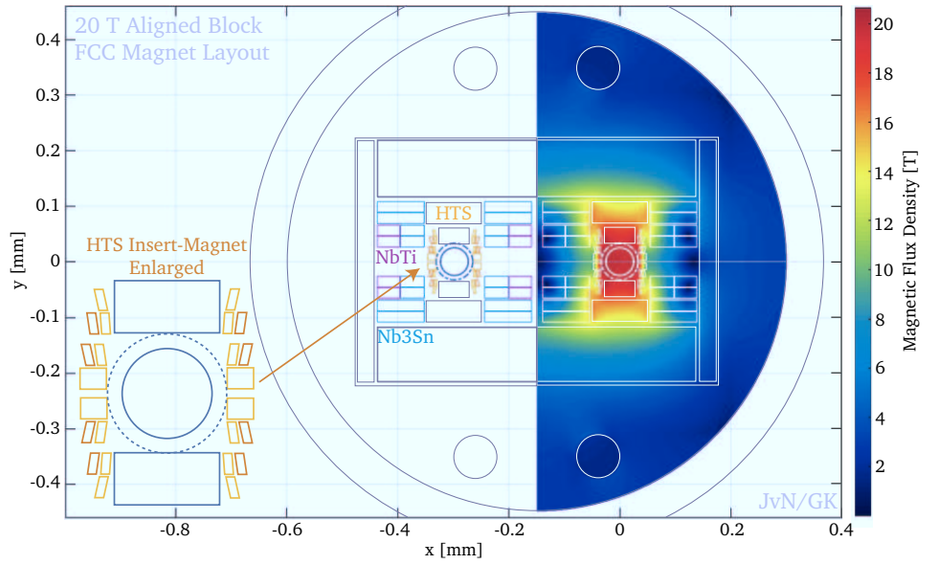


**Figure 1.13.** *Conductor cost Optimized hybrid layout for a* 20 T *Aligned Block insert, Block outsert magnet. On the left side the color represents the different types of conductor present. On the right side the color represents the magnetic field magnitude.*

The feasibility of the Aligned Block insert-magnet, is critical for the design of hybrid magnets that are capable of reaching magnetic fields in accelerator magnets beyond 16 T. So far little experience is available with HTS, especially when operating at low temperatures and high magnetic field. Therefore a case study for an Aligned Block demonstration magnet was performed. In parallel the EuCARD2 project started [55],

a successor to EuCARD1 [56, 57]. One of its work-packages is the design and construction of a 5 T stand-alone HTS accelerator dipole magnet. In order to properly align efforts with EuCARD2 the same technical requirements are used for the design studies, with the additional constraint that it can be used as an insert for the Fresca2 magnet [58, 59], designed to produce a magnetic field of 13 T in a 100 mm aperture. The requirements for the demonstration magnet to be developed are given as:

1. *Stand-Alone Magnetic Field* - The stand-alone nominal magnetic field of the insert is 5 T, when operating at 70% on the load-line. It is possible to use an iron yoke to increase the magnetic field.

2. *Accelerator Quality* - The stand-alone geometric magnetic field quality at 2/3 of the aperture radius is less than 20 units (explained in Section 1.7).

3. *Aperture Size* - The aperture diameter in stand-alone must be 40 mm and is accessible in order to perform field quality measurements using a rotating probe.

4. *Conductor* - A 10 kA class cable is used to wind the coil in order to accommodate future ramp-rates and quench protection (explained in Section 1.8).

5. *Outer Diameter* - The outer diameter of the magnet structure is less than 99 mm in order for it to fit inside Fresca2.

6. *Lorentz Forces Contained* - The mechanical structure must be able to contain the Lorentz forces in stand-alone mode and as insert in the Fresca2 background field. The magnet is not allowed to rely on Fresca2 for mechanical support.

The layout optimization studies, design, zero and one dimensional quench analysis, construction and testing of the demonstration magnet, now known as Feather-M2, together with a sub-scale model known as Feather-M0, are presented in detail in Chapter 2 of this thesis. In parallel at CEA Saclay in Paris a ReBCO cosine theta insert-magnet is developed [60, 61]. Because the outer diameter restriction prevented them from using two layers of the 12 mm wide Roebel cable, the load-line margin requirement on the stand-alone magnetic field of 5 T was dropped. This magnet will serve as a baseline in order to compare feasibility and results with the Feather-M2 Aligned Block layout.

## Numerical Design Tools for ReBCO Coated Conductors 1.6

Over the last two decades a significant number of numerical tools have been developed for the electro-magnetic and thermal analysis of LTS cables and coils. These tools are valuable for discovering new phenomena and to help understanding measurement data. In addition the tools can provide useful input for the design process of new magnets. An overview of all tools lies outside the scope of this thesis, however, worth mentioning are CUDI [62, 63], developed in 1995 at CERN in collaboration with the University of Twente. It uses and electrical and thermal network to approximate a Rutherford cable and was used extensively for analyzing the cables of the LHC. Later in 2011 a new variant was built at the University of Twente for studying Cable-in-Conduit Conductors

for the ITER fusion reactor. This model is named JackPot-AC [64, 65, 66, 67] and proved to be valuable for predicting AC losses and designing joints.

Existing tools used for LTS can relatively easily be modified for BSCCO by replacing the scaling relation, adding some material properties and if not present by adding current sharing. However, for ReBCO due to the large aspect ratio of the conductor, which is a flat tape, this conversion is not so straight forward. Therefore, over the last decade, new tools capable of simulating the electro-magnetic and in some cases thermal behavior in ReBCO coated conductors, have been developed by various groups. Because of the complexity that comes with persistent currents in the flat layer of the tape, which is of relevance for field quality analysis, many of these tools are two-dimensional, in order to keep computation time and memory requirements within acceptable bounds [68, 69, 70, 71]. In some cases only the steady state is computed in order to estimate the critical current [72]. Most of the quench analysis tools on the other hand use three dimensions, but approximate the coil-windings using a single block with anisotropic thermal conductivity. Complementary analysis of the Feather-M0 coil performed at the University of Tampere using such an approach is available from references [73, 74, 75, 76]. In some other cases only a small part of the coil is modeled [77], to study the effectiveness of quench heaters.

Only a few transient three-dimensional tools that include the surface of the ReBCO tape exist. These models are listed and compared in Table 1.3. Interesting is that the published results from these models usually only concern a single tape or a Roebel cable. Often only part of one of the tapes is modeled making heavy use of the available symmetry. In order to understand some of the relevant physics of multi-strand ReBCO coated conductor cables and ultimately coils under these operating conditions better, a new tool was developed as part of this work. The model is described in Chapter 3. In contrast to the other three-dimensional coated conductor models that use a Finite Element Method, in this model the cables are approximated using an Electro-Magnetic and Thermal Network, resulting in a set of equations that are similar to those of CUDI and JackPot-AC. By using a GPU version of the Multi-Level Fast Multipole Method for the mutual inductance calculation, the dense inductance matrix can be circumvented, making it possible to include a much larger geometry in the simulation than in the other models. In addition the electro-magnetic equations are fully coupled to the heat equation, which allows the model to simultaneously simulate both magnetization (see Chapter 4) and normal zone propagation and stability (see Chapter 5). Nevertheless, even for this numerical tool the limited scale is still an issue, making it not yet possible to model the full Feather-M2 coil without significant simplification of the network.

## 1.7 Magnetization and Field Quality

One of the concerns to be addressed for ReBCO based accelerator magnets is the magnetic field quality, which is a very important design parameter, since it affects the stability of the beam. The field in the aperture is represented as a series expansion in which different cylindrical solutions to the Laplace equation [87], i.e. dipole, quadrupole,

TABLE 1.3.
COMPARISON OF THREE DIMENSIONAL NUMERICAL MODELS FROM VARIOUS INSTITUTES DEVELOPED TO STUDY REBCO COATED CONDUCTOR.

| type | 1 | 2 | 3 | 4 |
|---|---|---|---|---|
| Institute | CERN | Kyoto University | KIT | University of Bath |
| Main author | J. van Nugteren | M. Nii | V.M.R. Zermeño | H. Zhang |
| Year published | 2015 | 2012 | 2013 | 2016 |
| References | this work and [78] | [79] | [80, 81] | [82] |
| Physics* | EM&T | EM | EM | EM |
| Method | Network Model | FEM T-form | FEM H-form | FEM T-form |
| Time | Transient | Transient | Transient | Transient |
| Geometry | 3D thin strip | 3D thin strip | 3D thin strip | 3D thin strip |
| Scale | Cable-Coil | Tape | Tape | Cable |
| Inductance | MLFMM [83, 84] | Dense | Dense | Dense |
| S.c. approx. | Sharing Model | Power Law | Power Law | Power Law |
| Symmetry | n.a. | Unit Cell | Unit Cell | n.a. |
| Software | MATLAB [85] | Homemade | COMSOL | COMSOL |
| Solver | Sundials-IDA [86] | Newton–Raphson | unknown | unknown |
| Hardware | Workstation | Workstation | Workstation | Workstation |
| Device | CPU-GPU | CPU | CPU | CPU |
| purpose† | QA-ACL-FQ | ACL-FQ | ACL | ACL |
| Striation | up to 5 lanes | No | No | No |

*: EM = Electro-Magnetic, T = Thermal
†: QA = Quench Analysis, ACL = AC Loss, FQ = Field Quality (in coils)

sextupole etc., also referred to as coil harmonics [6], are superimposed. A schematic drawing showing the different pseudo-harmonics is presented in Figure 1.14 and a mathematical description is provided in Appendix B.

A superconducting magnet is usually designed to generate a specific harmonic. All the other components, normalized with the main field, are therefore defined as the magnetic field error. In an accelerator, it is required by beam dynamics that the normalized field error, integrated over the length of the magnet, is less than a few times $10^{-4}$ (a few units) of the main field, within the area of 2/3 of the aperture radius. To ensure high field quality, the position and direction of the current inside the magnet's windings needs to be controlled precisely. This leads to tight construction tolerances and pre-stress to suppress the geometric field errors and small filament size to suppress field errors related to persistent currents. In addition the inter-strand resistance needs to be kept in a restricted range. The shape of the iron yoke must be optimized such that during a ramp of the current the non-linearity of its magnetization does not generate field errors.

However for a ReBCO coated conductor tape, some of these strategies are no longer applicable. Basically a coated conductor tape behaves as a thin and very wide but anisotrope mono-filament, resulting in large induced magnetization currents when a field is applied in the perpendicular direction, as is demonstrated in Figure 1.15. In-

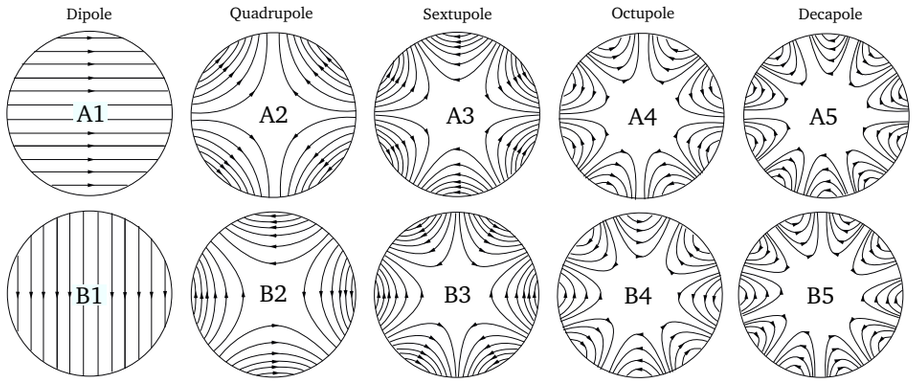


**Figure 1.14.** *Illustration showing the magnetic field lines for the first five cylindrical harmonics, which are commonly used to describe the magnetic field in the aperture of an accelerator magnet (adapted from [88]). The skew harmonics $A_n$ are often omitted because they are usually zero by symmetry. A mathematical description of the harmonics is available in Appendix B.*

side the tapes magnetization currents circulate to screen the applied magnetic flux lines. Note that these macroscopic magnetization currents are essentially the same as the microscopic currents around the flux lines. Attempts have been made to artificially scribe filaments into the ReBCO films using laser cutting [89, 90], a process also referred to as striating. In some of the possible cable structures, such as Roebel or Stacked, this does not lead to transposed filaments, thereby not fully resolving the issue. Also it can degrade the critical current density of the tapes significantly, especially when small defects are present in the tape before cutting.

In a magnet the effective area of the filaments can be suppressed by aligning the tapes with the magnetic field [78]. Although this suppresses the magnetization currents significantly, it does not control the position of the transport current. Unavoidable defects, variations in the critical current and cracks in the conductor change the path of the current making an exact prediction nearly impossible. In Chapter 4 it is explained how the electro-magnetic part of the Network Model is used to study the effect of the magnetization on the magnetic field quality. In addition a conceptual method to control magnetic field errors by inserting a set of so-called persistent mode compensation coils inside the aperture is introduced.

## 1.8 Stability and Quench

The detection of and protection against a thermal runaway, also referred to as quench, in HTS is still a not fully mastered problem. A thermal runaway can occur when the superconductor heats up locally over the current sharing temperature $T_{cs}$, in essence the temperature above which the superconductor can no longer carry the full current, at which point the excess current flows in the matrix, resulting in an effective low

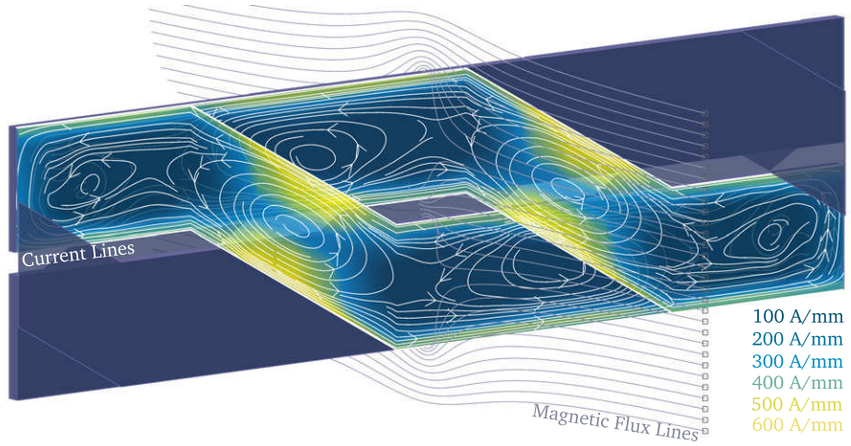


**Figure 1.15.** *Calculated surface current distribution in* A/mm *in a Roebel cable after applying a background field of* 0.6 T *in the x-direction with zero transport current. The current in only two tapes is shown using white lines. In addition a few flux lines are shown to demonstrate the shielding of the magnetic field.*

resistance zone. If the temperature increases further exceeding the critical temperature $T_c$, the superconductor can no longer sustain a superconducting current, causing all the current to flow in the matrix. In this work a normal zone is defined as a resistive zone and thus includes the temperature range between $T_{cs}$ and $T_c$. If the length of the normal zone in the tape or cable is sufficiently large, the Ohmic heating exceeds the cooling towards the ends, causing the normal zone to grow and propagate until the conductor is destroyed. If the heating is less than the cooling, the conductor recovers. In order to prevent the destruction of the tape, it is necessary to detect a thermal run-away on time, such that the electrical current can be extracted.

The amount of energy required to induce a propagating normal zone, is called the Minimum Quench Energy (MQE), which is a measure of conductor stability in a coil. To improve the thermal stability of the conductor, a fraction of the conductor's cross-section is made of copper or silver stabilizer. In LTS this is the matrix surrounding the superconducting filaments. In coated conductor this is the silver and copper cladding which is electroplated or laminated on one or both sides of the tape. Above the current sharing temperature the copper is a much better conductor than the superconductor. Therefore the overall resistivity and thus heating of the conductor is decreased, causing the minimum length for a propagating zone to be larger. In addition, the copper adds extra heat capacity to the conductor, increasing the energy needed to heat up the Minimum Propagation Zone.

In order to avoid the conductor to burn if a quench does occur, the voltage over the conductor is measured. Under normal operating conditions no or very low voltages (during ramping) are present. When the voltage rises this is an indication that a grow-

ing normal zone is present in the conductor, after which the magnet protection is triggered. In the case of small cables or coils, with low self-inductance, it can be sufficient to switch off the power supply. For big accelerator magnets, however, it is necessary to actively extract the magnetic energy by switching a dump resistor into the magnet's circuit. In addition, the entire conductor pack can also be deliberatively heated over the current sharing temperature, using a heater that is integrated into the coil-windings, causing the entire coil to become resistive, thereby spreading out the energy over a large volume. A relatively new approach is to use a Coupling Loss Induced Quench (CLIQ) system [91], which uses coupling losses instead of a heater, to warm up the conductor directly.

Because of the high critical temperature, ReBCO coated conductors can easily be operated with significant temperature margin and because the heat capacity increases rapidly with temperature under cryogenic conditions, the MQE can be up to three orders of magnitude higher than for LTS conductors. Therefore magnets constructed with ReBCO are expected to be very stable. At the same time, the normal zone if present propagates very slowly [92, 93], because it takes much more energy to push the front of the normal zone forward. The calculated one-dimensional temperature profiles along the conductor, under quench conditions, are shown for $Nb_3Sn$ in Figure 1.16 and for ReBCO, with exactly the same copper cross-section, in Figure 1.17. The peak temperature rises approximately at the same rate, but the length of the normal zone for LTS increases much faster. In Figure 1.18 the voltage drop over the normal zone is plotted against the peak temperature of the conductor. It can be seen that at the same detection voltage the peak temperature for HTS is much higher than for LTS. This means that voltage detection in HTS provides a relatively late warning. In a cable multiple superconducting strands are connected in parallel, causing for interesting behavior as shown for LTS in [94]. To study these effects in a multi-strand ReBCO Roebel cable and coil the electro-magnetic and thermal modules of the Network Model are used. The results are presented in Chapter 5.

## 1.9 Outline and Research Questions

The structure of the thesis is summarized in the flow chart shown in Figure 1.19.

In a high field HTS hybrid magnet, an HTS insert-magnet is combined with an LTS outsert-magnet. To study the ReBCO insert-magnet in detail, a case study is performed using the specifications of EuCARD2. A novel layout named Aligned Block was found, in which the anisotropic ReBCO tapes are aligned with the magnetic field, thereby increasing the critical current significantly. The design of the EuCARD2 Aligned Block insert-magnet, named Feather-M2, is described in Chapter 2.

For the application of ReBCO coated conductor in an accelerator magnet there are two main concerns, the effect of the cable magnetization on the field quality and the likelihood of thermal disruption. To study these issues an Electro-Magnetic and Thermal Network Model was implemented. This model is described in detail in Chapter 3.

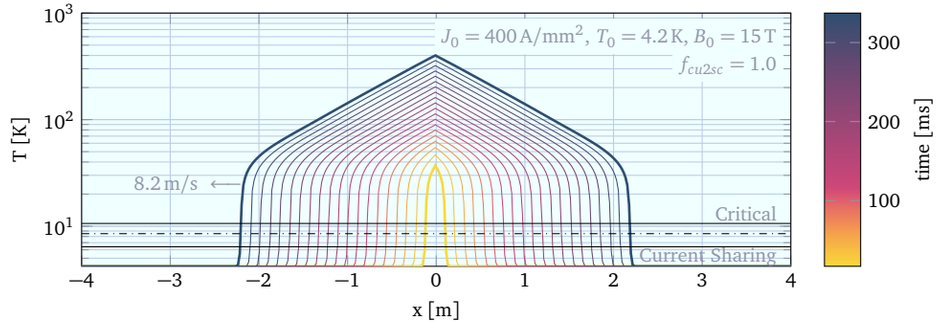


**Figure 1.16.** *Calculated one-dimensional temperature profiles for normal zone propagation in a $Nb_3Sn$ cable. Operational conditions are denoted inside the graph.*

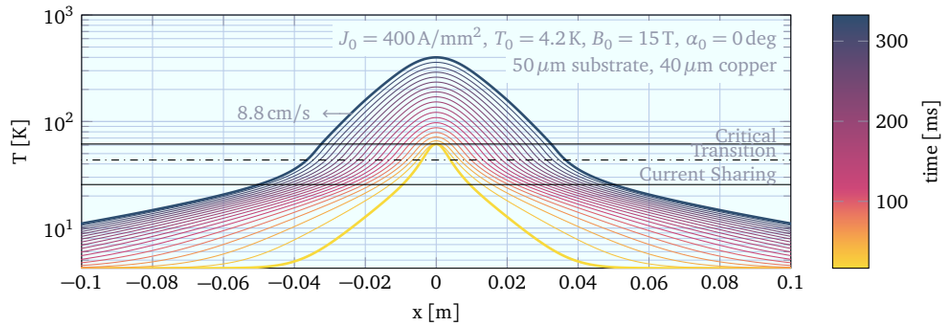


**Figure 1.17.** *Calculated one-dimensional temperature profiles for normal zone propagation in a ReBCO coated conductor. Operational conditions are denoted inside the graph. Note that the horizontal axises are not on the same scale.*

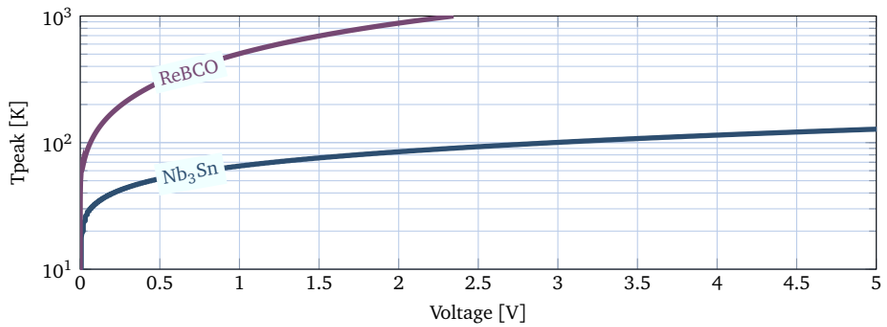


**Figure 1.18.** *Graph comparing the peak temperature versus the voltage between $Nb_3Sn$ and ReBCO coated conductor. The respective temperature profiles are shown in Figures 1.16 and 1.17.*

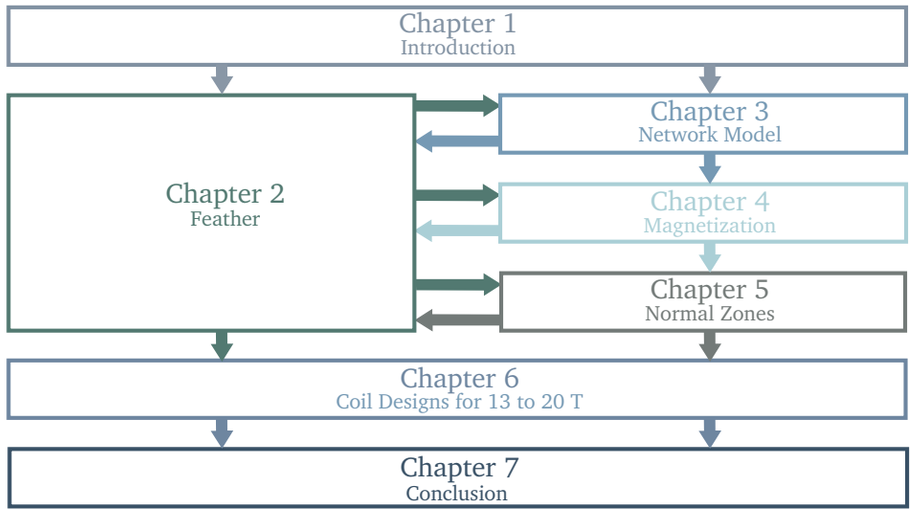


**Figure 1.19.** *Chart showing the interdependence of chapters and the flow of this thesis.*

The effect of the magnetization on the field quality is studied using the electro-magnetic part of the Network Model. Combining high node density, non-linear current-voltage characteristics and accurate mutual inductance calculations with acceptable computation time, this state-of-the-art three-dimensional model is able to make a detailed comparison between magnet geometries such as the CERN Feather-M2 and the CEA Cosine Theta. The results of such comparison are described in Chapter 4, together with a novel superconducting magnet concept, the persistent current shim coil, that can in theory improve the dynamic field quality of an accelerator magnet significantly.

In Chapter 5 is described how the electro-magnetic and thermal parts of the Network Model are combined to study thermal disruptions, first on a cable level but later also on the full coil geometry of Feather-M2.

In Chapter 6 all concepts and analyses come together in a layout study for hybrid high-field accelerator magnets operating in the magnetic field range of 13 to 20 T.

A series of research questions are outlined and will be answered in the concluding Chapter 7. The following questions obviously do not represent all details described in this thesis, but they represent a fair summary of its highlights. The questions are:

1. *Aligned Block* - Is it possible to design and construct an insert-magnet using ReBCO tape conductor, in which all tapes are aligned with the magnetic field throughout the coil?

2. *Roebel cable* - How to optimally use a ReBCO Roebel cable for accelerator coils in terms of coil-winding, insulation and impregnation?

3. *Test* - How to test an HTS magnet, while avoiding the risk of damaging the coils during the first series of ramps, due to overheating and thermal stress during a quench?

4. *Model* - Is it possible to represent a coated conductor tape reliably in terms of magnetization and quench dynamics using a network of superconducting elements and nodes?

5. *Mutual Inductance* - How to simulate a large electrical network while correctly taking into account the mutual coupling between all elements?

6. *Magnetization* - How does magnetization in a ReBCO Roebel cable geometry develop and is it fundamentally different from a collection of individual tapes?

7. *Field Quality* - What is the effect of the wide tape conductor on the dynamic magnetic field quality, is it necessary to compensate and if so, how can this be accomplished?

8. *Normal Zone Propagation* - In view of its high intrinsic thermal stability, is normal zone propagation in a multi-strand ReBCO Roebel cable geometry essentially different from Low Temperature Superconductors?

9. *Quench Detection* - Is it possible to provide early detection of a thermal runaway or its onset in a ReBCO Roebel cable, using other non-standard sensors such as pick-up coils and temperature probes?

10. *Limits of $Nb_3Sn$* - Can one realistically expect a 16 T accelerator magnet to be realized, using present or near future technology, with only Nb-Ti and $Nb_3Sn$ superconductors and what would be a suitable operating temperature for such a magnet?

11. *Hybrid Magnets using HTS* - What shape takes a 20 T hybrid magnet, including its force retaining structure and what is an optimal insert-outsert configuration?

# FIVE TESLA HTS R&D INSERT-MAGNET 2

> "There is a way out of every box, a solution to every puzzle; it's just a matter of finding it."
>
> JEAN-LUC PICARD, STAR TREK: TNG, S07E08, 1993

*This Chapter concerns the design, construction and testing of a Five Tesla High Temperature Superconductor (HTS) Research insert-Magnet for particle accelerator applications named FeaTHeR, constructed with ReBCO coated conductor.*

## Introduction and Chapter Layout 2.1

The magnet is designed to generate a 5 T central operating field, with a reasonable field quality, in a 40 mm aperture in stand-alone mode. To achieve a low-magnetic inductance and to allow in the future series operation with Nb-Ti/$Nb_3Sn$ coils, a 10 kA class cable is requested. By restricting the outer diameter of the magnet to 99 mm, leaving 0.5 mm margin on all sides for adding extra insulation sheets, and by adding additional mechanical structure, it can be tested as an insert of the Fresca2 magnet [58, 59]. In this case no restrictions are present on the field quality or aperture diameter of the insert, allowing for maximization of the magnetic field. The Aligned Block magnet that meets the EuCARD2 [55] requirements is named Feather-M2. As an intermediate development step, a sub-scale single racetrack coil named Feather-M0 is foreseen, which is intended as a test platform for coil-winding and quench protection, thereby avoiding wasting long lengths of expensive conductor. It can be operated in stand-alone mode in an iron yoke or as insert in the Fresca1 facility [95].

The ReBCO coated conductor tape is highly an-isotropic, implying that the critical current strongly depends on the magnetic field angle with respect to the surface of the tape (see Chapter 1). Therefore a novel Aligned Block (AB) layout is used, which is also published in [96, 97, 98, 99]. In this layout the tapes are oriented such that the magnetic field is with some tolerance parallel with the surface of the conductor, when operated as an insert inside a magnetic background field of 13 T, as for example can be supplied by the Fresca2 facility. This increases the coil's critical current in this scenario significantly, when compared to other non-aligned layouts, allowing it to operate at (almost) the same current as in stand-alone mode. Additionally, the alignment helps to reduce the magnetization, which improves the coil's dynamic field quality and reduces AC loss (see Section 4.4).

For this layout Roebel cable is selected, because in this cable the tapes have the same alignment, it is fully transposed and features a high conductor filling fraction. The shape details of the cable and its implications are presented in Section 2.2. The opti-

mization study of the Aligned Block layout for the Feather-M2 magnet is presented in Section 2.3. The position and orientation of the conductor in the coil-windings is optimized using two and three-dimensional analysis. The results are compared to other layout options. Feather-M0 is a single racetrack coil and its conductor is aligned with the background field as well. Another feature new to accelerator magnets is a set of Inductively Coupled Energy Dump (ICED) normal conducting turns or rings that are located around the coil pack. When the dump resistors are switched into the circuit, initiating a fast ramp-down, most of the current and thus energy is inductively transferred to these turns where it is dissipated. Quench analysis of the coil systems either operated in stand-alone mode or as insert, showing the effectiveness of the copper turns, is presented in Section 2.4.

When Feather-M2 is operated as insert, the peak magnetic peak field will be about 20 T and consequently the Lorentz forces are very high. The coil, however, can not rely on the outsert coil for mechanical support. This means that all forces need to be contained within the insert, while respecting stress limits. This, in combination with the limited space available and the organic shape of the Aligned Block layout, makes the design of the mechanical structure a challenging task as well. For this reason the mechanical design and test winding of Feather-M0 were performed as a first step, allowing for implementation of the findings and ideas into the Feather-M2 design. The mechanical designs of both Feather-M0 and Feather-M2 are presented in Section 2.5.

Due to the relatively high joint resistances between ReBCO conductors and the coil terminals, the joints to the current leads are considered to be challenging. To test joints under magnet operating conditions, without the risk of burning a magnet, a separate joint test is performed at cold before, as described in Section 2.6. The stress in the coil is well over 150 MPa, requiring high-quality epoxy impregnation. Since construction on Feather-M2 has just started, the winding and impregnation procedure, as well as preliminary cold testing, is presented for Feather-M0 only in Section 2.7. For Feather-M2 only the winding of the first exercise coils is presented in Section 2.8.

## 2.2 Cable Layout and Implications

*For ReBCO coated conductor tape it is not possible to use Rutherford type of cables, which are standard nowadays in accelerator magnets. In this Section the proposed Roebel type of cable and its implications are studied.*

### 2.2.1 Geometry

The Roebel cable was selected as a baseline for the EuCARD2 magnets following the arguments mentioned in Section 1.4, where an overview of different cable types was presented. It is the only cable at present that is fully transposed (all tapes/strands take all positions in the cable along its length), has a high filling factor and can accommodate the tight soft-way bending radius, which is needed for making ends inside the Fresca2 aperture. Also the tapes in the cable have the same orientation making

almost perfect alignment possible with the magnetic field as required for the Aligned Block layout. Tapes for Roebel cable[3], which can eventually be doubled with copper sheets or even other superconducting tapes to improve stability, are punched into a meandering shape and are folded together to form the cable (see Figure 2.1). Unfortunately this process causes loss of about half the material, thereby increasing the cost (expressed in kilo-Ampere meter) of the cable. In the future it can be expected that the deposition process of ReBCO is performed on a wider substrate such that multiple tapes can be cut from it, thereby reducing the loss of material. The punching also causes the edges of the tape to be no longer protected by the copper outer layer, leaving the superconductor exposed. This problem is resolved by punching the tapes before they are copper coated. Then by (re)applying the silver and copper layers the edges are sealed, which greatly improves the mechanical stability of the tape and prevents de-lamination. This process was developed by KIT in collaboration with SuperOx and is named punch-and-coat [100].

**Figure 2.1.** *Photograph of a Roebel cable by KIT assembled from Bruker ReBCO tapes. The cable shown here was later used in the Feather-M0.4 coil. A glass fiber rope was inserted into the central channel (visible) before winding and impregnation.*

The parameters defining the geometry of the meandering tapes in the cable are shown in Figures 2.2 and 2.3. The cable consists of two tape stacks on either side, the width of which is given by $W_r$. The stacks are separated by a channel, the width of which is given by $W_c$. This channel is necessary to assemble the cable with a machine. The total width of the cable is given by $W_t = 2W_r + W_c$. In the cable tapes cross-over from side-to-side under an angle given by $\Phi$, thereby transposing the cable. The width of the tape on the cross-over is given by $W_x$. A fillet, with radius $r_i$ for the inner corner and radius $r_o$ for the outer corner, is used at the cross-overs to smoothen the shape of the punching tool. For a cable with an even number of tapes the cross-overs are located above one another. For an odd number of tapes the cross-overs alternate from side to side. Obviously the cable pattern is repetitive for every twist pitch, but if the tapes are indistinguishable with respect to their index, a smaller repeated Unit Cell can be defined (see Figure 2.3).

The number of tapes in the cable, assuming single tapes, is limited by the length of the twist pitch $L_{\text{tp}}$, which is about 300 mm. The maximum number of tapes that fit within

[3]The 'tapes' that make up the Roebel cable are the equivalent to the 'strands' making up a Rutherford cable. The definition of a strand however is given as: "a thin thread of something". Therefore 'strand' is in-applicable to coated conductors, resulting in the use of 'tape' throughout this thesis.

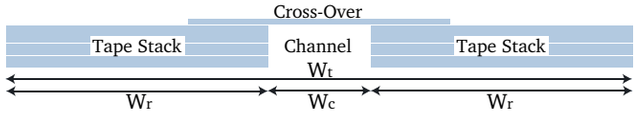


**Figure 2.2.** *Cross-section and definition of parameters of the Roebel cable. The geometry shown is for a cable with an odd number of tapes, resulting in alternating cross-overs along the length of the cable. Therefore in this cross-section the cross-over is only shown on one side. The parameters $W_r$ and $W_c$ are the widths of the tapes and the width of the central channel, respectively. The total width of the cable is given by $W_t$.*

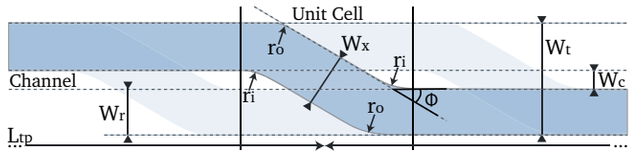


**Figure 2.3.** *Geometry and definition of parameters of the Roebel cable. For clarity only three of the tapes in the cable are shown. The width of the tape is given by $W_r$, the width of the tape at the cross-over by $W_x$, the width of the channel by $W_c$ and the total cable width by $W_t$. The angle defining the slope of the cross-over is given by $\Phi$ and the radius of the fillets around it by $r_i$ and $r_o$ for the inside and outside of the cable, respectively.*

TABLE 2.1.
ROEBEL CABLE PARAMETERS USED THROUGHOUT THIS THESIS.

| Symbol | Unit | SP-1 | Sun-Ox-1 | BHTS-1 | BHTS-2 | Description |
|---|---|---|---|---|---|---|
| tape | n.a. | SuperPower | Sunam | Bruker | Bruker | tape supplier |
| cabler | n.a. | KIT | SuperOx | KIT | KIT | cabling performed at |
| $N_s$ | n.a. | 15 | 15 | 15 | 13 | number of tapes |
| $d_s$ | $\mu$m | 100 | 110 | 150 | 150 | tape thickness |
| $d_c$ | mm | 0.8 | 0.9 | 1.7* | 1.1 | cable total thickness |
| $d_i$ | mm | 0.1 | 0.1 | 0.1 | 0.1 | insulation thickness |
| $W_r$ | mm | 5.5 | 5 | 5.5 | 5.9 | strand width |
| $W_t$ | mm | 12.0 | 12.0 | 12.0 | 12.0 | cable width |
| $W_x$ | mm | 5.5 | 6 | 5.5 | 5.9 | cross-over width |
| $W_c$ | mm | 1.0 | 2.0 | 1.0 | 0.2 | channel width |
| $\Phi$ | deg | 30 | 30 | 30 | 30 | cross-over angle |
| $L_{\mathrm{tp}}$ | mm | 226 | 300 | 300 | 300 | transposition pitch |
| $r_i$ | mm | 6.0 | 6 | 10 | 10 | inner radius |
| $r_o$ | mm | 0 | 6 | 0 | 0 | outer radius |
| $A_{\mathrm{tape}}$ | mm$^2$ | 8.25 | 8.85 | 12.4 | 11.5 | area of all tapes |
| $A_{\mathrm{bare}}$ | mm$^2$ | 9.6 | 10.8 | 20.4 | 13.2 | bare cable area |
| $A_{\mathrm{insu}}$ | mm$^2$ | 12.2 | 13.4 | 23.2 | 15.9 | total cable area |
| $R_{\mathrm{soft}}$ | mm | 11 | 12 | 16 | 16 | soft-way bend radius |
| $R_{\mathrm{hard}}$ | mm | 2 | 2 | 2 | 2 | hard-way bend radius |

* higher than nominal due to severe dog boning effect on the copper stabilizer.

the cable is then given as

$$N_{max} = \left\lfloor L_{\text{tp}} \frac{\sin\phi}{W_x} \right\rfloor. \qquad \text{Eq. 2.1}$$

In practice a lower number of tapes is used to avoid the tapes from interlocking, thereby allowing for some flexibility for winding coil-ends. The number of tapes also determines the thickness of the cable which is given as $\lceil N_s/2 \rceil d_s$. Within the EuCARD2 project various cables have been proposed and developed [101]. The specifications of the relevant cables are presented in Table 2.1. For the design of the 5 T coil, initially the SP-1 geometry, which uses SuperPower tapes with a substrate thickness of 50 $\mu$m, was used. However, to also accommodate tapes with different substrate thickness from other manufacturers, without lowering the number of tapes in the cable significantly, it was decided to allow for a variable cable thickness.

### Hard-Way Bending Test 2.2.2

A key issue in the three-dimensional design is the minimum hard-way bending radius of the cable since this mainly determines the shape of the side profile of the coil-end and layer jump. This mechanical property was not known for the ReBCO based Roebel cable and a bending test was performed. At the time of the experiment the conductor was fairly expensive ($\sim$ 10 kCHF/m, mainly depending on the number of superconducting tapes) and not readily available. Therefore it was decided to manufacture a stainless steel dummy cable first. The meandering strips were cut from of a 100 $\mu$m thick stainless steel sheet. At first water-jet cutting was used, but later chemical etching, which is the preferred method since it results in much cleaner edges showing no burrs. For the test geometry the specifications of the SP-1 cable layout are used, see Table 2.1. The cable itself, with a total length of 3 m, was assembled by hand.

With the dummy cable a hard-way bending test was performed (see Figure 2.4). The cable is bent into a curve with constant radius and held in place using polyimid tape, after which it was pressed between a flat surface and a glass plate. This to prevent the cable from bulging outward in the lateral direction (see Figure 2.5). The process was repeated at various bending radii. It was found that below a radius of 2 m the tapes started to crinkle near or at the bend. This crinkling would likely degrade the conductor and has to be avoided. To test the feasibility of the layer jump an S-shaped groove was machined in an aluminum plate using a radius of curvature of 2 m. The length of the layer jump becomes approximately 350 mm. Using tape and clamps the cable was put successfully in the slot (see Figure 2.6). The crinkling observed is within acceptable limits, the tape surfaces are rippled by an estimated 100 $\mu$m, but no plastic deformation occurs, making the layer jump possible. Note that the radius of curvature found in the test is nowhere near the theoretical limit of 0.9 m, imposed by the stress limit inside the tapes, but it is considered the practical limit for coil-winding and is therefore used for the magnet design.

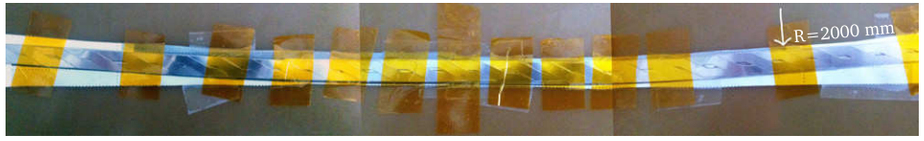


**Figure 2.4.** *Hard-way bend test on a stainless steel dummy Roebel cable comprising of* 15 *tapes, which have a thickness of* 100 µm*. The cable is fixed to a solid plate at a radius of* 2000 mm*, after which it is compressed under a glass plate, allowing the deformation of the tapes to be observed. At this radius the crinkling is within acceptable values.*

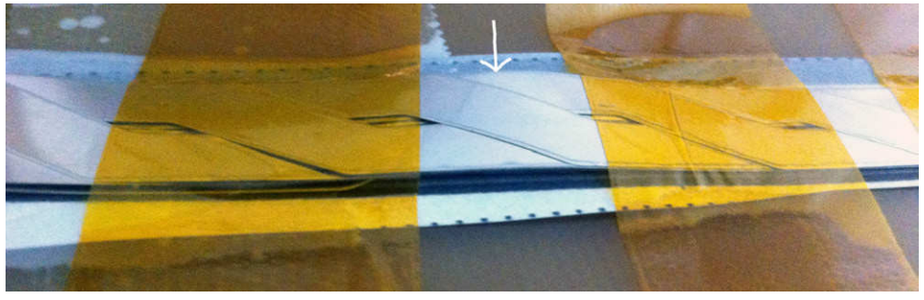

**Figure 2.5.** *Close up of the bending test on a* 15 *tapes stainless steel dummy Roebel cable before pressure is applied with the glass plate. The tapes have a thickness of* 100 µm*. Some of the tapes bend in the out of plane direction by approximately* 1 mm*, denoted with a white arrow. Controlling such shape distortions form a challenge when winding a coil that has a flared end.*

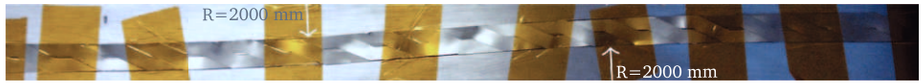


**Figure 2.6.** *Layer jump S-shape bending test on a* 15 *tapes stainless steel dummy Roebel cable. The tapes have a thickness of* 100 µm*. The reflection of the light on the tapes reveals some of the crinkling that occurs inside.*

### 2.2.3 Transverse Pressure, Impregnation and Delamination

Another important parameter is the cable's resistance against transverse pressure in terms of percentage of critical current degradation per MPa. ReBCO tapes are highly resistant against transverse pressure. The limit for single tapes was reported up to 600 MPa [102, 103, 104]. However, a Roebel cable has a more complex geometry in which the edges of the tapes cut into their neighbors, thereby generating very high pressure spots [105]. To quantify the effect, a compression test of a coil pack, consisting of ten Roebel cables, was performed up to an average pressure of 150 MPa, which is the load to survive a 20 T layout in which the forces are allowed to accumulate. In Figure 2.7 it can be seen that the adjacent cable is heavily imprinted in the tapes. In the case of real superconductor this would significantly degrade the cable. Similar results have been reported by other groups [106].

**Figure 2.7.** *Photograph of a dummy Roebel cable made with stainless steel tapes after performing a bare 10-stack test up to* 150 MPa *overall pressure. The cable shown was located near the middle of the stack. It can be seen that the surface pattern of the adjacent cable is heavily imprinted in the tape.*

To avoid these contact pressure effects, it is necessary that the cables are impregnated using a resin [107]. This however poses another problem. The layers of which the ReBCO tapes are composed of can be relatively easily separated, a process called de-lamination [108, 109]. When this occurs the superconducting layer is damaged resulting in degradation of the critical current. The amount of local tensile stress needed to de-laminate the tapes is in the wide range of 2-20 MPa and varies among tapes of various manufacturers. During the impregnation of the coil-winding pack the curing process of the resin, which likely occurs in a non-uniform manner, can result in stress. In addition when the coil pack is cooled down, the resin binds everything allowing for accumulation of thermal stress. Several sources have reported degradation of impregnated coated conductor coils due to these de-lamination effects [110, 32].

Several tests where performed to find an appropriate impregnation procedure. The thermal contraction of clear resin, when cooled down from 293 K to 10 K, is around 12 mm/m, whereas the thermal contraction of HTS tape, over this temperature range, is around 3.5 mm/m [111]. There is a high risk that this leads to de-lamination of the cross over tapes, when the resin contracts inside the channel. Therefore the first impregnations are performed with CTD-101G epoxy [112]. This epoxy is filled with alumina particles that reduce the thermal contraction to 6 mm/m (over the given temperature range). The cut ends of the samples are polished for inspection under an optical microscope (see Figure 2.8). A relatively large void was observed in the resin at the central channel of the cable. Some tapes in the cable are misplaced by up to 200 $\mu$m and seem to be at least partially in contact. Some de-lamination of the copper stabilizer is observed, mainly on or near the cross-overs. It is, however, hard to determine if this is caused by the resin or by the polishing of the sample. In addition it is observed that particles are filtered by the glass sleeve insulation (see Section 2.2.5), resulting in a variation of particle density over the length of the sample.

Later also a Feather-M0 exercise coil was impregnated with this resin, but it was proved again that the resin is too viscous and only part of the winding pack was impregnated. To resolve this issue, it was decided to switch to CTD101K [113] clear resin, the resin that is also used for impregnation of all $Nb_3Sn$ coils at CERN. To fill the void in the channel, a fiber-glass rope is inserted (see Figure 2.1). When impregnated the thermal contraction of the fiber-glass-epoxy is 1.9 mm/m, which is less than the thermal contraction of the conductor. The fiber-glass also acts as a capillary helping to fill the channel

during impregnation. The idea is tested on a dummy cable sample (see Figure 2.9). This time no significant voids are observed and the cable looks well impregnated. Inside the rope a fine insulated LTS wire can be inserted to act as a superconducting quench detector [114], but also to balance the inductive voltage in order to reduce noise on the voltage taps.

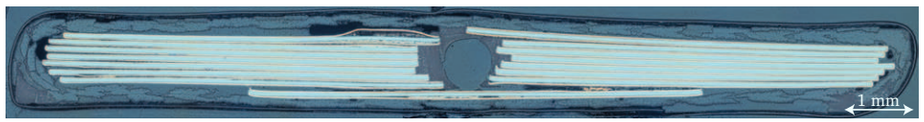


**Figure 2.8.** *Microscope picture of a Roebel cable cross-section impregnated with CTD-101G alumina filled epoxy. The picture shows the end part of the sample that is later used for AC loss measurements. In the channel a circular void in the resin is visible. The black areas were filled by a secondary resin during the preparation of the sample. These areas where likely opened up during the cutting of the sample and can be disregarded as artifacts.*


**Figure 2.9.** *Microscope picture of a Roebel cable cross-section impregnated with CTD-101K clear resin, with a glass rope inserted in the central channel. It can be seen that in contrast to Figure 2.8 no cavities are visible in the channel nor edges and the glass rope is impregnated perfectly.*

During the impregnation the coil pack is pressurized, ensuring that the tapes are in contact to allow for current sharing. In addition it can prevent de-lamination during the curing of the epoxy. A dummy 3 cable stack, which was impregnated with this method, is shown in Figure 2.10. The pressure prevented the resin from entering between the tapes. This might be an advantage because the tapes can to some extent slide with respect to each other avoiding the build-up of thermal stress. Another feature is the use of mold release on the former preventing the coil from being glued to the mechanical structure. This avoids the coil pack from being under transverse tension possibly also causing de-lamination.

### 2.2.4 Disintegration and Braiding

During the tests with the dummy cable it is observed that the cable can very easily disintegrate, making it difficult to handle. The reason is that the tapes are twisted, but not braided or inter-weaved. As demonstrated by KIT a solution to this problem can be the use of a very short twist pitch around 126 mm and tight packing of the tapes. This, however, poses a limit on the number of tapes in the cable following Equation 2.1. Also the channel width can be reduced to nearly zero to provide extra contact points for the tapes, thereby improving overall mechanical stability. This causes the cable to


**Figure 2.10.** *Internal inspection of an impregnated* 3 *stack of dummy Roebel cables. The tapes can be peeled off one by one because the resin did not enter in between the tapes.*

be more difficult to assemble, especially when using a cabling machine. With effort it can be assembled by hand.

If other options are insufficient or impractical, it was found that the cable can be sufficiently mechanically stabilized using (copper) bracelets or two (polyimid) ribbons that are braided (not to be confused with the glass sock) into the cable (see Figure 2.11). The braiding is achieved by wrapping around the two tape stacks making up the cable (shown in Figure 2.2). With both techniques the cable can be handled in practice for coil-winding, as demonstrated in Figure 2.12. This technique enables the use of much longer twist pitches, and allows for a high number of tapes in the cable and thus very high cable currents. When a copper rod or glass rope (see Section 2.2.3) is inserted into the central channel the bracelets or tapes can be wrapped around them to secure their position. This idea is filed as a provisional European Patent [115].

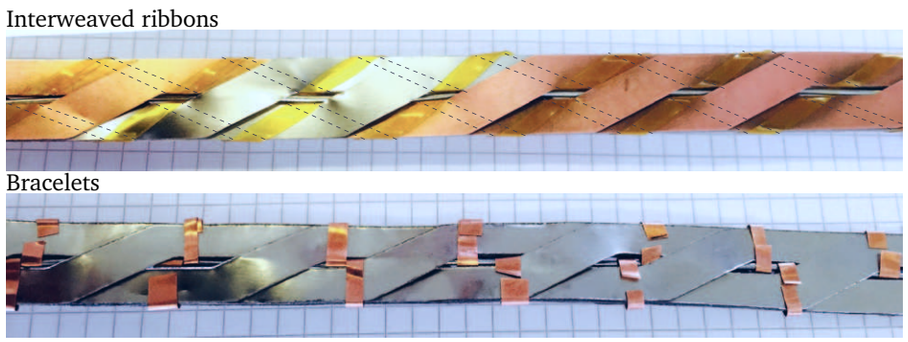


**Figure 2.11.** *Top view on Roebel cables equipped with inter-weaved ribbons or bracelets to improve mechanical stability of the Roebel cable. The dotted lines show how the polyimid ribbons are positioned on the backside of the cable.*

**Figure 2.12.** *A three-turns spiral with about* 40 mm *diameter for demonstration of the bracelet method for mechanically stabilizing the Roebel cable.*

### 2.2.5 Electrical Insulation

ReBCO Roebel cables were not used before in any accelerator magnet and no experience was available concerning a proper insulation system. For quench protection it is necessary that the insulation can withstand 1 kV turn-to-turn voltage. Also the insulation system must not restrict the hard-way bending of the cable. The tapes in the cable must be able to slide longitudinally with respect to each other to maintain the soft-way flexibility during coil-winding. Therefore the insulation must be able to slide over the cable during winding. The insulation must not locally compress the mechanically unstable cable in the lateral direction when applied. The tapes in the cable are preferred to be in electrical contact to allow redistribution of current during a thermal instability including quench. The insulation system must be compatible with resin impregnation (see Section 2.2.3). Also the insulation has to be relatively thin not to degrade the overall current density in the coil blocks too much. Note that presently the cost of the cable itself is very high, therefore the cost of the insulation is less relevant at this point.

For coils constructed with single tapes often an epoxy coating [116] or co-wound polyimide strips are used. For Roebel cable a surface coating is not appropriate because the surface of the cable is not smooth and has many sharp edges. Moreover the coating would insulate the tapes preventing current sharing. Co-winding strips can be considered but they are easily misplaced resulting in a short circuit at the edge of the coil-winding pack. Even if a short circuit is avoided, the distance from cable edge to edge for an arc to form, is very short. For certain solenoids it was shown that it is possible not to use electrical insulation between the cables [117], leaving electrical contact between the tapes everywhere. In this case stainless steel strips can be co-wound with the conductor to increase contact resistance. This approach, however, can not work for an accelerator type magnet, because it is necessary to ramp the magnet over a short time, implying high field-rates and subsequently high losses. During this time the path of the current must guarantee the field quality. In a non-insulated coil the current paths

converge over longer lengths of time. In addition when an insert-outsert combination is used, the shorted turns might allow very large induced currents, and thus forces, which could destroy the coil, when the quench protection of the outsert is switched in. For these reasons not using insulation is ruled out.

Polyimide wraps, as used for the LHC, require the cable to be stable in the lateral direction. The company General Cable (GC) has shown that a backing plate over the full width of the cable can stabilize the width, allowing for wrapping of the insulation. This increases the hard-way bending radius significantly. A solution could be to braid the cable as presented in Section 2.2.4 or to apply a braided sleeve around the cable. Because the cable will be impregnated, the advantage of having helium entering the cable through the voids in the wrap, a design feature of Nb-Ti Rutherford cables used in the LHC, no longer applies. Having excluded most of the other options, the type of insulation presently accepted is a braided sleeve, which is available of many materials (Kevlar, Dyneema, Nylon, PET). With the thermal contraction of fibre-glass epoxy in mind and the experience available from $Nb_3Sn$ magnets, a braided fiber-glass sleeve was selected.

To test the electrical limits of the insulation system a series of three stack samples using dummy cable were prepared applying different types of resin. The cables are placed in a staircase type layout to prevent an arc jumping over the ends, thereby bypassing the insulation (see Figure 2.13). The voltage is applied to the cable at several access holes that are placed at maximum separation distance, in order to increase the breakdown voltage through the air surrounding the cable. The breakdown voltages for the varying samples are presented in Table 2.2. Some of the tests were *destructive* for the insulation between the connected cables. Therefore in the last test, in which the breakdown voltage between the cables on the outside is measured, some of the samples were *already broken*. This can be considered an artifact of the method used and is not a sign of bad insulation. An arc over the surface means that the breakdown voltage through air between the leads connecting the sample was lower, than the breakdown voltage of the insulation. The results of such a test can be considered as a lower limit. The breakdown voltages are in the range of 2.5 to 7 kV and more than 6 kV for the CTD-101K, which is the resin selected for the final coils. This is a sufficiently high turn-to-turn breakdown voltage including safety margin, for the expected 1 kV applied over the coil, when running down the current during a quench.

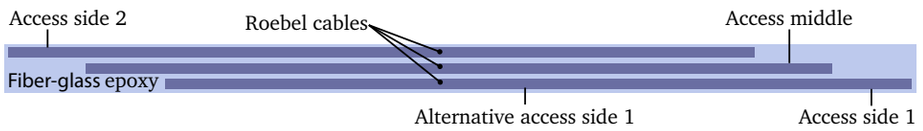


**Figure 2.13.** *Illustration showing a side view of the geometry of the three stack Roebel cable sample for the high voltage tests. The cables are placed in a staircase fashion to prevent an arc jumping over the ends, thereby bypassing the insulation. The position and labels of the high voltage leads are shown in the illustration.*

TABLE 2.2.
RESULTS OF THE INSULATION VOLTAGE BREAKDOWN EXPERIMENT. THE TEST IS PERFORMED AT A TEMPERATURE OF 22.5 °C AND A HUMIDITY OF 44% AT A RAMPRATE OF 100 V/s.

| Sample | Unit | Middle-Side 1 | Middle-Side 2 | Side 1-Side 2 |
|---|---|---|---|---|
| CTD.5.1 | kV | 7.2 (Destructive) | 8.2 (Destructive) | 0.2 (Already broken) |
| CTD 101K | kV | 6.2 (Destructive) | 6.7 (Arc over surface) | 6.3 (Arc over surface) |
| CTD 101G | kV | 5.0 (Destructive) | 3.9 (Destructive) | 0 (Already broken) |
| CTD 528 | kV | 4.4 (Destructive) | 2.4 (Destructive) | 0.1 (Already broken) |
| CB 521.540 | kV | 7.5 (Arc over surface) | 4.0 (Destructive) | 6.0 (Arc over surface) |

## 2.3 Winding Layout Optimization and Analysis

*In this Section several optimized cross-sectional layouts for the Feather-M2 Aligned Block magnet are presented and compared. A preferred cross-section is selected based on which a cable layout is generated.*

### 2.3.1 Two-Dimensional Layout Optimization

The first step in the design process is to generate a two-dimensional coil Aligned Block layout. The coil is designed to operate in two different scenarios, the first is stand-alone operation inside an iron yoke generating 5 T at the center of the aperture with reasonable field quality. The second is as insert in a 13 T background field and adding as much field as possible, without any field quality requirement. To maximize the magnetic field in the insert scenario, the off-vertical angle of the coil pack is adjusted to align the flat Roebel conductor with the magnetic field lines, including the background field. At the same time, the harmonics and coil pack widths needed to generate the magnetic field are optimized for the stand-alone case. The conductor performance is scaled to a target current density of 600 A/mm$^2$ in the tape at 20 T perpendicular applied magnetic field, corresponding to a scaling factor of 1.49 (see Appendix A).

The optimization is performed using the iterative algorithm described in Section 6.2. In this algorithm the coil pack is approximated by blocks of homogeneous current density, also referred to as the overall current density. For the design the SP-1 cable is used (see Table 1.2). The assumed performance of the coated conductor and the fractions to approximate this cable by an overall current density can be found in Table 2.3. The coil is designed to reach the required 5 T when operating at 70% on the load-line. The effect of the choice of margin on the thermal stability is evaluated later using transient thermal models of the cable (see Section 5.3.3).

Because of the angular dependence the intersection of the load-line with the critical surface needs to be determined at each point in the coil-windings. The change of field angle when operating at a different point on the load-line is not taken into account. The intersection with critical surface is calculated for the magnetic field angle at the operating current and thus not at the short sample. Furthermore it is assumed that the current is distributed homogeneously over the conductor, while in reality the current

TABLE 2.3.
SETTINGS USED FOR THE COIL-WINDINGS DURING THE 2D LAYOUT OPTIMIZATION.

| Symbol | Value | Description |
|---|---|---|
| $f_{\text{improv}}$ | 1.49 | scaling factor used to elevate scaling relation $Jc$ to specifications |
| $J_{c,20\,\text{T}}$ | $600\,\text{A/mm}^2$ | critical current density in the tape in 20 T transverse field and 4.2 K |
| $J_{c,15\,\text{T}}$ | $688\,\text{A/mm}^2$ | critical current density in the tape in 15 T transverse field and 4.2 K |
| $J_{c,12\,\text{T}}$ | $784\,\text{A/mm}^2$ | critical current density in the tape in 12 T transverse field and 4.2 K |
| $f_{\text{void}}$ | 0.20 | fraction of voids in cross-section of cable |
| $f_{\text{insu}}$ | 0.10 | fraction of insulation in cross-section of cable |
| $f_{\text{filling}}$ | 0.70 | fraction of tapes in cross-section of cable |

is not perfectly uniform and can redistribute over the width of the wide tapes gaining a significant amount of margin (see in Section 2.3.6).

As an example the magnetic field lines and calculated operating points are presented for the final Aligned Block layout in Figures 2.14 and 2.15, for stand-alone operation in a yoke and for operation as insert in 13 T background field, respectively. It can be seen that in the background field the conductor is well aligned and a performance of around 65% of the critical current at full alignment can be achieved. When the conductor is placed in a perpendicular magnetic field this is only 20%. By chance in the stand-alone case, in the high(er) field regions, the angle is also almost aligned, despite not having been optimized for this. In this case the performance is also around 65% of the critical current at full alignment. The resulting operating current densities for both scenarios are very similar. The higher magnetic field angle in stand-alone is essentially compensated for by the lower magnetic field.

The lowest margin is present at the edges of the blocks, whereas in the center of the blocks a band with high critical current density and low field angle resides. This distribution is very different from classical (non-angle dependent) LTS coils, where the highest percentage on the load-line is always located at the inner radius of the coil next to the aperture. As a first estimate of the pressure in the coil-windings, in order to check whether a design is mechanically viable, it is calculated from the Lorentz forces through integration in the direction perpendicular to the broad face of the cable (see Figure 2.16). A maximum pressure of 17 MPa is found when operated in stand-alone and a maximum pressure of 110 MPa when operated as insert in the 13 T background field. This pressure is within limits of the impregnated coil pack, which is more than 200 MPa [107]. Further mechanical analysis can be found in Section 2.5.

To make the coil resemble a real accelerator dipole and to be able to measure magnetic field quality, the aperture is decided to be open and accessible from both coil-ends. This also makes the insert a useful tool for high field cable tests after the project is finished. Although during the layout optimization all calculations are performed in two dimensions, it is necessary to already take into consideration the shape of the coil-ends. The three-dimensional trajectory of the cable has to stay outside the beam-pipe envelope and be within the Fresca2 aperture, additional support cylinder of 4 mm and

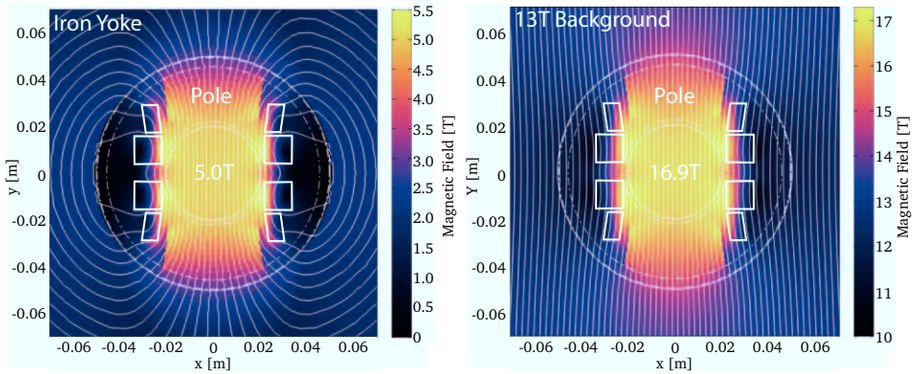


**Figure 2.14.** *Calculated magnetic field lines for a two-dimensional cross-section of the Feather-M2 magnet at design current. On the left side stand-alone coil in an iron yoke and on the right side as insert in a* 13 T *background field.*

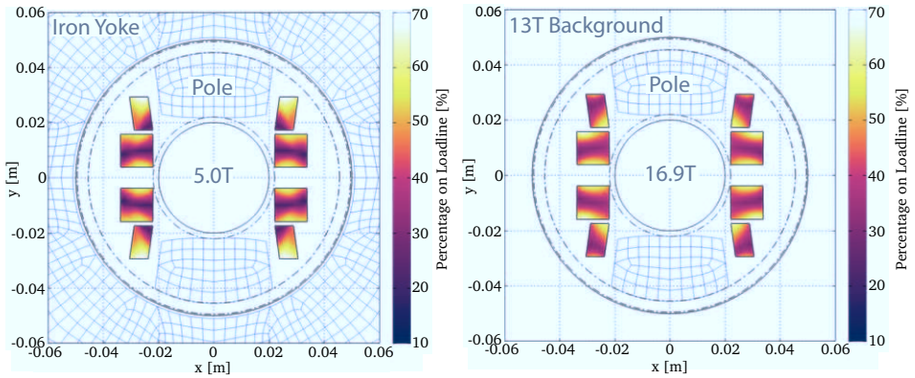


**Figure 2.15.** *Percentage on the loadline at design current inside the Feather-M2 magnet calculated separately for each pixel assuming a homogeneous current distribution. On the left side as stand-alone coil in an iron yoke and on the right side as insert in a* 13 T *background field.*

0.5 mm insulation sheets included. This means that above each block there must be space to move upward to make a flared-end, with a minimal bending radius of 16 mm (see Figure 2.17). This limits the coil design to a maximum of two decks[4], assuming 12 mm cable width. The decks making up the coil are named the central deck and the wing deck, respectively.

Because the space above the blocks is limited an additional restriction is put on the width of the blocks, leaving unfilled space on the outside of the coil in the cross-section.

[4]The definition of deck is given as: "any level, tier, or vertical section, as of a structure or machine". Here it is used for annotating the vertical levels of a (block) coil, in contrast to 'layers' which extend radially.

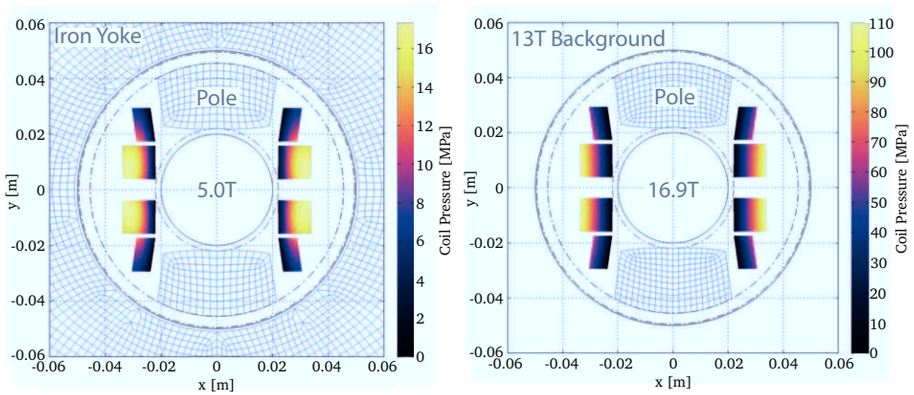


**Figure 2.16.** *Calculated pressure in the coil's cross-section, using integration, inside the Feather-M2 magnet. On the left side in stand-alone mode in an iron yoke and on the right side as insert in a* 13 T *background magnetic field.*

Axially the wing deck must be shorter in length than the central deck, in order to make space for the flared end of the central deck, making it all fit inside the limited Fresca2 aperture. This prevents the layer jump from being located inside the coil-ends, the method used for the so-called HD1 and HD2 $Nb_3Sn$ accelerator demo coils [19]. Therefore the layer jump needs to be located in the straight section forcing the inner edges of the blocks to be above one another. Getting the current leads in and out is trivial for the central deck. For the wing deck a more creative solution is required (see Section 2.3.4).

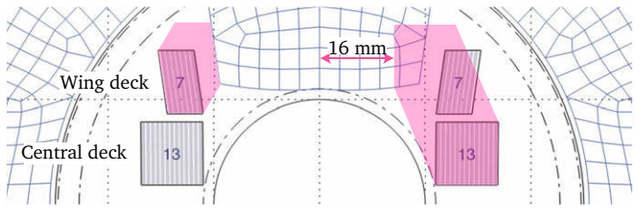


**Figure 2.17.** *Axial projection of the foreseen trajectory of the flared-end. On the left shown for the wing deck and on the right for the central deck. Note that in order to stay within the support cylinder the width of the blocks is limited by the coil-ends.*

These spatial requirements significantly reduce the degrees of freedom, such that achieving a good field quality becomes more difficult. The separation distance between the two poles, also referred to as the mid-plane separation distance, can be used to minimize the sextupole component $B_3$, thereby slightly reducing the effectiveness of the coil. Because it is not possible to add conductor blocks above the aperture (due to the alignment required for the layer jump), an iron pole piece can be added to help align-

ing the magnetic field with the conductor and to provide an extra 0.4 T at the center of the aperture. Also it reduces the $B_5$ harmonic component, without compromising the bending radius of the conductor. Between the iron pole and the conductor a clearance of 4 mm is maintained. The iron pole, however, introduces strong non-linearity in the coil harmonics. The non-linearity of the iron can be studied by calculating the harmonics of the coil as function of central field. As an example in Figure 2.18 is presented the harmonic shift in the final layout, while ramping the stand-alone coil and the insert coil, respectively. It can be seen that the sextupole component $B_3$ is affected severely starting at −190 units at low magnetic field, ending at only a few units near 5 T. When used in a real accelerator compensation for this effect is necessary. A possible solution could be the use of persistent current shim coils as presented in Section 4.5 in Chapter 4.

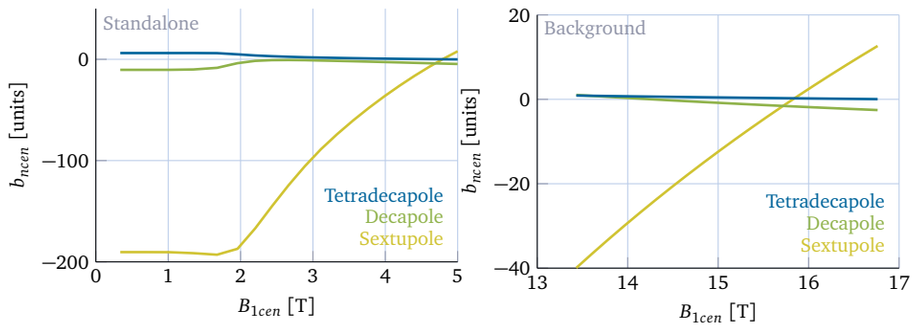


**Figure 2.18.** *Non-linearity in coil harmonics due to the iron pole, while ramping the final coil layout in stand-alone (left) and as insert in a background field (right). The harmonics are given as function of central magnetic field. The HB-curve used to calculated the iron magnetization is taken from Roxie [6].*

### 2.3.2 Comparison of Aligned Block Layout Options

Because of the restrictions a compromise between magnetic field quality and generated central magnetic field needs to be found. Five Aligned Block layout options designed with different compromises are explored and compared in Table 2.4 on Page 44. The first option (1) has high performance and good field alignment but lacks geometric field quality. The second (2) sacrifices some performance for field quality by opening the mid-plane, however, it has a non-linear iron pole. In the third option (3) no iron pole is used, making it no longer possible to reach 5 T. In addition $B_5$ field quality is not achieved because of insufficient conductor over the aperture due to space limitations. For completeness in the fourth (4) and fifth (5) layouts these space limitations are lifted by removing the Fresca2 aperture size restriction. An alternative is to test these coils in the so-called D1 [118] Nb-Ti separation dipole for the HL-LHC, which has an aperture of 150 mm but is limited to 6 T. This makes it possible to place a third deck, improving the geometric field quality significantly. Results are shown with and without iron pole

in the fourth and fifth designs, respectively. Note that the fifth layout uses about 1.5 times more conductor than the two deck layout with the iron pole.

For the Aligned Block layout it is of high interest to be able to operate inside Fresca2, because it is in a high background field that the conductor alignment pays off. Thanks to the alignment the calculated operating current is nearly the same for both stand-alone and insert mode of operation scenarios. In addition the combined magnetic field of the two magnets comes close to the 20 T target field specified by FCC. Mind that the insert only operates at 70% on the load-line and that Fresca2 is designed for 13 T, but may achieve at a short sample performance of 16 T. Therefore, not to miss a chance of achieving magnetic fields on the order of 20 T, it is decided to dismiss the three-deck layouts (4) and (5). The remaining question is how important the role of field quality is compared to reaching the stand-alone target field. It is expected that without striation [119], the wide ReBCO tapes will generate large persistent currents crippling the field quality in any case. Therefore it is decided to drop the third design (3) and allow for the non-linearity introduced by the iron poles. Since the cost difference between the remaining layouts (1) and (2) is only minor and keeping in mind that in three dimensions the coil-ends are slightly shorter because the flared ends need to clear a lower vertical distance, it was decided to study the medium field quality layout (2) in further detail.

### Comparison with Other Layout Options 2.3.3

In Table 2.5 on Page 45 the Aligned Block layout selected as motivated in the previous section is compared to other layout options. Because the Aligned Block (1) and the normal Block (2) are intrinsically the same, except for the alignment feature, the same design decisions apply. Therefore the overall layout looks very similar. However, it can be seen that the Block layout is outperformed by the Aligned Block on most issues. Because the angular dependence of the conductor at low magnetic field is weaker, only a 2% of extra conductor is needed to be able to generate 5 T in stand-alone mode. However, as insert in the background field the misalignment starts to play a role, resulting in a difference of current density and thus field contribution of 20% (3.9 T for Aligned Block against 3.2 T for Block). For the Cosine Theta the Aligned Block is compared to layouts designed at CEA Saclay [60, 61]. Because the 12 mm cable is too wide to make a dual layer coil, while retaining the structure inside the aperture of Fresca2, two layouts have been proposed.

The first (3) is a single layer coil, which has only a slightly higher conductor area in the cross-section than the Aligned Block. However, to reach 5 T it needs to operate at 80% on the load-line. Because it is possible to have more blocks, wedges are needed in any case for the non-keystoned Roebel cable, it has better geometric field quality than the aligned block. To achieve this the conductor is placed at a high angle resulting in a tight cable bending radius of 8 mm. The largest drawback of the Cosine Theta is that the conductor on the mid-plane is oriented perpendicularly with respect to the magnetic field. This causes the operating current and thus magnetic field to reduce with 44% when operated in a 13 T background field. Also the forces are directed such that

TABLE 2.4.
OVERVIEW SHOWING FIVE ALIGNED BLOCK LAYOUT OPTIONS FOR THE 2D-LAYOUT OF THE REBCO INSERT MAGNET.

| Parameter name<br>Optimized towards | 1 - Aligned Block<br>minimal conductor | 2 - Aligned Block<br>medium field quality | 3 - Aligned Block<br>same as 2, no-poles | 4 - Aligned Block<br>high field quality | 5 - Aligned Block<br>same as 4, no-poles |
|---|---|---|---|---|---|
| stand-alone coil layout | 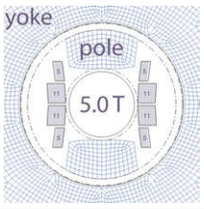 | 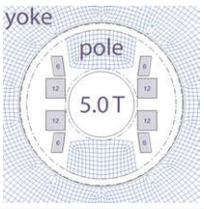 | 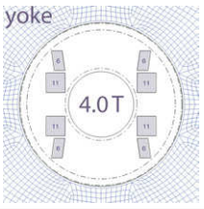 | 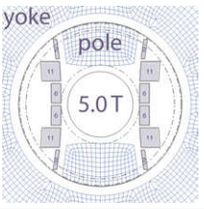 | 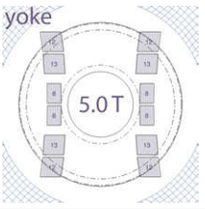 |
| GENERAL GEOMETRIC | | | | | |
| Aperture diameter | 40 mm (2 mm) | 40 mm (2 mm) | 40 mm (2 mm) | 40 mm (4 mm) | 40 mm (4 mm) |
| Nonlinear poles | yes | yes (Fig. 2.18) | no | yes | no |
| Midplane split | 1.50 mm | 7.65 mm | 14.26 mm | 1.50 mm | 1.50 mm |
| Required bending radius | 16 mm | 16 mm (Fig. 2.17) | 16 mm | 20 mm | 20 mm |
| Block shear angles | 3.4/7.2 deg | 0.5/8.0 deg | 0.1/6.7 deg | 0.5/4.0/8.0 deg | 1.0/4.0/8.0 deg |
| Number of turns | 11/5 (16) | 12/6 (18) | 11/6 (17) | 11/6/2 (19) | 8/13/12 (33) |
| Total area of all blocks | 790 $mm^2$ | 885 $mm^2$ | 873 $mm^2$ | 956 $mm^2$ | 1632 $mm^2$ |
| WHEN OPERATING IN STAND-ALONE IN AN IRON YOKE | | | | | |
| Percentage on loadline | 70% | 70% (Fig. 2.15) | 70% | 70% | 70% |
| Block current density | 674 A/$mm^2$ | 649 A/$mm^2$ | 642 A/$mm^2$ | 672 A/$mm^2$ | 575 A/$mm^2$ |
| Critical current density | 1454 A/$mm^2$ | 1216 A/$mm^2$ | 1194 A/$mm^2$ | 1268 A/$mm^2$ | 1051 A/$mm^2$ |
| Dipole $B_1$ | 5.0 T | 5.0 T | 4.0 T | 5.0 T | 5.0 T |
| Harmonics $b_3$ / $b_5$ / $b_7$ | 160 / 15 / 2 units | 8 / 5 / 0 units | 1 / 30 / 3 units | 0 / 0 / 0 units | 0 / 0 / 0 units |
| Maximum pressure | 17.1 MPa | 17.3 MPa (Fig. 2.16) | 14.9 MPa | 15.4 MPa | 18.8 MPa |
| WHEN OPERATING AS INSERT IN A 13 T BACKGROUND FIELD | | | | | |
| Percentage on loadline | 70% | 70% (Fig. 2.15) | 70% | n.a | n.a |
| Block current density | 769 A/$mm^2$ | 667 A/$mm^2$ | 640.4 A/$mm^2$ | n.a. | n.a. |
| Critical current density | 1279 A/$mm^2$ | 1282 A/$mm^2$ | 1258 A/$mm^2$ | n.a | n.a |
| Dipole $B_1$ | 17.3 T | 16.9 T | 15.9 T | n.a. | n.a. |
| Harmonics $b_3$ / $b_5$ / $b_7$ | 68 / 3 / 1 units | 13 / 3 / 0 units | 3 / 7 / 1 units | n.a. | n.a. |
| Maximum pressure | 117 MPa | 110 MPa (Fig. 2.16) | 102 MPa | n.a. | n.a. |

TABLE 2.5.
OVERVIEW COMPARING THE ALIGNED BLOCK LAYOUT TO OTHER AVAILABLE OPTIONS.

| Parameter name<br>Optimization | 1 - Aligned block<br>medium field quality | 2 - Normal block<br>medium field quality | 3 - Cosine Theta<br>CEA single [60, 61] | 4 - Cosine Theta<br>CEA double [60, 61] | 5 - Canted (CCT)<br>$\alpha = 20^o$, $f_p = 0.7$ |
|---|---|---|---|---|---|
| stand-alone coil layout | 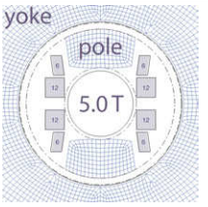 | 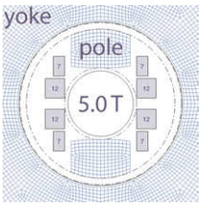 | 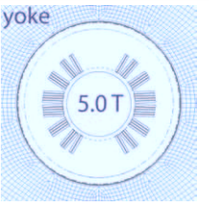 | 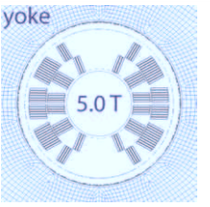 |  |
| GENERAL GEOMETRIC | | | | | |
| Aperture diameter | 40 mm (2 mm) | 40 mm (2 mm) | 40 mm (2 mm) | 40 mm (2 mm) | 40 mm (2 mm) |
| Cable width / thickness | 12 mm / 0.8 mm | 12 mm / 0.8 mm | 12 mm / 1.2 mm | 10 mm / 1.2 mm | 4 mm / 0.8 mm |
| Conlinear poles | yes | yes | no | no | no |
| Required bending radius | 16 mm | 16 mm | 8 mm | 8 mm | const. Perimeter req. |
| Number of turns | 12/6 (18) | 12/7 (19) | 5/4/3/2 (14) | 4/5/3 − 6/10/4 (32) | n.a. |
| Total area of all blocks | 885 $mm^2$ | 909 $mm^2$ | 956 $mm^2$ | 1827 $mm^2$ | 1557 $mm^2$ (real) |
| WHEN OPERATING IN STAND-ALONE IN AN IRON YOKE | | | | | |
| Percentage on loadline | 70% | 70% | 80% | 60% | 70% |
| Block current density | 649 $A/mm^2$ | 635 $A/mm^2$ | 683 $A/mm^2$ | 386 $A/mm^2$ | 533 $A/mm^2$ (real) |
| Critical current density | 1216 $A/mm^2$ | 1164 $A/mm^2$ | 843 $A/mm^2$ | 915 $A/mm^2$ | 945 $A/mm^2$ (real) |
| Dipole $B_1$ | 5.0 T | 5.0 T | 5.0 T | 5.0 T | 4.7 T |
| Harmonics $b_3$ / $b_5$ / $b_7$ | 8 / 5 / 0 units | 16 / 1 / 0 units | 0 / 0 / 0 units | 0 / 0 / 0 units | 0 / 0 / 0 units |
| Maximum pressure | 17.3 MPa | 16.9 MPa | 20 MPa | 20 MPa | n.a. |
| WHEN OPERATING AS INSERT IN A 13 T BACKGROUND FIELD | | | | | |
| Percentage on loadline | 70% | 70% | 70% | 70% | 70% |
| Block current density | 667 $A/mm^2$ | 530 $A/mm^2$ | 290 $A/mm^2$ | 283 $A/mm^2$ | 287 $A/mm^2$ (real) |
| Critical current density | 1282 $A/mm^2$ | 1068 $A/mm^2$ | 480 $A/mm^2$ | 477 $A/mm^2$ | 485 $A/mm^2$ (real) |
| Dipole ($Bcen1$) | 16.9 T | 16.2 T | 14.6 T | 15.8 T | 14.8 T |
| Harmonics $b_3$ / $b_5$ / $b_7$ | 13 / 3 / 0 units | 4 / 0 / 0 units | 0 / 0 / 0 units | 0 / 0 / 0 units | 0 / 0 / 0 units |
| Maximum pressure | 110 MPa | 87 MPa | 45 MPa | 51 MPa | n.a. |

the sharp edges of the tapes push into the insulation. For the second Cosine Theta layout (4) the cable width is decreased to 10 mm. This allows two layers to fit within the given space thereby maximizing the amount of conductor. With the lowest 5 T operating point of 60% (easier quench detection and protection) and the constant perimeter coil-ends it is probably the safest option for achieving the stand-alone mode magnetic field requirement. However, this layout suffers from the same problems as (3): tight bending radius and bad performance in magnetic fields.

The last design to compare to is the Canted Cosine Theta (5). In therms of efficiency this design has the worst performance for ReBCO because it suffers from both a lower packing factor and the presence of a perpendicular magnetic field component. Also to be able to wind the coil without hard-way bending it is necessary to develop a new former type in which the slots are not perpendicular with the surface of the cylinder, but instead are of constant perimeter type. This means that at present the Canted Cosine Theta is not a realistic option for use with a Roebel cable. In the future, when other cable types, such as CoRC, have achieved higher engineering current densities and better minimum bending radius the Canted Cosine Theta option can be reconsidered. In summary it is decided to make the selected Aligned Block layout, under the name of Feather-M2, the baseline.

### 2.3.4 Three-Dimensional Coil-End Geometry Calculation

To achieve an optimized conductor alignment with the magnetic field direction in three dimensions is challenging. Due to the alignment requirement only few coil-end options are available. The first is the Freeway Overpass/Underpass End designed at Brookhaven National Laboratory [39, 40]. This is a very promising coil-end because it needs almost no hard-way bending, can achieve field alignment and results in very short coil-ends (see Figure 2.19). However, for this project, these coil-ends would prevent the placement of the insert into an existing outsert as for example Fresca2. In the future this can be avoided by assembling the outsert on top of the insert, implying that the insert coil must be longer than the outsert. Since the outsert, Fresca2, is already under construction, it was decided that the Freeway Overpass/Underpass coil-end is too impractical. The remaining option is a flared end. These ends allow for longitudinal insertion into Fresca2, with the drawback that they unavoidably include some hard-way bending. In addition for a conventional flared end the coil pack is under an angle at the very end of the coil. This angle can be avoided by an S-shaped coil-end, at the cost of a 30% length increase. Because the ends are already quite long, due to the limited hard-way bending of the Roebel cable, it was decided not to use the S-shaped coil-end and stick to the conventional flared end.

To achieve the alignment it is necessary to rotate the conductor along its length. Existing software tools are not capable of performing such an operation, while avoiding self-intersection of the cable. Therefore a new method of generating such a geometry

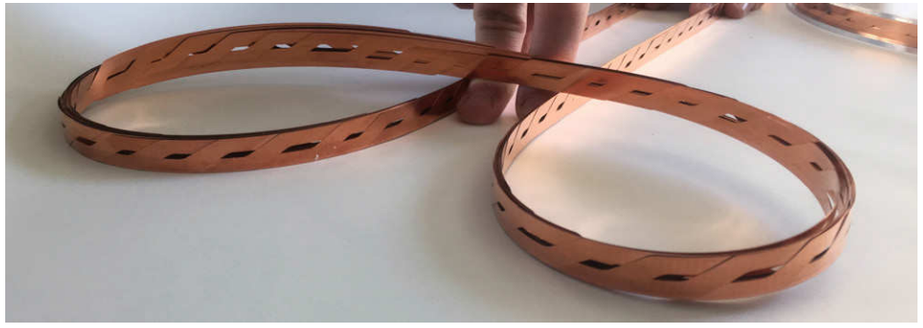

**Figure 2.19.** *Photograph showing the principle of the Freeway Overpass/Underpass coil-end developed by Brookhaven National Laboratory (photograph by CERN).*

is implemented in Field 2016[5] [120] to generate the three-dimensional geometry of Feather-M2 based on a side-profile and a top-profile. The generated geometry is later exported to other software packages such as Cobham Opera and COMSOL for complementary analysis. Using the profiles the shape of the aligned racetrack coil is generated (see Figure 2.20). The side-profile defines the out-of-plane $y$ location of the coil pack as function of the axial coordinate $z$ (pointing along the aperture) and thus the flaring of the end. The shape is mainly determined by the hard-way bending radius of the cable $R_{\text{hard}}$, determined experimentally to be 2 m, see Section 2.2.2. The angle at which the flared end deviates from the mid-plane of the magnet $a_{\text{end}}$, also determines the off-vertical angle at the end of the coil and is set to 4 deg, which determines the average local field angle there. To avoid intersecting the beam-pipe the end of the coil has to reach a vertical position of $h_{\text{req}}$ with respect to the straight section.

The side profile is divided in three sections: a straight section, a curved section and a sloped section. The profile is defined using a set of analytic equations. The deviation of a circular curve with radius $R$ from a line at a distance $x$ can be calculated using a function defined as

$$f_{\text{circ}}(x,R) = -R\cos\left(\arcsin\left(\frac{x}{R}\right)\right) + R. \qquad \text{Eq. 2.2}$$

The height of the curved section $h_1$, length of the curved section $L_1$ and the length of the sloped section $L_2$ are calculated using

$$h_1 = f_{\text{circ}}(L_1, R_{\text{hard}}), \quad L_1 = R_{\text{hard}}\sin(a_{\text{end}}), \quad L_2 = \frac{h_{\text{req}} - h_1}{\tan(a_{\text{end}})}. \qquad \text{Eq. 2.3}$$

[5] Field 2016 is a software package for three-dimensional magnetic field calculation of coil systems. The calculations are performed using a Multi-Level Fast Multipole Method (implemented on the GPU). The code of Field is implemented in a combination of the Matlab programming language, C++ (as mex files) and NVIDIA CUDA.

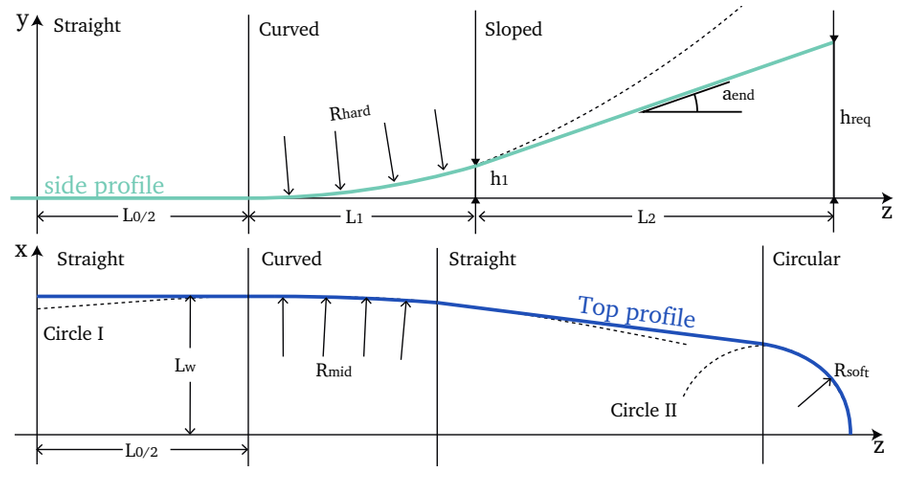


**Figure 2.20.** *Illustration showing the calculated side profile (left) and top profile (right) lines. By superimposing these profile lines the lower inner edge of the coil block is calculated (also see Figure 2.21).*

The side-profile line is then calculated using the conditional equation

EQ. 2.4
$$y_{\text{side}}(z) = \begin{cases} 0, & \text{if } z < L_0/2 \\ f_{\text{circ}}(z - L_0/2, R_{\text{hard}}), & \text{if } z > L_0/2 \;\&\; z < L_0/2 + L_1 \\ h_1 + (z - L_0/2 - L1)\tan(a_{\text{end}}), & \text{if } z > L_0/2 + L_1 \;\&\; z < L_0/2 + L_1 + L_2 \end{cases} .$$

The resulting profile is then mirrored in the $xy$-plane to represent the other end of the coil. When a wing deck is present, it re-uses the side-profile from the central deck, but with a different vertical offset $y_{\text{cen}}$.

The other profile is the top-profile, which determines the trajectory of the coil pack in the in-plane $x$ direction as function of the axial coordinate $z$. To keep the conductor within the specified cylinder it is required to move the conductor closer together, when it moves upward near the coil-end. This then leads to the typical diamond (rhombus) shape of the coil. The radius at the coil-end for the central deck is then limited by the conductor specification $R_{\text{soft}}$ to 16 mm. In addition, a less stringent (for bends in which space is not an issue) soft-way-bend radius $R_{\text{mid}}$ is defined, which is set at a radius of 200 mm. The width of the coil at the straight section is $L_w$. The top-profile is divided into four sections: straight, curved, sloped, curved. To calculate the profile line, first two circles are defined (see Figure 2.20), a large circle with zx-coordinates $(L_0/2, L_w - R_{mid})$ with radius $R_{mid}$ (denoted as circle I) and a small circle at $\left(L_0/2 + L_1 + L_2 - R_{soft}, 0\right)$ (denoted as circle II). The connection points defining the ends of the tangent between the two circles $(z_{t1}, x_{t1})$ and $(z_{t2}, x_{t2})$ are calculated analytically from the circle coordinates and radii. The top-profile line is then calculated

using the conditional equation

$$x_{\text{top}}(z) = \begin{cases} L_w, & \text{if } z < L_0/2 \\ L_w - f_{\text{circ}}(z - L_0/2, R_{\text{mid}}), & \text{if } z > L_0/2 \;\&\; z < z_{t1} \\ x_{t1} + \dfrac{x_{t2} - x_{t1}}{z_{t2} - z_{t1}}(z - z_{t1}), & \text{if } z > z_{t1} \;\&\; z < z_{t2} \\ x_{t2} - f_{\text{circ}}(z - z_{t2}, R_{\text{soft}}), & \text{if } z > z_{t2} \;\&\; z <= L_0/2 + L_1 + L_2 \end{cases} . \qquad \text{Eq. 2.5}$$

The profile is mirrored in both xy and yz-planes to create the four quadrants of the coil. In addition to the profiles also a local rotation $a_{\text{loc}}$ is defined as function of the axial coordinate. It is this rotation that causes the alignment the coil pack and cables with the magnetic field (see Figure 2.21). Because the coils move away from the mid-plane towards the ends, the influence of the other pole on the magnetic field at the coil block becomes weaker. This means that the field direction is more and more determined by the background field, allowing the conductor to twist to back vertical towards the coil-end. Because the separation distance between the poles $2y_{\text{side}}$ plays an important role, through trial and error the best equation for calculating the local rotation is found as

$$a_{\text{loc}}(z) = a_{\text{rot}}\left[1 - \frac{y_{\text{side}}(z)}{h_{\text{req}}}\right]^{p_{\text{twist}}}, \qquad \text{Eq. 2.6}$$

where $a_{\text{rot}}$ is the rotation of the conductor defined at the center of the magnet $z = 0$. At the coil-end the rotation is set to be zero (like a normal racetrack), to ensure that the coil-end is of constant perimeter type. The parameter $p_{\text{twist}}$ is determined iteratively as explained later.

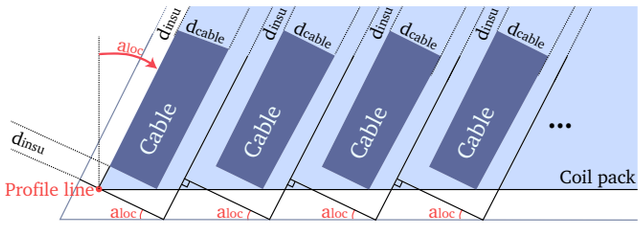


**Figure 2.21.** *Illustration of the cross-section of the coil-windings showing how the cables are rotated and the definition of the local rotation angle $\alpha_{loc}$.*

The shape of the coil pack and ultimately the cable is calculated using the given profiles. This task is performed using a coordinate transformation from the overall Cartesian coordinate system of the coil, with coordinates $x$, $y$ and $z$, to a local coordinate system originating from one edge of the coil pack, in which $\ell$ points along the coil, $t$ points in the transverse direction and $n$ points in the normal direction. A list of Cartesian coordinates defining the lower inner edge of the coil pack is calculated using the given Equations 2.4 and 2.5. A spacing of 1 to 2 mm is maintained between the nodes which are indexed by $i$. The result is an array of vectors defining the location of the nodes

with respect to the origin $\vec{X}_i$. To further clarify the notation, this vector is composed of components $x_i$, $y_i$ and $z_i$. On each node three orthogonal vectors, given as $\vec{X}_{\ell,i}$ (longitudinal vector), $\vec{X}_{t,i}$ (transverse vector) and $\vec{X}_{n,i}$ (normal vector), define the orientation of the local coordinate system, within the overall coordinate system. The direction vector pointing along the length of the coil pack is calculated and normalized using finite difference following

EQ. 2.7
$$\vec{X}_{\ell,i} = \frac{\vec{X}_{i+1} - \vec{X}_{i-1}}{\left|\vec{X}_{i+1} - \vec{X}_{i-1}\right|}.$$

The transverse vector $\vec{X}_{t,i}$ is perpendicular to $\vec{X}_{\ell,i}$ and must be located in the yz-plane. Its components are calculated as $x_{t,i} = 0$, $y_{t,i} = z_{\ell,i}$ and $z_{t,i} = y_{\ell,i}$. The normal vector must be orthogonal with the direction and radial vectors and is thus calculated using a vector product as $\vec{X}_{n,i} = \vec{X}_{\ell,i} \times \vec{X}_{t,i}$. Because the transverse and normal vectors are based on the longitudinal vector, they are normalized by default. The vectors defining the local coordinate system are illustrated in Figure 2.22. As an example Figure 2.23 shows the transverse and normal vectors in the Feather-M2 central deck. In addition to the coordinates a local rotation along the line defined as $a_{\mathrm{rot},i}$ at each node is calculated using Equation 2.6. This rotation defines the local coil pack shear angle and also the cable rotation. For some transformations it is necessary to know a node's position along the length of the conductor. This position is calculated as

EQ. 2.8
$$L_i = \sum_{k=1}^{i-1} \left|\vec{X}_{k+1} - \vec{X}_k\right|,$$

where $L_i$ is the $\ell$ coordinate of node $i$.

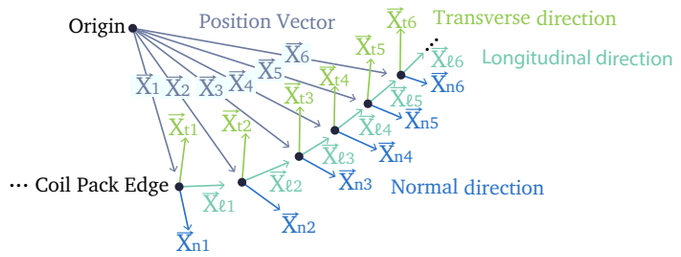


**Figure 2.22.** *Vectors and nodes used to define the local coordinate system originating from the edge of the coil-windings.*

In the local coordinate system with coordinates $\ell$, $t$ and $n$ it is easy to define the edges of the coil pack, cables and if needed the Biot-Savart elements used for the magnetic field calculation. The next step is to define a coordinate transformation that connects the local and Cartesian systems. This transformation is given here for a single coordinate. First an index $j$ is found at which $L_j < \ell < L_{j+1}$ is valid for $\ell$. Then through linear

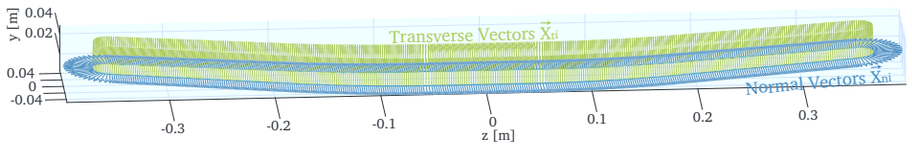


**Figure 2.23.** *Side-profile applied to top profile and vectors defining the local coordinate system for the central deck of the Feather-M2 coil.*

interpolation the transverse and normal vectors at position $\ell$ are calculated. In essence an intermediate node is added to Figure 2.22 using Equations

$$\begin{aligned}
\vec{X}(\ell) &= \vec{X}_j + \frac{(\ell - L_j)(\vec{X}_{j+1} - \vec{X}_j)}{L_{j+1} - L_j}, \\
\vec{X}_t(\ell) &= \vec{X}_{t,j} + \frac{(\ell - L_j)(\vec{X}_{t,j+1} - \vec{X}_{t,j})}{L_{j+1} - L_j}, \\
\vec{X}_n(\ell) &= \vec{X}_{n,j} + \frac{(\ell - L_j)(\vec{X}_{n,j+1} - \vec{X}_{n,j})}{L_{j+1} - L_j}.
\end{aligned} \qquad \text{Eq. 2.9}$$

The transformation itself is then defined as

$$\vec{X}(\ell, t, n) = \vec{X}(\ell) + t\vec{X}_t(\ell) + n\vec{X}_n(\ell). \qquad \text{Eq. 2.10}$$

This Equation is valid for any point in the coil pack. In practice it is convenient to translate the inner lower edge of the coil around in $t$ and $n$, while keeping the $L_i$ coordinate of the nodes constant. This vector Equation can easily be implemented without interpolation as

$$\vec{X}_i' = \vec{X}_i + t\vec{X}_{t,i} + n\vec{X}_{n,i}. \qquad \text{Eq. 2.11}$$

For Feather-M2 the Equation needs to be modified to apply the local rotation as a shear to the conductor block, turning its cross-sectional area into a diamond shape varying along the length of the coil. This is achieved by adding an extra shift depending on $t$ in the $n$ direction. The $n$ coordinate is divided by a cosine of the local angle to take into account the increased spacing between the cables when stacked under an angle. The modified Equation then becomes

$$\vec{X}_i' = \vec{X}_i + \vec{X}_{n,i}\left[\frac{n}{\cos\left(a_{\mathrm{rot},i}\right)} + t\tan\left(a_{\mathrm{rot},i}\right)\right] + t\vec{X}_{t,i}\cos\left(a_{\mathrm{rot},i}\right). \qquad \text{Eq. 2.12}$$

To ensure a smooth transition for the layer jump this equation is used to calculate the lower inner edge for the wing deck, by setting $t$ to the difference in $y_{\mathrm{cen}}$ between the two decks and $n$ to zero. When the $y$ coordinate of the wing deck exceeds the height of the beam-pipe it stops following the central deck and a circular coil-end is made to prevent it from intersecting the support cylinder. For the wing deck also a local

coordinate system is set up. The rotation angle $a_{\text{rot}}$ is usually different for the two decks.

To go into further detail the geometry of the cable is constructed. In Figure 2.24 a simplified winding scheme for Feather-M2 is shown. The exercise is necessary to ensure the return-end is symmetric, while the lead-end connects the turns with an increment. Note that the Central Deck is a clockwise spiral while the Wing Deck is anti clockwise. This because the decks are connected on the inside resulting in a current which flows clockwise in both. By starting on the inside and by using Equation 2.12 in one section at a time, the cable's lower inner edge is mapped to the Cartesian coordinates. In the circular section at the lead-end of the coil, the $n$ coordinate is incremented linearly with $d_{\text{cable}} + 2d_{\text{insu}}$, making a smooth transition between the turns. The $t$ coordinate is zero everywhere. This scheme is implemented by running over the individual sections and turns using a loop. Using the same approach as for the winding pack, now also a local coordinate system is set up for the cable. To distinguish between the two, additional subscript $c$ is added to denote that it concerns a cable. This time the individual cables need to be rotated instead of sheared. Therefore the local coordinate system of the cable is rotated using the equations

$$\begin{aligned} \vec{X}'_{c,t,i} &= \sin\left(a_{\text{crot},i}\right)\vec{X}_{c,n,i} + \cos\left(a_{\text{rot},i}\right)\vec{X}_{c,t,i}, \\ \vec{X}'_{c,n,i} &= -\sin\left(a_{\text{crot},i}\right)\vec{X}_{c,t,i} + \cos\left(a_{\text{rot},i}\right)\vec{X}_{c,n,i}. \end{aligned} \tag{Eq. 2.13}$$

After the coordinate system is rotated the layer jump is generated by connecting the two aperture side cable ends of the decks in an S-shape as generated with Equation 2.2. In this operation the local coordinate systems in the layer jump need to be rotated around the x-axis. Additional Gaussian curve can be added in the $x$ direction to move the layer jump away from the coil pack to allow space for the layer jump box. An offset $y_{\text{cen1}}$ is applied to the coils to move them in position. Then the cable geometry is generated using the standard non-sheared Equation 2.11. For Feather-M2, the cable is mirrored anti-symmetrically in the xz-plane, to generate the coils representing the other pole.

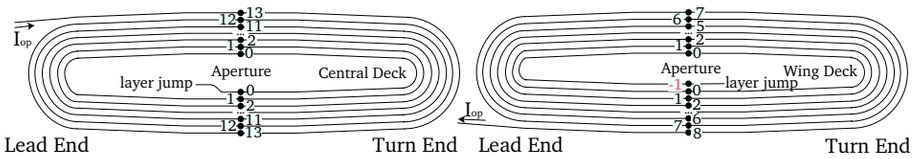


**Figure 2.24.** *Simplified Feather-M2 winding layout showing the numbering of the turns and their respective position in the cross-section of the coil-windings. It can be seen that the layer needs to move inward on the return-end in the central deck in order to connect with the wing deck.*

The resulting geometry and the definition of all geometric parameters is presented in Figures 2.25 and 2.26. Note that these figures show a shorter version of the coil for convenience. The values of the parameters used to define the Feather-M0 and Feather-M2 geometries are presented in Table 2.6. More on Feather-M0 can be found in Section 2.3.5. Because of the present scarcity of Roebel cable, in this coil the straight

section of Feather-M2 is only 100 mm long, which is the minimum required to fit the layer jump (part of the layer jump is located in the curved section). In the figures can be seen how the shape of the profiles is reflected in the coil's geometry. In the front view in Figure 2.27 it can be seen that the whole conductor is contained within the foreseen support cylinder with a wall thickness of 4 mm.

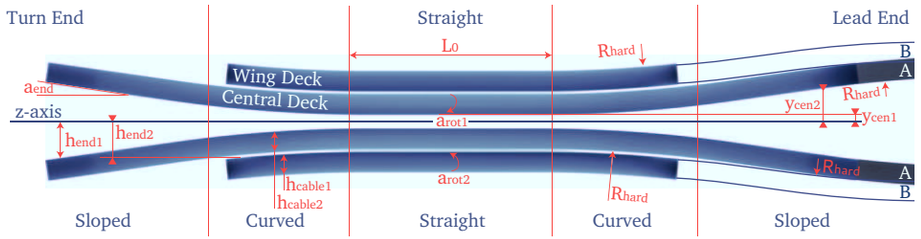


**Figure 2.25.** *Side view on the geometry of the aligned block coil and the definition of its geometric parameters. Respective values for the different coil layouts can be found in Table 2.6. Note that for convenience in the picture the coil-ends are shorter than in the final Feather-M2 coil design.*

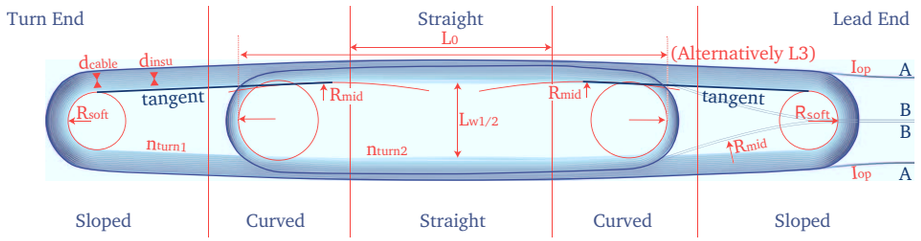


**Figure 2.26.** *Top view on the geometry of the aligned block coil and the definition of its geometric parameters. Respective values for the different coil layouts can be found in Table 2.6. Note that for convenience in the picture the coil-ends are shorter than in the final Feather-M2 coil design.*

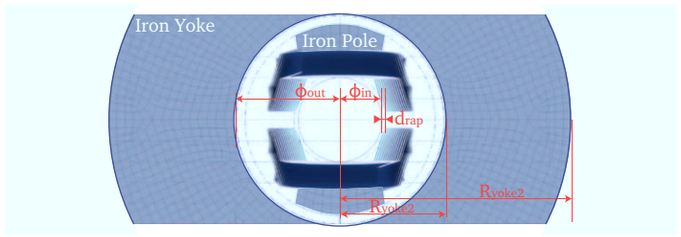


**Figure 2.27.** *Front view on the geometry of the aligned block coil and the definition of its geometric parameters. Respective values for the different coil layouts can be found in Table 2.6. In the picture the yoke has been truncated to save space.*

To complete the geometry the iron poles need to be added. The three-dimensional shape of the iron poles is modeled by extruding the iron cross-section shown in Figure 2.15.

TABLE 2.6.
GEOMETRIC SPECIFICATIONS OF THE THREE-DIMENSIONAL COIL LAYOUTS OF THE FEATHER-M0 AND FEATHER-M2 MAGNETS. PARAMETERS ARE CLARIFIED FURTHER IN FIGURES 2.25 TO 2.27.

| Symbol | Unit | FM0 | FM2 | Description |
|---|---|---|---|---|
| mirror | n.a. | none | anti-xz | mirror feature |
| $\phi_{\text{in}}$ | mm | 40.0 | 40.0 | magnet aperture diameter |
| $\phi_{\text{out}}$ | mm | 99.0 | 99.0 | magnet outer diameter |
| $d_{\text{rap}}$ | mm | n.a. | 2.0 | spacing between aperture and coil |
| $R_{\text{yoke1}}$ | mm | 36.0 | 51.0 | yoke inner radius |
| $R_{\text{yoke2}}$ | mm | 80.0 | 111.0 | yoke outer radius |
| $L_{\text{yoke}}$ | mm | 280.0 | 800.0 | yoke length |
| $d_{\text{cable}}$ | mm | 0.8 | 0.8 | thickness of cable |
| $d_{\text{insu}}$ | mm | 0.1 | 0.1 | thickness of insulation layer |
| $w_{\text{cable}}$ | mm | 12 | 12 | thickness of cable |
| $n_{\text{turn1}}$ | unitless | 5 | $2 \times 12$ | number of turns for central deck |
| $n_{\text{turn2}}$ | unitless | n.a. | $2 \times 6$ | number of turns for wing deck |
| $L_0$ | mm | 40.0 | 100.0 | straight section length |
| $L_3$ | mm | 440.0 | n.a. | enforced coil length |
| $L_w$ | mm | 40.0 | 44.0 | straight section width |
| $L_{co}$ | mm | 440 | 720 | total coil length |
| $y_{\text{cen1}}$ | mm | −6.0 | 3.8 | central deck y-position |
| $y_{\text{cen2}}$ | mm | n.a. | 17.3 | wing deck y-position |
| $h_{\text{req1}}$ | mm | 0.0 | 17.5 | central deck flaring height |
| $h_{\text{req2}}$ | mm | n.a. | 4.0 | wing deck flaring height |
| $a_{\text{end}}$ | deg | 0.0 | 4.0 | angle at end |
| $a_{\text{rot1}}$ | deg | 0.0 | 0.5 | central rotation angle |
| $a_{\text{rot2}}$ | deg | n.a. | 8.0 | wing rotation angle |
| $p_{\text{twist}}$ | unitless | n.a. | 0.6 | rotation angle factor |
| $R_{\text{easy}}$ | mm | 16.0 | 16.0 | easy-way bending radius |
| $R_{\text{mid}}$ | mm | 400 | 400 | medium coil bending radius |
| $R_{\text{hard}}$ | mm | 2000 | 2000 | hard-way bending radius |

TABLE 2.7.
PARAMETERS OF THE FEATHER MAGNET WHEN USING A CABLE THICKNESS DIFFERENT FROM THE ORIGINAL 0.8 mm THICK SP-1 CABLE.

| Symbol | Unit | FM0 | FM0 | FM2 | FM2 | FM2 | FM2 | FM2 | Description |
|---|---|---|---|---|---|---|---|---|---|
| $d_{\text{cable}}$ | mm | 0.8 | 1.7 | 0.8 | 0.9 | 1.0 | 1.1 | 1.2 | bare cable thickness |
| $n_{\text{turn1}}$ | n.a. | 5 | 3 | 13 | 12 | 11 | 10 | 9 | central # of turns |
| $n_{\text{turn2}}$ | n.a. | n.a. | n.a. | 7 | 6 | 6 | 5 | 5 | wing # of turns |
| $\ell_1$ | m | 4.8 | 2.9 | 20.0 | 18.4 | 16.9 | 15.3 | 13.8 | central cable length |
| $\ell_2$ | m | n.a. | n.a. | 6.0 | 5.2 | 5.2 | 4.4 | 4.4 | wing cable length |
| $\ell_{\text{leads}}$ | m | 1.2 | 1.2 | 2.0 | 2.0 | 2.0 | 2.0 | 2.0 | leads cable length |
| $\ell_{\text{total}}$ | m | 6.0 | 4.1 | 28.0 | 25.6 | 24.0 | 21.7 | 20.1 | total cable length |
| $L_{\text{self}}$ | $\mu$H | 10.4 | 3.8 | 450 | 370 | 320 | 260 | 220 | self inductance |
| $M_{\text{fr2}}$ | $\mu$H | n.a. | n.a. | 1320 | 1180 | 1100 | 980 | 900 | mutual inductance |

Towards the coil-ends, the width of the iron poles is reduced, such that a clearance of 4 mm with respect to the conductor is maintained (see Figure 2.28 and Figure 2.30). At the coil-ends the iron pole is as close as possible to the windings to straighten out the magnetic field. For the same reason extra pole pieces are added at the ends of the central deck. However at the lead-end the piece may be in the way of the current lead for the wing deck. When proven to be unfeasible the pole can be removed at the cost of slightly worse field angle of about half a degree and thus lower margin on the load-line. In stand-alone mode an additional iron yoke, with inner radius 51 mm and outer radius 111 mm is added, which functions as a flux return and straightens out the field. The yoke is 800 mm long covering the coil-ends to help straighten out the magnetic field in these regions. Note that in LTS magnets the yoke usually is shorter not covering the coil-ends to reduce the peak field.

The magnetic field is calculated using a Biot-Savart Multi-Level Fast Multipole Method (MLFMM) [83], which is part of Field 2016. The magnetic field contribution due to the magnetization of the iron is calculated using the Roxie Boundary Element Method coupled with the Finite Element Method (BEM-FEM) [121]. Later the calculation is verified by using Opera. The calculated magnetic field on the surface of the conductor, the coil geometry and the iron poles, when operated as insert in a uniform 13 T background field, is shown in Figure 2.28. Additionally, a series of cross-sections showing the magnetic field magnitude and direction, are provided in Figure 2.30. It can be seen that the magnetic field is highest in the straight section of the coil, in which the iron poles cause an increase of the magnetic field. The corresponding angle of the magnetic field with respect to the broad face of the cable can be calculated using $\arctan\left(B_n/\sqrt{B_t^2+B_\ell^2}\right)$, where $B_n$ is the magnetic field in the normal direction calculated as $\vec{B}\cdot\vec{X}_{c,n}$, $B_h$ the magnetic field in the transverse direction of the cable calculated as $\vec{B}\cdot\vec{X}_{c,t}$ and $B_\ell$ the magnetic field in the longitudinal direction of the cable calculated as $\vec{B}\cdot\vec{X}_{c,\ell}$. The calculated field angles on the surface of the conductor are presented in Figure 2.29. To minimize the magnetic field angle along the cable a proper value for the rotation parameter $P_{\text{twist}}$ was determined iteratively using an optimizer. The value chosen is 0.6. It can be seen that the largest angle of 14 deg is located at the edge of the cable in the coil-ends. At each position along the cable there is a point where the magnetic field angle is zero. The field angle averaged over the cross-section of the cable is less than 4 deg throughout its full length. The critical current at 4 deg and 20 T is estimated at 25 kA. When ramping along the load-line the magnetic field angle changes depending on the current. This causes the real short sample critical current to be lower.

### Sub-Scale Coil Feather-M0 2.3.5

Since the conductor and the proposed type of magnet is still new it is recommended to start tests with a less complex geometry. This allows for testing coil-winding, impregnation and quench detection and protection systems without risking long lengths of expensive cable. The sub-scale coil is named Feather-M0 and is a 400 mm long single racetrack coil. Because in a single racetrack the cable is already aligned as best as

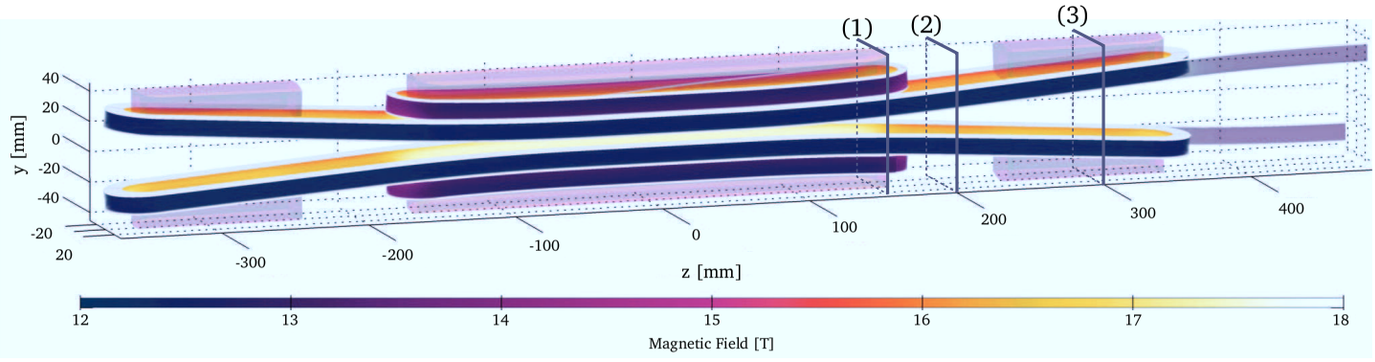


**Figure 2.28.** *Magnetic field magnitude shown, using a color map, on the surface of the conductor of Feather-M2 when inserted in a uniform background field of* 13 T. *Magnetic field (lines) in the numbered cross-sections are presented in Figure 2.30.*

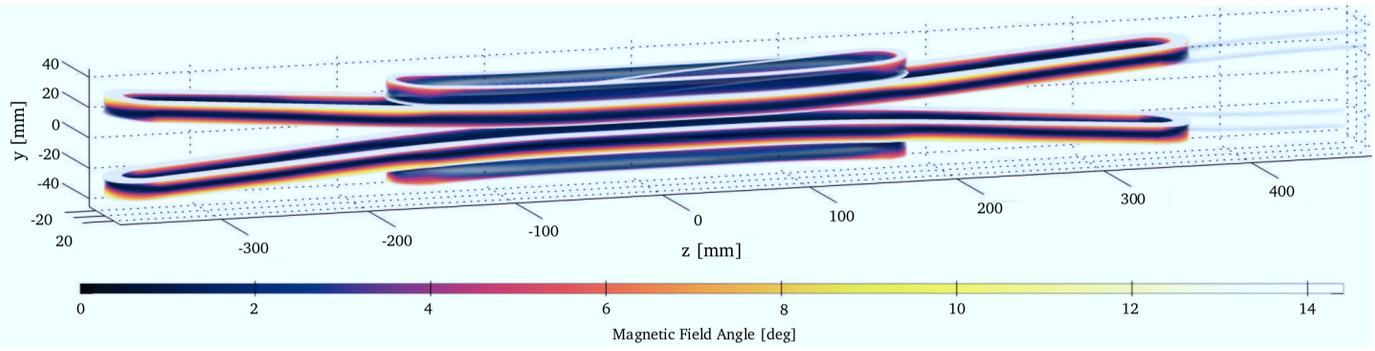


**Figure 2.29.** *Incident magnetic field angle shown, using a color map, on the surface of the conductor of Feather-M2 when inserted in a uniform background field of* 13 T. *A band of zero degree field angle runs along the length of the cable.*

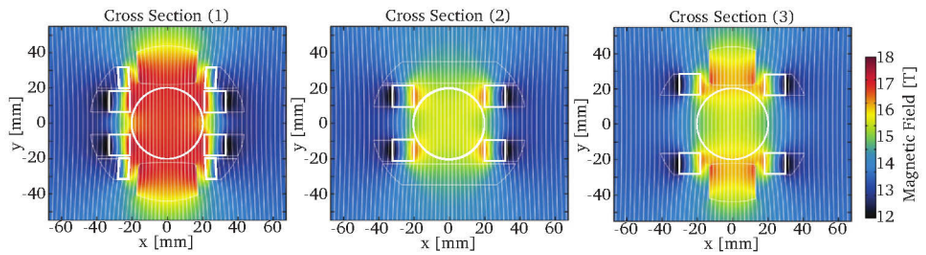


**Figure 2.30.** *Various cross-sections of Feather-M2, showing the calculated magnetic flux density and the magnetic field lines. The location of the cross-section with respect to the magnet is shown in Figure 2.28.*

possible with the background field that is present, no additional rotation of the cable is required. To make the coil layout representative for Feather-M2 the same bending radii are used. Also a layer jump is present which is needed to allow the current lead to exit the coil. The conductor layout of the Feather-M0 magnet is generated using the same equations as for Feather-M2. The geometry and definition of parameters is shown in Figure 2.31. The corresponding values defining the geometry can be found in Table 2.6. The first Feather-M0.4 is tested with the BHTS-1 cable (see Table 2.1) which is 1.7 mm thick. In Table 2.7 the specifications for the different cable thicknesses can be found. Because the magnet, including a support cylinder, is small enough to fit inside the Fresca1 bore, it can also be tested in a background field of approximately 8.5 T (see Figure 2.32), taking the peak field on the conductor to about 10 T. The average field angle is zero, but on the edges of the conductor, the location where the magnetic field angle is highest, the field angle is around 7 deg (see Figure 2.33).

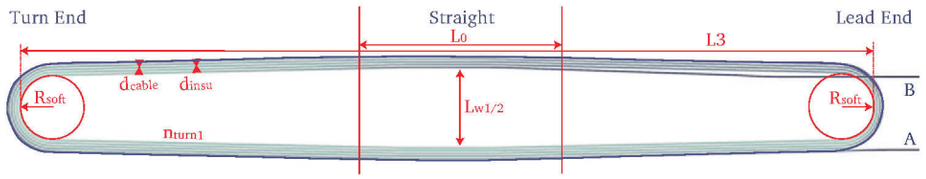


**Figure 2.31.** *Top view on the geometry of the Feather-M0 coil. Respective values for the different coil layouts can be found in Table 2.6.*

## Three-Dimensional Critical Current Calculation 2.3.6

Due to the angle dependence of the conductor and the current redistribution inside the tapes, the calculation of the critical current is not straight forward. For a more detailed study the Electro-Magnetic and Thermal Network Model, as described in Chapter 3, is used. Using the coordinate transformation described in Equation 2.11, the coordinates of the nodes and elements are mapped onto the coils (see Figure 2.34). Multiple methods for calculating the critical current from the geometry of the coil are proposed. The

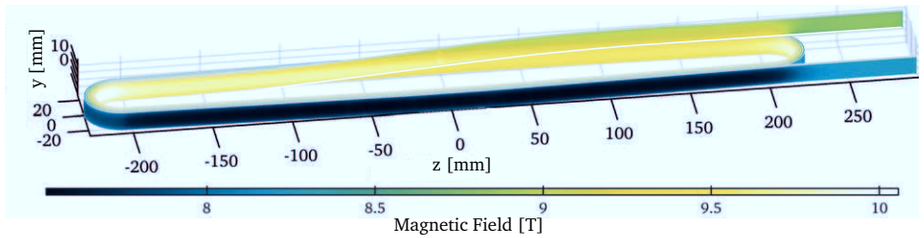


**Figure 2.32.** *Magnetic field on the surface of the conductor, represented using a color map, for Feather-M0 when operated at* 6 kA *in a uniform background field of* 8.5 T.

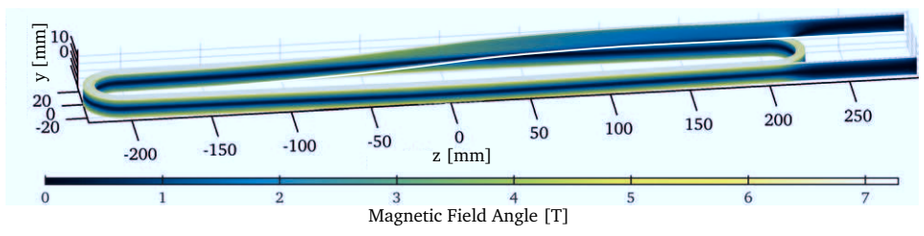


**Figure 2.33.** *Magnetic field angle on the surface of the conductor, represented using a color map, for Feather-M0 when operated at* 6 kA *in a uniform background field of* 8.5 T.

specifications of the two magnets including the calculated values for the critical current are given in Table 2.8. The first critical current $I_{c,\mathrm{I}}$ assuming conservatively that no current sharing can occur and that the current is limited by the lowest $J_c$ anywhere in the coil, can be calculated as

$$I_{c,\mathrm{I}} = \sum_{p}^{N_s} \min_{j} \left( W_r \min_{i} \left( J_{cel,p,i,j} \left( \left| \vec{B} \right|, \alpha, T \right) \right) \right), \qquad \text{Eq. 2.14}$$

where $J_{cel,p,i,j}$ is the critical current of the longitudinal elements (see Figure 3.1), where $p$ indexes into the tapes making up the cable, $i$ into the elements over the width of the tape and $j$ into the elements over the length of the tape (note that unit cell index $c$ is not used here, resulting in $j$ to run over the full length of the cable). This critical current is calculated by setting a homogeneous current density in the tapes, corresponding to an operating current $I_{cable}$, from which the required magnetic field $\vec{B}$ and field angle $\alpha$ are calculated at each element.

A temperature of 4.5 K is assumed, the boiling point of liquid helium. The cable current $I_{\mathrm{cable}}$ is increased until it matches the critical current $I_{c,\mathrm{I}}$. In this operation the magnetic field and its angle is recalculated every increment. The second critical current $I_{c,\mathrm{II}}$ assumes that current re-distribution can occur within the tape but not between the tapes. This is a logical assumption since the tapes, unless striated, are fully superconducting. Again a homogeneous current distribution is assumed for the magnetic field calculation. However this time the critical current is integrated over the width of each tape.

TABLE 2.8.
OPERATIONAL SPECIFICATIONS FOR FEATHER-M0 AND FEATHER-M2 WHEN OPERATED AT 4.2 K ASSUMING THE SP-1 CABLE (SEE TABLE 2.1).

| Symbol | Unit | FM0-sa | FM2-sa | FM0-bg | FM2-bg | Description |
|---|---|---|---|---|---|---|
| outsert | n.a. | Yoke | Yoke | Fresca | Fresca-2 | outsert magnet |
| $B_{bg}$ | T | 0.0 | 0.0 | 8.5 | 13.0 | background field |
| $B_{cen}$ | T | 1.5 | 5.0 | 9.2 | 16.9 | field in aperture |
| $P_{coil}$ | MPa | 4 | 17 | 23 | 110 | coil pressure |
| $I_{op}$ | kA | 6.00 | 7.92 | 6.00 | 8.14 | cable operating current |
| $J_{block}$ | A/mm$^2$ | 491 | 649 | 491 | 667 | block op. cur. density * |
| $J_{cable}$ | A/mm$^2$ | 625 | 824 | 625 | 847 | cable op. cur. density * |
| $I_{c,\mathrm{I}}$ | kA | 11.3 | 10.3 | 10.6 | 8.5 | first short sample † |
| $I_{c,\mathrm{II}}$ | kA | 14.0 | 11.8 | 13.2 | 11.6 | second short sample † |
| $I_{c,\mathrm{III}}$ | kA | 16.1 | 14.2 | 14.9 | 13.9 | third short sample † |
| $I_{c,el}$ | kA | 13.8 | 11.7 | 11.8 | 12.0 | electrical model s.s. † |

∗ the difference in block and cable current density is the insulation area
† see Section 2.3.6 for expanded explanation

The lowest values of all tapes are added to find the short sample current of the cable. The calculation is following

$$I_{c,\mathrm{II}} = \sum_{p}^{N_s} \min_{j} \left( \sum_{i}^{N_{et}} W_{12,el,p,i,j} J_{cel,p,i,j} \left( \left| \vec{B} \right|, \alpha, T \right) \right), \qquad \text{Eq. 2.15}$$

where $W_{12,el,p,i,j}$ is the width of the longitudinal elements, with the same indexing as $J_{cel,p,i,j}$. The third critical current $I_{c,\mathrm{III}}$ assumes full current sharing in and between the tapes. This can only occur if the contact resistance between the tapes is very low and is therefore likely an overestimate for ReBCO. It is calculated by integrating the critical current density over the cross section of the cable, after which the lowest value along its length is selected. This is defined as

$$I_{c,\mathrm{III}} = \min_{j} \left( \sum_{p}^{N_s} \sum_{i}^{N_{et}} W_{12,el,p,i,j} J_{cel,p,i,j} \left( \left| \vec{B} \right|, \alpha, T \right) \right). \qquad \text{Eq. 2.16}$$

To achieve a more realistic result the critical current of the cable can also be calculated using the steady-state solution of the Electro-Magnetic and Thermal Network Model (as described in Section 3.5.1). This critical current is given as $I_{c,el}$. The resistance of the contact elements between the tapes is set to 0.29 $\mu\Omega$m$^2$ [122]. The magnetic field contribution of the iron poles is again calculated using the Roxie BEM-FEM in the form of a set of field maps, which when solving are then interpolated at the cable current.The electrical currents inside all elements and the voltages at the nodes are then calculated. The main difference with the other solutions is that the current is no longer distributed homogeneously over the tapes, causing the magnetic field and its angle to be slightly

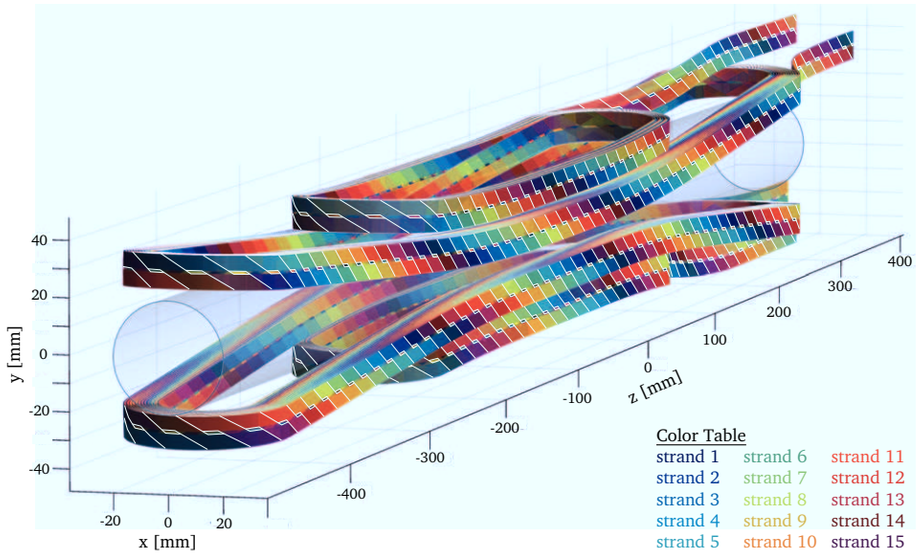


**Figure 2.34.** *Roebel cable with SP-1 cable parameters mapped onto the Feather-M2 geometry using a coordinate transformation. Visible are the individual tapes, each shown with a different color.*

different from the homogeneous case. The calculation is performed at several cable currents after which the critical current is determined by fitting the relation between the electric field and the current, using a power law with an electric field criterion of $10\,\mu\mathrm{V/m}$. A critical current of about 12.0 kA is found for both stand-alone and insert modes. This result is, as expected, in best agreement with $I_{c,\mathrm{II}}$. It is still to be analyzed (see Section 2.4) whether this current would be acceptable in terms of quench protection.

### 2.3.7 Insert Operation Inside Fresca2

The Feather-M2 magnet is designed to operate in the bore of the Fresca2 magnet. Of interest is the magnetic peak field enhancement of the Fresca2 magnet when the Feather-M2 is operated as insert. If the magnetic peak field of the outsert increases it is more likely to quench. Also an increment of the peak magnetic field indicates that the forces on the outsert magnet are increased. In order to study the combination of both magnets in detail a three-dimensional Cobham Opera model is made, in which the Fresca2 model is combined with the windings and iron pole pieces of the Feather-M2 model, that are exported from Field 2016. The magnetic field magnitudes in a vertical longitudinal cross-section and for a cross-section on the straight section of the coil are presented in Figure 2.35. For Fresca2 alone the peak magnetic field is 13.30 T, when operated at a central field of 13.00 T. For a combination of Fresca2 and Feather-M2 the peak magnetic field on Fresca2 is found slightly lower at 13.27 T, which indicates there

is almost no change. In both cases the peak magnetic field is located in the straight section.

## Simple Quench Analysis 2.4

*A simple quench analysis is presented of the Feather-M2 conductor, using a one-dimensional model. In addition an adiabatic model is used to estimate the effectiveness of the protection system in combination with the Inductively Coupled Energy Dissipation (ICED) copper loops. The models described in this section were used during the design of the magnet. A more detailed analysis, including the dynamic effects in the multi-strand cable, which was performed at a later time is described in Chapter 5.*

### One Dimensional Temperature Profiles 2.4.1

To model the quench a one dimensional finite difference method is used, previously validated experimentally in [123]. The model uses a series of temperature nodes indexed with $i$ connected with thermal resistors (see Figure 2.36). The temperature and position of the nodes along the tape are given as $T_i$ and $x_i$ respectively. Because the current can only follow one path, it is equal to the operating current $I_0$ for all elements and does not need to be evaluated. This makes the model run an analysis in a few seconds, making it suitable for parametric studies.

In the model the change of the temperature is calculated using a discretized heat balance equation given as

$$C_p(T_i)\frac{dT_i}{dt} = \overbrace{k\left(\frac{T_i+T_{i-1}}{2}\right)\frac{T_{i-1}-T_i}{x_i-x_{i-1}}}^{\text{Heat to Previous Node}} + \overbrace{k\left(\frac{T_{i+1}+T_i}{2}\right)\frac{T_{i+1}-T_i}{x_{i+1}-x_i}}^{\text{Heat to Next Node}} + P_i, \qquad \text{Eq. 2.17}$$

where $C_p(T)$ is the temperature-dependent heat capacity in J/mK and $k(T)$ the temperature-dependent thermal conductivity in Wm/K. Note that in the equation the terms between brackets are actually the temperature input of these functions. The temperature dependent material property interpolation tables are generated using CryoComp [124] and magneto resistance is included in the model (copper RRR is 150). Because the heat transfer occurs between the nodes the average temperature between the nodes is used for this property. $P_i$ is the power dissipation at node $i$, which is given as

$$P_i = \overbrace{\rho(T_i)\, I_{nc}\left(I_0, T_i, \left|\vec{B}\right|, \alpha, N\right)^2 \frac{x_{i+1}-x_{i-1}}{2}}^{\text{Ohmic Heating}} - \overbrace{h(T_i - T_{bath})\frac{x_{i+1}-x_{i-1}}{2}}^{\text{Cooling to Surroundings}} + P_{qh,i}(t), \qquad \text{Eq. 2.18}$$

where $\rho(T)$ is the temperature-dependent electrical resistivity in Ω/m (per meter cable). To calculate the normal conducting current the current sharing model described in Section 3.3.8 by Equation 3.49 is used. This equation needs, in addition to the temperature, the current $I_0$, the magnetic field $B_0$, its angle with respect to the tape surface $\alpha_0$ and the $N$ value, which is around 30 for ReBCO. A cooling term $h$, which

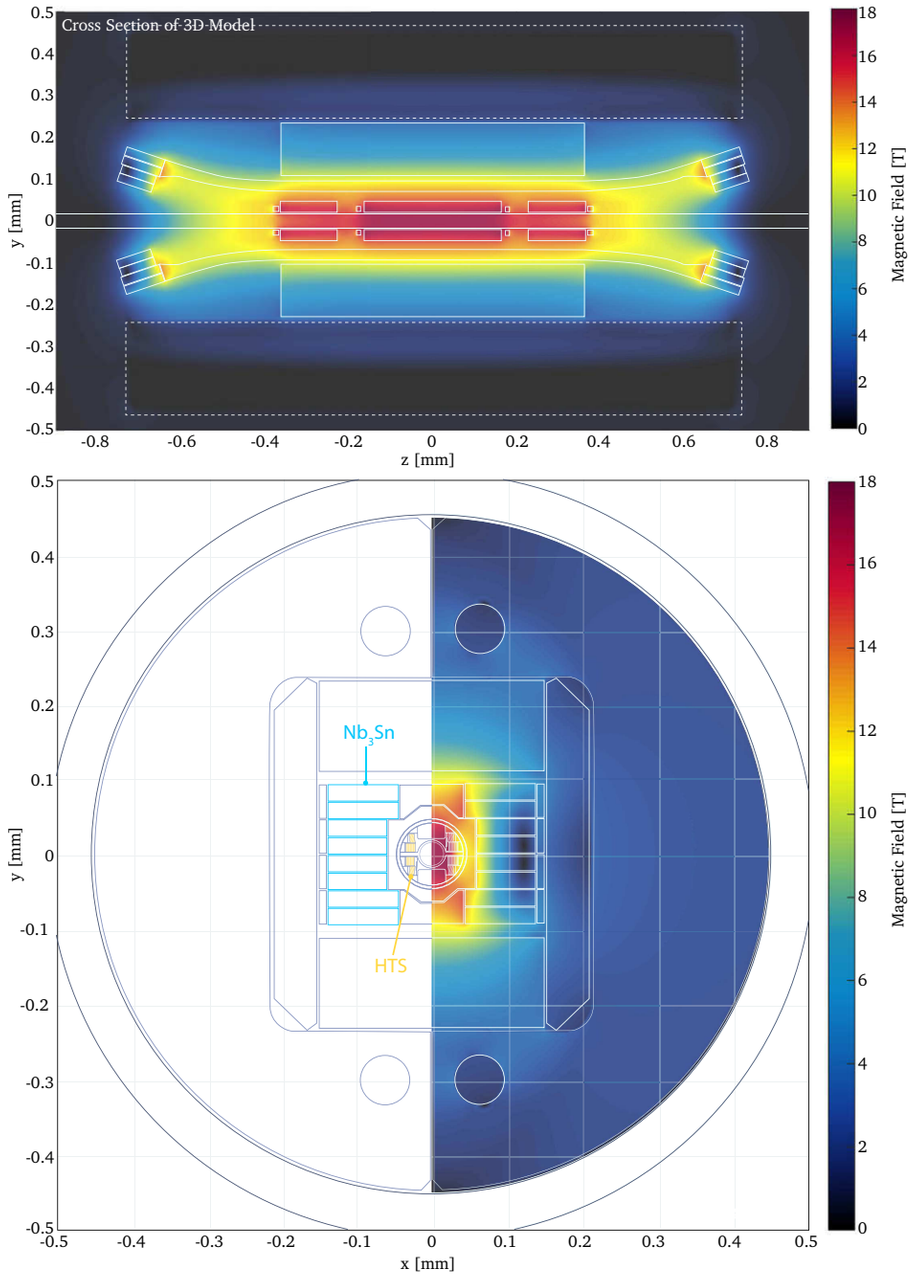


**Figure 2.35.** *Cross-section of the yz-plane at $x = 0$ (top) and cross-section of the xy-plane at $z = 0$ (bot), showing the calculated magnetic field magnitude of the three-dimensional Cobham Opera model of Feather-M2 integrated in Fresca2. The contribution to the central field by Fresca2 is* 13.0 T *(design field) and the contribution of Feather-M2 is* 3.9 T *(design field) resulting in a total magnetic field in the aperture of* 16.9 T.

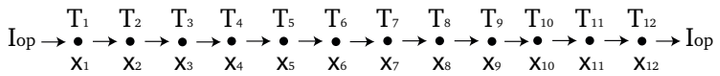


**Figure 2.36.** *One dimensional network model for quench analysis.*

represents the cooling to the surrounding material, can be included and is given in units of Watt/(Km).

To get an accurate description of the normal zone in HTS it is found that 401 equally spaced nodes are needed over a length of 400 mm (in the profile plots only the central part is shown). To initiate the quench a square heat pulse is deposited at the central node $i = 200$, with a typical duration of 10 ms, while the deposited energy is set using the peak value. To find the temperature profile as function of time $T_i(t)$, the $dT_i/dt$ needs to be evaluated and integrated using finite time steps. Because thermal problems are so called stiff differential equations [125], making them unstable when doing straight forward leap-frog integration (unless the time steps are very small), the Matlab *ode15s* solver, which is stabilized for these kind of problems, is used to perform the integration.

To make an estimate of the development of a quench in the Feather-M2 coil a single tape is modeled. Here the assumption is made that all tapes in the cable are hit in the same spot at the same time. For this scenario no current sharing between the tapes occurs. The magnetic field angle is set at 84 deg, the magnetic field to 20 T, the current density in the tape is 970 A/mm$^2$ (which corresponds to 8 kA in the cable). The tape consist of a 50 $\mu$m substrate and 40 $\mu$m of copper (the remaining 10 $\mu$m is unspecified). A heater pulse of 50 mJ is used to initiate the quench. The cooling term is not used in this case. The resulting transient evolution of the temperature profile along the length of the cable is presented in Figure 2.37. The length of the normal zone $\ell_{nz}$ is given as

$$\ell_{\mathrm{nz}}(t) = \sum_{T_i(t)>T_t} \frac{x_{i+1} - x_{i-1}}{2}, \qquad \text{Eq. 2.19}$$

from which the normal zone propagation velocity is derived as $V_{\mathrm{nzp}}(t) = 0.5 d\ell_{\mathrm{nz}}(t)/dt$. The velocity stabilizes at 370 mm/s after an initialization transient, which depends on the amplitude of the heat pulse. The peak temperature $\max(T_i)$ reaches 300 K in 45 ms, which starts to become challenging for the quench detection and protection system (compared to LTS where 50 to 100 ms is a common reaction time).

Since the amount of conductor within the available space is already maximized in the Aligned Block geometry, it is not possible to reduce the current density, or increase the copper fraction in the coil blocks without reducing the operating field. The initialization of the quench is perhaps not realistic, because the amount of energy needed to raise the temperature of the conductor over the current sharing temperature $T_{cs}$ is quite significant. The only likely source that can supply this energy in such a short time is resistive heating due to sudden mechanical damage to one or more tapes, which should not happen. Therefore it is more realistic that the energy is supplied over a larger time,

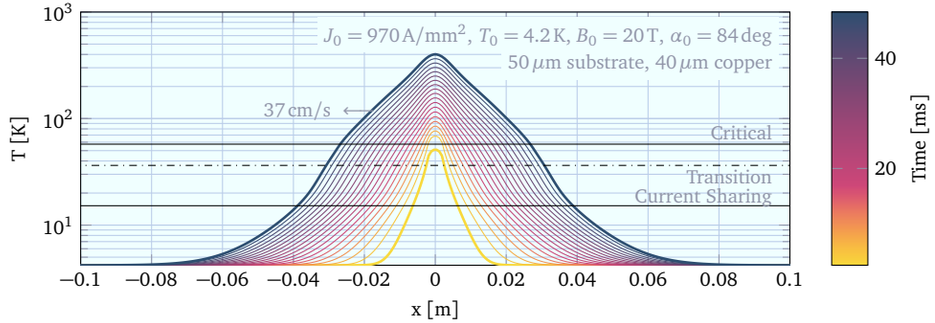


**Figure 2.37.** *Calculated one-dimensional temperature profiles of normal zone propagation in a SuperPower coated conductor with a substrate thickness of* 50 $\mu$m*. Operational conditions, denoted in the graph, are the same as in the Feather-M2 coil. The normal zone propagation velocity derived from the temperature profiles is* 370 mm/s*.*

for example due to joint heating. This means that the conductor temperature drifts away from the bath temperature, an event that can stretch over many seconds or even minutes. During this drift phase, also refer to Section 5.2.2, no significant voltage is present over the cable. When the temperature drifts over $T_{cs}$, the temperature suddenly rapidly increases. This sparked the idea of including many different types of detection systems to determine whether it is possible to detect the initialization of the normal zone.

To provide multiple opportunities to learn setting up the detection system, without damaging the conductor on the first attempt, it is decided to test the magnet at variable temperature, starting at 77 K. At higher temperature the critical current of the coil is much lower (a factor 5 between 4.5 and 77 K). Because the resistive heating scales with the operating current squared, much more time is available for the protection systems to react. By reducing the temperature in steps unexpected events can hopefully be avoided. In addition, to predict signals coming from the detection systems, amongst other things, a Thermal part was added to the Electro-Magnetic Network Model presented in Chapter 3. Using this model the initialization of a normal zone in a multi-strand cable is studied in Chapter 5.

### 2.4.2 Copper Layer Thickness Versus Reaction Time and Stability

When a quench occurs the current is diverted through the copper layer, electroplated around the bare tape for this purpose. Because copper has a relatively high electrical conductivity, the amount of resistive heating is significantly reduced. The added heat capacity slows down the temperature rise. The increased thermal conductivity spreads out the heat over the length of the conductor. These effects increase the stability of the tapes and thus result in an increase of the reaction time. However, the addition of copper also cause a reduction of the engineering current density, which in turn reduces the thermal margin. This makes the thickness of the copper layer an interesting parameter

in the design of the conductor (also see [126]). The one-dimensional quench model is used to study the effect of the copper thickness on the reaction time under Feather-M2 conditions and the results are presented in Figure 2.38. The reaction time is defined as the time it requires the conductor to reach 300 K from the moment the peak temperature exceeds the critical temperature $T_c$ (to avoid the initialization transients of the quench to be included). In the graph thickness is defined as the total thickness including the layers on both sides of the tape. The results are shown for different thicknesses of the substrate, because this determines the fraction of copper in the conductor. It can be seen that a low substrate thickness is favorable, because the copper fraction in the strands is higher. The study is performed at various overall current densities in the tape (denoted by numbers in the graph).

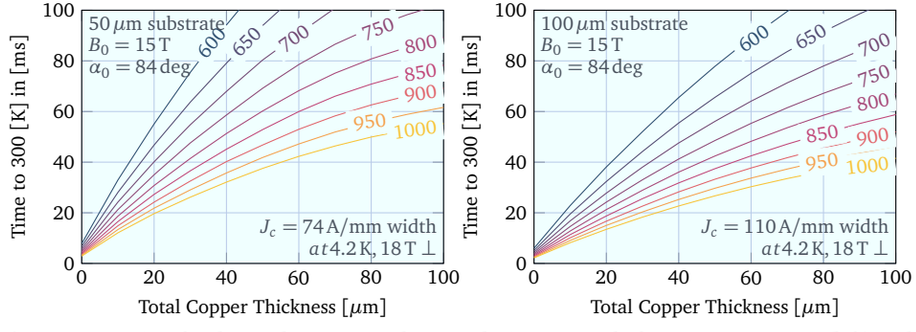


**Figure 2.38.** *Time for the conductor to reach* 300 K *during a quench, for SuperPower tape (left) and Bruker tape (right), with substrate thicknesses of* 50 $\mu$m *and* 100 $\mu$m *respectively, given as function of the copper thickness at various overall current densities (denoted by colored numbers).*

To find the Minimum Quench Energy (MQE), a simple search algorithm is used. A lower $E_{\text{low}}$ and higher $E_{\text{high}}$ estimate for the MQE are pre-set. These do not necessarily have to be the limits. First the algorithm tests if a quench does occur at $E_{\text{high}}$. The definition of a quench is here that the time derivative of the peak temperature at the last time step is positive. If it does not $E_{\text{low}}$ is set at $E_{\text{high}}$, after which $E_{\text{high}}$ is doubled. This step is repeated until a quench is found. If $E_{\text{high}}$ is correct the first time, the lower limit is checked. If a quench occurs at the lower limit, $E_{\text{high}}$ is set at $E_{\text{low}}$ and $E_{\text{low}}$ is halved. This step is repeated until no quench occurs at the lower limit. After these steps the MQE lies in the interval $\left[E_{\text{low}}, E_{\text{high}}\right]$. Then the model evaluates the occurence of a quench at $\left(E_{\text{low}} + E_{\text{high}}\right)/2$. If a quench occurs the higher limit is shifted to this energy, if it does not, the lower limit is shifted. The process is repeated until the difference between the higher and lower limit is less than a pre-set value. The resulting MQE values are shown as function of copper thickness and operating current density in Figure 2.39. It can be seen that an optimum exists around 40 $\mu$m, which shifts slightly with the current density. This optimum is caused by the balance between two effects, on the low side the heat capacity is too low and at the high end the margin is too small. It must be noted that the position of the optimum depends on the critical current of the tape and the operating conditions $B_0$ and $\alpha_0$. When relying on the stability and

Pre-Quench detection it is likely better to maximize the MQE over reaction time. For Feather-M2 the standard copper layer thickness of $2 \times 20\,\mu$m is close to the optimum.

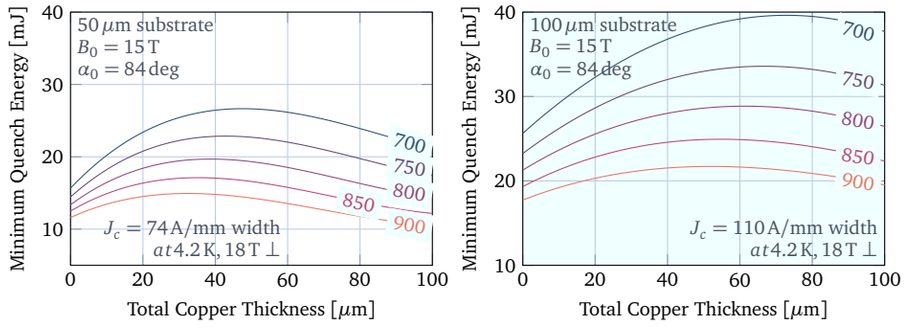


**Figure 2.39.** *Minimum Quench Energy per tape (*5.5 mm *width), for SuperPower tape (left) and Bruker tape (right), with substrate thicknesses of* 50 $\mu$m *and* 100 $\mu$m*, respectively, given as function of the copper thickness at various overall current densities (denoted by colored numbers).*

### 2.4.3 Protection of Feather-M2 in Stand-Alone and Insert Mode

During the testing of a high field HTS solenoid, constructed with ReBCO tapes, at Brookhaven National Laboratory [127], it was found that when the dump resistor was switched in to protect the magnet, the current was inductively transferred to a series of copper rings, that were included in the coil pack for providing additional cooling. This resulted in the current in the coils being reduced faster, thereby helping to protect the magnet. This idea inspired to purposely add Inductively Coupled Energy Dissipation (ICED) rings into the Feather-M2 magnet [98]. These resistive rings are located around the coil pack (see Section 2.5) filling up otherwise unused space. Similarly to the rings in the Brookhaven solenoid, these rings provide conductive cooling to the coil-windings and act as a transformer, extracting the current from the coil in the case of a fast dump. This effect is essentially the same as the quench-back often used to protect solenoids. To study the dynamics of the quench protection in the coil system, consisting of Fresca2, Feather-M2 and the ICED rings, a straight forward adiabatic model is used. In this model the longitudinal heat transfer terms are omitted in Equation 2.17 reducing the conductor to a single node, thereby creating a worst case scenario. In practice this kind of model leads to an estimated peak temperature, which is about 10 to 30% higher than in the non-adiabatic case. The adiabatic model was validated using experimental data from the LHC type MQM and MQY [128, 129] insertion magnets and was subsequently used for the design of many other magnets.

The model numerically solves the time dependent evolution of the peak temperature of the quenching coil $T_{\text{peak}}$ and the bulk temperature of all coils $T_{i,\text{bulk}}$. These coils can also include the ICED rings, which start at zero current and have no superconducting properties. At the start of the model only the peak temperature rises, until the voltage over the normal zone given as $V_{\text{qd}} = tV_{\text{nzp}}I_{\text{op}}(t)\rho\,(T_c)$ exceeds the quench detection

threshold (10 or 100 mV). The normal zone propagation velocity is calculated using an analytic Equation [4]. After a set validation of 5 ms for Feather-M2 or 20 ms for Fresca2, it is assumed that this large coil generates more noise, the protection systems are deployed. For both Feather-M2 and Fresca2 a dump resistor, which causes 1.0 kV over the coils, is switched in with a delay of 10 ms. In addition the Fresca2 coil is also protected using a dedicated heater, which heats 80% of the coil-windings over the critical temperature within 40 ms. The resulting current decay is calculated using the inductance matrix $M_{ij}$ of the system and the resistance $R_i$ of the bulk. The matrix contains the self and mutual inductances between all coils and is calculated using Field 2016. The matrix used for the calculations in this Section is given in Table 2.9 and the indexing of the ICED rings is shown in Figure 2.46. In the cases, in which not all components are present, the corresponding rows and columns can be omitted from the matrix. The current decay is then given as

$$M_{ij}\frac{dI_i}{dt} = V_i = I_i R_i, \qquad \text{Eq. 2.20}$$

which is solved every time step for $dI_i/dt$ using Matlab's *backslash* operator. Again the *ode15s* solver is used to integrate the change of temperature and the change of current over time, resulting in the transient evolution of the coil currents and temperatures.

TABLE 2.9.
CALCULATED INDUCTANCE MATRIX OF THE FEATHER-M2 (FM2) MAGNET INSERTED IN FRESCA2 (FR2), USED FOR THE QUENCH ANALYSIS. SELF-INDUCTANCES OF THE COILS ARE DENOTED IN MAGENTA. NOTE THAT IN THE MATRIX VARIOUS DIFFERENT UNITS ARE USED.

| | FR2 | FM2 | R1.1 | R1.2 | R2.1 | R2.2 | R3.1 | R3.2 |
|---|---|---|---|---|---|---|---|---|
| FR2 | 89.3 mH | 1.31 mH | 34.96 μH | 34.96 μH | 17.58 μH | 17.58 μH | 18.45 μH | 18.45 μH |
| FM2 | 1.31 mH | 0.45 mH | 13.11 μH | 13.11 μH | 6.64 μH | 6.64 μH | 4.64 μH | 4.64 μH |
| R1.1 | 34.96 μH | 13.11 μH | 0.71 μH | 0.19 μH | 0.19 μH | 80.4 nH | 0.12 μH | 60.1 nH |
| R1.2 | 34.96 μH | 13.11 μH | 0.19 μH | 0.71 μH | 80.5 nH | 0.19 μH | 60.1 nH | 0.12 μH |
| R2.1 | 17.58 μH | 6.64 μH | 0.19 μH | 80.5 nH | 0.37 μH | 51.3 nH | 0.24 μH | 39.9 nH |
| R2.2 | 17.58 μH | 6.64 μH | 80.4 nH | 0.19 μH | 51.3 nH | 0.37 μH | 39.9 nH | 0.24 μH |
| R3.1 | 18.45 μH | 4.64 μH | 0.12 μH | 60.1 nH | 0.24 μH | 39.9 nH | 0.41 μH | 32.3 nH |
| R3.2 | 18.45 μH | 4.64 μH | 60.1 nH | 0.12 μH | 39.9 nH | 0.24 μH | 32.3 nH | 0.41 μH |

First the Feather-M2 in stand-alone operation is studied. This case includes the magnet and six loops, three for each pole. A dump resistor of 125 mΩ is used which corresponds to 1.0 kV at $I_0$. The calculated current and temperatures as function of time are presented in Figure 2.40. It can be seen that the quench protection triggers at 15 ms after the start of the quench. After the validation time the dump resistor switches in and the majority of the current is transferred to the rings in about 1 ms, causing a current spike in the largest ring of 60 kA. The total ring current is 223 kA, which is about 67% of the total coil current calculated as $2N_t I_{op} = 332$ kA. The peak temperature reached is 255 K. The temperature of the rings reaches about 70 K, which represents the en-

ergy extracted from the coil. The average temperature of the magnet does not increase because it is purposely not covered by a heater.

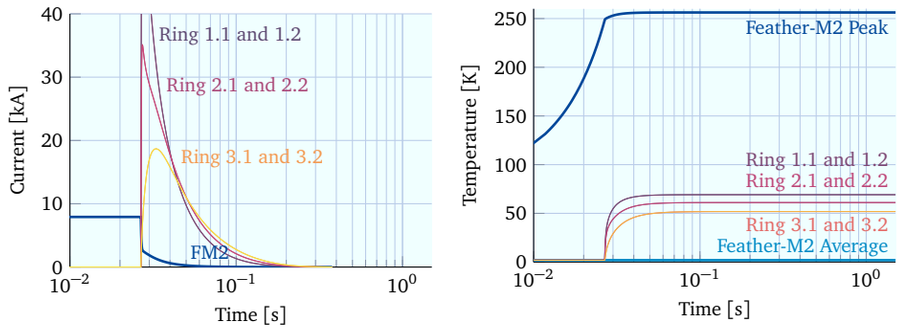


**Figure 2.40.** *Calculated current decay (left) and temperature rise (right) for a quench in Feather-M2 when operated in stand-alone mode. The quench detection trigger voltage is* 100 mV *with an integration time of* 5 ms*. After the quench protection is triggered, a dump resistor of* 126 mΩ *(*1000 V *at* $I_0$*) is switched in after a delay of* 10 ms*.*

The material of the ring determines its resistance and also its effectiveness. The current decay with and without ICED rings, made of copper with an RRR of 150 or aluminum with a very high (not realistic) RRR of 2000, is presented in Figure 2.41. The current decay without rings is 10 ms, which is 10 times slower than with protection ring. Unfortunately the reduction of the peak temperature is only 10 to 20 K, this is because the peak temperature is mainly determined by the quench detection time. However for future long accelerator magnets (operated in series), with high self-inductance, this probably shifts to the time to dump the current, making the rings much more effective. In order to test the idea at this point they are included in the design. As an additional advantage the highly thermal conductive rings provide cooling and heat capacity to the coil pack. aluminum is more effective for transferring the current, but copper has a volumetric heat capacity which is $\sim 2.4$ times higher than aluminum, $67\,\mathrm{kJ/(m^3K)}$ versus $28\,\mathrm{kJ/(m^3K)}$. Since the thermal contraction of copper matches better to the thermal contraction of the coil, for the first coils it was decided to use copper rings.

When the coil is operated as insert in a background field one of the concerns is that when the current in Fresca2 decays, its current is also transferred into the rings causing them to overheat, or into Feather-M2 causing it to quench. To ensure that in this model the physics are correctly implemented, Fresca2 is modeled first without insert. The peak temperature from the model is 180 K (with a quench protection delay of 60 ms), which is in good agreement with data provided for Fresca2 in literature [130]. With the Fresca2 model validated, Feather-M2 and rings are added to the model. The results are presented in Figures 2.42 and 2.43 for quenches originated from Feather-M2 and Fresca2 respectively. In this model there is not much difference between a quench in Fresca2 and a quench in Feather-M2, apart from the peak temperature being in a different coil. It can be seen that the rings indeed pick up some current from Fresca2,

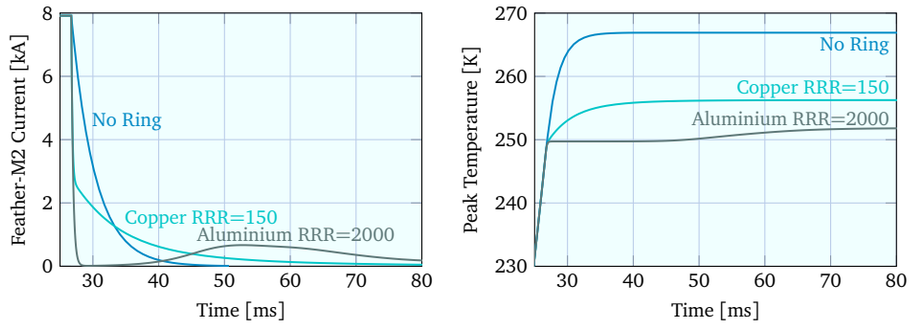


**Figure 2.41.** *Comparison of current and temperature versus time for a quench in Feather-M2 for different Ring materials. When the quench is detected a dump resistor of* 126 mΩ *(*1000 V *at* $I_0$*) is switched in after a delay of* 10 ms*.*

keeping the ring current stationary around 5 kA for when it dumps its current. This increases the final temperature of the rings by 10 K.

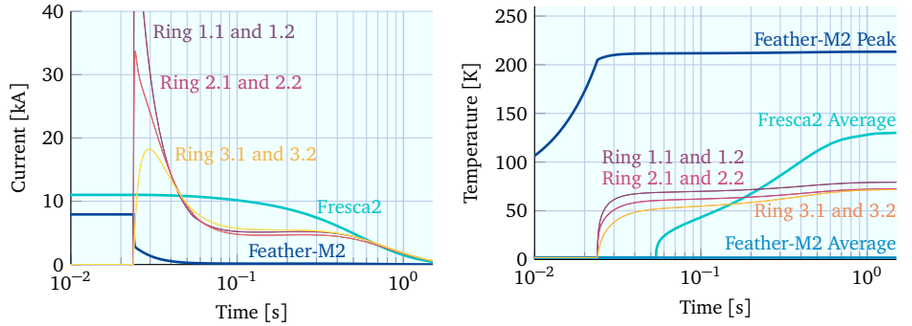


**Figure 2.42.** *Calculated current decay (left) and temperature rise (right) versus time for a quench in Feather-M2 when used as an insert for Fresca2. The quench detection trigger voltage is* 100 mV *with an integration time of* 5 ms *(for Feather-M2). After the quench detection is triggered, dump resistors, of* 126 mΩ *(*1000 V *at* $I_0$*) for Feather-M2 and* 90 mΩ *(*1000 V *at* $I_0$*) for Fresca2, are switched in after a delay of* 10 ms*. Additionally heaters hit* 80% *of the coil pack of Fresca2 after a delay of* 40 ms*.*

For Feather-M2 the dump resistor of 125 mΩ remains inside the circuit after the current is dumped. This almost completely prevents any current to be induced. This is in agreement with the results found for the EuCARD1 insert magnet [131], which has a higher mutual inductance than Feather-M2. It is therefore not necessary to open the circuit (after initial ramp-down) to protect the coil. The reduction of the coil temperature when operated in a background field, is attributed to the increased magneto-resistance in the higher magnetic field. This causes the quench to propagate more quickly and thus gives a faster rise in voltage. This in turn sets off the quench detection earlier causing the peak temperature to decrease.

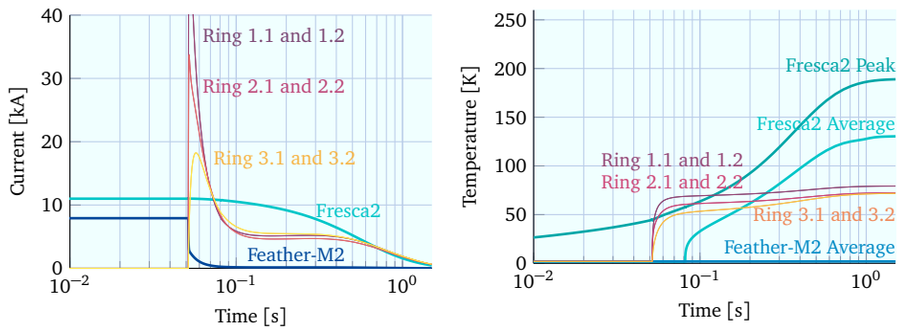


**Figure 2.43.** *Calculated current decay (left) and temperature rise (right) versus time for a quench in Fresca2 while Feather-M2 is used as an insert. The quench detection trigger voltage is* 100 mV *with an integration time of* 20 ms *(for Fresca2). After the quench detection is triggered, dump resistors, of* 126 mΩ *(*1000 V *at* $I_0$*) for Feather-M2 and* 90 mΩ *(*1000 V *at* $I_0$*) for Fresca2, are switched in after a delay of* 10 ms*. Additionally heaters hit* 80% *of the coil pack of Fresca2 after a delay of* 40 ms*.*

Important for the voltage detection, which will initially be the primary detection system, is the total delay time defined between the point where the conductor reaches the trigger voltage and the point were the dump resistor is switched in. Using the coil model the peak temperature is calculated as function of this delay time at different current densities. The results of this calculation are presented for trigger voltages of 10 mV and 100 mV in Figure 2.44. The studied stand-alone case in Figure 2.40 has a validation time of 5 ms and a trigger time of 10 ms therefore it is represented by a data marker in the plot at 15 ms. If the total delay time exceeds 20 ms the peak temperature in the coil reaches 300 K, which is in agreement with the one-dimensional tape model from Section 2.4.1.

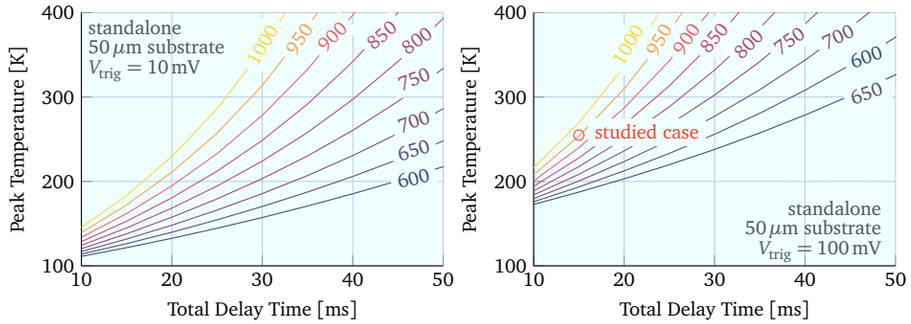


**Figure 2.44.** *The effect of delay times in the quench detection on the peak temperature in the stand-alone case, on the left for* 10 mV *trigger voltage, on the right for* 100 mV *trigger voltage. The delay time is the time between the trigger and the switching in of the dump resistor. The colored numbers in the graphs indicate the overall current density in the tape.*

## Mechanical Structure and Interfaces 2.5

*The mechanical structure[6] and assembly of the Feather-M0 and Feather-M2 magnets are presented.*

### Forces and Support Cylinder 2.5.1

The overall Lorentz force in the coil pack per meter for the straight part of the magnet is given as $\vec{F} = N_t \vec{I} \times \vec{B}$. The current is in the $\ell$ direction (as defined in the local coordinate system explained in Section 2.3.4) and because the cables are mostly aligned, the magnetic field is in the $t$ direction. The forces are in the $n$ direction (which is normal to the face of the conductor) pointing outward from the coil. To prevent the forces from causing de-lamination, the hastelloy or stainless steel substrate in the tape has to be positioned always on the outside, providing solid backing for the fragile ReBCO film.

The Equation calculating the force on the coil pack, can be simplified to $F_n = N_t I_{op} B_{av}$, where $F_n$ is the force in the normal direction. For Feather-M2 the average field in the coil pack $B_{av}$ is estimated using the average between the peak field 17.2 T and the background field 13 T, which is $\sim$ 15 T. The force on the central deck and the wing deck, at an operating current of 8 kA, is then estimated (for one pole) as 1.5 MN/m and 0.8 MN/m, respectively. When distributed over a 12 mm wide cable, this corresponds to stresses of 130 MPa for the central deck and 80 MPa for the wing deck, which is close to the values found in Figure 2.16. For Feather-M0 the magnetic field is lower resulting in lower forces and stresses of 0.36 MN/m and 30 MPa, respectively. In both cases a 5 mm thick cylinder is used supporting the outside of the coil. The hoop stresses are then calculated as the force of one pole (for Feather-M0 this is half of the coil) divided over the thickness of the cylinder. The cylinders are 5 mm thick, following the design of the EuCARD1 insert [56, 57], resulting in hoop stresses in the support cylinder of 36 MPa in stand-alone mode and 460 MPa in the background field. For the first an aluminum alloy (6063-T6) cylinder, with a yield strength of 250 MPa at room temperature, is used. The advantage of aluminum is that its thermal contraction, which is slightly higher than that of the coil, ensures a tight fit after cool-down. For the second a high grade steel (316L or In718), with a yield strength beyond 800 MPa at room temperature, is considered for the cylinder, which has additional support on the mid-plane.

From the forces and the Minimal Quench Energy (MQE), the distance over which the conductor needs to move, in order to cause a propagating quench due to magnetic friction is calculated. At operating current the MQE is estimated at about 100 mJ deposited over a distance of a centimeter. The force on a centimeter of cable is around 1.6 kN (assuming 8 kA, 20 T). The work $W$ performed when moving the cable over a

[6] Because the main focus of this thesis is on the thermo-electrical aspects, only the analytical estimates used to guide the initial mechanical design are presented here. For a more detailed analysis using a two- and three-dimensional Finite Element Method (FEM) the interested reader is referred to the future research thesis of Murtomäki [132].

transverse distance $s$ is then calculated as $W = Fs$. The corresponding distance found for the quench energy is then 60 $\mu$m. In LTS magnets, in which the margins are much smaller, movements are prevented by applying pre-stress to the coil. This stress is applied using a collaring system as in LHC or, for some research magnets, by a bladder and key system [133] as for example is used in Fresca2.

For Feather initially it is thought that a small 12 mm wide bladder pressurized with woods metal or wax could be used in order to apply pre-stress to the coil. However it was found that the design of such a bladder, that can apply pressures in the order of tens of MPa, is a complex task. Therefore and because the coil has a relatively low number of turns resulting in only small movement, it is decided to use a different approach and omit most of the pre-stress. This allows the coil pack to lean against the support cylinder and move under the accumulated pressure. Estimated distances for this movement is $\sim 10\,\mu$m, which occurs over the course of the ramp, still allowing time for cooling. To accommodate this movement it is of importance that the impregnated coil-windings do not stick to the former, which implies the use of mold release on most surfaces (see Section 2.2.3).

### 2.5.2 Former, Spacers and Rings

First the mechanical support for Feather-M0 was designed, which was then later used as a guideline for Feather-M2. A cross-sectional illustration of the structure is presented in Figure 2.45. For this test magnet it was decided to impregnate the coil pack separately after which it is mounted on the former. This has the advantage that the coil can be inspected and instrumented after the impregnation step. To perform the impregnation under pressure the coil is wound on the central support of the impregnation mold. A layer jump box is used to provide a flat surface for the coil pack next to it. This prevents sharp edges from damaging the conductor. The central support can be made of copper to use it as an ICED ring.

To accommodate instrumentation it is decided to leave a cavity, split in two halves by a bar, in the center of the former. Before the support cylinder is added the cavity is accessible from the top and bottom. To lead the instrumentation wiring out, the cavity can also be accessed by entrances located at both ends of the coil, but only through the lower half of the magnet. This because the upper half is blocked by the central support. Additional holes were added in the bar to connect the two sides for wiring. To fill the space between the former and the support cylinder two caps have been added to the former. The impregnated coil block is insulated from the former (and thus ground) using two G11 sheets. On the outside a copper spacer is added to transfer the forces to the support cylinder. This spacer can be adjusted to allow for tolerances in the thickness of the coil pack. Also it provides cooling and additional heat capacity to the coil.

For Feather-M2 a similar approach is used, the structure of which is presented in Figure 2.46. The design consists of two identical poles, constructed separately, after which they are inserted inside a support cylinder to form the magnet. For Feather-M2 it is decided to wind and impregnate the coil pack directly on the former, thereby reducing the complexity of the design significantly. Similar to Feather-M0, a layer jump

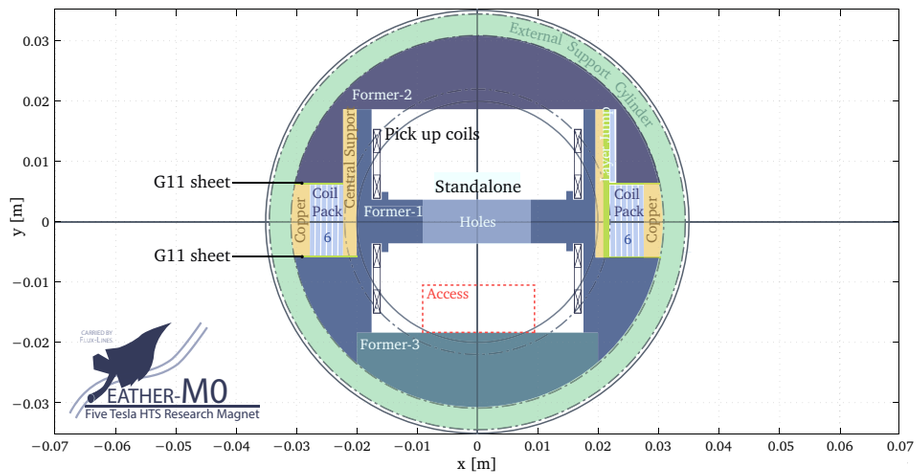


**Figure 2.45.** *Cross-section of the mechanical structure of the Feather-M0 magnet at its straight sections.*

box is used on one side of the magnet to keep the cable in place and to provide a flat surface. The central and wing decks are then wound in opposite direction.

In the space between the coil blocks and the support cylinder, where no conductor can be placed due to coil-end restrictions, three copper ICED rings are located in each pole. Between the rings and the coil blocks, spacers are used to enable insertion of the rings from the top. These spacers can also be adjusted to allow some tolerance in the thickness of the coil pack. This proved to be useful when cables of different thicknesses (than the design value) are used. Because of a restriction at the coil-end, the copper rings can not be inserted (or removed) after the coil has been impregnated. Therefore the rings are impregnated together with the coil, making it necessary to install and test all the instrumentation before this step. To simplify the shape of the impregnation mold the iron poles are also included in the impregnation.

The coil packs are insulated using two G11 sheets and one set of Kapton sheets, to keep the mid-plane as open as possible. This is necessary because further mechanical analysis showed that the deformation of the support cylinder, under the Lorentz forces in the background field, exceeded acceptable limits. Therefore when operated in Fresca2 a special enhanced support cylinder is used that is connected through the mid-plane to a central support tube of 4 mm (illustrated in the bottom right of Figure 2.46). This reduces the effective aperture to 32 mm. Because the high-strength cylinder is difficult to manufacture, it needs to be split longitudinally into several sections, to allow for wire cutting. Since most of the forces are in the transverse direction this does not cause mechanical issues.

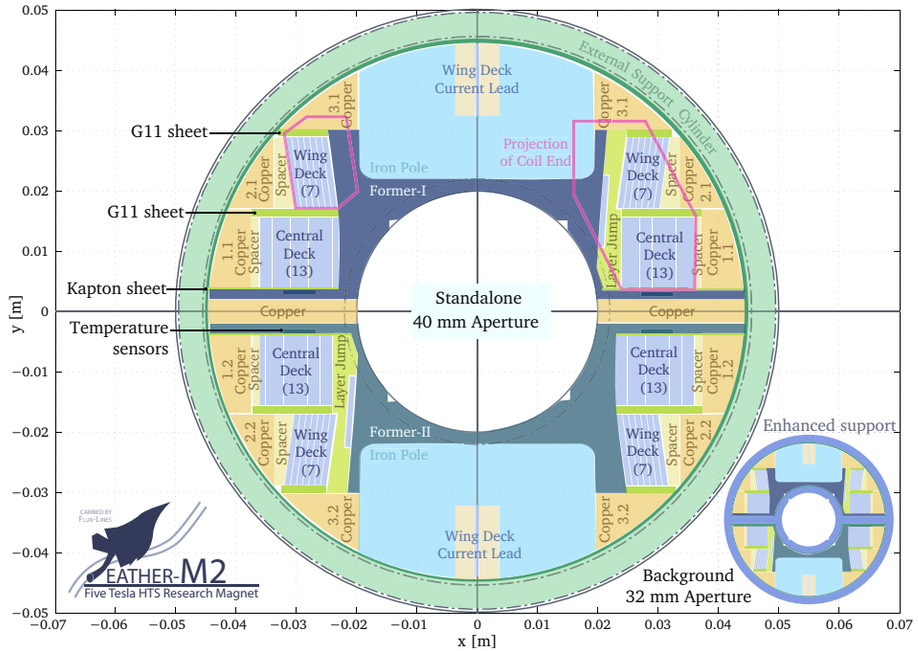


**Figure 2.46.** *Cross-section of the mechanical structure of the Feather-M2 magnet at its straight sections. Visible are the formers, one for each pole, on which the coils are wound. Each coil comprises a central deck with* 13 *turns and a wing deck with* 7 *turns. Next to the coil-windings a set of spacers are visible. At the center of the former a* 40 mm *free aperture is present. Above and below the aperture iron poles are present that increase the magnetic field. On the outside the structure is supported using an external support cylinder. When used in the very high field an alternative cylinder, connected through the mid-plane, is used. This cylinder is presented in the small illustration on the bottom right.*

### 2.5.3 Coil-Ends and Current Leads

The structure towards the coil-ends is similar to that of the straight section. At the coil-ends the coil-windings are supported by the copper rings surrounding it (see Figures 2.47 and 2.48 for two-dimensional cross-sections and Figure 2.49 for a three-dimensional exploded view). The spacers extend also to the coil-ends to allow for manufacturing tolerances and the mounting of the copper rings from the top. The copper rings are wedged between the former and the support cylinder, thereby transferring the forces on the coil-ends to these parts. Additional bolts, and on the return-end of the coil, iron poles are added to connect the copper rings to the former in order to provide additional support.

The insulation sheet on the mid-plane runs all the way towards the coil-end such that it can function as a trace to lead the instrumentation wiring out of the magnet. The other

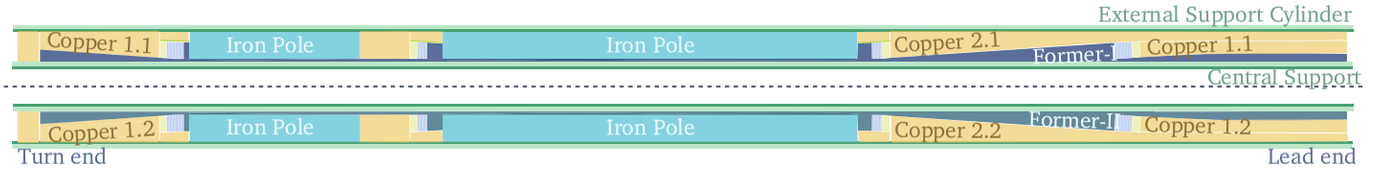


**Figure 2.47.** *Illustration of the vertical longitudinal cross-section through the mid-plane of the mechanical structure of the Feather-M2 magnet. Visible are the formers, one for each pole, on which the coils are wound. The shape of the former follows the side profile, as illustrated in Figure 2.20. The former supports the coil, the copper rings and the iron poles. Inside the former there is an aperture that is accessible on both sides of the magnet. above the aperture iron poles are present. See Figure 2.46 for an illustration showing a cross-section on the straight section.*

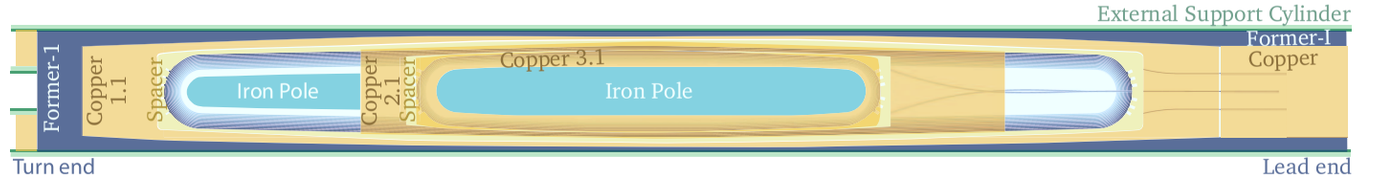


**Figure 2.48.** *Illustration of the horizontal longitudinal cross-section of the Feather-M2 magnet at a height of* 22 mm*. Only the top former is visible, together with the coils, iron poles and copper rings that are mounted on it. In between the coil and the copper ring the overall shape of the spacers is visible. On the outside there is the external support cylinder.*

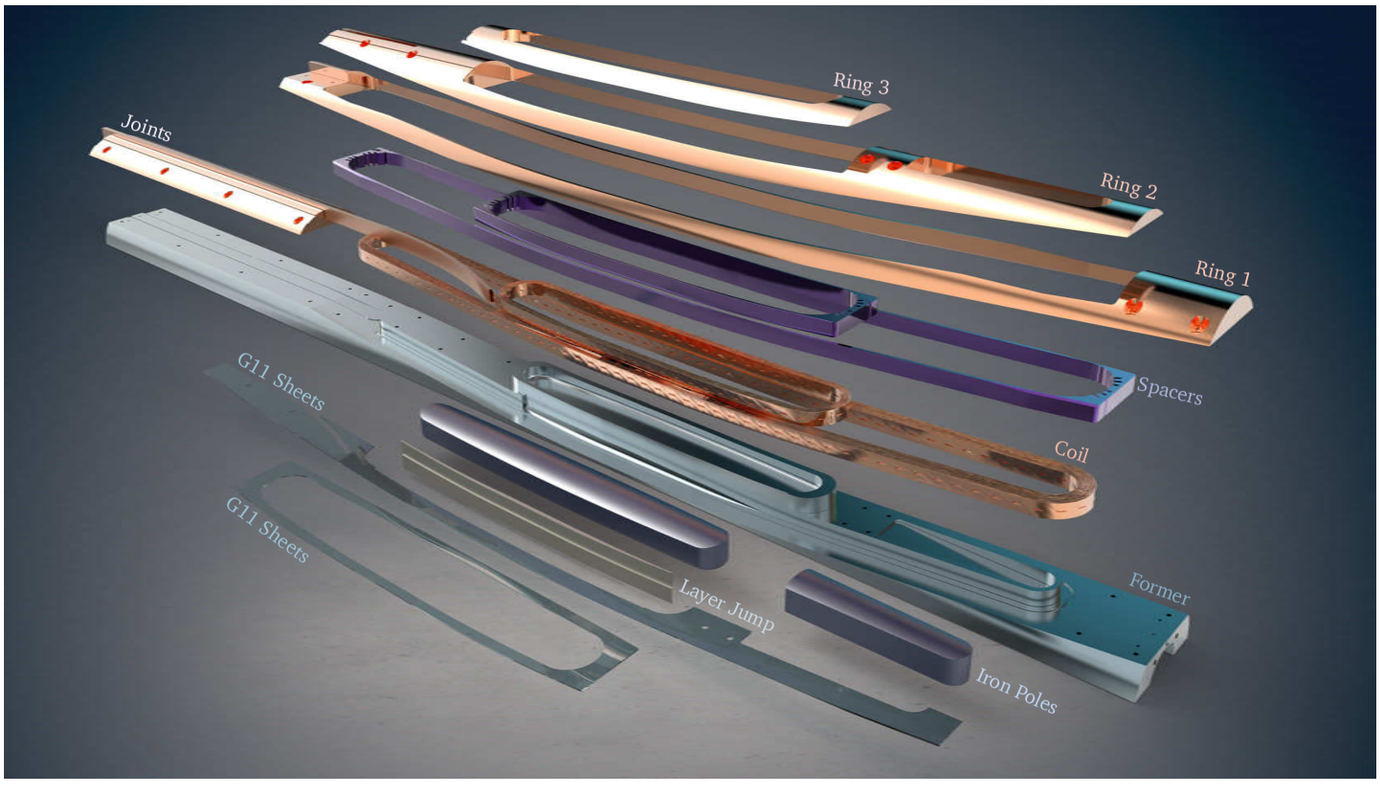


**Figure 2.49.** *Exploded view showing all the parts making up one of the Feather-M2 magnet poles. Visible from top to bottom are the copper rings, the spacers, the coil-windings and joint area, the former, the iron poles and the G11 insulation sheets.*

G11 insulation sheets between and above the coils are shorter to avoid intersection with the copper rings. The central sheet, which is 0.7 mm thick, can possibly house the distributed temperature sensor network. To take the current leads out of the magnet a copper channel, that partially cuts through the copper ring, is used. For this reason, to keep the cross-sectional area constant, to avoid local heating when the current is transferred to the rings during a quench, the rings are wider at the coil-ends than on the straight section.

## Joint Design and Cold Testing 2.6

*Joints are the weak point of the magnet, especially for ReBCO due to delamination issues, therefore careful consideration is needed. This section describes the design and cold testing of the used joints.*

### Joint Procedure 2.6.1

A joint is necessary in order to connect the coil to the current leads. An intermediate joint inside the magnet connecting the relatively fragile Roebel cable to a ductile Nb-Ti cable was considered. This would, however, prevent magnet testing at variable temperature making it impractical for these first Feather-M0 and Feather-M2 demonstration coils. Therefore the Roebel cable, which is part of the coil, is led out of the magnet to the current leads, where a joint is made. Between the coil and the current leads the Roebel cable can be stabilized using additional copper sheets.

Inside the joint a single twist pitch length of 300 mm is pre-soldered, in order to provide good electrical contact between the tapes, see Figure 2.50. The soldering is performed using a no-clean lead free low melting point $Sn_42Bi_57Ag_1$ solder paste [134]. The melting point of this solder is 138 °C. The advantage of this particular solder is that it can be applied between the tapes of the cable using a brush, without heating. After the solder is applied it is mounted in a dedicated mold in which a relatively low pressure of 3 MPa is applied to the cable. It is then heated to 110 °C over a time scale of 180 s, subsequently the temperature is rapidly increased to 170 °C, which is maintained for about 10 s after which the sample is cooled down. This procedure was recommended by the supplier.

After pre-soldering the cooled cable is clamped inside the current lead together with a sheet of indium. The joint is protected using a copper cover. When disassembling the joint after the test it is recommended to soften the indium using a heat gun, to avoid delamination of the tapes inside the joint.

### Joint Cold Test 2.6.2

The joint test comprises of a U-shaped cable that has a joints on either side connecting to the current leads, see electrical diagram in Figure 2.51. Along the cable and on the joints a series of voltage taps is positioned. The voltage taps on the cable were

**Figure 2.50.** *The Roebel cable after pre-soldering with the $Sn_4 2Bi_5 7Ag_1$ solder paste.*

soldered to individual tapes. On the cable and on the joints additional Cernox sensors were mounted to monitor the temperature. The goal of the test was to validate the joint design and to verify the thermal stability of the copper current leads, which are part of the used cryostat, when operated at variable temperature.

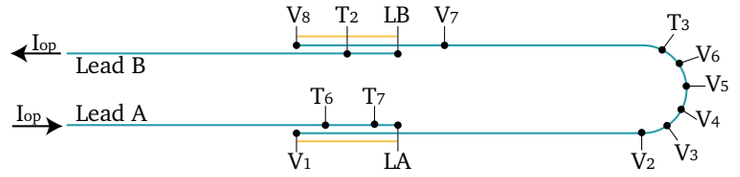


**Figure 2.51.** *Schematic diagram of the joint test showing the position of the voltage taps and temperature sensors.*

The test was performed with the current leads in gas. The central part of the cable was located in liquid helium. The measured voltages and temperatures as well as the supplied current are presented as function of time in Figure 2.52. The ramp was performed first in steps of 100 A up to 1.0 kA and then in steps of 1.0 kA up to 5 kA, which was the limit of the used power supply. During the test the temperature of the joints was allowed to drift away from equilibrium and reaches a maximum of about 10 K at 5 kA. The voltages show inductive spikes during ramping followed by a plateau, during which a slow drift is observed. The voltages over the joints show strongest dependence with the current.

The voltages on the plateaus are isolated and plotted as function of current in Figure 2.53. By fitting the slope the joint resistances are determined at approximately 6 nΩ for both joints, which is acceptable for an accelerator magnet. The drift of the voltages, was first thought to be the current redistribution between the tapes in the cable. In Figure 2.53 the time constants of the voltage decays are determined for every plateau. The decay times are on the order of several hundred to several thousand seconds and increase with the current. These time constants, however, can not be explained by the tape-to-tape inductance matrix and the measured joint resistances, resulting in time constants of a few seconds. Therefore, it is more likely that the drift in the voltages is caused by

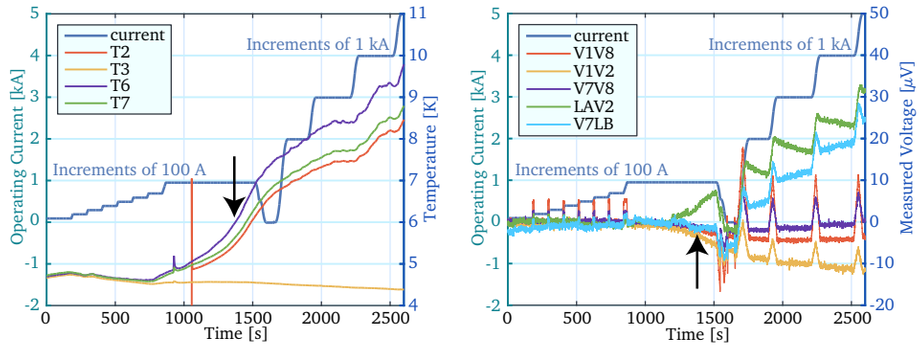


**Figure 2.52.** *Measured temperatures and voltages as function of time during the joint test shown on the left and right of the plot, respectively. Location of voltage taps and temperature sensors is shown in Figure 2.51.*

a thermal effect. In the plot it is visible, denoted by the arrows, that the start of the temperature rise corresponds with the first voltage drift.

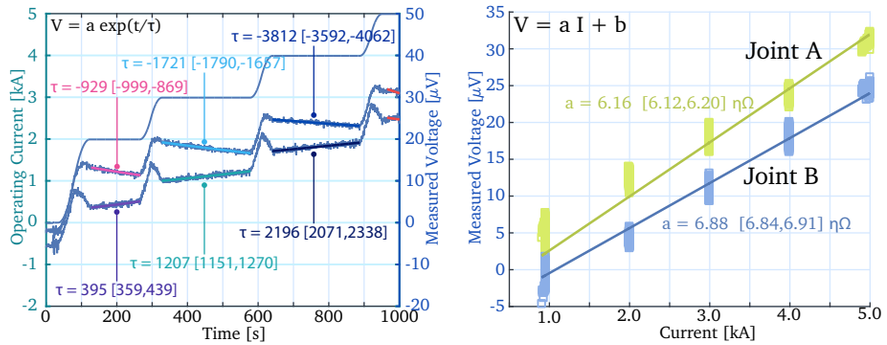


**Figure 2.53.** *Fitted time constants during ramping with increments of* 1 kA *on the left and voltage as function of current during the plateaus on the right.*

## Construction and Testing of the Sub-Scale Coil 2.7

*Several Feather-M0 sub-scale coils were constructed. Four exercise coils with dummy cable, in order to test winding and impregnation and one real coil that has also undergone first cold tests. In this section the construction and cold testing of the Feather-M0 coils is described.*

### 2.7.1 Coil-Winding and Impregnation

At present four exercise and one real coil with the Feather-M0 layout have been manufactured. In Figure 2.54 a photograph of the four exercise coils using dummy Roebel cable is shown. The used winding tooling and impregnation molds follow concepts previously used for the $Nb_3Sn$ RMC racetrack coils [135]. The impregnation is performed vertically in a vacuum chamber, however, due to the design of the mold, it was not possible to use overpressure, an issue that was fixed for the Feather-M2 mold.

It is noted that the length of the coil, of approximately 400 mm, does not match an integer number of twist pitches of the cable, as proposed in [136] in order to reduce length differences between the trajectories of the tapes inside the cable, and thus minimizing longitudinal sliding. This could be a potential problem because it causes the cross-overs to become interlocked. This solution was discovered too late for incorporation in the Feather magnet designs.

A description of each of the produced Feather-M0 coils, illustrating the learning process, is provided below:

- *Feather-M0.0 Exercise Coil* - First time winding and impregnating the coil. A stainless steel dummy cable with the SP-1 layout is used (see Table 2.1). The winding is performed under a very light tension of 0.5 kg to avoid damage to the cable. Some sliding of the tapes with respect to each other is observed, resulting in slight meandering in the cable due to interlocking. The coil was impregnated using CTD101-K clear resin without problems. Part of the coil was cut and studied under a microscope.
- *Feather-M0.1 Exercise Coil* - The winding tension was increased to 5 kg as proposed by [137], making the cable to behave much better, resulting in significant reduction of meandering. In addition, cable exits at current leads were tested and improved. The cable was soldered over a length of 10 to 20 mm in order to seal the mold.
- *Feather-M0.2 Exercise Coil* - This coil was impregnated using CTD101-G, an alumina filled epoxy, which was originally intended to reduce the thermal contraction of the resin. The turns at the lead-end were separated in order to perform high voltage insulation tests. However, the resin, which entered the mold from the turn-end, was not able to propagate throughout the entire coil leaving part of the lead-end dry. Based on this result it was decided to revert to the CTD101-K clear resin, with the addition of glass rope inside the channel (see Section 2.2.3).
- *Feather-M0.3 Exercise Coil* - The fourth coil was used to test the inclusion of the glass rope during the winding and impregnation. Furthermore the winding procedure and lead end were perfected. At the leads the stainless steel cable was copper platted to perform preliminary tests for soldering the joints.
- *Feather-M0.4 Superconducting Coil* - The first real coil uses a cable with the BHTS-1 layout (see Table 2.1), which was nick-named the Frankenstein [138] cable, because it was assembled from all sorts of tapes of different batches and because

the copper plating was not yet perfected. The latter resulted in a significant variation of the tape thickness, an effect also referred to as dog-boning. In addition the process used was coat-and-punch instead of punch-and-coat leaving the tape edges exposed (see Section 2.2.1). Due to the cable thickness of 1.8 mm only three turns were included. Winding and impregnating the coil with Roebel cable was relatively straight forward at this point and no significant problems were encountered. The coil on the winding table is shown in Figure 2.55 and a photograph of the impregnated coil-windings is shown in Figure 2.56. Because initially it was planned to solder Nb-Ti current leads to the Roebel cable, before the variable temperature testing was introduced (see Section 2.7.3), the Roebel cable current leads were too short. Therefore they were extended with Roebel cable introducing a secondary set of Roebel-to-Roebel cable joints. These splices are soldered and do not rely on indium clamping.

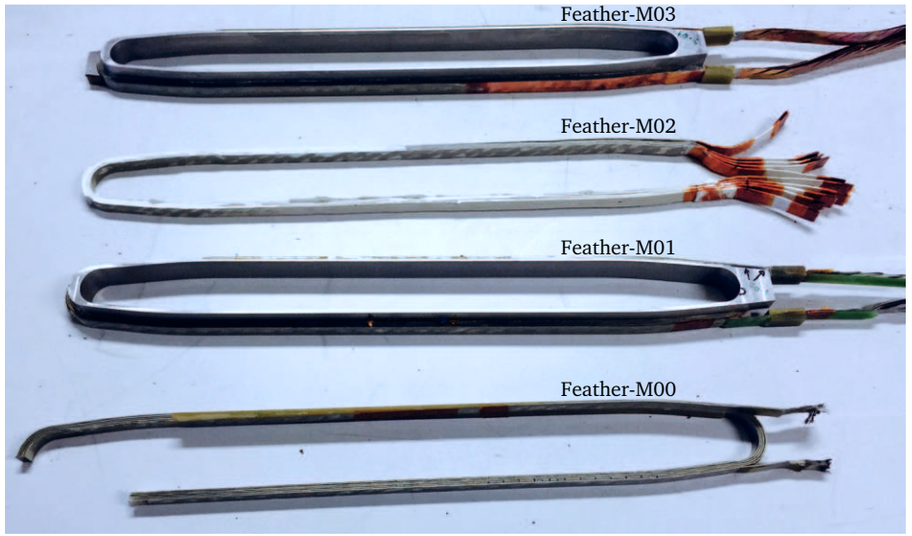


**Figure 2.54.** *Photograph showing the series of Feather-M0 exercise coils side by side, produced to study the winding and impregnation procedures.*

## Instrumentation 2.7.2

One of the main purposes of Feather-M0 is to test instrumentation before implementation in the Feather-M2 coil. In Section 5.3.4 it is shown that thermal drift or a pre-quench, both early warnings for an imminent quench, can be detected using a variety of temperature sensors and pick-up coils, respectively. The position and implementation of the various sensors in Feather-M0 is shown in Figure 2.57 and an electrical diagram is shown in Figure 2.58. Visible is an array of Carbon Ceramic Sensors (CCS) that are

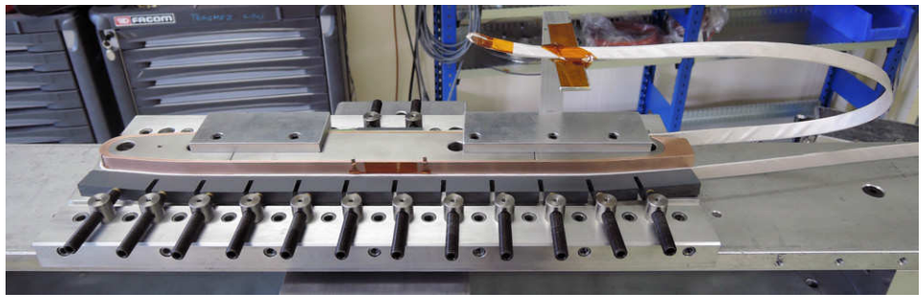

**Figure 2.55.** *Winding of the Feather-M0.4 coil using real Roebel cable with the BHTS-1 layout, based on Bruker tapes and cable assembled at KIT.*

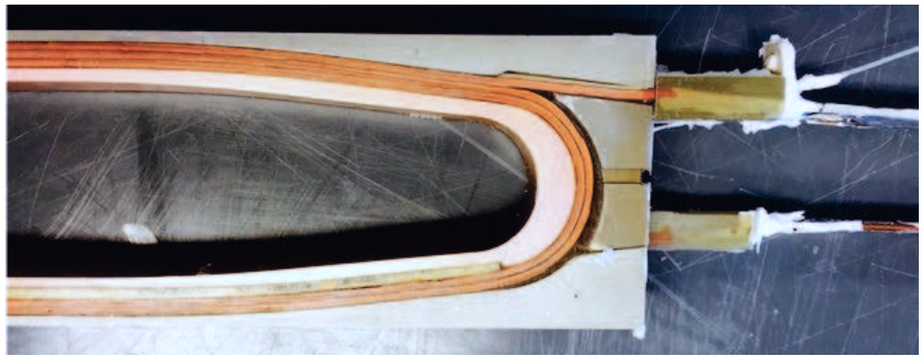

**Figure 2.56.** *Photograph showing part of the Feather-M0.4 coil and some of the spacers after removal from the impregnation mold.*

located on top of the coil-windings. A secondary array is located at the other side of the coil next to the windings. The CCS array is not calibrated and can only detect changes in temperature. Therefore, an additional calibrated CCS sensor is added to the copper ring. The temperature of the coil-windings is also measured using an optical fiber. Inside the aperture two hall probes are located, which are used to measure the magnetic field.

Inside the aperture a series of pick-up coil arrays are located. These pick-up coils consist of copper lanes on a Kapton sheet. The design of these traces is generated using computer code and is shown in Figure 2.59. By stacking multiple layers the number of turns in the pick-up coils can be increased. In Feather-M0.4 the number of turns is 200. The pick-up coil arrays are positioned above and below the mid-plane of the coil as shown previously in Figure 2.45. This suboptimal position was added to the design before the numerical results were available. In fact the coil in Feather-M0 is short enough to only locate pick-up coils on the current leads, an option that is considered for the next coil.

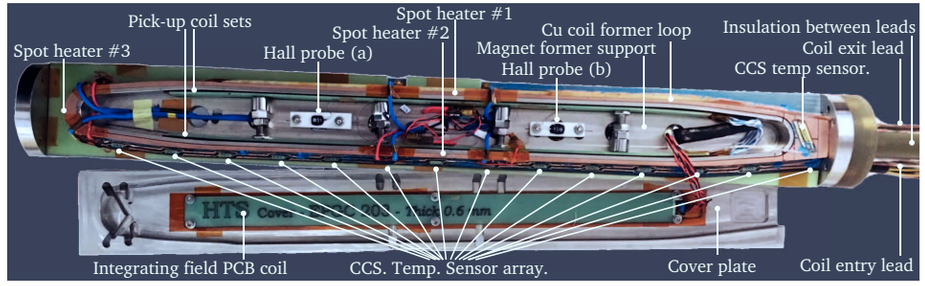


**Figure 2.57.** *Photograph of the instrumentation of the Feather-M0.4 coil and labels indicating the position of pick-up coils, temperature sensors, hall probes and spot heaters.*

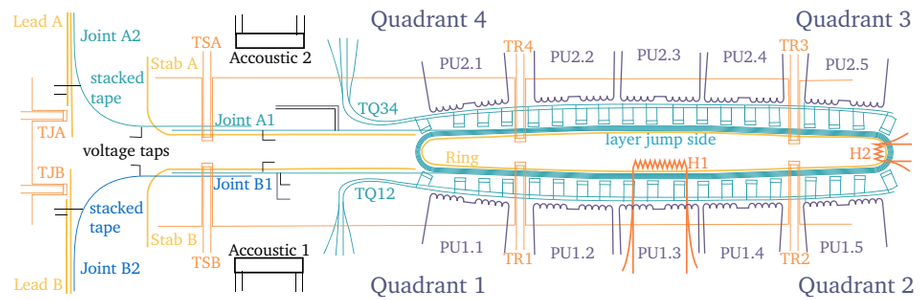


**Figure 2.58.** *Conceptual circuit diagram showing all envisioned instrumentation for the Feather-M0. Abbreviations with TQ are the distributed un-calibrated temperature arrays for quench detection, TR are the calibrated temperature sensors on the copper quench protection rings, PU are the pickup coils, TS are the calibrated temperature sensors in the lead stabilizers, TJ are the calibrated temperature sensors on the joints. Black lines denote the positions of the voltage taps.*

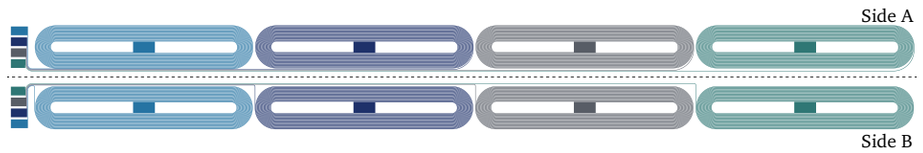


**Figure 2.59.** *Computer generated pick-up coil array layout for Feather-M0 on a two sided circuit board. At the center of each coil a series of holes connects the two sides. Two pickup coils, from different strips, can be anti-series connected in order to cancel out changes in the background field. The strips can be stacked to increase the number of turns.*

### 2.7.3 Cold Testing of the Coil

To provide multiple opportunities to learn setting up the detection system, without damaging the conductor on the first attempt, the magnet is tested at variable temperature in helium gas, starting at 70 K. This reduces thermal margin and critical current such that the coil can be quenched at much lower operating currents. Because the resistive heating scales with the operating current squared, much more time becomes available for the protection system to react. When sufficient confidence in the protection system is achieved, the coil test temperature can be reduced in steps in order to increase the critical current. In addition, at high temperature, the critical current of the coil is much lower (a factor 5 between 4.2 K and 77 K). This makes it possible to measure the critical current without risking damage to the coil. The measured critical current and resulting quench recordings can then be extrapolated in order to keep the system predictable. The calculated critical current as function of temperature and the time period between a voltage drop of 100 mV and a peak temperature of 300 K as function of operating current, is shown for Feather-M0.4 in stand-alone mode in Figure 2.60.

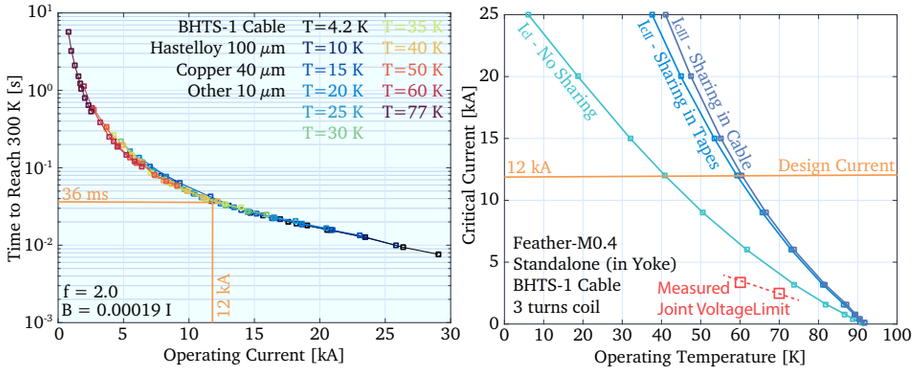


**Figure 2.60.** *Calculated critical current in Feather-M0.4 as function of temperature based on the different criterions described in Section 2.3.6 (left) and the time period between* 100 mV *voltage drop and a peak temperature of* 300 K *as function of operating current (right).*

The test of the Feather-M0.4 magnet was performed at the SM18 test station at CERN in August 2016. During the test the Feather-M0.4 was first cooled down to a temperature of 4.5 K in liquid helium. The temperature difference over the coil was kept within 20 K to avoid damage due to differential thermal contraction. During the cooldown the RRR of the coil was measured at around 20, which is in good agreement with data from the University of Geneva, presented previously in Figure 1.9. At the expected critical temperature of 93 K only a gradual transition was observed, which is explained by the thermal gradient over the coil, causing the transition to be asynchronous.

The coil was powered with a 600 A power supply and it was shown that the coil was superconducting. The splice resistances for Roebel-to-Roebel joints A1 and B1 (see

Figure 2.58) were determined to be 2.4 nΩ and 6.4 nΩ, respectively, well within acceptable limits for an HTS coil. The resistance of the clamped current lead joints, A2 and B2 together, was determined to be 100 nΩ. The coil inductance was determined by measuring the voltage while ramping up and down and was found at approximately 4 $\mu$H, as expected from numerical predictions (see Table 2.7).

After initial tests in liquid helium, the switch was made to operation in helium gas. A 20 kA power supply was connected and the operating temperature was increased to 60 K. The coil was protected using a dump resistor of 80 mΩ. The thermal variation at higher operating temperatures in gas flow was found within 1 K, better than expectations. The energy extraction was tested by manually triggering the protection. After triggering the current was extracted from the coil within 4 ms. Then the coil was powered using a staircase profile and above 2.6 kA the voltage over joint B1 was slowly increasing. After increasing the helium gas flow from 1.5 g/s to about 3 g/s, in order to provide extra cooling, the current was incremented further, up to 3 kA, at which point a thermal runaway occurred in or near to the affected joint. The quench protection was triggered normally causing the current to be extracted. This effect could be reproduced and no degradation of the critical current was caused. The test was repeated at 70 K by which the maximum current of the joint was about 1.9 kA. Although the joint probably could still reach the design current of 12 kA at liquid helium temperatures, as predicted by extrapolation using the ReBCO critical surface, it was decided to remove the coil from the cryostat in order to visually inspect the joint, add additional cooling and add improvements if necessary.

No visual damage was found on the current leads and additional cooling was added. Sub-cooling the leads about 10 K below the coil temperature proved to be sufficient to move the thermal runaway into the coil. Likely during the first tests a thermal gradient was present, the lower part of the coil was lower in temperature than the upper part containing the leads. The fact that the weak spot moved into the coil proves that the entire cable was close to its short sample operating limits. This is confirmed further by measurement data taken on the 12 mm wide Bruker tape at 77 K in self-field prior to cabling. When the performance of the tape is scaled to 5.5 mm and multiplied by 15, the number of tapes in the cable, a value of 896 A is found [139]. This point is just below the quench current found at 77 K, which shows that the cable was not degraded during cabling, impregnation and cool-down. The initial estimate shown in Figure 2.60 was likely too high due to the scaling relation used. Note that the temperature dependence is strongly related to the use of doping.

After the initial tests at higher temperatures, the temperature was decreased in steps thereby increasing the quench current. The currents found are presented in Figure 2.61. The coil reached its nominal current of 12 kA at 25 K. All quenches were preceded by thermal drift in the coil, which could actually be reversed by increasing the helium gas flow, thereby averting the quench. If this behavior persists when the coil is operated in liquid helium yet remains to be seen. The coil was protected using a trigger voltage of 10 mV with a filter time of 20 ms. No degradation was observed between any of the quenches, showing that the voltage protection was sufficient. Multiple 12 kA quenches were invoked and as expected the coil did not exhibit any training. The variation of the

quench current, visible in the graph, is a result of the inaccuracy of the temperature control.

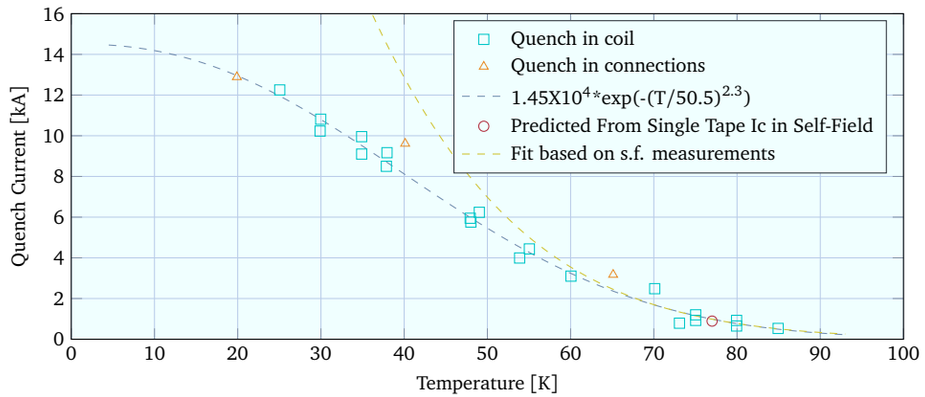


**Figure 2.61.** *Measured quench current as function of temperature for the Feather-M0.4 demonstrator magnet operated in helium gas. The measurements were performed in the SM18 test station at CERN. The joints and current leads were cooled* 10 K *below the temperature of the coil in order to prevent quenches at these locations.*

Measurement data from the pick-up coils during the quenches were analyzed. Unfortunately no Pre-Quench signals (explained in Section 5.3.4) were found. This could be explained by the type of quench. The quench was initiated by ramping the coil over the critical current, which means that no margin was left in any of the tapes and thus no current re-distribution could occur. In the next series of tests, which are presently (October 2016) ongoing, the quench heaters will be used to induce the quench in order to find the Minimal Quench Energies as function of operating current. The Pre-Quench phase is more likely to occur during these tests. However, the location of the pick-up coils in the present Feather-M0 design is not optimal. The distance from the coil windings is more than 5 mm and the copper ring, located between the pick-up coils and the windings, reduces the signal due to screening currents. In addition two pick-up coils should be connected anti-series to reduce noise levels. These issues will be addressed in the next coils, which are expected to be tested by the end of 2016 and early 2017.

## 2.8 Coil-Winding Tests of the Full-Scale Coil

*For Feather-M2 thus far only winding was performed using dummy cable. In this section the tooling and first results of the coil-winding test are described.*

### 2.8.1 Tooling Design and Winding Steps

The Feather-M2 magnet consists of two poles that are wound and impregnated separately. The winding and impregnation of one of the poles is illustrated step-by-step in

Figure 2.62. The roman numerals in the text correspond to those in the figure. The coil-winding is performed on the base plate of the impregnation mold. The tooling is coated with a Teflon layer to prevent the resin from adhering to it.

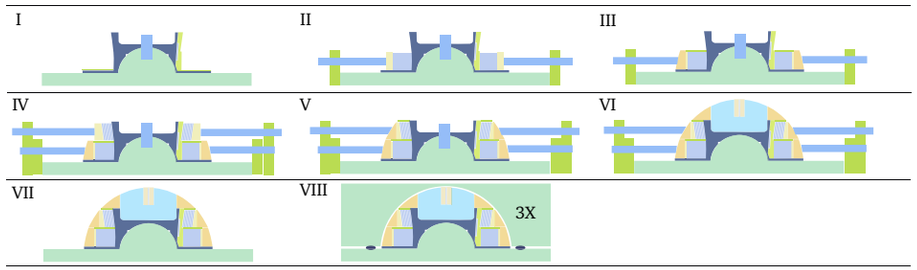


**Figure 2.62.** *Illustration of the steps required to wind and impregnate a pole of the Feather-M2: I. Mounting of layer jump, II. Winding of Central deck, III. Mounting of Ring 1, IV. Winding of wing deck, V. Mounting of Ring 2, VI. Mounting of poles and Ring 3, VII. Remove winding tooling, VIII. Add impregnation mold and perform impregnation.*

The former and layer jump box, containing the cable are mounted (I). The central deck is wound onto the former (II). Special pushing pins hold the coil-windings in place. The copper spacers are mounted on the outside of the coil. The spacers are clamped or glued in order to mount the first copper ring (III). After the copper ring is mounted a second layer of pushing pins is added to the tooling. Using these pins the wing deck is wound (IV), followed again by a spacer and the second copper ring (V). Then the iron poles and third copper ring are mounted (VI). The structure is temporarily held in place using clamps or glue (VII), in order to mount the impregnation mold (VIII). The top half of the mold comprises three longitudinal sections. The ends of the mold are sealed using end plates, that contain air tight feedthroughs for the current leads. In contrast to Feather-M0 this mold can be fully sealed allowing for over pressure impregnation.

### Coil-Winding Tests 2.8.2

For Feather-M2 at present two exercise poles were wound using dummy cable. The poles are indexed separately as allowing recombination into a magnet later on. A description of each of the produced Feather-M2 poles thus far is provided below:

1. *Feather-M2.00 Exercise Pole* - This exercise pole was produced, in order to test whether it was possible to wind Feather-M2, bearing in mind the required hard-way bending of the cable. The preliminary former was printed in plastic using rapid prototyping, which was then glued onto the winding table. The tooling and impregnation mold were not yet available and thus some improvisation took place. A bare dummy cable with SP-1 layout was wound onto the former. Some meandering of the cable was observed, which could be reduced to acceptable levels by tightening the winding clamps. This however caused the weak plastic

former to deform and the aperture to collapse. Nevertheless, it was shown that winding a Feather-M2 pole is possible.

2. *Feather-M2.0 Exercise Pole* - This is a winding test of the final design including all the parts and tooling. The former was machined out of 316L stainless steel. A fiber glass rope was inserted into the 30 m length of BHTS-2 dummy cable (see Table 2.1), supplied by General Cable in New Zealand. A fiber glass sleeve was applied on the outside in order to insulate the cable. The produced coil after winding the central deck and applying the copper ring is shown in Figures 2.63 and 2.64. In these photographs it can be seen that some meandering is present due to the absence of compression. This issue is resolved by adding some additional shims to fill up the space. The mounting of the copper rings was proven to be possible by holding the spacers in place using thin pushing pins. These pins are then retracted one by one during the mounting of the rings. The impregnation mold was closed and the impregnation of this magnet is presently ongoing.

Thus far no significant issues were discovered in winding and assembly of the Feather-M2 magnet and first cold tests using a superconducting coil are planned at the start of 2017, unfortunately beyond the scope of this work.

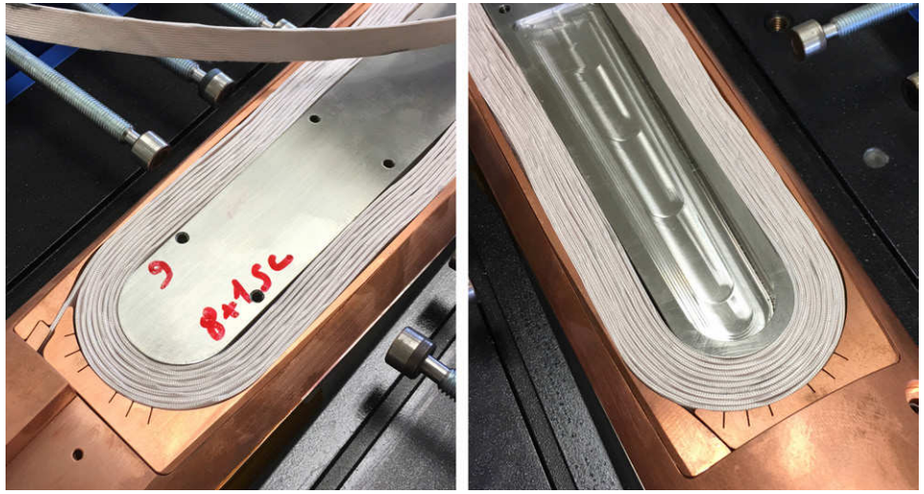


**Figure 2.63.** *Photograph of the lead-end (left) and the turn-end (right) of Feather-M2.0 after winding of the central deck and the mounting of the copper rings (step III in Figure 2.62). Visible are the individual turns, the copper spacer and ring, the former and part of the winding and impregnation tooling.*

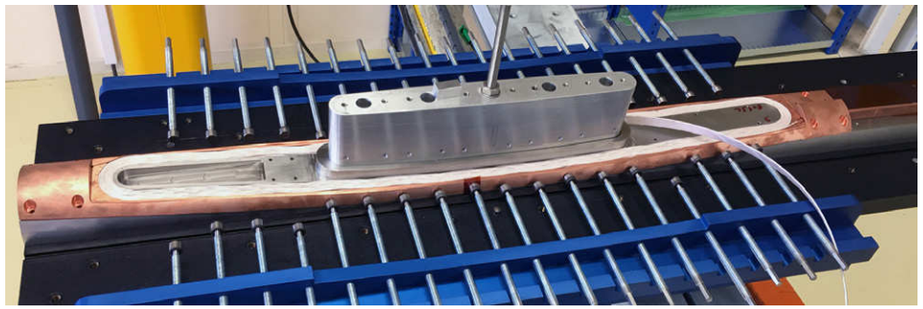

**Figure 2.64.** *Photograph showing an overview of Feather-M2.0 after winding of the central deck and the mounting of the copper rings (step III in Figure 2.62). Visible are the individual turns, the copper spacer and ring, the former and the winding and impregnation tooling.*

## Conclusion 2.9

The design and construction of the Feather-M2 magnet, featuring various new ideas for optimal use of ReBCO Roebel cables, quench protection and structural support, was presented. In addition, a second sub-scale exercise model magnet named Feather-M0 was designed and constructed in order to test coil-winding strategies and quench protection without risking long lengths of expensive conductor.

For the design, a ReBCO Roebel cable was selected because it is fully transposed, it has a reasonable minimum bending radius and allows for a high packing factor of conductor in windings, which together with the alignment of all the tapes, results in a very high in-field critical current density in the optimum parallel magnetic field direction. The drawback of the Roebel cable is its low transverse stress resistance when used in its bare form. When the coil is operated as insert in a background field of 13.0 T, the transverse pressure is around 130 MPa. Therefore it is necessary to impregnate the cable using resin in combination with a glass fiber insulation sock and a rope that fills the otherwise empty central channel of the cable. The thermal contraction of the resulting glass fiber epoxy is close to that of the conductor, thereby reducing de-lamination effects that are a common problem in impregnated ReBCO coils made so far.

To optimize the design, an in depth layout study was performed. By including the angular dependence of the in field critical current density in this study (the percentage on the load-line is distributed very differently from classical LTS magnets), a new layout type for ReBCO coated conductor dipole coils, named Aligned Block, was developed. This layout takes advantage of the anisotropy of the conductor by optimizing the alignment of the tapes with respect to the magnetic field lines. Depending on the ReBCO tape characteristics, which are slightly different for various manufacturers, this can improve the critical current of the tapes up to a factor five, making the design much more efficient and thermally stable. In the design, iron poles are necessary to meet the strict magnetic field requirement imposed. This introduces non-linear behavior into the magnetic field harmonics of the coil. When operated in stand-alone mode, the coil

can be inserted in an iron yoke to increase the magnetic field and to improve the field angle on the conductor.

It proved to be difficult to align the tapes in the coil-end within the mechanical limits of the cable. After careful study, a three-dimensional conductor geometry was found in which the maximum deviation of the average field angle in the cross section of the cable is only 4 deg along the length of the cable. The three-dimensional layout is described fully parametric inside a coil calculation package named Field 2016, allowing for easy modification of the basic shape. Because current can flow freely in the tapes from side-to-side, the calculation of the critical current is not straight-forward. Different methods for the calculation of the critical current were introduced and compared to a steady-state calculation using the new Electro-Magnetic and Thermal Network Model.

Because the Aligned Block magnet allows for a very high current density, it is challenging to protect it against quench. In order to dump the current sufficiently fast, extra copper rings are positioned on the outside of the coil pack. When a dump resistor is switched into the current circuit, most of the current transfers inductively to these rings. The rings also provide additional cooling and heat capacity to the coil pack increasing the stability of the magnet. Coil, spacers, copper rings, instrumentation and all other parts are mounted on a former and are then co-impregnated using epoxy resin, one pole at a time. Two poles are assembled inside a high-strength support cylinder, the shape of which depends on whether the magnet is operated as insert or in stand-alone mode. The cylinder counteracts the forces of the coil pack. The joints that connect the poles to one another and to the current leads are located outside of the magnet. During the impregnation the cable exits the impregnation mold through a hole which is sealed using solder. Integration studies were performed for operation in stand-alone in the INFN test facility in Milan (Italy) and for operation in the background field inside the Fresca2 dipole magnet at CERN.

Preliminary cold tests of Feather-M0.4 were performed up to 3 kA at 60 K, at which point a thermal runaway occurred at one of the joints. The result could be reproduced and no degradation was observed. It was decided to remove the magnet from the cryostat and reinforce the affected joint before further testing. The issue with the current lead was resolved and during further testing the nominal current of 12 kA was reached at an operating temperature of 25 K. The conductor was not damaged during the cabling, impregnation and cool-down. Also many quenches where induced by ramping over the critical current (up to 12 kA) without observing any degradation and as expected also no training behavior was present. The signals from the pick-up coil were analyzed and thus far no signs of a pre-quench were found.

Further testing will involve determination of the Minimum Quench Energies in various coil parts using the built-in spot heaters. This testing is foreseen in Fall 2016, which lies beyond the scope of this thesis. For Feather-M2, winding and impregnation tests have just started and so far no critical issues have been found. The first cold tests of Feather-M2 are expected early 2017.

# Electro-Magnetic and Thermal Network Model

# 3

> "There are times, when men of good conscience cannot blindly follow orders."
>
> Jean-Luc Picard, Star Trek: TNG, S03E16, 1990

*In this Chapter an Electro-Magnetic and Thermal Network Model for Coated Conductor Cables implemented in Matlab [85] is introduced. The model allows for the time dependent modeling of magnetization and thermal runaways in Roebel, CORC and Twisted-Stack type of cables. The solving strategies and representation of the network partially resemble that of JackPot-AC [64, 65, 66, 67], a code developed at the University of Twente for analyzing Cable-in-Conduit Conductors and joints for the magnets in the ITER fusion reactor project.*

## Introduction and Chapter Layout 3.1

ReBCO coated conductors come with properties very different from classical LTS conductors. The tapes act as wide mono-filaments resulting in large screening currents that not only cause high AC losses, but also can negatively affect a magnet's field quality. The dramatically enhanced temperature margin (at 4.5 K) results in quench energies that are a few orders of magnitude higher than in LTS conductors. Therefore magnets constructed with ReBCO have proven to be very stable. However, when a quench does occur, the normal zone propagates relatively slowly, making quench detection and protection more complicated. In view of the high stability it is an open question whether an HTS magnet operating at 4.5 K can quench at all due to a transient.

To improve the understanding of magnetization, thermal stability and thermal runaway, a three-dimensional time dependent Electro-Magnetic and Thermal Network Model capable of simulating coated conductor cable structures was developed. The new model is capable of simulating Roebel, CORC [32] and Twisted-Stack type of cables. In the model an electrical network with both superconducting and resistive elements is mapped to the geometry of the cable as described in Section 3.2. The dynamic behavior of the network can then be described using a system of equations. The electro-magnetic part of these equations is described in Section 3.3. The system can be extended to also include thermal effects as described in Section 3.4. The system of equations is a so called Differential Algebraic Equation (DAE), which is an equation in the form $f(y'(t), y(t), t) = 0$, where $y$ can be a vector. Because such a system needs to be solved quasi implicitly at every time step, it is much more difficult to solve numerically than an Ordinary Differential Equation (ODE), which can be solved by integrating its time derivative.

The inclusion of superconducting properties introduces non-linearity into the system, thereby adding more complexity to the model. In addition the mutual inductance matrix, which is dense, can not be stored due to memory limitations. Therefore only a small band of the matrix is stored, whereas the other interactions are calculated using the Multi-Level Fast Multipole Method (MLFMM) [83, 84]. The chain that allows for solving this system is described in Section 3.5.

## 3.2 Network Geometry

*In this section the geometry of the electrical network which is used to approximate the geometry of the cable is presented. The setup of such a network is partially different for the three cable types: Roebel, CORC and Twisted-Stack. The Roebel cable is used as the prime example. Specifics for CORC and Twisted-Stack are provided in Sections 3.2.2 and 3.2.3, respectively.*

### 3.2.1 Roebel Cable

In the model, the tape surfaces are represented by a grid of nodes and superconducting elements also referred to as a Partial Element Equivalent Circuit [140] (PEEC) (see Figure 3.1). The elements pointing along the tape are called the longitudinal elements and the elements pointed across the tape are called the transverse elements, from now on denoted using subscripts $l$ and $t$ respectively. Although current can only flow in these directions, when the grid is fine enough it is able to sufficiently approximate the behavior of a superconducting surface. To generate the coordinates of the nodes and elements in a Roebel cable, first a line is defined along the edge of the meandering tapes, using the following two arrays containing cable coordinates (as described in Section 2.3.4):

EQ. 3.1
$$\begin{aligned} t_{\text{edge}} &= [0, 0, W_r + W_c, W_r + W_c, 0, 0], \\ \ell_{\text{edge}} &= \left[0, 0.5L_{\text{str}}, 0.5L_{\text{str}} + L_{\text{cr}}, 1.5L_{\text{str}} + L_{\text{cr}}, 1.5L_{\text{str}} + 2L_{\text{cr}}, L_{tp}\right], \end{aligned}$$

where the parameters are given as presented in Figures 2.2 and 2.3 and Table 2.1. The length of the crossover is calculated as $L_{\text{cr}} = (W_r + W_c)\,/\tan(\phi)$ and the length of the straight section as $L_{\text{str}} = \left(L_{\text{tp}} - 2L_{\text{cr}}\right)/2$. Through linear interpolation the function $t_{\text{edge}}(\ell)$ is acquired, which represents one edge of one of the strands. The surface of a tape in $\ell$ and $t$ is now defined as $t_e(\ell_{\text{surf}}) + t_{\text{surf}}$, where $\ell_{\text{surf}}$ is in the range $[0, L_{\text{tp}}]$ and $t_{\text{surf}}$ is in the range $[0, W_r]$. The coordinate in the normal direction, defining the elevation of the surface is calculated from two additional profile lines, given by the coordinates

EQ. 3.2
$$\begin{aligned} \ell_1 &= \left[0, 0.5L_{\text{str}} + L_{\text{cr}}, 1.5L_{\text{str}} + L_{\text{cr}}, L_{tp}\right], \\ \ell_2 &= \left[0, 0.5L_{\text{str}}, 1.5L_{\text{str}} + 2L_{\text{cr}}, L_{tp}\right], \\ n_1 &= n_2 = [0, 0.5d_c, -0.5d_c, 0], \end{aligned}$$

where $d_c$ is the total thickness of the cable given as $d_s N_s/2$. Through linear interpolation the functions $n_1(\ell)$ and $n_2(\ell)$ are found. The elevation of the surface is now defined by $\ell$ and $t$ using

$$n_{\text{surf}} = \begin{cases} n_1(\ell), & \text{if } t \leq W_r \\ \left[\frac{t-W_r}{W_c}\right] n_1(\ell) + \left[1 - \frac{t-W_r}{W_c}\right] n_2(\ell), & \text{if } t > W_r \;\&\; t < W_r + W_c \\ n_2(\ell), & \text{if } t \geq W_r + W_c \end{cases} . \qquad \text{Eq. 3.3}$$

In Figure 3.2 the resulting surface and its elevation in $n$ are shown. As can be seen, the cross over is less wide than the rest of the cable. To accommodate for different cross over widths $W_x$, the current carrying capacity of the elements and surface area of the nodes on the cross-over are artificially increased.

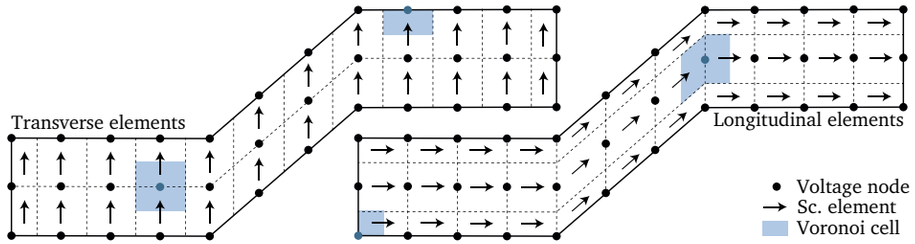


**Figure 3.1.** *Approximation of a strand in a Roebel cable using voltage nodes and superconducting elements, shown separately for the longitudinal and transverse directions. For clarity a very coarse version of the network is shown. For some nodes the Voronoi cells used for the determination of the tape-to-tape contact areas are shown.*

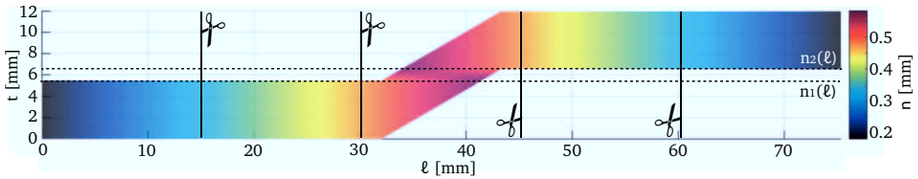


**Figure 3.2.** *Roebel strand surface and elevation. It can be seen that near the cross-over a gradient in n is present in both the $\ell$ and t directions. The horizontal dotted lines are the lines used to define the elevation. The vertical lines show the edges of the unit cells.*

Next the surface is subdivided, along the vertical lines shown in Figure 3.2, into shorter tape sections with length $L_{\text{tp}}/N_{\text{tape}}$, which is the length of a unit cell. The $N_s$ number of tape sections that result from one twist pitch are then numbered with index $p$ with increments along the length and shifted in $\ell$ such that all sections are located in the same unit cell. This cell can be repeated along $\ell$ to form longer cables. However, to reduce calculation time when setting up the electrical network, especially when calculating

the overlapping areas for determining the contact resistances, it is first performed for a single cell, after which the network itself is copied and repeated. The tape sections come in five elementary shapes, which are presented for a cable with an odd number of elements in Figure 3.3. It can be seen that (b) is symmetric with (c) and (d) is symmetric with (e). When the number of strands in the cable is even, (b) and (c) are replaced with a mirror of (a). In each unit cell the nodes of all tapes coincide at the same cross-section. This prevents the contact resistances to be directed in the longitudinal direction. To ensure that these cross-sections also coincide with the corners of the cross-overs, the cell is subdivided into 5 sub-sections using the dotted vertical lines that are shown in Figure 3.3.

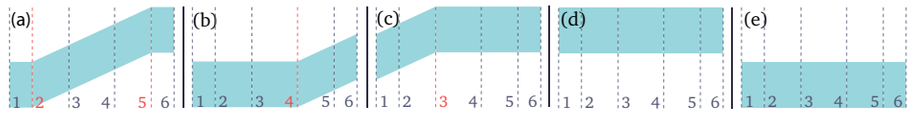


**Figure 3.3.** *Illustration of the elementary shapes in a Roebel cable with an odd number of tapes (alternating cross over results in additional b and c) in arbitrary sequence. To ensure that the nodes coincide with the corners of the shapes, the unit cell is subdivided further into five sections using the vertical lines shown.*

Now nodes are placed in an equally spaced rectangular or rhombus (on the cross over) shaped grid on these tape sub-sections. The number of nodes of each grid in the longitudinal direction $N_{nl}$ is determined using the requested element length, which is commonly set around 1.2 mm. In the notation used here $N$ is always used for an integer number subscript, $n$ stands for nodes and subscripts $l$ and $t$ for the longitudinal and transverse directions, respectively. The number of nodes of each grid in the transverse direction $N_{nt}$ is pre-set by the user, commonly around 14. The effect of this value is studied in Section 4.2.3. Nodes in neighboring sections are now combined, resulting in the coordinate matrices $\ell_{n,p,i,j}$, $t_{n,p,i,j}$ and $n_{n,p,i,j}$, where $p$ is the index of the tape element and $i$ and $j$ are the indexes indicating the position of the nodes within the grid in the transverse and longitudinal direction, respectively. Note that all tape sections in the unit cell are now represented by matrices of equal size. These nodes are also numbered using a grouped index $Q$, which is calculated from the other indices using $Q = pN_{nl}N_{nt} + jN_{nl} + i$ equivalent to the reshape function in Matlab. This provides an alternative method of indexing into the nodes as $\ell_{n,Q}$, $t_{n,Q}$ and $n_{n,Q}$, representing the values of the matrices as arrays. Index $Q$ runs from 1 to $N_{nu} = N_s N_{nl} N_{nt}$, which is the total number of nodes in the unit cell $u$.

At the next step the contact areas between the nodes in the elemental shapes are calculated. These areas are required to include the electrical and thermal contact resistances between the tapes in the model. The calculation is performed by using the overlapping area of the two dimensional Voronoi [141] cells, formed between the nodes that are located in the same tape section. A few examples of Voronoi cells are shown in Figure 3.1. These can be easily obtained by refining the grid containing all nodes by one level. The Voronoi cells are then found by walking on the refined grid around each node. For the

edge and corner nodes the shape is somewhat different. The projected overlap between the cells is calculated in the $\ell$-$t$ plane as shown in Figure 3.4. This is performed using Matlab's build in *polybool* operation to calculate the overlapping polygon and *polyarea* operation to calculate its area. This operation is performed only for nodes that have a higher $n$ coordinate than the source node to avoid forming the elements twice.

To avoid contact elements to form for tapes that are separated by another third tape, a contact pair matrix is used. For the Roebel cable this matrix is given as

$$\boldsymbol{M}_{\mathrm{sc}} = \begin{bmatrix} 0 & 1 & 0 & & 0 & 0 & 1 \\ 1 & 0 & 1 & \cdots & 0 & 0 & 0 \\ 0 & 1 & 0 & & 0 & 0 & 0 \\ & \vdots & & \ddots & & \vdots & \\ 0 & 0 & 0 & & 0 & 1 & 0 \\ 0 & 0 & 0 & \cdots & 1 & 0 & 1 \\ 1 & 0 & 0 & & 0 & 1 & 0 \end{bmatrix}, \qquad \text{Eq. 3.4}$$

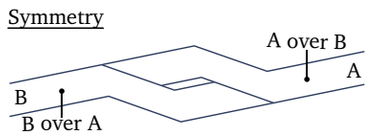


where the rows represent the source strand sections and the columns the target tape sections, making the size of the matrix $N_s \times N_s$. The ones represent the tape section pairs that are direct contact. The matrix is symmetric because a contact pair, in the Roebel cable, is overlapping in both directions, see small illustration besides the Equation. By only performing the pairing operation on these combinations of tape sections and directions, incorrect pairings are fully avoided.

The number of polygon operations, which can take a long computation time, can be reduced further, by only calculating the overlap areas for node pairs that have a separation distance which is less than 5 mm (several times the element size). Indexes of the source and target nodes are then stored as $k_{1,i}$ and $k_{2,i}$. The corresponding contact area is then given as $A_{12,i}$. The number of contact elements in the unit cell $N_{uec}$ (subscript $c$ stands for contact) depends on the geometry and can not be predicted in advance. In addition to the contact areas the Voronoi cells are also used to calculate the tape surface area represented by each node $A_{n,Q}$. These areas are later required to calculate properties such as the nodal heat capacity.

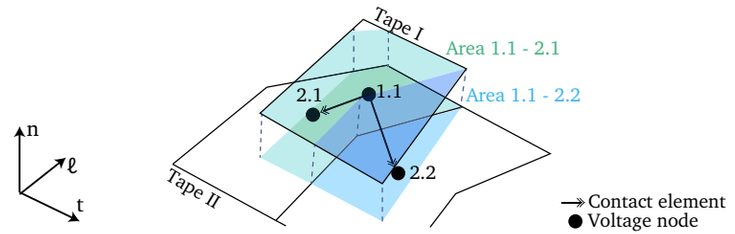


**Figure 3.4.** *Example showing the calculation of contact areas between the nodes of two tapes by projecting their respective Voronoi cells.*

At this point the nodes inside the unit cell are copied many times and shifted in $\ell$ to form the cable, after which they are transformed to Cartesian coordinates. A new index $c$ is

created, which runs from 1 to $N_u$, which is the number of unit cells. The transformation is performed before the elements are created because it avoids rotation of the vector elements during the coordinate transformation. In the case of a non-straight trajectory of the cable, such as in coil-windings, Equation 2.11 is used (using $Q$ indexes). For a straight cable the coordinates can be transformed one-to-one (i.e. $x = n$, $y = t$, $z = \ell$). The resulting coordinates of the nodes are $x_{n,c,Q}$, $y_{n,c,Q}$ and $z_{n,c,Q}$. For clarity these three components are grouped in a vector array $\vec{X}_{n,c,Q} = \vec{X}_{n,c,p,i,j}$. The transverse elements are now generated in each unit cell using

Eq. 3.5
$$\vec{X}_{et,c,p,i,j} = 0.5\left(\vec{X}_{n,c,p,i+1,j} + \vec{X}_{n,c,p,i,j}\right), \quad \vec{D}_{et,c,p,i,j} = \vec{X}_{n,c,p,i+1,j} - \vec{X}_{n,c,p,i,j} \ ,$$

where $\vec{X}_{et,c,p,i,j}$ is the coordinate vector of the transverse elements and where $\vec{D}_{et,c,p,i,j}$ is the direction vector of the transverse elements (subscript $et$ stands for transverse elements). Index $i$ runs from 1 to $N_{et,t} = N_{nt} - 1$, which is the number of transverse elements in the transverse direction. Index $j$ runs from 1 to $N_{et,l} = N_{nl}$, which is the number of transverse elements in the longitudinal direction. Similarly as for the nodes, the transverse elements are indexed using a group index chosen to be $P$, which is calculated from the node indexes as $P = pN_{et,t}N_{et,l} + jN_{et,t} + i$. Index $P$ runs from 1 to $N_{uet} = N_t N_{et,t} N_{et,l}$, which is the total number of transverse elements in each unit cell.

Similarly the longitudinal elements are generated using

Eq. 3.6
$$\vec{X}_{el,c,p,i,j} = 0.5\left(\vec{X}_{n,c,p,i,j+1} + \vec{X}_{n,c,p,i,j}\right), \quad \vec{D}_{el,c,p,i,j} = \vec{X}_{n,c,p,i,j+1} - \vec{X}_{n,c,p,i,j} \ ,$$

where $\vec{X}_{el,c,p,i,j}$ are the coordinates of the longitudinal elements and where $\vec{D}_{el,p,i,j}$ are the direction vectors of the longitudinal elements (subscript $el$ stands for longitudinal elements). Index $i$ runs from 1 to $N_{el,t} = N_{nt}$, which is the number of longitudinal elements in the transverse direction. Index j runs from 1 to $N_{el,l} = N_{nl} - 1$, which is the number of longitudinal elements in the longitudinal direction. Again an alternative index $R$ is defined as $R = pN_{el,t}N_{el,\ell} + jN_{el,t} + i$, which runs from 1 to $N_{uel} = N_s N_{el,t} N_{el,l}$ , which is the total number of longitudinal elements in each unit cell.

The flat tape surface is approximated by single line elements. Each line element represents a surface element that resembles a ribbon. Each line element should be located at the center of this surface element, such that it averages the current of this ribbon correctly. Therefore the elements running along the edges of the strands need to be moved slightly inward (see Figure 3.1). This is achieved by changing the position vectors using

Eq. 3.7
$$\begin{aligned} \vec{X}_{el,c,p,1,j} &= 0.75\vec{X}_{el,c,p,1,j} + 0.25\vec{X}_{el,c,p,2,j} \ , \\ \vec{X}_{el,c,p,N_{el,t},j} &= 0.75\vec{X}_{el,c,p,N_{el,t},j} + 0.25\vec{X}_{el,c,p,N_{el,t}-1,j} \ , \end{aligned}$$

for the longitudinal elements and using

Eq. 3.8
$$\begin{aligned} \vec{X}_{et,c,p,i,1} &= 0.75\vec{X}_{et,c,p,i,1} + 0.25\vec{X}_{et,c,p,i,2} \ , \\ \vec{X}_{et,c,p,i,N_{et,\ell}} &= 0.75\vec{X}_{el,c,p,i,N_{et,\ell}} + 0.25\vec{X}_{et,c,p,i,N_{et,\ell}-1} \ , \end{aligned}$$

for the transverse elements. To keep track of the connectivity of the elements the source and target connected to it, are found by generating a matrix $Q_{p,i,j}$ using the indexing provided by $Q$. The start and end nodes of the elements, $m_{et,1,c,P}$ and $m_{et,2,c,P}$ for the transverse elements, respectively, and $m_{el,1,R}$ and $m_{el,2,R}$ for the longitudinal elements, respectively, are then found using

$$\begin{aligned} m_{et,1,c,p,i,j} &= Q_{p,i,j}\ , \quad m_{et,2,c,p,i,j} = Q_{p,i+1,j}\ , \\ m_{el,1,c,p,i,j} &= Q_{p,i,j}\ , \quad m_{el,2,c,p,i,j} = Q_{p,i,j+1}\ . \end{aligned} \tag{Eq. 3.9}$$

Each element is assigned a length, which is calculated using Pythagoras as

$$L_{12,et,c,P} = \sqrt{\vec{D}_{et,c,Q} \cdot \vec{D}_{et,c,Q}}\ , \quad L_{12,el,c,R} = \sqrt{\vec{D}_{el,c,R} \cdot \vec{D}_{el,c,R}}\ , \tag{Eq. 3.10}$$

for the transverse and longitudinal elements, respectively. In addition a width $W_{12}$ is assigned, which is determined using

$$W_{12,et,c,p,i,j} = \left(L_{12,el,c,p,i,j} + L_{12,el,c,p,i,j+1}\right)/2, \tag{Eq. 3.11}$$

for the transverse elements. For the longitudinal elements the widths are determined using

$$W_{12,el,c,p,i,j} = W_r/(N_{el,t} - 1), \quad W_{12,el,c,p,i,j} = W_x/(N_{el,t} - 1), \tag{Eq. 3.12}$$

on the straight section and cross-over, respectively and divided by 2 on the edges. The orientation of the elements is required to calculate the incident field angle for the angle dependent critical current. The orientation is defined using the vectors along the tape $\vec{L}_{et,P}$ and $\vec{L}_{el,R}$, the vectors in the transverse direction $\vec{T}_{et,P}$ and $\vec{T}_{el,R}$ and the vectors in the face normal direction $\vec{N}_{et,P}$ and $\vec{N}_{el,R}$. The orientation vector arrays are calculated from the existing direction vector arrays using

$$\begin{aligned} \vec{L}_{et,c,p,i,j} &= \left[\vec{D}_{el,c,p,i,j} \quad \vec{D}_{el,c,p,i,N_{el,l}}\right], & \vec{L}_{el,c,p,i,j} &= \vec{D}_{el,c,p,i,j}, \\ \vec{T}_{et,c,p,i,j} &= \vec{D}_{et,c,p,i,j}, & \vec{T}_{el,c,p,i,j} &= \begin{bmatrix} \vec{D}_{et,c,p,i,j} \\ \vec{D}_{et,c,p,N_{et,t},j} \end{bmatrix}, \\ \vec{N}_{et,c,p,i,j} &= \vec{T}_{et,c,p,i,j} \times \vec{L}_{et,c,p,i,j}, & \vec{N}_{el,c,p,i,j} &= \vec{T}_{el,c,p,i,j} \times \vec{L}_{el,c,p,i,j}. \end{aligned} \tag{Eq. 3.13}$$

After creation, all orientation vectors are divided by their length in order to normalize them. The position and direction vector arrays of the contact elements are generated similarly to the transverse and longitudinal elements from their respective node coordinates using

$$\vec{X}_{ec,i} = 0.5\left(\vec{X}_{n,k_{1,i}} + \vec{X}_{n,k_{2,i}}\right), \quad \vec{D}_{ec,i} = \vec{X}_{n,k_{2,i}} - \vec{X}_{n,k_{1,i}}, \tag{Eq. 3.14}$$

where $\vec{X}_{ec,i}$ is the coordinate vector array and $\vec{D}_{ec,i}$ the direction vector array. For each unit cell the properties of the elements and the nodes are now collected and combined

into large (vector) arrays using

$$\text{EQ. 3.15}\qquad \begin{aligned}
\vec{X}_{e,c,K} &= \begin{bmatrix}\vec{X}_{et,c,P} & \vec{X}_{el,c,R} & \vec{X}_{ec,c,i}\end{bmatrix}, & \vec{D}_{e,c,K} &= \begin{bmatrix}\vec{D}_{et,c,P} & \vec{D}_{el,c,R} & \vec{D}_{ec,c,i}\end{bmatrix},\\
\vec{L}_{e,c,K} &= \begin{bmatrix}\vec{L}_{et,c,P} & \vec{L}_{el,c,R} & \vec{0}_{(1,N_{uec})}\end{bmatrix}, & \vec{T}_{e,c,K} &= \begin{bmatrix}\vec{T}_{et,c,P} & \vec{T}_{el,c,R} & \vec{0}_{(1,N_{uec})}\end{bmatrix},\\
\vec{N}_{e,c,K} &= \begin{bmatrix}\vec{N}_{et,c,P} & \vec{N}_{el,c,R} & \vec{0}_{(1,N_{uec})}\end{bmatrix}, & L_{12,c,K} &= \begin{bmatrix}L_{12,et,c,P} & L_{12,el,c,R} & L_{12,ec,c,i}\end{bmatrix},\\
W_{12,c,K} &= \begin{bmatrix}W_{12,et,c,P} & W_{12,el,c,R} & 0_{(1,N_{uec})}\end{bmatrix}, & A_{12,c,K} &= \begin{bmatrix}0_{(1,N_{uet})} & 0_{(1,N_{uel})} & A_{12,ec,c,R}\end{bmatrix},\\
m_{1,c,K} &= \begin{bmatrix}m_{et,1,c,P} & m_{el,1,c,R} & m_{ec,1,c,i}\end{bmatrix}, & m_{2,c,K} &= \begin{bmatrix}m_{et,2,c,P} & m_{el,2,c,R} & m_{ec,2,c,i}\end{bmatrix},\\
\vec{X}_{n,c,Q} &= \vec{X}_{n,Q}, & A_{n,c,Q} &= A_{n,Q},
\end{aligned}$$

where $K$ is the index into all elements of the unit cell independent of element type, which runs from 1 to $N_{ue} = N_{uel} + N_{uet} + N_{uec}$, which is the total number of elements in the unit cell. The matrices $0_{(a,b)}$ and $\vec{0}_{(a,b)}$ are of dimensions $a \times b$ and are filled with zeros and zero vectors respectively. The vectors are used to fill the space when no information is available. For example the orientation of the contact elements is filled with zeros because it is not defined. To keep track of element type the elements are labeled using the integer array

$$\text{EQ. 3.16}\qquad e_{\text{type},c,K} = \begin{bmatrix}1_{(1,N_{uet})} & 2_{(1,N_{uel})} & 3_{(1,N_{uec})}\end{bmatrix},$$

where 1 stands for transverse elements, 2 stands for longitudinal elements and 3 stands for contact elements (later more element types are added). To keep track of the tape an array with indexes $p$ is stored as

$$\text{EQ. 3.17}\qquad e_{\text{tape},c,K} = \begin{bmatrix}1_{(1,N_{uet}+N_{uel})}\ 2_{(1,N_{uet}+N_{uel})} & \dots & (N_s-1)_{(1,N_{uet}+N_{uel})}\ (N_s)_{(1,N_{uet}+N_{uel})}\ 0_{(1,N_{uec})}\end{bmatrix},$$

To group the elements further index $C$ is defined which groups the unit cells. Index $C$ is calculated as $C = cN_{ue} + K$. The nodes are grouped using $S = cN_{un} + Q$. The source and target nodes of the elements need to be re-indexed to

$$\text{EQ. 3.18}\qquad m'_{1,c,K} = m_{1,c,K} + (c-1)N_{un}, \quad m'_{2,c,K} = m_{2,c,K} + (c-1)N_{un}.$$

Because the tapes in the cable are transposed the index of the tapes are re-indexed using

$$\text{EQ. 3.19}\qquad e'_{\text{tape},c,K} = e_{\text{tape},c,K} + c - N_s\left\lfloor\frac{c}{N_s}\right\rfloor,$$

To summarize, the network representing the cable is now fully defined using arrays

$$\text{EQ. 3.20}\qquad \text{network} = \begin{Bmatrix}
\vec{X}_{e,C}, & \vec{D}_{e,C}, & \vec{L}_{e,C}, & \vec{T}_{e,C}, & \vec{N}_{e,C},\\
L_{12,C}, & W_{12,c,K}, & A_{12,C}, & m'_{1,C}, & m'_{2,C},\\
e_{\text{type},C}, & e'_{\text{tape},C}, & \vec{X}_{n,S}, & A_{n,S}, &
\end{Bmatrix}$$

As a final step, to connect the unit cells electrically, nodes that are overlapping between two unit cells are combined into a single node, thereby requiring a final re-indexing of $m$. A side view illustrating the nodes and elements is presented in Figure 3.5.

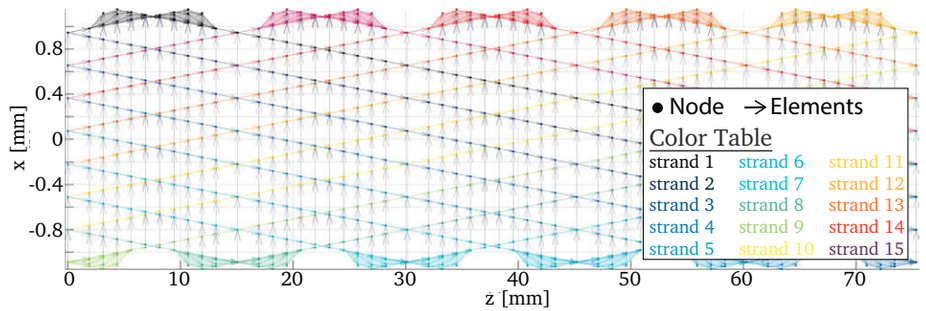


**Figure 3.5.** *Side view of the electrical network representing an example Roebel cable consisting of* 5 *unit cells. The contact elements between the tapes are represented by the gray arrows running along the $x$ direction. Note that the picture is not to scale.*

## Cable on Round Core 3.2.2

The setup of the Cable on Round Core (CORC) cable geometry is different from Roebel. The CORC cable is built up of multiple layers, each consisting of three tapes spiraling around one another in a triple helix (per layer), the direction (clock wise and anti clockwise) alternates from layer to layer. The helices running along the center of each of the tapes are defined in $t$, $n$ and $\ell$ coordinates using

$$
\begin{aligned}
t_{\mathrm{hlx},p,j} &= R_{\lfloor p/3 \rfloor} \sin\left(2\pi\theta_j + \phi_{\lfloor p/3 \rfloor} + \omega_{\mathrm{shift},p}\right), \\
n_{\mathrm{hlx},p,j} &= (-1)^{\lfloor p/3 \rfloor} R_{\lfloor p/3 \rfloor} \cos\left(2\pi\theta_j + \phi_{\lfloor p/3 \rfloor} + \omega_{\mathrm{shift},p}\right), \\
\ell_{\mathrm{hlx},p,j} &= \theta_j L_{\mathrm{tp},\lfloor p/3 \rfloor},
\end{aligned}
\qquad \text{Eq. 3.21}
$$

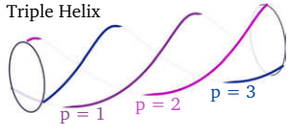


where $p$ is the index of the tape, $R_i$ is the radius of each of the layers indexed as $i$, $\phi_i$ is the rotational off-set of each of the layers, which is usually set as a list of random numbers on the interval $[0, 2\pi]$, $L_{\mathrm{tp},i}$ is the twist pitch given per layer and $\theta_j$ is a running parameter on the interval $[0, 1]$, with increments of $L_e/L_{\mathrm{tp}}$, in which $L_e$ is the requested element length. The brackets $\lfloor \ldots \rfloor$ denote rounding down of the value inside to the nearest integer using Matlab's floor function. The phase shift of the tapes is given as

$$
\omega_{\mathrm{shift},p} = (p - 3\lfloor p/3 \rfloor)\,\frac{2\pi}{3}. \qquad \text{Eq. 3.22}
$$

Because the orientation vectors of the cable coordinate system $\vec{L}$, $\vec{N}$ and $\vec{T}$ in this cable geometry do not correspond to the orientations of the tapes, a second tape coordinate coordinate system is constructed on the spiral using vectors $\vec{L}'$, $\vec{N}'$ and $\vec{T}'$. The accent denotes that the vectors are constructed inside the cable coordinate system. The geometry of the cable is then generated using two coordinate transformations, first from tape to cable and then from cable to coil. For convenience the coordinates $t_{\mathrm{hlx},p,j}$, $n_{\mathrm{hlx},p,j}$ and $\ell_{\mathrm{hlx},p,j}$ are grouped into position vector array $\vec{X}'_{\mathrm{hlx},p,j}$. The orientation vector

arrays along the spiral constructing the coordinate system of the individual tapes are now given as

$$\begin{aligned}\vec{L}'_{\mathrm{hlx},p,j} &= \vec{X}'_{\mathrm{hlx},p,j+1} - \vec{X}'_{\mathrm{hlx},p,j},\\ \vec{N}'_{\mathrm{hlx},p,j} &= \left[t_{\mathrm{hlx},p,j}, n_{\mathrm{hlx},p,j}, 0\right],\\ \vec{T}'_{\mathrm{hlx},p,j} &= \vec{L}'_{\mathrm{hlx},p,j} \times \vec{N}'_{\mathrm{hlx},p,j}\ .\end{aligned} \tag{Eq. 3.23}$$

The surface of the tapes is now given as where $t'$ is in the interval $[-W_t/2, W_t/2]$ and where $\ell'$ is in the interval $\left[0, L_{s,p}\right]$, where $L_{\mathrm{hlx},p}$ is the length of the helix (acquired through numerical integration).

Similarly to the Roebel, nodes are now placed on an equally spaced grid over the surface of the tape. This time it is not necessary to subdivide the tape, because there are no corners in the geometry. The coordinates of the nodes are now transformed once into cable coordinates. To ensure that all nodes are located on a cylindrical surface their coordinates are transformed to cylindrical coordinates in which the radius is fixed at $R_{\lfloor p/3 \rfloor}$. The calculation of the contact areas is the same as for Roebel, with the exception that it is performed in cylindrical coordinates. The three tapes of each layer are now in contact with the three tapes of the next layer. The contact matrix is then defined as

$$M_{\mathrm{sc}} = \begin{bmatrix} 0_{(3,3)} & 1_{(3,3)} & 0_{(3,3)} & 0_{(3,3)} & \cdots & 0_{(3,3)} \\ 0_{(3,3)} & 0_{(3,3)} & 1_{(3,3)} & 0_{(3,3)} & \cdots & 0_{(3,3)} \\ 0_{(3,3)} & 0_{(3,3)} & 0_{(3,3)} & 1_{(3,3)} & & 0_{(3,3)} \\ & \vdots & & & \ddots & 1_{(3,3)} \\ 0_{(3,3)} & 0_{(3,3)} & 0_{(3,3)} & 0_{(3,3)} & 0_{(3,3)} & 0_{(3,3)} \end{bmatrix}, \tag{Eq. 3.24}$$

where $n_{(a,b)}$ is an $a$ by $b$ matrix filled with $n$ at every index, $0_{(3,3)}$ for example is a three by three all zero matrix. From this point onwards the same equations are followed as for the Roebel cable, starting at Equation 3.5. An example geometry of the CORC cable is presented in Figure 3.6.

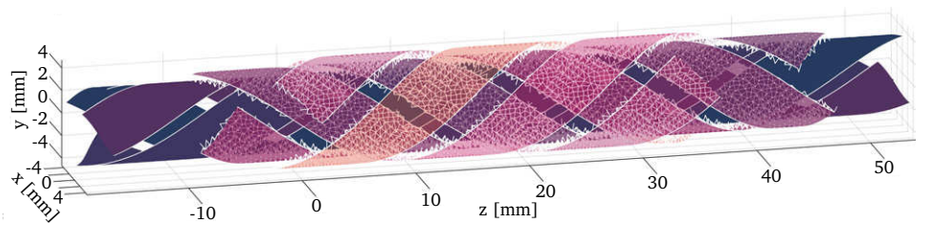


**Figure 3.6.** *Illustration showing the geometry of a CORC cable with arbitrary geometry. White lines represent the contact elements resulting from the contact area calculation.*

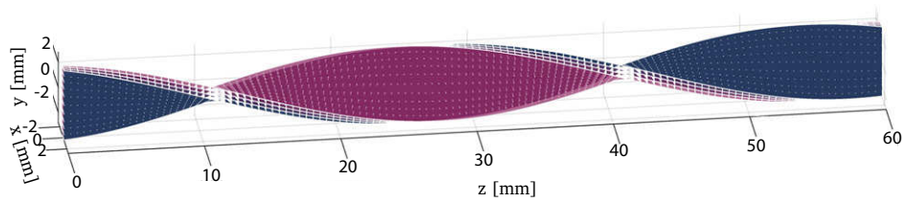


**Figure 3.7.** *Illustration showing the geometry of a Twisted-Stack cable with arbitrary geometry. White lines represent the contact elements resulting from the contact area calculation.*

## Twisted-Stack 3.2.3

The Twisted-Stack is easiest to setup of the available cable types. The location of the nodes for a non-twisted-stack of tapes are given in cable coordinates as a three dimensional uniform grid using

$$\begin{aligned} t_{p,i,j} &= iW_t/(N_{nt}-1) - W_t/2, \\ n_{p,i,j} &= pd_c/(N_s-1) - d_c/2, \\ \ell_{p,i,j} &= jL_{\text{tp}}/N_{n\ell} - L_{\text{tp}}/2. \end{aligned} \qquad \text{Eq. 3.25}$$

Each tape $p$ is only in contact with the next tape $p+1$. The contact matrix therefore becomes

$$M_{\text{sc}} = \begin{bmatrix} 0 & 1 & 0 & 0 & & 0 & 0 \\ 0 & 0 & 1 & 0 & \dots & 0 & 0 \\ 0 & 0 & 0 & 1 & & 0 & 0 \\ 0 & 0 & 0 & 0 & & 0 & 0 \\ & \vdots & & & & \vdots & \\ 0 & 0 & 0 & 0 & & 0 & 1 \\ 0 & 0 & 0 & 0 & \dots & 0 & 0 \end{bmatrix}. \qquad \text{Eq. 3.26}$$

Before the cable coordinates are transformed to Cartesian coordinates, a twist can be added to the tape stack using a coordinate transformation defined as

$$\begin{aligned} t'_{p,i,j} &= \sqrt{t_{p,i,j}^2 + n_{p,i,j}^2}\cos\left(\arctan\left(\frac{n_{p,i,j}}{t_{p,i,j}}\right) + 2\pi\frac{\ell_{p,i,j}}{L_{\text{tp}}}\right), \\ n'_{p,i,j} &= \sqrt{t_{p,i,j}^2 + n_{p,i,j}^2}\sin\left(\arctan\left(\frac{n_{p,i,j}}{t_{p,i,j}}\right) + 2\pi\frac{\ell_{p,i,j}}{L_{\text{tp}}}\right), \\ \ell'_{p,i,j} &= \ell_{p,i,j}. \end{aligned} \qquad \text{Eq. 3.27}$$

From this point onwards the same equations are followed as for the Roebel cable, starting at Equation 3.5. An example geometry of the twisted-stack cable is presented in Figure 3.7.

## 3.3 Electrical Equations

*In this section the system of equations responsible for the electric part of the model is discussed. Although the geometry is different, the electrical equations used here are very similar to the Cable-In-Conduit Cable (CICC) model JackPot-AC [64, 65] developed at the University of Twente. At a later stage the heat balance equation is added to the system (see Section 3.4).*

### 3.3.1 System of Equations

In the model Kirchhoff's Current and Voltage laws (KCL and KVL respectively) are solved. The first represents conservation of charge and states that the directed sum of the currents at each node in the network graph has to be zero. The currents in each of the elements is given as $I_r$. The second represents conservation of energy and states that the directed sum of voltages over any loop in the network has to be zero. Because finding all elementary circuits in an undirected three dimensional graph is not a trivial task [142], it was decided to implement the second law by keeping track of the voltages at the nodes. The voltage drop over each element $V_j$ has then to be equal to the differential voltage between the two nodes to which it is connected.

The linear part of the system, with the exception of the Multi-Level Fast Multipole Method (MLFMM), is implemented using Sparse matrices [143] and the non-linear part as functions. The notation used for the construction of such matrices is described in Section 3.3.2. During the solution of the system these equations are valid at each time step. The overall system of electric equations is then given as:

EQ. 3.28

$$\overbrace{\begin{bmatrix} G_{ij} & M_{\mathrm{kcl},ir} \\ M_{\mathrm{kvl},qj} & R_{qr} \end{bmatrix}}^{\text{Time Independent Linear}} \begin{bmatrix} V_j \\ I_r \end{bmatrix} + \overbrace{\begin{bmatrix} 0 \\ V_{\mathrm{nl},q}\left(I_r, T_r, \left|\vec{B}_r\right|, \alpha_r\right) \end{bmatrix}}^{\text{Time Independent Non-linear}} + \overbrace{\begin{bmatrix} I_{s,i} + I_{\mathrm{bg},i}\left(\frac{\partial \vec{B}_{bg}}{\partial t}\right) \\ V_{s,q} + V_{\mathrm{bg},q}\left(\frac{\partial \vec{B}_{bg}}{\partial t}\right) \end{bmatrix}}^{\text{External Sources}} + \overbrace{\begin{bmatrix} 0 & 0 \\ 0 & L_{qr} + M_{\mathrm{S2T},qr} \end{bmatrix} \begin{bmatrix} \frac{\partial V_j}{\partial t} \\ \frac{\partial I_r}{\partial t} \end{bmatrix} + \begin{bmatrix} 0 \\ V_{\mathrm{mlfmm},q}\left(\frac{\partial I_r}{\partial t}\right) \end{bmatrix}}^{\text{Time Dependent Linear}} = \overbrace{\begin{bmatrix} I_{\mathrm{res},i} \\ V_{\mathrm{res},q} \end{bmatrix}}^{\text{Residual}} \cong \vec{0}, \tag{3.28}$$

in which the first and second row of the equation represent Kirchhoff's Current and Voltage laws [144], respectively. In the equation indexes $i$ and $j$ are used here for the nodes and indexes $q$ and $r$ are used for the elements. Terms in the equation that have two indexes are matrices. After matrix vector multiplication and function resolution, equations with only indexes $i$ and $q$ remain. The first summing over currents and the second over voltages, resulting in residuals $I_{\mathrm{res},i}$ and $V_{\mathrm{res},q}$ respectively, which have to be equal to zero.

The connectivity of the network is given in the Kirchhoff's matrices $M_{\mathrm{kcl},ir}$ and $M_{\mathrm{kvl},qj}$, the construction of which is described in Section 3.3.3. The contact elements are either represented by resistance elements in matrix $R_{qr}$ or as conductances in matrix $G_{ij}$.

The second option is preferred because it reduces the number of equations. The resistance and conductance matrix are described in Section 3.3.7. The voltage over the superconducting elements is non-linear and is therefore calculated using a function that calculates $V_{\mathrm{nl},q}$ with as input the current $I_r$ through the element, the temperature at the element $T_r$, which is the bath temperature when performing an electro-magnetic only calculation, magnetic flux density at the element $\left|\vec{B}_r\right|$ and magnetic field angle $\alpha_r$ at the element. The superconducting elements, the function and its input are described in Section 3.3.8.

Between each element pair in the system the mutual inductance is calculated: a changing current in one element induces in a voltage across all other elements. The matrix containing all mutual inductances is dense and of size $N_e$ by $N_e$. For most network solvers this matrix places a huge strain on the available memory. To avoid this the mutual inductances are calculated using the MLFMM. For pre-conditioning purposes it is useful to store and use the matrix elements of the direct interaction step $M_{\mathrm{S2T},qr}$. The mutual inductance calculation is explained in further detail in Section 3.3.4. In addition to the mutual inductances each element also has a self-inductance: a changing current in an element induces a voltage over the element itself. The self-inductance is represented by matrix $L_{qr}$. For the self-inductance it is no longer possible to approximate the tapes using infinitely thin line elements. Therefore an analytical expression is used that depends on the shape of the element. This process is described in Section 3.3.6.

A cable is usually part of a larger system, for example a coil. To avoid modeling the entire object, several time dependent external source terms are available to drive the equations. External current can be applied to nodes using $I_{s,i}$ and external voltage can be applied across elements using $V_{s,q}$. Because the cable's transport current can also be part of a magnet it is also possible to apply a time-changing magnetic field using the functions $I_{\mathrm{bg},i}$ and $V_{\mathrm{bg},q}$. All source terms are described in more detail in Section 3.3.9.

## Sparse Matrix Notation 3.3.2

A sparse matrix is defined as a matrix in which sufficient elements are zero, such that it becomes worthwhile to store only the non-zero elements. This is achieved by storing the row indexes, column indexes and the value in a set of arrays $n_c$, $m_c$ and $v_c$ respectively, where $c$ runs from 1 to $N_{nz}$, which is the number of non-zero entries in the matrix. The size of the matrix is stored in scalars $N_1$ for the number of rows and $N_2$ for the number of columns. The example matrix

$$M_{ij} = \overbrace{\begin{bmatrix} 10 & 0 & 0 & 0 & -2 & 0 \\ 3 & 9 & 0 & 0 & 0 & 3 \\ 0 & 7 & 8 & 7 & 0 & 0 \\ 3 & 0 & 8 & 7 & 5 & 0 \\ 0 & 8 & 0 & 9 & 9 & 13 \\ 0 & 4 & 0 & 0 & 2 & -1 \end{bmatrix}}^{\text{Full}} = \overbrace{\begin{bmatrix} 10 & \cdot & \cdot & \cdot & -2 & \cdot \\ 3 & 9 & \cdot & \cdot & \cdot & 3 \\ \cdot & 7 & 8 & 7 & \cdot & \cdot \\ 3 & \cdot & 8 & 7 & 5 & \cdot \\ \cdot & 8 & \cdot & 9 & 9 & 13 \\ \cdot & 4 & \cdot & \cdot & 2 & -1 \end{bmatrix}}^{\text{Sparse}}, \qquad \text{Eq. 3.29}$$

which contains many zero entries (annotated using the dots) can be represented by such arrays as

Eq. 3.30
$$
\begin{aligned}
n_c &= \begin{bmatrix} 1 & 2 & 4 & 2 & 3 & 5 & 6 & 3 & 4 & 3 & 4 & 5 & 1 & 4 & 5 & 6 & 2 & 5 & 6 \end{bmatrix}, \\
m_c &= \begin{bmatrix} 1 & 1 & 1 & 2 & 2 & 2 & 2 & 3 & 3 & 4 & 4 & 4 & 5 & 5 & 5 & 5 & 6 & 6 & 6 \end{bmatrix}, \\
v_c &= \begin{bmatrix} 10 & 3 & 3 & 9 & 7 & 8 & 4 & 8 & 8 & 7 & 7 & 9 & -2 & 5 & 9 & 2 & 3 & 13 & -1 \end{bmatrix}, \\
N_1 &= N_2 = 6,
\end{aligned}
$$

which is one of many ways to represent a sparse matrix. Note that this is not the most memory efficient method, but probably the most convenient from a notation point of view. Therefore Matlab uses this definition on the user side, but internally, somewhat hidden from the user, uses a more efficient version. Because many sparse matrices are used in the system of equations, it is useful for understanding the model, to mathematically describe their structures (sparsity patterns). A mathematical notation for constructing these matrices in the form of a sparse function is defined here, following the definition in Matlab:

Eq. 3.31
$$
M_{ij} = \underset{N_1 \times N_2}{\text{sparse}}\left(n_c, m_c, v_c\right) = \begin{cases} v_c & \text{if} \quad i = n_c \quad \text{and} \quad j = m_c \quad \text{for any} \quad c \\ 0 & \text{if otherwise} \end{cases}
$$

where $i$ runs from 1 to $N_1$, $j$ runs from 1 to $N_2$ and $c$ runs from 1 to $N_{nz}$, which is the number of non-zero elements in the matrix. The sparse function now conveniently constructs the matrix from the respective indexes. It should be noted that in the model the full matrices are never constructed nor used. Often the indexes $n_c$ and $m_c$ are arrays of integers running from 1 to $N$ with increments of 1. The notation of such an array is simplified using the double dot array notation to $1{:}N$ (again following Matlab).

### 3.3.3 Kirchhoff's Connectivity Matrices

To couple the current to the voltage equations, the current law matrix $M_{kcl,ir}$ and the voltage law matrix $M_{kvl,qj}$ are used [6]. The matrices contain information on the element to node connectivity of the network, such that the first calculates the voltage drop over an element by taking the differential voltage of the nodes it is connected to and the second calculates the current flowing towards each node (the sum of which should be zero every time step), from the currents in all elements. These statements are given in equation form as

Eq. 3.32
$$
I_i = M_{\text{kcl},ir} I_r, \quad V_q = M_{\text{kvl},qj} V_j.
$$

Due to symmetry the KCL and KVL matrices are each others transpose $M_{\text{kcl},ir} = {M_{\text{kvl},qj}}^T$. Because the network geometry does not change over time the matrices are constructed before solving from the element connectivity arrays $m_{1c}$ and $m_{2c}$ using

Eq. 3.33
$$
\begin{aligned}
M_{\text{kcl},ir} &= \underset{N_n \times N_e}{\text{sparse}}\left(m_{2c}, 1{:}N_e, 1_{1,N_e}\right) - \underset{N_n \times N_e}{\text{sparse}}\left(m_{1c}, 1{:}N_e, 1_{1,N_e}\right), \\
M_{\text{kvl},qj} &= \underset{N_e \times N_n}{\text{sparse}}\left(1{:}N_e, m_{2c}, 1_{1,N_e}\right) - \underset{N_e \times N_n}{\text{sparse}}\left(1{:}N_e, m_{1c}, 1_{1,N_e}\right),
\end{aligned}
$$

where the sparse function and double dot array notation are defined in Section 3.3.2. As an example the sparsity pattern for a simple example network, consisting of 7 nodes and 8 elements (illustration of this network is shown next to the equation) is provided as

$$M_{\text{kcl}} = {M_{\text{kvl}}}^T = \begin{bmatrix} -1 & -1 & \cdot & \cdot & \cdot & \cdot & \cdot & \cdot \\ 1 & \cdot & -1 & \cdot & \cdot & \cdot & \cdot & \cdot \\ \cdot & 1 & \cdot & -1 & \cdot & \cdot & \cdot & \cdot \\ \cdot & \cdot & 1 & 1 & -1 & -1 & \cdot & \cdot \\ \cdot & \cdot & \cdot & \cdot & 1 & \cdot & -1 & \cdot \\ \cdot & \cdot & \cdot & \cdot & \cdot & 1 & \cdot & -1 \\ \cdot & \cdot & \cdot & \cdot & \cdot & \cdot & 1 & 1 \end{bmatrix} \Leftarrow$$

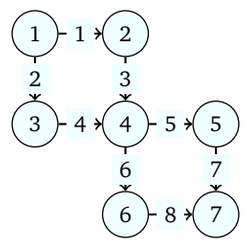


Eq. 3.34

in which the dots are used to annotate the non-existent zero entries of the sparse matrix.

## Mutual Inductance 3.3.4

To calculate the mutual inductance between two elements the time derivative of the vector potential is used. To calculate the vector potential from the currents in each element a Biot Savart type of approach can be used. In this approach all elements are approximated as a point source located at the center of the element. For a source current with index $r$ and a target element with index $q$ (see Figure 3.8) the equation for calculating the time derivative of the vector potential becomes [66]

$$\frac{d\vec{A}_q}{dt} = \frac{\mu_0}{4\pi}\frac{dI_r}{dt}\frac{\vec{D}_r}{\left|\vec{D}_r\right|}\log\left[\frac{k_1}{k_2}\right], \qquad \text{Eq. 3.35}$$

where $k_1$ and $k_2$ are given by

$$k_1 = \frac{b+a}{2\sqrt{a}} + \sqrt{\frac{1}{4}a + \frac{1}{2}b + c}, \quad k_2 = \frac{b-a}{2\sqrt{a}} + \sqrt{\frac{1}{4}a - \frac{1}{2}b + c}, \qquad \text{Eq. 3.36}$$

where $a$,$b$ and $c$ are defined by

$$a = \vec{D}_r \cdot \vec{D}_r = \left|\vec{D}_r\right|^2, \quad b = 2\vec{D}_r \cdot \left(\vec{X}_q - \vec{X}_r\right), \quad c = \left(\vec{X}_q - \vec{X}_r\right) \cdot \left(\vec{X}_q - \vec{X}_r\right). \qquad \text{Eq. 3.37}$$

The induced voltage in the target element can then be calculated using the dot product, between the direction vector of the element and the time derivative of the vector potential (this follows from the electric field $\vec{E} = -\nabla\phi - d\vec{A}/dt$, where $\phi$ is the electric potential), as

$$V_{\text{ind},q} = \vec{D}_q \cdot \frac{d\vec{A}_q}{dt}. \qquad \text{Eq. 3.38}$$

The full mutual inductance matrix $M_{qr}$ can then be calculated element wise by setting all $dI_r/dt$ to 1.0 A/s, resulting in units of Vs/A. The induced voltage in each element $V_{\text{mut},q}$ can then be calculated using a simple matrix vector product $V_{\text{mut},q} = M_{qr}dI_r/dt$.

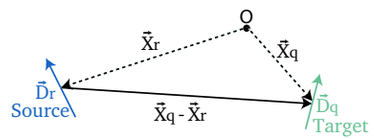


**Figure 3.8.** *Definition of the variables used for the calculation of the magnetic field with the Biot-Savart Law.*

The $M_{qr}$ matrix is fully populated requiring a large amount of memory to store. To illustrate, for a relatively small system containing $10^4$ elements ($\sim$ 3 unit cells), the number of matrix entries would be $(10^4)^2 = 10^8$, which corresponds to about 750 MB of memory. To overcome this the mutually induced voltages in the system are calculated using a Multilevel Fast Multipole Method (MLFMM) [7].

The MLFMM can calculate both the magnetic vector potential $A$ (and the magnetic field $B$) at any point from the currents in the elements $I_r$. Intrinsically it is also possible to calculate the time derivative of the vector potential $dA/dt$ (and thus the induced voltages) from the time derivative of the current $dI_r/dt$. This method employs Multipoles and Localpoles as intermediate steps to reduce the computational complexity of N-body problems, in this case of the Biot Savart type for magnetic field computation, from $O\left(N^2\right)$ to $O\left(N\right)$. A Multipole approximates the field generated by a group of line currents inside a sphere and is only valid at a certain distance, larger than its radius, from the sphere's center. A Multipole is a series expansion consisting of spherical harmonics [147, 148] (all possible solutions of the Laplace equation) in turn consisting of Legendre polynomials [149].

Because the vector potential has 3 components, the Multipoles here also need to consist of three separate expansions, in contrast to the original MLFMM algorithm, which has only one. A Localpole is the opposite of the Multipole. It represents the field of elements far away from the origin inside the sphere. The reduction of complexity acquired by the MLFMM is illustrated in Figure 3.9, in which a Multipole to Localpole transformation is used to transfer the field. It can be seen that the number of operations (represented by the gray lines) in considerably less than for the direct approach. It is also possible to translate and add Multipoles (at the same point) together to form a larger Multipole. The same applies to Localpoles which can also be translated and superimposed.

In reality the source and target elements can all be scrambled together. To avoid the Multipoles and Localpoles from intersecting (for which the transformation becomes invalid) a Multi-Level grid is used (see Figure 3.10 for overview of the algorithm). The grid is constructed starting from a (Parent) box that encloses all elements, into eight smaller boxes (Children). Each of these smaller boxes are then subdivided further into

[7] A full mathematical description of the Multi Level Fast Multipole Method lies outside the scope of this thesis. Therefore only a a description capturing the concept is provided here, interested readers are referred to Greengard [83, 84, 145] for the source material and Kurzak [146] for a detailed description. The GPU implementation of the MLFMM used for the Network Model is described in detail in van Nugteren [120].

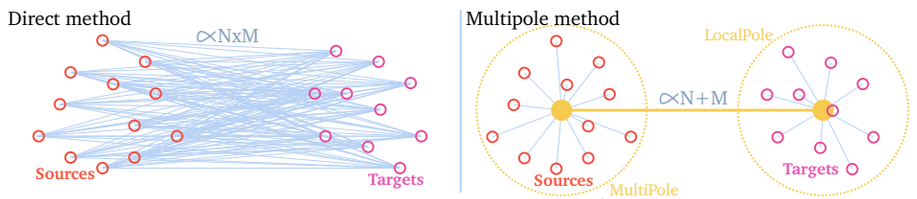


**Figure 3.9.** *Schematic representation showing the reduction of computation complexity when Multipoles and Localpoles are used as intermediate step in an N-body problem.*

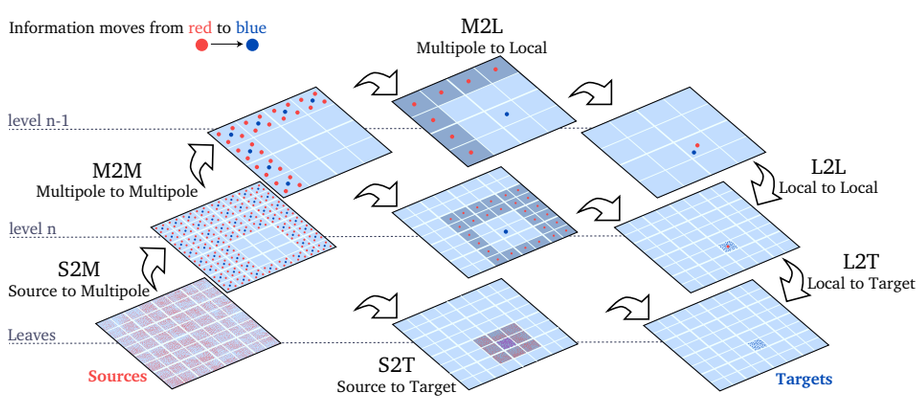


**Figure 3.10.** *Schematic two dimensional representation of the steps used in the Multi-Level Fast Multipole Method (concept of representation from [150]).*

eight even smaller boxes. This process is repeated recursively until the average number of source elements or target positions is less than a predefined number. The optimum for this predefined amount depends on the hardware and the number of expansions used. In order to increase memory efficiency only the boxes that contain source elements or target positions are stored (empty boxes are removed from the tree structure). Each box now corresponds to its own node in the tree, where the root of the tree, by definition level zero, is the most coarse level and the leaves are the most fine level. All nodes, with exception of the leave nodes, now contain eight or less child nodes. The leaves contain any number of source and/or target elements. For each node also two interaction lists are stored. The direct interaction list contains only indexes of the nodes whose boxes are in direct contact with the box of the corresponding node. The approximate interaction list contains the indexes of the nodes that are those children of the neighbors of the parent node, that are *not* contained in the direct interaction list. Spatial decomposition of these lists is shown in Figure 3.11. Each node stores also the center position of their box.

After the oct-tree construction is complete, the MLFMM algorithm traverses up and down its structure using following steps:

1. *S2M - Source to Multipole* - For all leaf nodes a multiPole expansion is formed at the center of their respective boxes representing the field of all the source elements contained inside.

2. *M2M - Multipole to Multipole* - The Multipole expansions propagate up the tree starting at the leaf level by translating their origin, to the center of the box of their parent node. The eight translated Multipole expansions are added to form a larger Multipole expansion. This process is repeated until the root level is reached. When this step is finished each node contains a Multipole expansion that represents the field generated by the source elements inside (all its children).

3. *M2L - Multipole to Localpole* - For each node at all levels the Multipole expansions are converted into Localpole expansions at the position of the nodes in their approximate interaction lists. This is the most computationally intensive step of the MLFMM and can take up 90% of its computation time.

4. *L2L - Localpole to Localpole* - The Localpole expansions propagate down the tree by translating them from each node, starting at the root level, to the positions of their children. When this step is finished all nodes contain a Localpole expansion representing the field generated by all elements that are not in its children nor in the children of the nodes in its direct interaction list.

5. *L2T - Localpole to Target* - For each leaf node the magnetic field or vector potential generated by its Localpole is evaluated at the target positions contained in its box.

6. *S2T - Source to Target* - Finally for each target position the field or voltage generated by all source elements in the parent node and the nodes in the direct interaction list of the parent node is evaluated directly. The self-inductance is excluded here. For the Network Model this last step is replaced by the sparse matrix $M_{\mathrm{S2T},qr}$ (the entries of which are calculated using Equation 3.35). The advantage is that this matrix can then also be used to approximate the MLFMM in the pre-pre-conditioner matrices (see Section 3.5 and Equations 3.66 and 3.70).

In the solver, instead of using a matrix vector product, now the MLFMM function is used as $V_{\mathrm{mut},q} = V_{mlfmm,q}(dI_r/dt) + M_{\mathrm{S2T},qr} dI_r/dt$, where the first term is a function with array input $dI_r/dt$ and the second term is a matrix vector product. It should be noted that, despite the majority of the matrix is not stored, this part of the system is still linear and can be solved using standard iterative solvers (that allow for function input) such as the conjugate gradient method. Because most of the translations and transformations used in the algorithm have no interdependence they can be executed in parallel. To exploit this parallelism to the maximum, the MLFMM is implemented to run on Graphics Processing Units (GPU). These devices allow ten-thousands of threads to be executed in parallel, at a relatively low clock rate. The speed-up found over the standard parallelized Central Processing Unit (CPU) code, which also makes use of the parallelism, is approximately 15 to 40 times for hardware of a similar price.

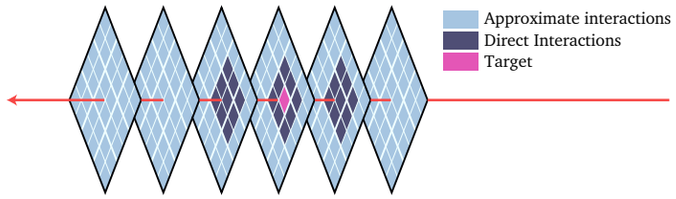


**Figure 3.11.** *Illustration showing the three dimensional spatial decomposition of the direct and approximate interaction lists used in the MLFMM(figure from [151]).*

### Magnetic Field Calculation 3.3.5

For the non-linear superconducting elements (see Section 3.3.8) the magnetic field value at each element $\left|\vec{B}_r\right|$ and field angle $\alpha_r$ are needed for the calculation of the critical current. The magnetic field $\vec{B}_r$ can be calculated using Biot Savart which is given in discrete form as

$$\vec{B}_r = \frac{\mu_0}{4\pi} \sum_{q=1}^{N_e} \frac{I_q \vec{D}_q \times \left(\vec{X}_q - \vec{X}_r\right)}{\left|\vec{X}_q - \vec{X}_r\right|^3}, \qquad \text{Eq. 3.39}$$

which has the same problem as with the Mutual inductance resulting in an $O\left(N^2\right)$ complexity. This can be avoided by using the MLFMM. But instead of using the time derivative of the current as input, now the current itself is used. In the L2T (final) step a different equation is used to calculate the magnetic field instead of the vector potential and in the S2T step Equation 3.39 is used. The magnetic field calculated from the elements is superimposed with the (time dependent) background field vector $\vec{B}_{\text{bg}}$. Note that this does not introduce inductive coupling with the background field in the system (this is described in Section 3.3.9).

To acquire the field angle with respect to the surface of the tape, $\alpha_r$, the orientation vectors $\vec{N}_r$, $\vec{T}_r$ and $\vec{L}_r$ of the elements, calculated in Equation 3.13, are used. The magnetic field in the direction of these vectors is calculated using the dot product as

$$B_{Nr} = \vec{N}_r \cdot \vec{B}_r, \quad B_{Tr} = \vec{T}_r \cdot \vec{B}_r, \quad B_{Lr} = \vec{L}_r \cdot \vec{B}_r, \qquad \text{Eq. 3.40}$$

where $B_{Nr}$ is the field along $\vec{N}_r$, $B_{Tr}$ the field along $\vec{T}_r$ and $B_{Lr}$ the magnetic field along $\vec{L}_r$. The in-plane components can then be combined as

$$B_{LTr} = \sqrt{B_{Tr}^2 + B_{Lr}^2}, \qquad \text{Eq. 3.41}$$

where $B_{LTr}$ is the in-plane magnetic field and where $B_{Nr}$ remains the out of plane magnetic field. The field angle $\alpha_r$ is then calculated from these components as

$$\alpha_r = \arctan\left(\frac{\left|\vec{B}_{Nr}\right|}{B_{LTr}}\right). \qquad \text{Eq. 3.42}$$

### 3.3.6 Self-Inductance

The self-inductance of the elements is calculated using an analytic equation depending on its shape. For the tape elements an equation is used for ribbons [152] given as

EQ. 3.43
$$L_{\text{rib},q} = 200 L_{12q}\left[\log\left(\frac{2L_{12q}}{W_{12q}+d_s}\right)+0.5+0.235\left(\frac{W_{12q}+d_s}{L_{12q}}\right)\right],$$

The required length of the elements $L_{12r}$ is originally calculated in Equation 3.10 and the required element width $W_{12r}$ in Equations 3.11 and 3.12. For the contact elements (if not included as conductances) an equation is used for round wires [153]. The diameter of the wires is calculated from the contact area as $d_q = \sqrt{A_{12q}/\pi}$. The contact area originates from the overlap between the Voronoi cells (Figure 3.4). The inductance of a wire element is given as

EQ. 3.44
$$L_{\text{con},q} = 200 L_{12q}\left[\log\left(\frac{2L_{12q}}{d_q}\left(1+\sqrt{1+\left[\frac{d_q}{2L_{12q}}\right]^2}\right)\right)-\sqrt{1+\left[\frac{d_q}{2L_{12q}}\right]^2}+\frac{\mu_r}{4}+\frac{d_q}{2L_{12q}}\right],$$

where $\mu_r$ is the permeability constant which is 1 in non-magnetic materials. The self-inductance of each element is stored on the diagonal of the matrix $L_{qr}$. The construction of the self-inductance matrix is then defined as

EQ. 3.45
$$L_{qr} = \underset{N_e \times N_e}{\text{sparse}}\left(1{:}N_e, 1{:}N_e, L_{e,q}\right),$$

where $L_{e,q}$ is the self-inductance of the element with index $q$ calculated as

EQ. 3.46
$$L_{e,r} = \begin{cases} L_{rib,q} & \text{if} \quad e_{type,q} = 1 \quad \text{or} \quad e_{type,q} = 2 \\ L_{con,q} & \text{if} \quad e_{type,q} = 3 \end{cases},$$

Note that when the inter strand resistance is modeled as part of the conductance matrix to reduce the number of elements, the contact elements can not have a self- or mutual inductance. This has almost no effect on the model because the contact elements are very short and therefore have nearly no self-inductance.

### 3.3.7 Inter-Strand Conductance and Resistance

From the overlapping area the resistance is calculated from a set contact resistance $\rho_{\text{contact}}$, estimated at $0.288\,\mu\Omega\text{m}^2$ [154, 155, 156], a value used unless stated otherwise. Recent measurements have shown a lower limit on the order of $0.1\,\text{n}\Omega\text{m}^2$ [157], which is three orders of magnitude lower. The contact resistances can be included in the system of equations using two different methods. The first is by including them as additional elements on the diagonal of the resistance matrix as

EQ. 3.47
$$R_{qr} = \underset{N_e \times N_e}{\text{sparse}}\left(1{:}N_e, 1{:}N_e, \frac{\rho_{\text{contact}}}{A_{12c}}\right).$$

The matrix can be used to calculate the resistive voltages as $V_q = R_{qr} I_r$. The second is by including their contribution to the node currents through the conductance matrix, which is given as

$$G_{ij} = \underset{N_n \times N_n}{\text{sparse}}\left(m_{1c}, m_{2c}, \frac{A_{12c}}{\rho_{\text{contact}}}\right) + \underset{N_n \times N_n}{\text{sparse}}\left(m_{2c}, m_{1c}, \frac{A_{12c}}{\rho_{\text{contact}}}\right) - \underset{N_n \times N_n}{\text{sparse}}\left(m_{2c}, m_{2c}, \frac{A_{12c}}{\rho_{\text{contact}}}\right) - \underset{N_n \times N_n}{\text{sparse}}\left(m_{1c}, m_{1c}, \frac{A_{12c}}{\rho_{\text{contact}}}\right). \quad \text{Eq. 3.48}$$

The additional current at the nodes can then be calculated as $I_i = G_{ij} V_j$. Note that when the elements are implemented in the conductance matrix they no longer require a separate equation in the system, thereby reducing complexity. This comes at the cost of ignoring the self- and mutual inductances of these elements.

### Non-Linear Superconducting Elements 3.3.8

The superconducting elements have a non-linear voltage-to-current behavior. This introduces hysteresis into the model [158], but also allows for accurate quench propagation predictions. During a quench the current density of the elements strongly exceeds the critical one, therefore it is not sufficient to model these elements using only a basic power law, with exponent $N_{\text{sc}}$ (which set to be 30 unless stated otherwise). Instead, a current sharing model is used in which the superconductor runs in parallel with the normal conducting matrix. To calculate the fraction of the total current in the element $I_q$ that runs in the superconductor $I_{\text{sc},q}$ an implicit equation (residual $r$ should equal zero) is used, which is given as

$$I_q - \overbrace{\frac{E_0}{\rho_{tq}\left(\left|B_q\right|, T_q\right)}\left[\frac{I_{\text{sc},q}}{I_{c,q}(\left|B_q\right|, T_q, \alpha_q)}\right]^{N_{\text{sc}}}}^{\text{Normal Conducting Current}} - I_{sc,q} = r \cong 0, \quad \text{Eq. 3.49}$$

where $\rho_{tq}$ is the resistance of the tape element (in most cases dominated by the copper) in Ohm per meter length. The resistance of the element is calculated by placing the various materials making up the layers of the tape in parallel. The resulting Equation is

$$\frac{1}{\rho_{tq}\left(\left|B_q\right|, T_q\right)} = \sum_{\text{mat}} \frac{W_{12q} d_{\text{mat}}}{\rho_{\text{mat},q}\left(\left|B_q\right|, T_q\right)}, \quad \text{Eq. 3.50}$$

where $d_{\text{mat}}$ is the thickness of the (material) layer and where the individual material resistivity $\rho_{mat,q}$ given in Ωm is interpolated from data generated by Cryocomp [124] and various other sources. This interpolation relies on both the temperature $T_q$ and the magnetic flux density $\left|\vec{B}_q\right|$ (to include the magneto resistance). By using fixed increments for the temperature in the data tables, searches through the table can be avoided, making it likely the fastest method for accessing material property data. The electric field criterion $E_0$ in units of V/m is given as $10\,\mu$V/m. The critical current $I_{c,q}$,

given by Equation A.10, depends on the magnetic flux density $\left|\vec{B}_q\right|$, temperature $T_q$ and magnetic field angle $\alpha_q$ of the respective element. After the equation is solved for the superconducting current running in each element, the normal conducting current is calculated as $I_{\mathrm{nc},q} = I_q - I_{\mathrm{sc},q}$, from which the voltage drop of the element is calculated as $V_{\mathrm{nl},q} = I_{\mathrm{nc},q}\rho_q L_{12q}$. For the electric model the temperature $T_q$ is given by the temperature of the coolant bath $T_{\mathrm{bath}}$. For the thermal model the temperature of the element is calculated by averaging the temperature of the connected nodes (see Section 3.4.1). The magnetic field and its angle are calculated from the element currents using the MLFMM (this is described in Section Sections 3.3.4 and 3.3.5).

Equation 3.49 is implicit and the superconducting current $I_{\mathrm{sc},q}$ thus needs to be solved numerically through the following steps:

1. A higher and lower bound are set for the superconducting current at $I_{\mathrm{sc,low},q} = 0$ and $I_{\mathrm{sc,high},q} = I_q$ respectively.
2. The residual $r$ is calculated for current $I_{\mathrm{sc,try},q} = \left(I_{\mathrm{sc,low},q} + I_{\mathrm{sc,high},q}\right)/2$.
3. If $r < 0$ the tried superconducting current is too high and the upper bound is moved: $I_{\mathrm{sc,high},q} = I_{\mathrm{sc,try},q}$.
4. If $r > 0$ the tried superconducting current is too low and the lower bound is moved: $I_{\mathrm{sc,low},q} = I_{\mathrm{sc,try},q}$.
5. If $\left|I_{\mathrm{sc,high},q} - I_{\mathrm{sc,low},q}\right| < 10^{-7}$ convergence is reached and the superconducting current is found. Otherwise the process is repeated from step 2.

This algorithm is in essence a simplified (and in this specific case faster) version of the Newton-Raphson [159] algorithm. Because there is no interdependence, the solution can be obtained using parallel threads, one for each element. As an example the current sharing between the matrix and the superconductor is presented in Figure 3.12. It can be seen that the saturation of the superconductor consists of a very smooth transition, allowing for large excess currents of 1.5 times the critical current, with only a small fraction of the current running in the matrix.

In the pre-conditioner and Jacobian functions (see Section 3.5) it is necessary to linearize the resistance of the superconducting elements. For the pre-conditioner this is achieved by approximating the resistance of the superconducting elements using Ohm's law as $r_{\mathrm{nl},r} = V_{\mathrm{nl},r}/I_r$. The resistances are then placed on the diagonal of the non-linear resistance matrix as

EQ. 3.51
$$R_{\mathrm{nl},qr} = \underset{N_e \times N_e}{\mathrm{sparse}}\left(1{:}N_e, 1{:}N_e, r_{\mathrm{nl},r}\right).$$

For the Jacobian function the local derivative $dV_r/dI_r$ is needed. This derivative is determined by solving Equation 3.49 twice for $I_r - \Delta I/2$ and for $I_r + \Delta I/2$, resulting in voltages $V_{\mathrm{nl1},r}$ and $V_{\mathrm{nl2},r}$ respectively. The derivative is then given as $dV_r/dI_r = \left(V_{\mathrm{nl2},r} - V_{\mathrm{nl1},r}\right)/\Delta I$. The value of $\Delta I$ needs to be high enough to be above the noise of

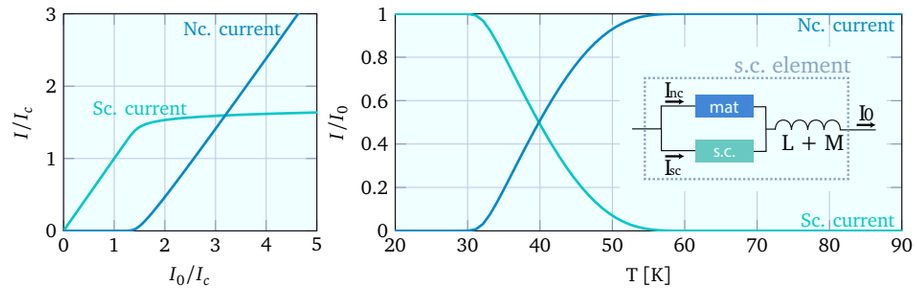


**Figure 3.12.** *Current sharing between the superconductor and the matrix in the case of excess current (left) and as function of temperature (right). The current in the superconductor $I_{sc}$ and the matrix $I_{nc}$ are calculated (implicitly) using the relation in Equation* 3.49.

the iterative solver and is chosen to be 0.1 A. The derivative is stored on the diagonal of the matrix $M_{\mathrm{dVdI},qr}$, which is constructed as

$$M_{\mathrm{dVdI},qr} = \underset{N_e \times N_e}{\mathrm{sparse}}\left(1{:}N_e, 1{:}N_e, \frac{dV_r}{dI_r}\right). \qquad \text{Eq. 3.52}$$

## External Coupling 3.3.9

To reduce the computational complexity usually a short length of cable, which can be part of a larger coil system, is simulated. To drive the current in the cable on either end a current source and sink can be connected (see Figure 3.13). This is performed by adding an extra entrance node, to which all the nodes at the end of each tape are connected through additional elements, which have been assigned an $e_{\mathrm{type}}$ of 4 and 5 for the source and sink, respectively. By setting the time dependent source current $I_{s,i}$ at these nodes the tape currents can be controlled directly. If the current re-distribution over the cable is of interest, for example during quench simulations, an additional cable entrance node is added to which all the entrance nodes of the tapes are connected through additional elements, which have been assigned an $e_{\mathrm{type}}$ of 9 and 10 for the source and sink, respectively. To include the self-inductance of the coil, these elements can be assigned an additional self-inductance and mutual inductance (off diagonal) in the $L_{qr}$ matrix.

Usually the cable is situated in a time-changing background magnetic field generated by the coil the cable is part of. A time-changing magnetic field introduces an electric field, which induces screening currents through the electro-motive force. The coupling between the elements and the background field is calculated from the cross product between the Vector Potential $\vec{A}$ and the direction vector $\vec{D}$. The vector potential is defined as $\vec{B}_{\mathrm{bg}} = \vec{\nabla} \times \vec{A}_{\mathrm{bg}}$, which is written out as

$$B_{\mathrm{bg},x} = \overline{\frac{\partial A_{\mathrm{bg},z}}{\partial y}} - \frac{\partial A_{\mathrm{bg},y}}{\partial z}, \quad B_{\mathrm{bg},y} = -\frac{\partial A_{\mathrm{bg},x}}{\partial z} + \overline{\frac{\partial A_{\mathrm{bg},z}}{\partial x}}, \quad B_{\mathrm{bg},z} = \overline{\frac{\partial A_{\mathrm{bg},y}}{\partial x}} - \frac{\partial A_{\mathrm{bg},x}}{\partial y}, \qquad \text{Eq. 3.53}$$

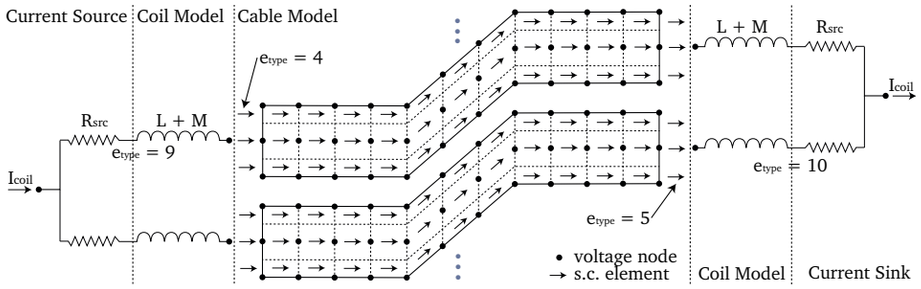


**Figure 3.13.** *Connection diagram of the sources and sinks with the cable model. For clarity only* 2 *out of* $N_t$ *tapes are shown.*

because of the nature of the vector potential it can represent the same magnetic field $\vec{B}$ in different ways and is therefore not uniquely defined. The definition of the vector potential as function of the background field is therefore a free choice. In the model the vector potential as function of the background field $\vec{B}_{\mathrm{bg}}$ is given by only the over-bracketed terms in Equation 3.53. By straight forward integration the vector potential becomes

EQ. 3.54 $$A_{\mathrm{bg},x} = 0, \quad A_{\mathrm{bg},y} = xB_{\mathrm{bg},z}, \quad A_{\mathrm{bg},z} = yB_{\mathrm{bg},x} - xB_{\mathrm{bg},y},$$

where $x$, $y$ and $z$ is the position at which the vector potential is defined. The induced voltages however come from a time-changing magnetic field and thus vector potential, therefore the derivatives are given as

EQ. 3.55 $$\frac{dA_{\mathrm{bg},x}}{dt} = 0, \quad \frac{dA_{\mathrm{bg},y}}{dt} = x\frac{dB_{\mathrm{bg},z}}{dt}, \quad \frac{dA_{\mathrm{bg},z}}{dt} = y\frac{dB_{\mathrm{bg},x}}{dt} - x\frac{dB_{\mathrm{bg},y}}{dt},$$

When the position $x$, $y$ and $z$ is equal to the position vector of the elements $\vec{X}_e$, the induced voltage over the elements is provided by Equation 3.38.

## 3.4 Adding Thermal Equations

*For analyzing the thermal behavior of cable, for example during a quench, the electrical equations can be coupled to the heat balance equation [160]. The use of these additional equations is optional and can be enabled or disabled when required.*

### 3.4.1 System of Equations

The new system of equations consists of both an electrical part and a thermal part. In addition to the voltages $V_j$ and the currents $I_r$, the temperature at each node is added $T_p$, where indexes $p$ and $s$ are added to index the temperature nodes, which are the same as the voltage nodes. After matrix multiplication and function resolution now three sets of equations with indexes $i$, $q$ and $s$ remain. The equations with index $s$ sum

over the heat flux towards each of the temperature nodes. Unlike Kirchhoff's Current Law the heat can be stored in a nodes through the heat capacity of the node. For some of the functions it is necessary to have the temperature also at the elements $T_r$. These are calculated by taking the average between the temperatures of nodes indexed with $m_{1r}$ and $m_{2r}$. The full system of equations is then given as

$$\overbrace{\begin{bmatrix} G_{ij} & M_{\mathrm{kcl},ir} & 0 \\ M_{\mathrm{kvl},qj} & R_{qr} & 0 \\ 0 & 0 & K_{sp}-K_{\mathrm{cool},sp} \end{bmatrix}\begin{bmatrix} V_j \\ I_r \\ T_p \end{bmatrix}}^{\text{Time Independent Linear}} + \overbrace{\begin{bmatrix} 0 \\ V_{\mathrm{nl},q}\left(I_r, T_r, \left|\vec{B}_r\right|, \alpha_r\right) \\ P_{\mathrm{nl},s}\left(I_r, T_r, \left|\vec{B}_r\right|, \alpha_r\right) + P_{G,s}\left(V_j\right) + P_{R,s}\left(I_r\right) \end{bmatrix}}^{\text{Time Independent Non-linear}} +$$

$$\overbrace{\begin{bmatrix} I_{s,i} + I_{\mathrm{bg},i}\left(\frac{\partial \vec{B}}{\partial t}\right) \\ V_{s,\mathrm{q}} + V_{\mathrm{bg},q}\left(\frac{\partial \vec{B}}{\partial t}\right) \\ P_{s,s} + K_{\mathrm{cool},ss}T_{\mathrm{bath}} \end{bmatrix}}^{\text{External Sources}} + \overbrace{\begin{bmatrix} 0 & 0 & 0 \\ 0 & L_{qr}+M_{\mathrm{S2T},qr} & 0 \\ 0 & 0 & -C_{p,sp} \end{bmatrix}\begin{bmatrix} \frac{\partial V_j}{\partial t} \\ \frac{\partial I_r}{\partial t} \\ \frac{\partial T_p}{\partial t} \end{bmatrix} + \begin{bmatrix} 0 \\ V_{\mathrm{mlfmm},q}\left(\frac{\partial I_r}{\partial t}\right) \\ 0 \end{bmatrix}}^{\text{Time Dependent Linear}} = \overbrace{\begin{bmatrix} I_{\mathrm{res},i} \\ V_{\mathrm{res},q} \\ P_{\mathrm{res},s} \end{bmatrix}}^{\text{Residual}} \cong \vec{0}, \quad \text{Eq. 3.56}$$

where the heat equation matrices $K_{sp}$ and $C_{p,sp}$ comprising thermal conductivity and heat capacity, respectively, are described in Section 3.4.2.

The coupling between the electro-magnetic and thermal systems is mainly provided by the electrical power generation causing additional heat to be deposited into the nodes in the system. The power generation by the conductors and resistors is non-linear and is described by the functions $P_{G,s}\left(V_j\right)$ and $P_{R,s}\left(I_r\right)$ respectively. The non-linear power generation of the superconducting elements relies on the current sharing and is therefore described by a separate function $P_{nl,s}$. In addition to the internal power generation it is also possible to externally add power to the nodes, for example to initiate a quench. This power is represented by the source term $P_{s,s}$. The power matrices and functions are described in Section 3.4.3. The last term $K_{\mathrm{cool},sp}$ represents the cooling from the nodes on the cable's surface to the surrounding coil structure and ultimately cryogen with temperature $T_{\mathrm{bath}}$. The cooling and the matrix is described in Section 3.4.4. Because the matrices $K_{sp}$, $C_{p,sp}$ and $K_{cool,sp}$ rely on the temperature dependent material properties it is necessary to re-assemble them each time step.

## Thermal Conductivity and Heat Capacity 3.4.2

$K_{sp}$ is the thermal conductivity matrix. The matrix is defined such that $K_{sp}T_p$ is the heat flux towards each node in W. The sparsity pattern of the thermal conductivity is assembled as

$$\begin{aligned} K_{sp} = &\underset{N_n \times N_n}{\mathrm{sparse}}\left(m_{1c}, m_{2c}, k_{tc}\right) - \underset{N_n \times N_n}{\mathrm{sparse}}\left(m_{1c}, m_{1c}, k_{tc}\right) + \\ &\underset{N_n \times N_n}{\mathrm{sparse}}\left(m_{2c}, m_{1c}, k_{tc}\right) - \underset{N_n \times N_n}{\mathrm{sparse}}\left(m_{2c}, m_{2c}, k_{tc}\right), \end{aligned} \quad \text{Eq. 3.57}$$

where $k_{tc}$ is the thermal conductivity of the elements in units of Watt per Kelvin, and is calculated for the superconducting elements from the thermal conductivity of the

individual materials making up the layers of the tapes. For the contact elements the thermal conductivity is estimated at $k_{\text{contact}} = 100\,\text{W}/(\text{m}^2\text{K})$ [154, 161], which is the value used unless stated otherwise. The thermal conductivity of the elements then becomes

EQ. 3.58
$$k_{tq} = \begin{cases} \sum_{\text{mat}} \dfrac{k_{\text{mat}}\left(T_q\right) W_{12q}}{L_{12q}}, & \text{if} \quad e_{\text{type},q} = 1 \quad \text{or} \quad e_{\text{type},q} = 2 \\ k_{\text{contact}} A_{12q} & \text{if} \quad e_{\text{type},q} = 3 \end{cases},$$

where $k_{\text{mat}}$ is the thermal conductivity between each of the layers interpolated from a data table generated with CryoComp [124]. The temperature rise in the tape is controlled by the heat capacity matrix, which a diagonal matrix given as

EQ. 3.59
$$C_{p,sp} = \underset{N_n \times N_n}{\text{sparse}}\left(1{:}N_n, 1{:}N_n, C_{pt,c}\right).$$

The heat capacity of each node $C_{pt,c}$ in J/K is calculated as

EQ. 3.60
$$C_{pt,Q} = \sum_{\text{mat}} C_{p,\text{mat}}\left(T_p\right) A_{n,Q} d_{\text{mat}},$$

where $C_{p\text{mat}}$ is the heat capacity in $\text{J}/(\text{m}^3\text{K})$, interpolated from a data table generated with CryoComp [124] and other sources.

### 3.4.3 Power Generation

All losses included in the model, in essence coupling, hysteresis and transport excess current, are eventually included in the form of electric power dissipation, which is non-linear because it is by definition given as the square of the current or voltage $P = I^2R = V^2/R = IV$ (derived from Ohm's law). Other loss factors, caused by for example mechanical motion, are not included in the model itself, but can be added using the external source term $P_{s,s}$. The power generation is linearized each time step by re-calculating the matrices $I_{G,sj}$ and $V_{R,sr}$ for the conductances and resistors respectively. The first matrix is given as

EQ. 3.61
$$I_{G,sj} = \underset{N_n \times N_n}{\text{sparse}}\left(k_{1c}, k_{2c}, \frac{I_{\text{con},c}}{2}\right) - \underset{N_n \times N_n}{\text{sparse}}\left(k_{1c}, k_{1c}, \frac{I_{\text{con},c}}{2}\right) - \underset{N_n \times N_n}{\text{sparse}}\left(k_{2c}, k_{1c}, \frac{I_{\text{con},c}}{2}\right) + \underset{N_n \times N_n}{\text{sparse}}\left(k_{2c}, k_{2c}, \frac{I_{\text{con},c}}{2}\right),$$

where $I_{con}$ is the current in the conductance elements, calculated as $I_{con,i} = M_{kvl} V_j A_{12,i} / \rho_{\text{contact}}$. The second matrix is given as

EQ. 3.62
$$V_{R,sr} = \underset{N_n \times N_e}{\text{sparse}}\left(m_{1c}, 1{:}N_e, \frac{R_{cc} I_c}{2}\right) + \underset{N_n \times N_e}{\text{sparse}}\left(m_{2c}, 1{:}N_e, \frac{R_{cc} I_c}{2}\right).$$

Because the linearisation matrices depend on the voltages $V_j$ and currents $I_r$ at that specific time, they need to be updated each time step. For convenience the matrices

are also used in the conductance and resistance power generation functions to calculate the power at the nodes using

$$P_{G,s}\left(V_j\right) = I_{G,sj} V_j, \quad P_{R,s}\left(I_r\right) = V_{R,sr} I_r, \tag{Eq. 3.63}$$

with the advantage that the connectivity of the nodes to the elements is already included in the matrices.

The power generation in the non-linear superconducting elements is described by the function $P_{\mathrm{nl},r}\left(I_r, T_r, \left|\vec{B}_r\right|, \alpha_r\right)$ which depends on the element current, temperature, magnetic flux density and the field angle respectively. The function uses Equation 3.49 to calculate the resistive voltage drop over the element $V_{\mathrm{nl},q}$ (note that no inductive components are included here). The power is then calculated from the voltage drop as $P_{\mathrm{nl},r} = V_{\mathrm{nl},r} I_{\mathrm{nc},r}$. The source power term $P_{s,s}$ is used to externally supply power to the nodes in the system. This array is time dependent and is updated each time step using an external signal function (for example a square pulse).

For the Jacobian (see Section 3.5) the local dependence of the power at the nodes $P_s$ on the element current $I_q$ and the node temperatures $T_p$ is required. Because the power is generated in the elements the derivatives $dP_q/dI_q$ and $dP_q/dT_q$ are calculated first using finite difference similar to the non-linear voltages (see Section 3.3.8). The Jacobian matrices, used to calculate the local power derivatives at the nodes, are then constructed from these arrays using

$$\begin{aligned} M_{\mathrm{dPdI},sp} &= \underset{N_n \times N_e}{\mathrm{sparse}}\left(m_{1c}, 1{:}N_e, \frac{1}{2}\frac{dP_c}{dI_c}\right) + \underset{N_n \times N_e}{\mathrm{sparse}}\left(m_{2c}, 1{:}N_e, \frac{1}{2}\frac{dP_c}{dI_c}\right), \\ M_{\mathrm{dPdT},sr} &= \underset{N_n \times N_e}{\mathrm{sparse}}\left(m_{1c}, m_{1c}, \frac{1}{4}\frac{dP_c}{dT_c}\right) + \underset{N_n \times N_e}{\mathrm{sparse}}\left(m_{1c}, m_{2c}, \frac{1}{4}\frac{dP_c}{dT_c}\right) + \\ &\quad \underset{N_n \times N_e}{\mathrm{sparse}}\left(m_{2c}, m_{1c}, \frac{1}{4}\frac{dP_c}{dT_c}\right) + \underset{N_n \times N_e}{\mathrm{sparse}}\left(m_{2c}, m_{2c}, \frac{1}{4}\frac{dP_c}{dT_c}\right). \end{aligned} \tag{Eq. 3.64}$$

### Cooling Term 3.4.4

Additional cooling can be added to the surface nodes of the network. The surface nodes are labeled by finding the nodes that have only contact elements connected to them from one side. The cooling from the surface to the surroundings $k_{\mathrm{cool},p}$ can be a fixed value in Watt per Kelvin, but can also (as a rough approximation) be made dependent on the average temperature of the surface nodes. For nodes that are not surface nodes $k_{\mathrm{cool},p}$ is zero. The diagonal cooling matrix is then given as

$$K_{\mathrm{cool},sp} = \underset{N_n \times N_n}{\mathrm{sparse}}\left(1{:}N_n, 1{:}N_n, k_{\mathrm{cool},c}\right). \tag{Eq. 3.65}$$

The cooling matrix is used twice in the system of equations, see Equation 3.56, to acquire the differential temperature between the surface nodes and the bath.

## 3.5 Solving the System of Equations

*Once the matrices are setup the electrical system in Equation* 3.28 *or the thermo-electric system in Equation* 3.56 *needs to be solved. In order to scale all equations to the same order of magnitude, thereby simplifying the solution, the system and its matrices are scaled to* μV*,* A *and* mW *for the Voltages, Currents and Heat Fluxes/Generation respectively. Also one single Voltage equation (the first row and column of the matrix) is removed from the system to represent the zero voltage node* $V_1 = 0$*. There are two solvers types available. The first is a steady state solver that ignores the time dependent terms in the equations. Because the mutual inductance is avoided it allows for solving much larger systems. However, because the distribution of the current in a superconductor depends on the unknown history (i.e. hysteresis), it must be noted that the steady state solution are non-unique. The second is a time dependent solver that takes all terms into account and leads to a unique solution.*

### 3.5.1 Steady State Solution

The steady state solution of the system is calculated using Sundials KINSol [86], which is a solver for non-linear algebraic systems. Alternatively also Matlab's built-in *fsolve* function can be used. KINSol needs a series of functions as input:

1. *System Function* - Calculates the residual current $I_{\text{res},i}$, voltage $V_{\text{res},r}$ and heat $P_{\text{res},s}$ as function of the voltage $V_i$, current $I_r$ and temperature $T_p$ using the time-independent parts of electric system Equation 3.28, or thermo-electric system Equation 3.56.

2. *Pre-conditioner Function* - The pre-conditioner function solves a linearized system of equations of the form of $\boldsymbol{A}_{\text{ss,pre}} p = r$, where $\boldsymbol{A}_{\text{ss,pre}}$ is the pre-conditioner matrix (see Equation 3.66) representing the linearized system.

3. *Pre-conditioner Setup Function* - To speed-up the pre-conditioner the pre-conditioner matrix $\boldsymbol{A}_{\text{ss,pre}}$ is factorized during this setup step. There are many different techniques available for matrix factorization, which are explored in Section 3.5.3. The factorized matrix can be used many times in the pre-conditioner function before another factorization is required.

4. *Jacobian Times Vector Function* - The non-linear part is solved using a Jacobian Times Vector Function (JTVFun). The JTVFun describes the change of the residuals $\Delta I_{\text{res},i}$, $\Delta V_{\text{res},r}$, $\Delta dP_{\text{res},s}$ as function of a change of system variables, voltage $\Delta V_i$, current $\Delta I_r$ and temperature $\Delta T_p$ (which are part of the vector $v$). The function then outputs matrix vector product $\boldsymbol{J}_{\text{ss}} v$, where $J_{\text{ss}}$ is the Jacobian matrix (see Equation 3.67).

The solver determines the order in which, and how often, the functions are called, thereby calculating a steady state solution. The factorization of the pre-conditioner is updated automatically when needed. The pre-conditioner matrix of the steady state

solver is given as

$$\boldsymbol{A}_{\text{ss,pre}} = \begin{bmatrix} G_{ij} & M_{\text{kcl},ir} & 0 \\ M_{\text{kvl},qj} & R_{qr} + R_{\text{nl},qr} & 0 \\ I_{G,sj} & V_{R,sr} & K_{sp} - K_{\text{cool},sp} \end{bmatrix}. \qquad \text{Eq. 3.66}$$

The Jacobian matrix, used in the JTVFun function, for the steady state solution is given as

$$\boldsymbol{J}_{\text{ss}} = \begin{bmatrix} G_{ij} & M_{\text{kcl},ir} & 0 \\ M_{\text{kvl},qj} & R_{qr} + M_{\text{dVdI},qr} & 0 \\ I_{G,sj} & V_{R,sr} + M_{\text{dPdI},sr} & K_{sp} - K_{\text{cool},sp} + M_{\text{dPdT},sp} \end{bmatrix}. \qquad \text{Eq. 3.67}$$

It must be noted that because the electro-magnetic and thermal systems are inherently unstable, a steady state solution including the thermal part is very uncommon and that usually for the steady state only the electrical equations are used. When far below the critical current, the non-linear voltage $V_{\text{nl},q}$ is zero and only one or two iterations are needed to find a solution. At higher currents the non-linear part becomes active making it necessary to use several tens of iterations.

### Transient Solution of the System 3.5.2

The transient solution of the system is calculated using Sundials IDA [86], which is a package for solving time dependent differential algebraic equations. The advantage of this solver over other available packages is that it is matrix-free (including the Jacobian) avoiding the need to store the mutual inductance matrix allowing to use the MLFMM instead. Sundials IDA requires a set of initial values and derivatives (not following from the steady state solution) for the variables $V_j$, $I_r$ and $T_p$. To find proper values it is assumed that the (source) currents and thus voltages at the initial time are zero. This is a reasonable starting point because it assumes that there is no history, other than from cooldown. The initial temperatures are provided by the user. To find the initial step for $V_j$ and $I_r$ the following linear system of electrical equations is solved for $\Delta V_j$ and $\Delta I_r$ using the biconjugate gradients stabilized method (BICGSTAB) [162]

$$\begin{bmatrix} G_{ij} & M_{\text{kcl},ir} \\ M_{\text{kvl},qj} & R_{qr} \end{bmatrix} \begin{bmatrix} \Delta V_j \\ \Delta I_r \end{bmatrix} + t_{cj} \begin{bmatrix} 0 & 0 \\ 0 & L_{qr} + M_{\text{S2T},qr} \end{bmatrix} \begin{bmatrix} \Delta V_j \\ \Delta I_r \end{bmatrix} + \begin{bmatrix} 0 \\ V_{\text{mlfmm},q}\left(t_{cj}\Delta I_r\right) \end{bmatrix} = - \begin{bmatrix} I_{\text{bg},i}\left(\frac{\partial \vec{B}}{\partial t}\right) \\ V_{\text{bg},q}\left(\frac{\partial \vec{B}}{\partial t}\right) \end{bmatrix}, \qquad \text{Eq. 3.68}$$

where the time constant $t_{\text{cj}}$ is given as $1/(\Delta t)$, where $\Delta t$ is in this case the pre-set initial time step (commonly 0.1 ms). The initial derivatives for the voltages and currents

are calculated as $dV_q/dt = \Delta V/\Delta t$ and $dI_r/dt = \Delta I/\Delta t$. The temperature equations are not implicit and therefore the initial change of temperature can easily be calculated as $dT_s/dt = \left(I_{G,sj}V_j + V_{R,sr}I_r + P_{s,s}\right)/C_{p,ss}$. Instead of solving the initial system of equations it is also possible to set the values externally, or to continue from an existing calculation. The initial values are inserted into the IDA solver, which starts integrating at $t = \Delta t$.

Similar to KINSol, IDA also requires a set of input functions. A flow diagram showing the inter dependencies of the elements of the transient solver is provided in Figure 3.14. The relevant input functions are then given as:

1. *System Function* - Calculates the residual Current $I_{\text{res},i}$, Voltage $V_{\text{res},r}$ and the heat flux (including heat generation) $P_{\text{res},s}$ (if enabled) as function of the voltage $V_i$, current $I_r$ and temperature $T_p$ using the electro-magnetic system Equation 3.28, or electro-magnetic and thermal system Equation 3.56. Updates the thermal matrices by calling the Thermal Setup Function and updates the linearization by calling the Nonlinear Ic Function.

2. *Pre-Conditioner Function* - Solves linearised system of equations (see Equation 3.69) using the Generalised Minimal Residual Method GMRES [163, 164]. Normally using such an iterative solver, as pre-conditioner, is not recommended, but in this case is a necessity because $V_{fmm}(\partial I/\partial t)$ is not represented by a matrix and can therefore not be solved directly. Therefore as input for GMRES the Sub-Pre-Conditioner function is used instead of the usual matrix. In order to pre-condition GMRES the Pre-Pre-Conditioner function is used.

3. *Pre-Pre-conditioner Function* - Solves a simplified linearised system of equations given as $\boldsymbol{A}_{\text{tdprepre}}p = z$ using the provided factorization. Where $\boldsymbol{A}_{\text{tdprepre}}$ is the pre-pre-conditioner matrix (see Equation 3.70). Instead of using the full MLFMM only its S2T step is used in the form of the $M_{\text{S2T}}$ matrix.

4. *Sub-Pre-conditioner Function* - Calculates the matrix vector product as given by Equation 3.69 for the pre-conditioner. This includes the MLFMM.

5. *Pre-Conditioner Setup Function* - Factorizes the matrix $\boldsymbol{A}_{\text{tdprepre}}$ to speed up the solution of the pre-pre-conditioner. There are many different techniques available for matrix factorization, which are explored in Section 3.5.3. Calls the Nonlinear-Ic Function to update the linearization.

6. *Jacobian Times Vector Function* - Calculates the Jacobian vector product using the MLFMM (see Equation 3.71). Calls the non-linear Ic function to update the linearization.

7. *Thermal Setup Function* - Re-calculates the thermal matrices dependent on material properties $K_{sp}$, $K_{\text{cool},sp}$, $C_{p,sp}$.

8. *Nonlinear Ic Function* - Linearizes the system by recalculating the matrices $R_{\text{nl},qr}$, $M_{\text{dVdI},qr}$, $M_{\text{dPdI},sr}$, $I_{G,sj}$, $V_{R,sr}$ and $M_{\text{dPdT},sp}$.

Again the solver determines the order in which, and how often, the functions are called, thereby integrating over time to find a transient solution for $V_j$, $I_r$ and if needed $T_p$. The values are stored to the hard drive every time step. This allows for post-analysis of the solution and for continuing the integration in the case of processor failure. The pre-conditioner setup function is automatically called to update the factorization when needed. The pre-conditioner system is given as

$$\begin{bmatrix} G_{ij} & M_{\mathrm{kcl},ir} & 0 \\ M_{\mathrm{kvl},qj} & R_{qr}+R_{\mathrm{nl},qr} & 0 \\ I_{G,sj} & V_{R,sr}+V_{\mathrm{nl},sr} & K_{sp}-K_{\mathrm{cool},sp} \end{bmatrix} \begin{bmatrix} V_j \\ I_r \\ T_p \end{bmatrix} + t_{\mathrm{cj}} \begin{bmatrix} 0 & 0 & 0 \\ 0 & L_{qr}+M_{\mathrm{S2T},qr} & 0 \\ 0 & 0 & -C_{p,sp} \end{bmatrix} \begin{bmatrix} V_j \\ I_r \\ T_p \end{bmatrix} + \begin{bmatrix} 0 \\ V_{\mathrm{mlfmm},q}\left(t_{\mathrm{cj}} I_r\right) \\ 0 \end{bmatrix} = \begin{bmatrix} I_{\mathrm{res},i} \\ V_{\mathrm{res},q} \\ P_{\mathrm{res},s} \end{bmatrix}, \quad \text{Eq. 3.69}$$

where, similar to the initial step, $t_{\mathrm{cj}}$ is the time stepping constant, which is automatically updated by IDA. It is noted here that the MLFMM despite being linear is not stored in matrix form. Therefore this system of equations is linear and can be solved by GMRES pre-conditioned using the pre-pre-conditioner matrix given as

$$\boldsymbol{A}_{\mathrm{tdprepre}} = \begin{bmatrix} G_{ij} & M_{\mathrm{kcl},ir} & 0 \\ M_{\mathrm{kvl},qj} & R_{qr}+R_{\mathrm{nl},qr} & 0 \\ I_{G,sj} & V_{R,sr}+V_{\mathrm{nl},sr} & K_{sp}-K_{\mathrm{cool},sp} \end{bmatrix} + t_{\mathrm{cj}} \begin{bmatrix} 0 & 0 & 0 \\ 0 & L_{qr}+M_{\mathrm{S2T},qr} & 0 \\ 0 & 0 & -C_{p,sp} \end{bmatrix} \quad \text{Eq. 3.70}$$

The non-linear part of the solution is guided with the Jacobian Times Vector Function given as

$$\boldsymbol{J}_{td} \begin{bmatrix} V_j \\ I_r \\ T_p \end{bmatrix} = \begin{bmatrix} G_{ij} & M_{\mathrm{kcl},ir} & 0 \\ M_{\mathrm{kvl},qj} & R_{qr}+M_{\mathrm{dVdI},qr} & 0 \\ I_{G,sj} & V_{R,sr}+M_{\mathrm{dPdI},sr} & K_{sp}-K_{\mathrm{cool},sp}+M_{\mathrm{dPdT},sp} \end{bmatrix} \begin{bmatrix} V_j \\ I_r \\ T_p \end{bmatrix} + t_{\mathrm{cj}} \begin{bmatrix} 0 & 0 & 0 \\ 0 & L_{qr}+M_{\mathrm{S2T},qr} & 0 \\ 0 & 0 & -C_{p,sp} \end{bmatrix} \begin{bmatrix} V_j \\ I_r \\ T_p \end{bmatrix} + \begin{bmatrix} 0 \\ V_{\mathrm{mlfmm},q}\left(t_{\mathrm{cj}} I_r\right) \\ 0 \end{bmatrix}. \quad \text{Eq. 3.71}$$

### Pre-Conditioner Matrix Factorization 3.5.3

After profiling the solver it is noted that approximately 70% of solution time is spend in pre-pre-conditioner and another 20% of solution time is spend in the MLFMM. Because the MLFMM was already previously optimized, effort is taken to speed-up the

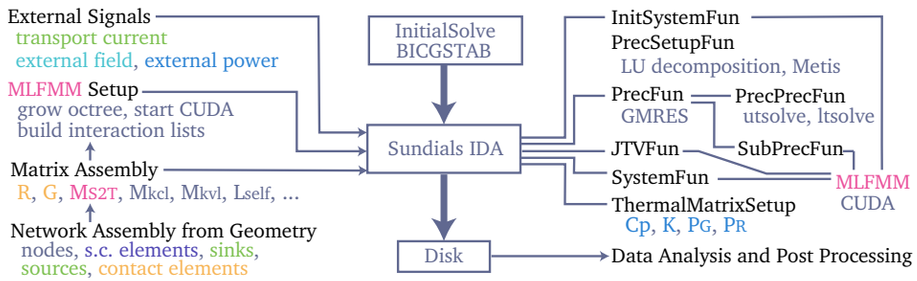


**Figure 3.14.** *Flow chart diagram showing the solver setup used to solve the electro-magnetic and thermal network equations.*

pre-pre-conditioner. The pre-conditioner setup function plays a very minor role and therefore the setup time is not so important. Many algorithms for factorizing a matrix are available. An overview and comparison is provided in Table 3.1. The most commonly used is LU [165] decomposition which decomposes/factorizes for example (sparse) $\boldsymbol{A}$ into a (sparse) lower $\boldsymbol{L}$ and upper $\boldsymbol{U}$ triangular matrix such that $\boldsymbol{A} = \boldsymbol{LU}$. To increase the sparsity of $\boldsymbol{L}$ and $\boldsymbol{U}$ commonly also re-ordering matrices $\boldsymbol{P}$, $\boldsymbol{Q}$ and $\boldsymbol{R}$ are provided such that $\boldsymbol{P}(\boldsymbol{R}^{-1}\boldsymbol{A})\boldsymbol{Q} = \boldsymbol{LU}$. The sparsity can be improved further by using a specialised re-ordering algorithm such as METIS [166, 167]. The electrical pre-pre-conditioner matrix is symmetric and can benefit from re-ordering both the columns and rows. The thermal matrix is non-symmetric and can only benefit from column re-ordering. An example of the sparsity pattern of the original matrix and re-orderings is shown in Figure 3.15 on Page 123.

With the factorized matrices the solution to the system $\boldsymbol{A}x = b$, is then given as $x = \boldsymbol{Q}(\boldsymbol{U}^{-1}(\boldsymbol{L}^{-1}(\boldsymbol{P}(\boldsymbol{R}^{-1}b))))$. Because the matrices are triangular, simple forward and back substitution can be used to solve the equations. The LU decomposition is implemented natively in Matlab but also in KLU [168] and UMFPACK [169] which are part of SuiteSparse [170]. The drawback of the forward and back substitutions is that it is inherently serial and can not be parallelized for full matrices, thereby making less efficient use of the multi-core processor(s) that are available. For sparse matrices the parallelism of the algorithm depends on the sparsity pattern of the matrix. Solvers that try to make use of this are MUMPS [171, 172] and cuSolverRf [173]. The last of which uses NVIDIA CUDA to run on the GPU. The model available NVIDIA GTX780/GTX980 unfortunately has reduced calculation speed in double precision, which is the only option available for this solver, compared to the professional models.

The LU factorization provides an exact solution. For the pre-conditioner this is not necessary. This is used by the Incomplete LU (ILU) decomposition [174] that increases the sparsity by providing an approximate solution instead of an exact solution. Besides LU some other matrix decomposition algorithms are available such as QR implemented in SuiteSparse [175] and LDL implemented in PARDISO [176]. As a bonus the Algebraic Multi-Grid solver implemented in AMGX [177] was tried. This solver is again implemented in parallel using NVIDIA CUDA. Communication with this solver is per-

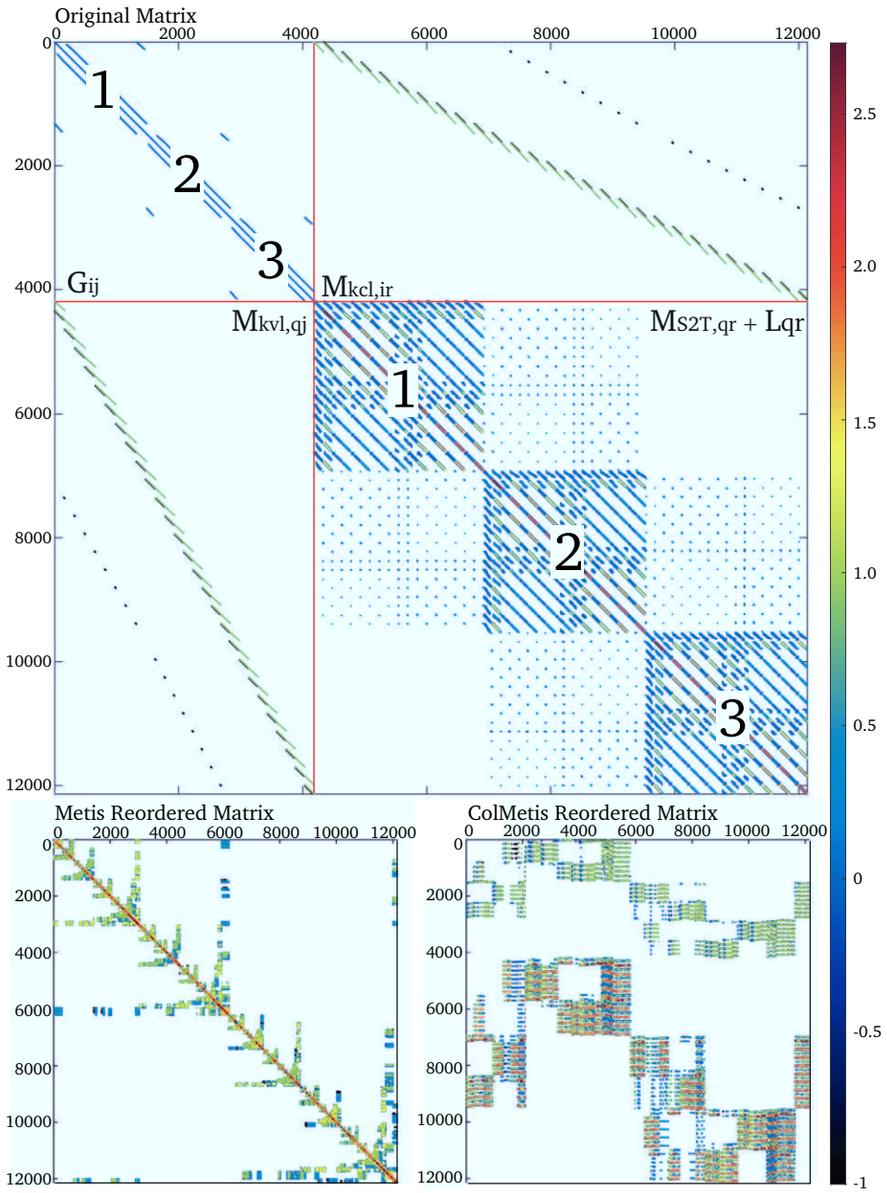


**Figure 3.15.** *Sparsity pattern of the pre-pre-conditioner matrix $A_{prepre}$ and possible reordering schemes for an electrical only system of equations. The system was setup for a cable consisting of three unit cells. On the top the original matrix is shown, in the bottom left the matrix with (symmetric) column and row reorderings using Metis and on the bottom right the matrix with only column reordering using Metis.*

TABLE 3.1.
COMPUTATION TIMES FOR VARIOUS PRE-PRE-CONDITIONERS FOR A NETWORK CONSISTING OF 3 UNIT CELLS WITH A TOTAL OF 22214 EQUATIONS. COMPARISON PERFORMED ON AN INTEL X990 I7 CPU RUNNING AT 3.47 GHz (UNLESS STATED OTHERWISE).

| Solver | Source | Setup [s] | Solve* [ms] | Remarks |
|---|---|---|---|---|
| LU | Matlab | 5.74 | 62.4 | v2015a |
| ILU | Matlab | 5.85 | 17.5 | slower GMRES convergence than LU |
| KLU | SuiteSparse | 31.3 | 61.4 | targeted towards SPICE application |
| UMFPACK | SuiteSparse | 7.53 | 64.2 | probably the same as Matlab LU |
| QR | SuiteSparse | 2.15 | 793 | part of Factorise sub-package |
| COD | SuiteSparse | 2.21 | 291 | part of Factorise sub-package |
| LDL | SuiteSparse | 1.00 | 79.8 | part of Factorise sub-package |
| CuSolverRf | NVIDIA | 6.06 | 35.0 | on a NV-GTX780 graphics card† |
| MUMPS | CERFACS | 0.51 | 15.6 | fastest solver |
| PARDISO | INTEL | 0.73 | 15.8 | requires license |
| AMGx | NVIDIA | n.a. | n.a. | unable to solve pre-con matrix |
| SPAI | TUTI | n.a. | n.a. | interesting, no Matlab interface |

* Time includes overhead due to communication between Matlab and the solver.
† Double precision is not well suited for this type of gaming card.

formed using a home made Matlab interface. The final solver considered is the SParse Approximate Inverse implemented in MSPAI [178]. This one constructs an approximated inverse of matrix $A$, such that $b = A^{-1}x$. Because the matrix vector product can be executed fully in parallel, it is considered a promising option. Unfortunately so far the Matlab interface to this solver is not working. The best results were obtained with the MUMPS solver which solves the pre-pre-conditioner matrix approximately 4 times faster than the native Matlab solution. Moreover, it also has the lowest setup time.

## 3.6 Conclusion

To analyze electro-magnetic and thermal phenomena in coated conductor cables, a new Network Model was implemented. At present three fully parametric cable geometries are available: Roebel, CORC and Twisted-Stack type of cables. This allows to make a comparative study between the cable types within the same model.

In the model the flat tapes are approximated as partial element equivalent circuits consisting of superconducting line elements and voltage/temperature nodes. Between the tapes, resistive contact elements approximate the electrical and thermal resistances between them. The currents in the elements together with the voltages and temperatures at the nodes are solved time dependently using a system equation comprising Kirchhoff's Current Law (summing the current at the nodes), Kirchhoff's Voltage Law (summing the voltages over the elements) and the discrete heat equation.

The thermal equations, when enabled, are fully coupled to the electrical ones and solved simultaneously. The non-linear superconducting elements are modeled as a

parallel path consisting of the copper matrix and the superconductor. The implicit current sharing relation between these two layers is then solved using a Newton Raphson method.

The critical current of the superconducting layer depends on the magnetic field, its angle with respect to the tape surface and temperature. Additional source currents can be added at any node to simulate an externally imposed transport current in the cable. A time-changing background field can be coupled to the elements as an externally induced voltage. The self-inductance is calculated using analytical expressions for ribbons and wires, modelling the superconducting and the contact elements respectively.

The mutual inductances between all line elements and the elements' self-fields are included using a Multi-Level Fast Multipole Method (MLFMM), which reduces the computational complexity of the resulting N-body problem, from $O(N^2)$ to $O(N)$. The inclusion of this algorithm makes this specific network solver unique and capable of modeling much larger structures than most other solvers.

The system is then solved, as function of time, using the Sundials IDA solver. Because of the MLFMM, the mutual inductance is only known as a function and no physical matrix is available. This means that the system can only be preconditioned using an iterative solver, such as the Generalized Minimal Residual Method (GRMES). To precondition this solver, the system matrix needs to be approximated, which is achieved by only including the interactions in the source-to-target (S2T) step of the MLFMM, which is responsible for the direct interactions, into the pre-conditioner matrix, which in turn is factorized and solved using the direct MUMPS solver. This method was selected as the fastest from a variety of direct solvers.

The combination of multiple coated conductor cable and coil geometries, fully coupled three-dimensional thermal and electrical physics and the large scale of the systems that can be solved, while maintaining fine tape-level details, makes this new model unique and state-of-the-art. The model allows to simulate the screening currents induced in a dipole coil geometry as described in Chapter 4. In addition it is possible to study the initialization transients and propagation of a normal zone in ReBCO cables and coils, including current redistribution between the tapes, leading to unique and interesting results, as described in Chapter 5.

# 4 Magnetization and Field Quality

"You may test that assumption at your convenience."

Jean-Luc Picard, Star Trek: TNG, S03E17, 1990

*The electro-magnetic part of the Network Model, described in Chapter 3, is applied here to study magnetization in ReBCO coated conductor cables and coils. The issue of field quality is discussed in depth and a possible solution by using additional persistent current shim coils is proposed.*

## 4.1 Introduction and Chapter Layout

For accelerator magnets wound with ReBCO coated conductor, achieving a high dynamic field quality is a main concern and requires an in depth study. Due to the several mm wide tapes, in comparison to the 5 to 50 $\mu$m diameter filaments in LTS, the position of the current can not be fully pre-determined down to a microscopic scale. When the cables in the coil are not operated at short sample current, it is possible that large screening currents are induced, introducing additional dynamic variations in the magnetic field expressed in terms of so-called coil harmonics. In order to study these primary and induced currents, in coated conductor tapes, cables and ultimately coils, an Electro-Magnetic and Thermal Network Model was implemented (see Chapter 3). To ensure that the Electro-Magnetic part of the model (the Thermal part is not used in this chapter) is implemented correctly, it needs to be validated by comparing results to experimental data.

Several reports on the magnetization loss in Roebel cables were published by the University of Kyoto [179], Industrial Research Ltd [180, 181, 182], Ohio State University [183, 184] and Karlsruhe Institute of Technology (KIT) [185, 186, 186]. However, most data were collected for use in electrical power applications and are therefore at 77 K and frequencies above 10 Hz. In most cases the in-field angular dependence was not considered. The model published here was bench-marked through a series of tests that qualitatively, but not quantitatively, verify the electrical part of the model. These benchmark tests are described in Section 4.2. Later an effort was initiated to measure coupling current and hysteresis AC loss under conditions that are more relevant to accelerator magnets, i.e. at low temperature, low frequency. Two cable samples were assembled from punched meandering tapes by KIT, impregnated at CERN, and sent to the University of Southampton and the University of Twente for measurement as described in depth in references [187] and [78, 188], respectively.

In order to model screening currents in the cross-section of a coil, multiple cables are stacked to form the blocks of windings in the coil. From the currents in the elements

the transient harmonic content is calculated, which is presented in Section 4.4. Although the resulting dynamic field errors are lower than initially expected, it may still be necessary to reduce them. In addition, the non-linearity of the iron poles needs to be compensated for. This can be achieved using a set of shim coils, operating in persistent-mode inside the aperture, which is a novel concept to accelerator magnets. These coils, by topology, act as a filter dynamically shielding any harmonics from the aperture, thereby improving the dynamic field quality by an order of magnitude over the full range of the magnetic field. This concept is generally applicable not only to HTS magnets, but also to LTS magnets and can be vital for the success of a Future Circular Collider, irrespective the choice between 16 or 20 T. The persistent current shim coils are elaborated further in Section 4.5.

## 4.2 Initial Benchmark Tests

*In this Section several initial benchmark tests are performed to check the validity and characteristics of the model. The tests were performed before the availability of the measurement data collected by the University of Southampton and the University of Twente.*

### 4.2.1 Current Profiles

The ability to directly present the position and density of the electrical currents in the tapes is one of the advantages that the model has over a practical experiment. However, because the time dependent currents are solved in the elements of the electrical network, not providing a vector field on the surface of the tapes, plotting the current or current density is not as straight forward as for example in the Finite Element Method (FEM). To transform the element currents into a vector field some post-analysis is necessary. First the current density in each of the elements is calculated by dividing the current with element width $J_r = I_r / W_{12r}$. Then the longitudinal current density is calculated at each of the nodes by averaging the current density of the longitudinal elements connected to it. Similarly the transverse current density can be calculated from the transverse elements. The nodes belonging to the same tape are selected using their identifier $e_{\text{tape},r}$. Because the order of the nodes was not changed during the network setup, their respective current densities can be shaped back into a matrix resulting in the current density vector field on the surface of the tape, consisting of transverse and longitudinal components (see Figure 4.1). From this vector field the stream function [189] is calculated using the mathematical description and code provided in [190]. The contour plot of the stream function generates the current stream-lines which are then mapped onto the surface of the tape. It is noted that, because current can run through the contact resistances, potentially the stream lines are allowed to jump from tape to tape. The contour lines of the stream function are always closed, therefore this approach should only be considered as an approximation that is used for visualization purposes. When significant contact currents are present, it is better to use Matlab's build-in *stream* functions, which integrate the current lines numerically, thereby not closing the loops.

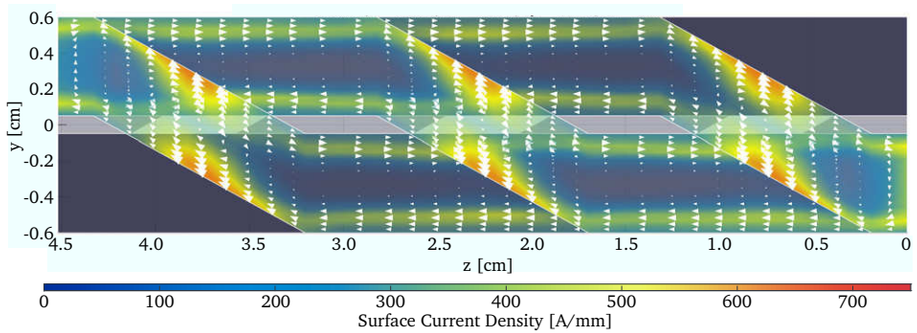


**Figure 4.1.** *Calculated vector field, which indicates the overall current direction for a Roebel cable, shown for an perpendicular uniform applied magnetic field of* 0.7 T*, which was ramped over the virgin curve using a frequency of* 0.1 Hz*. The operating temperature is set at* 4.5 K*. The engineering current density of the conductor is scaled to* 527 A/mm$^2$ *at* 20 T $\perp$ 4.5 K *and* 4.4 kA/mm$^2$ *at* 20 T $\parallel$ 4.5 K *in the* 100 $\mu$m *thick tape.*

The stream lines representing the screening currents are shown at various amplitudes of the applied magnetic field, for a magnetization loop with maximum amplitude 2.0 T and frequency 0.1 Hz in Figure 4.2. It is found that the position of the currents is frequency independent, as expected since the hysteresis losses predicted by literature are also independent of frequency. It can be seen here and in Figure 4.3 that the magnetic flux, and thus the screening currents, are located at the edges of the cable as expected from Bean's Critical State Model [191]. Because the geometry is different from Bean's infinite slab model, some gradient is present. In the cross-section it can be seen that the tapes on the outside of the stacks, on either side of the cable, shield the tapes on the inside of the stacks, causing the penetration depth to vary. Because the critical current density is angular dependent, the current density along the edges of the tapes, is lower than slightly inward (also refer to Section 4.2.4). The time dependence of the current profiles is presented in detail in Figure 4.4, where the currents across the width of the tapes are presented for a tape located in the stack and for a tape located at the cross-over. It is noted that the calculated currents are basically a macroscopic description of the Abrikosov vortices [192] and their pinning (explained in Chapter 1). The inclusion of pinning was effectively achieved by implementing the critical current into the model as explained in [158]. The model, however, does not include the Meissner state [16, 17], which directly emerges when the superconductor is cooled below its critical temperature. Because the Meissner state only occurs at very low magnetic field it is expected that its influence on the magnetization loops is negligible.

In the cable it can be seen that the flux penetrates much deeper into the tapes at the cross-overs, which show full penetration at around 0.3 T. This can be explained by the collaborative effect of the tapes, i.e. the screening currents are not divided over seven or eight tapes, but are only flowing through a single tape on the cross-over. A large fraction of the AC loss is therefore originated from this part of the cable, as previously

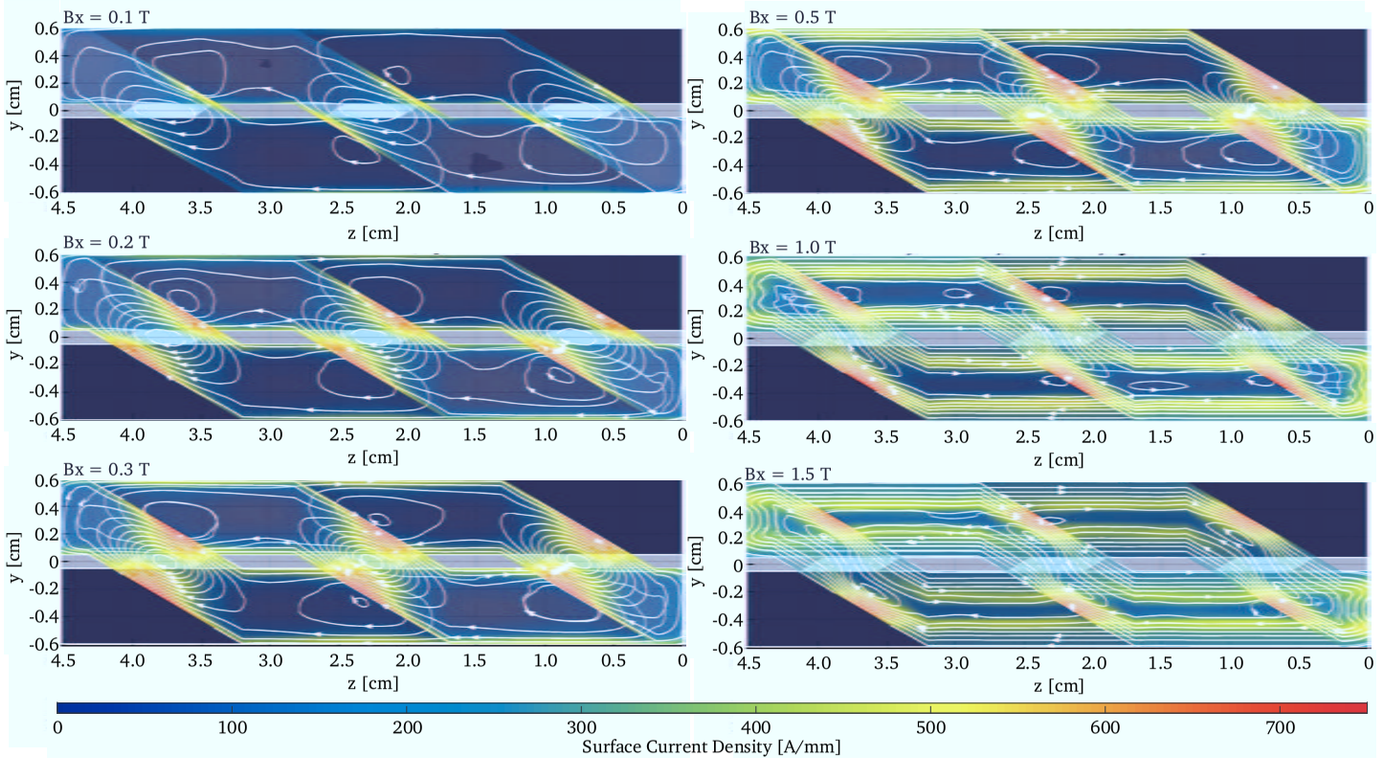


**Figure 4.2.** *Calculated magnetization currents in a Roebel cable, shown for applied magnetic field amplitudes of* 0.1, 0.2, 0.3, 0.5, 1.0 *and* 1.5 T *respectively (top to bottom, left to right), and are located along the virgin curve of a magnetization loop, that has a perpendicular uniform applied magnetic field amplitude of* 2.0 T *and a frequency of* 0.1 Hz. *The operating temperature is* 4.5 K. *The engineering current density of the conductor is scaled to* 527 A/mm$^2$ *at* 20 T $\perp$ 4.5 K *and* 4.4 kA/mm$^2$ *at* 20 T $\parallel$ 4.5 K *in the* 100 $\mu$m *thick tape. It can be seen that the cross-over magnetizes before the rest of the cable.*

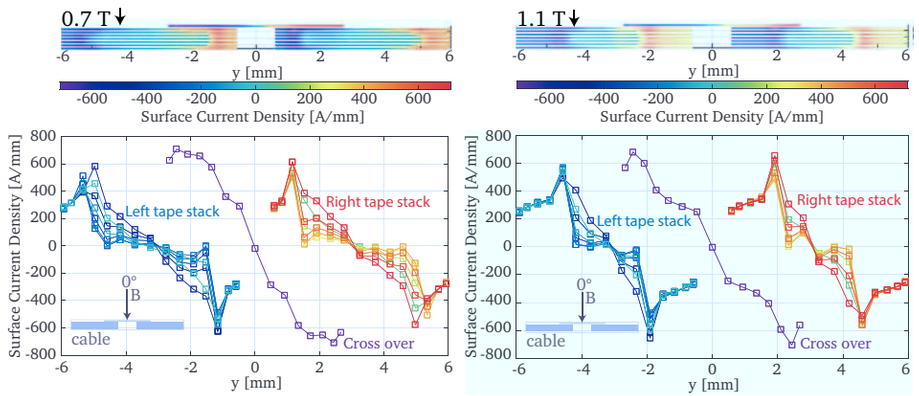


**Figure 4.3.** *Calculated screening currents in the cross-section at* $z = 2.26\,\mathrm{cm}$ *of a Roebel cable, shown for applied magnetic field amplitudes of* 0.7 *and* 1.1 T *respectively (left to right), and are located along the virgin curve of the magnetization loop, that has a perpendicular uniform applied magnetic field amplitude of* 2.0 T *and a frequency of* 0.1 Hz*. The operating temperature is* 4.5 K*. The engineering current density of the conductor is scaled to* $527\,\mathrm{A/mm^2}$ *at* $20\,\mathrm{T} \perp 4.5\,\mathrm{K}$ *and* $4.4\,\mathrm{kA/mm^2}$ *at* $20\,\mathrm{T} \parallel 4.5\,\mathrm{K}$ *in the* $100\,\mu\mathrm{m}$ *thick tape.*

also reported in [193, 80]. When the external magnetic field is increased further the tapes in the stack are penetrated up to around 1.5 T, at which point the whole cable shows full saturation. This behavior means that the tapes in the cable influence one another and therefore it is necessary, for magnetization studies, to take the full geometry of the cable and eventually the entire coil-winding pack into account. This is verified by switching off the mutual inductances in the Network Model, thereby removing this influence, in which case the penetration of the flux is observed simultaneously in all tapes.

### Hysteresis Loop and Loss Calculation 4.2.2

The geometry of a Roebel cable with the SP-1 geometry (see Table 2.1) consisting of $N_u = 3$ unit cells is constructed. The scaling relation used to describe the angular dependent critical current of the tapes is presented in Appendix A. The critical current density is scaled to 52.7 A/mm width, which equals an engineering current density of $527\,\mathrm{A/mm^2}$ in a $100\,\mu\mathrm{m}$ thick tape, in 20 T perpendicular applied field at 4.5 K. The tape surface is approximated using 14 elements, that have a length close to 1.2 mm, homogeneously distributed over its width. A time-varying uniform magnetic field given by $B_0 \sin(2\pi f t)$, with amplitude $B_0 = 0.7\,\mathrm{T}$ and frequency $f = 0.1\,\mathrm{Hz}$, is applied in the perpendicular direction, with respect to the tape surface. The resulting magnetization in units of $\mathrm{Am^2}$ is then calculated at each time step from the currents using the position

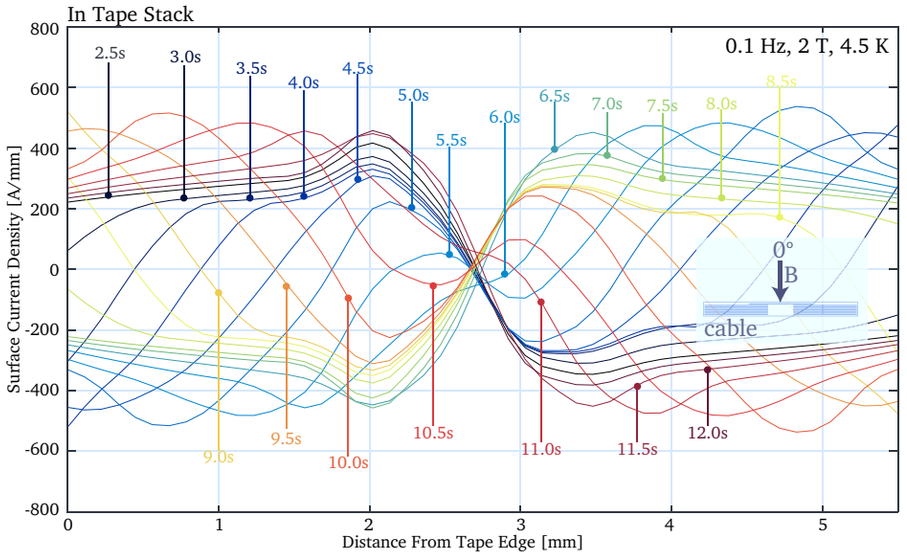


**Figure 4.4.** *The calculated surface current density inside a tape located in the stack (top) and the cross-over (bot), respectively. The current density is shown as function of distance from the tape's edge, in a cross-section in the xy-plane at* $z = 22.6\,\mathrm{mm}$*. The profiles are shown at various time steps, denoted with colored markers. The current density is calculated for a perpendicular uniform applied magnetic field with an amplitude of* $2.0\,\mathrm{T}$ *and a frequency of* $0.1\,\mathrm{Hz}$*. The operating temperature is* $4.5\,\mathrm{K}$*. The engineering current density of the conductor is scaled to* $527\,\mathrm{A/mm^2}$ *at* $20\,\mathrm{T} \perp 4.5\,\mathrm{K}$ *and* $4.4\,\mathrm{kA/mm^2}$ *at* $20\,\mathrm{T} \parallel 4.5\,\mathrm{K}$ *in the* $100\,\mu\mathrm{m}$ *thick tape.*

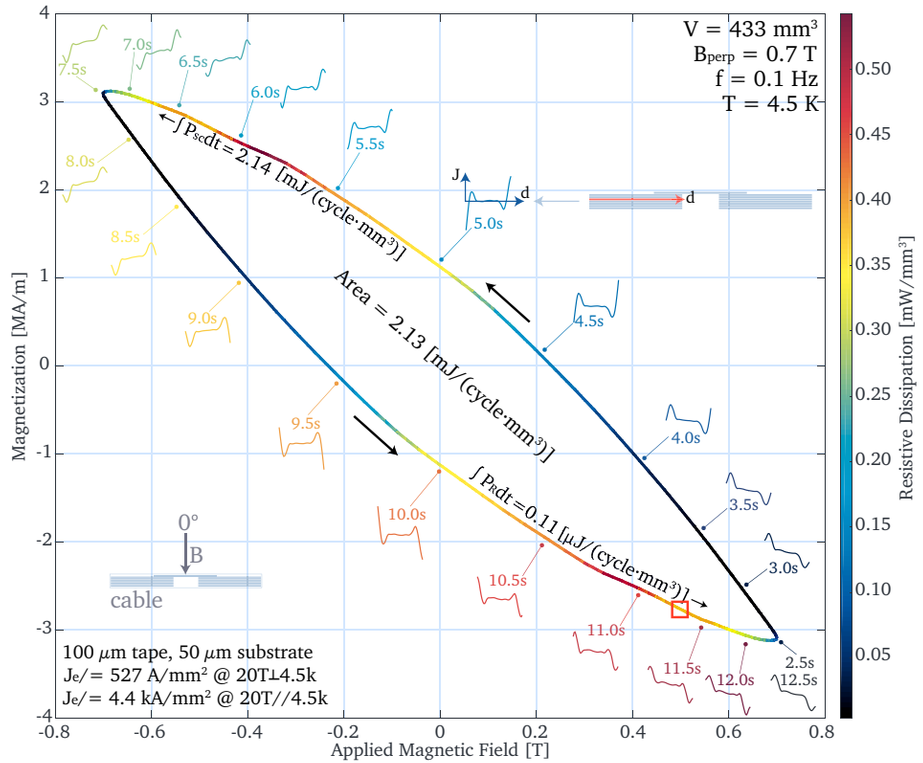


**Figure 4.5.** *Magnetization versus applied magnetic field and power dissipation versus time of an SP-1 Roebel cable for a uniform applied magnetic field with amplitude* 0.7 T *in the perpendicular direction, at a bath temperature of* 4.5 K *and a frequency of* 0.1 Hz*. The data is presented in a hysteresis loop, where the color of the line represents the power dissipation. The times and schematic current profiles for a tape located in the stack are shown around the loop. The engineering current density of the conductor is scaled to* 527 A/mm$^2$ *at* 20 T $\perp$ 4.5 K *and* 4.4 kA/mm$^2$ *at* 20 T $\parallel$ 4.5 K *in the* 100 $\mu$m *thick tape.*

and the direction vectors as

$$\vec{M} = 0.5 \sum_{i=1}^{N_e} \vec{X}_{e,i} \times \vec{D}_{e,i} I_i. \qquad \text{Eq. 4.1}$$

The magnetization is commonly expressed per unit of volume resulting in units of A/m. The modeled cable volume is calculated as $d_c \times W_t \times (N_u/N_s) L_{\text{tp}}$ (ignoring the insulation). In this specific case the volume of the cable is found to be 433 mm$^3$. The magnetization losses in the model can now be determined using two fundamentally different methods:

1. *Loop Area* - The magnetization loss per cycle should be equal to the area of the hysteresis loop. The area is determined using the Matlab build in *polyarea* function.

2. *Power Integration* - The loss per cycle is determined by integrating the resistive power dissipation of all the elements in the network. The inductive voltages are ignored. In this case hysteresis losses can be distinguished from coupling losses by calculating the power separately for the superconducting elements and for the normal conducting elements respectively. Also the position of the losses can be determined.

To avoid including the virgin curve, the magnetization currents and voltages are calculated for two periods of the applied field, after which only the second period is included. The calculated combined hysteresis and coupling losses are $2.14\,\mathrm{mJ/(cycle \cdot mm^3)}$. The numerical difference between methods 1 and 2 is only $\sim 0.1\%$, providing confidence that Electro-Magnetic part of the model is correctly implemented. The calculation is illustrated in Figure 4.5, which shows the power dissipation in the elements along the calculated hysteresis loop. It can be seen that the power dissipation occurs at two points along the hysteresis curve causing the main frequency of the power dissipation to be $2f$. It is also observed that the power dissipation has a strong co-incidence with the curvature of the (convex) loop, which in turn has a strong relationship to its surface area. Essentially if the loop consists of two straight lines the surface area equals zero, therefore curvature is required in order for the surface area to be non-zero.

### 4.2.3 Number of Elements and Calculation Accuracy

As a second check, the convergence with the number of longitudinal elements over the width of the tapes $N_{el,t} = N_{nt}$ is studied. The loss has to converge to a constant value when using a high number of elements. If not, then this is an indication that there is some scaling problem with the element width. Not surprisingly, because it depends on the screening currents inside the tapes and thus the elements representing it, the hysteresis loss converges much slower with the number of elements than the coupling loss. Also the amplitude of the applied magnetic field is important. When the amplitude is low, the flux penetrates only at the very edges of the tapes, requiring more elements in this location to provide an accurate solution. The convergence of the AC loss calculation with the number of elements, across the width of the tape, and the position of the hysteresis loss is presented in Figure 4.6. At 0.3 T the solution at 14 elements is only 3% different from the 26 elements solution. However, when the amplitude is low the penetration depth decreases. For 0.075 T amplitude the hysteresis loss calculation is not yet converging. Thus for now 0.15 T is taken as a lower limit for hysteresis loss until a better solution is found. This also means that under very shallow field angles the model does not portray hysteresis loss accurately. The overall current trajectories, however, are not affected by this shortcoming. This means that it is not considered an issue for field quality predictions.

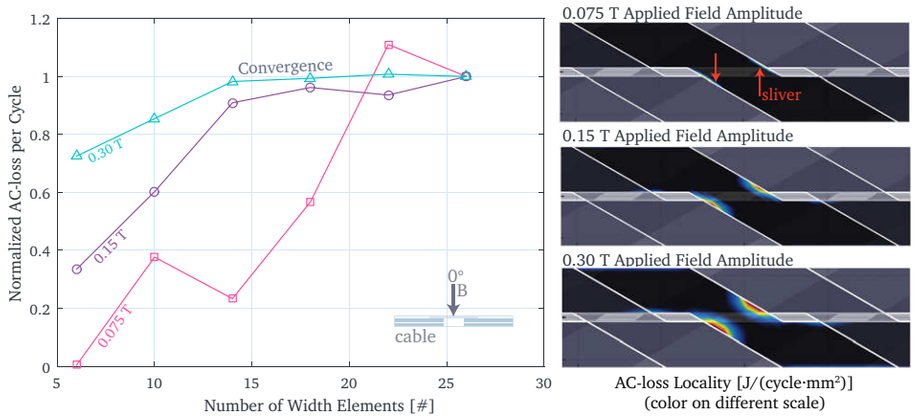


**Figure 4.6.** *Illustration of the convergence of AC loss calculations with number of width elements at various applied magnetic field amplitudes (left). Because the AC loss in these three cases are orders apart, they are normalized with respect to the AC loss in the* 26 *elements case. The AC losses are calculated by integrating the resistive power dissipation from the individual elements. The assumed cable geometry is the SP-1. The engineering current density of the conductor is scaled to* $527\,\mathrm{A/mm^2}$ *at* $20\,\mathrm{T} \perp 4.5\,\mathrm{K}$ *and* $4.4\,\mathrm{kA/mm^2}$ *at* $20\,\mathrm{T} \parallel 4.5\,\mathrm{K}$ *in the* $100\,\mu\mathrm{m}$ *thick tape. It can be seen that the cross-over magnetizes before the rest of the cable and that at magnetic field amplitudes of* 0.15 *and* $0.3\,\mathrm{T}$ *good convergence is found. In addition the positions of the AC losses throughout the cable are shown (right).*

### Inclusion of the Self Field 4.2.4

In the model the magnetic field generated by the elements themselves, the self field, is superimposed to the background field. When including the self field an extra call to the MLFMM is needed when the field is calculated. Also the critical current of each element, used for determining current sharing, becomes dependent on the current of all other elements. This increases the complexity slowing down the solver by approximately a factor 2. Therefore in many other cable models the self field is omitted. To study the effect of this omission, the currents are calculated as function of time (and thus the hysteresis loop), with and without the inclusion of the self field. The comparison in terms of resulting currents in an uniform harmonic applied magnetic field with amplitude of $0.5\,\mathrm{T}$ and a frequency of $0.1\,\mathrm{Hz}$ at an operating temperature of $4.5\,\mathrm{K}$ is presented in Figure 4.7 and the loops are compared in Figure 4.8. The losses are 0.93 and $0.99\,\mathrm{mJ/(cycle \cdot mm^3)}$, with and without self field respectively, which corresponds to a difference of 6%. The current profiles and the time appearance of the losses are also slightly different. The likely cause is that the magnetic field angle $\alpha_r$ at the edges of the tapes, causes a reduction of the local critical current density and thus the current (refer to Figure 4.4). In addition it is observed that the convergence with the number of elements, across the width of the tape, is slightly slower when the self field is enabled. Because the difference between with and without is significant it is decided to run all calculations with the inclusion of the self field.

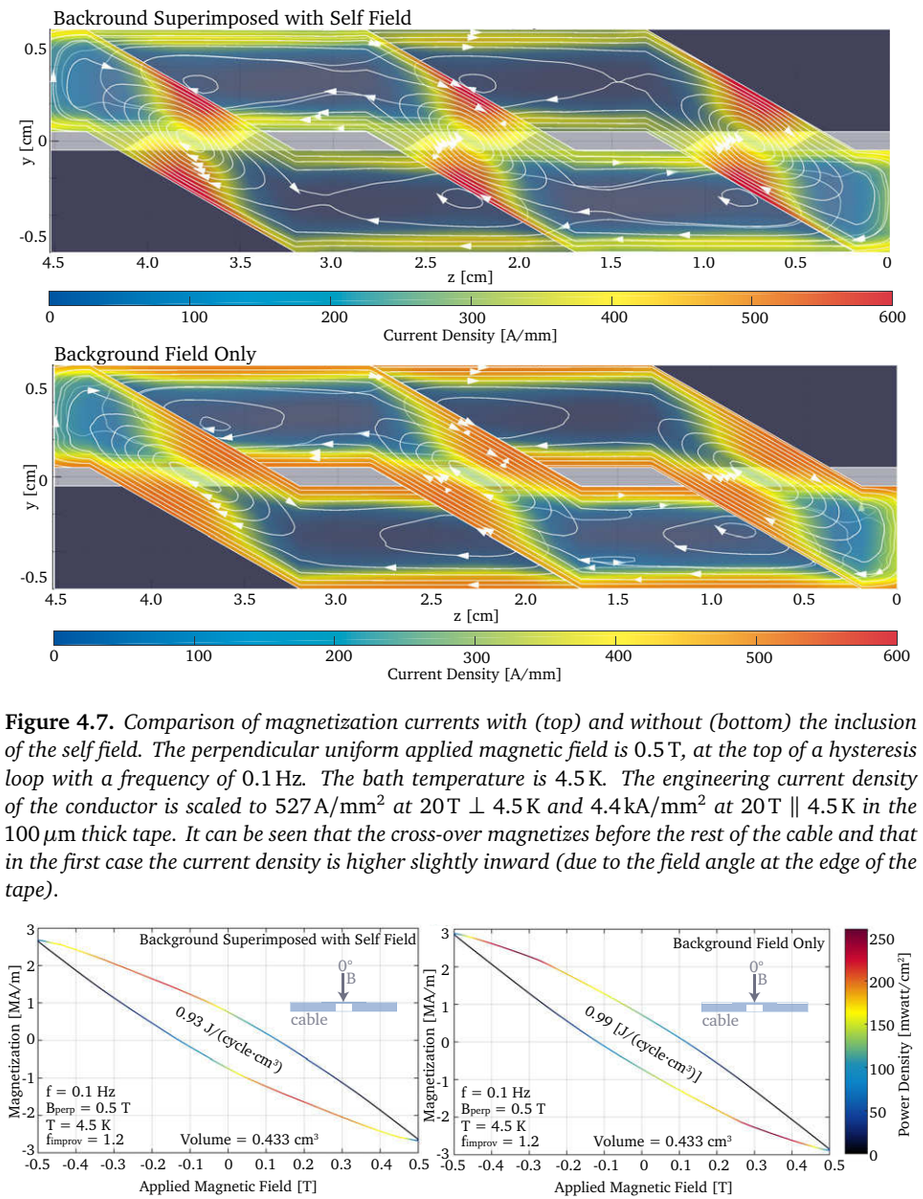


**Figure 4.7.** *Comparison of magnetization currents with (top) and without (bottom) the inclusion of the self field. The perpendicular uniform applied magnetic field is* 0.5 T*, at the top of a hysteresis loop with a frequency of* 0.1 Hz*. The bath temperature is* 4.5 K*. The engineering current density of the conductor is scaled to* 527 A/mm$^2$ *at* 20 T $\perp$ 4.5 K *and* 4.4 kA/mm$^2$ *at* 20 T $\parallel$ 4.5 K *in the* 100 $\mu$m *thick tape. It can be seen that the cross-over magnetizes before the rest of the cable and that in the first case the current density is higher slightly inward (due to the field angle at the edge of the tape).*




**Figure 4.8.** *Comparison between between hysteresis loops with (left) and without (right) the inclusion of the self field. The amplitude of the uniform applied magnetic field is in both cases* 0.5 T *at a frequency of* 0.1 Hz*. The bath temperature is* 4.5 K*. The engineering current density of the conductor is scaled to* 527 A/mm$^2$ *at* 20 T $\perp$ 4.5 K *and* 4.4 kA/mm$^2$ *at* 20 T $\parallel$ 4.5 K *in the* 100 $\mu$m *thick tape.*

### Contact Elements between Tapes 4.2.5

The contact elements between the tapes, also referred to as inter-tape resistances, are determining the coupling losses in the model. To ensure that these elements are implemented correctly in the model, two different implementations are compared:

1. *Resistances* - The contact elements are represented by additional elements, and thus additional degrees of freedom in the system of equations. The distribution of resistances of the contact elements is represented by the matrix $R_{qr}$. The advantage is that for the inductance calculations the network is guaranteed to consist of closed loops ensuring consistent coupling with the background field. The disadvantage is that the computation time is much longer due to the extra elements.

2. *Conductances* - The contact elements are represented by conductances in the matrix $G_{ij}$. This means that current is transferred between two nodes without a physical element. Because this violates Kirchhoff's Current Law, this approximation is only applicable when the contact elements are very small compared to the rest of the system.

The coupling losses, defined as dissipation in the contact elements, are calculated for both implementations using a Roebel cable consisting of a full twist pitch (comprising of 15 unit cells), to ensure all possible current loops are present in the model. The external magnetic field with amplitude 0.5 T at 0.1 Hz is applied in the parallel direction to maximize the coupling losses. It is indeed found that in this direction coupling losses are the dominant term (see Section 4.3.1). The calculated losses are $2.65\,\mathrm{J/(cycle \cdot m^3)}$. The numerical difference between the conductance and resistance cases is found to be 0.07%, which provides confidence that the inter-tape resistances are implemented correctly.

## Experimental Validation of the Network Model 4.3

*In this section numerical and experimental AC loss data are presented and compared.*

### Numerical Prediction 4.3.1

After the initial benchmarks the model is used to predict the magnetization loss as function of amplitude and angle of the applied magnetic field in SuperPower tapes based Roebel cable (see SP-1 in Table 2.1) with a twist pitch of 226 mm. Again the scaling relation from Appendix A is scaled to an engineering current density of $527\,\mathrm{A/mm^2}$ in 20 T perpendicular applied field at 4.5 K in the 100 $\mu$m thick SuperPower tapes. The temperature of the cable is set at 4.5 K and the frequency is fixed at 0.1 Hz. The contact resistance between the tapes is set at the default $0.288\,\mu\Omega\mathrm{m^2}$ (see Section 3.3.7). The losses are calculated directly from the current elements as described in Section 4.2.2. The magnetization and the AC losses in units of MA/m and $\mathrm{mJ/(cycle \cdot mm^3)}$ respectively are calculated based on the bare cable dimensions of $0.8 \times 226 \times 12 = 2170\,\mathrm{mm^3}$.

The resulting magnetization losses are presented in Figure 4.10 and the corresponding magnetization loops for an applied field in the perpendicular direction Figure 4.9. The model predicts that in the perpendicular field direction the AC loss is dominated by hysteresis loss and in the parallel direction, at lower fields, by coupling loss. In the second case it must be noted that the model uses infinitely thin current sheets to approximate the superconducting tapes and therefore the superconducting layer can not magnetize in the transverse direction.

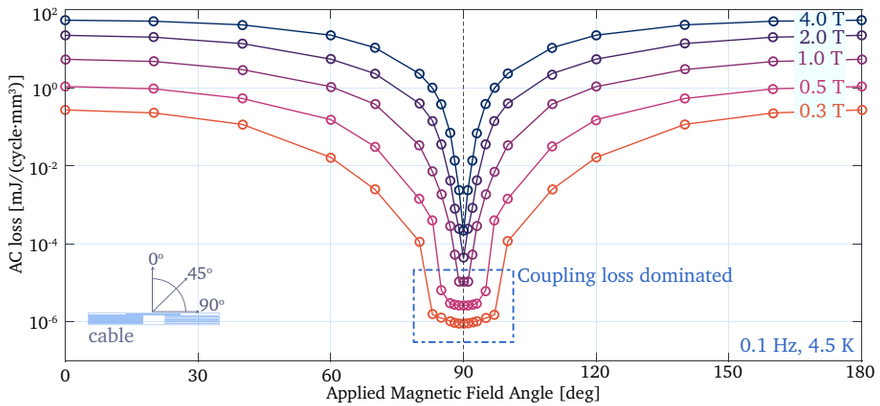


**Figure 4.9.** *Numerical prediction of the AC losses as function of applied magnetic field amplitude and applied magnetic field angle in a SP-1 Roebel cable. The frequency is* 0.1 Hz *and the operating temperature is* 4.5 K*. The engineering current density of the conductor is scaled to* 527 A/mm$^2$ *at* 20 T $\perp$ 4.5 K *and* 4.4 kA/mm$^2$ *at* 20 T $\parallel$ 4.5 K *in the* 100 $\mu$m *thick tape.*

### 4.3.2 Experimental Aspects

The Roebel cable for the two AC loss test samples was assembled with SuperPower tapes by KIT. The geometry of the cable is equal to the one used for the numerical prediction (cable SP-1 in Table 2.1). The samples were then prepared and impregnated at CERN, to ensure that the impregnation procedure closely match the foreseen coils. The samples were insulated with a 16 mm wide S2-glass (33 Tex) sleeve. Both cable samples were impregnated using CTD 101G, which is an alumina-loaded resin. Later it was found necessary to switch to CTD 101K (clear epoxy), see Section 2.2.3. The 300 mm long mold, shown in Figure 4.11, was designed specifically to allow the filled resin to penetrate the cable from the edge. This reduces the filtering of the alumina particles by the glass sleeve. An adjustment shim is added into the mold to fine-tune the pressure on the wide face of the cable to around 3 MPa. This ensures that all tapes are in good electrical contact. The pressure was verified using Fuji paper [194]. After impregnation the cable was removed from the mold by pressurized air forced through a hole below the sample, to avoid unnecessary strain. After impregnation the cable samples were cut at both ends to a length of 226 mm, i.e. a single transposition length,

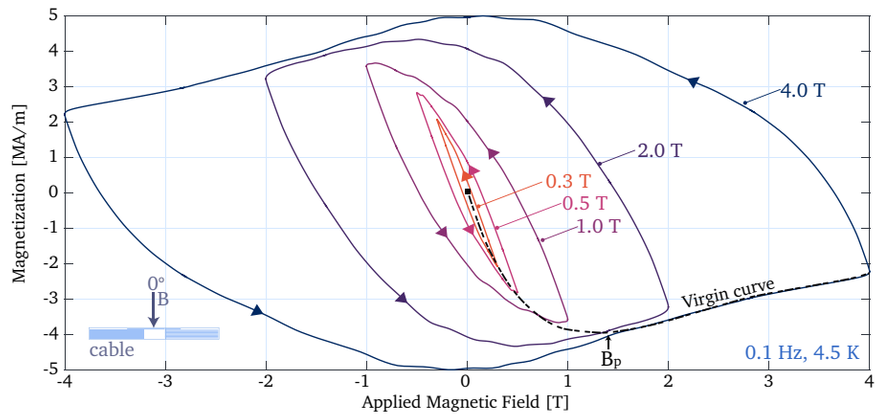


**Figure 4.10.** *Numerical prediction of the magnetization versus applied magnetic field in the perpendicular direction in a SP-1 Roebel cable. The loops are shown for various amplitudes of the applied magnetic field. The frequency is* 0.1 Hz *and the operating temperature is* 4.5 K*. The engineering current density of the conductor is scaled to* 527 A/mm$^2$ *at* 20 T $\perp$ 4.5 K *and* 4.4 kA/mm$^2$ *at* 20 T $\parallel$ 4.5 K *in the* 100 $\mu$m *thick tape.*

and cleaned, to ensure no electrical contact between the tapes is present at their ends. The cut ends of the samples were polished for inspection with an optical microscope (see Figure 2.8, in Chapter 2).

The cable sample was mounted on a dedicate sample-holder at the University of Twente, which was inserted in a time varying magnetic field of a given amplitude, angle and frequency. The AC losses in the sample are measured using two different methods:

1. *Calorimetric Method* - The losses induced by the applied field are obtained by measuring the average flow of Helium that is evaporated by the sample over a relatively high number of periods. This is achieved by placing the sample inside a partially enclosed volume into which liquid Helium is able to enter through the bottom and produced helium gas is able to escape at the top, where it is measured by a gas-flow-meter outside the cryostat at room temperature.

2. *Inductive Method* - The applied changing magnetic field magnetizes the sample. The in-time-averaged magnetization is measured using two pickup coils: one for the perpendicular component of the magnetization and one for the parallel component. The pick-up coil voltage consists of many frequencies and phases, but only the part of the signal, which has the same frequency as the applied magnetic field and is in-phase with it contributes to the AC loss in the sample. To allow for amplification of this relatively small signal, the pick-up coils are anti-series connected to an empty coil, thereby canceling the majority of the out-of-phase component. The in-phase signal is measured using a lock-in amplifier. Because the position of the currents in the sample are unknown and varying, it is not possible to determine directly which part of the flux returns within the

pickup coils, making it impossible to determine the losses directly. This implies that a non-constant fill factor has to be introduced to scale the results, which then requires a calibration using for example the calorimetric measurement.

An illustration of a simplified electrical diagram of the setup is shown in Figure 4.12. The first method is more direct and accurate, but has a high noise floor and therefore only works for samples with high loss. The second has a lower noise floor, but is less direct and does not always translate easily to absolute numbers of losses. Usually the inductive measurement data is gauged to the calorimetric data, combining the higher sensitivity of the inductive method, with the accuracy of the calorimetric method. This results in a filling factor for each pickup coil. However, for the HTS Roebel cable, the position of the magnetization and coupling current paths can strongly depend on the magnetic field amplitude, angle and frequency. Therefore, data analysis and comparison need to be performed with special care.

### 4.3.3 Hysteresis Loss in Perpendicular Magnetic Field

For uniform time-varying magnetic fields applied in the perpendicular direction, hysteresis loss was predicted by the Network Model as the dominant contribution. In Figure 4.13 the calculated and measured AC losses per cycle and volume as function of magnetic field amplitude, for a Roebel cable with the SP-1 geometry (see Table 2.1) are presented. The frequency of the applied magnetic field is 0.1 Hz. In addition the calculated AC loss is also shown for a Stacked conductor comprising of 1 to 6 tapes. The tape in the stack is 40 mm long and 5.5 mm wide, is not twisted and uses the same scaling relation as the Roebel cable. The separation distance between the tapes is 100 $\mu$m,


**Figure 4.11.** *The impregnated sample in the specifically designed* 300 mm *long impregnation mold for single tapes at CERN. Visible are the channels that allow the resin to penetrate the cable from its edges.*

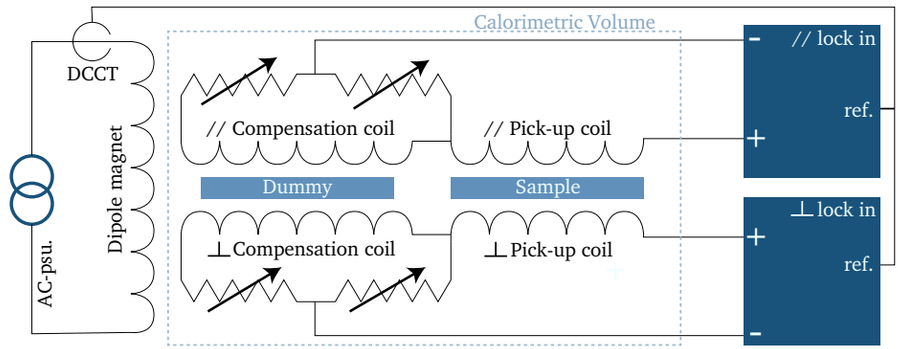


**Figure 4.12.** *Simplified electrical diagram of the experimental setup at the University of Twente showing both the parallel and perpendicular pickup coils, with their ant-series connected compensation coils and the connection to a lock-in amplifier. Sample and pick-up coils are positioned in the bore of a dipole magnet driven by an AC power supply.*

equal to the tape thickness. Because the power dissipation in the perpendicular magnetic field direction is dominated by relatively high hysteresis loss, it was possible to calibrate the pick-up coil data to the calorimetric measurement, which is also shown in the graph. It can be seen that in the magnetic field range of 0.15 to 0.4 T, where the numerical result overlaps with the calorimetric and inductive measurement data, very good agreement is found between the three.

The experimental data lies far below the magnetic field of full penetration and shows a cubic scaling with the magnetic field amplitude. This scaling is more-or-less constant over the entire range indicating that the effective pick-up coil fill factor does not change significantly. The numerical data for the Roebel cable at its lower end also exhibits a cubic scaling with magnetic field, but at higher fields a transition towards linear scaling with magnetic field amplitude occurs. This transition happens at the so-called penetration magnetic field $B_p$ at which point the tapes are saturated. For the stack of tapes at lower magnetic fields a quartic scaling is found with the magnetic field amplitude and at the higher end a linear scaling is found.

The quartic scaling found below the penetration field and the linear scaling above is in agreement with theoretical models for an infinity thin film, with finite dimensions and a one-dimensional current distribution [195, 196, 193]. In some other analytic models, in which a two dimensional current distribution is assumed, cubic scaling is found [197]. When a mixture of one- and two-dimensional current distribution is present the scaling of the losses with magnetic field amplitude has the strong tendency to become cubic [198]. Apparently the Roebel cable, in which the loss is dominated by local spots, essentially the cross-overs, as previously shown in Figure 4.2, behaves in a more two-dimensional manner causing the cubic scaling with magnetic field amplitude to become dominant. In addition the stacks screen out most of the flux increasing the

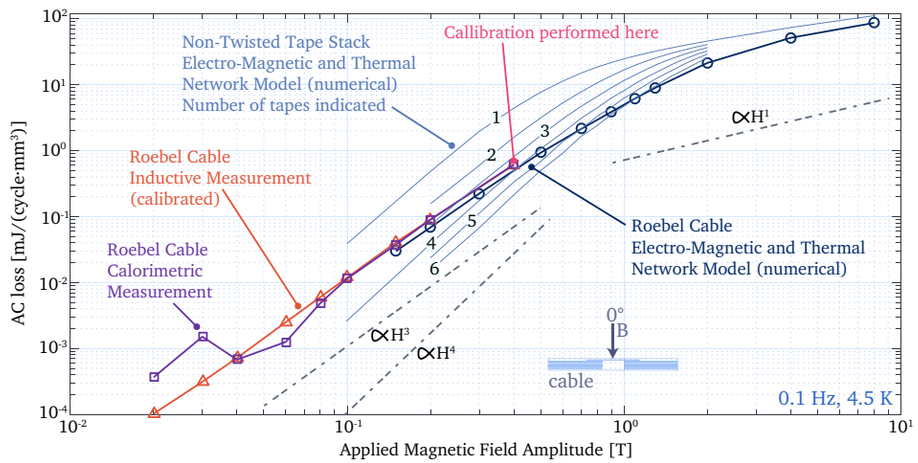


**Figure 4.13.** *Comparison between measured and numerically predicted AC losses in the perpendicular applied magnetic field direction in a Roebel cable, with the SP-1 layout (see Table 2.1). Shown as function of applied magnetic field amplitude at a constant frequency of* 0.1 Hz *and temperature of* 4.5 K*. For comparison also the AC loss of a Stack with varying numbers of tapes is shown. In the model the engineering current density of the conductor is scaled to* 527 A/mm$^2$ *at* 20 T $\perp$ 4.5 K *and* 4.4 kA/mm$^2$ *at* 20 T $\parallel$ 4.5 K *in the* 100 $\mu$m *thick tape.*

effective magnetic field amplitude inside the channel and thus on the cross-over, likely contributing to the effect.

In order to find the penetration field $B_p$ the losses are divided with the applied magnetic field amplitude as $\Gamma = Q/B_0^2$, where $Q$ is the AC loss. In Figure 4.14, $\Gamma$ is shown as function of applied magnetic field amplitude. The transition between quartic or cubic and linear is now visible as a peak, on which the scaling is quadratic. The penetration field of the Roebel cable lies at 1.7 T, which corresponds to the penetration field of a stack of about 5 tapes, explained by the combination of the single cross-over and the stacks of 7 tapes in the cable. The transition from cross-over to tape stack penetration causes the peak to be much wider than for the tape stacks. The penetration fields of the tape stacks are 0.6, 0.9, 1.2, 1.5, 1.7 and 1.9 T for 1 to 6 tapes, respectively. The penetration field flattens off with the number of tapes due to the reduction of the critical current at the penetration field. This is confirmed through the relation $B_p/J_e\left(B_p, T, \alpha\right) \propto N_{\text{tape}}$. Which is fitted with a line of slope $0.0127 \pm 0.0003$, with $J_e$ in A/mm$^2$.

The frequency of the applied field normally has no influence on the hysteresis loss. These relations are checked by measuring the AC losses in the cable sample as function of applied field amplitude and frequency. The results are presented together with the predicted numerical data in Figure 4.15. As expected, no frequency dependence is observed in both measurement and model, within the provided accuracy. Again good

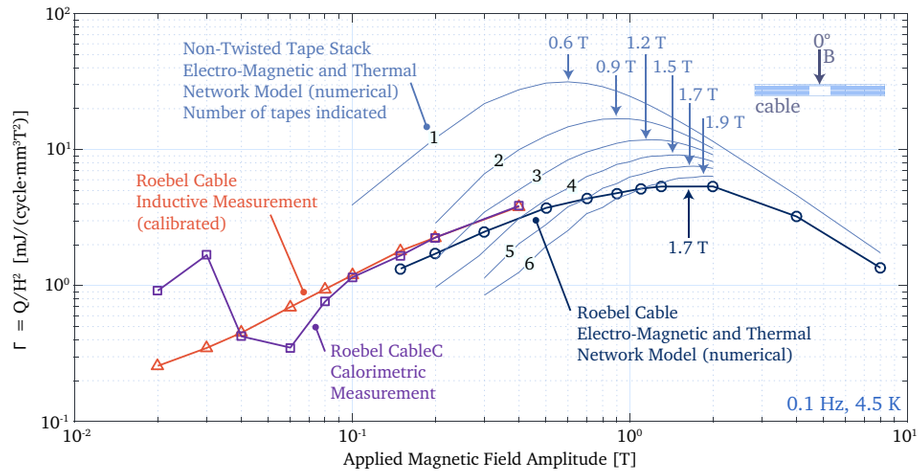


**Figure 4.14.** *Comparison between measured and numerically predicted AC loss in a Roebel cable, with the SP-1 layout (see Table 2.1), divided by the applied magnetic field squared, as function of applied magnetic field amplitude. The magnetic field is applied in the perpendicular direction. The frequency and temperature are constant at* 0.1 Hz *and* 4.5 K*, respectively. For comparison the results are also shown for a Stack with varying numbers of tapes. In the model the engineering current density of the conductor is scaled to* 527 A/mm$^2$ *at* 20 T ⊥ 4.5 K *and* 4.4 kA/mm$^2$ *at* 20 T ∥ 4.5 K *in the* 100 $\mu$m *thick tape.*

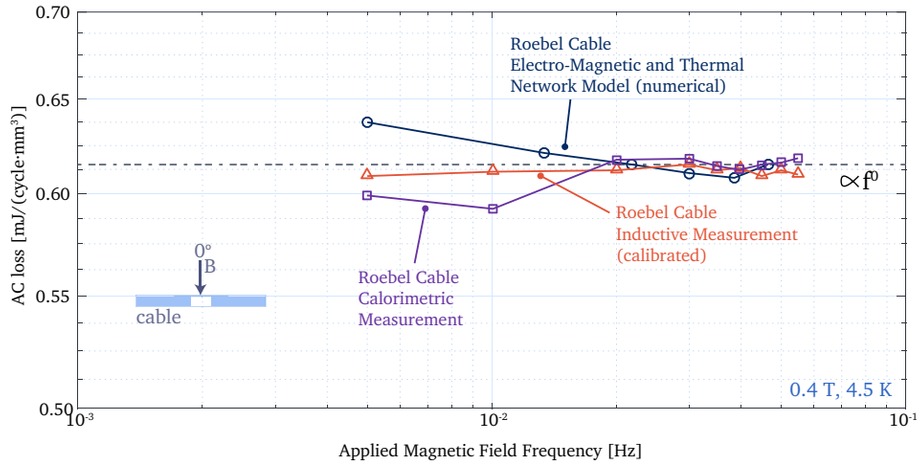


**Figure 4.15.** *Comparison between measured and numerically predicted magnetization losses in the perpendicular applied magnetic field direction in a Roebel cable, with the SP-1 layout (see Table 2.1). Shown as function of frequency at constant magnetic field amplitude of* 0.4 T *and temperature of* 4.5 K*. In the model the engineering current density of the conductor is scaled to* 527 A/mm$^2$ *at* 20 T ⊥ 4.5 K *and* 4.4 kA/mm$^2$ *at* 20 T ∥ 4.5 K *in the* 100 $\mu$m *thick tape.*

agreement is found between the numerical model and the measurement. It is concluded that in the perpendicular direction hysteresis is the main loss component and that the hysteretic loss calculation in the superconducting elements of the Network Model is functioning correctly.

### 4.3.4 Coupling Loss in Parallel Magnetic Field

The amplitude dependence is also measured in the parallel direction (see Figure 4.16). Because the losses are relatively small, no calorimetric data is available, leaving the measurement uncalibrated. This unfortunately prohibits verification of the used value for the contact resistance between the tapes (responsible for the amplitude of the coupling losses). However, it can be seen that the data scale with the second power of the magnetic field $H^2$, indication of pure coupling losses, which is the same as the model prediction. The model predicts a linear dependence with the frequency, again indicative of coupling loss. In the measurement only a small frequency dependence is found, which could indicate a mixture of both coupling and hysteresis. The cause of this discrepancy between both sweeps is possibly a small misalignment of the sample during the second measurement. This can not be verified at this time.

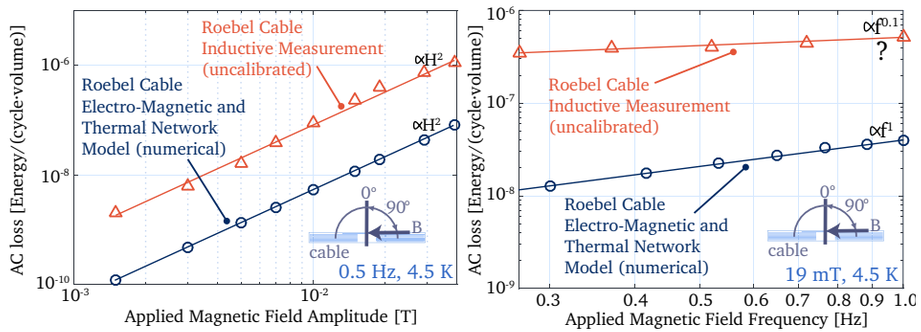


**Figure 4.16.** *Comparison between measured and numerically predicted magnetization losses in the parallel applied magnetic field direction in a Roebel cable, with the SP-1 layout (see Table 2.1). Shown on the left as function of applied magnetic field amplitude at constant frequency of* 0.5 Hz *and temperature of* 4.5 K *and on the right as function of frequency at a magnetic field amplitude of* 19 mT *and temperature of* 4.5 K*. In the model the engineering current density of the conductor is scaled to* 527 A/mm$^2$ *at* 20 T $\perp$ 4.5 K *and* 4.4 kA/mm$^2$ *at* 20 T $\parallel$ 4.5 K *in the* 100 $\mu$m *thick tape. Because the measured data is uncalibrated only a qualitative comparison can be made.*

## 4.4 Hysteresis in Coil-Windings and Field Quality

*This section concerns the dynamic field quality inside coils constructed with ReBCO coated conductor based Roebel cables. The current distribution in coil-windings and thus the field quality is calculated using the Electro-Magnetic and Thermal Network Model.*

### Current Distribution and Magnetic Field 4.4.1

To calculate the dynamic field quality of the Feather-M2 magnet it was first attempted to solve the time dependent currents of the full coil structure using the electro-magnetic part of the Network Model. Unfortunately the memory requirements for performing the LU-decomposition on the S2T matrix proved to be too high (more than the available 64 GB). Therefore as a first approximation the coil was modeled using a slice through the straight section. Figure 4.17 shows an example of such a geometry for the Cosine Theta and Aligned Block. The voltages and currents are only solved inside the slice indicated in red, which has the length of a single unit cell. By only including the length of one single unit cell, the pattern of this slice repeats longitudinally. In addition to further simplify the model, the time-dependent currents are only solved in one quadrant of the coil. The elements in the remaining quadrants and in the repeated slices are included as mirror images for the calculation of the magnetic field and induced voltages. The positions of the cables in the slice are set using the two-dimensional straight section model of the coils. Each tape in each cable is connected to a separate current source, implying that the sum of the currents on the boundary is fixed. Because of the symmetry provided by the mirror elements the boundaries on both sides of the slice show identical currents within the numerical errors. The iron poles and yokes are not included in the simulation because the induced voltages due to their magnetization, are at present not implemented.

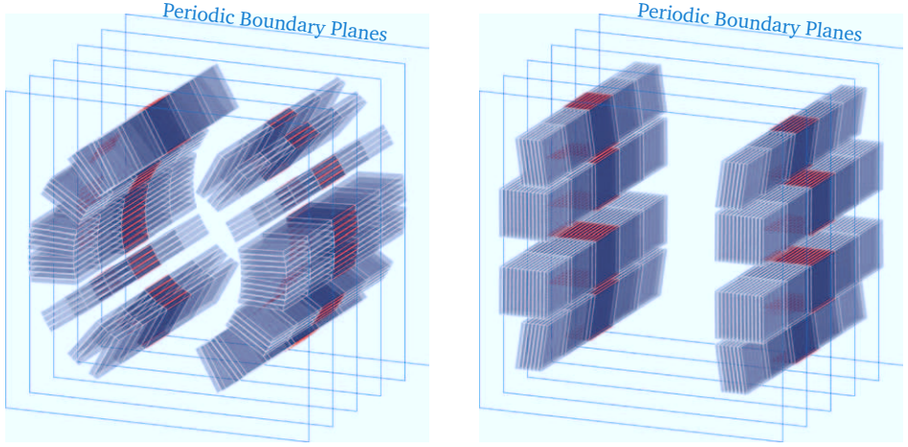


**Figure 4.17.** *Quasi three-dimensional geometry used to perform the coil cross-section simulations, for the Cosine Theta (left) and the Aligned Block coil (right). The voltages and currents are solved for the unit cells marked in red. The elements are copied and repeated across the periodic boundary planes for the mutual inductance calculations.*

Under study are two coil geometries (Aligned Block and Cosine Theta) and two operating scenarios (stand-alone mode and operating as insert in a background field), resulting in the following four cases:

1. *Cosine Theta in Stand-alone Mode* - The Cosine Theta layout [60, 61] designed by CEA for the 1.2 mm BHTS-2 ReBCO Roebel cable (see Table 2.1) is operated at 4.2 K in stand-alone mode and is powered twice to its design current of 7 kA. The ramping up and down occur over a time span of 20 min with a ramp-rate of 5.83 A/s, and between the ramps a plateau of 100 s is maintained. The critical current in the 150 $\mu$m thick tape is approximated using the scaling relation described in Appendix A scaled to 527 A/mm$^2$ in 20 T perpendicular applied magnetic field and 4.4 kA in parallel applied magnetic field.

2. *Aligned Block in Stand-alone Mode* - The CERN Feather-M2 Aligned Block (see Chapter 2) layout designed for the 0.8 mm SP-1 ReBCO Roebel cable is operated at 4.2 K in stand-alone mode and is powered twice to its design current of 8 kA. The ramping up and down occur over a time span of 20 min, with a ramp-rate of 6.66 A/s, and between the ramps a plateau of 100 s is maintained. The critical current in the 100 $\mu$m thick tape is approximated using the scaling relation described in Appendix A scaled to 527 A/mm$^2$ in 20 T perpendicular applied magnetic field and 4.4 kA in parallel applied magnetic field.

3. *Cosine Theta as Insert in Background Field* - The Cosine Theta layout [60, 61] designed by CEA for the 1.2 mm BHTS-2 ReBCO Roebel cable is operated at 4.2 K in a co-ramped background field of 13 T and is powered twice to its design current of 7 kA. The ramping up and down occur over a time span of 20 min, with a ramp-rate 5.83 A/s, and between the ramps a plateau of 100 s is maintained. The critical current in the 150 $\mu$m thick tape is approximated using the scaling relation described in Appendix A scaled to 527 A/mm$^2$ in 20 T perpendicular applied magnetic field and 4.4 kA in parallel applied magnetic field.

4. *Aligned Block as Insert in Background Field* - The CERN Feather-M2 Aligned Block (see Chapter 2) layout designed for the 0.8 mm SP-1 ReBCO Roebel cable is operated at 4.2 K in a co-ramped background field of 13 T and is powered twice to its design current of 8 kA. The ramping up and down occurs over a time span of 20 min, with a ramp-rate 6.66 A/s, and between the ramps a plateau of 100 s is maintained. The critical current in the 100 $\mu$m thick tape is approximated using the scaling relation described in Appendix A scaled to 527 A/mm$^2$ in 20 T perpendicular applied magnetic field and 4.4 kA in parallel applied magnetic field.

Due to the complexity of the geometry, since many tapes are located in a small volume, the calculation time for each of these cases is 2-4 weeks[8]. It is noted that, due to the absence of the iron, the coil study performed here has to be be regarded as a qualitative and relative comparison and not as a prediction of the precise harmonic content of the

[8] Calculation times are given on the available hardware which comprises of a *Intel(R) Core(TM) i7-5820K CPU* operating at 3.3 GHz and a *NVIDIA GTX980* graphics card.

coils. A two dimensional representation of the axial tape surface current density in the four scenarios at various times throughout the powering cycle are shown in the Figures 4.18 to 4.21 on Pages 148, 150, 152 and 154, respectively.

The surface current densities shown are in essence a superposition of both magnetization and transport current density. The magnetization currents are characterized by axial current density equal in both directions, while the transport current applies an offset, causing more axial current density to flow in one direction. In all the scenarios the currents fill up the tapes and cables from their edges, where they run approximately the critical current, while at the center of the tapes the current density is near zero. The magnetic field angle is usually larger on the edges due to the self field. Therefore, similar to the results from a single cable, the surface current density is often lower on the edges of the cables than slightly inward. When the magnets are ramped down, in all cases a remnant superconducting current and thus magnetic field remains inside the windings. As previously observed for the cable, the cross-over tapes magnetize first, followed by the tapes in the stack. clear interaction is visible between the cables making up a conductor block. The outer cables magnetize before the inner ones. The penetration field of such a stack can exceed 7 T.

For the Cosine Theta in stand-alone mode it can be seen that almost no magnetization currents and thus only the transport current is present. This would be different for a two layer layout, in which the inner layer generates a perpendicular magnetic field on the outer layer and vice-versa, resulting in screening currents. Inside the coil pack the magnetic field is near zero. The transport current at the operating current of 7 kA only utilizes the outer 1 to 2 mm of the cables, showing that a significant amount of margin is left. In the Aligned Block in stand-alone mode the upper deck is located in perpendicular magnetic field and thus screening currents are induced at this location. With an iron yoke and pole it is expected that this effect is weaker than shown due to the better magnetic field alignment. Note that the Block layout uses a smaller tape thickness than the Cosine Theta, resulting lower surface current density. The central deck is in near parallel magnetic field and has only a transport current.

When the layouts are operating as insert in the background field the roles are reversed. Due to the misalignment of the tapes on the mid-plane in the Cosine Theta coil very large screening currents flow in the tapes. Cables that have a larger inclination reach full penetration at a later time than the cables located on the mid-plane. When reaching the operating current of 7.0 kA and a background magnetic field of 13 T, the coil is almost at its short sample, causing the transport current to occupy about 70% of the conductor cross section, thereby suppressing most of the magnetization currents. The Aligned Block by topology avoids flux perpendicular to the tape surface resulting in almost no magnetization currents. When operating at 8.0 kA and a background magnetic field of 13 T, only 1 to 2 mm of the edges of the cable are filled with a relatively high current density, resulting from the alignment of the conductor with the magnetic field. This shows that a significant margin is left and that the coil can potentially reach much higher operating currents.

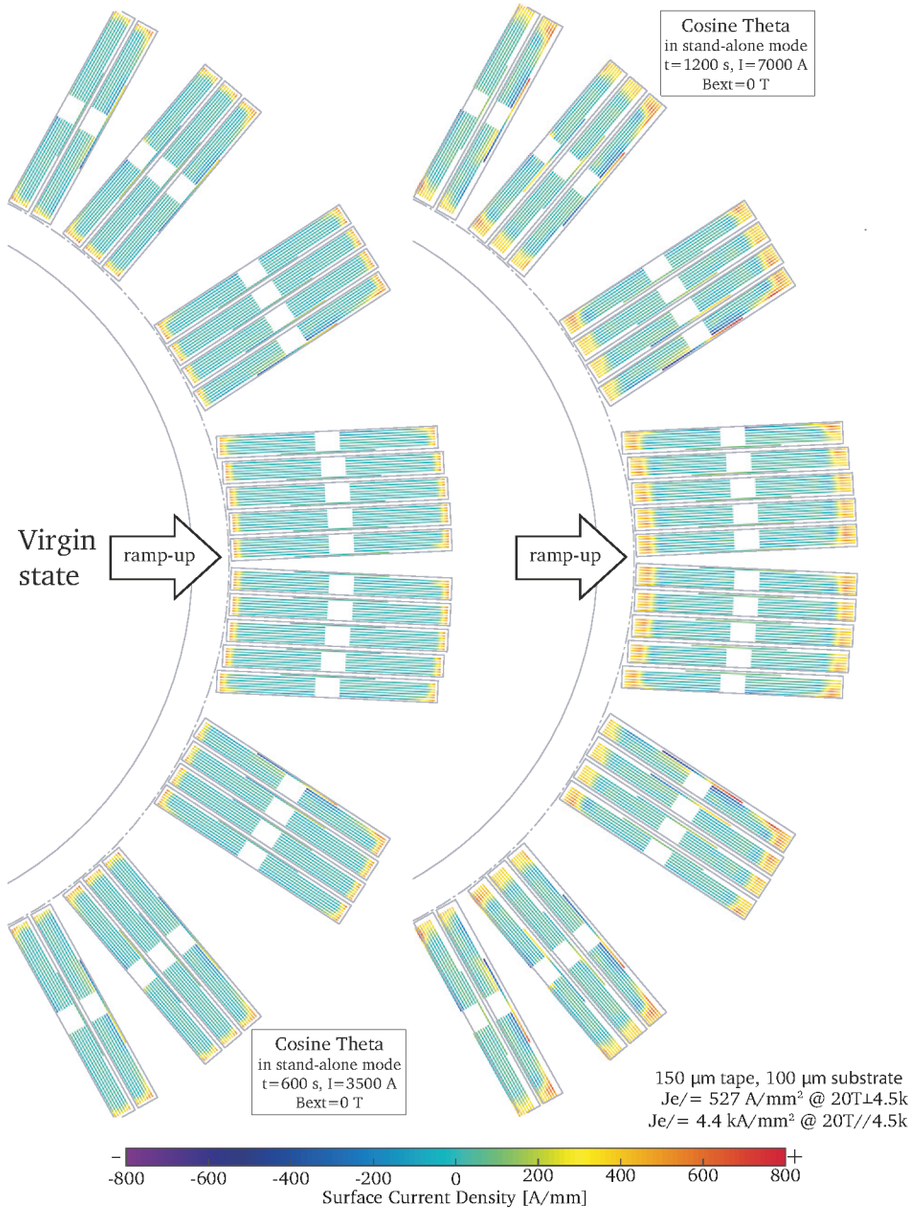


**Figure 4.18.** *The calculated axial surface current density distribution at various times on the straight section of the CEA Cosine Theta coil [60, 61] during powering in stand-alone mode as given by Case 1 (see Section 4.4.1). The calculation of the local current density is performed in a three-dimensional slice of the coil using the electro-magnetic part of the Network Model. The engineering current density of the conductor is scaled to* $527\,\mathrm{A/mm^2}$ *at* $20\,\mathrm{T} \perp 4.5\,\mathrm{K}$ *and* $4.4\,\mathrm{kA/mm^2}$ *at* $20\,\mathrm{T} \parallel 4.5\,\mathrm{K}$ *in the* $150\,\mu\mathrm{m}$ *thick tape. The iron yoke was not included in the calculation.*

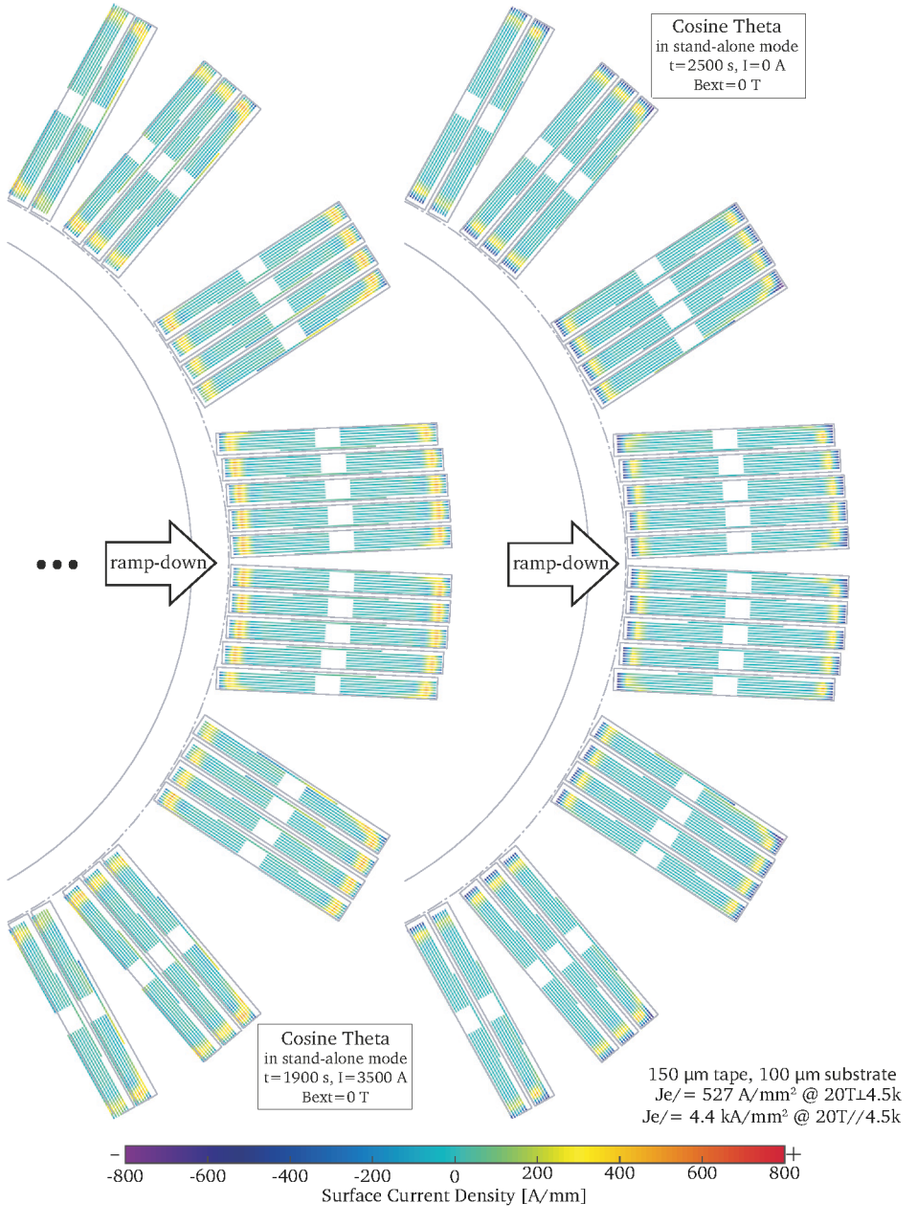
Cosine Theta
in stand-alone mode
t=2500 s, I=0 A
Bext=0 T
ramp-down
ramp-down
Cosine Theta
in stand-alone mode
t=1900 s, I=3500 A
Bext=0 T
150 µm tape, 100 µm substrate
Je/= 527 A/mm² @ 20T⊥4.5k
Je/= 4.4 kA/mm² @ 20T//4.5k
-
+
-800
-600
-400
-200
0
200
400
600
800
Surface Current Density [A/mm]

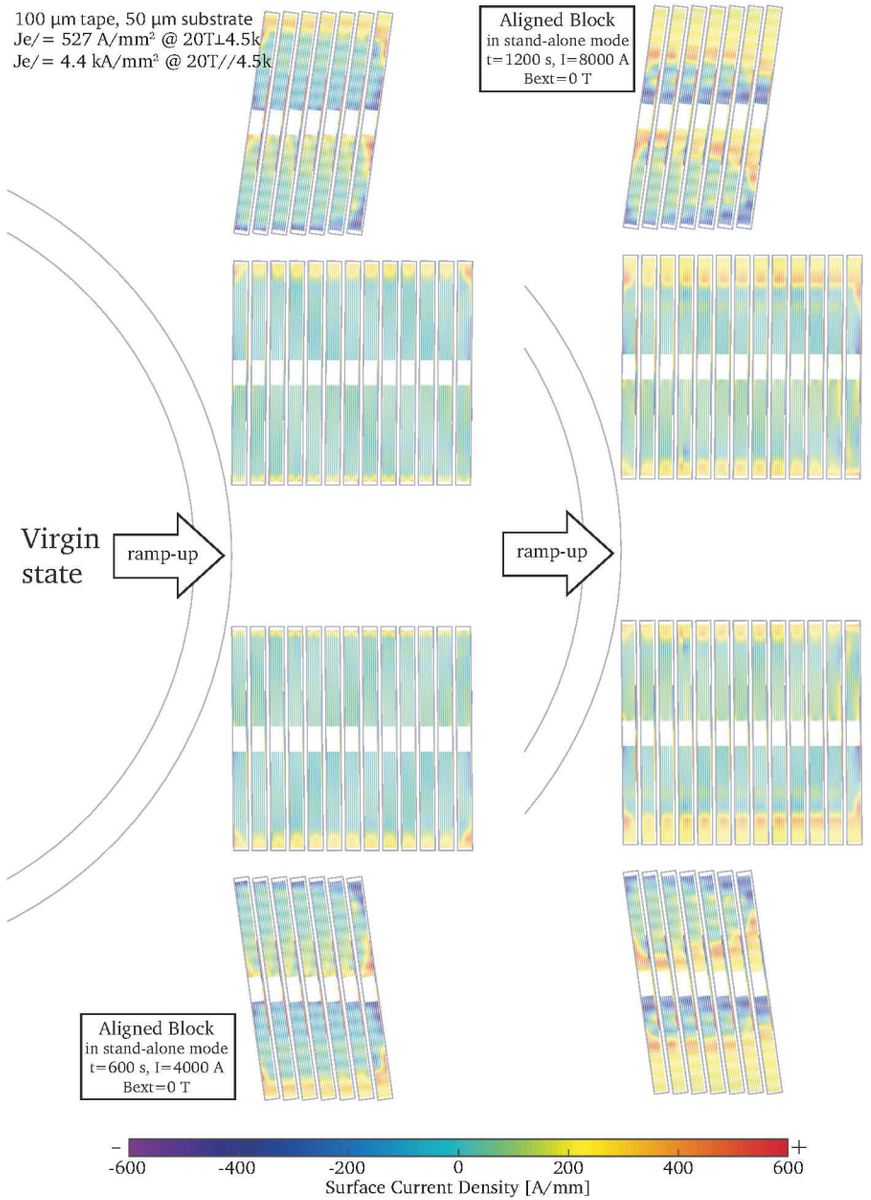


**Figure 4.19.** *The calculated axial surface current density distribution at various times on the straight section of the Feather-M2 Aligned Block during powering in stand-alone mode as given by Case 2 (see Section 4.4.1). The calculation of the local current density is performed in a three-dimensional slice of the coil using the electro-magnetic part of the Network Model. The engineering current density of the conductor is scaled to* $527\,\mathrm{A/mm^2}$ *at* $20\,\mathrm{T} \perp 4.5\,\mathrm{K}$ *and* $4.4\,\mathrm{kA/mm^2}$ *at* $20\,\mathrm{T} \parallel 4.5\,\mathrm{K}$ *in the* $100\,\mu\mathrm{m}$ *thick tape.The iron poles and yoke were not included in the calculation.*

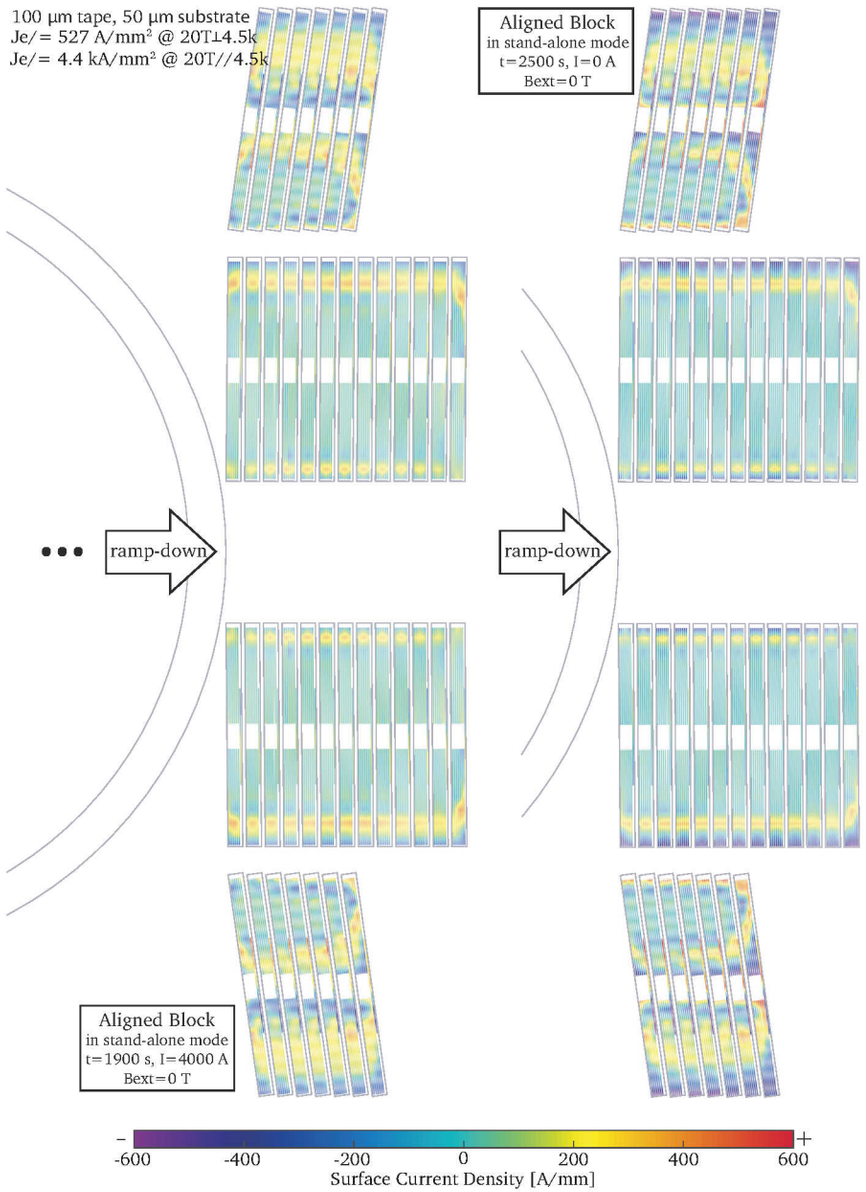
100 μm tape, 50 μm substrate
Je/= 527 A/mm² @ 20T⊥4.5k
Je/= 4.4 kA/mm² @ 20T//4.5k
Aligned Block
in stand-alone mode
t=2500 s, I=0 A
Bext=0 T
ramp-down
ramp-down
Aligned Block
in stand-alone mode
t=1900 s, I=4000 A
Bext=0 T
−
+
-600
-400
-200
0
200
400
600
Surface Current Density [A/mm]

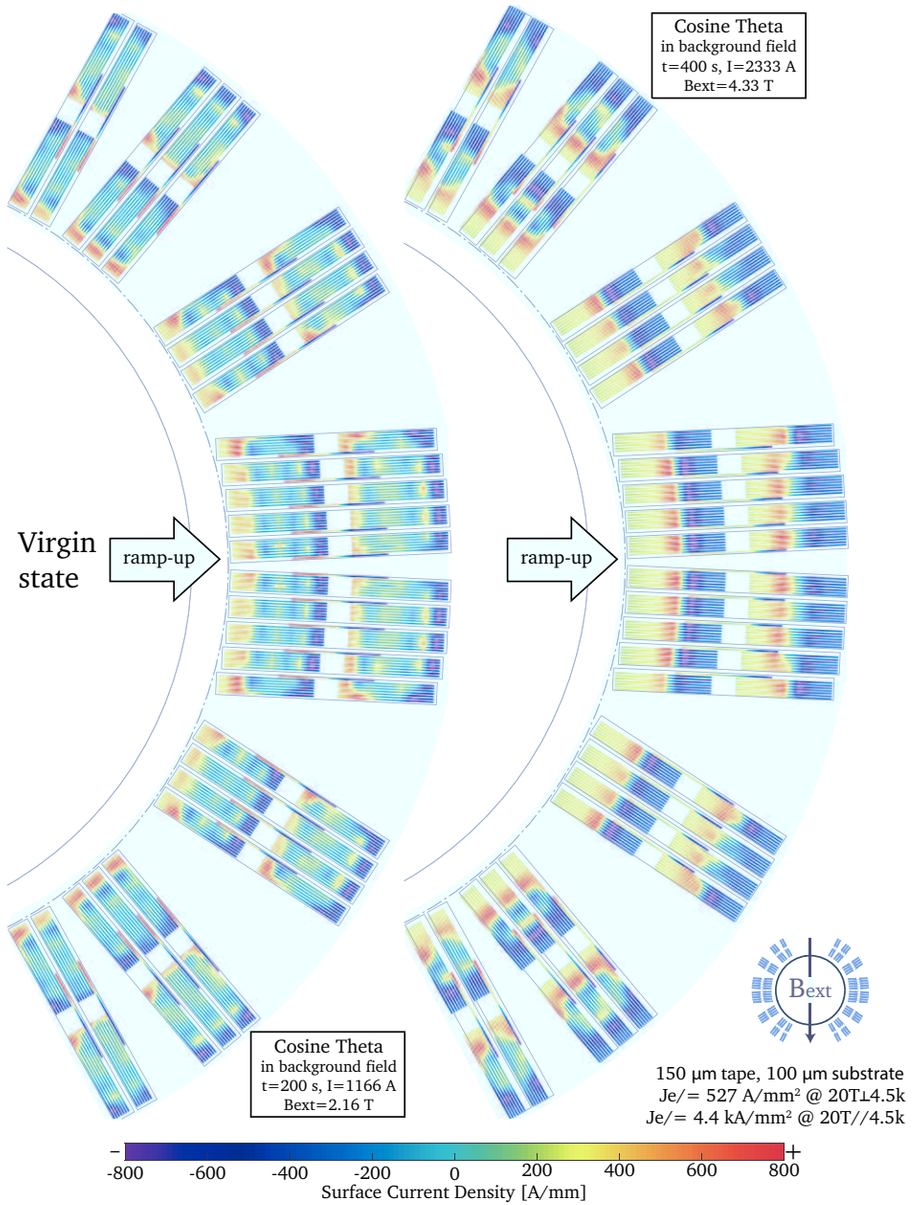


**Figure 4.20.** *The calculated axial surface current density distribution at various times on the straight section of the CEA Cosine Theta coil [60, 61] during powering as insert in a co-ramped background magnetic field with amplitude* 13 T *as given by Case 3 (see Section 4.4.1). The calculation of the local current density is performed in a three-dimensional slice of the coil using the electro-magnetic part of the Network Model. The engineering current density of the conductor is scaled to* 527 A/mm$^2$ *at* 20 T $\perp$ 4.5 K *and* 4.4 kA/mm$^2$ *at* 20 T $\parallel$ 4.5 K *in the* 150 µm *thick tape.*

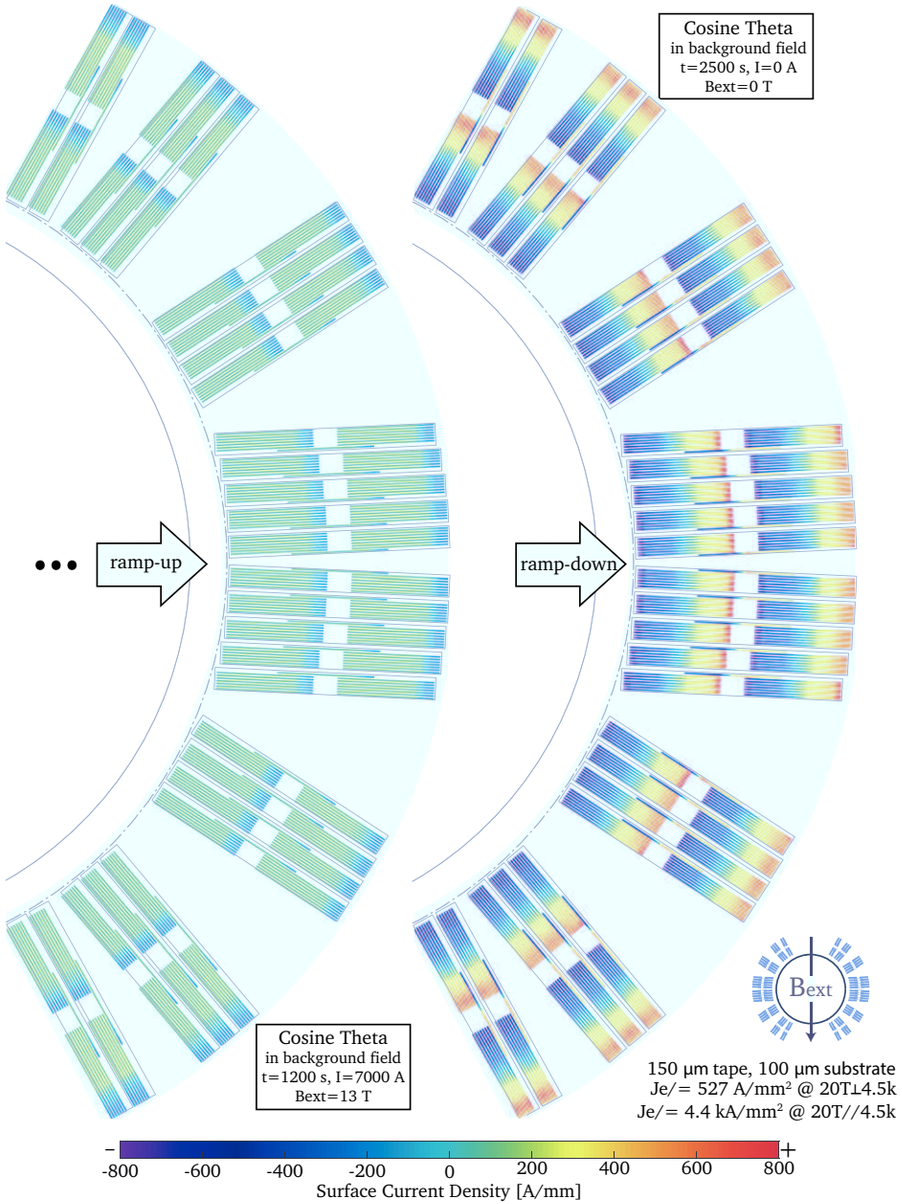
Cosine Theta
in background field
t=2500 s, I=0 A
Bext=0 T
ramp-up
ramp-down
Cosine Theta
in background field
t=1200 s, I=7000 A
Bext=13 T
Bext
150 µm tape, 100 µm substrate
Je/= 527 A/mm² @ 20T⊥4.5k
Je/= 4.4 kA/mm² @ 20T//4.5k
–
+
-800
-600
-400
-200
0
200
400
600
800
Surface Current Density [A/mm]

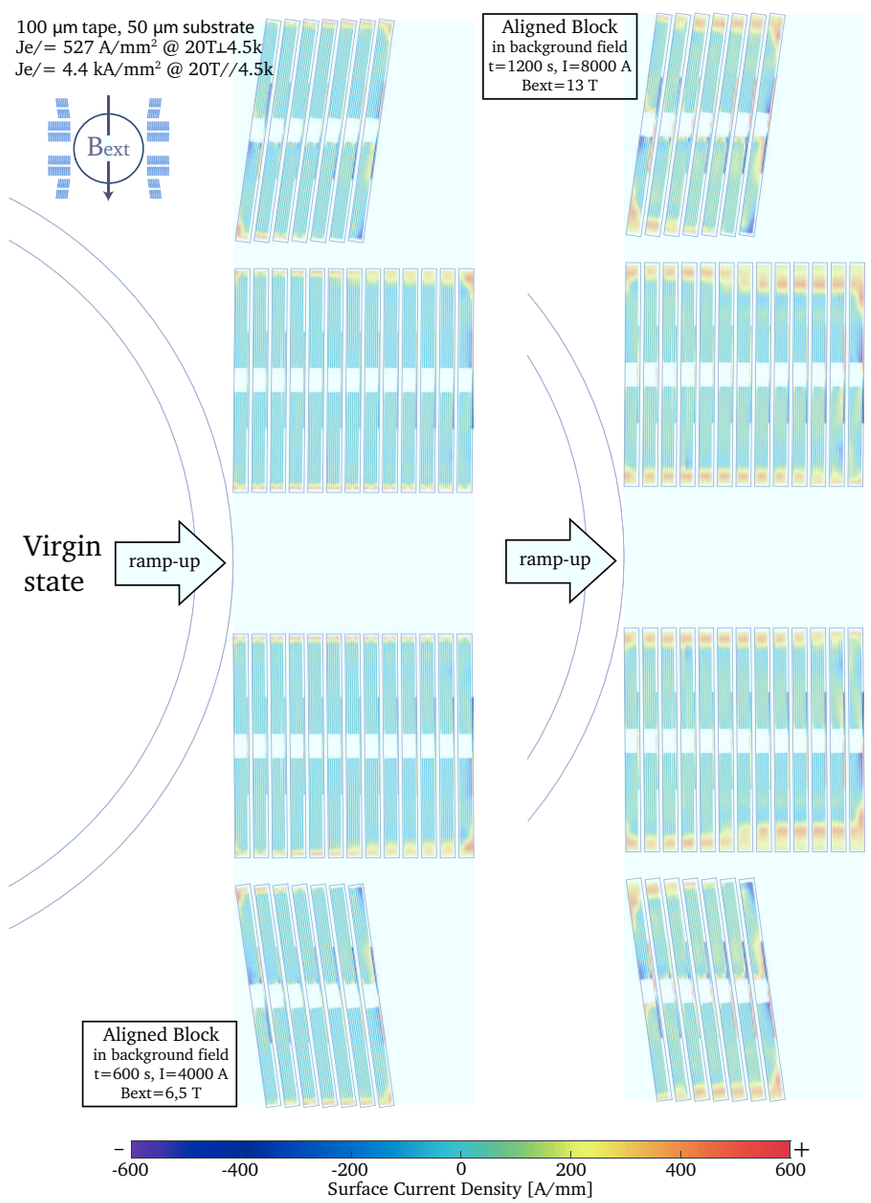


**Figure 4.21.** *The calculated axial surface current density distribution at various times on the straight section of the Feather-M2 Aligned Block during powering as insert in a co-ramped background magnetic field with amplitude* 13 T *as given by Case 4 (see Section 4.4.1). The calculation of the local current density is performed in a three-dimensional slice of the coil using the electromagnetic part of the Network Model. The engineering current density of the conductor is scaled to* 527 A/mm$^2$ *at* 20 T ⊥ 4.5 K *and* 4.4 kA/mm$^2$ *at* 20 T ∥ 4.5 K *in the* 100 µm *thick tape. The iron poles were not included in the calculation.*

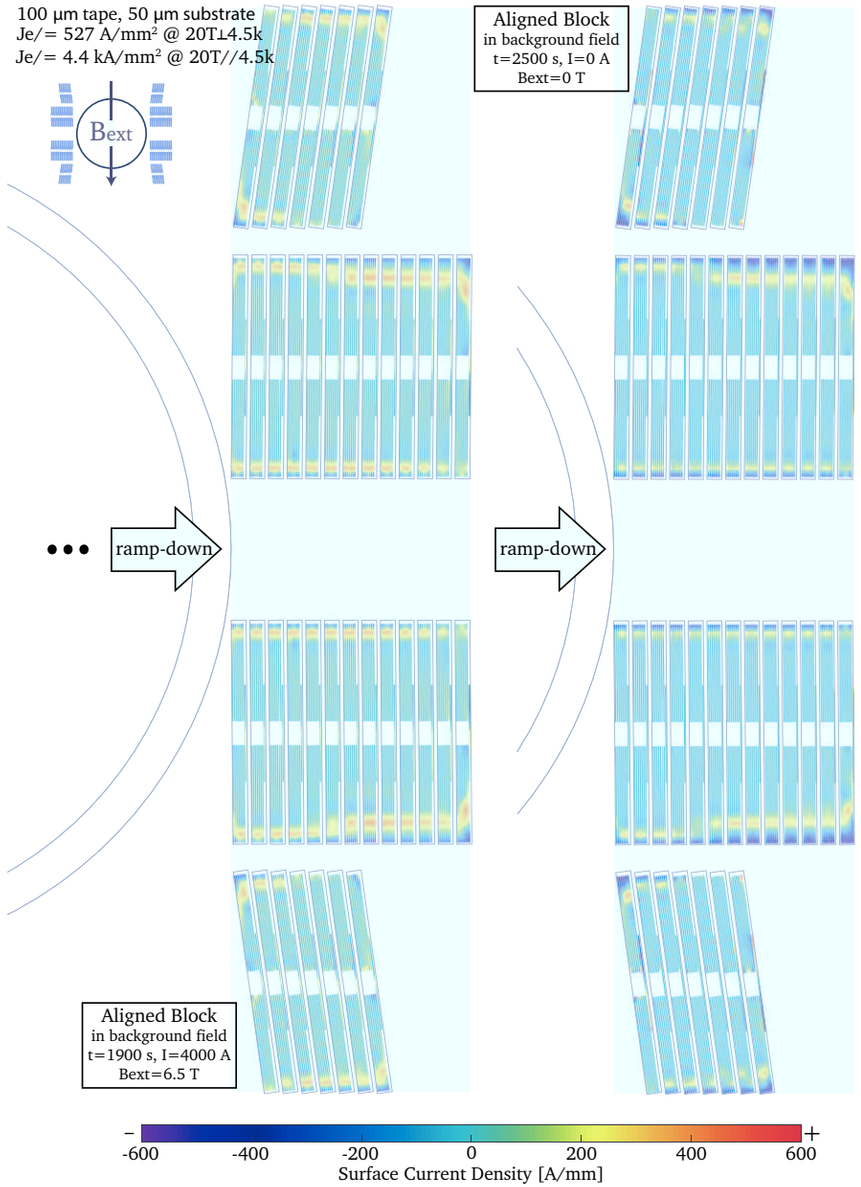
100 µm tape, 50 µm substrate
Je/= 527 A/mm² @ 20T⊥4.5k
Je/= 4.4 kA/mm² @ 20T//4.5k
Bext
Aligned Block
in background field
t=2500 s, I=0 A
Bext=0 T
ramp-down
ramp-down
Aligned Block
in background field
t=1900 s, I=4000 A
Bext=6.5 T
–
+
-600
-400
-200
0
200
400
600
Surface Current Density [A/mm]

Because the magnetization currents inherently shield the flux from the superconductor and because the width of the superconducting layer in the tapes, in fact a flat filament, is orders of magnitude larger than for LTS, the magnetic field inside the coil pack during ramping is very a-typical, as is presented in Figure 4.22. In this figure the magnetic field is calculated at 400 s for a Cosine Theta coil, which was co-ramped with a background field (case 3). The current in the cable is 2333 A and the background field is 4.33 T. It can be seen that in the coil pack, near the mid-plane, the magnetic field is still zero due to the screening currents, while outside the windings the magnetic field, a superposition of self- and background magnetic field, already reached $\sim 7$ T.

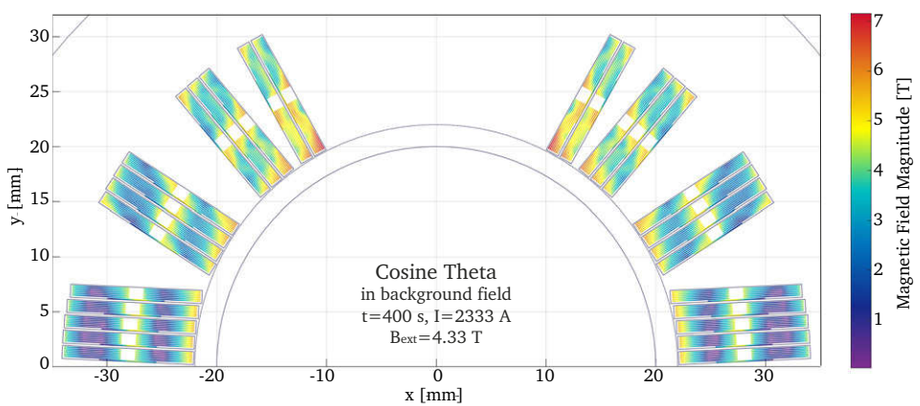


**Figure 4.22.** *Cross-section showing the a-typical magnetic field distribution on the conductor, as calculated from the screening currents in the Electro-Magnetic and Thermal Network Model, inside the CEA Cosine Theta layout when co-ramped with a background field (Case 3). The field is calculated at* 400 s *during the powering of the magnet. At this time the current in the cable is* 2333 A *and the background field is* 4.33 T. *The corresponding current density is presented in Figure 4.20 (second illustration).*

### 4.4.2 Dynamic Field Quality

From the calculated time dependent currents in the model elements the dynamic field quality is calculated. This is achieved by calculating the magnetic field on a reference circle, located in the xy-plane, centered at $[0, 0, 0]$, with a radius of 13.33 mm, corresponding to 2/3 times the radius of the aperture. Note that the field quality for points inside the circle is always better than on the circle. The value of the harmonic components then follow from the Discrete Fourier Transform (DFT) of the radial magnetic field.

The dynamic variation of the coil harmonic content throughout the powering cycles is then calculated for every time step and is represented as function of time for the Cosine Theta in stand-alone (Case 1) in Figure 4.23. It can be seen that the coil geometry is optimized for the sextupole and the decapole components that are near-zero throughout

the majority of the ramp. When the coil reaches zero current after the first ramp-down at 2500 s, the remnant currents that were presented in Section 4.4.1 generate various harmonic components. Because, the remnant currents generate a dipole component opposite to the main field direction, it crosses zero. This causes the harmonic components, which are normalized with the dipole field, to exhibit asymptotic behavior. This behavior is commonly avoided in an accelerator by injecting the particles at the so-called minimum injection field, which is nonzero. The injection field for the Cosine Theta in stand-alone in order to stay within 10 units, is about 0.3 T out of the 2.2 T generated. Note that the dipole component is slightly lower than in the design, even without iron yoke, because the simulated geometry, despite the mirror images used, turned out to be too short to fully represent the coil.

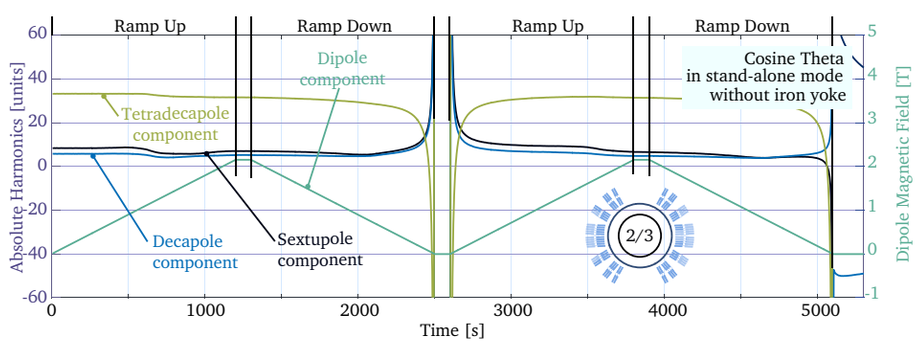


**Figure 4.23.** *Calculated absolute coil harmonics as function of time on the straight section of the CEA Cosine Theta coil layout during the powering in stand-alone mode (Case 1 in Section 4.4.1). The calculation is performed in a three-dimensional slice of the coil using the electro-magnetic part of the Network Model.*

In Figure 4.24 the harmonic variation of the components are presented as function of time for the Aligned Block in stand-alone mode (Case 2). The reason only the variation is shown, is that the absence of the iron pole in the calculations, would lead to a very large offset in the harmonics, making graphical representation difficult. In this case large variations on the order of 100 units are visible in the sextupole component. These variations are caused by the magnetization currents in the upper deck, which are presented in Section 4.4.1. The other components seem much less affected. The field quality at first ramp-up is different from the second ramp, because the coil is ramped from the virgin state. After the initial ramp the pattern repeats, which provides additional confidence in the correctness of the developed coil models. The injection field to stay below 10 units is about 2.5 T out of the generated 3 T, which is unacceptable for an accelerator magnet.

Now both cases are studied in the background field. The harmonic components as function of time are presented for the Cosine Theta insert in a uniform background field (Case 3) in Figure 4.25. For the insert cases the dipole component resulting from the background field is included in the calculation. In contrast to the stand-alone case

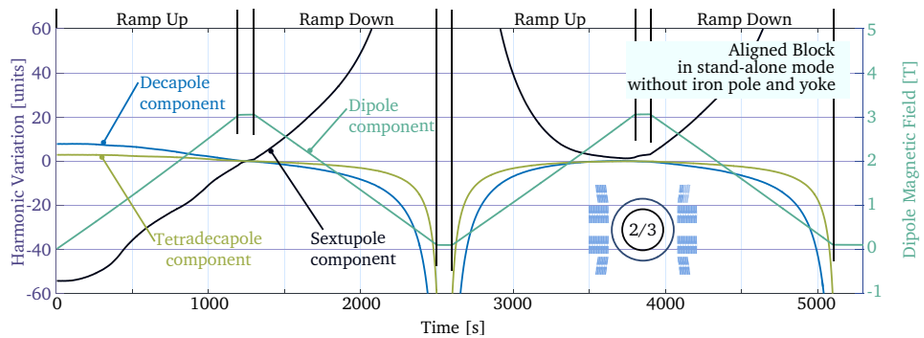


**Figure 4.24.** *Calculated harmonic variation in the coil harmonics as function of time on the straight section of the Feather-M2 Aligned Block coil layout during the powering in stand-alone mode (Case 2 in Section 4.4.1). The calculation is performed in a three-dimensional slice of the coil using the electro-magnetic part of the Network Model.*

a variation of about 60 units is present in the sextupole component during the virgin ramp. The injection field below 10 units is about 12 T out of the 15 T at maximum magnetic field, which is unacceptable for an accelerator magnet. In addition it can be seen that the coil pack reaches full magnetic field penetration at approximately 8 T, which is the only case in which full penetration is observed. All other cases are below penetration and therefore their harmonic content does not exhibit the classical loop, which is commonly presented in, for example, the LHC magnets. Therefore it is likely that the coil harmonics in these cases keep increasing further, when the current is increased beyond the operating current of 8 kA.

For the Aligned Block insert the variation of the harmonic components in a uniform background field can be found in Figure 4.26. Because almost no magnetization currents are present and because the transport current is located on the edges of the conductor and barely moving inward during the ramp, the harmonic components show almost no variation. This in contrast to the stand-alone case. The injection field is about 1 T, limited by the sextupole component, out of the 16 T generated, which is actually acceptable for accelerator magnets.

### 4.4.3 AC loss and Temperature

Although the magnetization losses assuming constant temperature have no direct effect on the beam dynamics, they are still of relevance for conductor thermal stability and possible local thermal runaway leading to a quench. The AC loss is calculated every time step directly from the elements, after which it is summed. The total loss per meter coil, including the four coil quadrants, is presented as function of time for the four cases (see Section 4.4.1) in Figure 4.27. AC loss is observed mainly during ramp-up and ramp-down. Between the ramps an exponential decay is visible.

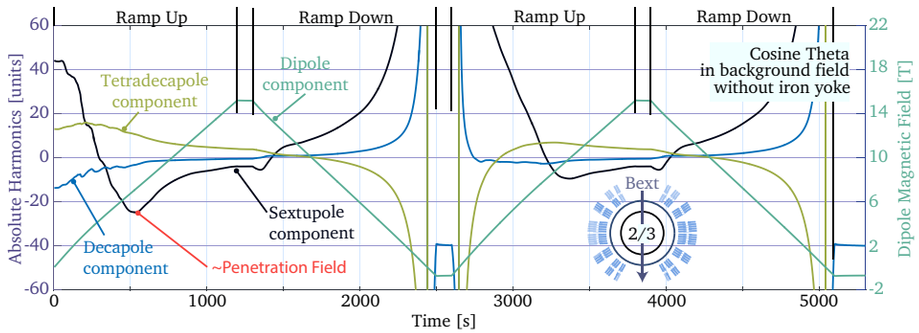


**Figure 4.25.** *Calculated absolute coil harmonics as function of time on the straight section of the CEA Cosine Theta coil layout during the powering as insert in co-ramped uniform background field (Case 3 in Section 4.4.1). The calculation is performed in a three-dimensional slice of the coil using the electro-magnetic part of the Network Model.*

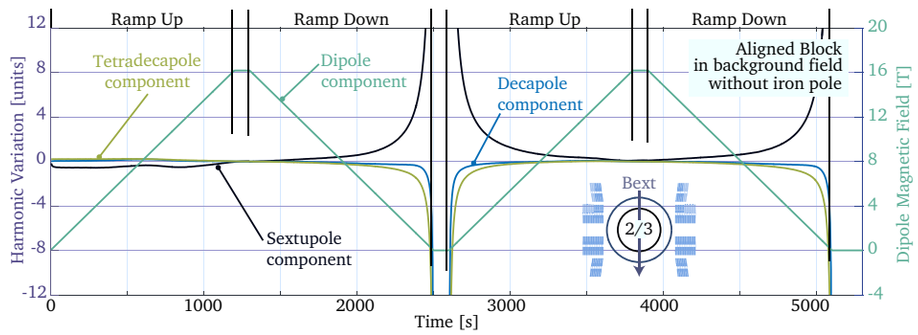


**Figure 4.26.** *Calculated harmonics variation as function of time on the straight section of the Feather-M2 Aligned Block coil layout during the powering as insert in co-ramped uniform background field (Case 4 in Section 4.4.1). The calculation is performed in a three-dimensional slice of the coil using the electro-magnetic part of the Network Model.*

The amount of magnetization in the coil-windings, presented in Section 4.4.1, corresponds directly to the power dissipation. A peak dissipation of 0.17, 2.0, 24 and 0.49 W/m is found for the Cosine Theta in stand-alone (Case 1), the Aligned Block in stand-alone (Case 2), the Cosine Theta as insert in co-ramped background magnetic field (Case 3) and the Aligned Block as insert in a co-ramped background magnetic field (Case 4), respectively (see Table 4.1). During the virgin ramp the time averaged power dissipation is calculated for the four cases at 0.059, 0.68, 12 and 0.11 W/m, respectively. The power dissipation during the virgin ramp is slightly higher than the second ramp, which is normal behavior also present in LTS magnets. The estimated average power dissipation during the second ramp for the four cases is 0.014, 0.17, 8.3 and 0.024 W/m, respectively. Considering the cryogenic penalty factor at liquid helium temperature, which is about 10000, the cosine theta would require an average

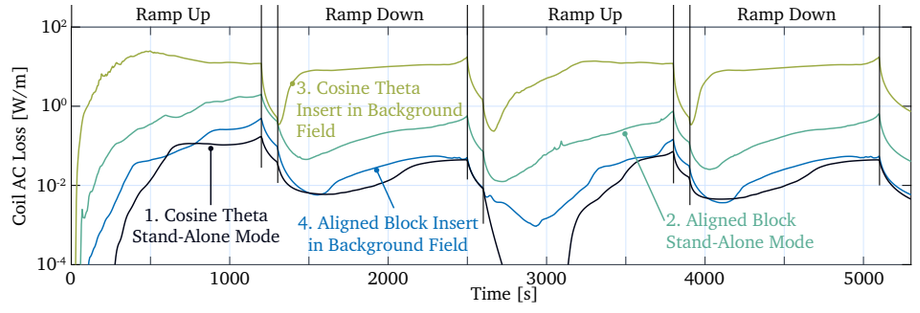


**Figure 4.27.** *The calculated power dissipation as function of time on the straight section of the Cosine Theta and Aligned Block coil layouts during the powering of the coils as given by the four cases described in Section 4.4.1. The calculation is performed in a three-dimensional slice of the coil using the electro-magnetic part of the Network Model.*

of 83 kW of cooling power per meter coil. This value is much higher than in the LHC where 500 W/m per aperture is required and would be impractical for a large accelerator, making the novel Aligned Block layout a much better option for ReBCO high field inserts for accelerators.

TABLE 4.1.
CALCULATED POWER DISSIPATION DURING POWERING OF THE ALIGNED BLOCK AND COSINE THETA COILS IN STAND-ALONE MODE OR AS INSERT IN A CO-RAMPED BACKGROUND FIELD.

| Case | | 1. | 2. | 3. | 4. |
|---|---|---|---|---|---|
| Type | | Cosine Theta | Aligned Block | Cosine Theta | Aligned Block |
| Operation | | stand-alone | stand-alone | insert | insert |
| Peak Power | W/m | 0.17 | 2.0 | 24 | 0.49 |
| Average Power 1st | W/m | 0.059 | 0.68 | 12 | 0.11 |
| Average Power 2nd | W/m | 0.014 | 0.17 | 8.3 | 0.024 |

In order to further characterize the power dissipation in the Cosine Theta layout, when operated as insert in the background field, the loss is plotted as function of time per tape in Figure 4.28. It is observed that the cables that have a higher inclination angle with respect to the coil mid plane, in general have lower losses. The individual tapes show that the local AC losses are also more localized in time. The subsequent spikes then average out in time. The spikes can be explained by two factors. The first is that only a limited number of 10 elements was used over the width of the tapes. When an element fills up, the current is pushed to its neighboring elements, temporarily increasing the power output. This is a numerical effect that is averaged out in time. The second factor is that the magnetization does not occur simultaneously in all tapes. In essence, the inclined cables magnetize at a different time than the cables on the mid-plane, resulting in a temporal shift in the losses between these areas.

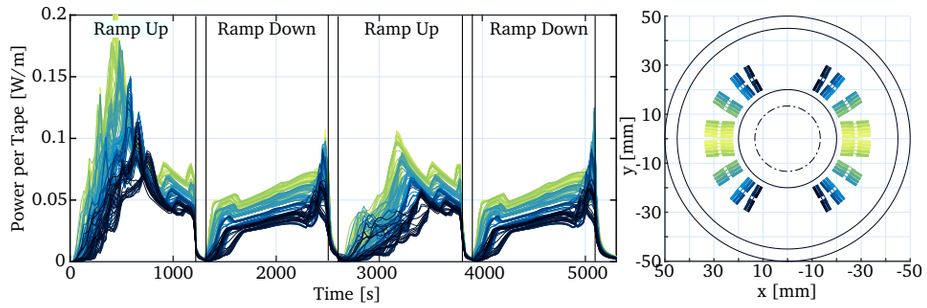


**Figure 4.28.** *Power dissipation per tape for the Cosine Theta operated as insert in a uniform co-ramped background magnetic field, corresponding to Case 3 in Section 4.4.1.*

### Inhomogeneous Force Density Distribution 4.4.4

Since the current is not homogeneously distributed in the conductor, the Lorentz forces in the coil pack are also inhomogeneous. In Figure 4.29, the Lorentz forces divided by the surface area of the tape acted upon, i.e. the Lorentz force density, is shown for the Feather-M2 Aligned Block insert at full magnetic field, corresponding to Case 4 at 1200 s. A sketch of the surrounding structure is shown in order to clarify the position of the Roebel cables, making up the coil-windings. The arrows represent the overall direction and the color represents the magnitude of the surface force density in units of MPa. Note that this is just a representation of the forces acting on the superconducting layer and is in no way related to the von Mises stress. Because the tapes are aligned with the magnetic field, the forces are more-or-less perpendicular with their surface. The edges of each tape experience a force density of approximately 6 MPa, while in the middle of the tape almost no pressure is present. On the three outer turns of the central deck it can be seen that the cross overs experience forces pointing in both directions, this due to the magnetization currents. Each cable has 7 tapes on each side (stack), while the central deck has 13 cables, resulting in an accumulated edge pressure of 546 MPa, which is close to the limit of what individual tapes can stand [102, 103, 104]. This means that further mechanical analysis, in which the current distribution in the coil pack is taken into account, is necessary.

## Persistent Current Shim Coils 4.5

*A conceptual method is introduced to control dynamic and static magnetic field errors by inserting a set of compensation coils operating in persistent-mode inside the main coil aperture. A similar technique is applied or considered to improve the magnetic field homogeneity of NMR magnets [199]. It is to mention that a similar concept was tried out on a fast ramping magnet at CEA in 1973 [200]. In this Section the shape of the compensation coils is described, together with a numerical simulation exploring the effect of such coils on the coil harmonics.*

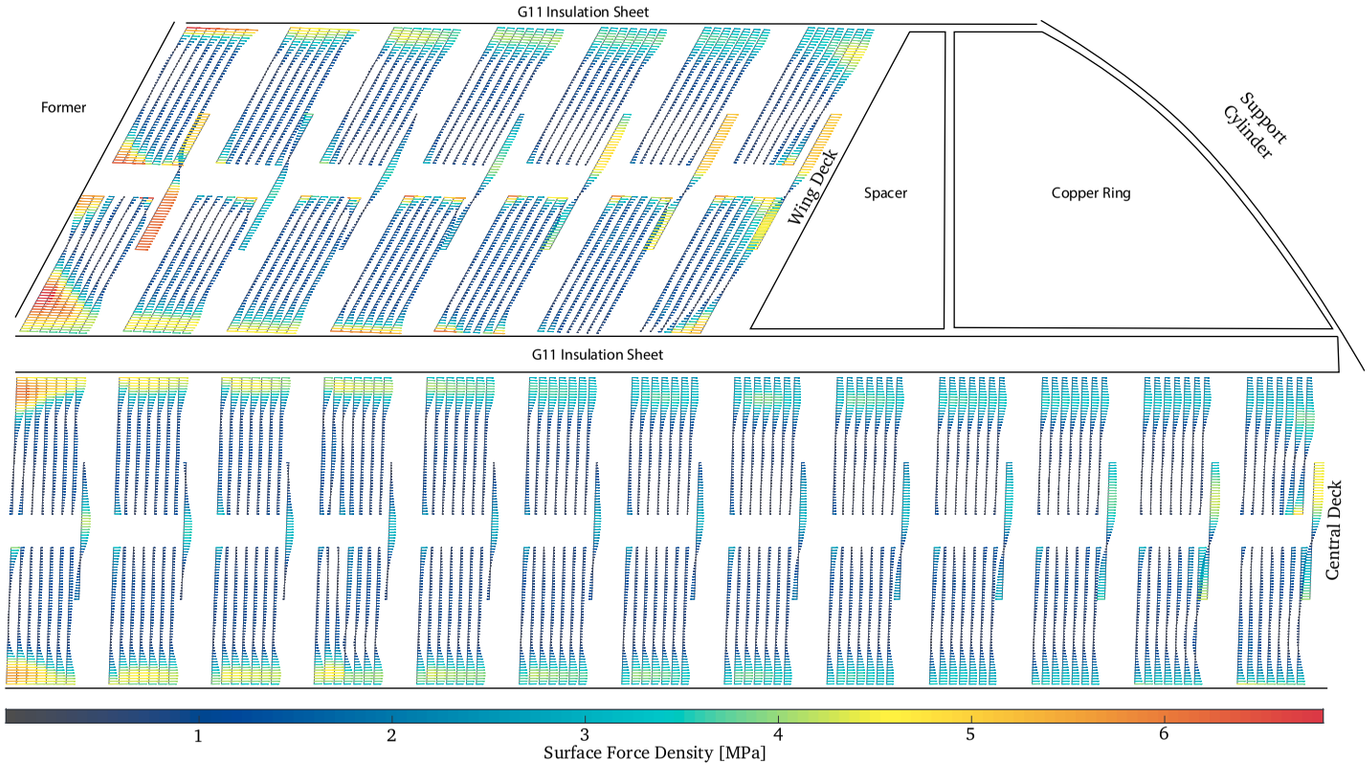


**Figure 4.29.** *Surface force density distribution (pressure) resulting from the current distribution in an aligned block coil pack when operated at* 8 kA *in a background field of* 13 T. *The vectors indicate the direction of the force and the color the magnitude. Note that the geometry is not shown to scale.*

### Concept 4.5.1

To improve the field quality, one or multiple nested shim coils are added inside the aperture. The shim coils are connected in persistent-mode, such that resistance-free current is induced. By topology the current induced in each resistance-free shim coil cancels out only one specific harmonic component of the field, independent of the origin, acting as a filter. This moves the issues concerning field quality, away from the coil pack, such that the main coil-windings can be optimized for current density and efficiency, in essence by maximizing the magnetic field. This principle does not only apply to HTS magnets but also to LTS magnets. The technique may help to solve field quality problems in future accelerators. Tight tolerances and filament size are still required for the compensation coils. Since the shimming coils are not restrained by current density and generally are much smaller than the magnet itself, different manufacturing techniques can be applied making the accuracy needed more easily achievable. However there also drawbacks. The first is that the coils require valuable space inside the aperture. The second drawback is the technical risk of imperfect shim coils since there is the hard requirement that the shim coils have to show perfect persistent-mode operation, which can be challenging.

### Shim Coil Geometry 4.5.2

Since the coils act both as antenna and as compensation, it is very important that each coil is only sensitive to the specific harmonic component they are intended to shield. A heater has to be incorporated either on the joint or the windings to allow the persistent currents to be reset to zero, at a suitable point along the magnetization loop, when the integration error becomes too large. The coils can be constructed using multiple racetracks connected in series, but can also be of a helical type [201], also referred to as Canted ($n$-)Cosine Theta coils, which inherently does not suffer from end effects. The focus here is on the helical type.

The respective shapes for the first three higher order harmonics are presented in Figure 4.30. The center-line defining the shape of the correction coil is described using the equation

$$\vec{x} = \vec{e}_x R_0 \cos(\theta) + \vec{e}_y R_0 \sin(\theta) + \vec{e}_z \left[ \frac{R_0 \sin(n\theta)}{n \tan(\alpha)} + \frac{\omega\theta}{2\pi} \right], \qquad \text{Eq. 4.2}$$

where $R$ is the radius of the coil, $\alpha$ the angle of the wires on the mid-plane (so called skew angle), $2n$ the number of poles ($n$ must be integer), $\theta$ the running parameter between $-n_t\pi/2$ and $n_t\pi/2$, where $n_t$ is the number of turns. The step size of $\theta$ is $2\pi/n_{pt}$ radians, where $n_{pt}$ is the number of elements per turn. The axial shift parameter $\omega$ is calculated as $\omega = (d_r + d_w)/\sin(\alpha)$, where $d_r$ is the spacing between two turns on the mid-plane and $d_w$ the diameter of the wire. The magnetic length is then calculated as $\ell_{\text{mag}} = n_t\omega$. For the second layer the radius is slightly increased, depending on the wire thickness, the running parameter is reversed and the skew angle is negative. The start and end of both layers are located on top of one another. The coils can be rotated around the z-axis by $\pi/2$ rad to create coils sensitive to the respective

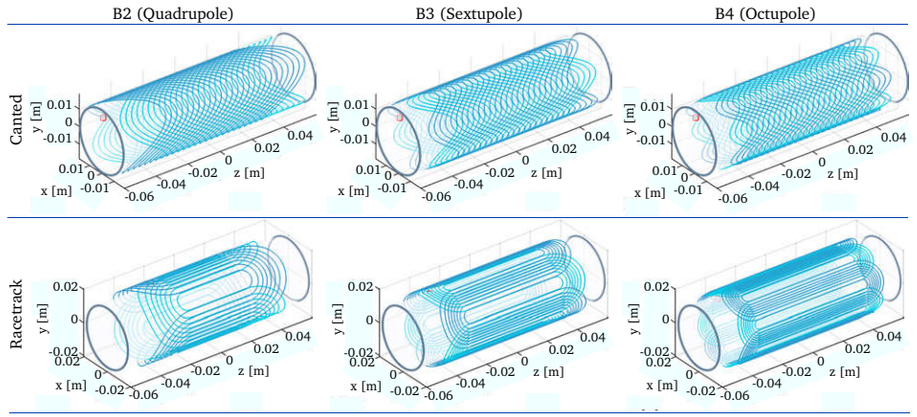


**Figure 4.30.** *Coil shape for each of the first three coil harmonics with both racetrack and canted winding variations. Both variations consist of two separate layers represented by the light and dark blue lines respectively. A semi-transparent white cylinder was added inside the coils for viewing purposes.*

skew harmonics $A_n$. The strength of the harmonic component, $B_n$ in tesla, generated by each layer (1 coil consists of at least 2 layers), at reference radius $r_0$, is calculated analytically using [41]

EQ. 4.3
$$B_n = \left[\frac{r_0}{R_0}\right]^{n-1} \frac{\mu_0 I_0 \cot(\alpha)}{2\omega},$$

where $\mu_0$ is the permeability of vacuum and $I_0$ the induced current in the coil. Using this equation the strength at short sample can be determined by replacing $I_0$ by the critical current $I_c$, calculated at the magnetic field located on the compensation coils (thereby neglecting the self field). However, a margin is needed because at the critical current the resistance is not equal to zero.

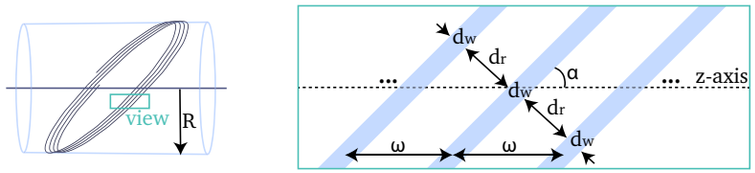


**Figure 4.31.** *Definition of the parameters that define the shape of the helical coils. The part on the right is a view on the mid-plane as indicated on the left.*

### Simple Numerical Evaluation 4.5.3

To evaluate and demonstrate the effectiveness of the shim coils a numerical model was developed. In the study, a non-optimized dipole geometry is used (see Figure 4.32), which has a bad geometric field quality. Inside its aperture various sets of shim coils are inserted. All shim coils in this study have a radius $R_0$ of 25 mm and a skew angle $\alpha$ of 35 deg. The rib thickness $d_r$ is 0.3 mm and the wire diameter $d_w$ is 0.6 mm, which results in axial shift length $\omega$ of 2.13 mm. The current in the shim coils is calculated by approximating the system as a transformer (see Figure 4.33), with the dipole magnet and its power supply in the primary circuit and the shim coil with a persistent joint in the secondary circuit. The change of current in the secondary circuit $I_2$ is then calculated from the change of current in the primary circuit $I_1$ using

$$\frac{dI_2}{dt} = \frac{M_{12}}{L_2}\frac{dI_1}{dt}, \qquad \text{Eq. 4.4}$$

where $M_{12}$ is the mutual inductance between the two circuits and $L_2$ the self-inductance of the secondary circuit. When multiple shim coils of the same order are included into the circuit, it is necessary to take the mutual inductances between these coils into account. Therefore in the model a slightly more complex, but essentially similar matrix equation is solved to find the currents.

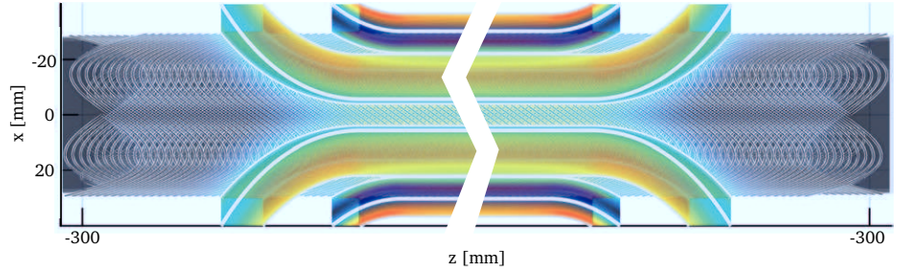


**Figure 4.32.** *A single long sextupole harmonic shim coil inserted inside a non-optimized bad field quality dipole magnet geometry. Note that for the visualization purposes most of the straight section has been removed.*

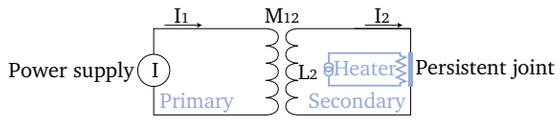


**Figure 4.33.** *The circuit diagram used in the numerical model to calculate the induced current in each of the shim coils.*

The self- and mutual inductances are calculated using a Biot-Savart type of approximation, where all coils are split into many short infinitely thin line elements. All mutual

interactions between all line elements representing the two coils are summed to calculate the mutual inductance. For the self-inductance the same approach is used except for the interaction of each line element with itself. In this specific case the inductance is calculated analytically using Equation 3.44. The accuracy of the inductance calculations is critical in order to find the correct current. Note that in this approach the harmonic content of the magnetic field in the aperture is *not* used to directly set the induced currents. Therefore it is now possible to safely study the effect of the shim coils on the field quality. This is useful to determine the position, length and type of the measurement probe for experimental validation later on.

The length of the shim coil determines its effect on the pseudo coil harmonics along the axis, as shown for the sextupole component in Figure 4.34, although the result is similar for harmonics of different order. Therefore the following cases consisting of one or multiple shim coils with different length are considered:

1. *Single short shim coil* - The shim coil is much shorter than the length of the dipole it is inserted in, only covering part of the straight section. The coil consists of 80 turns, resulting in a magnetic length of 170.4 mm. It is observed that the integrated harmonic, corresponding to the shim, is compensated perfectly over its magnetic length.

2. *Single long shim coil* - The shim coil is longer than the length of the magnet and extends from its ends. The number of turns of the shim is set at 280, resulting in a magnetic length of 596 mm. The magnetic field generated by the dipole is nearly zero beyond its coil-ends. The integrated harmonics are then compensated when integrated over the full length of the magnet, however, local deviations are naturally there.

3. *Multiple short shim coils* - The shim consists of five adjacent shim coils, containing 50 turns each, resulting in an individual magnetic length of 106 mm. The spacing between the coils is chosen such that their magnetic lengths are in contact. The total magnetic length of the shim then becomes 532 mm. Note that in this case, since the shim coils are of the same order, the mutual inductances between them have to be taken into account. Having multiple coils however comes at the cost of multiple persistent joints. It is observed that each shim zeros out the integrated harmonic over its magnetic length, thereby locally improving the field quality.

4. *Distributed shim coil* - The shim consists of two tubes each containing 250 individual persistent loops covering the full length of the magnet. The total of 500 loops are only inductively coupled, but not connected electrically. This case can be interesting when the coils are manufactured by layer deposition (see Section 4.5.6). It is found that despite the coils not being connected, the integrated harmonics still become zero. In addition, with the exception of the coil-ends, the harmonic content is corrected locally. Such a layout still needs further study to be able to reset the currents to zero.

Multiple shim coils of different order (and type) can be nested together to simultaneously filter multiple harmonics from the aperture (see Table 4.2 and Figure 4.35). The

shim coils do not affect one another because the inductance between shims of different harmonics is zero (in essence the system of equations is near orthogonal). The sequence in which the coils are placed has a small effect on the result. In the numerical model the best results are obtained when the lower order coils are nearest to the aperture center. The resulting field quality is very good with deviations of less than a unit. These deviations are likely caused by the numerical in-accuracy of the inductance calculations.

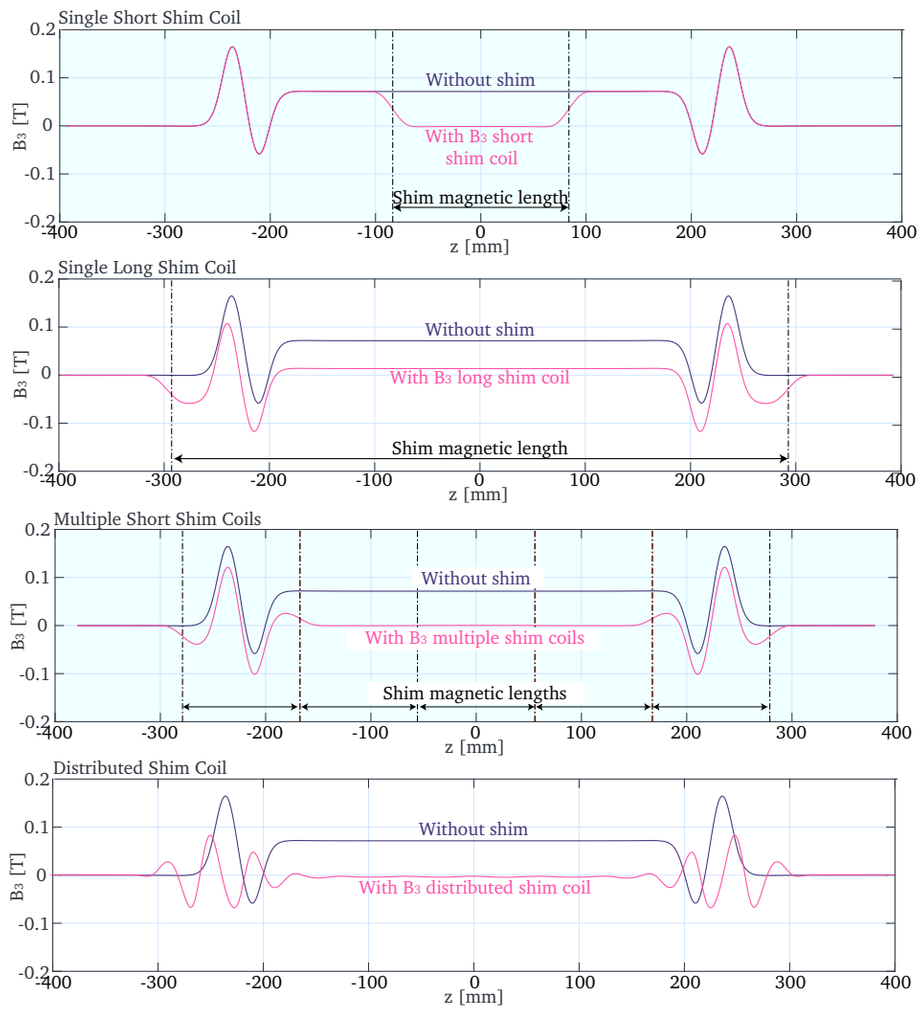


**Figure 4.34.** *Calculated sextupole component at* 18 mm *radius in the aperture as function of the axial position, with and without shim coil, shown for various sextupole shim coil configurations that are described in detail in Section 4.5.3.*

TABLE 4.2.
INTEGRATED HARMONIC CONTENT, AT A RADIUS OF 18 mm, OVER THE FULL LENGTH OF THE COMBINED COIL (SHIM + DIPOLE) FOR VARIOUS CONFIGURATIONS.

| Configuration | none | B3 | B3-B5 | B5-B3 | B3-B7 | B7-B3 | B3-B9 | B9-B3 |
|---|---|---|---|---|---|---|---|---|
| $b_3$ [units] | −419.9 | 0.18 | 0.23 | 0.18 | −0.93 | −0.19 | −0.09 | 0.19 |
| $b_5$ [units] | −24.5 | −24.49 | −0.22 | −0.26 | −0.27 | −0.27 | −0.22 | −0.27 |
| $b_7$ [units] | −29.1 | −29.1 | −29.1 | −29.1 | −0.22 | −0.53 | −0.27 | −0.52 |
| $b_9$ [units] | −42.9 | −42.9 | −42.9 | −42.9 | −42.9 | −42.9 | −0.56 | −1.24 |

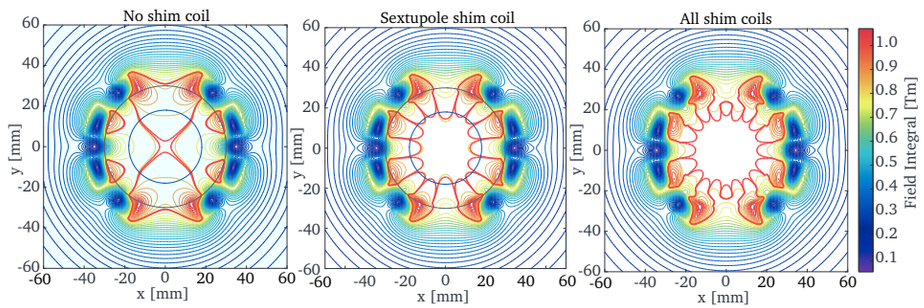


**Figure 4.35.** *Magnetic field integrated in the direction of the z-axis over the magnetic length of the shim coils, for the case where the shim coil is longer than the magnet itself. The integration is performed separately for the x- and y-components, after which the integrated components are used to determine the magnetic field magnitude. The red line encloses the region where the field integral deviates less than* 0.1% *from the field integral on the z-axis.*

### 4.5.4 Quench Analysis

A Quench or a fast ramp-down of the main magnet is not a concern because in this case the current in the shim coils is inductively driven down. However, the shim coils have a stored energy. The single long shim coil with a self-inductance of 0.33 mH and an operating current of 250 A is assumed, with all other parameters the same as given in Section 4.5.3. The copper to superconductor fraction is set to 1, which is a common value for LTS superconductors. The normal zone propagation velocity is calculated analytically using an analytic equation [4]. The energy is dissipated in the wire only, since no quench protection system is present. The resulting temperature evolution and current decay is presented in Figure 4.36. It can be seen that the wire reaches a peak temperature of some 100 K, which is acceptable. For full size long magnets further studies are recommended. Splitting the coils into multiple sections will reduce the stored energy and thus helps reducing the peak temperature. It is likely that after a quench the shim coil needs to be reset with the build-in heater, since incorrect persistent currents of the main magnet may be frozen in when the shim coil is cooled down.

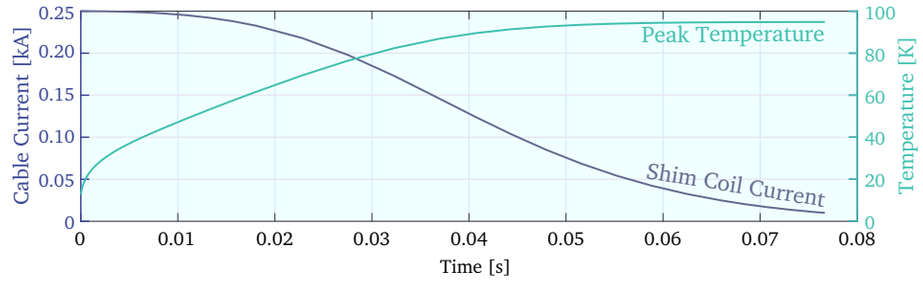


**Figure 4.36.** *Adiabatic quench analysis of a* 0.8 m *long sextupole shim coil operating at* 250 A *showing current decay and temperture rise, without quench protection system.*

## Sensitivity Analysis 4.5.5

The effect of errors in the harmonics of the shim coil will have an effect on the harmonics when the main coil is combined with the shim coil. Different types of errors can be considered (see Figure 4.37). The errors are applied to the coil using a random number generator with different seeds, after which a statistical analysis can be performed on the resulting harmonics. This method is known as Monte Carlo. The errors are applied at 30 nodes per turn. The other deviations of the coil position are interpolated from these nodes using a cubic spline. As an example the windings of a sextupole coil with an over-exaggerated error in the parallel direction is shown in Figure 4.38. The calculated standard deviations on the shim's harmonics are presented in Table 4.3. To relate the effect of these errors for the entire coil system, the study is repeated for the shim coils combined with the main magnet. The results are presented in Table 4.4. The standard deviation of the respective harmonic of the shim coil is clearly the dominant term. This, because the current induced or the stored energy of the shim, is partially used to generate other harmonics. This means that the shim coil is no longer able to fully compensate out the harmonic it is sensitive to. For random errors applied in the n-direction the results are similar to the p-direction. A misalignment in the xy-plane gives minor errors on $b_2$ and $a_2$, this because the shim is no longer co-axial with the axis on which the harmonics are calculated. A rotational error in the $\theta$-direction generates the respective skew harmonic. The $\alpha$ error unbalances the solenoidal contribution between layers, which is not visible in the pseudo harmonics. Therefore part of the induced current in the shim is used for the solenoid, resulting in non-full compensation. This then results in a error in the respective harmonic.

## CAD Models, Prototyping and Manufacturing 4.5.6

One of the challenges is the manufacturing of these persistent coils. Since the space in the aperture is scarce, the nested coils have to be as thin as possible. For a first demonstrator a Nb-Ti wire will be inserted in a slot in a cylinder, also referred to as former (see Figure 4.40). This slot can either be machined into a tube using a three-axis milling machine or the tube including the slot can be printed directly using rapid prototyping.

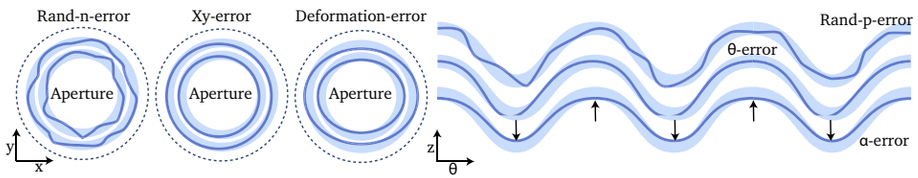


**Figure 4.37.** *Different types of errors on the wire position in a CCT type correction coil. On the left the view is along the z-axis. On the right the view is normal to the surface of the support cylinder looking directly at the slots.*

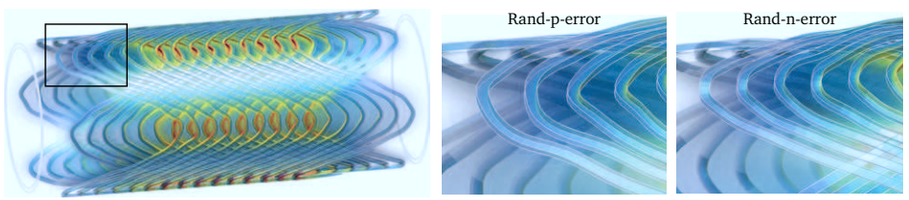


**Figure 4.38.** *Over-exaggerated random positional errors added to the geometry of a sextupole shim coil in the direction parallel to the surface of the support cylinder (left) and face-normal to the surface of the support cylinder (right). Visible are in inner cylinder and the wires making up the coils (colored in the magnitude of the magnetic field).*

TABLE 4.3.

SENSITIVITY OF THE INTEGRATED HARMONIC CONTENT OF THE SHIM COILS THEMSELVES TO RANDOM NOISE IN THE P-DIRECTION. HARMONICS ARE GIVEN WITH RESPECT TO THE MAIN COMPONENT OF THE RESPECTIVE COIL.

| Coil description | | Standard deviation $\sigma$ of the integrated harmonics in units | | | | | | | | | | | | | |
|---|---|---|---|---|---|---|---|---|---|---|---|---|---|---|---|
| Coil | Error | $b_1$ | $b_2$ | $b_3$ | $b_4$ | $b_5$ | $b_6$ | $b_7$ | $a_1$ | $a_2$ | $a_3$ | $a_4$ | $a_5$ | $a_6$ | $a_7$ |
| $B_3$ | 50 $\mu$ rand-p | 0.45 | 0.51 | 0.00 | 0.40 | 0.33 | 0.23 | 0.17 | 0.42 | 0.53 | 0.55 | 0.41 | 0.32 | 0.24 | 0.19 |
| $B_5$ | 50 $\mu$ rand-p | 1.17 | 1.35 | 1.30 | 1.03 | 0.00 | 0.59 | 0.43 | 1.07 | 1.36 | 1.24 | 1.08 | 0.93 | 0.62 | 0.47 |
| $B_7$ | 50 $\mu$ rand-p | 2.89 | 3.48 | 3.40 | 2.65 | 2.21 | 1.50 | 0.00 | 2.71 | 3.52 | 3.20 | 2.81 | 2.14 | 1.58 | 1.36 |

In order to create a proper program for these machines a CAD input model is required. For the milling machine this complicated intermediate step can possibly be bypassed by inputting Equation 4.2, or a polar coordinate version of it, directly into the machine. To make the CAD model for a Canted Cosine Theta magnet two different methods were developed:

1. *Import of xyz points* - The xyz-coordinates representing the lines on the four edges of the cable are imported through a comma separated value file. After the points are imported each cable edge is fitted using a spline, resulting in a smooth curve. Then by performing a *loft* operation the geometry of the cable is created. The advantage of this method is that it is not limited to the Canted Cosine Theta and works equally well for any cable geometry. However, in CATIA [202] the

importing of the points is performed using a visual basic interface implemented in excel, which proved to be very slow, resulting in computing time of many hours, when importing the necessary 40 k points. A better implementation is found in SolidWorks [203], which imports the points and sets up the geometry in a few seconds.

2. *Through analytic equation* - The curve representing the position of the cable given by Equation 4.2 is directly imported in CATIA, which then draws the line. Using the line and the condition that the slot is perpendicular to the surface of the cylinder the geometry of the former is then generated. The advantage is that the parametrization of the curve remains intact, making it easy to change the geometry and even number of poles of the coils on the fly. This type of solution is not available in SolidWorks. In difficult cases the equation can be generated by fitting a Fourier series or a polynomial.

In the CAD model it is necessary to set a manufacturing tolerance to be able to fit the cable in the slot. Therefore in most cases the geometry of the cable is produced twice. Once as the cable itself and once as a cutout surface (see Figure 4.39). To simplify the winding and to improve the accuracy, the second layer can be wound on top of the first layer by using different depths for the slots in the same cylinder (see Figure 4.40). For achieving higher magnetic field a $Nb_3Sn$ wire can be used, with the additional requirement that the cylinder and insulation can withstand the necessary reaction temperatures.

The design and manufacture of a first set of shim coils will allow for demonstration of the technology. However the resulting cylinders are relatively thick, taking up valuable space in the aperture. For a real application one can consider vapor deposition of $Nb_3Sn$ on a cylinder, as is currently under development for superconducting accelerator cavities [204]. After depositing the $Nb_3Sn$ layer the lanes can be either machined or cut using a laser. Another more advanced possibility is vapor deposition of ReBCO

TABLE 4.4.
SENSITIVITY OF THE INTEGRATED HARMONIC CONTENT OF THE SHIM COMBINED WITH THE MAIN DIPOLE. VALUES OF INTEREST ARE DENOTED IN MAGENTA.

| Coil description | | Standard deviation $\sigma$ of the integrated harmonics in units | | | | | | | | | | | | | |
|---|---|---|---|---|---|---|---|---|---|---|---|---|---|---|---|
| Coil | Error | $b_1$ | $b_2$ | $b_3$ | $b_4$ | $b_5$ | $b_6$ | $b_7$ | $a_1$ | $a_2$ | $a_3$ | $a_4$ | $a_5$ | $a_6$ | $a_7$ |
| $B_3$ | 50 $\mu$ rand-p | 0.00 | 0.02 | 0.20 | 0.01 | 0.01 | 0.01 | 0.00 | 0.01 | 0.01 | 0.02 | 0.01 | 0.01 | 0.01 | 0.01 |
| $B_5$ | 50 $\mu$ rand-p | 0.00 | 0.00 | 0.00 | 0.00 | 0.13 | 0.00 | 0.00 | 0.00 | 0.00 | 0.00 | 0.00 | 0.00 | 0.00 | 0.00 |
| $B_7$ | 50 $\mu$ rand-p | 0.00 | 0.01 | 0.01 | 0.01 | 0.00 | 0.00 | 0.06 | 0.01 | 0.01 | 0.01 | 0.01 | 0.00 | 0.00 | 0.00 |
| $B_3$ | 50 $\mu$ rand-n | 0.00 | 0.01 | 0.12 | 0.01 | 0.01 | 0.01 | 0.00 | 0.01 | 0.01 | 0.01 | 0.01 | 0.01 | 0.00 | 0.00 |
| $B_3$ | 50 $\mu$ $x$ | 0.00 | 0.70 | 0.13 | 0.00 | 0.00 | 0.00 | 0.00 | 0.00 | 0.00 | 0.00 | 0.00 | 0.00 | 0.00 | 0.00 |
| $B_3$ | 50 $\mu$ $y$ | 0.00 | 0.00 | 0.00 | 0.00 | 0.00 | 0.00 | 0.00 | 0.00 | 0.72 | 0.00 | 0.00 | 0.00 | 0.00 | 0.00 |
| $B_3$ | 50 $\mu$ $xy$ | 0.00 | 0.73 | 0.13 | 0.00 | 0.00 | 0.00 | 0.00 | 0.00 | 0.69 | 0.00 | 0.00 | 0.00 | 0.00 | 0.00 |
| $B_3$ | 0.5 deg $\theta$ | 0.00 | 0.00 | 0.05 | 0.00 | 0.00 | 0.00 | 0.00 | 0.00 | 0.00 | 4.21 | 0.00 | 0.00 | 0.00 | 0.00 |
| $B_3$ | 0.5 deg $\alpha$ | 0.00 | 0.00 | 0.43 | 0.00 | 0.00 | 0.00 | 0.00 | 0.00 | 0.00 | 0.00 | 0.00 | 0.00 | 0.00 | 0.00 |

on a cylinder, which allows for use in even higher magnetic fields. For the latter two techniques, it is important that the lane widths are small, such that magnetization currents do not affect the field quality negatively. Possibly the lanes can be striated. To avoid manufacturing of a persistent joint between the two layers the coils can consist of continuous single turns, like the distributed shim coil case described in Section 4.5.3. The inductive coupling ensures correct cancellation of the solenoidal field between both layers.

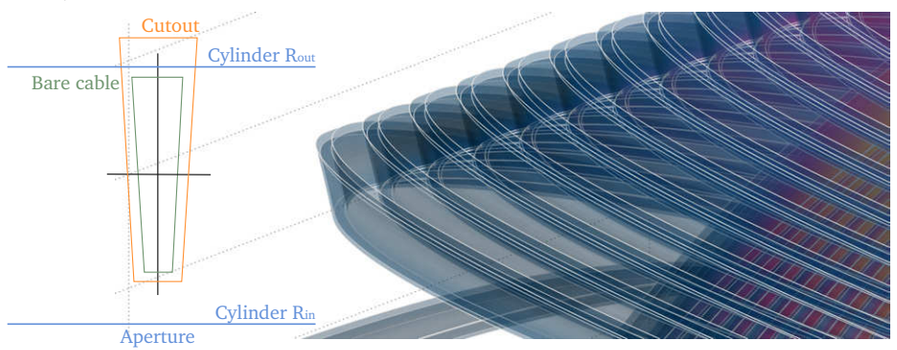


**Figure 4.39.** *Close up of the conductor layout of the MiniWhale, a CCT demonstration coil developed at CERN [205]. It can be seen that outside of the bare cable there is the cutout surface taking into account the insulation and extra spacing required for the 3D printing. This cutout can be subtracted in a CAD programme from a cylinder to create the basic shape of the former.*

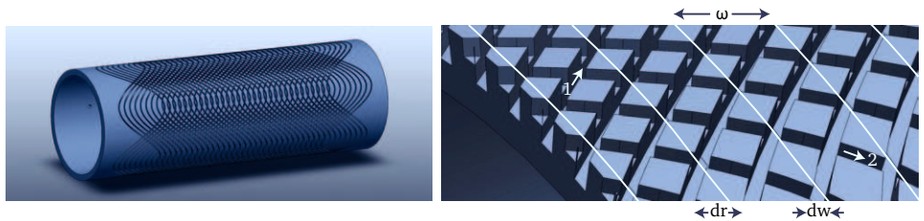


**Figure 4.40.** *CAD drawing showing the geometry of the support cylinder for a sextupole shim coil demonstrator. In this configuration the two layers, making up the shim coil, are wound onto the same former.*

## 4.6 Conclusion

The effect of magnetization in cables and coils was studied using the electro-magnetic part of the Network Model, introduced in Chapter 3. To ensure that the physics was implemented correctly in the model, a series of benchmark tests were performed. The screening currents and thus the flux lines penetrate the tapes from the edges, as predicted by Bean's Critical State Model. The fact that the model captures this correctly

is somewhat remarkable, because the pinning of these flux lines, and thus hysteresis, is implemented in the model simply by using a non-linear critical current density and by taking into account the self- and mutual inductances between all elements.

The calculated area of the hysteresis loop, representing the dissipated energy per cycle, corresponds almost exactly with the integrated resistive power dissipation of all elements. Because these two methods of calculating AC losses are fundamentally different, it is another indication that the electro-magnetic predictions of the model are realistic.

Next the relation between the convergence and the number of elements was checked. It was shown that when the magnetic field amplitudes are low, flux only penetrates at the very edges of the sample. In order to acquire accurate losses it is necessary to have a very high number of elements in order to have a sufficiently fine network in these areas. Since the number of elements is limited by the amount of available memory and computing power, this means that for very low hysteresis loss the model is not sufficiently accurate. Also it is observed that when multiple tapes are combined in a cable, the tapes collaboratively shield the magnetic flux from the conductor pack. This means that the penetration field of a cable, and even more so for that of a coil, is different from that of a single tape. This effect is nicely visible in the Roebel cable by the fact that the strands that cross-over show full penetration at around 0.3 T. The two tape stacks making up the sides of the cable, on the other hand, are fully penetrated only at around 2.0 T. This implies that at lower applied magnetic field amplitudes the majority of the losses are located at the cross-overs.

In order to validate the electro-magnetic part of the model further an effort was initiated to measure magnetization losses in the SP-1 Roebel cable. Initial calculations showed that when a time-varying magnetic field is applied perpendicular with respect to the tape surface, hysteresis loss is dominant. When the time-varying magnetic field is applied in the parallel direction, coupling loss becomes more apparent. The AC losses were measured at the University of Twente using both a very sensitive inductive method and a more direct calorimetric method. Because analysis of the inductive measurement necessitates to assumptions on the position of the current flow inside the sample, it is not possible to determine the absolute losses directly. Therefore the inductive measurement is calibrated using the calorimetric measurement.

For the hysteresis very good agreement is found between the model and theory. For the coupling loss comparison is more difficult because the losses are on the order of microjoule per cycle, which is far below the accuracy of the calorimetric method. Therefore only qualitative agreement can be concluded in terms of scaling with magnetic field. This implies that the value of contact resistance between tapes, responsible for coupling loss, could not be verified. For the frequency scaling in the parallel measurement some discrepancy was found, possibly caused due to an alignment issue. In summary, it is concluded that the electrical part of the model seems to be working correctly.

To study the effect of the magnetization inside coil-windings on the magnet's field quality, multiple cables were inserted into the same model, representing a slice of the straight section of the coil. To reduce the complexity of the model, only a quadrant of

the coil is included in the model, which is then mirrored to the other quadrants and repeated longitudinally to include the magnetic field contribution by these parts. The Feather-M2 Aligned Block coil layout presented in Chapter 2 and, for comparison, the CEA Saclay Cosine Theta layout were studied in both stand-alone mode and as insert in a uniform background field. Since the magnetic field contribution of the iron poles and yokes were not included in the model, the results only provide a qualitative comparison between the different layouts.

When operated in stand-alone mode, the Aligned Block coil loses alignment (mainly in the upper deck), locally resulting in screening currents. These currents can easily generate 100 units of dynamic variation in the relevant harmonic components. In terms of dynamic field quality, the single layer cosine theta performs better in stand-alone mode due to its symmetry and due to the fact that only transport currents are seen at the edges of the cable, resulting in only a few units of variation.

When operated as an insert coil in a background field, however, the roles are reversed. The Aligned Block shows only small magnetization currents, resulting in only a few units of dynamic variation. However, in this case, the flux has not fully penetrated the coil pack and thus the transport currents may drift around, making it still necessary to compensate for these effects. The Cosine Theta in the background field magnetizes strongly, due to the perpendicular alignment of the conductor near the mid-plane with respect to the background field, resulting in 60 units of dynamic variation, which is lower than expected due to radial orientation of the tapes. These results are also reflected in the predicted power dissipation due to hysteresis loss, which could exceed the prohibitively high value of 20 W/(mcoil) in the Cosine Theta when operated a co-ramping background field. Because of the inhomogeneous distribution of the currents in the coil pack, the forces are also distributed inhomogeneously and therefore further study is required.

The field quality study has demonstrated that it is necessary to find a method to compensate for these dynamic effects. Due to the wide ReBCO layer in the tape, and anisotropic nature of the tapes it can not be guaranteed that the dynamic effects are fully predictable. Therefore, a novel method, based on using passive persistent-mode shim coils was proposed. These additional thin coils are inserted in the aperture, where they may simultaneously act as pick-up and correction coils. By topology the persistent currents induced in the shim coils, each cancel out a specific harmonic, thereby acting as a harmonic filter. This allows for correcting the field errors independent of their origin or nature.

A first-order numerical evaluation, in which the self- and mutual inductances are used to calculate the current in the shim coils, confirmed that the concept can work. This new technology is not necessarily limited to only high temperature superconducting magnets and but may also provide a solution for $Nb_3Sn$-based accelerator magnets, in which the filament size is a limiting factor to the critical current density as well. Further preliminary analysis of quench and sensitivity to manufacturing tolerances have not unveiled any possible show-stoppers.

# Thermal Drift and Runaway in ReBCO Cables

5

"Things are only impossible until they're not!"

Jean-Luc Picard, Star Trek: TNG, S01E17, 1988

*The Electro-Magnetic and Thermal Network Model described in Chapter 3 is employed to study thermal runaway in ReBCO type coated conductor cables and coils. Included are possible methods for timely detection of normal zone propagation.*

## Introduction and Chapter Layout

5.1

The engineering current density of ReBCO tapes at present is rapidly increasing, almost doubling every two years. Mechanisms for increasing the engineering current density are: adding Zirconium doping to the ReBCO layer to create artificial pinning centers only improves the perpendicularly applied in-field performance, increasing the ReBCO layer thickness, improving the quality of the ReBCO itself, decreasing the copper layer thickness and reducing the substrate thickness. Using Zirconium doping in the ReBCO layer [37, 206], it has already been proven on short lengths that very high levels of current densities exceeding $4\,\mathrm{kA/mm^2}$ in perpendicular applied field of $20\,\mathrm{T}$ at $4.5\,\mathrm{K}$ are possible. When such current densities become available in longer lengths of tape, a conductor efficient, low cross-sectional area, very high-field magnet becomes a possibility. The Aligned Block magnet described in Chapter 2 already prospects into this future by alignment of the ReBCO tapes with the magnetic field, to optimally use the critical current density. However, when such a coil quenches, the high current density causes the conductor temperature to rise rapidly, leaving barely time for activating the protection systems.

Due to the higher critical temperature as well as the increased heat capacity at elevated temperatures, the energy needed to initiate a propagating normal zone is three orders of magnitude larger than in an LTS conductor. This implies that such magnets are not likely to quench when operated at a safe margin with respect to the critical surface. Quench initiation mechanisms present in LTS such as conductor motion (see Section 2.5.1) or flux jumping are not probable causes for a quench in an HTS magnet, even when operating at $4.5\,\mathrm{K}$ and $20\,\mathrm{T}$ (also refer to Figure 5.1). It is therefore not likely that HTS magnets exhibit classical training behavior, making it unnecessary to purposely quench the magnet by ramping it over its critical current.

When a local defect is present or when the magnet suddenly degrades due to mechanical stress (fatigue effects in ReBCO coated conductors require further study) accidental operation over the critical current can occur. These mechanisms, however, are caused by manufacturing or design errors, and shall not be present in a fully developed future

accelerator magnet. Magnetization loss, mainly consisting of hysteresis, can cause significant heating in the coil (see Section 4.4.3). It was shown though, that these losses can be reduced significantly by designing the magnet such that the tapes in the coil-windings are aligned with the magnetic field lines. In addition, the global and relatively slow nature of the magnetization loss causes the entire coil to heat up relatively slowly, making it possible to early detect temperature increase using temperature sensors, long before the current sharing temperature is reached. This is likely also true for normal levels of beam loss (in accelerators) and cryogenic failure scenarios.

At present the cause of a possible quench in an HTS coil, when operated at safe margin, is not known and can only be found through real magnet tests. To be able to study quench initialization it is decided to characterize losses by the time frame over which the heating occurs, slow and fast, and the locality of the heat deposition, either local or global. This spectrum is illustrated in Figure 5.1. Because of heat diffusion and energy requirements, all disruption scenarios form a diagonal band in this graph. Since slow and global losses are easier to detect, due to the large volume hit, the focus here is mainly on fast and local losses with durations of about 50 ms, affecting only one or a few tapes in the cable.

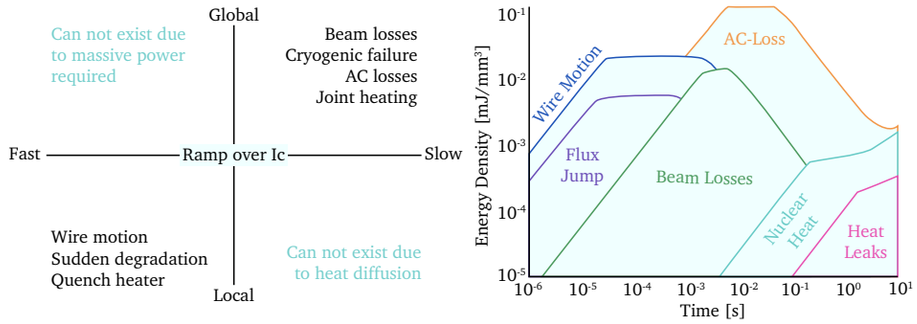


**Figure 5.1.** *Sources of disturbing heat generation in a ReBCO conductor or coil at* 4.5 K *and high field (left) and the conceptual categorization into the size of the volume hit and the time frame over which the heating occurs (right, adapted from [4, 207]).*

For LTS conductor it is shown in literature that the interaction between adjacent strands in a Rutherford cable plays an important role in the initialization transients of a quench. When a normal zone develops in a strand the current in the strand redistributes to neighboring strands, until the heat is transferred, eventually causing them to quench as well, leading to an avalanche [94]. Because the time scale on which this happens is very short, this effect is usually omitted from quench analysis simulations, in which the conductor is commonly modeled using a uniform current density throughout the cable. However, because of the significant thermal margin in HTS, the heat needed to initiate a normal zone in the neighboring tapes is much higher. It was thus expected that the initialization of a propagating normal zone is a relatively slow process. If these initialization transients, in essence being current redistributions, can be detected, they

can provide an early warning, allowing more time for the quench protection to switch off the magnet even at high current density.

Thermal disruptions and stability of ReBCO cables and coils are studied in more detail using the Electro-Magnetic and Thermal Network Model described in Chapter 3. To ascertain the correctness of the thermal part of the model first a benchmarking step is described in Section 5.2. The model is used to predict the quench initialization transients in a single tape and a short Roebel cable section, when part of the Feather-M2 inductive load. The normal zone propagation velocities and minimum quench energies are then compared to a previously validated one-dimensional model [123, 92].

After validation the model is employed for predicting quenches in the full Feather-M0 and Feather-M2 coil geometries taking into account the current redistribution along the entire cable/coil, as described in Section 5.3. The stability of the coil in terms of Minimum Quench Energy (MQE) as function of operating current is evaluated and possible detection of the current redistribution using pick-up coils is explored.

## Normal Zone Propagation in Coated Conductors 5.2

*The thermal part of the Electro-Magnetic and Thermal Network Model is benchmarked by comparing its predictions on a single tape and a multi-strand cable to a previously validated one-dimensional finite difference model.*

### Normal Zone Propagation in a Single Tape 5.2.1

First, normal zone propagation in single tape is considered. The temperature evolution of the tape can be computed using three different models:

1. *Nodal Model* - The Nodal model is based on Matlab's built-in *ode15s* solver and was previously validated in [123, 92]. The tape is approximated using a string of temperature nodes connected with heat conducting elements. The current is assumed equal throughout the tape and no electrical equations are solved. The nodal model was previously used for the Feather-M2 quench analysis and is described in Section 2.4.1.

2. *Network Model 1D* - Or by using the Electro-Magnetic and Thermal Network Model based on the Sundials IDA solver. Again the tape is approximated as a string of temperature nodes connected with elements. In this case the currents in the elements are needlessly included in the calculation, since all elements have the same current, because they are connected in series.

3. *Network Model 2D* - In addition to the one-dimensional case, the network model can also model the two-dimensional flat surface of the tape, allowing the current to redistribute across its width. In this case the geometry is set up by using the stacked cable geometry consisting of only a single tape and no twist.

The two solvers are inherently different as the first uses stabilized forward integration while the second uses backward integration.

With the three models a 5.5 mm wide and 100 $\mu$m thick SuperPower tape is simulated at 4.5 K in a background field of 17 T applied under an angle of 86 deg with respect to the tape surface, resembling the conditions in the Feather-M2 magnet. The critical current is calculated using the scaling relation described in Appendix A. The engineering current density is scaled to 600 A/mm$^2$ in a 20 T perpendicularly applied magnetic field at 4.5 K and 5 kA/mm$^2$ in a 20 T parallel applied magnetic field also at 4.5 K. The operating current is kept constant and no protection is assumed. The same material properties, including magneto resistance of the copper, are used in all three models. In the two-dimensional model the heat pulse is chosen to deposit on the tape's edge (see Figure 5.2). It is observed that the current quickly redistributes to the other side of the tape, when a homogeneous current density is assumed as initial condition. The increased current density at this location causes the normal zone and thus the current to quickly spread, within about 10 ms, over the width of the tape, practically resulting in the same current and temperature distributions as in the one-dimensional case.

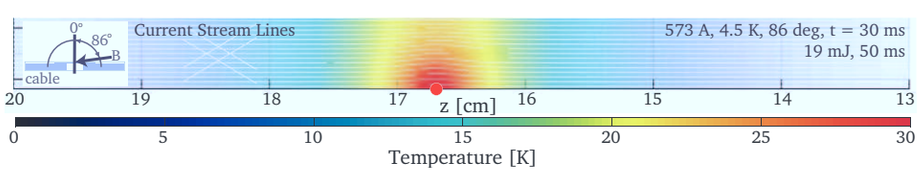


**Figure 5.2.** *Calculated temperatures around a normal zone in a single tape. The origin of the quench is located at the edge of the tape. The current redistributes in a few milliseconds to the other side of the tape.*

The normal zone propagation velocities are calculated in all models from the time derivative of the length of conductor that exceeds the transition temperature $T_t = (T_c + T_{cs})/2$. The velocity is divided by 2, since there are two fronts. The MQE is found in all models by applying the search algorithm described in Section 2.4.2. The resulting normal zone propagation velocities and minimum quench energies are presented at various tape currents in Table 5.1. It shows that the calculated propagation velocities and minimum quench energies are very similar between the different models, with some deviation at lower current. This observation provides confidence that the implementation of the heat equation in the Electro-Magnetic and Thermal Network Model was correctly performed.

### 5.2.2 Normal Zone Propagation in a Roebel Cable

Next the SP-1 Roebel cable geometry is considered (see Table 2.1). Simulating propagation in the entire Feather-M2 magnet is too calculation intensive and some simplification (see Section 5.3) is needed. The model is constraint to run a cable section consisting of a single twist pitch comprising 15 unit cells and 226 mm length. The

TABLE 5.1.
CALCULATED NORMAL ZONE PROPAGATION VELOCITIES AND MINIMUM QUENCH ENERGIES IN A SINGLE SUPERPOWER TAPE. COMPARISON OF THE ONE-DIMENSIONAL NODAL MODEL (NODAL) WITH THE ONE AND TWO-DIMENSIONAL ELECTRO-MAGNETIC AND THERMAL NETWORK MODEL (NM).

| Current [A] | Velocity [mm/s] | | | Minimal Quench Energy [mJ] | | |
|---|---|---|---|---|---|---|
| | Nodal | NM 1D | NM 2D | Nodal | NM 1D | NM 2D |
| 50 | 14.3 | 21.4 | 22.1 | 234 | 278 | 247 |
| 150 | 76 | 76.9 | 78.0 | 84.9 | 97.5 | 92.8 |
| 250 | 140 | 144 | 145 | 57.1 | 64.0 | 59.7 |
| 400 | 259 | 277 | 278 | 32.1 | 35.0 | 33.6 |
| 600 | 500 | 547 | 552 | 16.8 | 18.0 | 17.3 |
| 1000 | 1500 | 1660 | 1710 | 7.2 | 7.2 | 7.3 |

Tape conditions are: 5.5 mm width, 50 $\mu$m Hastelloy substrate, 40 $\mu$m Cu sheeting, 2 $\mu$m Ag layer, 17 T applied magnetic field, 86 deg magnetic field angle, 4.5 K operating temperature.

same input settings are used as for the single tape (Section 5.2.1). The electrical and thermal contact resistances between the tapes are set at the default 0.2888 $\mu\Omega m^2$ and 100 $W/(m^2K)$, respectively. The cable current is set at a constant 8.0 kA and the current density is initially uniform. This initial condition provides an easy valid solution for the solver.

To model the remainder of the Feather-M2 coil, the strands are connected at their ends to a single node through a network of elements that are mutually coupled using an inductance matrix (see Figure 3.13). The values contained in this tape-to-tape inductance matrix, are presented for Feather-M0 and Feather-M2 in Appendix C. They are are obtained from the full coil geometry of the three-dimensional models that are also used for the critical current calculations described in Section 2.3.6. The self-inductances of the tapes, located on the diagonal of the matrix, are 11.1 $\mu$H and 463 $\mu$H for Feather-M0 and Feather-M2, respectively and correspond to the self-inductance of the coil wound with a 0.8 mm thick cable presented in Table 2.7.

It is assumed here that the modeled cable section and thus the normal zone is located somewhere in the middle of the magnet on one of the poles in the case of Feather-M2, leaving maximum distance between the joints and the position of the expanding normal zone. For Feather-M2 it is also assumed that the current can redistribute in the joints connecting the two poles. Therefore, as an approximation, because it includes the mutual inductance between the poles, the inductance values in the matrix are divided by two.

The normal zone is initiated using a heat pulse that is deposited on a single node located at the corner of the cross-over along the edge of one of the tapes (labeled number 9 out of 15, see Figure 5.3). This area is known to exhibit the highest stresses when the cable is under longitudinal tension [208] and is thus a likely weak spot of the cable. The heat pulse is characterized by its duration, usually 50 ms, unless stated otherwise, and the energy it contains. Alternatively the normal zone can also be initiated using

sudden degradation across one of the tapes in the cable. In this case the defect only results in a normal zone in the entire cable section, when the cable is operated in the so-called single strand regime (see Section 5.2.3). In this regime similar results are found as for the more versatile heat pulse case, which is pursued further.

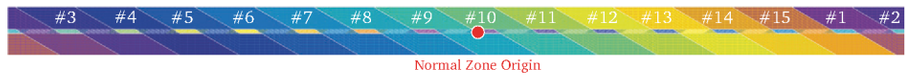


**Figure 5.3.** *Numbering and color coding of the tapes in the Roebel cable model. A hot spot is introduced at the position of the red dot.*

The calculated temperature and current distributions are shown at various time steps in Figures 5.4 and 5.5. The current redistributes from the heated tape (number 9) to its two neighboring tapes (numbers 8 and 10). When the majority of the current is transferred, the normal zone stops propagating after which the heat seeps to the neighboring tapes causing them to quench. In literature this type of propagation is referred to as Adjacent Propagation, as opposed to Cross Propagation [94], which is impossible in Roebel cables due to the separation of the stacks by the central channel.

Because the normal zone started on the surface of the cable, heat transfer to tape 10 is slower than to tape 8, causing the normal zone to propagate anti-symmetrically. Interesting is that the tapes located at the other side of the cable, number 1 and 2, initially decrease in current while no normal zone is present in them. This is likely an inductive effect, where the coupling with tapes 8 and 10 is higher than the coupling with tape 9. In addition these tapes are located furthest away from the quenching tape and thus receive the lowest current from the redistribution. The current distribution inside the tapes is, similar to the two-dimensional single tape model, almost homogeneous. The sequence in which the tapes quench is independent of current, in contrast to the time-scale, which does depend on the current.

The initialization transients of the normal zone can be studied in further detail in Figure 5.6, which shows the currents in the tapes located at the hot-spot $z = 11\,\mathrm{cm}$ and their respective derivatives as function of time. The red arrows indicate the three time steps shown in Figures 5.4 and 5.5. The figure also presents as function of time the peak temperature in each tape, the voltage drop over the coil, including additional inductance elements at the cable ends, the power dissipation in the contact elements and the power dissipation in all elements. Three phases can be distinguished:

1. *Thermal Drift* - The local temperature slowly increases, drifts away from the operating temperature due to an external heat source (heater, joint, magnetization, etc.). The current sharing temperature is not yet exceeded anywhere, no current redistribution occurs and no voltages are present. This phase can, depending on the heat source, last for many seconds or even minutes. Thermal Drift can occur in both single and multi-tape conductors.

2. *Pre-Quench* - The local temperature exceeds the current sharing temperature in one of the tapes and part of the electrical current is transferred to the matrix.

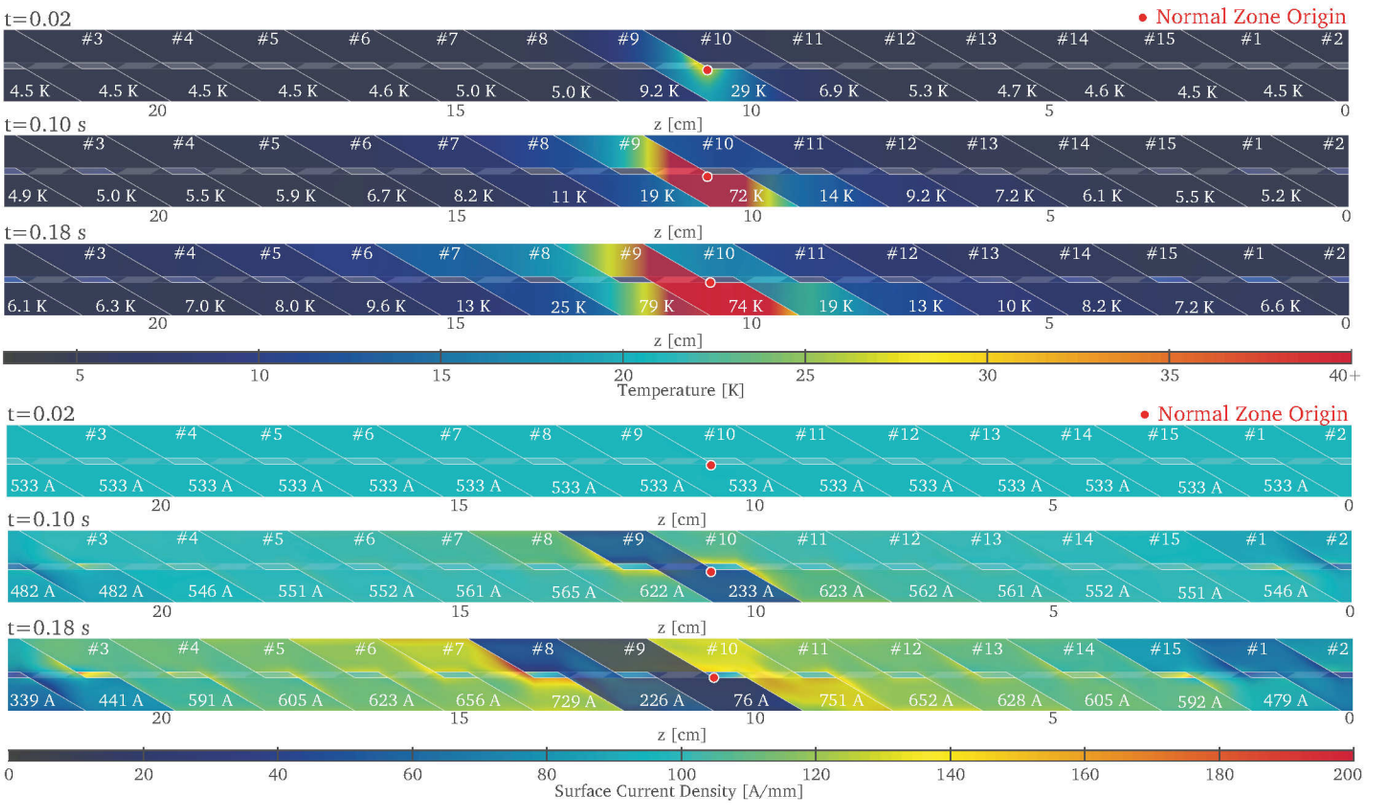


**Figure 5.4.** *Temperature (top three plots) and surface current density (bottom three plots) represented on the surface of the strands at* 0.02, 0.10 *and* 0.18 s, *respectively, calculated for a normal zone propagating in a Roebel cable in an applied magnetic field of* 17 T, *under an applied angle of* 86 deg *at* 4.5 K *and current of* 8.0 kA. *The normal zone is initiated using a heat pulse of* 100 mJ *injected over a duration of* 200 ms *starting at* 0 s. *At the end of each strand a self- and mutual inductive element (see Section 3.3.9) representing the inductance matrix of one of the Feather-M2 poles is used. The inductance matrix is given in Appendix C (divided by two in order to represent only one of the poles). More details on the transient development of the normal zone is provided in Figure 5.6.*

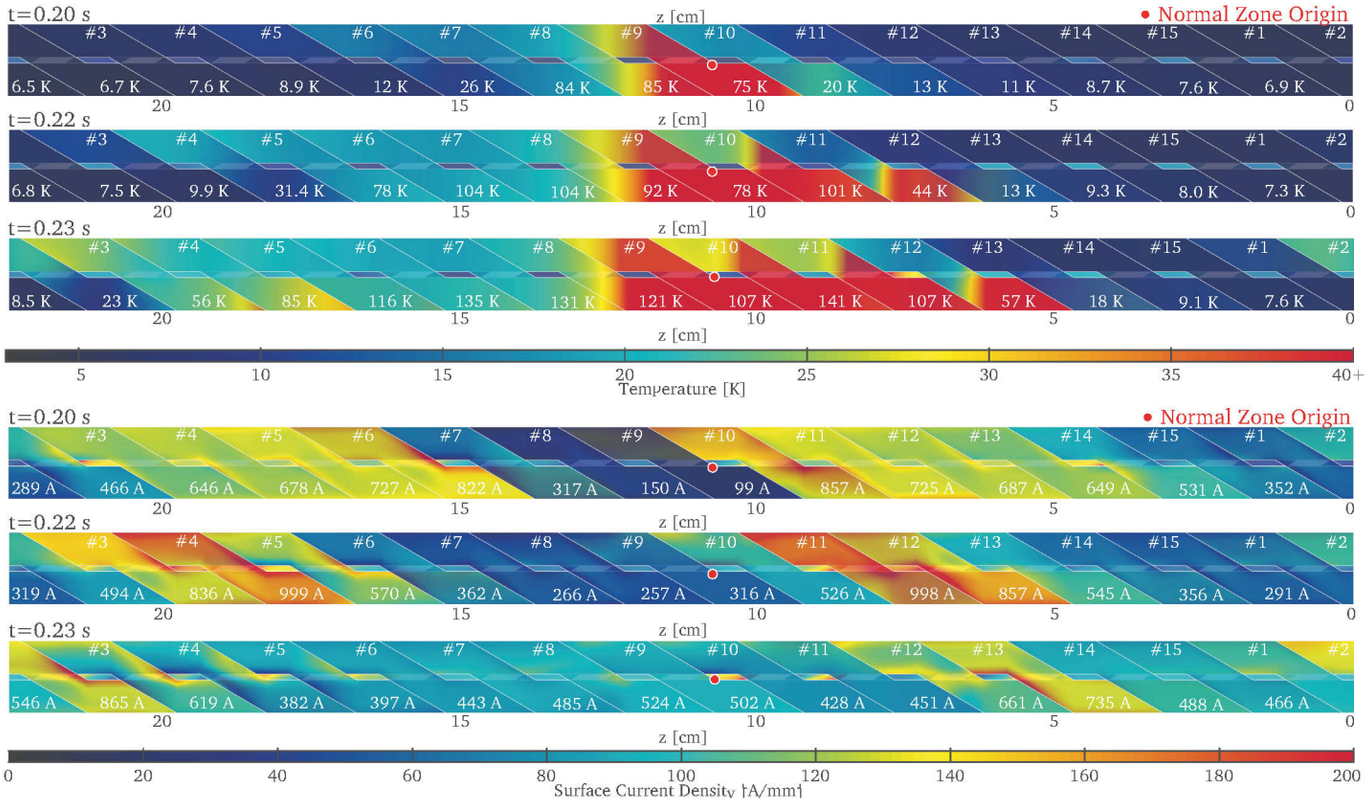


**Figure 5.5.** *Temperature (top three plots) and surface current density (bottom three plots) represented on the surface of the strands at* 0.20, 0.22 *and* 0.23 s*, respectively, calculated for a normal zone propagating in a Roebel cable in an applied magnetic field of* 17 T*, under an applied angle of* 86 deg *at* 4.5 K *and current of* 8.0 kA*. The normal zone is initiated using a heat pulse of* 100 mJ *injected over a duration of* 200 ms *starting at* 0 s*. At the end of each strand a self- and mutual inductive element (see Section 3.3.9) representing the inductance matrix of one of the Feather-M2 poles is used. The inductance matrix is given in Appendix C (divided by two in order to represent redistribution over only one of the poles). More details on the transient development of the normal zone is provided in Figure 5.6.*

However, the other tapes have sufficient margin left, resulting in a current redistribution to these tapes. This redistribution initially occurs locally through the contact resistances between the tapes, followed by a transition to global redistribution over the joints. In the second case the current does not necessarily redistribute to the neighboring tapes. The heat dissipated during the redistribution seeps relatively slowly, strongly dependent on the thermal boundary resistance, to the neighboring tapes resulting in a cascading effect, until none of the tapes have margin left. The cascading can occur over several hundreds of milliseconds prior to the quench, causing inductive voltage spikes to appear over the coil that are only in the several mV range (refer to Figure 5.6). This Pre-Quench phase can only occur in multi-tape conductors.

3. *Quench* - All tapes in the cable section exceed the current sharing temperature, leaving no margin for redistribution, resulting in a propagating normal zone in the entire cable. The voltage drop over the coil rises quickly over 100 mV and should easily be detectable using voltage taps. This last phase behaves essentially the same as a quench in a single tape and lasts usually several tens of milliseconds for the conductor to reach 500 K. Here good agreement is found with the reaction times of the one-dimensional Nodal model shown in Figure 2.38.

It is confirmed that due to the higher thermal margin the durations of the first and second phases are generally much longer in HTS than in LTS cables at 4.5 K. The level of current redistribution characterizes the Pre-Quench phase. It is concluded that the inductances and thus the length the magnet and the position of the quench are important factors that define the initialization of the normal zone. However, by using the tape-to-tape inductance matrix to represent the coil a significant simplification has been made, as outside of the modeled cable the current can not redistribute. This implies that the current redistribution either occurs within the modeled cable section or over the far-away joints, resulting in a higher effective resistance between the strands than in reality, causing the current redistribution to be slower. This problem is addressed by modeling the full coil using only one element over the width of the tape. The results presented in Section 5.3.

### Comparing Minimum Quench Energies 5.2.3

The parameter that indicates the stability of a coil is the Minimum Quench Energy (MQE) or $E_{MQE}$. It is the minimum amount of energy required to cause a conductor to quench. In Figure 5.7 the calculated MQEs are shown as function of current in the SP-1 Roebel cable (see Table 2.1), when applying various models. In the plot each marker represents the energy of the first model over the MQE found using the algorithm described in Section 2.4.2. In this algorithm, about ten iterations are needed to find the final MQE within 1%. This implies that such a plot comprises hundreds of simulations. The MQE is shown for different inductive loads connected to the ends of the cable, represented by the inductance matrices of the coils, as provided for both Feather-M0 and Feather-M2 in Appendix C. For Feather-M2 both the half inductance and full inductance cases are shown. The first assumes that there is a joint between the

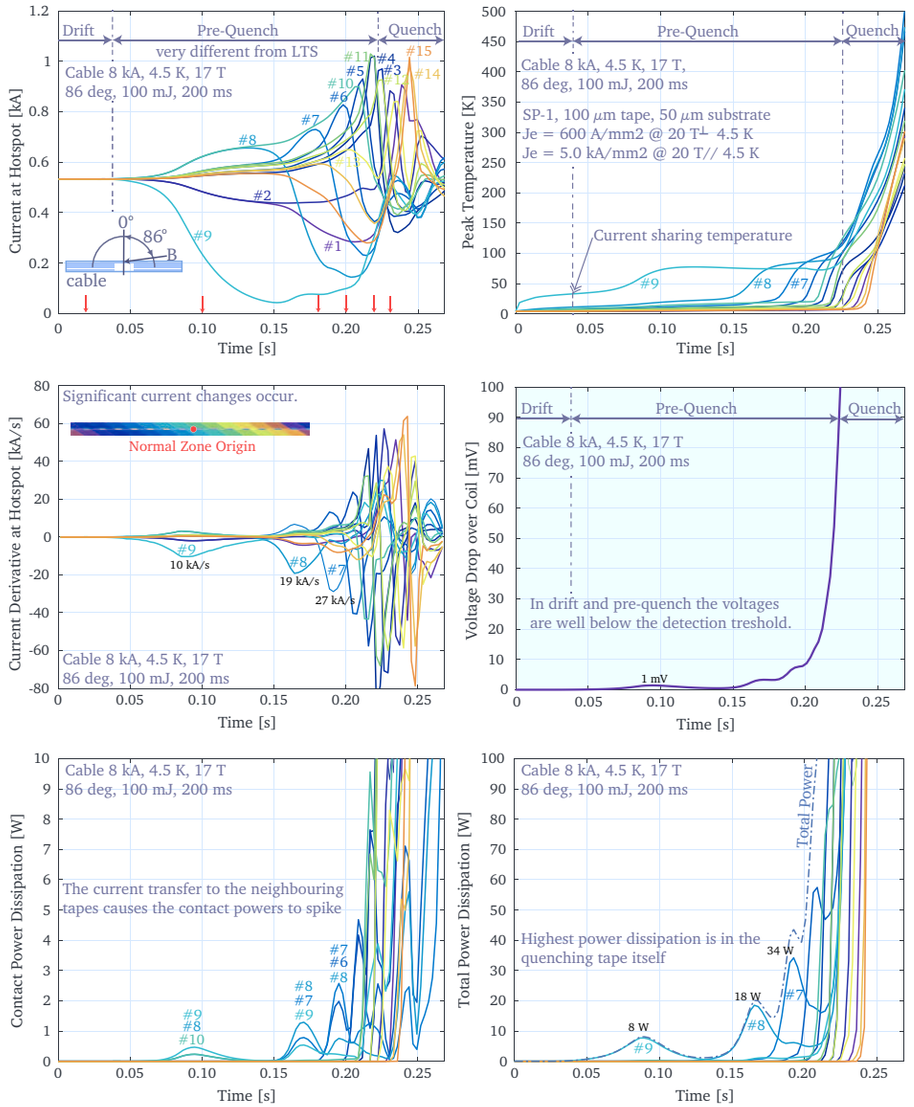


**Figure 5.6.** *Transient analysis of a quench in an SP-1 Roebel cable in applied magnetic field of* 17 T*, under an angle of* 86 deg *at* 4.5 K *operated at* 8.0 kA*. The normal zone is initiated using a heat pulse of* 100 mJ *over a duration of* 200 ms *starting at* 0 s*. At the end of each strand a self- and mutual inductive element (see Section 3.3.9) representing the inductance matrix of one of the Feather-M2 poles is used. The inductance matrix is given in Appendix C (divided by two in order to represent redistribution over only one of the poles).*

poles through which the current can redistribute. The second assumes that the coil is constructed from a single cable or that the joint between the poles only connects single tapes. In addition, the MQE is shown for the one and two-dimensional single strand models. In these cases the operating current on the horizontal axis is multiplied by the number of tapes in the cable.

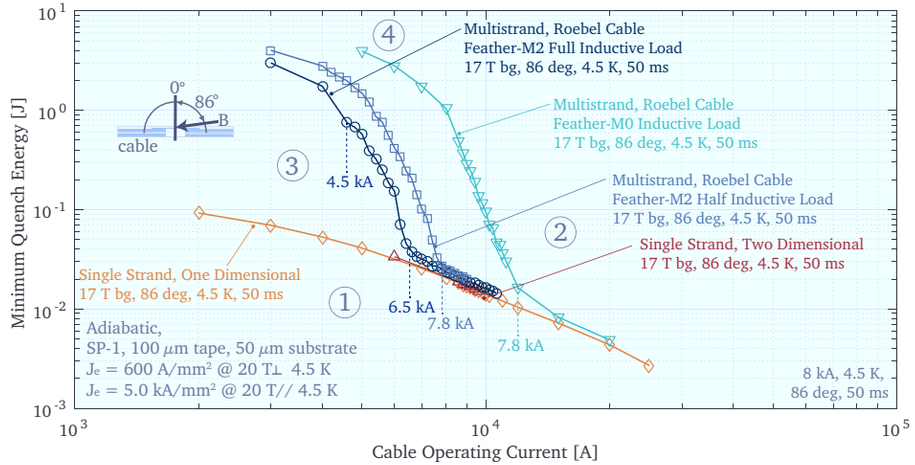


**Figure 5.7.** *Calculated Minimum Quench Energies as function of current in an SP-1 Roebel cable section and for a single tape operated at* 4.5 K *in a magnetic field of* 17 T *applied under an angle of* 86 deg*. The inductive loads, used by the model to approximate the behaviour of the Feather-M0 and Feather-M2 coils, are provided in Appendix C. The duration of the heat pulse is kept constant at* 50 ms *and the heat deposited is controlled by peak value. For the single tape models the operating current is multiplied by the number of tapes (*15*) in the Roebel cable. The areas indicated by the encircled numbers are explained in Section 5.2.3.*

The classical transition, also called kink, between the single- and multi-strand regimes is also present in ReBCO Roebel cables, causing the MQE to rapidly rise at lower currents. The kink is located for Feather-M0 around 13 kA. For Feather-M2 the kink is located around 8 kA and 7 kA for half and full coil inductances, respectively. To maximize stability the kink needs to be be located at a high current. The position of the kink is dependent on the electrical and thermal contact resistances between the tapes (see Section 5.3.3). Further distinction in the multi-strand regime resulting in multiple kinks is not clearly visible in these data. At higher current, however, the MQE of the cable perfectly falls onto the MQE of the single tape. This means that the energy to quench a single tape is sufficient to quench the entire cable. This good agreement between single tape and cable models provides further validation of the thermal part of the Electro-Magnetic and Thermal Network Model. In Figure 5.7 four areas [62], also indicated by the encircled numbers, can be distinguished:

1. *No Current Sharing* - The heat pulse does not contain enough energy to cause a single strand to exceed the current sharing temperature. The strand cools down and recovers without current redistribution.

2. *Single-Strand Quench* - The heat pulse causes one of the strands in the cable to exceed the current sharing temperature. The current redistributes to the other strands while releasing part of the stored energy as heat. The amount of energy released is enough to cause the other strands to exceed the current sharing temperature one-by-one until no further margin is available.

3. *Multi-Strand Recovery* - The heat pulse causes one of the strands in the cable to exceed the current sharing temperature. The current redistributes to the other strands while releasing part of the stored energy in the form of heat. The energy released is not sufficient to cause further strands to exceed the current sharing temperature and the cable recovers to the superconducting state.

4. *Multi-Strand Quench* - The heat pulse causes one of the strands in the cable to exceed the current sharing temperature. The current redistributes to the other strands while releasing part of the stored energy as heat. The energy released, with the additional heat from the heater pulse, causes other strands to exceed the current sharing temperature until no further margin is available at which point the cable quenches.

The value of the transition current between the single and multi-strand regimes depends, amongst other things, on the used inductive load connected to the end of the cable. The values in the inductance matrix determine to what extend the current redistributes to the neighboring strands, as these have the strongest mutual coupling. In the single-strand regime the MQE is several tens of millijoules, about three orders of magnitude higher than for LTS in which the order is about tens of microjoules. In the multi-strand regime the MQE is on the order of joules compared to millijoules in LTS cables, again three orders difference.

The MQE at low current is so high, that it is not possible to initiate a propagating normal zone in the cable within the given 50 ms heat pulse duration, using a local spot heater, without immediately burning the strand the heater is attached to, due to the heat supplied by the pulse itself. In practice this could be circumvented by applying the heat to a larger area. However, this would affect the resulting initialization transients. To avoid this there are no data available below an operating current of around 4 kA.

## 5.3 Quench Analysis of the Full Scale Coil

*From the initial benchmark tests is has become clear that the current redistribution in the multi-strand conductor plays as significant role in the initialization transients of the normal zone. Therefore, to be able to properly include these redistributions, the propagation of a normal zone is modeled in the full scale Feather-M0 and Feather-M2 coils using a simplified network.*

### Model for Entire Coil 5.3.1

To include the current redistribution effects throughout the conductor in the entire coil it is necessary to run the full coil model. The geometry of the SP-1 Roebel cable cable is mapped onto the geometry of the coils using Equation 2.11. The number of unit cells is set such that the modeled cable equals the length of the conductor in the coil. However the resulting number of elements is, especially in the case of Feather-M2, too high for the time dependent solver. Therefore the network is simplified by removing the transverse elements and by recombining the longitudinal elements and nodes over the width of the tape. During this step the areas and widths are added and the length, position and direction are averaged. The contact elements need to be reconnected to the new recombined nodes as well. Resulting duplicate contact elements connecting to the same nodes in the network are added into a single element. Each flat tape is now represented by a one-dimensional wire.

The advantage of simplifying the network over the use of one width element from the start, is that the contact areas are calculated more accurately. By using one element over the width of the tape it is no longer feasible to model screening currents and thus hysteresis effects. In addition, the magnetic field angle and all other related properties, are assumed equal over the width of the entire tape. Note that these compromises are likely acceptable for quench analysis, since the normal zone quickly homogenizes over the width of the tape (as shown in Section 5.2.1), but obviously not for calculating magnetization loss and field quality.

To demonstrate the effect of the simplification on the complexity of the models the following geometries are compared:

1. *Feather-M0 Full* - The tapes are modelled using 8 elements over their width and the longitudinal element length is 2 mm. The total number of superconducting elements, nodes and contact elements, included in the conductance matrix $G_{ij}$, are 405 k, 214 k and 249 k, respectively. The MLFMM requires 9 levels and uses a grid size of 1.0 mm. The resulting S2T matrix consists of 27 M non-zeros and requires 204 MB to store. It is possible to run this model, but the calculation time for a single quench analysis is on the order of one week[8], making it impractical for parametric studies and MQE searches.

2. *Feather-M0 Simplified* - The network is simplified using only 1 element over the width of the tape. The length of the longitudinal elements is 2 mm. The total number of superconducting elements, nodes and contact elements, included in conductance matrix $G_{ij}$, are 23 k, 23 k and 23 k, respectively. The MLFMM requires 8 levels with a grid size of 2.0 mm. The resulting S2T matrix consists of 1.1 M non-zeros and takes only 8.4 MB to store. A quench analysis with this model takes only a few hours to run for each case and several cases can be run in parallel.

3. *Feather-M2 Full* - The tapes are modeled using 8 elements over tape width. The length of the longitudinal elements is 2 mm. The total number of superconducting elements, nodes and contact elements, included in conductance matrix $G_{ij}$,

are 2195 k, 1162 k and 1353 k, respectively. The MLFMM requires 10 levels with a grid size of 0.98 mm. The resulting S2T matrix takes 2541 MB to store and has 333 M non-zeros. Factorization of the system matrix is not possible using the available 64 GB memory. Simplification of the network is necessary to be able to run the model on present hardware.

4. *Feather-M2 Simplified* - The network is simplified using only 1 element over the width of the tape. The length of the longitudinal elements is 2 mm. The total number of superconducting elements, nodes and contact elements, included in conductance matrix $G_{ij}$) are 129 k, 129 k and 129 k, respectively. The MLFMM requires 9 levels with a grid size of 1.98 mm. The resulting S2T matrix takes 70.9 MB to store and the number of non zeros is 9.2 M. A quench analysis using this model takes about a day to run for each case[8], but several cases can be run in parallel.

To keep the computation time within acceptable limits, especially considering MQE searches, the use of the simplified models is unavoidable to study both Feather-M0 and Feather-M2. For comparison the models are both run at a temperature of 4.5 K, under adiabatic conditions, and in a constant background field of 13 T, which is superimposed on the self field generated by the coil. In the case of Feather-M2 the magnetic field generated by the other pole is included by mirroring the elements in the xz-plane. The iron poles in Feather-M2 are omitted from the calculation.

The ends of the cable, comprising one pole in the Feather-M2 case, are connected to single node using a 5 n$\Omega$ joint resistance. This allows the current to redistribute among the tapes over the joint and through the contact resistances. The normal zone is initiated using a 50 ms heat pulse located in both coil geometries on the layer jump, unless stated otherwise, in the corner of the cross-over in tape number 9, similar to the cable section model. A total energy of 287 mJ is required to cause a quench in the entire cable, after the Pre-Quench phase. The coil operating current is kept constant throughout the full development of the normal zone thereby assuming no energy extraction. The electrical and thermal contact resistances between the tapes are again set at the default 0.2888 $\mu\Omega m^2$ and 100 $W/(m^2K)$, respectively.

### 5.3.2 Initialization Transients, Voltages and Current Redistribution

The calculated quench initialization transients for the full coil analysis at 8.0 kA are presented in Figure 5.8, which shows a selection of relevant properties as function of time, similar to the results of a cable in series with an inductive load presented in Figure 5.6. After the normal zone is initiated in tape 9 it propagates through a series of current and temperature redistributions, named the Pre-Quench phase, to the other tapes in the cable. It is re-confirmed here that the current redistributes first to the neighboring strands 8 and 10. The anti-symmetry due to the normal zone being initiated at the cable surface, causes the normal zone to first propagate to 8, 7 and 6, with the respective current redistributions, before it propagates to strand 10 on the other side.

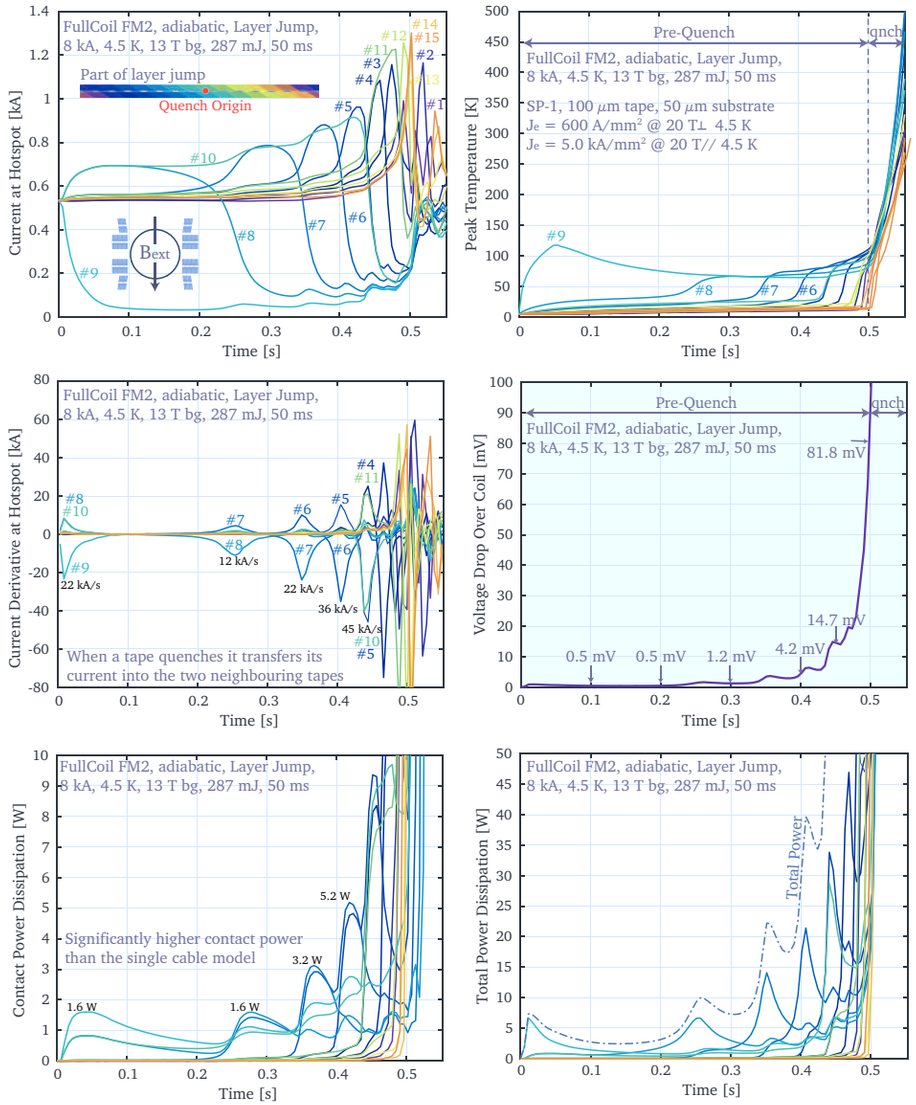


**Figure 5.8.** *Transient analysis of a quench in the Feather-M2 magnet operated in a background magnetic field of* 13 T *at* 4.5 K*. The coil current is* 8.0 kA*, which is the design current at* 16.9 T *central field (including the background magnetic field). The quench is initiated using a heat pulse of* 287 mJ *over a duration of* 50 ms *starting at* 0 s *in tape number* 9*. This initiates a normal zone that then propagates through a series of current and temperature redistributions, named the Pre-Quench, to tapes* 8*,* 7*,* 6*,* 5*,* 10 *and* 4*, with increasing frequency, after which the whole cable quenches.*

The rate at which the current at the hot-spot changes during the first redistribution is around 22 kA/s, which is about twice that of the cable model, in which the rate is around 10 kA/s. During the Pre-Quench phase the current redistribution between tapes occurs more often than in the cable model, causing it to last longer, around 500 ms compared to 250 ms. These differences can be attributed to the lower effective resistance between the strands, resulting from the increased contact area by taking the entire coil into account. This is also reflected in the higher contact power dissipation during the current redistribution peaks. The total power, which includes the dissipation in the tapes, is more or less the same as in the cable section model. After all tapes are normal conducting at around 0.5 s, the Quench phase starts, in which all the tapes heat up at the same rate. The Quench phase itself takes only 36 ms, at which a temperature of 500 K is reached. Again, as in the cable model, good agreement is found with the reaction times calculated with the single strand model, using a similar current density. The voltage drop over the coil in the first peak is again around 1 mV, a level very hard to detect in a reliable way using classical voltage detection methods in a noisy environment.

The duration of the Pre-Quench and Quench phases as function of coil operating current are compared in Figure 5.9. Note that these durations are calculated using a heater pulse, which has an energy exceeding MQE by only 1% (also see Section 5.3.3). When energies much larger than the MQE are used, the temperature of the first quenching tape is higher, resulting in faster heat transfer to the neighboring tapes, which causes the Pre-Quench duration to be slightly shorter. For example, at 7 kA at pulse energies of 443 (MQE), 450, 500, 600 and 800 mJ, the duration of the Pre-Quench is given as 0.91, 0.86, 0.72, 0.65 and 0.61 s, respectively. Although the Pre-Quench times are not always consistently decreasing and seem to be very sensitive to numerical variation, it is also observed that at higher currents, in the single strand regime, the dependence of the Pre-Quench duration on the pulse energy is less strong.

In Figure 5.9 it can be seen that the Pre-Quench and Quench durations both decrease with the operating current. Both are fitted using a basic power law with respective exponents −2.3 and −1.8. While the durations of both phases depend on ohmic heating, which scales quadratically with current, the duration of the Pre-Quench phase, in contrast to the Quench phase, depends as well on the margin, i.e. the number of tapes that quench before no margin is left. This can explain why it has a stronger scaling with current, since the operating current also determines the amplitude of the magnetic field and its incident angle with respect to the tape surface. Good agreement is found for the quench duration calculated with the single strand and the Electro-Magnetic and Thermal Network Model. Over the full current range the duration of the Pre-Quench phase is approximately an order of magnitude longer than the duration of the Quench phase. If the first current redistribution spike during the Pre-Quench phase is always present and can be detected (see Section 5.3.4), it can provide means to protect multi-strand HTS cables and coils at high current densities, as then there is sufficient time to take protection measures.

While the temperature rise near the hot-spot is very local, the resulting current redistribution due to the difference in effective resistance between the strands, affects almost

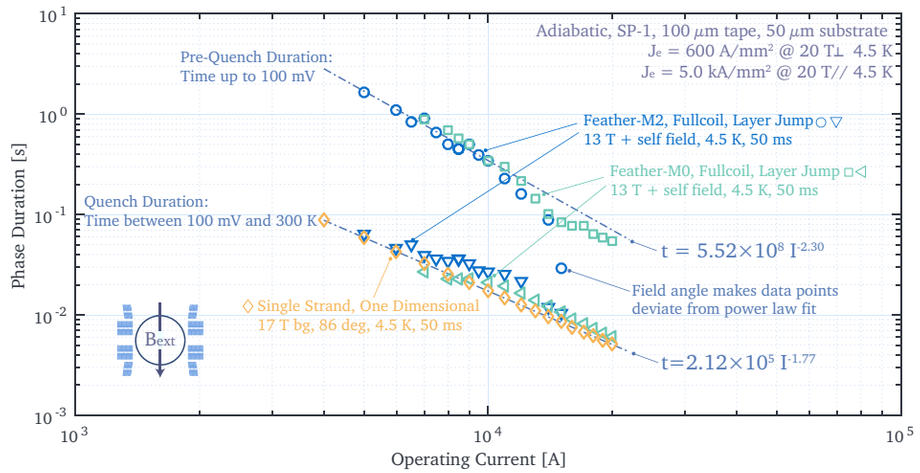


**Figure 5.9.** *Calculated duration of the Pre-Quench and Quench phases as function of operating current for heat pulses with energies just above the Minimum Quench Energy located on the layer jump of both the Feather-M0 and the Feather-M2 magnet. Both magnets are operated in a background field of* 13 T *at a temperature of* 4.5 K*. In addition the duration of the quench in the single tape model is shown.*

the whole coil. This is demonstrated for a quench in Feather-M2 at 8.0 kA and 4.5 K in Figure 5.10, in which the surface current density in the tapes is plotted on their surface at various time steps. It can be seen that the redistribution of current to the neighboring strands is not instantaneous in the entire coil. Instead the redistribution starts at the hot-spot, in this case the layer jump, and then propagates towards the coil-ends. This is illustrated further in Figure 5.11 in which the current of each of the tapes in the cable is plotted along their length at various time steps. The propagation of the current redistribution along the cable is governed by the resistance of the normal zone, the contact resistance between the tapes in the cable and their respective self- and mutual inductances, which prevents the current from redistributing directly over the joints, as it would happen in the steady state solution.

Similarly the voltages represented on the surface of the tapes in the coil are shown in Figure 5.12. The voltage drop is largest over tape 9 at the layer jump. This becomes more apparent in Figure 5.13, which shows a step at 20 m, the position of the layer jump, in the voltage of tape 9. The voltages are directly responsible for driving the contact currents. The voltage in tape 9 in front of the normal zone is higher than in the other tapes, thereby driving the current to them. Behind the normal zone the voltage is lower making the current return. Because the tapes are connected to the joints at their ends the voltage at this location is almost equal for all tapes. It is therefore not necessary to put multiple voltage taps on the cable near the joints. The voltage drop over the entire coil, from the current source to the current sink remains on the order of a few milliVolts during the Pre-Quench phase. The differential voltage between specific

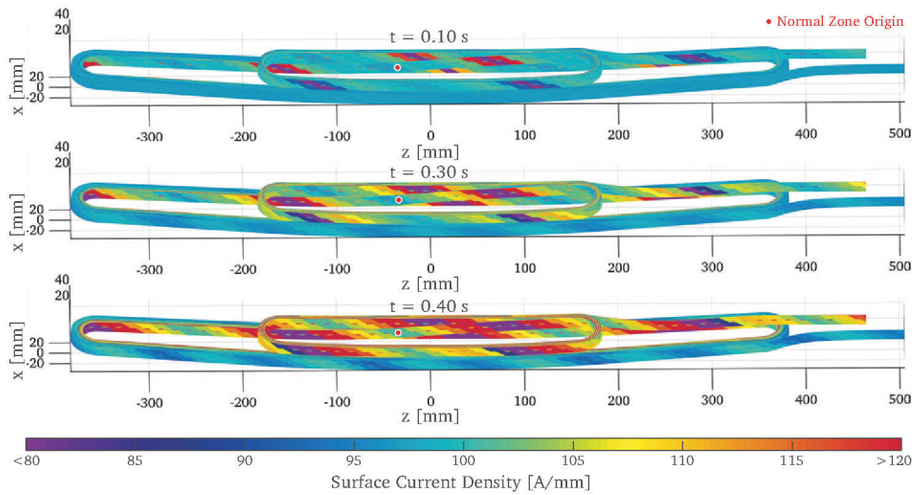


**Figure 5.10.** *Calculated surface current density shown on all tapes in the three-dimensional Feather-M2 coil model at times of* 0.1 s, 0.3 s *and* 0.4 s *throughout the Pre-Quench phase, for a quench at* 8.0 kA *when operated in a background field of* 13 T *at a temperature of* 4.5 K. *The quench is initiated using a heat pulse of* 287 mJ *over a duration of* 50 ms *starting at* 0 s. *The extremities of the color scale indicate currents that are smaller or larger than fit on the scale. The origin of the quench is indicated by the red dot. Note that the other pole, which is not shown here, was included in the calculation by mirroring the elements in the zx-plane.*

spots in the coil can be much higher. This means that the positioning of voltage taps for quench detection needs to be considered carefully.

### 5.3.3 Coil Stability and Minimum Quench Energies

Considering the difficulty of detecting and protecting ReBCO based magnets at high current density, the level of coil stability is a vital parameter. It has already been shown that HTS conductors, due to their higher thermal margin, have MQEs that are three orders of magnitude higher than for LTS. This implies that an HTS coil has an extremely high level of stability, provided sufficient margin is maintained. This is reflected in the MQEs calculated for the Feather-M0 and Feather-M2 coils, which are presented as function of operating current in Figure 5.14. In this case the transition between the single and multi-strand regimes is visible at respective currents of around 10 kA and 11 kA, which is a few kiloamperes higher than in the cable section model. The difference between Feather-M0 and Feather-M2 is only small despite the difference in coil inductances between the two. The transition is characterized by the four areas described in Section 5.2.3, labeled 1 to 4. For Feather-M2 also a secondary kink is visible which indicates the presence of another transition. The MQEs in the coil are higher than in the single tape model. This is explained by the difference in magnetic field angle, which is fixed at 86 deg for the single tape, while in the coil it depends on

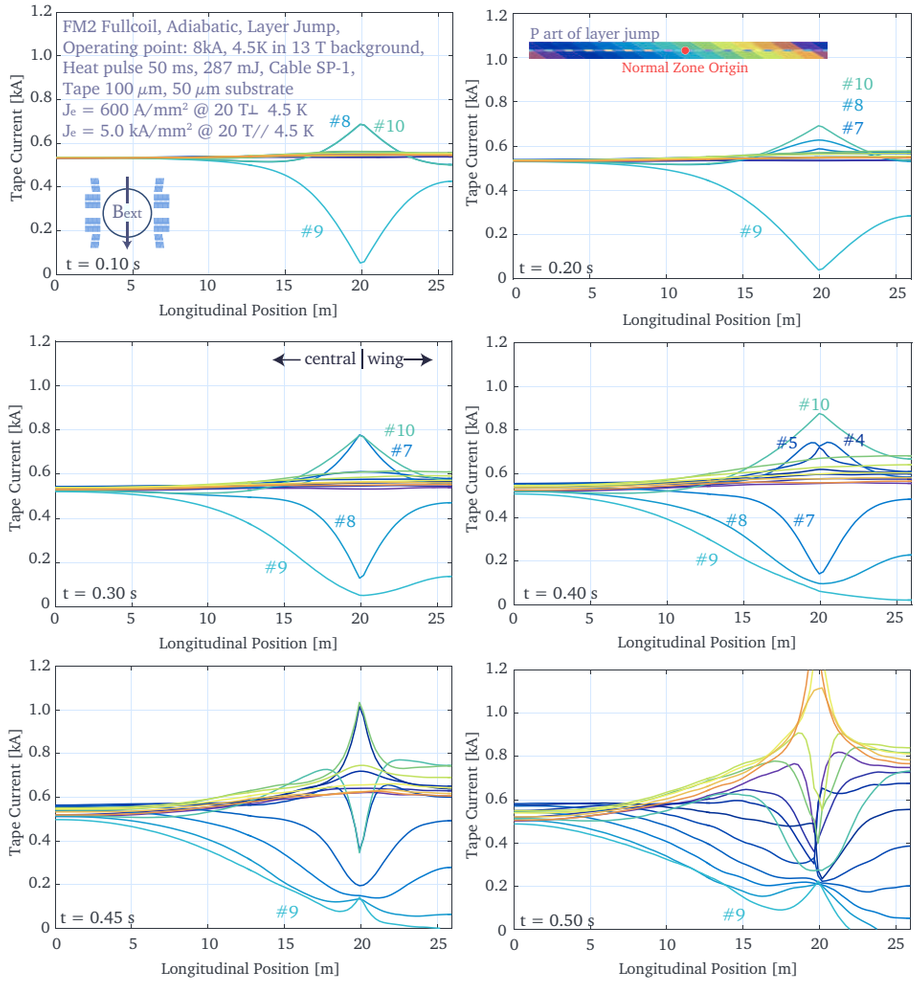


**Figure 5.11.** *Calculated current distribution along cable in the three-dimensional Feather-M2 coil at various time steps, indicated in the plots, during the Pre-Quench phase, for a quench at* 8.0 kA *when operated in a background field of* 13 T *at a temperature of* 4.5 K*. The quench is initiated using a heat pulse of* 287 mJ *over a duration of* 50 ms *starting at* 0 s*. The central deck runs from* 0 *to* 20 m *and the wing deck runs from* 20 *to* 26 m*. The normal zone is located on the layer jump at* 20 m.

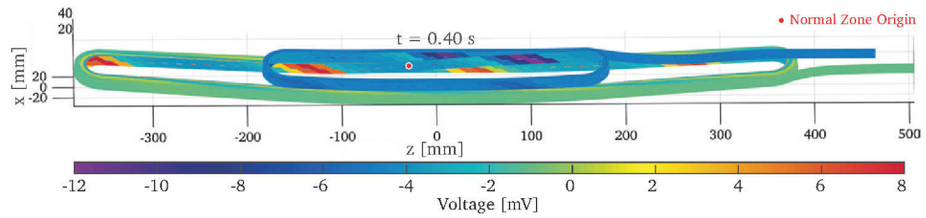


**Figure 5.12.** *Calculated voltages shown on the surface of the three-dimensional coil geometry at a time of* 0.4 s*, for a quench in Feather-M2 at* 8.0 kA *when operated in a background field of* 13 T *at a temperature of* 4.5 K*. The quench is initiated at the red dot positioned on the layer jump using a heat pulse of* 287 mJ *over a duration of* 50 ms *starting at* 0 s*.*

the operating current, due to the inclusion of self field. At higher current, exceeding the design current of 8.0 kA, the magnetic field angle in the coil increases as well, making the two curves come closer. In the single strand regime the energies are on the order of several tens of millijoules. In the multi strand regime the energies exceed several hundreds to several thousands of millijoules. The MQE at the design current of 8.0 kA, which corresponds to 70% on the load-line, is around 287 mJ and is safely in the multi-strand regime.

Interesting parameters are the electrical and thermal contact resistances. The contact areas can be increased by applying pressure to the coil-windings during impregnation, as done for the Feather magnets. In Figure 5.15 the MQE is shown as function of current at various values for the contact resistance. It can be seen that the position of the kink depends on the value. It is located at currents of about 7, 8, 10 and 14 kA for contact resistance values of $2.88 \times 10^{-5}$, $2.88 \times 10^{-6}$, $2.88 \times 10^{-7}$ and $2.88 \times 10^{-8}\,\Omega\text{m}^2$, respectively. It is noticed that at lower resistance the model becomes more difficult to solve, taking a much longer calculation time.

To maximize stability it is important to have a high electrical contact resistance. It looks like the secondary transitions are located at a varying distance from the kink, indicating that the contact resistance affects the manner in which the normal zone propagates. The calculated duration of the Pre-Quench and Quench phases as function of the current and contact resistance are shown in Figure 5.16. It can be seen that, although the data is noisy, the duration of the Pre-Quench lasts clearly depends on the contact resistance. A lower contact resistance results in a longer Pre-Quench. This occurs because the current can redistribute more easily and thus closer to the normal zone, causing less heat to be deposited when a tape quenches. Therefore it takes longer for the heat to spread throughout the cable. The duration of the Quench phase itself is not significantly affected.

The electrical contact resistance is usually related to the thermal conductivity. Materials that have a good electrical conductivity are also good heat conductors [209]. When the pressure on the cable is increased, the number of contact points between the tapes increases, thereby effectively increasing the thermal conductivity and reducing the con-

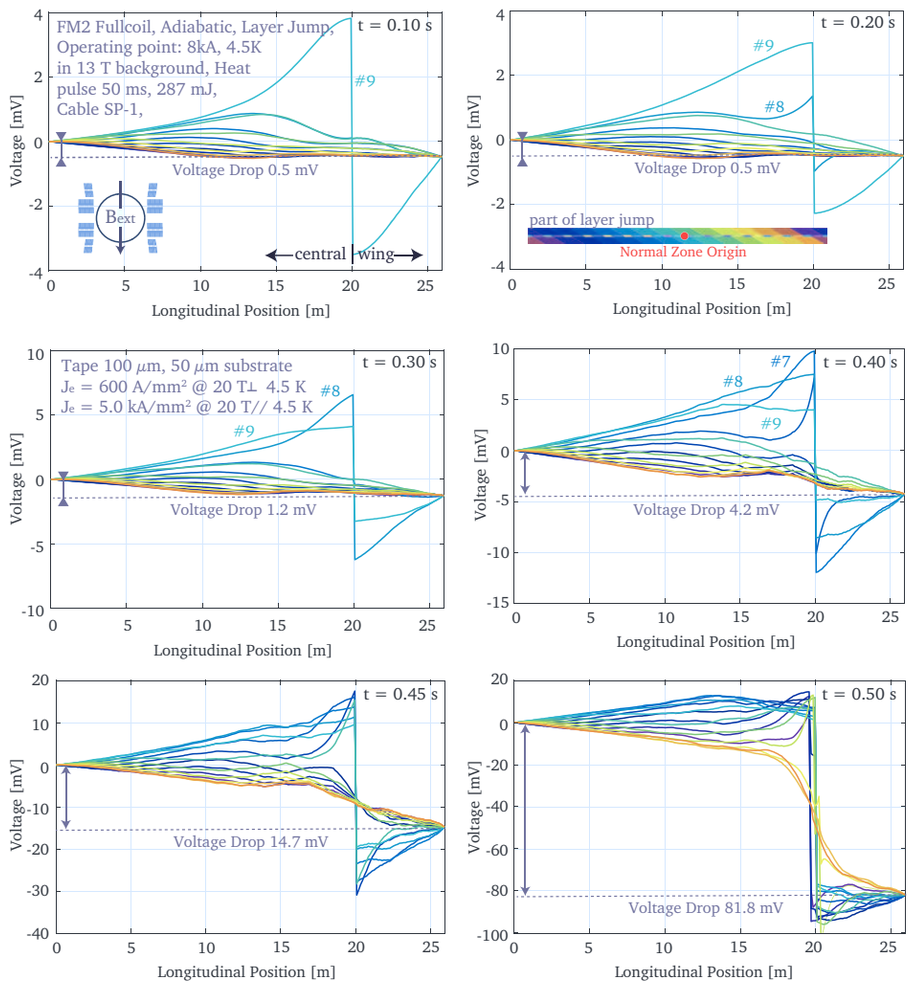


**Figure 5.13.** *Calculated voltages along the tapes in the three-dimensional Feather-M2 coil at various time steps, indicated in the plots, during the Pre-Quench phase, for a quench at* 8.0 kA *when operated in a background field of* 13 T *at a temperature of* 4.5 K. *The quench is initiated using a heat pulse of* 287 mJ *over a duration of* 50 ms *starting at* 0 s. *The central deck runs from* 0 *to* 20 m *and the wing deck runs from* 20 *to* 26 m. *The normal zone is located on the layer jump at* 20 m.

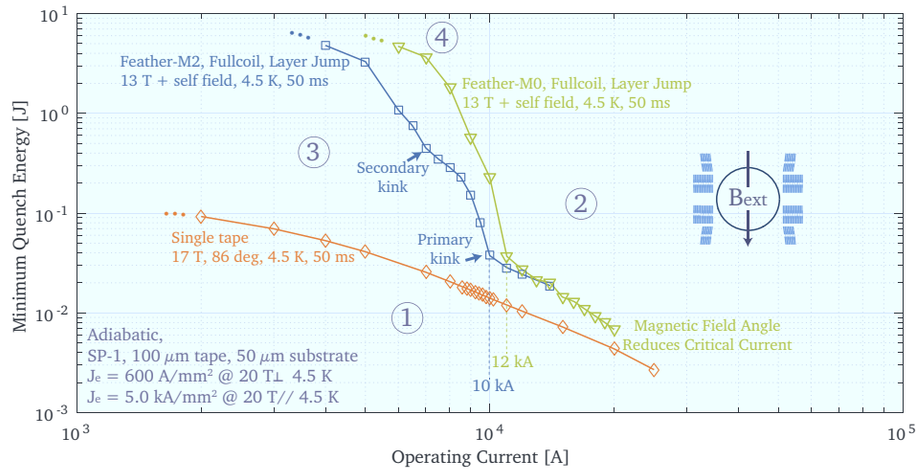


**Figure 5.14.** *Calculated Minimum Quench Energies in the Feather-M0 and Feather-M2 coils as function of operating current when operated in a background magnetic field of* 13 T *at a temperature of* 4.5 K*. The normal zone is initiated on the layer jump by a heat pulse, which has a duration of* 50 ms*. The energy of the heat pulse is controlled by its peak value. For the calculations the simplified model is used that approximates the tapes in the coil using only one element across their widths. The areas indicated by the encircled numbers are explained in Section 5.2.3.*

tact resistance. Data on the relation between the two values for contact boundaries are not widely available. Therefore the effect of the thermal contact resistance on the MQE is studied here separately. The MQE as function of the operating current and various values of the thermal contact resistance are presented in Figure 5.17. The electrical contact resistance is kept at a constant $2.88 \times 10^{-7}\,\Omega\mathrm{m}^2$. The kink is found at currents of 10, 11 and 12 kA for thermal contact resistances of 100, 50 and $10\,\mathrm{W/(Km^2)}$, respectively. To optimize stability the thermal conductivity between the tapes should be as low as possible. This prevents the heat from transferring to the neighboring tapes, preventing them from quenching. The heat then diffuses longitudinally or even to the surroundings (not included in the model). This is also reflected in the duration of the Pre-Quench phase, which becomes longer, as shown in Figure 5.18. The duration of the Quench phase is again almost unaffected.

To maximize the thermal stability of the coil it is necessary to decrease both the electrical contact resistance and thermal conductivity between the tapes, in order to enhance the current redistribution and to prevent the normal zone from spreading. Unfortunately this is a non-trivial task. Some manufacturers have the option of electro-plating a solder layer onto the copper stabilizer. This layer can be melted in a small oven after the coil is wound, thereby increasing the electrical contact, but also increasing the thermal conductivity, and thus the effect is at least partially negated. Adding thermal insulation sheets between the tapes, also reduces the electrical contact between them. Therefore, it is proposed here to apply a patch of solder every few meters of

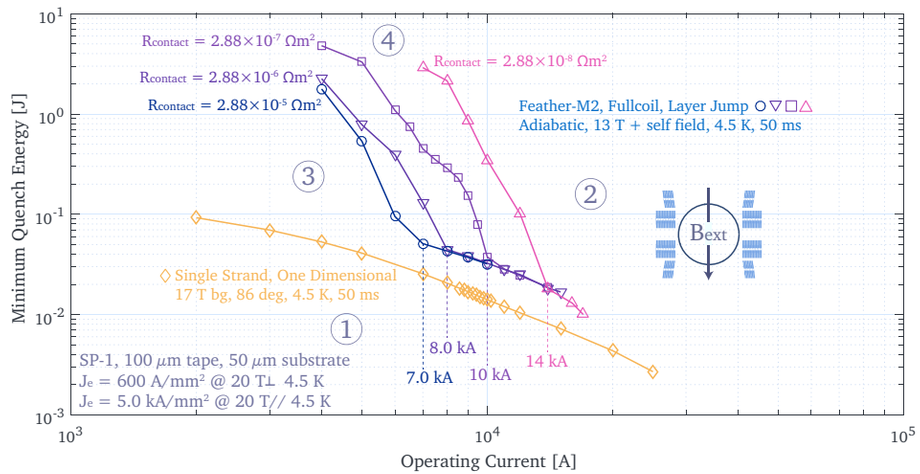


**Figure 5.15.** *Calculated Minimum Quench Energies as function of current for various values of the electrical contact resistance between the tapes, for the Feather-M2 coil when operated in a background magnetic field of* 13 T *at a temperature of* 4.5 K*. The normal zone is initiated on the layer jump by a heat pulse, which has a duration of* 50 ms*. The energy of the heat pulse is controlled by its peak value. For the calculations the simplified model is used that approximates the tapes in the coil using only one element across their widths. The areas indicated by the encircled numbers are explained in Section 5.2.3.*

cable during the coil-winding process, to still allow the tapes to slide longitudinally. These patches allow the current to redistribute between the strands, effectively reducing the electrical resistance between the strands. Note that this is in essence the same as reducing the distance to the joint and thus the inductive load. If the normal zone is located in a non-solder location, which comprises the majority of the coil, the thermal conductivity remains unaffected. To reduce the chances of a normal zone developing inside the patches, they can be placed in relatively safe places. For example, in the straight section, where the field is parallel to the tape surface. The distance between the patches needs to be an integer number of twist pitches to prevent large coupling currents from being induced. Further study on the effectiveness of this method and on the implications on the winding process is necessary.

### Early Detection During the Thermal Drift or Pre-Quench phases 5.3.4

If the high stability proves to be insufficient for preventing a quench in the magnet, a scenario that must be considered especially in prototype HTS magnets, early detection of a thermal disruption during the Thermal Drift or Pre-Quench phases is vital to providing sufficient time for the magnet protection, when operated at high current density. Classical voltage taps based detection, across coil sections is relying on a 100 mV or more trigger level, which is too late for a high current density coil as demonstrated

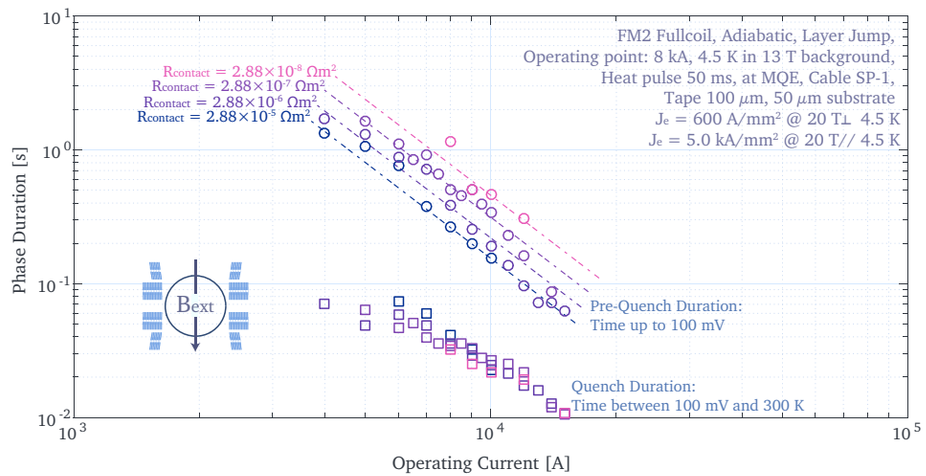


**Figure 5.16.** *Calculated durations of the Pre-Quench and Quench phases as function of current for various values of the electrical contact resistance between the tapes, for the Feather-M2 coil when operated in a background magnetic field of* 13 T *at a temperature of* 4.5 K*. The normal zone is initiated on the layer jump by a heat pulse, which has a duration of* 50 ms*. The energy of the heat pulse is controlled by its peak value. For the calculations the simplified model is used that approximates the tapes in the coil using only one element across their widths.*

before. The trigger will come when the normal zone is developed into a full quench, leaving little time to react. Nevertheless, since voltage taps are easy to implement, it is still recommended to use them because they might provide insight in the development of the normal zone and can act as a backup when other protection mechanisms described in this section fail, something that is likely to happen in early prototype coils.

If the heat is deposited relatively slowly and thus globally (see Figure 5.1), for example, due to joint heating, continuous beam losses or cryogenic failure, the Thermal Drift phase can last 100 s or more. In this scenario the conductor exceeds the current sharing temperature when none of the tapes have margin left, thereby reducing the time of the Pre-Quench to nearly zero. Assuming the Thermal Drift phase happens over a longer time span, a larger area of the coil heats up allowing the detection of this phase using distributed temperature sensors. In this case it is not even necessary to monitor absolute temperature with high precision, since a significant change of the temperature is already indicative of heating. Possible temperature sensing techniques include:

1. *Classical Temperature Sensors* - These sensors have to be located in critical areas such as coil-ends and joints. If absolute temperature is required one can consider for example calibrated sensors, such as Cernox [210]. For detecting only a change in temperature it is also possible to use cheap diodes [211]. Multiple sensors can be connected in series or parallel, for redundancy, to form a distributed grid covering the coil-windings.

2. *Superconducting Quench Detection (SQD)* - The change in temperature is detected using the superconducting transition of a superconductor that has a lower transition temperature than the main conductor. This concept was explored using Nb-Ti wires or thin films in $cm^2$ type sensors or lay chips [114]. The so-called SQDs are actually used in a few magnets like for instance the ATLAS magnet system [212]. Also an insulated Nb-Ti wire can be inserted in the central channel of the cable for the same purpose. This would also allow for balancing inductive voltages for the voltage detection system. This technique is limited by the critical field of the used wire or film, which for Nb-Ti is about 11 T. For 20 T class magnets it is necessary to use a superconductor with a higher critical magnetic field. This could be a $Nb_3Sn$ wire, film or tape [213], increasing the complexity. Another option to be considered is the use of $MgB_2$ fibres [214, 215], which have an upper critical magnetic field of 55 T at 1.5 K and a critical temperature of about 38 K.

3. *Optical Fiber* - An optical fiber sensitive to local stress caused by temperature changes is inserted in the coil pack. Provided that the fiber allows for a sufficiently tight bending radius, it can even be inserted in the central channel of the Roebel cable. The fiber can be based on Rayleigh scattering, allowing for fully distributed sensing or on Brag gratings [216, 217, 218, 219]. The drawback of

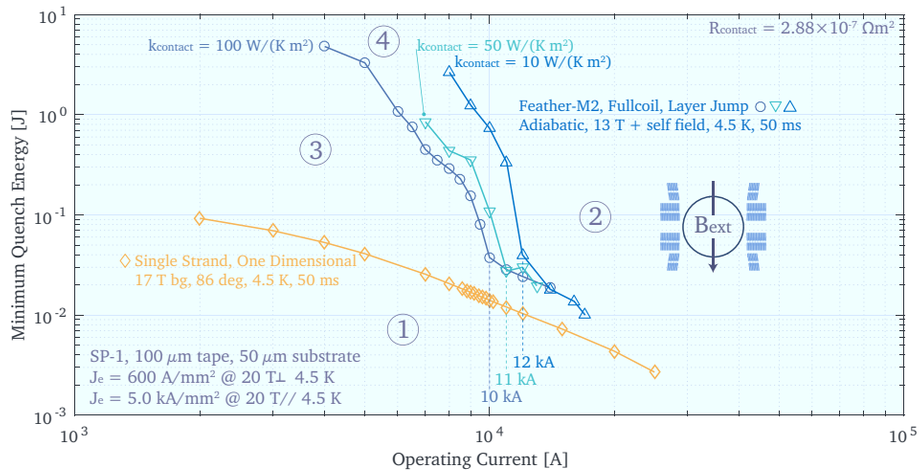


**Figure 5.17.** *Calculated Minimum Quench Energies as function of current for various values of the thermal contact resistance between the tapes, for the Feather-M2 coil when operated in a background magnetic field of* 13 T *at a temperature of* 4.5 K*. The normal zone is initiated on the layer jump by a heat pulse, which has a duration of* 50 ms*. The energy of the heat pulse is controlled by its peak value. For the calculations the simplified model is used that approximates the tapes in the coil using only one element across their widths. The areas indicated by the encircled numbers are explained in Section 5.2.3.*

optical fibers is that they rely on thermal contraction and are therefore not (very) sensitive at temperatures below 30 K (this is the area of interest for Thermal Drift detection). The advantage is that optical fibers are totally insensitive to electromagnetic noise and can therefore provide a very clean signal (in an otherwise noisy environment).

For physical sensors the best location is close to, or inside, the coil pack, where they are not in direct contact with liquid helium. Copper heat conductor strips can be considered to further improve thermal contact with the coil pack. It should not be necessary to remove cooling from the coil to aid the temperature sensors, because this would negatively affect thermal stability.

If the heat is deposited fast and thus locally (see Figure 5.1), for example, due to sudden degradation of the critical current in one of the tapes or perhaps a ramp over the critical current, the Thermal Drift phase is short. However, because the heat is not distributed evenly over the tapes in the cable, it is likely that most of them have margin left, resulting in a Pre-Quench phase. During this phase the current redistributes between the tapes at a rate of about 22 kA/$s$. This current change occurs over lengths of tens of meters, which in the case of Feather-M2 encompasses the major part of the coil. The change of position of the current inside the cable is reflected by a change in magnetic field around it, which can be measured magnetically anywhere along the cable. A basic version of this concept was explored at Lawrence Berkely National Lab-

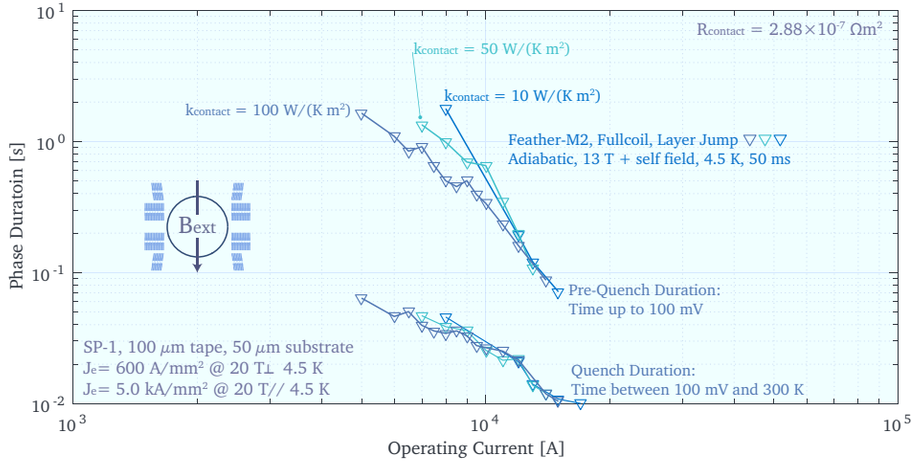


**Figure 5.18.** *Calculated durations of the Pre-Quench and Quench phases as function of current for various values of the thermal contact resistance between the tapes, for the Feather-M2 coil when operated in a background magnetic field of* 13 T *at a temperature of* 4.5 K. *The normal zone is initiated on the layer jump by a heat pulse, which has a duration of* 50 ms. *The energy of the heat pulse is controlled by its peak value. For the calculations the simplified model is used that approximates the tapes in the coil using only one element across their widths.*

oratory [220]. It was proven that by slicing a tape into two halves along its length, the current redistribution between the two halves and thus a quench can be detected using a hall-probe. Because the two tape stacks in the Roebel cable resemble this geometry, the idea of using a similar concept for these cables was triggered. Because hall probes lose their sensitivity at high magnetic field and because only the change of magnetic field is of interest, it is decided to try using a set of pick-up coils instead, a concept very similar to a so-called quench antenna [221]. The induced signal on these coils can be calculated by representing the coil with line elements. The induced voltage on each element is calculated using Equation 3.38, where the time derivative of the vector potential is calculated directly from the elements using the MLFMM.

Further study unveiled that the positioning and topology of the pick-up coils is vital for achieving a good signal [222, 223]. To avoid picking up main dipole field, the pick-up coils are oriented parallel with the magnetic field lines. In the Aligned Block coil design this is also parallel with the cable surface. Figure 5.19 illustrates the magnetic field change around a meandering tape in a Roebel cable that has a time-changing current. Areas exist with both positive and negative out-of-plane flux change. A pick-up coil that is centered on the cross-over ($V_2$) does not experience a change of total flux and thus the voltage signal from this coil is zero. The signals coming from $V_1$ and $V_3$ are of opposite sign and can be subtracted. To ensure that the pick-up coil array is sensitive to current changes in any tape inside the cable each twist pitch is divided into $2N$ (minimal 4 and 6 for redundancy) coils. The proposed $N = 2$ configuration in the Feather-M2 magnet is shown in Figure 5.20. This remedies the problem that occurs when a coil is located on the cross-over of the quenching tape, because in this case at least 2 other coils are still located in the good position, providing redundancy. Calculated voltages of such a pick-up coil array (200 turns per coil) for the quench positioned in the layer jump, as described in Section 5.3.2 are presented in Figure 5.21. An accumulated voltage spike with an amplitude of a few mV per coil is found, 0.45 s prior to the Quench phase.

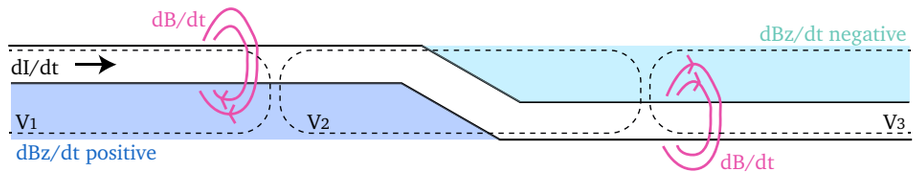


**Figure 5.19.** *Illustration showing the magnetic field around a strand and the proposed positioning of the pick-up coils. When the current in the tape changes, the pick-up coil labeled $V_1$ experiences a positive total flux change, the coil labeled $V_2$ experiences no total flux change and the coil labeled $V_3$ experiences a negative total flux change.*

The signal can be increased further by physically connecting the coils in anti-series that have a separation of half a twist pitch (i.e. every $N$ coils). This reduces the number of wires required and also counter-acts changes in the background field, which can be regarded as noise, from the signal. More coils located along the cable or coil pack

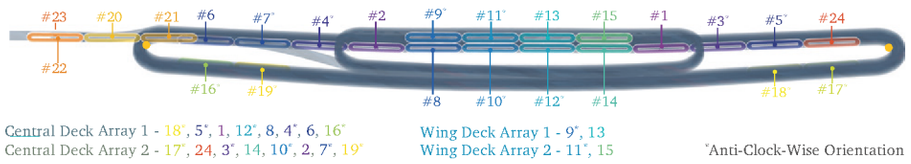


**Figure 5.20.** *Possible position of pick-up coils when integrated inside Feather-M2. The asterisk denotes anti-clockwise orientation with respect to the outside of the magnet, otherwise the coil is clock-wise.*

can be included in these sets to increase the sensitivity of the array. In the Feather-M2 magnet all coils located along the central deck are combined in two sets: Central Deck Array 1 (CDA1) and CDA2. The coils in the wing deck are combined into: Wing Deck Array 1 (WDA1) and WDA2 (each containing only 2 coils). The signals on these arrays are also shown in the plot by the dotted lines. The first voltage spike for CDA1, CDA2, WDA1 and WDA2 is now 15 mV, 30 mV, 8 mV and 5 mV respectively. Absolute values from the different arrays can be superimposed by the data acquisition system, to further increase the first peak to 50 mV. If this numerical prediction also proves to work in practice, this could be a valuable method for early detection of imminent quenches in ReBCO cables, resulting from fast and local heat deposition. Because the coils are not directly connected to the cable it is expected that noise levels are much lower than for voltage taps. To avoid picking up slow signals, such as current redistribution during ramping or the flux change due to the main field, a *high* pass filter with a cut-off frequency of a few hertz can be considered. The signals of the pick-up array depend on the duration of the Pre-Quench phase and thus on the operating current. As an example the signal on the CDA2 are given as function of time at different operating currents in Figure 5.22. All signals have an initial spike at the start of the graph.

### 5.3.5 Effect of the Position

In order to investigate if the pick-up coils can work independent of the origin of the quench, the current distribution and pick-up coil signals are calculated for a variety of quenches, starting at different locations in the Feather-M2 coil, shown in Figure 5.23. These locations are located on critical areas, such as the joints, the coil-ends and the layer jump, both on the inside and the outside of the coil. At each of these locations the normal zone is initiated using a heat pulse in a tape located either on the cross-over or in the stack.

The resulting MQE, the Pre-Quench phase duration, the Quench phase duration and pick-up array voltages for the initial spike are presented for all studied cases in Table 5.2. It can be seen that significant variation is present in the MQE. Lowest values are found at the inside of the coil-ends, locations 4 and 6, which can be explained by the misalignment of the conductor at these locations. This misalignment was unavoidable due to mechanical restrictions of the cable (see Section 2.3.4). The MQE for quenches that originate in the tape stack are generally lower than quenches orig-

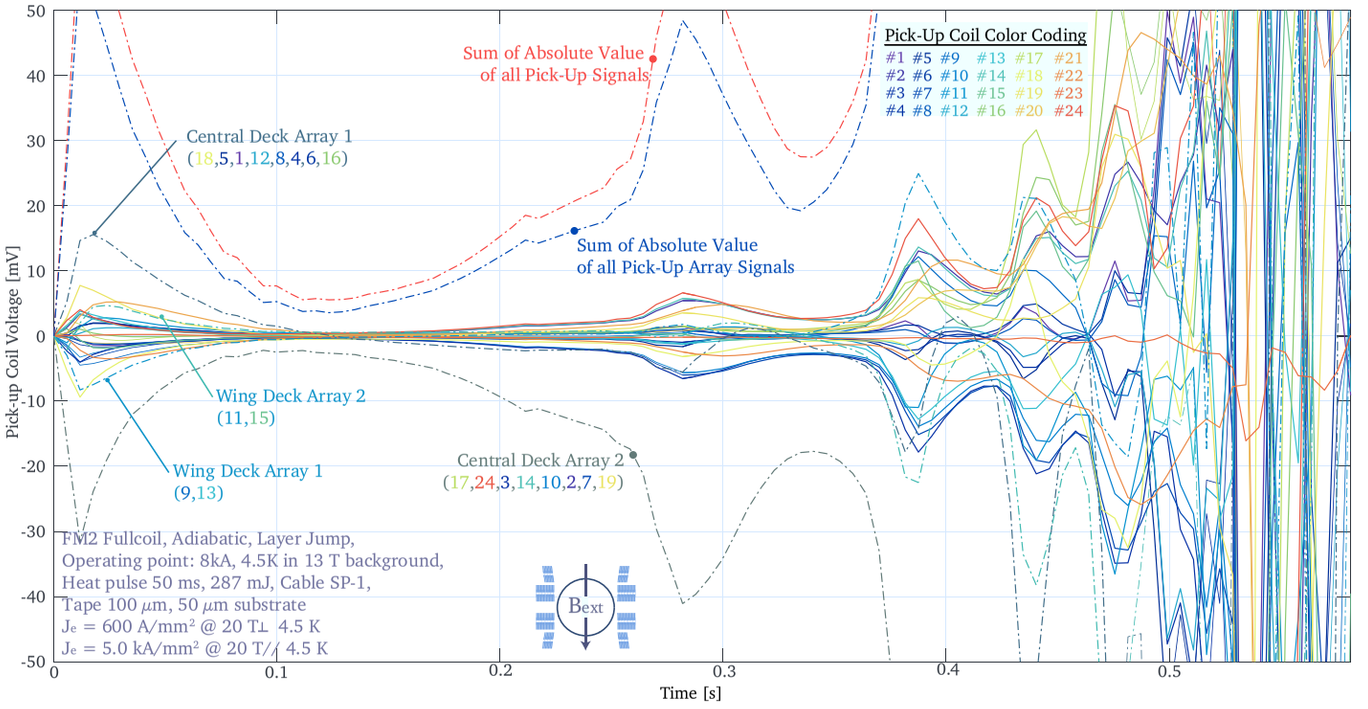


**Figure 5.21.** *Numerical prediction of the voltages over the pick-up coils in Feather-M2. The induced voltages are calculated from the time derivative of the currents. The color coding of the lines corresponds to the coloring of the pick-up coils in Figure 5.20. Because the screening currents are not included using this method, it is likely an over estimate. Further description of the quench can be found in Figure 5.6.*

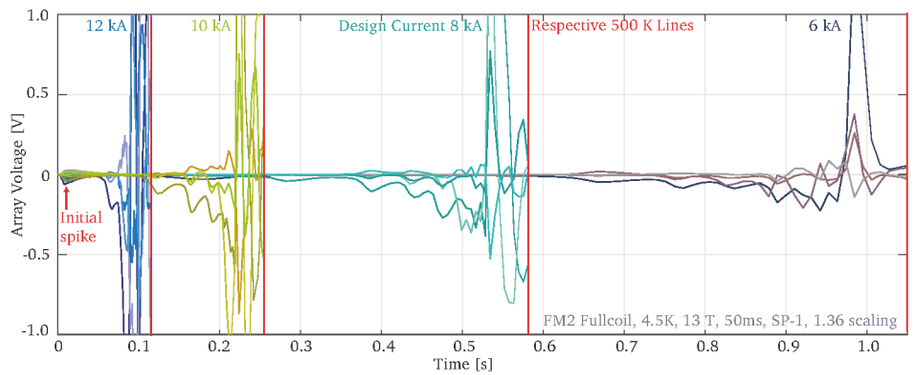


**Figure 5.22.** *Calculated signals from the Central Deck Array 2 at various operating currents for the Feather-M2 magnet operated in a* 13 T *background field at* 4.5 K.


**Figure 5.23.** *Normal zone origin locations used to study the effect of the location on the characteristics of the quench.*

inating on the cross-over. This is likely due to the heat from the initial quench being redistributed over two tapes instead of one. The quenches originating on the cross-over have a longer Pre-Quench phase. Because the normal zone propagates mainly in one direction, it takes longer to heat up the same number of tapes. The duration of the Quench phase, however, depends mainly on Ohmic heating and is nearly unaffected by the location. The signals on the pick-up array clearly depend on the distance of the quench origin from their location at the center of the coil. For the outer turns and layer jump the signals sometimes drop below 10 mV making them harder to detect. However, in these cases the coils located on the leads start picking up a strong signal. It is therefore recommended to place additional pick-up coils on the current leads in the Feather-M2.

In Table 5.3 the order in which the tapes quench and the corresponding times are presented. It can be seen that the normal zone almost always propagates to the neighboring tapes. In some rare cases a tape is skipped, but it can be seen that the timing is nearly simultaneous. The timing of the individual tape quenches seems to depend on many factors and is not clearly defined. In Figure 5.24 the current redistribution is given for some of the cases. It can be seen that the normal zones starting in the tape stacks propagate in a symmetrical manner. The shapes of the graphs are all different (note that the horizontal axis is not to scale), making it an interesting topic for further study.

TABLE 5.2.

ANALYSIS OF A LARGE VARIETY OF QUENCHES IN THE FEATHER-M2 COIL, AT VARIOUS LOCATIONS ALONG THE COIL-WINDINGS (SEE FIGURE 5.23), FOR HEAT PULSES IN BOTH THE CROSS-OVER (CR) AND THE TAPE STACK (ST).

| Case† | | Tape | Pos. | $I_{\text{cable}}$ | MQE | $t_{\text{pre}}$ | $t_q$ | $V^*_{\text{CDA1}}$ | $V^*_{\text{CDA2}}$ | $V^*_{\text{WDA1}}$ | $V^*_{\text{WDA2}}$ | $V_{22}$ | $V_{23}$ |
|---|---|---|---|---|---|---|---|---|---|---|---|---|---|
| | # | #(type) | [m] | [kA] | [mJ] | [ms] | [ms] | [mV] | [mV] | [mV] | [mV] | [mV] | [mV] |
| 1 | 1 | 5 (cr) | 0.06 | 8.0 | 1620 | 1124 | 31 | 9.94 | 7.59 | 1.41 | 0.86 | 1.23 | 35.9 |
| 2 | 1 | 1 (st) | 0.06 | 8.0 | 1000 | 611 | 27 | 6.47 | 6.40 | 0.68 | 1.07 | 1.85 | 27.5 |
| 3 | 2 | 1 (cr) | 0.91 | 8.0 | 309 | 614 | 30 | 4.39 | 4.39 | 0.69 | 0.86 | 0.53 | 9.37 |
| 4 | 2 | 5 (st) | 0.91 | 8.0 | 124 | 225 | 30 | 2.45 | 1.61 | 0.29 | 0.37 | 0.11 | 3.30 |
| 5 | 3 | 8 (cr) | 9.84 | 8.0 | 239 | 456 | 29 | 10.9 | 13.9 | 0.30 | 1.08 | 0.42 | 1.61 |
| 6 | 3 | 4 (st) | 9.84 | 8.0 | 101 | 457 | 30 | 6.24 | 7.81 | 0.73 | 0.20 | 0.21 | 0.94 |
| 7 | 4 | 1 (cr) | 19.6 | 8.0 | 55 | 322 | 28 | 2.04 | 20.6 | 0.92 | 0.78 | 1.79 | 0.09 |
| 8 | 4 | 5 (st) | 19.6 | 8.0 | 38 | 249 | 28 | 12.0 | 4.97 | 1.52 | 1.81 | 0.35 | 0.08 |
| 9 | 5 | 14 (cr) | 20.0 | 8.0 | 550 | 750 | 29 | 29.1 | 40.7 | 10.9 | 22.3 | 2.19 | 0.22 |
| 10 | 5 | 3 (st) | 20.0 | 8.0 | 225 | 306 | 32 | 33.9 | 14.4 | 17.8 | 11.0 | 2.93 | 0.26 |
| 11 | 6 | 6 (cr) | 20.6 | 8.0 | 73 | 452 | 32 | 14.1 | 17.2 | 1.16 | 10.9 | 1.11 | 0.06 |
| 12 | 6 | 2 (st) | 20.6 | 8.0 | 150 | 156 | 31 | 16.8 | 19.1 | 13.7 | 2.13 | 3.06 | 0.20 |
| 13 | 7 | 4 (cr) | 25.2 | 8.0 | 253 | 536 | 27 | 19.8 | 2.32 | 2.64 | 1.17 | 12.4 | 0.42 |
| 14 | 7 | 8 (st) | 25.2 | 8.0 | 141 | 416 | 29 | 1.51 | 14.7 | 0.15 | 1.56 | 3.87 | 0.13 |
| 15 | 8 | 14 (cr) | 25.9 | 8.0 | 1460 | 1297 | 49 | 9.30 | 15.0 | 6.57 | 6.82 | 55.5 | 2.89 |
| 16 | 8 | 3 (st) | 25.9 | 8.0 | 775 | 760 | 41 | 14.3 | 7.45 | 4.72 | 3.99 | 12.0 | 0.29 |

* The pick-up voltages are given on the arrays in Figure 5.20 for the first redistribution only.

† Locations for the quench origin as shown in Figure 5.23.

TABLE 5.3.

THE ORDER IN WHICH TAPES QUENCH AND THE TIME AT WHICH THE QUENCH OCCURS FOR THE CASES THAT ARE PRESENTED IN TABLE 5.2.

| Case | Order and Timing during Pre-Quench phase given in: Tape Index ([ms]) | | | | | | | | |
|---|---|---|---|---|---|---|---|---|---|
| # | #1 | #2 | #3 | #4 | #5 | #6 | #7 | #8 | #9 |
| 1 | 5(12) | 4(448) | 6(790) | 3(1040) | 7(1080) | 2(1110) | n.a. | n.a. | n.a. |
| 2 | 1(7) | 2(243) | 15(243) | 14(545) | 3(558) | 12(598) | 5(604) | n.a. | n.a. |
| 3 | 1(20) | 15(431) | 4(576) | 2(596) | 3(596) | 14(596) | 5(603) | 6(609) | n.a. |
| 4 | 5(30) | 4(174) | 6(174) | 3(191) | 7(191) | 8(196) | 2(204) | 9(212) | 1(217) |
| 5 | 8(20) | 7(366) | 9(406) | 6(416) | 10(441) | 5(451) | n.a. | n.a. | n.a. |
| 6 | 4(35) | 3(362) | 5(387) | 2(418) | 6(423) | 7(443) | 1(453) | n.a. | n.a. |
| 7 | 1(51) | 2(223) | 3(252) | 4(271) | 5(289) | 6(304) | 15(311) | 7(315) | 8(318) |
| 8 | 5(50) | 4(196) | 6(196) | 3(214) | 7(214) | 2(225) | 8(228) | 1(231) | 9(231) |
| 9 | 14(16) | 15(567) | 1(654) | 2(694) | 13(694) | 3(718) | 12(734) | 4(742) | n.a. |
| 10 | 3(18) | 2(187) | 4(187) | 1(244) | 5(244) | 6(269) | 15(269) | n.a. | n.a. |
| 11 | 6(40) | 5(330) | 4(375) | 3(400) | 2(420) | 7(420) | 1(430) | 15(440) | n.a. |
| 12 | 2(18) | 1(84) | 3(84) | 15(112) | 4(114) | 14(124) | 5(126) | 13(140) | 6(150) |
| 13 | 4(17) | 3(321) | 5(425) | 2(478) | 6(501) | 7(501) | 8(513) | 9(524) | n.a. |
| 14 | 8(23) | 9(314) | 11(365) | 10(374) | 5(383) | 7(388) | 6(393) | 12(393) | 4(411) |
| 15 | 14(14) | 13(688) | 15(715) | 1(1110) | 2(1220) | 12(1250) | 3(1270) | 4(1290) | 10(1290) |
| 16 | 3(8) | 2(315) | 4(315) | 5(655) | 1(664) | 6(722) | 15(722) | n.a. | n.a. |

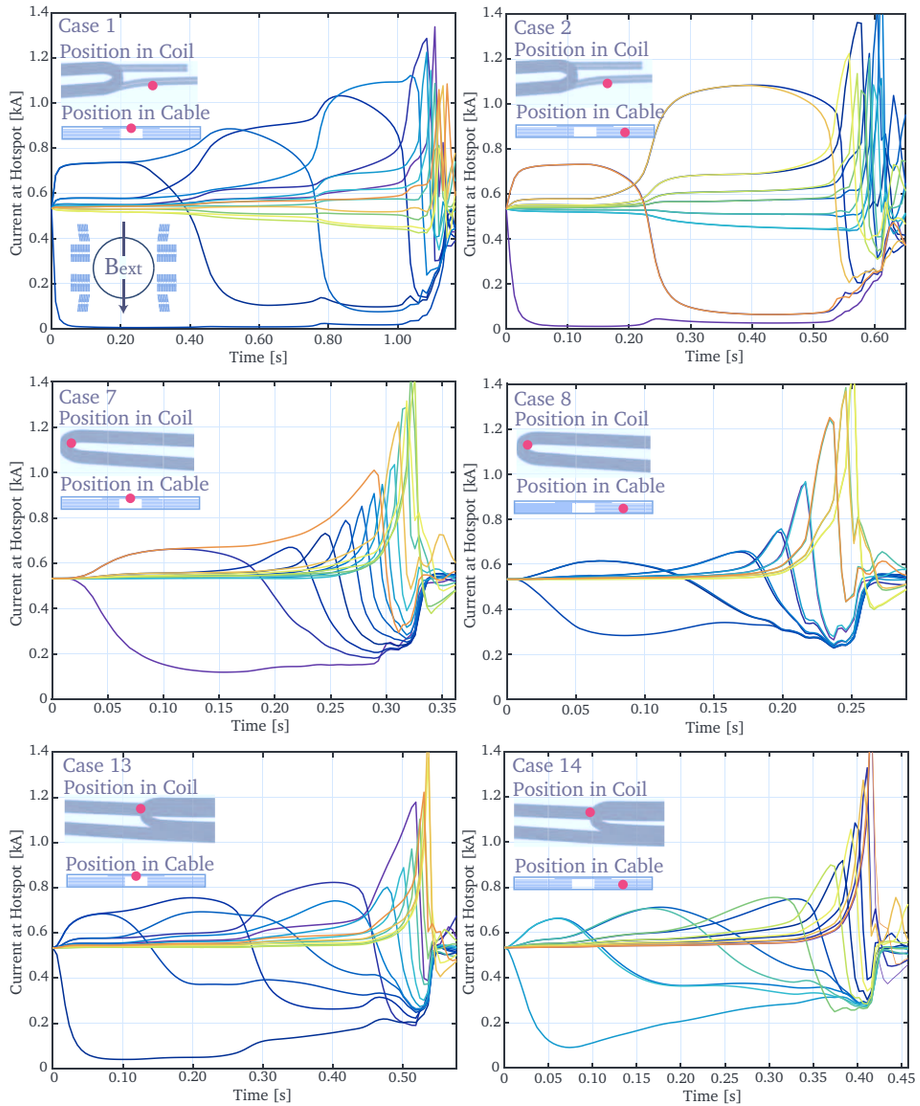


**Figure 5.24.** *Current redistribution for quenches at different origins throughout the Feather-M2 coil. The case indexes shown correspond to the cases shown in Tables 5.2 and 5.3. Note that the horizontal axises are not on the same scale.*

## Conclusion 5.4

Normal zone initialization and development into a full quench is studied in ReBCO Roebel cables and coils in detail with the Electro-Magnetic and Thermal Network Model described in Chapter 3. First a few initial benchmark tests were performed comparing the normal zone velocities and Minimum Quench Energies in a single tape with a previous experimentally validated one-dimensional model. Good agreement was found between the two models providing validation of the thermal part of the Electro-Magnetic and Thermal Network Model. It is found that when the surface of the tape is modeled as a two-dimensional surface, the normal zone very quickly spreads over the tape width due to current redistribution. This implies that in principle a one-dimensional tape model is sufficient to perform an adequate quench analysis.

Next a quench in a Roebel cable section consisting of a single transposition length was modeled, still using two-dimensional surfaces. To include the inductive load of the entire coil the mutual inductance matrices, containing the tape-to-tape mutual inductances of the Feather-M2 magnet, were included using additional elements at the end of each tape. It was found that three distinct phases can be identified in the development of a normal zone in a Roebel cable, which were named Thermal Drift, Pre-Quench and Quench. These phases are known to be present in classical LTS cables, but the network model predicts that they also occur in ReBCO Roebel cables and allows to study them in detail. Due to the much higher thermal margin, the duration of the Thermal Drift and Pre-Quench phases is much longer than in LTS, potentially providing means for early quench detection.

The Minimum Quench Energies were calculated both for the single tape and for the Roebel cable model. It was discovered that the single and multi-strand regime that were demonstrated to be present in LTS cables, are also evident in the simulation results of Roebel cables. The transition between the regimes, characterized by a kink in the MQE versus current plot, was found to depend strongly on the self-inductance of the coil. Above the transition the Minimum Quench Energies agreed perfectly with the single tape model. This observation provides additional validation of the thermal part of the Electro-Magnetic and Thermal Network Model.

During the Pre-Quench phase, current redistribution between strands plays an important role. However, modelling approaches that approximate the remainder of the coil using single elements that are only inductively connected through the tape-to-tape mutual inductances matrix, do not correctly account for current redistribution in this part of the coil. This means that the effective contact resistance is higher than in reality. To avoid this problem, the full geometry of the coil was modeled as well. To keep the number of elements in the model within acceptable levels the tapes were approximated using only a single element across their widths, an approach that was earlier proven to be acceptable for the single tape and cable section models. This allowed to demonstrated that in the full coil model the Pre-Quench phase was significantly longer than in the cable section model, likely due to the decreased effective resistance between the strands.

Also the current redistribution along the cable in the entire coil was studied dynamically. It was shown that the current does not directly redistribute over the joints as would be the case in a steady state solution. Instead the redistribution propagates along the cable as a wave. The voltage drop over the entire coil was found to be only a few mV during the Pre-Quench phase. The Minimum Quench Energy values in the full coil model were slightly higher than those calculated in the cable section model. This could be attributed to the difference in magnetic field angle between the models. The transition between single and multi-strand regimes was found to occur around 10 kA and 11 kA for Feather-M0 and Feather-M2, respectively. At an operating current of 8.0 kA and a temperature of 4.5 K, the Minimum Quench Energy for a quench on the layer jump was found at 287 mJ.

The calculations show that an HTS magnet is much more stable than an LTS one and therefore a quench due to transients is unlikely to occur when the magnet is operated at a safe margin. Nevertheless, several quench detection mechanisms were explored. It was necessary to differentiate between slow-global and fast-local heat deposition. The first type causes the Thermal Drift phase to be detectable as a local rise in temperature. This can be captured using various classical temperature sensors, but also, according to literature, optical fibers or SQDs may be an option. The second type causes the Thermal Drift phase to be short but involves a Pre-Quench phase during which the current redistributes between the strands in the cable. This current redistribution affects almost the entire coil and can be detected using either hall-probes or pick-up coils. The signals on these pick-up coils from the current redistribution in the magnet were calculated and it was shown how a series of voltage spikes provide means of early detection.

By optimizing the position of the pick-up coils around the coil and by combining their signals, the amplitude of the first spike could be increased to around 50 mV, which is detectable using conventional data acquisition systems. Using these detection techniques, an early warning of an impending quench can be feasible provided that sufficient margin with respect to the critical surface is maintained. Alignment of the tapes with the magnetic field is very useful in this respect. The type of quench and the corresponding effective detection methods need to be explored further experimentally, which is the primary goal of the Feather-M0 and Feather-M2 prototype cold tests. The time gained for the magnet protection could increase the limit on the operating current density for ReBCO coils significantly, which results in conductor-efficient very high-field coil cross-sections.

# Conductor Cost Optimized Coil Designs for 13 to 20 T

6

> "It is possible to commit no mistakes and still lose. That is not a weakness; that is life."
>
> Jean-Luc Picard, Star Trek: TNG, S02E21, 1989

*Optimized hybrid coil layouts for the magnetic field range of* 13 *to* 17 T *using Nb-Ti and* $Nb_3Sn$ *are presented. In addition a first survey is presented of solutions for reaching* 20 T*, using a ReBCO based High Temperature Superconducting insert. The optimization of the graded hybrid layouts is performed using a newly developed algorithm.*

## Introduction and Chapter Layout 6.1

For very high field superconducting accelerator magnets it is necessary to use a graded and hybrid layout in order to minimize the cost. However, optimizing such layouts is a non-trivial task. The magnetic field of the outsert-magnet can not simply be superimposed when used in an insert-outsert configuration. The insert increases the magnetic peak field on the outsert thereby reducing its critical current significantly. This means that the magnetic field magnitude and the optimal operating points need to be studied for the combination of the insert- and outsert-magnets. Before work on the Feather-M2 insert started (described in Chapter 2), a two-dimensional layout optimization algorithm was implemented [21]. This algorithm was used to perform a preliminary layout study for such hybrid accelerator magnet layouts. This algorithm is described in Section 6.2.

The algorithm was used to perform a preliminary layout study for graded hybrid coils reaching 20 T at 20% margin. Although some interesting observations were made it was concluded that there were too many unknowns concerning the design of the Aligned Block ReBCO insert. For example, knowledge on the feasibility of conductor alignment in the coil-ends, the effect of magnetization on the field quality and the quench detection and protection was very limited. Therefore, it was decided to focus first on the design of the Aligned Block Feather-M2 insert magnet, in order to revisit the 20 T layout study at a later time. The nevertheless interesting preliminary results of the 20 T survey are presented in Section 6.3.

The implemented algorithm was used to perform a study at the limit of the capacity of $Nb_3Sn$ conductor in the magnetic field range of 13 to 17 T. The results from this survey are presented in Section 6.4. This section can be regarded simultaneously as a study of the LTS outsert-coil for a 20 T magnet as well as a study for the FCC 16 T accelerator dipole magnets, not using an HTS insert.

## 6.2 Layout Generating Algorithm

*Before the layouts can be optimized towards, for example, cost, it is necessary to ensure that the layout is valid in terms of central magnetic field, load-line margin and field quality. For a multi-layer hybrid coil this is a non-trivial task. This section describes a new iterative algorithm for finding a valid coil layout through a systematic survey.*

### 6.2.1 Two-Dimensional Magnetic Field Evaluation

Fast two-dimensional calculation of the magnetic field at a set of target points is necessary, because during the optimization studies this operation is required hundreds of times. For the calculation of the magnetic field the winding domains are subdivided into infinitely long line elements pointing in the axial direction of the coil. Note that these elements are only a mathematical representation of the current distribution and are not to be confused with strands. The magnetic field contribution of each of these elements is then superimposed to calculate the magnetic field generated by the block. The elements for a block type domain are equally spaced throughout its surface, as shown in Figure 6.1. Therefore the current is equally distributed over all elements. The position and shape of the block domain is denoted by x-coordinates $x_1$ and $x_2$ and y-coordinates $y_1$ and $y_2$. The sector coil is subdivided in cylindrical coordinates (see Figure 6.1). This means that the current elements are equally spaced in radial direction and in azimuthal direction. For the distribution of the current there are three options:

1. The current is distributed equally over all the elements resulting in a radially graded current density. This is the current distribution used for a cosine-theta coil.
2. The current is scaled with the surface area represented by the element. This results in a homogeneous current density.
3. The current is distributed similarly as in 1 but is multiplied by cosine-theta, resulting in a perfect dipole field inside the sector. This is the current distribution used for a Canted Cosine Theta coil.

The position and shape of the sector coil is denoted by azimuthal coordinate $\varphi_1$, angle $\alpha$, and radii $r_1$ and $r_2$.

The winding domains can be automatically mirrored in the x-axis and anti-mirrored in the y-axis to create a dipole symmetry. The resulting quadrants are then numbered counter-clockwise from 1 to 4. The coil blocks in quadrants 1 to 4 can then be mirrored again in the y-axis and displaced to produce the second aperture. The quadrants of the second aperture are numbered clockwise 5 to 8. In the case of a dual aperture the shield coils (see Section 6.4.7) are mirrored positively in the y-axis and not mirrored to the other aperture but are displaced to the center of the coil system. Because of the symmetry, the calculation of peak fields, current densities and forces only needs to be performed in quadrant 1 for a single aperture and in quadrants 1 and 2 for a dual aperture layout.

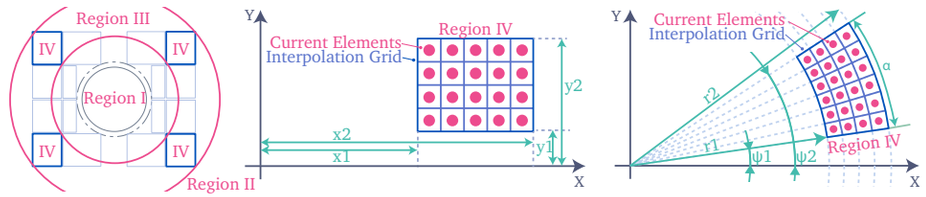


**Figure 6.1.** *Subdivision of the coil cross-section into computational domains (left) and the subdivision of the coil domains into infinite line currents for magnetic field calculation (right). In addition the interpolation grids used to avoid evaluation of the field close to the line currents are shown.*

To calculate the magnetic field generated by the line elements, the field contribution of each of the source elements must be calculated and summed at each target position. The relative position between the target and the source $\vec{r}$ is calculated as $\vec{r}_2 - \vec{r}_1$ (see Figure 6.2). The field in the azymuthal direction in a cylindrical coordinate system centered on the source $B_{theta}$ is then calculated as

$$B_\theta = \frac{\mu_0 I}{2\pi |\vec{r}|}, \qquad \text{Eq. 6.1}$$

where $\mu_0$ is the permeability of vacuum ($\mu_0 = 4\pi 10^{-7}$ Tm/A by definition) and $I$ is the current inside the element. The field at the target position in cartesian coordinates is then calculated as

$$\vec{B} = B_\theta \sin(\theta)\vec{e}_x - B_\theta \cos(\theta)\vec{e}_y, \qquad \text{Eq. 6.2}$$

where theta is the azymuthal component of the relative position calculated as $\theta = \arctan\left(r_y / r_x\right)$, $\vec{e}_x$ and $\vec{e}_y$ are the unit vectors in the $x$ and $y$ directions, respectively. This process is repeated for each source element. Because the field contribution of a source does not depend on the other sources, evaluation of the sum can be implemented using parallel code. The solenoidal component results in a magnetic field in the axial direction. In order to calculate this solenoidal field a Matlab based parallel implementation of SOLENO[9] is used [205].

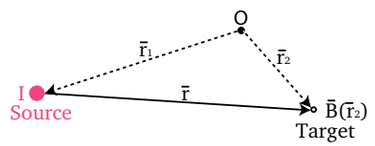


**Figure 6.2.** *Illustration showing the definition of parameters for the two-dimensional magnetic field calculation using the Biot-Savart Law.*

[9] SOLENO is a magnetic field and inductance calculation package developed at the University of Twente originally for excel by G. Mulder. Later, in 1999 it was upgraded by E. Krooshoop to improve the accuracy of the field calculation inside the winding packs. Now SOLENO is further improved using a multi-threaded MEX-function for Matlab.

Using Equations 6.1 and 6.2, close to a source elements the field becomes infinite. This unphysical result is present because the line elements have an infinite current density. To avoid the calculation close to the line elements when calculating the magnetic field inside the winding packs the field is first calculated on the intersections of the interpolation grid (see Figure 6.1), which lie exactly between the current elements [224]. The magnetic field at the required target points inside the coil domain is then calculated from the grid through two-dimensional linear interpolation. To check the validity of this method the calculated magnetic peak field was compared to values calculated by ROXIE [6], which is well established for magnetic field calculation. The difference found was less than 1%, which validates the used new algorithm.

When the magnetic field needs to be calculated at many points within the central or remote region it is much faster to evaluate the field using the harmonics expansion instead of evaluating the field of each source at each target. The harmonic expansions for the central and remote regions are described in Appendix B. When using the harmonics as intermediate step, the number of operations scales with $N_s + N_t$ instead of $N_s \times N_t$, where $N_s$ is the number of source line currents and $N_t$ the number of target points. This trick is essentially a highly simplified version of the Fast Multipole Method (FMM) described in Section 3.3.4. Note that the magnetic field within the coil-windings still has to be calculated by using (interpolated) Biot-Savart. To keep this region as small as possible the harmonics and field are evaluated separately for each block and its mirror images.

The magnetic field contribution of the iron can be calculated using the BEM-FEM algorithm from ROXIE [6]. The two-dimensional BEM-FEM requires as input the vector potential, resulting from the line elements, in the axial direction at the boundary nodes of the used mesh. The contribution of each element to the vector potential is calculated as

EQ. 6.3 $$A_z = \frac{\mu_0 I}{2\pi} \log(|\vec{r}|) .$$

Based on this input, the BEM-FEM algorithm outputs the magnetic field contribution at the specified target points, where it is superimposed with the magnetic field generated by the elements (Equation 6.2).

### 6.2.2 Model Structure and Nesting Conditions for a Graded Coil Layout

An object oriented structure is used, which was introduced into Matlab as of version 2008a, in the form of classes. A model of a coil containing multiple blocks and layers can then be represented by an hierarchical tree structure, as shown in Figure 6.3. At the root of the tree is a model object, which contains the optimization properties and methods. It also passes down magnetic field calculation commands to its layers, which are connected to it. In addition to the connected blocks, each layer also contains a superconductor object. This object allows the layer to compute the engineering current density at a certain magnetic field, temperature, operating point and field angle in the case of ReBCO. At the top of the tree there are all the coil blocks providing methods for

the computation of the magnetic field. Because there is a difference between the block and the sector coils, some of the methods are different and therefore, there are separate classes. The methods and properties that are the same for these two block/layer types, are implemented in so called super-classes. The blocks inside the layers are often labeled using the index of their respective layer and the position in this layer. For example, BL23 implies the third block, as counted from the mid-plane, in the second layer. This indexing is identical for both Cosine Theta and Block coils.

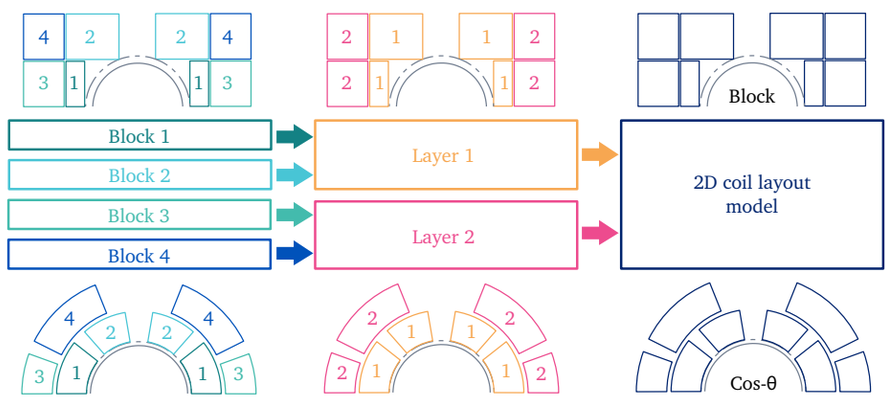


**Figure 6.3.** *Hiararchical tree structure used to manage all the coil-winding blocks in a two dimensional multi-layer layout.*

During optimization, the layer thicknesses $\delta_i$ and gap sizes $\delta_{\text{gap},i}$ are constantly updated. Therefore, after each step the position of the coil blocks inside the layers need to be updated. This is implemented in the so-called nesting function. Preventing the blocks from intersecting is trivial for a Cosine Theta coil, however, for a Block coil it is not. In order to place multiple layers of different type in one another, it is necessary to have all different types of layers behave in a similar way. For each layer a thickness $\delta$ and a gap size $\delta_{\text{gap},i}$ is specified. Based on these parameters and the diameter of the aperture, the nesting-function calculates the radius $R_i$ of each of the layers using

$$R_i = R_{\text{ap}} + \sum_{j=1}^{i-1} R_j + \delta_{\text{gap},j}. \qquad \text{Eq. 6.4}$$

For a Cosine Theta layer, the inner and outer radii of the blocks are set to $R_i$ and $R_i + \delta_{\text{gap},i}$, respectively. For a block coil layer inner and outer wall conditions are set, which determine how the $x_1$ and $x_2$ coordinates of the blocks interact with the circles at radii $R_{\text{in},i} = R_i$ and $R_{\text{out},i} = R_i + \delta_{\text{gap},i}$, for the inner and outer conditions, respectively. As an example, several of the available nesting conditions are shown in Figure 6.4. The available nesting conditions are:

1. *Wallin (WI)* - All walls are on a straight line fitting inside the circle. If set as inner condition $x_1 = \sqrt{R_{\text{in},i}^2 - y_{2,\max}^2})$ and if set as outer condition $x_2 = \sqrt{R_{\text{out},i}^2 - y_{2max}^2})$, where $y_{2\max}$ is the $y_2$ of the last coil block inside the respective layer.

2. *Wallout (WO)* - All walls are on a straight at the circle radius. If set as inner condition $x_1 = R_{\text{in},i}$ and if set as outer condition $x_2 = R_{\text{out},i}$.

3. *Radiusin (RI)* - The outer corners of all blocks are on the circle. If set as inner condition $x_1 = \sqrt{R_{\text{in},i}^2 - y_2^2})$ and if set as outer condition $x_2 = \sqrt{R_{out,i}^2 - y_2^2})$.

4. *Radiusout (RO)* - The inner corners of all blocks are on the circle. If set as inner condition $x_1 = \sqrt{R_{\text{in},i}^2 - y_1^2})$ and if set as outer condition $x_2 = \sqrt{R_{\text{out},i}^2 - y_1^2})$.

5. *Radiusout-sqe (ROe)* - Same as Radiusout with the exception of the the evenly numbered blocks which have the same $x_1$ or $x_2$ coordinate, for inner and outer conditions, as the previous block. This condition is used to ensure that a layer jump can be made between double decks.

6. *Radiusout-sqo (ROo)* - Same as Radiusout with the exception of the odd numbered blocks that have the same $x_1$ or $x_2$ coordinate, for inner and outer conditions, as the previous block (with exception of the first block which behaves normally). This condition is used to ensure that a layer jump can be made between double decks, where two of the decks are combined over the mid-plane.

7. *Beam-Pipe (BP)* - Same as Radiusout but with a minimum bending radius constraint on $x_1$. This condition can not be used on the outer wall and is usually only applied for the innermost layer.

8. *Moving (MO)* - Same as Wallout but with x-shift optimization that optimizes the magnetic field to be equal on the next layer. This condition can not be used as outer condition on the last layer.

9. *Smoothshear (SS)* - Smooth inner wall for Aligned Block coils, which sets $x_1 = x_{\text{prevblock}} + (y_2 - y_1)\tan(a_{\text{shear}})$, where $x_1 = R_{\text{in},i}$ for the first block. Can not be used as outer condition.

10. *Follow (FO)* - In the case of inner condition, $x_1$ follows the $x_2$ coordinate of the same block in the previous layer with offset x-shift. Can not be set as outer condition.

On top of these pre-set nesting conditions it also possible to, either manually or by using a steepest descent optimizer linked to a target, apply an x-shift of walls of individual blocks, thereby creating any layout possible. The quantity of conductor, and thus the magnetic field contribution, is now directly linked to the thickness of the layer. Therefore, the layout generator can treat each layer the same way. After each step in the optimization process the radii of the layers and the positions of the blocks are recalculated. In some cases blocks are omitted from a layer, allowing the block from the previous layer to span to the outer wall condition of the next layer (span2next).

This is often required when a $Nb_3Sn$ coil has layer of Nb-Ti at its core. All layouts are mirrored inside a 2-in-1 configuration. The spacing between the outer blocks of the two apertures is fixed at constant distance $d_{sep}$.

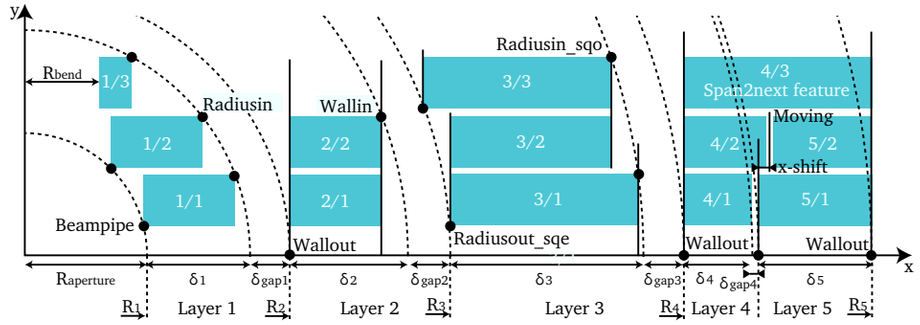


**Figure 6.4.** *Highly hypothetical coil layout demonstrating most of the different nesting conditions available in the layout generation algorithm. The numbers inside the coil blocks indicate the layer/block numbers.*

## Lorentz Force and Required Gap Size 6.2.3

In a high field magnet layout the Lorentz forces on the coil pack are significant and proper force containment is a challenge. This led to the idea of mechanically separating the insert coil from the outsert coil. The required wall thickness between the layers, in order to contain the forces is calculated from the total force exerted by the coil blocks on the wall. This feature can be enabled between layers to set the gap size, based on the yield strength of the material. If disabled the forces accumulate to the next layer, until the outer boundary of the coil is reached. To calculate the force acting on and generated by coil blocks the Lorentz force contributions of the line elements are summed. The force on a single current element can be calculated as

$$\vec{F} = \sum_{j=1}^{N_e} I_j \vec{\ell} \times \vec{B}_j, \qquad \text{Eq. 6.5}$$

where $\vec{F}$ is the total force in N/m, $I_j$ is the current in the line element $j$ in the block, $N_e$ is the number of line elements, $\vec{\ell}$ is the direction vector of the current and $\vec{B}_j$ is the magnetic field calculated at the position of element $j$. If the current only flows in the z-direction, i.e. $\vec{\ell} = \vec{e}_z$ the cross product can be simplified to

$$\vec{F} = \sum_{j=1}^{N_e} I_j B_{yj} \vec{e}_x - I_j B_{xj} \vec{e}_y. \qquad \text{Eq. 6.6}$$

The gap size between the insert and the outsert is the space which is available for mechanical structure to balance the Lorentz forces generated by the insert. The required

gap size can be estimated based on a maximum allowable stress inside the mechanical structure. First the Lorentz forces on the wall are calculated using Equation 6.6. For the stress equation there are several options available. The first option is to calculate the hoop stress from the Lorentz force as

Eq. 6.7 $$\sigma_{max} = \frac{W}{\delta_{\text{gap}}},$$

where $W$ is the total Lorentz force on the wall in $N/m$ calculated in the second quadrant only and $\delta_{gap}$ the width of the gap and thus the thickness of the wall (see Figure 6.4). This equation is mainly used for circular walls.

For straight walls, common in Block coil designs, a more advanced equation is needed. For a straight wall with thickness $d$ and length $L$, a distributed force $W$ is applied (see Figure 6.5). The distributed force $W$ in N is force from the insert coil blocks combined. A distinction between closed and open mid-plane outsert magnets is made, where the length of the wall and the distributed force is halved in the second case. The total stress is a combination of the shear stress and the stress caused by the moment. The shear stress $\tau$ at the edges of the wall can be calculated as

Eq. 6.8 $$\tau = \frac{W}{2\delta_{\text{gap}}}.$$

The stress caused by the moment, as illustrated in Figure 6.6, can be calculated in the wall as function of $y$ using [225, 226]

Eq. 6.9 $$\sigma = \frac{My}{I}, I = \frac{\delta_{\text{gap}}^3}{12}, M = \frac{WL}{12},$$

where $y = 0$ is defined as the mid-plane of the beam. The stress is highest at the surfaces of the wall. Solving for $\sigma$ at $y = -\delta_{\text{gap}}/2$ then gives the peak stress

Eq. 6.10 $$\sigma_{max} = -\frac{6M}{\delta_{\text{gap}}^2}.$$

The shear stress and the bending stress can then be combined using the Von Mises relation given as

Eq. 6.11 $$\sigma_{\text{vm}} = \sqrt{\sigma^2 - \sigma\tau + \tau^2} = \sigma_{\text{req}},$$

where $\sigma_{\text{req}}$ is the maximum allowable stress in the beam. Combining Equations 6.8, 6.10 and 6.11 gives

Eq. 6.12 $$\sqrt{\left[-\frac{6M}{d_{\text{gap}}^2}\right]^2 + \frac{6MW}{2\delta_{\text{gap}}^3} + \left[\frac{W}{2\delta_{\text{gap}}}\right]^2} - \sigma_{\text{max}} = 0,$$

which is solved implicitly for $\delta_{gap}$ using Matlab's *fzero* function to get the required thickness of the beam and thus the gap-size.

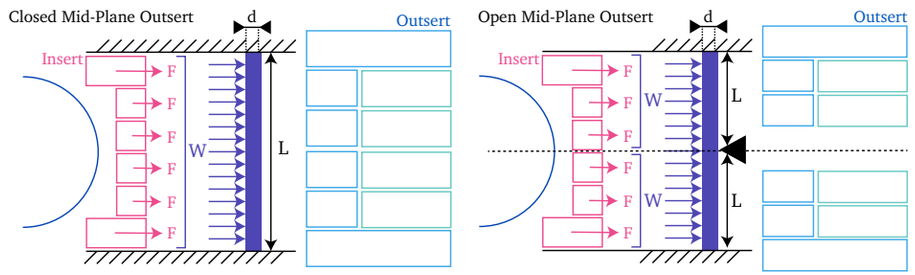


**Figure 6.5.** *Definition of the parameters for the analytical calculation of the required gap size between layers in order to keep the Von Mises stress, resulting from the coil Lorentz forces, within acceptable limits, while containing the forces. The difference between an open mid-plane and a closed mid-plane outsert configuration is shown.*

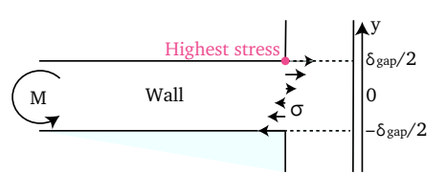


**Figure 6.6.** *Illustration showing the stress counteracting a moment applied on a fixed wall. Note that in the case described in this section, the wall is fixed at both ends.*

### Engineering and Overall Current Density 6.2.4

It is required to calculate the engineering current density of the coil blocks in order to calculate the operating current density. The critical current of the superconductor as function of magnetic field, temperature and magnetic field angle, in the case of ReBCO, is provided by the scaling relations given as $J_c\,(B, T, \theta)$ that are described for Nb-Ti, $Nb_3Sn$ and ReBCO in Appendix A. Because the critical current of the $Nb_3Sn$ conductor is still likely to improve in the future, it is scaled using an improvement factor $f_{Nb_3Sn}$, that can vary between 0.8 and 1.5, where the second number is the target for the FCC study.

For the LTS conductors the engineering current density of the strands in the cable is then given as $J_e(B, T) = J_c(B, T)/(1 + f_{cu2sc})$, where $f_{cu2sc}$ is the copper to superconductor ratio, which can be set at a fixed value, or can be calculated using the quench model described in Section 6.2.5. In the coil block the overall current density $J_{ov}(B, T)$ is defined by by the void and insulation factors, $f_{void}$ and $f_{insu}$, which are set to 0.2 and 0.1 respectively unless stated otherwise. The overall current density is then calculated as $J_{ov}(B, T) = (1 - f_{void} - f_{insu})J_e$. The Low Temperature Super conductors in this work are assumed to operate at 80% on the load-line, $f_{load} = 0.8$, unless stated otherwise. The resulting approximate temperature margins are 2 K and 4 K, for the Nb-Ti and $Nb_3Sn$ respectively. This means that the operating current density is calculated as $J_{op}(B, T) = f_{load}J_{ov}(B/f_{load}, T)$.

For ReBCO coated conductor a layer thickness of 2 $\mu$m was assumed for the fit. To get the engineering current density of the tape, the critical current is multiplied by the thickness of the tape divided by the thickness of the superconductor. Using a linear scaling factor $f_{\mathrm{ReBCO}}$ the engineering current density $J_{\mathrm{e}}(B, T, \alpha)$ is scaled to 600 A/mm$^2$ at 20 T perpendicularly applied magnetic field and a temperature of 4.5 K. The void and insulation fraction in the Roebel cable are set at 0.2 and 0.1. The load-line critical surface intersection is performed for each computation node in the computation grid (see Section 6.2.1), after which the lowest current is selected, as described for the Feather-M2 magnet in Section 2.3.1. The operating current for ReBCO coated conductor is taken at 70% on the load-line, resulting in a thermal margin between 20 and 50 K.

### 6.2.5 Quench Model and Copper to Superconductor Ratio

In order to control the peak temperature, an adiabatic quench model is applied. Based on its results, the copper to superconductor fraction is adjusted such that the peak temperature is a fixed value, usually set to 200 K unless stated otherwise. The model is essentially the same as described in Section 2.4.3. In the model the multiple coil layers are connected in series. A common a detection trigger level of 100 mV is used. The voltage growth over the normal zone is derived from the normal zone propagation velocity, which is calculated using an analytical equation [3, 4]. After the quench is detected a 20 ms validation time is used. After the validation another 40 ms is taken into account for activation of the protection heaters, which heat up 80% of the coil-windings over the critical temperature. The RRR of the copper is set to 150. In the future a CLiQ [91] system should be seriously considered in order to achieve considerably faster response times.

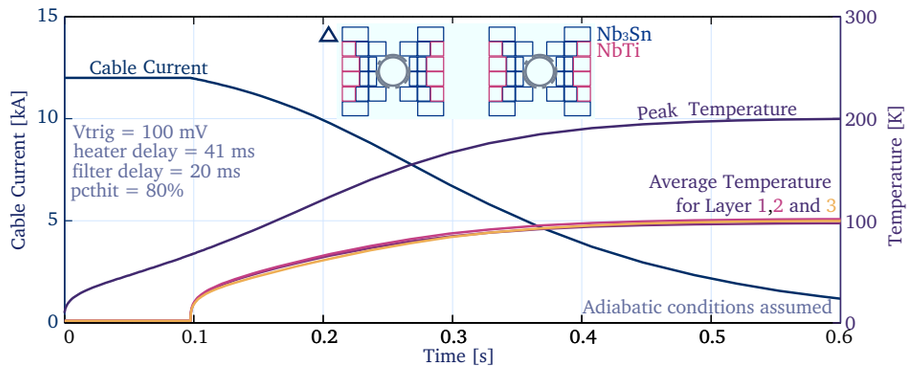


**Figure 6.7.** *Peak temperature and current decay for a characteristic quench in a thermally optimized* 16 T *layout, shown in the axis, with graded $Nb_3Sn$ and Nb-Ti. The peak temperature is* 200 K *and the bulk temperatures are equal for the three layers. The copper to superconductor fractions of the layout are about* 0.7, 2.5 *and* 1.6, *for the low current density $Nb_3Sn$ conductor, the high current density $Nb_3Sn$ conductor and the Nb-Ti conductor respectively.*

The required coil self-inductance per meter is calculated from the energy stored in the self- and mutual inductances between the line elements (iron if present is ignored). Based on the calculated peak $T_{\text{peak}}$ and bulk temperatures $T_{i,\text{bulk}}$, the copper to superconductor fraction is set such that the average temperatures between the layers are equal and the peak temperature is at a pre-set value of usually 200 K. A lower limit of 0.6 is used for the copper to superconductor fraction, to stay within bounds for strand manufacturers. The calculated temperature transients for a characteristic quench in a Block coil of 3 layers at 16 T with a 20% margin is shown in Figure 6.7. With the quench model enabled, the current density in the outer layers is suppressed and in the inner layers is increased, thereby reducing the advantages of grading with many layers.

### Iterative Layout Convergence Algorithm 6.2.6

The iterative algorithm requires a starting layout as input, which is then converged to a layout that is valid in terms of load-line margin and magnetic field quality and other constraints. The advantage is that in this case, since the number of variables and targets are equal, a single converged solution exists. Outside the iterative algorithm a real optimizer can be used to find, for example, the optimal distribution of magnetic field contribution over the layers. This can be a steepest descent optimizer, a genetic algorithm or just a plain pattern search. The cost optimization algorithm calls the iterative cycle many times, with slightly different input models and parameters, in order to generate a large set of layouts, which are all stored for comparison at a later time. In the future the combination of the iterative cycle and the conductor cost optimizer can be replaced using a multi-objective optimizer, using exact-achieve targets. This option requires further investigation beyond the scope of this thesis.

The starting layout basically is a rough sketch of the coil and does not necessarily need to meet any requirements. It contains geometric settings such as the type of the layers, the nesting conditions, the aperture size, the hight and angles of the blocks, but also contains targets and variables for the magnetic field quality and angle optimizations. The initial values set for the layer thickness and gap sizes have to be in a realistic range. The iterative algorithm itself is presented in the form of a flow chart in Figure 6.8. To stabilize the convergence of the algorithm a damping factor $f_{\text{damp}}$, with a value between 0.2 and 0.4 is applied. The main steps in the algorithm are then:

1. *Set Current Density* - The current density is set such that the layer generates exactly the required magnetic field (no damping).

2. *Calculate Overall Current Density* - The overall critical current density $J_{ov}$ is calculated using the peak magnetic field, calculated on the nodes of the interpolation grid (see Section 6.2.1) and the operating temperature, using the scaling relations and load-line settings explained in Section 6.2.4.

3. *Scale Layer Thickness* - The layer thickness is scaled using the set current density and the calculated overall current density using $\delta_{new} = \delta_{\text{old}}(f_{\text{damp}}\,(J_{\text{set}}/J_{\text{ov}} - 1) + 1)$.

4. *Set Gap Size* - For the layers which have to contain their own force, the required gap width is calculated based on the forces exerted by the coils and the maximum stress in the support structure following the steps in Section 6.2.3.

5. *Redistribute Breq* - Redistributes the required field over the layers such that the thicknesses of pre-set groups of layers becomes equal. This is useful, for example, in a double layer Cosine Theta coil, in which the cable width is constant.

6. *Optimize Moving Walls* - Shifts the position of moving boundaries between layers consisting of block coils to minimize the variation of field magnitude over the blocks. These shifts are performed such that the total area of the coil domains does not change.

7. *Optimize Field Quality and Aligned Block Angles* - Optimizes a predefined set of variables and targets using a Matlab built-in optimizer. This function can for example be used to minimize certain field harmonics or maximize the current density by adjusting the shear angle of the blocks in an Aligned Block coil. The variables and targets can be subdivided in groups such that they are not all optimized at once. If the number of variables is equal to the number of targets, a unique solution is found.

8. *Set Copper to Superconductor Fractions* - Set copper to superconductor fractions according to the quench model described in Section 6.2.5.

9. *Check Convergence* - If the change of the geometry is less than 0.001% on all parameters, convergence is reached, and the model is output, otherwise all the steps are repeated.

After each of these steps the layers are re-nested to keep the layout of the magnet organized (see Section 6.2.2). Converging a single layout, without iron, can be performed within a few minutes and thus allows for external optimization.

## 6.3 Designs for 20 T using a ReBCO insert

*In this section a preliminary survey for graded hybrid* 20 T 20% *margin layouts is presented. This survey was performed before the layout study using only Nb-Ti and* $Nb_3Sn$.

### 6.3.1 Overview

The survey comprises a large set of combinations of inserts and outserts, which are compared and presented for ReBCO in Figure 6.9. Each data point in the figure represents a two dimensional dual aperture coil layout. A selection of these layouts is presented in Figure 6.10. The cost of the layouts is based on a cost ratio of 1 to 4 to 16 for the Nb-Ti, $Nb_3Sn$ and ReBCO, respectively. Note that this ratio is a far future prediction and is different from survey presented in Section 6.4. In this initial survey the copper to superconductor ratio was not adjusted using the quench model, because it was at

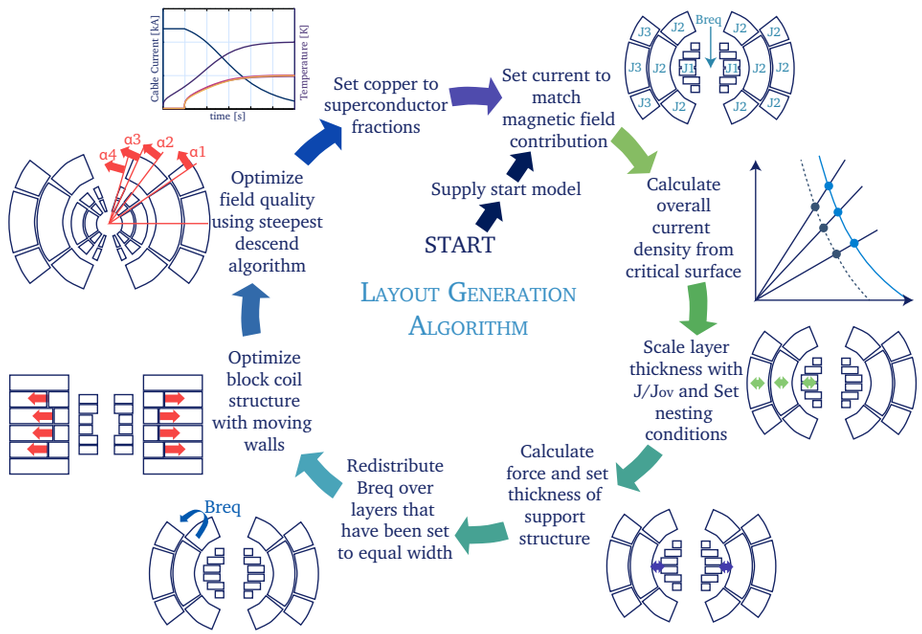


**Figure 6.8.** *Flow chart explaining the various steps of the iterative layout generation algorithm, which ensures that the output layout meets the design rules.*

the time unknown how to protect the ReBCO insert part. Through a pattern search, the magnetic field contribution between layers and in some cases the height and angles of the coil blocks, are optimized towards lower total conductor cost (horizontal axis) and smaller aperture separation distance (vertical axis). The data points, representing each family, then form a so-called Pareto front [227] on which the optimal designs lie. The fronts show that the most cost efficient layout is usually not the smallest layout. These type of plots can be made for different sets of variables allowing for a more in depth study.

The layouts based on a ReBCO insert show a large spread regarding total conductor costs. This spread can be explained by the strong anisotropy of the conductor. A small amount of extra current density in the insert has a large effect on the cost of the total magnet. A higher critical current density in the insert can be achieved when the tapes are aligned with the magnetic field lines (see Section 1.3), resulting in the Aligned Block layout. The Aligned Block insert coils are optimized taking into account the magnetic field of the outsert. Therefore, the outsert coils are higher than in other designs. This can be accomodated using an open mid-plane, see Section 6.3.2. The Aligned Block insert is followed by the inserts based on block that have partial alignment usually within 30 deg. For the outsert it is more cost effective to use a Block than a Cosine Theta, because in the preliminary study the Block is hybrid and the Cosine Theta is not.

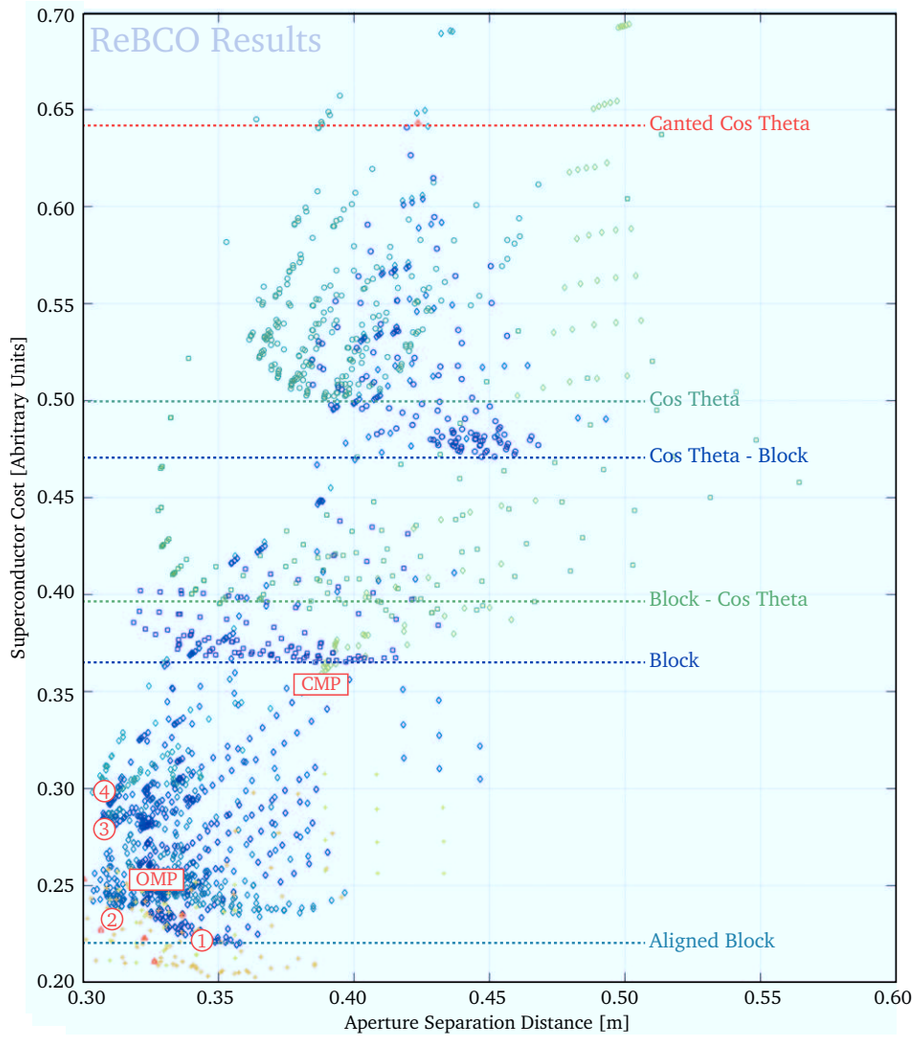


**Figure 6.9.** *Overview of showing all the layouts in the* 20 T *survey as data markers on a scatter plot comparing the conductor cost and the aperture separation distance.*

The Block insert coil is followed by the Cosine Theta insert coil, which has perpendicular magnetic field on the mid-plane, causing its current density to be significantly lower and thus much more material is needed for the magnetic field. Here also a graded Block outsert is more efficient than a non-graded Cosine Theta outsert. The least effective design is the Canted Cosine Theta, because it has both perpendicular magnetic field on the mid-plane and a reduced filling fraction of superconductor due to the ribs.

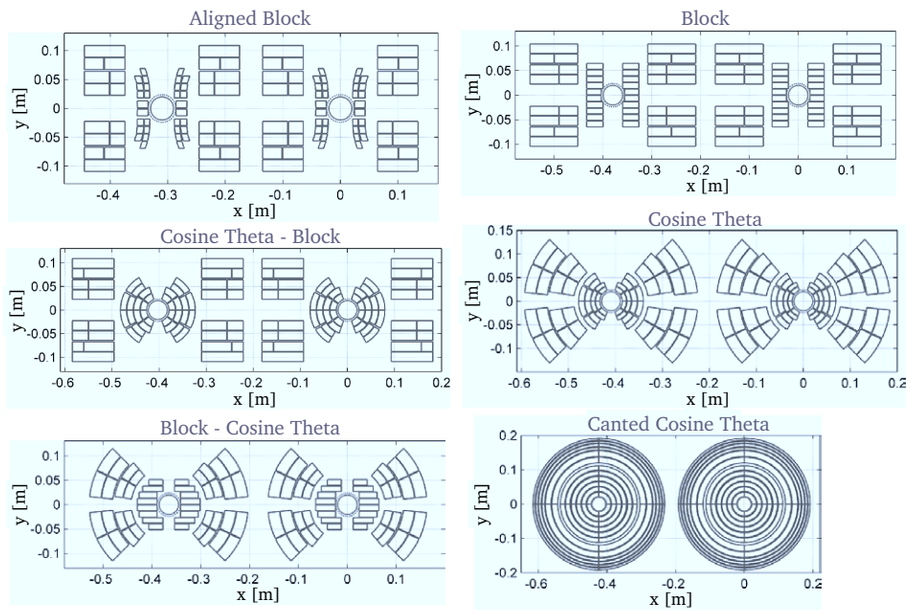


**Figure 6.10.** *Selection of layouts from the* 20 T *ReBCO survey (also see Figure 6.9). Note that the chosen axis limits are different for each layout.*

From the survey it also has become clear that the Aligned Block HTS insert preferably contributes about 7 T and the outsert about 13 T to the 20 T desired magnetic field in the aperture. This ratio is different from the 5 to 15 T ratio found by [53], because of the alignment of the conductor. It is also found that when the critical current density of the ReBCO improves, something that is likely to happen in the future (see Section 5.1), the ratio shifts towards the ReBCO. One layout that should be considered in the future is ReBCO with a Nb-Ti outsert, without $Nb_3Sn$. For such a layout it is likely that only the inner, high magnetic field, part of the ReBCO is aligned with the magnetic field. The outer part is then needed to provide background magnetic field. This can be taken to the extreme using only ReBCO, partially aligned at the high magnetic fields. This would also allow operation at higher temperatures.

### Open and Closed Outsert Mid-Plane 6.3.2

In addition it was found that an Open Mid-Plane (OMP) outsert results in a lower conductor cost than a Closed Mid-Plane (CMP) one. The latter provides additional space for the support structure to keep the forces in the insert contained. The wall separating the insert from the outsert can then be supported on the mid-plane causing its effective length to be more than halved. This reduces the required wall thickness around the insert, allowing the separated outsert-coils to be located closer to the aperture (also

refer to Section 6.2.3). This counteracts the reduction of efficiency resulting from not having conductor on the mid-plane and in some cases results even in a slightly more cost effective layout. Additional advantages are that the open mid-plane allows the LTS outsert-coils to become flat racetracks and therefore do not require flared coil-ends and that the relatively sensitive LTS outsert-coils are less exposed to the synchrotron radiation, which is strongest on the mid-plane. The mechanical structure of the magnet can then consist of a strong and rigid mid-plane piece, surrounding the beam-pipe, acting as a reference, onto which all the other components are placed.

### 6.3.3 Outsert Grading

Grading is useful when conductor performance is not limited by the quench model. This becomes the case when the conductor is pushed towards its limits, causing the operating current density to fall bellow 300 A/mm$^2$. If the current density of the entire coil is then determined by the peak field located on the inner part, as would be the case in a non-graded coil, the design becomes very inefficient. Different levels of grading in the outsert magnet are shown in Figure 6.11. The encircled numbers in Figure 6.9 correspond to the layouts in the plot. When the level of grading is increased, generally the conductor cost will decrease. However, due to the presence of extra internal splices, as well as application of various coil-winding, heat treatment and impregnation techniques, the complexity, risk and cost of coil-winding tends to increase. This implies that a compromise between cost reduction and increased complexity is to be determined.

## 6.4 Optimized Hybrid Nb-Ti and $Nb_3Sn$ Coils for 13 to 17 T

*A layout survey is described for dipole magnets at the magnetic field limit of the $Nb_3Sn$ conductor. This survey can simultaneously be regarded as a study for the outsert-coil of a* 20 T *magnet and as a study for the* 16 T *dipole magnets for the FCC.*

### 6.4.1 Studied Layout Options

In order to find a consistent set of layouts, which are in theory all technically feasible, the iterative algorithm described in Section 6.2.6 is employed. A large collection of different input models is applied. An overview of the input models is provided in Table 6.1, in which the nesting conditions, layer types and special features are outlined. The indexes in the table are used throughout this section to label the corresponding data markers in the plots. The magnetic field contribution from the iron yoke is omitted from the study, except in Section 6.4.7, describing the effect of the yoke separately. For all layouts the aperture diameter is set at 50 mm following the FCC requirements, unless stated otherwise. The separation distance between the outer coil layers of the two apertures is set at 80 mm. This is an arbitrary choice and needs to be reconsidered, based on cross-talk between the coils and whether it is possible to compensate either

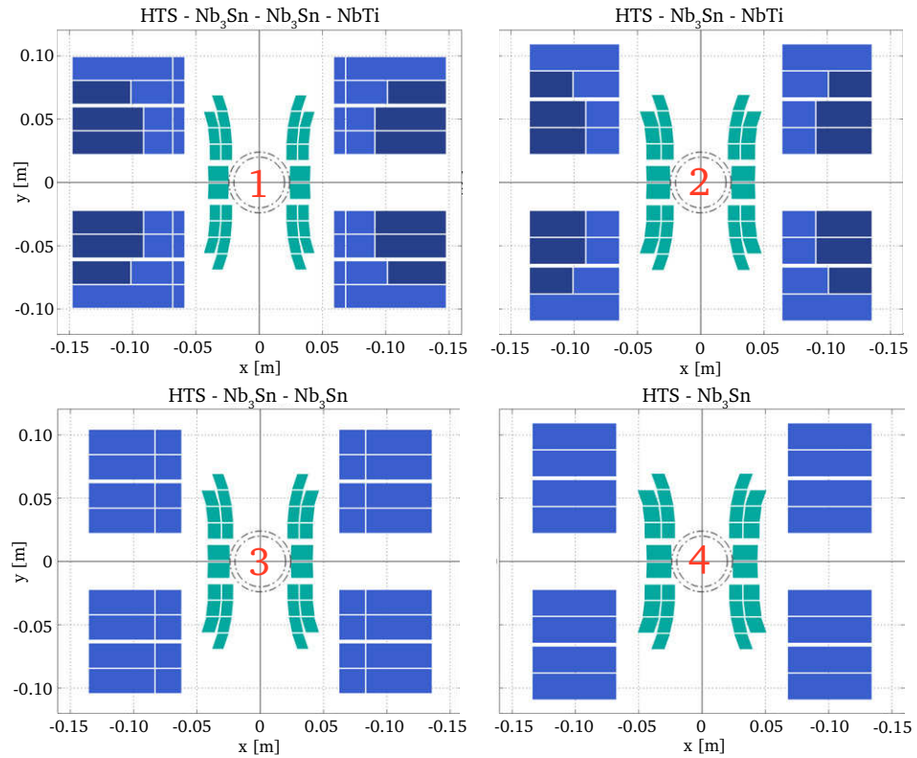


**Figure 6.11.** *Different levels of grading in an Aligned Block insert and Block outsert magnet. The effect on the cost is shown in Figure 6.9, where the layouts are represented by the numbers* 1-4.

by shifting coil blocks anti-symmetrically or by using shim coils, as described in Section 4.5. The quench protection times for setting the copper to superconductor ratio are described in Section 6.2.5. The conductor scaling relations for Nb-Ti and $Nb_3Sn$ are as given in Section 6.2.4, where the improvement factor for the $Nb_3Sn$ is $f_{Nb_3Sn}$, is included in the parametric study.

The height or angle of the winding blocks, for the Block and Cosine Theta coils, respectively, and the distribution of magnetic field between the layers, is controlled by the external conductor cost optimizer, which in this case is a pattern search algorithm. The cost of the layers is approximated per unit volume based on practical superconductor. The volumetric cost ratio between the Nb-Ti and $Nb_3Sn$ is taken as 1 to 10 [228]. The calculated conductor cost is then normalized with respect to the optimal 50 mm aperture, 16 T, 1.9 K, 20% margin, 200 K peak temperature at quench and $f_{Nb_3Sn}$ Block layout with index 9. The scaling of the conductor cost with the improvement factor is assumed negligible. Note that potential risk factors resulting from heat treatment, internal splices and complexity are not included in the cost model. Each layout has

TABLE 6.1.
DIFFERENT LAYOUTS THAT WERE INCLUDED DURING THE 16 T LAYOUT SURVEY.

| idx | Type* | Grading | Config | Layout † | Special Features |
|---|---|---|---|---|---|
| 1 | BL | non | 2 deck | BP-BL-WO | - |
| 2 | BL | non | 3 deck | BP-BL-WO | - |
| 3 | BL | $Nb_3Sn$ | 2 deck | BP-BL-WO-BL-WO | - |
| 4 | BL | $Nb_3Sn$ | 3 deck | BP-BL-WO-BL-WO | - |
| 5 | BL | $Nb_3Sn$ | 3 deck | BP-BL-WO-BL-WO | BL13 removed |
| 6 | BL | $Nb_3Sn$,Nb-Ti | 2 deck | BP-BL-WO-BL-MO-BL-WO | - |
| 7 | BL | $Nb_3Sn$,Nb-Ti | 2 deck | BP-BL-WO-BL-MO-BL-WO | BL22 spans next |
| 8 | BL | $Nb_3Sn$,Nb-Ti | 3 deck | BP-BL-WO-BL-MO-BL-WO | BL23 spans next |
| 9 | BL | $Nb_3Sn$,Nb-Ti | 3 deck | BP-BL-WO-BL-MO-BL-WO | BL13 removed, BL23 spans next |
| 10 | CT | non | 4 layers | RI-CT-RI(4X) | all layers same current density |
| 11 | CT | $Nb_3Sn$ | 2 layers | RI-CT-RI(2X) | - |
| 12 | CT | $Nb_3Sn$ | 3 layers | RI-CT-RI(3X) | - |
| 13 | CT | $Nb_3Sn$ | 4 layers | RI-CT-RI(4X) | - |
| 14 | CT | $Nb_3Sn$,Nb-Ti | 4 layers | RI-CT-RI(4X) | BL31 and BL41 are Nb-Ti |
| 15 | CCT | $Nb_3Sn$ | 6 layers | RI-CCT-RI(6X) | - |

*CT = Cosine Theta, BL = Block, CCT = Canted Cosine Theta.
† Nesting conditions and abbreviations are presented in Section 6.2.2.

a $B_3$ harmonic component that is zero, which is achieved in the Block coil by moving the $x_1$ of BL12 and BL13 (if existent) simultaneously. For the Cosine Theta the field quality is achieved by moving $\varphi_2$ of the last block of the first layer. The angles of the remaining layers are cost optimized.

### 6.4.2 Effects of Magnetic Field and Operating Temperature

Under study is the effect of the magnetic field in the aperture and the operating temperature on the conductor cost. The choice of magnetic field is important because it is in essence a trade-off with the diameter of the accelerator ring, as described in Section 1.1. The temperature is important because it determines the critical current density of the superconductor and thus the required conductor volume to reach a certain magnetic field. At lower operating temperature the critical current increases, but also the cooling cost, resulting in another trade-off.

In Figures 6.12 and 6.13 the normalized conductor cost for realizing a design is shown versus the magnetic dipole field strength for $Nb_3Sn$ improvement factors $f_{Nb_3Sn}$ that are in the range of 0.8 to 1.5, at operating temperatures of 1.9 and 4.5 K, respectively. The magnetic field at a fixed margin of 20% can be translated directly to a margin at a fixed magnetic field, in this case 16 T. For example, a 16 T magnet with 11.7% margin has the same cost as a 14.5 T magnet with 20% margin. The 20% margin is kept here as a baseline, since in the LHC it has been shown that above this point the magnets start to train significantly [229], making it difficult to operate an entire accelerator. The training is likely related to the transition between the multi-strand and single-strand

regimes in cable stability [94] (in thesis also shown to exist in HTS, see Chapter 5), that occurs at about 80% on the load-line, and is therefore difficult to circumvent. Since at high magnetic field the margin is very costly, further study on magnet training could be vital.

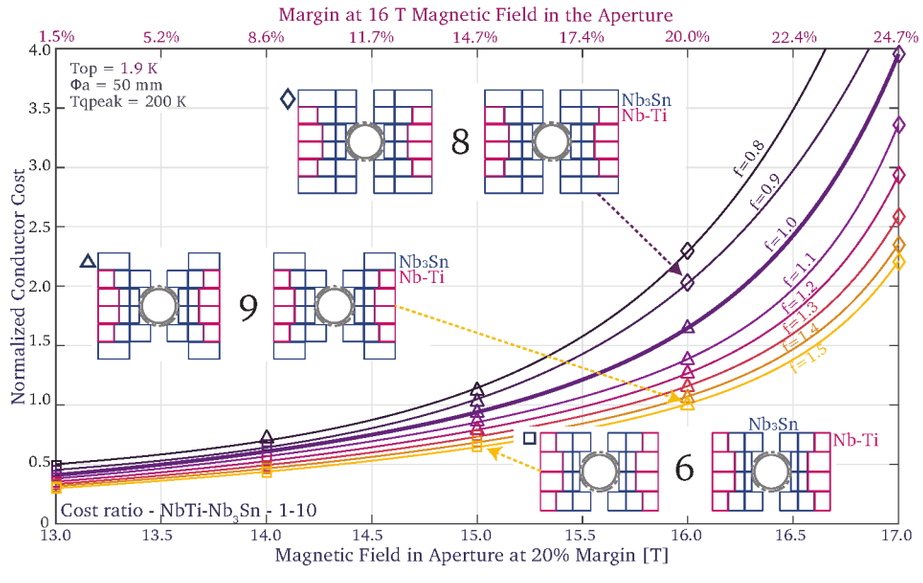


**Figure 6.12.** *Normalized conductor cost for fully graded Block coils (reproduced from [21]) operated at* 1.9 K*, versus the central magnetic field at a margin of* 20% *(bottom axis) or versus the corresponding margin at a central field of* 16 T *(top axis). The numbers* 6*,* 8 *and* 9 *inside the layouts correspond to the indexes of Table 6.1. The aperture size is* 50 mm *and the peak temperature at quench is* 200 K.

For convenience both, magnetic field at a fixed margin of 20% and margin at fixed magnetic field of 16 T, are shown on the horizontal axis at the bottom and at the top of the plot, respectively. The results are shown for the Block coil, but for the Cosine Theta coil the results are similar. All layouts in the plots comprise two layers of $Nb_3Sn$ and one layer of Nb-Ti and can exhibit 2 or 3 decks. It is found that different types of layout are optimal for different sets of input parameters. At 1.9 K the 16 T, 20% margin layouts all consist of three decks (per quadrant), although at higher $f_{Nb_3Sn}$ it is possible to omit the third block of the first layer (BL13), while maintaining magnetic field quality using the second block of the first layer (BL12). This is no longer possible for lower values of $f_{Nb_3Sn}$ without violating the minimal bend radius constraint in the Beampipe wall condition in the first layer. At lower magnetic fields it becomes more optimal to use a two deck layout and at higher magnetic fields the option in which BL13 is removed is no longer feasible.

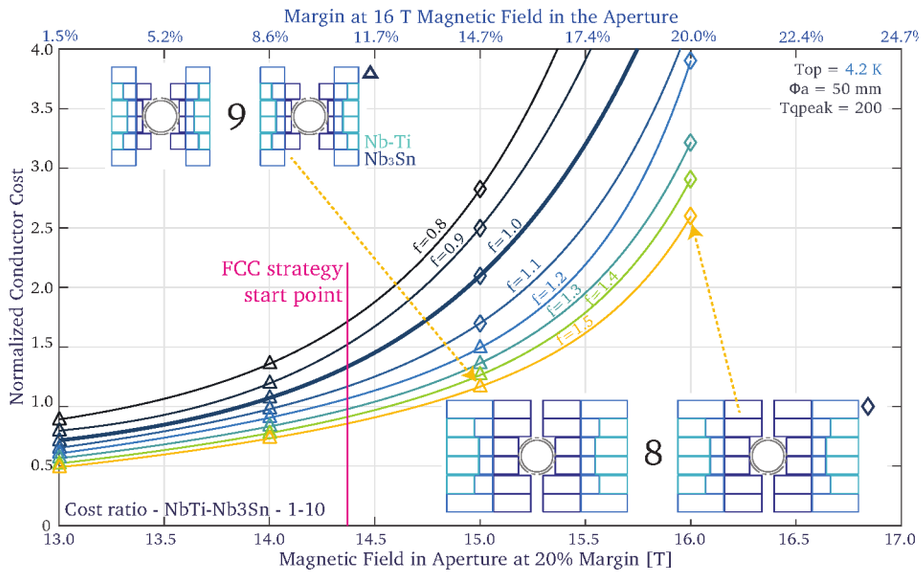


**Figure 6.13.** *Normalized conductor cost for fully graded Block coils (reproduced from [21]) operated at* 4.5 K*, versus the central magnetic field at a margin of* 20% *(bottom axis) or versus the corresponding margin at a central field of* 16 T *(top axis). The* 8 *and* 9 *inside the layouts correspond to the indexes of Table 6.1. The aperture size is* 50 mm *and the peak temperature at quench is* 200 K.

When comparing Figures 6.12 and 6.13, between 1.9 and 4.5 K, a 1.2 T or 7% margin shift is observed. Causing 17 T 20% margin magnets to become impossible and 16 T 20% margin magnets to become very expensive. Also the layout types are shifted by about 1.2 T causing the border between 2 and 3 decks to be around 14.5 T. The current density improvement factor $f_{\mathrm{Nb_3Sn}}$ when increased from 1.0 to 1.5, which is the target for the FCC project, results in another 1.0 T or 5.3% margin shift. The 16 T 20% margin is just within reach at 1.9 K although it lies at the point where the curves rapidly start to increase. For a 16 T layout to be possible having both a 1.9 K operating temperature and an $f_{\mathrm{Nb_3Sn}}$ of 1.5 is highly recommended in order to minimize quantities of conductor. For the FCC project a $Nb_3Sn$ magnet with, 20% margin and an operating point of 14 T would be a much easier target to achieve. Within the FCC project it is decided to start with a 16 T 10% margin magnet at an operating temperature of 4.5 K (FCC start point in Figure 6.13) [20]. With the added 1.2 T from reducing the temperature this would correspond to 17% margin at 16 T and 1.9 K.

### 6.4.3 Effect of Grading

Next the effect of the level of grading on the conductor cost is studied. In Figure 6.14 conductor cost is shown versus magnetic field at 20% margin for various Block layouts with different levels of grading. In all cases the layouts comprise 2 decks at the lower

magnetic fields and 3 decks at the higher magnetic fields. When the coil is sub-graded in the $Nb_3Sn$, thus using low and high current density $Nb_3Sn$, an additional very significant 1.7 T, corresponding to 10% margin, can be obtained. When the coil is graded further, including Nb-Ti, then another 0.5 T, corresponding to 2.5% margin, is obtained for similar conductor cost. Additional advantage is that the high stress areas of the coil are filled with stress resistant Nb-Ti instead of $Nb_3Sn$. The optimal magnetic field contribution in the aperture, of the Nb-Ti layer, is around 5.5 T. When increased beyond this point the current density of the Nb-Ti reduces significantly causing the conductor cost to increase.

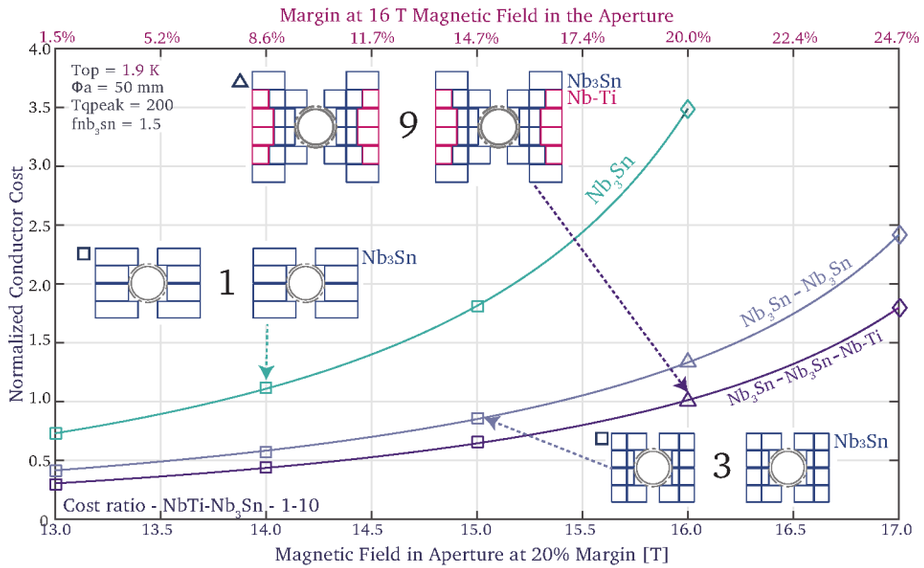


**Figure 6.14.** *Normalized conductor cost for Block coils with various levels of grading (reproduced from [21]), operated at* 1.9 K*, plotted against the central magnetic field at a margin of* 20% *(bottom axis) or against the corresponding margin at a central field of* 16 T *(top axis). The numbers provided inside the layouts correspond to the indices of Table 6.1. The aperture size is* 50 mm *the peak temperature at quench is* 200 K *and the* $f_{Nb_3Sn}$ *is set at* 1.5*, which is the FCC target performance.*

Although grading seems obvious to reach a magnetic field of about 16 T, it introduces a series of splices between the $Nb_3Sn$ layers and between the $Nb_3Sn$ and Nb-Ti. These splices need to be made in the straight section or in the coil-ends. However, due to the heat treatment of the $Nb_3Sn$ it is unknown how and when in the assembly process such joints can be made and research and development is required. In addition, the ratio of current densities between the low and high current density $Nb_3Sn$ is about a factor 2. Because in the block coil the deck height determines the width of the cable, it is not preferred to use cables of different width. Therefore, in a conventional Rutherford cable, the grading has to be introduced by using different diameters of strands. This, however, puts a high constraint on the strand diameters, which then have to be about

0.7 and 1.4 mm, respectively. These diameters are the outer limits of what is possible for $Nb_3Sn$. A way around this problem could be found in other cable configurations such as a two stage Rutherford cable.

The results obtained for Cosine Theta layouts are very similar to those of the block coil. Here the difference between a $Nb_3Sn$ graded and a non-graded layout is about a 2.0 T, corresponding to about 11% margin. This is slightly more than for the Block coil because the grading is applied over four $Nb_3Sn$ layers instead of two. When grading including Nb-Ti an additional 0.3 T is gained, corresponding to 2% margin. In the Cosine Theta it is possible to vary the thickness of the layers in order to allow different cable widths. This makes it possible to acquire the grading with only one strand diameter. This is a clear advantage of the Cosine Theta over the Block.

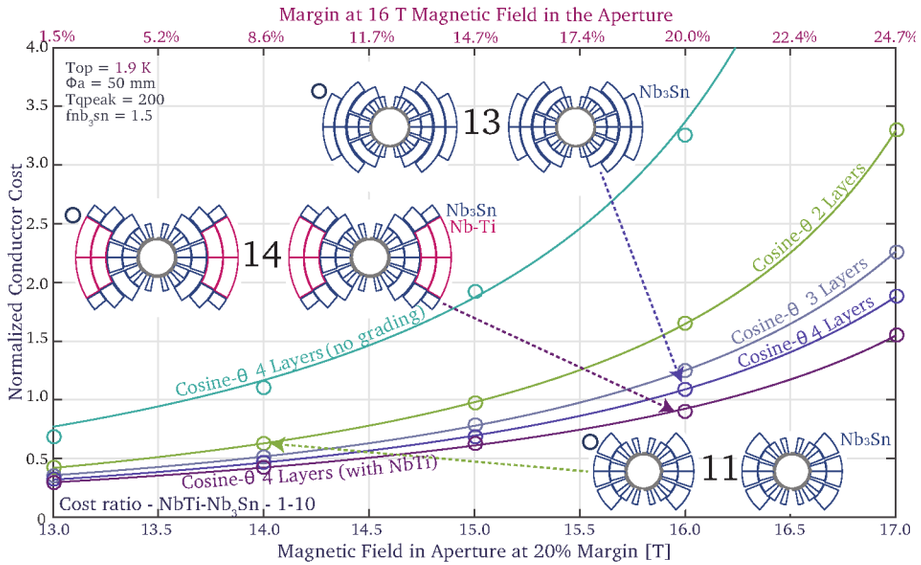


**Figure 6.15.** *Normalized conductor cost for Cosine Theta coils with various levels of grading (reproduced from [21]), operated at* 1.9 K*, versus the central magnetic field at a margin of* 20% *(bottom axis) or versus the corresponding margin at a central field of* 16 T *(top axis). The numbers provided inside the layouts correspond to the indices of Table 6.1. The aperture size is* 50 mm *the peak temperature at quench is* 200 K *and the* $f_{Nb_3Sn}$ *is set at* 1.5*, which is the FCC target performance.*

### 6.4.4 Effect of Type of Coil Layout

In Figure 6.16 the Block, Cosine Theta and Canted Cosine Theta layouts are compared in terms of conductor cost versus magnetic field and margin. The Canted Cosine Theta is approximated with a sector coil that has a perfect cosine-theta current distribution, superimposed with a from layer to layer alternating azimuthal current (see Section 6.2.1). The axial magnetic field contributes to a small increase of the peak

magnetic field. The Canted Cosine Theta is fully graded over all layers. This grading could be achieved like the Cosine Theta with the width of the cable. The Block and Cosine Theta coils share about the same cost. It looks like the extra mechanical structure in the aperture of the Block is balanced by the wedges needed for the inner layer of the Cosine Theta coil. The difference between the Canted Cosine Theta and the other layouts is about 0.7 T, corresponding to 5% margin. This difference is attributed to the space taken by the ribs, reducing the effective filling fraction of the conductor to about 70%. Because the margin plays a critical role at these high magnetic fields, it is required to experimentally determine the influence of the layout type and its complexity on the training behavior and thus the achievable margin.

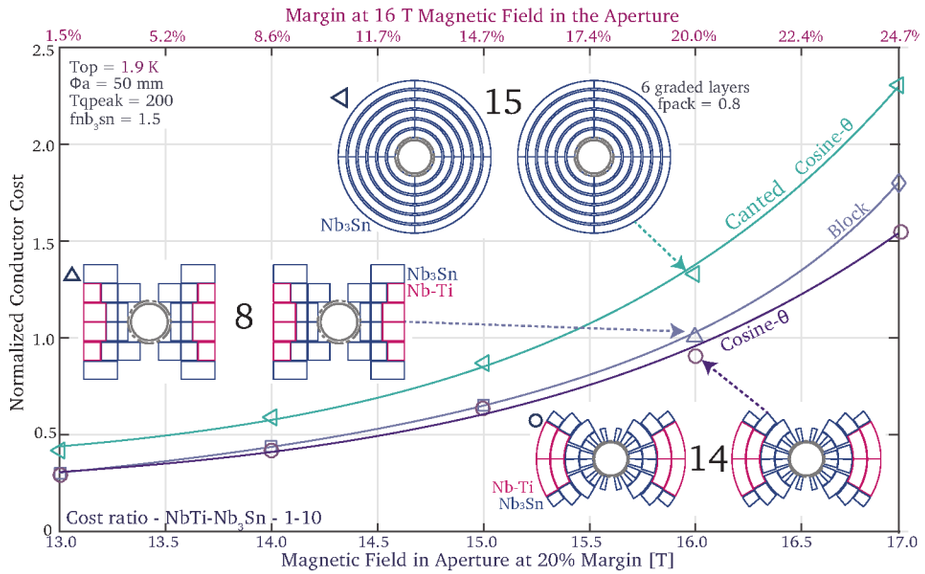


**Figure 6.16.** *Normalized conductor cost for the Block, Cosine Theta and Canted Cosine Theta coil layouts (reproduced from [21]), operated at* 1.9 K*, versus the central magnetic field at a margin of* 20% *(bottom axis) or versus the corresponding margin at a central field of* 16 T *(top axis). The numbers provided inside the layouts correspond to the indices of Table 6.1. The aperture size is* 50 mm *the peak temperature at quench is* 200 K *and the* $f_{Nb_3Sn}$ *is set at* 1.5*, which is the FCC target performance.*

## Effect of Aperture Size 6.4.5

The aperture size is required to allow space for the beam screen with cooling pipes, achieving field quality for the beam and the beam itself. In order to extract the energy deposited by the very high level of synchrotron radiation it was found that additional cooling pipes are necessary for the FCC, resulting in an increase of aperture size from

the original 40 to 50 mm. Certain minimum aperture diameter is also mandatory when applying an insert-magnet, where the insert needs to fit in the LTS outsert.

The effect of the aperture diameter on the cost is presented in Figure 6.17. In theory the conductor cost scales linearly with the aperture diameter. However, in the figure a small curvature can be seen. This curvature is explained by the inclusion of the thermal model. When the coil size increases, the stored energy per conductor volume increases as well. Therefore it becomes harder to protect and more copper is required to keep the peak temperature at the set 200 K. The inclusion of this extra copper in turn makes the coil less cost-efficient. The effect of the aperture size on the mechanical structure and possible additional wall thickness required is not (yet) included in the study. The effect on cost is therefore expected to be slightly stronger than shown in the plot. At larger aperture size, it becomes more efficient to use 2 or 4 decks, depending on cable width, resembling the design of the Fresca2 magnet. At lower aperture sizes it is more efficient to use 3 decks.

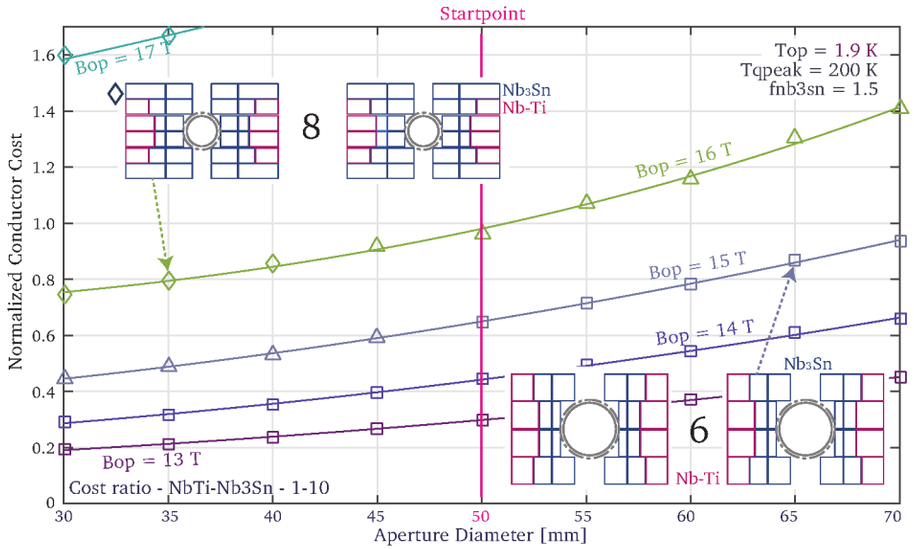


**Figure 6.17.** *Normalized conductor cost for the fully graded Block coil layouts (reproduced from [21]), operated at* 1.9 K*, versus the size of the aperture. The numbers provided inside the layouts correspond to the indices of Table 6.1. The peak temperature at quench is* 200 K *and the* $f_{Nb_3Sn}$ *is set at* 1.5*, which is the FCC target performance.*

### 6.4.6 Effect of Peak Temperature at Quench

The inclusion of the quench model in the cost optimization causes the amount of copper in the inner layers to reduce, thereby improving their current density. In the outer

layers the amount of copper is increased, and thus the current density is reduced. Characteristic values for the copper to superconductor ratio in a fully graded 16 T, 20% margin Block layout, with a peak temperature of 200 K, are 0.7, 2.5 and 1.6 for the $Nb_3Sn$, $Nb_3Sn$ and Nb-Ti layers, respectively. The effect of the maximum peak temperature on the conductor cost is presented in Figure 6.18. When the peak temperature is requested too low, the amount of copper needed rapidly increases, resulting in an asymptotic behavior. At higher temperatures the requested peak temperature has almost no effect on the cost. In essence it is no longer possible to remove material from the coil without increasing the peak temperature significantly.

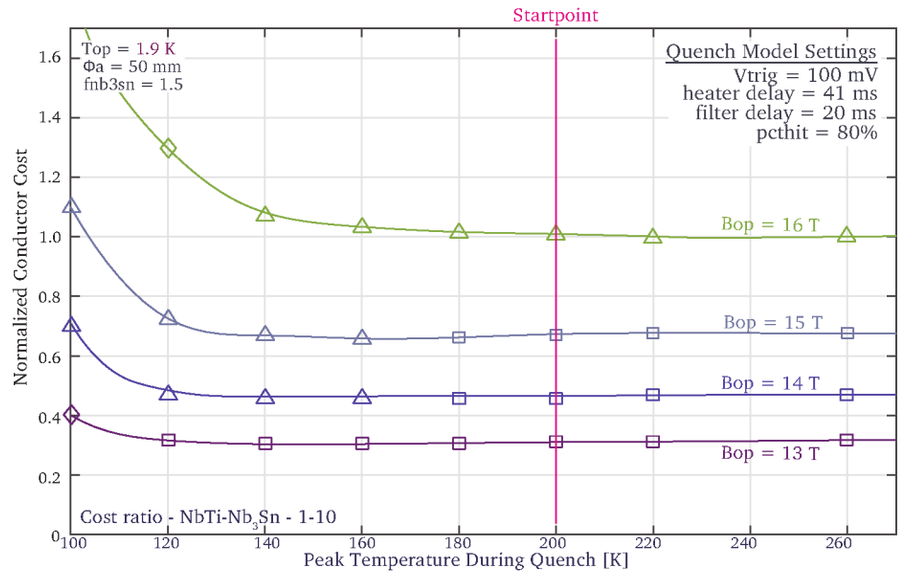


**Figure 6.18.** *Normalized conductor cost for the fully graded Block coil layouts (reproduced from [21]), operated at* 1.9 K*, against the allowable peak temperature during a quench. The aperture size is* 50 mm *and the* $f_{Nb_3Sn}$ *is set at* 1.5*, which is the FCC target performance. The settings used for the quench model are shown inside the graph.*

## Iron Yoke or Active Shielding 6.4.7

Thus far the iron yoke for shielding purposes was not included in the study in order to limit computation times. However, it is necessary in an accelerator magnet to apply flux return, in order to reduce the stray magnetic field. This can be achieved using either an iron yoke or active magnetic shielding coils, a concept commonly used in MRI magnets. An iron yoke has the advantage that it generates as by-product a magnetic field in the apertures of approximately 1 T practically for free. The peak magnetic field in the outer coil layers is reduced slightly as well allowing for a more efficient coil. The layout of the yoke is fairly straight forward and an example is shown in Figure 6.19.

The magnetization and the shape of the yoke is updated every step during the iterative cycle. The distance between the yoke and the coil pack is maintained at 30 mm by the optimizer. Furthermore the shape of the yoke is designed to reduce the quadrupole harmonic, resulting from the antisymmetry in a dual aperture coil layout. However, the iron has a saturation field of about 2.1 T, requiring a large iron shell thickness to shield all the flux in high field accelerator magnets.

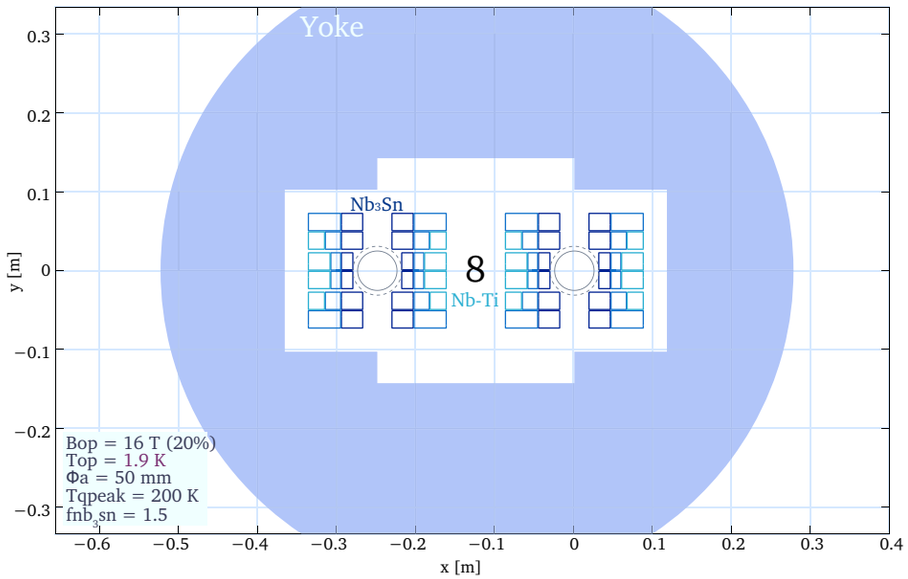


**Figure 6.19.** *Example* 16 T 20% *margin fully graded Block layout including an iron yoke as used during the survey. The aperture size is* 50 mm*, the peak temperature at quench* 200 K *and the* $f_{Nb_3Sn}$ *is set at* 1.5*, which is the FCC target performance. The shape of the yoke is automatically generated during the iterative cycle. The picture is cropped on the vertical axis.*

Shielding coils do not require a large diameter and can potentially be useful when size or weight become an issue. The position of the shielding coils can be calculated using the remote harmonics (see Appendix B) originating from a point centered between the apertures. Because a dual aperture dipole is basically a quadrupole, it is the first non-zero term and therefore needs to be shielded. Note that this case is different than an MRI magnet, where the first non-zero harmonic is the spherical equivalent of the dipole. The quadrupole component decays much faster with distance from the coils and is therefore easier to shield. This is also the case for the iron yoke. As an example, a set of optimized quadrupole shielding coils is shown for a 16 T layout in Figure 6.20. The 10 mT line lies at a distance of approximately 150 mm from the shield. More higher order shielding coils can be added to improve the effect further at the cost of complexity. However, it is found in MRI magnets that when a quench occurs, there is a so-called blooming field effect, due to a small phase difference between the main and

shielding coil currents, a spike in the magnetic stray field occurs [230]. The amplitude of this spike and its effect on the surrounding electronics should be investigated before application in an accelerator. The shielding coils do not necessary need to be inside the same cryostat as the main dipoles and can in theory also be made of HTS, $MgB_2$ or, when the distance is allowed to be large, plain copper at low current density.

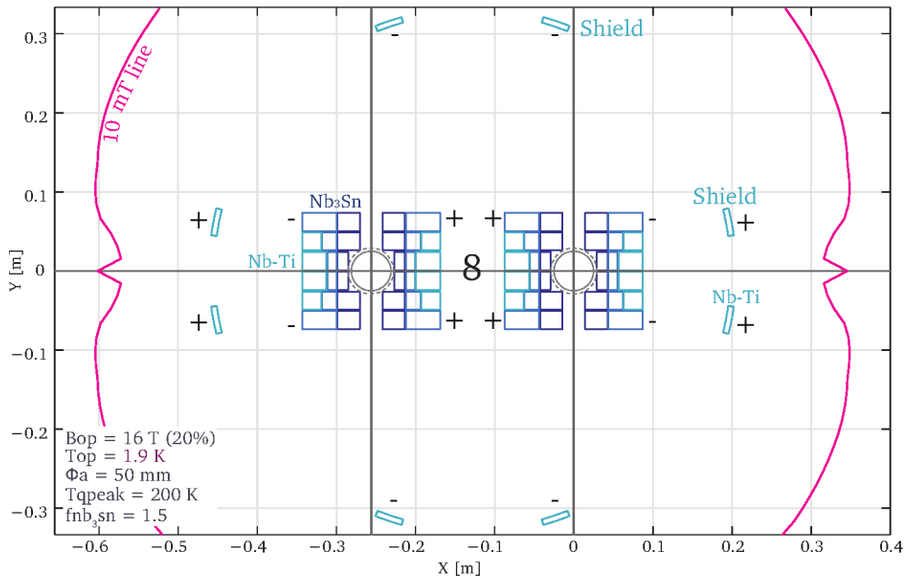


**Figure 6.20.** *Example* 16 T *fully graded Block layout showing the position of the optimized quadrupole shield coils. The aperture size is* 50 mm*, the peak temperature at quench* 200 K *and the* $f_{Nb_3Sn}$ *is set at* 1.5*, which is the FCC target performance. In addition the* 10 mT *line is visible in order to demonstrate the size of the stray field.*

The effect of iron yoke and shielding coils on the conductor cost is shown in Figure 6.21. The difference between the iron and the non-shielded layout at the same conductor cost is approximately 0.25 T, corresponding to a margin of 1.2%. At the same magnetic field, the conductor cost is reduced by about 15%. Note that the cost of the iron, which could be relevant to this result, is not included. For the layout with the shielding coils magnetic field is reduced by 0.15 T at the same conductor cost, with respect to the non-shielded layout. This reduction corresponds to about 0.7% margin. The total difference between shielding coils or an iron yoke is thus 0.4 T, corresponding to 1.9% margin.

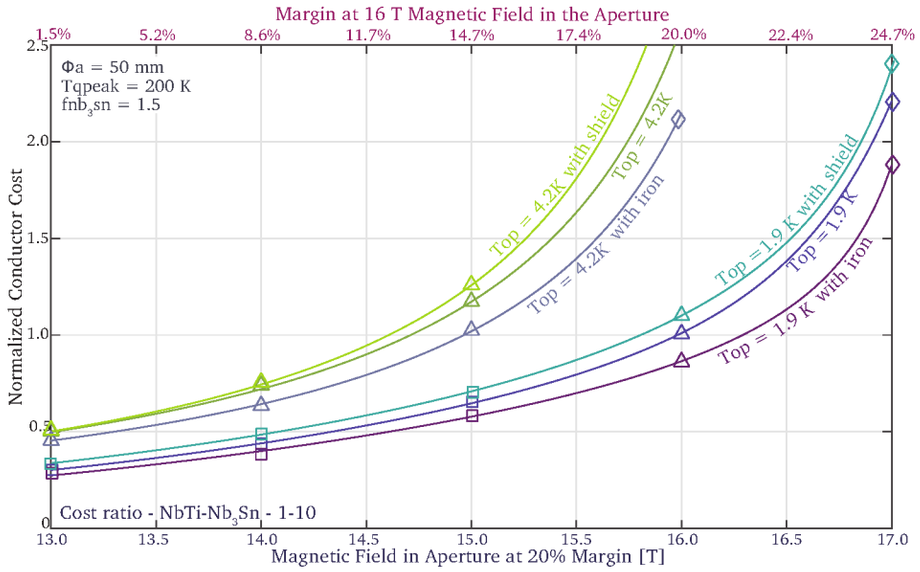


**Figure 6.21.** *Normalized conductor cost for fully graded Block coil layouts (reproduced from [21]), with iron yoke or active magnetic shield coils, operated at* 1.9 K*, plotted against the central magnetic field at a margin of* 20% *(bottom axis) or against the corresponding margin at a central field of* 16 T *(top axis). The aperture size is* 50 mm *the peak temperature at quench is* 200 K *and the* $f_{Nb_3Sn}$ *is set at* 1.5*, which is the FCC target performance.*

## 6.5 Conclusion

A new and original algorithm was developed to optimize the layout of graded hybrid accelerator coils. Since in such a design exercise current density, magnetic peak field, coil magnetic field harmonics, position of the blocks and thickness of the layers, are all related, it is necessary to use an iterative approach. The iterative cycle takes an initial layout and then converges it into a design that meets all requirements, such as magnetic field quality and load-line margins. Outside the iterative cycle a cost optimization is performed, finding the optimal distribution of magnetic field between the layers and optimal height or angles within the layers.

The iterative algorithm was used to study hybrid coil layouts for a 20 T magnet that makes use of a ReBCO insert. This study was only preliminary since there were too many unknowns concerning the ReBCO part of the coil. Nevertheless, some interesting observations could be made. It was found that the magnetic field angle in the ReBCO insert has a strong influence on the overall conductor cost. In order to make effective use of the ReBCO coated conductor, the tapes can be aligned with the magnetic field lines, thereby maximizing their critical current. This led to the so-called Aligned Block layout that is studied in detail in the EuCARD2 insert-magnet, as discussed in Chapter 2.

In order to keep the Lorentz forces on the insert and the resulting stress within acceptable levels, it is more cost effective to have an open mid-plane outsert-magnet instead of a thicker wall between both insert and outsert. This has the additional advantage that the coils in the outsert can consist of simple flat racetracks. It is also found that different levels of grading in the outsert can help to reduce the cost further. Because there were too many unknowns related to the ReBCO insert, it was decided to focus on the Feather-M2 insert first, with the intent to revisit the layout study with HTS at a later time.

In parallel, a layout survey at the limit of the present performance boundaries of $Nb_3Sn$ conductors was performed. This survey can be regarded both as a study for the 16 T option for the Future Circular Collider and as a study for the LTS outsert for an HTS insert reaching 20 T. The optimization layout survey provides a rich collection of alternatives. Obviously it is impossible to present all details in this context, so that only a few specific but highly relevant observations are presented here.

For a given conductor cost it is found that grading the $Nb_3Sn$ causes an increase of the magnetic field by approximately 1.7 T, equivalent to a 10% margin gain. Grading is a must to achieve cost-efficient magnets beyond 14 T. When additionally grading using Nb-Ti is considered, an extra 0.5 T, or 2.5% margin can be attained. As an extra advantage the Nb-Ti is positioned in the high stress regions of the coil, instead of the stress sensitive $Nb_3Sn$. In order to achieve effective grading it is necessary to impose different cross-sectional areas for the cables. For the Cosine Theta and the Canted Cosine Theta, this can be achieved varying the width of the cable. For the Block design it is necessary to change the strand diameter or resort to alternate cable geometries.

Operation at 1.9 K instead of 4.5 K yields a magnetic field increase of 1.2 T, corresponding to 7% margin gain at the same conductor cost. Improving the conductor critical current density by a factor $f_{Nb_3Sn}$ of 1.5 can yield an increase of magnetic field of 1.0 T, corresponding 5.3% margin, for the same conductor cost. For a 16 T layout with 20% margin layout to be realistic, a combination of grading, 1.9 K operation will be needed. Improvement of the $Nb_3Sn$ critical current density with a factor 1.5 is highly recommended to further reduce conductor cost.

# 7 General Conclusion and Outlook

> "Seize the time... Live now! Make now always the most precious time. Now will never come again."
>
> Jean-Luc Picard, Star Trek: TNG, S05E25, 1992

*In this concluding chapter the research questions introduced in Section 1.9 are answered. These answers represent a fair summary of the highlights contained in this work. In addition, some general observations on the future of HTS accelerator magnets are made.*

This thesis considers the use of High Temperature Superconductor (HTS) for application in particle accelerator magnets. The HTS conductor selected for this study was ReBCO, which is only available in the form of tapes. The critical current density in this conductor is highly anisotropic, implying that it depends strongly on the angle of the magnetic field with respect to the surface of the tapes. A new type of layout named Aligned Block was introduced in which all the tapes in the coil-windings are aligned with the magnetic field in order to maximize their critical current density.

Although it is simple to achieve conductor alignment in the straight sections of an accelerator magnet, it becomes more complicated in a full three-dimensional layout involving also the coil-ends. This led to Research Question 1: *Is it possible to design and construct an insert-magnet using ReBCO tape conductor, in which all tapes are aligned with the magnetic field throughout the coil?* - Within this context the EuCARD2 Feather-M2 insert-magnet with the novel Aligned Block layout was designed and developed. For this magnet the Roebel cable was selected because it is fully transposed, has a high cross-sectional conductor fraction and provides alignment of the tapes. In contrast to previous HTS insert designs this magnet has an accessible aperture of 40 mm. Moreover, the magnet had to meet a stringent outer diameter restriction of 99 mm in order for it to be tested in the LTS Fresca2 outsert-magnet. Within the envelope of these two diameters and given the mechanical restrictions of the selected Roebel cable it was possible to find a trajectory and orientation of the cable, such that at the operating magnetic field of 16.9 T (including 13 T background magnetic field) the cross-section average magnetic field angle inside the cable does not exceed more than 4 deg. The maximum magnetic field angle at operating point, located on the edges of the cable, is approximately 12 deg. This degree of alignment not only leads to higher critical current but also helps to improve the magnetic field quality and reduces magnetization loss. The structure of the magnet has been fully designed and construction has just started. First winding tests are positive.

Feather-M2 is the first accelerator magnet that will use a ReBCO Roebel cable at low temperature and high magnetic field. Because of the high forces involved it is necessary

to impregnate the coil with epoxy resin. However, in literature it was reported that differential thermal contraction may easily lead to delamination of the ReBCO coated conductor when impregnated, causing degradation of the critical current. This led to Research Question 2: *How to optimally use a ReBCO Roebel cable for accelerator coils in terms of coil-winding, insulation and impregnation?* - The likelyhood of delamination is significantly reduced when the epoxy has the same thermal contraction as the tape. Attempts were made to use an alumina filled epoxy, however, its increased viscosity lead the impregnation of one of the exercise coils to fail, leaving the coil dry. The solution is to use a fiber glass insulation sleeve in combination with a glass rope that fills the central channel of the Roebel cable. When the coil is impregnated such a cable is surrounded with fiber glass epoxy that has the same thermal contraction as the coated conductor tapes. When winding the coil some longitudinal sliding of the tapes in the cable is necessary to allow for sufficient flexibility at the coil-ends. By applying a winding tension of 5 kg, the cross-overs act as springs mitigating most of the sliding at the coil-ends and thus prevent the cross-overs from interlocking.

Due to the relatively slow normal zone propagation velocity, quenches in HTS magnets are harder to detect using the voltage based method common in LTS coils, which led to Research Question 3: *How to test an HTS magnet, while avoiding the risk of damaging the coils during the first series of ramps, due to overheating and thermal stress during a quench?* - In order to prevent unexpected quenches at very high operating currents, the magnet is first tested at variable temperature in helium gas. This reduces the thermal margin, making it possible to quench the magnet at much lower currents. Reaction times for the protection increase accordingly, allowing for the setting-up the quench protection system without risk for the magnet. The temperature can then be reduced in steps in order to keep the system predictable.

In order to study coated conductor cables and coils in detail in terms of magnetization, normal zone propagation and stability, it was necessary to develop a numerical model. Both at CERN and at the University of Twente experience was already available with solving electro-magnetic network equations in previous models named CUDI and JackPot-AC. In these models the round strands are approximated as a single line current. However, coated conductor tapes are wide and flat surfaces. This led to Research Question 4: *Is it possible to represent a coated conductor tape reliably in terms of magnetization and quench dynamics using a network of superconducting elements and nodes?* - A new Electro-Magnetic and Thermal Network Model was developed, adapting the solver strategy of JackPot-AC. The flat surfaces of the tapes are represented by a rectangular grid of nodes and superconducting elements. The voltages at the nodes and the currents through the elements are solved using Kirhoff's Voltage and Current Laws. In addition a discrete heat equation is added in order to calculate also the temperature at the nodes. This full coupling with thermal physics was never implemented before and constitutes a unique feature of this study. It is noted that the currents in this grid are unable to flow under a 45 deg angle with respect to the grid. Because locally current can only flow either longitudinally or transverse to the tape, a maximum error of a factor $\sqrt{2}$ is introduced. However, in most cases the current only flows along the edges of the cable and is thus unaffected by this problem. The model was validated

using experimental AC loss data from the University of Twente and good agreement was demonstrated. In terms of quench dynamics it was found that it is not necessary to include the full two-dimensional surface of the tape, because a quench quickly spreads over its width due to current redistribution. Apart from this initial effect, the model behaves essentially one-dimensional. The normal zone propagation was compared to a one-dimensional model and good agreement was found in terms of normal zone propagation velocity and minimum quench energy.

The resulting electrical network, especially for coil geometries, can be rather large comprising several tens of thousands of elements. Solving the resulting system of equations is a non-trivial task. This led to Research Question 5: *How to simulate a large electrical network while correctly taking into account the mutual coupling between all elements?* - The system of equations is represented using sparse matrices (and some additional non-linear functions) only storing their non-zero entries. The system is then solved using the Sundials IDA solver. However, the matrix containing all mutual inductances between all elements becomes fully populated and would require too much memory to store. Therefore, the Multi-Level Fast Multipole Method (MLFMM) was implemented, a feature adapted from JackPot-AC but unique to HTS tape models. This method reduces the complexity of N-body calculations from $O\left(N^2\right)$ to $O\left(N\right)$. However, since in this method the matrix is no longer physically stored it is necessary to use an iterative solver, such as GMRES, in the pre-conditioner of IDA. This iterative solver is then pre-conditioned using a sparse matrix representation of the MLFMM source-to-target (S2T) step.

Tape and cable magnetization may have an important impact on the magnetic field quality. Although well understood for single tapes, for cable geometries only limited knowledge of the magnetization profile is available, leading to Research Question 6: *How does the magnetization in a ReBCO Roebel cable geometry develop and is it fundamentally different from a collection of individual tapes?* - Magnetic field penetration in a cable was indeed found to be different from a single tape. More layers of superconductor are available to screen the magnetic flux. Therefore the penetration magnetic field, applied in the transverse direction, is about 1.7 T, much higher than for a single tape. However, the cross-over tapes are not screened by any other tapes, therefore the magnetic flux can more easily penetrate at this location. The detailed geometry of the cable has a strong influence on the magnetization and resulting AC loss and it is therefore necessary to study the cable and ultimately the coil as a whole.

The ultimate example of such calculations is the magnetic field quality in a dipole coil geometry. This led to Research Question 7: *What is the effect of the wide tape conductor on the dynamic magnetic field quality, is it necessary to compensate and if so, how can this be accomplished?* - With the electro-magnetic part of the Network Model it was possible to simulate screening currents inside a slice of the Feather-M2 aligned block and in the CEA Cosine Theta coil. It is observed that when the magnetic field is perpendicular to the surface of the conductor, significant magnetization currents occur, generating coil harmonics, and thus the field quality is affected negatively. In a background magnetic field the Cosine Theta layout shows about 60 units of dynamic variation. In the Aligned Block, in which the tapes are nearly parallel to the magnetic field, almost no dynamic

variation occurs. However, the transport current fills the tapes from their edges still causing some variation in the coil harmonics. To compensate for these effects a novel concept was introduced in the form of persistent current shim coils. These thin coils, by design, can screen one specific harmonic component from the aperture, thereby acting as a passive harmonic filter. This technique is not only useful for HTS accelerator magnets, but can also be used for LTS and could potentially be a game-changer for future accelerator magnets.

The Electro-Magnetic and Thermal Network Model can also be used for quench analysis in ReBCO cables and coils. Since the thermal margin in HTS magnets at operating current is much larger than in LTS ones, much more energy is required to initiate a quench. This led to Research Question 8: *In view of its high intrinsic thermal stability, is normal zone propagation in a multi-strand ReBCO Roebel cable geometry essentially different from Low Temperature Superconductors?* - Using the network model the development of a normal zone was studied, first in a cable but later on also in a coil. In the model current redistribution and thermal contact between strands in the Roebel cable were included. It was found that quench initialization is similar to what occurs in LTS in terms of the mechanism involved. When a tape quenches, the current is transferred to neighboring tapes, which are driven to quench as well when the heat is transferred. However, due to the large thermal margin, the duration of this so-called Pre-Quench phase is much longer in ReBCO than in LTS. Similarly, when a small heat source is present, for example due to joint heating, it takes much longer to reach the current sharing temperature, resulting in a much longer temperature Drift phase.

These observations directly lead to Research Question 9: *Is it possible to provide early detection of a thermal runaway or its onset in a ReBCO Roebel cable, using other non-standard sensors such as pick-up coils and temperature probes?* - If either the thermal Drift or Pre-Quench phase can be detected reliably, a significant amount of time is gained to protect the magnet. This allows to run the magnet at higher current density and thus allowing for more efficient coil layouts. With the Electro-Magnetic and Thermal Network Model it was possible to predict the signal on a series of pick-up coils located on the inner surfaces of the coil and on the current leads. It is found that the current redistribution resulting from a normal zone in one of the tapes covers a significant length of cable. The calculated signal on the pick-up coil array is about 50 mV for the first redistribution, making it easily detectable. Detection of the temperature rise can be achieved with various temperature sensors. Their respective signals are difficult to predict as it would require an assumption on the heat source power. Therefore additional experimental input, testing the various systems, is necessary.

The conductor orientation of the Feather-M2 insert-magnet was optimized to operate in a background magnetic field. Realistically this background magnetic field can be provided with a combined Nb-Ti and $Nb_3Sn$ outsert. Additionally, for FCC a 16 T magnet using only the LTS materials Nb-Ti and $Nb_3Sn$ is considered for the main bending dipoles. This led to Research Question 10: *Can one realistically expect a* 16 T *accelerator magnet to be realized, using present or near future technology, with only Nb-Ti and* $Nb_3Sn$ *superconductors and what would be a suitable operating temperature for such a magnet?* - An algorithm was developed that allows to optimize graded hybrid magnet

layouts. The algorithm was used to perform an extensive parametric study on the overall conductor cost. It was shown that a 16 T layout with 20% load-line margin is at the point where conductor cost rapidly increases with magnetic field. Therefore this kind of design is only possible at an operating temperature of 1.9 K and when grading is used in the $Nb_3Sn$ coil layers. Further improvement of the critical current density of practical $Nb_3Sn$ conductor is useful and recommended.

In order to exceed 16 T in an accelerator magnet, it is necessary to use HTS, leading to Research Question 11: *What shape takes a* 20 T *hybrid magnet, including its force retaining structure and what is an optimal insert-outsert configuration?* - The concept of splitting the coils into an HTS insert and LTS outsert was introduced in order to contain the forces of the insert, such that the pressure in the outsert would not exceed the stress limit of $Nb_3Sn$. To minimize the conductor cost of the expensive HTS insert an Aligned Block layout is proposed. A Block layout for the outsert best accommodates this type of insert. It was found that by using an open mid-plane for the outsert, it is possible to provide additional mechanical support to the insert, using the space that thus becomes available. In addition the outsert coils can be placed at a higher angle, helping with the alignment of the magnetic field in the insert. Another advantage is that the outsert coils become flat racetracks which are much easier to wind. The thick mid-plane mechanical support plate, containing the apertures, can then be used as a reference during assembly of the coils.

With all the initial research questions answered, the overall impression is that the use of HTS ReBCO coated conductor in an accelerator magnet is in principle possible and that the related technical difficulties can be overcome. This opens the door for very high magnetic field accelerator magnets, offering magnetic fields even in excess of 20 T. The main issue though for practical application is the manufacturing cost of the coated conductor itself. Even in a hybrid insert-outsert configuration a large fraction of the conductor cost is attributed to the HTS insert. It may thus be concluded that the feasibility of HTS accelerator magnets hinges not primarily on technical issues but essentially on financial arguments.

# SUPERCONDUCTOR SCALING RELATIONS A

*The critical current density in the superconductor is calculated, using its scaling relation, the local magnetic field B, the operating temperature T and in the case of ReBCO the magnetic field angle θ as well. In this appendix the scaling relations for the three superconductors and the values of the fitting parameters are provided.*

## Niobium-Titanium A.1

For Nb-Ti the scaling relation is given Bottura [231]. The used reference critical current density is $J_{c,\mathrm{ref}} = 3200\,\mathrm{A/mm^2}$ at 5 T and 4.2 K [232]. Standard LHC settings are used for the remaining parameters as presented in Table A.1. The normalized temperature given by $t = T/T_{c0}$. The second critical field required to normalize the magnetic field is given by Lubell's equation [233] as $B_{c2} = B_{c20}(1 - t^{1.7})$. The normalized magnetic field is then $b = B/B_{c2}$. The critical current is then calculated using

$$J_c = J_{\mathrm{ref}} \frac{C_0}{B} b^{\alpha}(1-b)^{\beta}(1-t^n)^{\gamma}. \qquad \text{Eq. A.1}$$

The equation is only valid for $B < B_{c2}$ otherwise the critical current is zero. For reference the resulting critical current as function of magnetic field and temperature is shown in Figure A.1.

TABLE A.1.
VALUES OF THE FITTING PARAMETERS FOR NIOBIUM-TITANIUM.

| symbol | $C_0$ | $\alpha$ | $\beta$ | $\gamma$ | $n$ | $B_{c20}$ | $T_{c0}$ | $J_{\mathrm{ref}}$ |
|---|---|---|---|---|---|---|---|---|
| unit | [T] | [-] | [-] | [-] | [-] | [T] | [K] | [$\mathrm{A/m^2}$] |
| value | 31.4 | 0.63 | 1.0 | 2.3 | 1.7 | 14.7 | 9.2 | 3200 |

## Tri-Niobium Tin A.2

For $Nb_3Sn$ superconductor the Godeke scaling relation is used [234]. The assumed critical current is $1400\,\mathrm{A/mm^2}$ at 4.2 K and 15 T corresponding to $2000\,\mathrm{A/mm^2}$ at 1.9 K and 15 T. The fitting parameters are then given in Figure A.2. This scaling relation depends on axial strain $\epsilon_{ax}$ as well. In the thesis it is assumed to be zero. The strain dependence is left in the equation for reference.

$$\epsilon_{\mathrm{shift}} = \frac{C_{a2}\epsilon_{0a}}{\sqrt{C_{a1}^2 - C_{a2}^2}}, \qquad \text{Eq. A.2}$$

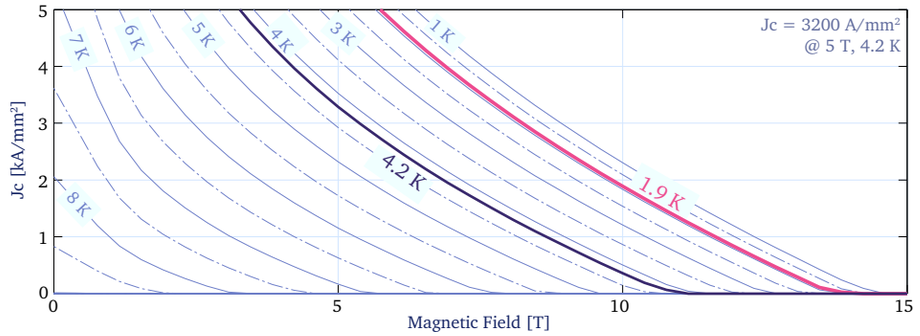


**Figure A.1.** *Critical current density in Nb-Ti superconductor as function of magnetic field at various temperatures. The critical current density was calculated using the Bottura scaling relation [233, 231]. Highlighted are the* 1.9 K *and* 4.5 K *curves, representing the temperatures for superfluid and boiling helium at* 1.26 bar*, respectively.*

the strain dependence can be given by

EQ. A.3
$$S = \frac{C_{a1}(\sqrt{\epsilon_{\text{shift}}^2 + \epsilon_{0a}^2} - \sqrt{(\epsilon_{\text{ax}} - \epsilon_{\text{shift}})^2 + \epsilon_{0a}^2}) - C_{a2}\epsilon_{\text{ax}}}{1 - C_{a1}\epsilon_{0a}} + 1.$$

The strain dependent critical temperature is given as $T_c = T_{cm}S^{(1/3)}$. The temperature is then normalized as $t = T/T_c$. The strain dependent critical field is calculated as $B_{c2} = B_{c2m}S(1 - t^{1.52})$. The normalized magnetic field is $h = B/B_{c2}$. The critical current is given as

EQ. A.4
$$J_c = \frac{C_1 S(1-t^{1.52})(1-t^2)h^p(1-h)^q}{B}.$$

Similar to Nb-Ti here the equation is only valid for $B < B_{c2}$ otherwise the critical current is zero. The critical current, as function of applied magnetic field and temperature $J_c(B, T)$, is shown for an improvement factor of 1.0 in Figure A.2.

TABLE A.2.
VALUES OF THE FITTING PARAMETERS FOR TRINIOBIUM-TIN.

| symbol | $C_{a1}$ | $C_{a2}$ | $\epsilon_{0a}$ | $C_1$ | $B_{c2m}$ | $T_{cm}$ | $p$ | $q$ |
|---|---|---|---|---|---|---|---|---|
| unit | [-] | [-] | [-] | [MAT/mm$^2$] | [T] | [K] | [-] | [-] |
| value | 47.6 | 6.4 | 0.00136 | 225 | 27.2 | 17.9 | 0.5 | 2 |

## A.3 Rare-Earth Barium Copper Oxide

For the ReBCO coated conductor an angular dependent scaling relation is used [46, 235], which is based on data provided by Fujikura [28]. The angular dependent critical

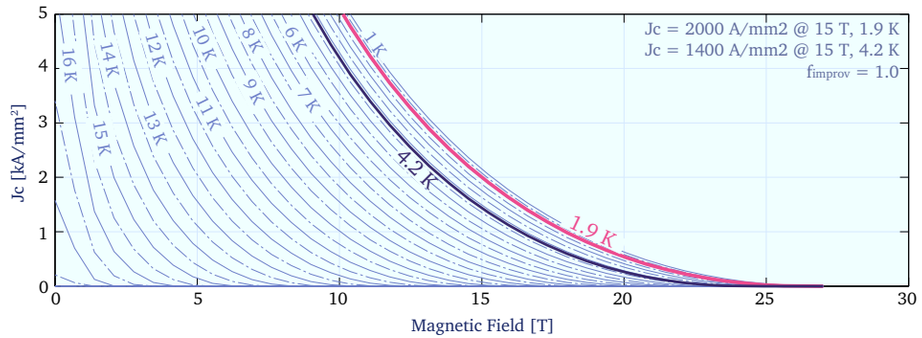


**Figure A.2.** *Critical current density in $Nb_3Sn$ superconductor as function of magnetic field at various temperatures. The critical current density was calculated using the Godeke scaling relation [234]. Highlighted are the* 1.9 K *and* 4.5 K *curves, corresponding to the temperatures for superfluid and boiling helium at* 1.26 bar*, respectively.*

surface calculated using this fit was previously shown in Figure 1.8 in Section 1.3. The values of the fitting parameters are given in Table A.3. For convenience the fit is repeated here, together with some modifications that where necessary to make the fit more stable.

As input the fit requires $B$, $T$ and $\theta$. The temperature is converted to the unit-less temperature $t$ using $t = T/T_{c0}$. The fit is not valid for very low values of the magnetic field. Therefore, it is necessary to place a lower limit of 0.1 T on $B$, causing $B$ to become equal to this value if it falls below it. In order to also make the magnetic field magnitude unitless, the irreversibility field is required, which is given as

$$B_{i,\mathrm{ab}} = B_{i0,\mathrm{ab}}\left((1-t^{n_1})^{n_2} + a\,(1-t^{n})\right), \qquad \text{Eq. A.5}$$

for the parallel direction and

$$B_{i,\mathrm{c}} = B_{i0,\mathrm{c}}(1-t^{n}), \qquad \text{Eq. A.6}$$

for the perpendicular direction, also referred to as $ab$ and $c$ directions. The unit-less magnetic field is then given as $b_{\mathrm{ab}} = B/B_{i,ab}$, and $b_{\mathrm{c}} = B/B_{i,c}$, for the two directions, respectively. The critical current density is first calculated separately for pure perpendicular and for pure parallel magnetic field. The first is given as

$$J_{c,\mathrm{ab}} = \frac{\alpha_{\mathrm{ab}}}{B} b_{\mathrm{ab}}{}^{p_{\mathrm{ab}}}(1-b_{\mathrm{ab}})^{q_{\mathrm{ab}}}\left((1-t^{n_1})^{n_2} + a\,(1-t^{n})\right)^{\gamma_{\mathrm{ab}}}, \qquad \text{Eq. A.7}$$

provided that $t < 1$ and that $b_{i,c} < 1$, otherwise $J_{c,\mathrm{ab}} = 0$. The second is given as

$$J_{c,\mathrm{c}} = \frac{\alpha_{\mathrm{c}}}{B} b_{\mathrm{c}}{}^{p_{\mathrm{c}}}(1-b_{\mathrm{c}})^{q_{\mathrm{c}}}\,(1-t^{n})^{\gamma_{\mathrm{c}}}, \qquad \text{Eq. A.8}$$

also provided that $t < 1$ and that $b_{i,ab} < 1$, otherwise $J_{c,\mathrm{c}} = 0$. The angular dependence is included in the anisotropy factor $g\,(B, T)$, which depends on both temperature $T$ and

magnetic field magnitude $B$. The anisotropy factor is calculated as

EQ. A.9 $$g(B,T) = g_0 + g_1 \exp(-[g_2 \exp(g_3 T)]B).$$

Using the parallel end perpendicular critical current densities and the anisotropy factor the critical current densities at magnetic field angle $\theta$, given in radians, is now calculated as

EQ. A.10 $$J_c(B,T,\theta) = \min\left(J_{c,\mathrm{c}}(B,T), J_{c,\mathrm{ab}}(B,T)\right) + \frac{\max\left(0, (J_{c,\mathrm{ab}}(B,T) - J_{c,\mathrm{c}}(B,T)\right)}{1 + \left[\frac{\theta - \pi/2}{g(B,T)}\right]^{\nu}},$$

where the min and the max functions take the highest value of their two inputs. This addition is required to prevent strange behavior when $J_{c,\mathrm{c}}$ is higher than $J_{c,\mathrm{ab}}$, which happens at high temperature. The calculated critical current is given at an electric field criterion of $10\,\mu$V/m. The thickness of the superconducting layer is $2\,\mu$m.

TABLE A.3.
VALUES OF THE FITTING PARAMETERS FOR FUJIKURA REBCO COATED CONDUCTOR. THE ASSUMED THICKNESS OF THE REBCO LAYER IS $2\,\mu$m.

| symbol | $g_1$ | $g_2$ | $g_3$ | $g_4$ | $T_{c0}$ | $p_c$ | $q_c$ | $B_{i0c}$ | $\gamma_c$ | $\alpha_c$ |
|---|---|---|---|---|---|---|---|---|---|---|
| unit | [-] | [-] | [-] | [-] | [K] | [-] | [-] | [T] | [-] | [MAT/mm$^2$] |
| value | 0.03 | 0.25 | 0.06 | 0.058 | 93 | 0.5 | 2.5 | 140 | 2.44 | 1.86 |
| symbol | $\nu$ | $n$ | $n_1$ | $n_2$ | $p_{ab}$ | $q_{ab}$ | $B_{i0ab}$ | $a$ | $\gamma_{ab}$ | $\alpha_{ab}$ |
| unit | [-] | [-] | [-] | [-] | [-] | [-] | [T] | [-] | [-] | [MAT/mm$^2$] |
| value | 1.85 | 1 | 1.4 | 4.45 | 1 | 5 | 250 | 0.1 | 1.63 | 68.3 |

At a temperature of 4.5 K a 20% deviation was found with the measurement data and at 50 K temperature a 30% deviation (for more detail see [235]). Because of the variation in the critical current density between manufacturers and even between batches from the same manufacturer, this fit is deemed acceptable for now in terms of accuracy. However, for future magnet design, it is useful to acquire more detailed data as function of magnetic field, temperature and angle, on tapes from all manufacturers. In addition the effect on artificial doping on the angular dependence should be studied.

# Harmonics

# B

*Two dimensional coil harmonics are often used for transverse field accelerator magnets to describe and optimize the magnetic field quality inside the aperture and the magnetic stray field outside the coil [6]. In this Appendix a mathematical description of the cylindrical harmonics is provided.*

## Introduction B.1

The coil harmonics can be seen as a series expansion which originate at a certain point, usually but not necessarily the center of the aperture, describing the magnetic field generated by a set of current elements using a number of source constants. Each source constant represents the magnitude of a specific multipole (i.e. dipole, quadrupole, sextupole etc.). There are two types of harmonic expansions, central and remote, the first of which describes the magnetic field inside a circle with a radius equal to the distance of the nearest current element and the second describes the field outside a circle with a radius equal to the distance of the furthest current element. Often used origin locations and coil regions in which the expansions are valid are shown in Figure B.1. Note that there remains a region in the coil where the magnetic field is not described by either of the harmonic expansions. In this region the Biot-Savart method can be used to calculate the magnetic field.

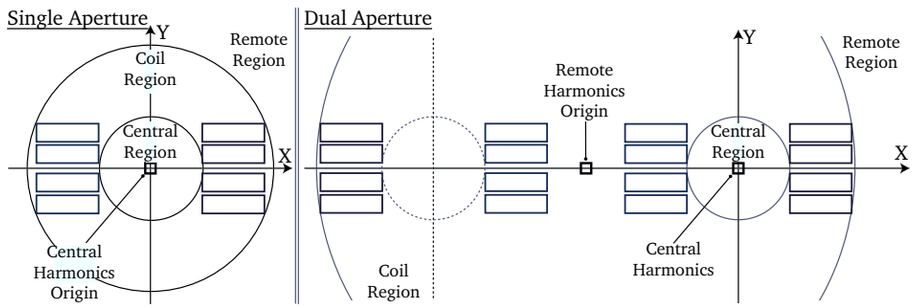


**Figure B.1.** *Illustration showing often used positions for the origins of both central and remote harmonics and the coil regions in which their expansions are valid, for both single and dual aperture coil configurations.*

## B.2 Central Harmonics

The coefficients, $A_{ncen}$ and $B_{ncen}$, for the central region can be calculated directly from the two dimensional coil geometry by summing the contribution of each of the line current elements representing the coil blocks. The contribution of each line current is given as

EQ. B.1
$$A_{ncen}(r_0) = \frac{\mu_0 I}{2\pi r_c}\left(\frac{r_0}{r_c}\right)^{n-1}\sin(n\varphi_c),$$

EQ. B.2
$$B_{ncen}(r_0) = \frac{\mu_0 I}{2\pi r_c}\left(\frac{r_0}{r_c}\right)^{n-1}\cos(n\varphi_c),$$

where $\mu_0$ is the permeability of vacuum, $I$ is the current in the line element, $r_c$ is the relative radial position coordinate of the element, $\varphi$ is the relative azymuthal coordinate of the element, $n$ is an integer value and corresponds to a specific harmonic constant of the field and $r_0$ is the reference radius, which can be chosen arbitrarily (but is usually set to be 2/3 of the aperture radius). The field in the central region can be calculated from the coefficients, by superimposing the magnetic field contributions of each using

EQ. B.3
$$B_r(r,\varphi) = \sum_{n=1}^{\infty}\left(\frac{r}{r_0}\right)^{n-1}\left(B_{ncen}(r_0)\sin(n\varphi) + A_{ncen}(r_0)\cos(n\varphi)\right),$$

EQ. B.4
$$B_\varphi(r,\varphi) = \sum_{n=1}^{\infty}\left(\frac{r}{r_0}\right)^{n-1}\left(B_{ncen}(r_0)\cos(n\varphi) - A_{ncen}(r_0)\sin(n\varphi)\right),$$

where $B_r$ and $B_\varphi$ are the field components in cylindrical coordinates. Note that in a real magnet the influence of higher order harmonics is negligible and therefore $n$ can run to a finite number. The magnetic field quality is usually expressed in so-called "units". The source constants in units are normalized with the main magnetic field component of the respective magnet and multiplied by $10^4$.

## B.3 Remote Harmonics

Similarly to the source constants for the central region, the remote source constants, $A_{nrem}$ and $B_{nrem}$, can also be calculated from infinitely long line current elements as

EQ. B.5
$$A_{nrem}(r_0) = \frac{\mu_0 I}{2\pi r_c}\left(\frac{r_c}{r_0}\right)^{n+1}\sin(n\varphi_c),$$

EQ. B.6
$$B_{nrem}(r_0) = \frac{\mu_0 I}{2\pi r_c}\left(\frac{r_c}{r_0}\right)^{n+1}\cos(n\varphi_c),$$

where the parameters are the same as in Appendix B.2. The field in the remote region is then defined from the source constants using

$$B_r(r,\varphi) = \sum_{n=1}^{\infty} \left(\frac{r_0}{r}\right)^{n+1} \left(B_{nrem}(r_0)\sin(n\varphi) + A_{nrem}(r_0)\cos(n\varphi)\right), \qquad \text{Eq. B.7}$$

$$B_\varphi(r,\varphi) = \sum_{n=1}^{\infty} \left(\frac{r_0}{r}\right)^{n+1} \left(-B_{nrem}(r_0)\sin(n\varphi) + A_{nrem}(r_0)\sin(n\varphi)\right). \qquad \text{Eq. B.8}$$

# C Feather Inductance Tables

*The tape-to-tape mutual inductances tables for Feather-M0 and Feather-M2 were produced for calculating the current redistribution between the tapes in the coils. These matrices can be useful input for other numerical models and are therefore provided in this Appendix.*

## C.1 Feather-M0

The tape-to-tape mutual inductances matrix for Feather-M0, assuming the SP-1 cable with 5 turns, is presented in Table C.1. It can be seen that the self-inductances of the tapes (numbers on the diagonal) correspond approximately to the self-inductance of the coil previously presented in Table 2.7. Small differences can be explained by the meandering of the tapes causing the trajectory to be slightly longer.

Table C.1.
Matrix containing the self- and mutual inductances of the individual strands of the Feather-M0 magnet. Values are in $\mu$H and self inductances are shown in magenta.

| | | | | | | | | | | | | | |
|---|---|---|---|---|---|---|---|---|---|---|---|---|---|
| 11.13 | 10.83 | 10.64 | 10.40 | 10.11 | 9.85 | 9.65 | 9.50 | 9.50 | 9.65 | 9.85 | 10.12 | 10.40 | 10.64 | 10.83 |
| 10.83 | 11.13 | 10.83 | 10.64 | 10.39 | 10.11 | 9.85 | 9.65 | 9.50 | 9.50 | 9.65 | 9.85 | 10.11 | 10.40 | 10.64 |
| 10.64 | 10.83 | 11.13 | 10.83 | 10.64 | 10.39 | 10.11 | 9.85 | 9.65 | 9.49 | 9.49 | 9.65 | 9.85 | 10.11 | 10.40 |
| 10.40 | 10.64 | 10.83 | 11.13 | 10.82 | 10.63 | 10.39 | 10.10 | 9.84 | 9.64 | 9.49 | 9.49 | 9.65 | 9.85 | 10.11 |
| 10.11 | 10.39 | 10.64 | 10.82 | 11.12 | 10.82 | 10.63 | 10.38 | 10.09 | 9.83 | 9.63 | 9.49 | 9.49 | 9.64 | 9.85 |
| 9.85 | 10.11 | 10.39 | 10.63 | 10.82 | 11.11 | 10.81 | 10.62 | 10.37 | 10.09 | 9.83 | 9.64 | 9.49 | 9.49 | 9.65 |
| 9.65 | 9.85 | 10.11 | 10.39 | 10.63 | 10.81 | 11.10 | 10.80 | 10.61 | 10.37 | 10.09 | 9.84 | 9.64 | 9.49 | 9.50 |
| 9.50 | 9.65 | 9.85 | 10.10 | 10.38 | 10.62 | 10.80 | 11.10 | 10.80 | 10.62 | 10.38 | 10.10 | 9.85 | 9.65 | 9.50 |
| 9.50 | 9.50 | 9.65 | 9.84 | 10.09 | 10.37 | 10.61 | 10.80 | 11.10 | 10.81 | 10.63 | 10.39 | 10.11 | 9.86 | 9.66 |
| 9.65 | 9.50 | 9.49 | 9.64 | 9.83 | 10.09 | 10.37 | 10.62 | 10.81 | 11.11 | 10.82 | 10.64 | 10.40 | 10.12 | 9.86 |
| 9.85 | 9.65 | 9.49 | 9.49 | 9.63 | 9.83 | 10.09 | 10.38 | 10.63 | 10.82 | 11.12 | 10.83 | 10.65 | 10.40 | 10.12 |
| 10.12 | 9.85 | 9.65 | 9.49 | 9.49 | 9.64 | 9.84 | 10.10 | 10.39 | 10.64 | 10.83 | 11.13 | 10.84 | 10.65 | 10.41 |
| 10.40 | 10.11 | 9.85 | 9.65 | 9.49 | 9.49 | 9.64 | 9.85 | 10.11 | 10.40 | 10.65 | 10.84 | 11.14 | 10.84 | 10.65 |
| 10.64 | 10.40 | 10.11 | 9.85 | 9.64 | 9.49 | 9.49 | 9.65 | 9.86 | 10.12 | 10.40 | 10.65 | 10.84 | 11.14 | 10.84 |
| 10.83 | 10.64 | 10.40 | 10.11 | 9.85 | 9.65 | 9.50 | 9.50 | 9.66 | 9.86 | 10.12 | 10.40 | 10.65 | 10.84 | 11.13 |

## C.2 Feather-M2

The tape-to-tape mutual inductances matrix for Feather-M2, assuming the SP-1 cable with 13 turns for the central deck and 7 turns for the wing deck, is presented in Table C.2. It can be seen that the self-inductance of the tapes corresponds approximately

to the self-inductance of the coil previously presented in Table 2.7. Small differences can be explained by the meandering of the tapes causing the trajectory to be slightly longer.

TABLE C.2.

MATRIX CONTAINING THE SELF- AND MUTUAL INDUCTANCES OF THE INDIVIDUAL STRANDS OF THE FEATHER-M2 MAGNET. VALUES ARE IN $\mu$H AND SELF INDUCTANCES ARE SHOWN IN MAGENTA.

| | | | | | | | | | | | | | | |
|---|---|---|---|---|---|---|---|---|---|---|---|---|---|---|
| 463.8 | 459.0 | 456.1 | 452.7 | 448.9 | 445.2 | 442.1 | 439.6 | 439.6 | 442.1 | 445.1 | 448.7 | 452.6 | 456.0 | 459.0 |
| 459.0 | 463.8 | 459.0 | 456.1 | 452.7 | 448.8 | 445.2 | 442.2 | 439.6 | 439.6 | 442.1 | 445.2 | 448.8 | 452.7 | 456.0 |
| 456.1 | 459.0 | 463.8 | 459.0 | 456.1 | 452.7 | 448.9 | 445.3 | 442.3 | 439.7 | 439.7 | 442.2 | 445.3 | 449.0 | 452.7 |
| 452.7 | 456.1 | 459.0 | 463.9 | 459.1 | 456.1 | 452.8 | 449.0 | 445.5 | 442.4 | 439.8 | 439.8 | 442.3 | 445.4 | 448.9 |
| 448.9 | 452.6 | 456.1 | 459.1 | 463.9 | 459.1 | 456.2 | 452.9 | 449.1 | 445.5 | 442.4 | 439.8 | 439.8 | 442.3 | 445.3 |
| 445.2 | 448.8 | 452.7 | 456.1 | 459.1 | 463.9 | 459.1 | 456.3 | 452.9 | 449.1 | 445.4 | 442.3 | 439.7 | 439.7 | 442.2 |
| 442.1 | 445.2 | 448.9 | 452.7 | 456.2 | 459.1 | 464.0 | 459.2 | 456.3 | 452.9 | 449.0 | 445.3 | 442.2 | 439.6 | 439.6 |
| 439.5 | 442.1 | 445.3 | 449.0 | 452.9 | 456.3 | 459.2 | 464.1 | 459.3 | 456.3 | 452.8 | 448.9 | 445.3 | 442.2 | 439.6 |
| 439.6 | 439.6 | 442.3 | 445.4 | 449.1 | 452.9 | 456.3 | 459.3 | 464.1 | 459.2 | 456.1 | 452.7 | 448.8 | 445.2 | 442.1 |
| 442.1 | 439.6 | 439.7 | 442.4 | 445.5 | 449.1 | 452.9 | 456.3 | 459.2 | 463.9 | 459.0 | 455.9 | 452.5 | 448.7 | 445.1 |
| 445.1 | 442.1 | 439.7 | 439.8 | 442.4 | 445.4 | 449.0 | 452.8 | 456.1 | 459.0 | 463.7 | 458.8 | 455.8 | 452.5 | 448.7 |
| 448.7 | 445.2 | 442.2 | 439.8 | 439.8 | 442.3 | 445.4 | 448.9 | 452.7 | 456.0 | 458.8 | 463.6 | 458.8 | 455.9 | 452.5 |
| 452.6 | 448.8 | 445.3 | 442.3 | 439.8 | 439.7 | 442.2 | 445.3 | 448.8 | 452.6 | 455.9 | 458.8 | 463.6 | 458.9 | 455.9 |
| 456.0 | 452.7 | 449.0 | 445.4 | 442.3 | 439.7 | 439.7 | 442.2 | 445.3 | 448.8 | 452.5 | 455.9 | 458.9 | 463.7 | 458.9 |
| 459.0 | 456.0 | 452.7 | 449.0 | 445.3 | 442.2 | 439.6 | 439.6 | 442.1 | 445.2 | 448.7 | 452.5 | 455.9 | 458.9 | 463.8 |

# BIBLIOGRAPHY


[1] M. Tinkham, Introduction to Superconductivity. Book, Dover Publications INC (1996).

[2] M. Cyrot and D. Pavuna, Introduction to Superconductivity and High-Tc Materials. Book, World Scientific (1992).

[3] M. Wilson, Superconducting Magnets. Book, Clarendon Press (1983).

[4] Y. Iwasa, Case Studies in Superconducting Magnets. Book, Springer Science, 2nd edn. (2009).

[5] K.-H. Mess, P. Schmüser and S. Wolff, Superconducting Accelerator Magnets. Book, World Scientific (1996).

[6] S. Russenschuck, Field Computation for Accelerator Magnets. Book, Wiley (2010).

[7] H. Wiedemann, Particle Accelerator Physics. Book, Springer (1993).

[8] G. Stancari, V. Previtali, A. Valishev et al., Conceptual design of hollow electron lenses for beam halo control in the Large Hadron Collider. Technical report, CERN and Fermilab (2014).

[9] C. Wyss, LHC Arc Dipole Status Report. Technical report, CERN (2008).

[10] L. Rossi, "State-of-the-art superconducting accelerator magnets". *IEEE Transactions on Applied Superconductivity*, vol. 12, no. 1, pp. 219–227 (2002).

[11] W. Barletta, M. Battaglia, M. Klute et al., "Future hadron colliders: From physics perspectives to technology R&D". *Nuclear Instruments and Methods*, vol. 764, pp. 352–368 (2014).

[12] I. Hinchliffe, A. Kotwal, M. Mangano et al., "Luminosity goals for a 100 TeV pp collider". *International Journal of Modern Physics A*, vol. 30, no. 23 (2015).

[13] F. Zimmermann, M. Benedikt, D. Schulte et al., "Challenges for Highest Energy Circular Colliders". Proceedings of the 5th International Particle Accelerator Conference, edited by C. Petit-Jean-Genaz, G. Arduini, P. Michel and V. Schaa (2014).

[14] J. Osborne, "FCC Civil Engineering". Pdf copy of oral presentation at FCC week in Rome (2016).

[15] H. Kamerlingh Onnes, "Sur les Résistances Électriques". *Communications from the Physical Laboratory of the University of Leiden*, vol. 29, pp. 1–11 (1911).

[16] W. Meissner and R. Ochsenfeld, “Ein neuer Effekt bei Eintritt der Supraleitfähigkeit”. *Naturwissenschaften*, vol. 21, p. 787–788 (1933).

[17] J. Bardeen, L. Cooper and J. Schrieffer, “Theory of superconductivity”. *Physical Review B*, vol. 108, no. 5, pp. 1175–1204 (1957).

[18] P. Kapitza, “Viscosity of liquid helium below the $\lambda$-point”. *Nature*, vol. 141, no. 74 (1938).

[19] G. Sabbi, S. Bartlett, S. Casp et al., “Design of HD2: a 15 Tesla $Nb_3Sn$ Dipole with a 35 mm Bore”. *IEEE Transactions on Applied Superconductivity*, vol. 15, no. 2, p. 1128 (2015).

[20] D. Schoerling, H. Bajas, M. Bajko et al., “Strategy for Superconducting Magnet Development for a Future Hadron-Hadron Circular Collider at CERN”. *Proceedings of science* (2015).

[21] J. van Nugteren, D. Schoerling, G. Kirby et al., “Layout Study for the Dipole Magnets of the Future Circular Collider Using Nb-Ti and $Nb_3Sn$”. *IEEE Transactions on Applied Superconductivity*, vol. 26, no. 4, pp. 1–6 (2016).

[22] A. Ballarino, “Prospects for the use of HTS in High Field Magnets for Future Accelerator Magnets”. Proceedings of the 5th International Particle Accelerator Conference, edited by C. Petit-Jean-Genaz, G. Arduini, P. Michel and V. Schaa, pp. 974–979 (2014).

[23] H. Maeda, Y. Tanaka, M. Fukutomi and T. Asano, “A New High-Tc Oxide Superconductor without a Rare Earth Element”. *Japanese Journal of Applied Physics*, vol. 27, no. 2A (1988).

[24] A. Golovashkin, O. Ivanenko, Y. Kudasov et al., “Low temperature direct measurements of $H_{c2}$ in HTSC using megagauss magnetic fields”. *Physica C: Superconductivity*, vol. 185, pp. 1859–1860 (1991).

[25] T. Sekitani, Y. Matsuda, N. Miura et al., “Measurement of the Upper Critical field of Optimally-Doped $YBa_2Cu_3O_{7-\delta}$ in Megagauss Magnetic Fields”. *New Journal of Physics*, vol. 9, no. 47, pp. 1–11 (2007).

[26] D. Larbalestier, J. Jiang, U. Trociewitz et al., “Isotropic round-wire multifilament cuprate superconductor for generation of magnetic fields above 30 T”. *Nature Materials*, vol. 13, p. 375–381 (2014).

[27] M. Wu, J. Ashburn, C. Torng et al., “Superconductivity at 93 K in a new mixed-phase Y-Ba-Cu-O compound system at ambient pressure”. *Physical Review Letters*, vol. 58, no. 9, pp. 908–910 (1987).

[28] Fujikura, Y-based high temperature superconductor. Company leaflet at ICEC (2014).

[29] P. Pahlke, M. Sieger, P. Chekhonin et al., “Local Orientation Variations in YBCO Films on Technical Substrates - A Combined SEM and EBSD Study”. *IEEE Transactions on Applied Superconductivity*, vol. 26, no. 3 (2016).

[30] A. Goyal, M. P. Paranthaman and U. Schoop, “The RABiTS Approach: Using Rolling-Assisted Biaxially Textured Substrates for High-Performance YBCO Superconductors”. *MRS Bulletin*, vol. 29, no. 8, pp. 552–561 (2004).

[31] C. Senatore, C. Barth, M. Bonura et al., “Field and temperature scaling of the critical current density in commercial REBCO coated conductors”. *Superconductor Science and Technology*, vol. 29, no. 1 (2016).

[32] C. Barth, N. Bagrets, K.-P. Weiss et al., “Degradation free epoxy impregnation of REBCO coils and cables”. *Superconductor Science and Technology*, vol. 26, no. 5 (2013).

[33] D. van der Laan, L. Goodrich and T. Haugan, “High-current dc power transmission in flexible RE–$Ba_2Cu_3O_{7-\delta}$ coated conductor cables”. *Superconductor Science and Technology*, vol. 25 (2012).

[34] D. van der Laan, P. Noyes, G. Miller et al., “Characterization of a high-temperature superconducting conductor on round core cables in magnetic fields up to 20 T”. *Superconductor Science and Technology*, vol. 26 (2013).

[35] D. van der Laan, “$YBa_2Cu_3O_{7-\delta}$ coated conductor cabling for low AC loss and high-field magnet applications”. *Superconductor Science and Technology*, vol. 22 (2009).

[36] D. van der Laan, “Compact $GdBa_2Cu_3O_{7-\delta}$ coated conductor cables for electric power transmission and magnet applications”. *Superconductor Science and Technology*, vol. 24, no. 4 (2011).

[37] A. Xu, L. Delgado, N. Khatri et al., “Strongly enhanced vortex pinning from 4 to 77 K in magnetic fields up to 31 T in 15 mol.% Zr-added (Gd, Y)-Ba-Cu-O superconducting tapes”. *Applied Materials*, vol. 2, no. 4 (2014).

[38] G. Nielsen, N. Zangenberg, D. Hazelton et al., “Transverse Pressure Dependence of the Critical Current in Epoxy Impregnated ReBCO Roebel Cables”. *Physics Procedia*, vol. 36, pp. 824–829 (2012).

[39] R. Gupta, M. Anerella and J. Cozzolino, “Next Generation IR Magnets for Hadron Colliders”. *IEEE Transactions on Applied Superconductivity*, vol. 13, no. 2, pp. 1351–1354 (2003).

[40] R. Gupta, “High Field Magnet R&D at BNL for Future High Energy Colliders”. presented at the Low Temperature Superconductor Workshop (2016).

[41] L. Brouwer, Canted-Cosine-Theta Superconducting Accelerator Magnets for High Energy Physics and Ion Beam Cancer Therapy. Ph.D. thesis, University of California, Berkely (2015).

[42] D. van der Laan, J. Weiss, P. Noyes et al., “Record current density of 344 A/mm$^2$ at 4.2 K and 17 T in CORC accelerator magnet cables”. *Superconductor Science and Technology*, vol. 29 (2016).

[43] M. Takayasu, L. Chiesa, L. Bromberg and J. Minervini, “Cabling Method for High Current Conductors Made of HTS Tapes”. *IEEE Transactions on Applied Superconductivity*, vol. 21, no. 3 (2011).

[44] J. Maguire, F. Schmidt, S. Bratt et al., “Development and Demonstration of a HTS Power Cable to Operate in the Long Island Power Authority Transmission Grid”. *IEEE Transactions on Applied Superconductivity*, vol. 17, no. 2 (2007).

[45] W. Goldacker, A. Frank, R. Heller et al., “ROEBEL Assembled Coated Conductors (RACC): Preparation, Properties and Progress”. *Applied Superconductivity, IEEE Transactions on*, vol. 17, no. 2, pp. 3398–3401 (2007).

[46] J. Fleiter, A. Ballarino, W. Goldacker and A. Kario, “Characterization of Roebel cables for potential use in high-field magnets”. *IEEE Transactions on Applied Superconductivity*, vol. 25, no. 3 (2014).

[47] J. Himbele, A. Badel and P. Tixador, “HTS Dipole Magnet for a Particle Accelerator Using a Twisted Stacked Cable”. *IEEE Transactions on Applied Superconductivity*, vol. 26, no. 3 (2016).

[48] L. Roebel, “Electrical conductor”. US Patent 1,144,252 (1915).

[49] W. Goldacker, Roebel Cable from Coated Conductors. Technical report, KIT (2005).

[50] L. Clelland, C. Bumby and R. Badcock, “Machine for producing transposed cable”. WO Patent Application PCT/NZ2013/000,198 (2014).

[51] N. Long, R. Badcock, C. Bumby and Z. Jiang, Superconductivity: Recent Developments and New Production Technologies, chap. Production and Characterisation of HTS Roebel cable. Nova publishers (2012).

[52] P. McIntyre and A. Sattarov, “On the Feasibility of a Tripler Upgrade for LHC”. Proceedings of the 2005 Particle Accelerator Conference, pp. 634–636 (2005).

[53] L. Rossi and E. Todesco, “Conceptual design of 20 T dipoles for high-energy LHC”. The High-Energy Large Hadron Collider, edited by E. Todesco and F. Zimmermann, pp. 13–19, CERN (2011).

[54] W. van de Camp, Critical Current versus Transverse Stress and Thermal Stability of a RRP $Nb_3Sn$ Rutherford Cable. Master’s thesis, University of Twente (2012).

[55] L. Rossi et al., “The EuCARD-2 Future Magnets project: the European collaboration for accelerator quality HTS magnets”. *IEEE Transactions on Applied Superconductivity*, vol. 25, no. 3 (2014).

[56] G. de Rijk, “EuCARD Magnet Development”. The High-Energy Large Hadron Collider, edited by E. Todesco and F. Zimmermann, pp. 45–49, CERN (2011).

[57] G. de Rijk, “The EuCARD High Field Magnet Project”. *IEEE Transactions on Applied Superconductivity*, vol. 22, no. 3 (2012).

[58] P. Ferracin, M. Devaux, M. Durante et al., “Development of the EuCARD $Nb_3Sn$ dipole magnet FRESCA2”. *IEEE Transactions on Applied Superconductivity*, vol. 23, no. 3 (2013).

[59] P. Manil, B. Baudouy, S. Clément et al., “Development and Coil Fabrication Test of the $Nb_3Sn$ Dipole Magnet FRESCA2”. *IEEE Transactions on Applied Superconductivity*, vol. 24, no. 3 (2014).

[60] C. Lorin, M. Durante, P. Fazilleau et al., “Cos-theta design of dipole inserts made of YBCO-Roebel or BiSCCo-Rutherford cables”. *IEEE Transactions on Applied Superconductivity* (2014).

[61] C. Lorin, Cos-$\theta$ magnet design option. Technical report, CEA Saclay (2015).

[62] A. Verweij, CUDI: Users Manual. CERN, public version available since September 2005 (1992).

[63] A. Verweij, Electrodynamics of Superconducting Cables in Accelerator Magnets. Ph.D. thesis, University of Twente (1995).

[64] E. P. A. Van Lanen and A. Nijhuis, “Simulation of interstrand coupling loss in cable-in-conduit conductors with JackPot-AC”. *IEEE Transactions on Applied Superconductivity*, vol. 21, no. 3 PART 2, pp. 1926–1929 (2011).

[65] E. van Lanen, J. van Nugteren and A. Nijhuis, “Full-scale calculation of the coupling losses in ITER size cable-in-conduit conductors”. *IEEE Superconductor Science and Technology*, vol. 25 (2012).

[66] G. Rolando, Notes about the functioning of the code JackPot-AC. University of Twente (2011).

[67] G. Rolando, Cable-in-Conduit Superconductors for Fusion Magnets. Ph.D. thesis, University of Twente (2013).

[68] F. Grilli, R. Brambilla and L. Martini, “Modeling High-Temperature Superconducting Tapes by Means of Edge Finite Elements”. *IEEE Transactions on Applied Superconductivity*, vol. 17, no. 2, pp. 3155–3158 (2007).

[69] F. Grilli, R. Brambilla, L. F. Martini et al., “Current Density Distribution in Multiple YBCO Coated Conductors by Coupled Integral Equations”. *IEEE Transactions on Applied Superconductivity*, vol. 19, no. 3, pp. 2859–2862 (2009).

[70] E. Pardo, J. Kováč and J. Šouc, “Power Loss in ReBCO Racetrack Coils Under AC Applied Magnetic Field and DC Current”. *IEEE Transactions on Applied Superconductivity*, vol. 23, no. 3 (2013).

[71] E. Pardo, “Modeling of AC loss in Coils Made of Thin Tapes Under DC Bias Current”. *IEEE Transactions on Applied Superconductivity*, vol. 24, no. 3 (2014).

[72] V. Zermeño, F. Sirois, M. Takayasu et al., “A self-consistent model for estimating the critical current of superconducting devices”. *Superconductor Science and Technology*, vol. 28, no. 8 (2015).

[73] E. Härö and A. Stenvall, “Reducing Modeling Domain to Speed-Up Quench Simulations of HTS Coils”. *IEEE Transactions on Applied Superconductivity*, vol. 24, no. 3 (2014).

[74] E. Härp̈, A. Stenvall, J. van Nugteren and G. Kirby, “Modeling of Minimum Energy Required to Quench an HTS Magnet With a Strip Heater”. *IEEE Transactions on Applied Superconductivity*, vol. 25, no. 6 (2015).

[75] E. Härö, A. Stenvall, J. van Nugteren and G. Kirby, “Hot Spot Temperature in an HTS Coil: Simulations With MIITs and Finite Element Method”. *IEEE Transactions on Applied Superconductivity*, vol. 25, no. 2 (2015).

[76] E. Härö, A. Stenvall, T. Lecrevisse et al., “Quench Considerations and Protection Scheme of a High Field HTS Dipole Insert Coil”. *IEEE Transactions on Applied Superconductivity*, vol. 23, no. 3 (2013).

[77] T. Salmi, Optimization of Quench Protection Heater Performance in High-Field Accelerator Magnets through Computational and Experimental Analysis. Ph.D. thesis, Tampere University of Technology (2015).

[78] J. van Nugteren, B. van Nugteren, P. Gao et al., “Measurement and Numerical Evaluation of AC losses in a ReBCO Roebel Cable at 4.5 K”. *IEEE Transactions on Applied Superconductivity*, vol. 26, no. 3, pp. 1–7 (2016).

[79] M. Nii, N. Amemiya and T. Nakamura, “Three-dimensional model for numerical electromagnetic field analyses of coated superconductors and its application to Roebel cables”. *Superconductor Science and Technology*, vol. 25 (2012).

[80] V. Zermeño, F. Grilli and F. Sirois, “A full 3-D time-dependent electromagnetic model for Roebel cables”. *IEEE Superconductor Science and Technology*, vol. 26, no. 5 (2013).

[81] F. Grilli, R. Brambilla, F. Sirois et al., “Development of a three-dimensional finite-element model for high-temperature superconductors based on the H-formulation”. *Cryogenics*, vol. 53, pp. 142–147 (2013).

[82] H. Zhang, J. Zhu, W. Yuan and M. Qiu, “Electromagnetic Analysis of YBCO Superconducting Cables With High Current Transporting for Electric Devices”. *IEEE Transactions on Applied Superconductivity*, vol. 26, no. 7 (2016).

[83] L. Greengard and V. Rokhlin, “A fast algorithm for particle simulations”. *Journal of Computational Physics*, pp. 325–348 (1987).

[84] L. Greengard and R. Beatson, A short course on fast multipole methods. Book, Oxford University Press (1997).

[85] Mathworks, “available at: http://www.mathworks.com”.

[86] A. Hindmarsh, P. Brown, K. Grant et al., “SUNDIALS: Suite of Nonlinear and Differential/Algebraic Equation Solvers”. *ACM Transactions on Mathematical Software*, vol. 31, no. 3, pp. 363–396, also available as LLNL technical report UCRL-JP-200037 (2005).

[87] D. Griffiths, Introduction to Electrodynamics. Book, Pearson Education, Inc. (2008).

[88] D. Brandt, ed., CERN Accelerator School: Specialised course on Magnets, CERN (2010).

[89] E. Demenčík, M. Vojenciak, A. Kario et al., “AC Loss and Coupling Currents in YBCO Coated Conductors With Varying Number of Filaments”. *IEEE Transactions on Applied Superconductivity*, vol. 24, no. 6 (2014).

[90] E. Demenčík, F. Grilli, A. Kario et al., “AC Magnetization Loss and Transverse Resistivity of Striated YBCO Coated Conductors”. *IEEE Transactions on Applied Superconductivity*, vol. 25, no. 3 (2015).

[91] E. Ravaioli, CLIQ: A New Quench Protection Technology for Superconducting Magnets. Ph.D. thesis, University of Twente (2015).

[92] J. van Nugteren, M. Dhallé, S. Wessel, E. Krooshoop, A. Nijhuis and H. ten Kate, “Measurement and analysis of normal zone propagation in a ReBCO coated conductor at temperatures below 50 K”. *Physics Procedia*, vol. 67, p. 945 – 951 (2015).

[93] M. Bonura and S. Senatore, “An equation for the quench propagation velocity valid for high field magnet use of ReBCO coated conductors”. *Applied Physics Letters*, vol. 108, no. 24 (2016).

[94] G. Willering, Stability of Superconducting Rutherford Cables: For Accelerator Magnets. Ph.D. thesis, University of Twente (2009).

[95] A. Verweij, J. Genest, A. Knezovic et al., “1.9 K test facility for the reception of the superconducting cables for the LHC ”. *Applied Superconductivity, IEEE Transactions on*, vol. 9, no. 2, pp. 153–156 (1999).

[96] J. van Nugteren, Case Study for a Five Tesla HTS Research Insert-Magnet. Technical report, CERN, Geneva 23, Geneva, Switzerland (2014).

[97] J. van Nugteren, G. Kirby, G. de Rijk et al., “Study of a 5 T Research Dipole Insert-Magnet Using an Anisotropic ReBCO Roebel Cable”. *IEEE Transactions on Applied Superconductivity*, vol. 25, no. 3, pp. 1–5 (2015).

[98] G. Kirby, J. van Nugteren, A. Ballarino et al., “Accelerator Quality HTS Dipole Magnet Demonstrator Designs for the EuCARD-2, 5 T, 40 mm Clear Aperture Magnet”. *IEEE Transactions on Applied Superconductivity*, vol. 25, no. 3 (2014).

[99] G. Kirby, L. Rossi, M. Bajko et al., “Status of the Demonstrator Magnets for the EuCARD-2 Future Magnets Project”. *IEEE Transactions on Applied Superconductivity*, vol. 26, no. 3 (2016).

[100] A. Molodyk, A. Markelov, A. Blednov et al., “"Punch-and-Coat”: a novel approach to mechanically strong 2G HTS Roebel cables”. Presented at MEM 2016 Tallahassee FL (2016).

[101] A. Badel, A. Ballarino, C. Barth et al., Advances in the Development of a 10 kA Class REBCO cable for the EuCARD2 Demonstrator Magnet. Technical report, CERN (2016).

[102] T. Takao, S. Koizuka, K. Oi et al., “Characteristics of Compressive Strain and Superconducting Property in YBCO Coated Conductor”. *IEEE Transactions on Applied Superconductivity*, vol. 17, no. 2, pp. 3517–3519 (2007).

[103] N. Cheggour, J. Ekin, C. Clickner et al., “Transverse compressive stress effect in Y-Ba-Cu-O coatings on biaxially textured Ni and Ni-W substrates”. *IEEE Transactions on Applied Superconductivity*, vol. 13, no. 2, pp. 3530–3533 (2003).

[104] C. Barth, G. Mondonico and C. Senatore, “Electro-Mechanical Properties of REBCO Coated Conductors from various Industrial Manufacturers at 77 K, self-field and 4.2 K, 19 T”. *Superconductor Science and Technology*, vol. 28, no. 4 (2015).

[105] J. Fleiter and A. Ballarino, The effective transverse section of a Roebel cable. Technical report, CERN (2014).

[106] D. Uglietti, R. Wesche and P. Bruzzone, “Effect of transverse load on the critical current of a coated conductor Roebel cable”. *Superconductor Science and Technology*, vol. 26, no. 7 (2013).

[107] S. Otten, Transverse Pressure Dependence of the Critical Current in Epoxy Impregnated ReBCO Roebel Cables. Master’s thesis, University of Twente (2014).

[108] D. van der Laan, J. Ekin, C. Clickner and T. Stauffer, “Delamination strength of YBCO coated conductors under transverse tensile stress”. *Superconductor Science and Technology*, vol. 20, no. 8, p. 765 (2007).

[109] Y. Yanagisawa, H. Nakagome, T. Takematsu et al., “Remarkable weakness against cleavage stress for YBCO-coated conductors and its effect on the YBCO coil performance”. *Physica C: In Superconductivity*, vol. 471, no. 15–16, p. 480–485 (2011).

[110] T. Takematsu, R. Hu, T. Takao et al., “Degradation of the performance of a YBCO-coated conductor double pancake coil due to epoxy impregnation”. *Physica C: Superconductivity*, vol. 470, no. 17–18, pp. 674–677 (2010).

[111] G. Kirby, V. Datskov, S. Clement et al., Thermal Contraction of Future Magnet Materials at Cryogenic Temperatures. Technical report, CERN (2016).

[112] Composite Technology Development, CTD-101G, Cryogenic, Alumina Filled, Anhydride Cured Epoxy. Available at: http://www.CTD-materials.com (2006).

[113] Composite Technology Development, CTD-101G, Epoxy Resin System. Available at: http://www.CTD-materials.com (2003).

[114] A. Dudarev, T. Mulder, W. van de Camp, E. Ravaioli, A. Teixeira and H. ten Kate, “New Fast Response Thin Film-Based Superconducting Quench Detectors”. *IEEE Transactions on Applied Superconductivity*, vol. 24, no. 3, pp. 1–4 (2014).

[115] “Continuously transposed conducting cable”. Provisional European Patent Application: EP15179513.5. (2015).

[116] G. Nielsen, N. Zangenberg, D. Hazelton et al., “Dipole Magnet from High Tc Superconductor”. *Physics Procedia*, vol. 36, pp. 824–829 (2012).

[117] S. Hahn, D. K. Park, J. Bascunan and Y. Iwasa, “HTS Pancake Coils Without Turn-to-Turn Insulation”. *IEEE Transactions on Applied Superconductivity*, vol. 21, no. 3, pp. 1592–1595 (2011).

[118] T. Nakamoto, M. Sugano, Q. Xu et al., “Model Magnet Development of D1 Beam Separation Dipole for the HL-LHC Upgrade”. *IEEE Transactions on Applied Superconductivity*, vol. 25, no. 3, pp. 1–5 (2015).

[119] C. Cobb, P. Barnes, T. Haugan et al., “Hysteretic loss reduction in striated YBCO”. *Physica C: Superconductivity*, vol. 382, no. 1, pp. 52–56 (2002).

[120] J. van Nugteren, Internship Report: CERN, Software development for the Science and Design behind Superconducting Magnet Systems. Technical report, Twente University: Energy Materials and Systems and CERN: ATLAS magnet team (2011).

[121] S. Kurz, J. Fetzer and W. Rucker, Coupled BEM-FEM methods for 3D field calculations with iron saturation. Technical report, Universität Stuttgart, Institut für Theorie der Elektrotechnik (2000).

[122] K. Yagotintsev, P. Gao, M. Dhalle et al., “AC loss tests on CORC and stacked tape ReBCO cables”. Poster presented at ASC 2014, Charlotte (SC), USA (2014).

[123] J. van Nugteren, Normal Zone Propagation in a YBCO Superconducting Tape. Master’s thesis, University of Twente (2012).

[124] Eckels Engineering, 3322 Ebenezer Chase Drive, Florence, SC 29501, CryoComp 5.0 for Windows. Available at: www.eckelsengineering.com (2009).

[125] L. Shampine and C. Gear, "A user's view of solving stiff ordinary differential equations". *SIAM Review*, vol. 21, no. 1, p. 1–17 (1979).

[126] E. Härö and A. Stenvall, The effect of Cu Thickness on stability of ReBCO Tape. Technical report, Tampere University of Technology (2015).

[127] R. Gupta, M. Anerella, A. Ghosh et al., "High Field HTS Solenoid for a Muon Collider Demonstrations, Challenges and Strategies". *IEEE Transactions on Applied Superconductivity*, vol. 24, no. 3 (2014).

[128] R. Ostojic, N. Lasheras, G. Kirby et al., "Status of production of the superconducting matching quadrupoles for the LHC insertions". *IEEE Transactions on Applied Superconductivity*, vol. 15, no. 2, pp. 1094–1097 (2005).

[129] N. Catalán Lasheras, G. Kirby, R. Ostojic et al., "Performance of the Superconducting Matching Quadrupoles for the LHC Insertions". Proceedings of EPAC, pp. 1615–1617 (2004).

[130] P. Fazilleau, M. Devaux, M. Durante et al., "Protection of the 13 T $Nb_3Sn$ Fresca2 Dipole". Proceedings of the Workshop on Accelerator Magnet, Superconductor, Design and Optimization, edited by E. Todesco, pp. 65–69 (2013).

[131] A. Stenvall, E. Haro, P. Fazilleau et al., Protection of the 6 T YBCO Insert in the 13 T $Nb_3Sn$ Fresca-II Dipole. Technical report, CERN (2013).

[132] J. Murtomäki, Mechanical Aspects of High Temperature Superconducting Dipole Insert Magnets. Ph.D. thesis, University of Tampere, CERN, draft version, to be defended (2018).

[133] S. Caspi, S. Gourlay, R. Hafalia et al., "The use of pressurized bladders for stress control of superconducting magnets". *Applied Superconductivity, IEEE Transactions on*, vol. 11, no. 1, pp. 2272–2275 (2001).

[134] Sirius, LMP Solder Paste Dispensing Grade, Sirius$^{TM}$ 1 LF (2013).

[135] J. Perez, H. Bajas, M. Bajko et al., "16 T $Nb_3Sn$ Racetrack Model Coil Test Result". *IEEE Transactions on Applied Superconductivity*, vol. 26, no. 4 (2016).

[136] W. Goldacker, A. Kario, R. Nast et al., "Properties of HTS-Roebel Cables and the Approach for EuCARD-2". Presented at the first workshop on accelerator magnets in HTS (2014).

[137] N. Long and M. Oomen. Private communication during WAM-HTS workshops.

[138] M. Shelley, Frankenstein; or, The Modern Prometheus. Book, Lackington, Hughes, Harding, Mavor & Jones (1818).

[139] L. Bottura, “Tapes and Cables EuCARD2 2016.xlsx”. Spreadsheet (2016).

[140] A. Ruehli, “Equivalent Circuit Models for Three-Dimensional Multiconductor Systems”. *IEEE Transactions on Microwave Theory and Techniques*, vol. 22, no. 3 (1974).

[141] G. Dirichlet, “Über die Reduktion der positiven quadratischen Formen mit drei unbestimmten ganzen Zahlen”. *Journal für die Reine und Angewandte Mathematik*, vol. 40, p. 209–227 (1850).

[142] M. Prabhaker and D. Narsingh, “On Algorithms for Enumerating All Circuits of a Graph”. *SIAM Journal on Computing*, vol. 5, no. 1, pp. 90–99 (1976).

[143] N. Gibbs, W. Poole and P. Stockmeyer, “A Comparison of Several Bandwidth and Profile Reduction Algorithms”. *ACM Transactions on Mathematical Software*, vol. 2, no. 4, pp. 322–330 (1976).

[144] P. Horowitz and W. Hill, The Art of Electronics. Book, Cambridge University Press, 2nd edn. (1989).

[145] N. Gumerov and R. Duraiswami, Fast Multipole Methods for the Helmholz Equation in Three Dimensions. Technical report, Oxford (2005).

[146] J. Kurzak and B. M. Pettitt, “Fast multipole methods for particle dynamics”. *Molecular Simulation*, vol. 32, no. 10-11, pp. 775–790 (2006).

[147] E. Hobson, The Theory of Spherical and Ellipsoidal Harmonics. Book, Chelsea Green Publishing (1955).

[148] C. Müller, Spherical Harmonics, vol. 17. Book, Springer, Lecture Notes in Mathematics (1966).

[149] I. Gradshteyn and I. Ryzhik, Table of Integrals, Series and Products. Book, Academic Press, 7th edn., edited by A. Jeffrey and D. Zwillinger (2007).

[150] R. Yokota and A. Barba, Treecode and fast multipole method for N-body simulation with CUDA. Technical report, Boston University (2011).

[151] J. Nugteren van, MLFMM-GPU Enhancement of JackPot-AC. Technical report, Twente University: Energy Materials and Systems (2011).

[152] B. Wadell, Transmission line design handbook. Book, Artech House (1991).

[153] F. Grover, Inductance Calculations. Book, Dover Publications (2004).

[154] J. Ekin, Experimental Techniques for Low-Temperature Measurements. Book, Oxford Univeristy Press (2006).

[155] K. Yagotintsev, P. Gao, M. Dhalle et al., “AC loss tests on CORC and stacked tape ReBCO cables”. Poster presented at the Applied Superconductivity Conference (2014).

[156] Otten. private communication via e-mail (2016).

[157] A. Grether, C. Scheuerlein, A. Ballarino and L. Bottura, “Electromechanical behaviour of HTS tape lap splices under transverse compressive loading”. Presented at the 8th Workshop on Mechanical and Electromagnetic Properties of Composite Superconductors MEM 2016 (March).

[158] A. Bossavit, “Remarks about hysteresis in superconductivity modelling”. *Physica B: Condensed Matter*, vol. 275, no. 1–3, pp. 142–149 (2000).

[159] P. Deuflhard, Newton Methods for Nonlinear Problems, Affine Invariance and Adaptive Algorithms. Book, Springer (2004).

[160] H. Carslaw and J. Jaeger, Conduction of Heat in Solids. Book, Oxford University Press, 2nd ed. edn. (1959).

[161] E. Gmelin, M. Asen-Palmer, M. Reuther and R. Villar, “Review: Thermal boundary resistance of mechanical contacts between solids at sub-ambient temperatures”. *Physics D: Applied Physics*, vol. 32, no. 6, pp. 19–43 (1999).

[162] H. A. Van der Vorst, “Bi-CGSTAB: A Fast and Smoothly Converging Variant of Bi-CG for the Solution of Nonsymmetric Linear Systems”. *SIAM Scientific and Statistical Computing*, vol. 13, no. 2, p. 631–644 (1992).

[163] Y. Saad and M. Schultz, “GMRES: A Generalized Minimal Residual Algorithm for Solving Nonsymmetric Linear Systems”. *SIAM J. Sci. Stat. Comput.*, vol. 7, no. 3, pp. 856–869 (1986).

[164] R. Barrett, M. Berry, T. Chan et al., Templates for the Solution of Linear Systems: Building Blocks for Iterative Methods. Book, SIAM, Philadelphia, PA, 2nd edition edn. (1994).

[165] J. Bunch and J. Hopcroft, “Triangular factorization and inversion by fast matrix multiplication”. *Mathematics of Computation*, vol. 28, no. 125, p. 231–236 (1974).

[166] G. Karypis and V. Kumar, “A fast and high quality multilevel scheme for partitioning irregular graphs”. International Conference on Parallel Processing, pp. 113–122 (1995).

[167] G. Karypis and V. Kumar, “A fast and high quality multilevel scheme for partitioning irregular grap”. *SIAM Journal on Scientific Computing*, vol. 20, no. 1, pp. 359–392 (1999).

[168] T. Davis and E. Palamadai Natarajan, “KLU, A Direct Sparse Solver for Circuit Simulation Problems”. *ACM Transactions on Mathematical Software*, vol. 37, no. 3 (2010).

[169] T. Davis, “UMFPACK V4.3-an unsymmetric-pattern multifrontal method”. *ACM Transactions on Mathematical Software*, vol. 30, no. 2, pp. 196–199 (2004).

[170] T. Davis, “FACTORIZE: an object-oriented linear system solver for MATLAB”. *ACM Transactions on Mathematical Software*, vol. 39, no. 4 (2013).

[171] P. R. Amestoy, I. S. Duff, J. Koster and J.-Y. L’Excellent, “A Fully Asynchronous Multifrontal Solver Using Distributed Dynamic Scheduling”. *SIAM Journal on Matrix Analysis and Applications*, vol. 23, no. 1, pp. 15–41 (2001).

[172] P. R. Amestoy, A. Guermouche, J.-Y. L’Excellent and S. Pralet, “Hybrid scheduling for the parallel solution of linear systems”. *Parallel Computing*, vol. 32, no. 2, pp. 136–156 (2006).

[173] NVIDIA, The cuSOLVER library user guide v7.5. Available at: http://docs.nvidia.com (2015).

[174] Y. Saad, Iterative Methods for Sparse Linear Systems. Book, PWS Publishing Company (1996).

[175] T. Davis, “SuiteSparseQR: Multifrontal multithreaded rank-revealing sparse QR factorization”. *ACM Transactions on Mathematical Software*, vol. 38, no. 1 (2011).

[176] O. Schenk, M. Bollhöfer and R. Römer, “On Large-Scale Diagonalization Techniques for the Anderson Model of Localization”. *SIAM Review*, vol. 50, no. 1, pp. 91–112 (2008).

[177] NVIDIA, AMGX Reference Manual (2014).

[178] T. Huckle, A. Kallischko, A. Roy, M. Sedlacek and T. Weinzierl, “An Efficient Parallel Implementation of the MSPAI Preconditioner”. *Parallel Computing*, vol. 36, no. 5-6, pp. 273–284 (2010).

[179] T. Komeda, N. Amemiya, R. Buckley et al., “Experimental comparison of AC loss in ReBCO Roebel cables consisting of six strands and ten strands”. *IEEE Transactions on Applied Superconductivity*, vol. 24 (2014).

[180] L. Lakshmi, N. Long et al., “Magnetic AC loss characteristic of 2G Roebel cable”. *IEEE Transactions on Applied Superconductivity*, vol. 19 (2009).

[181] L. Lakshmi, M. Sumption et al., “Frequency dependence of magnetic AC loss in a five strand YBCO Roebel cable”. *IEEE Superconductor Science and Technology*, vol. 23 (2010).

[182] L. Lakshmi, N. Long, J. Emhofer et al., “Magnetic and transport AC loss in HTS Roebel cable”. *IEEE Transactions on Applied Superconductivity*, vol. 21 (2011).

[183] L. Lakshmi, N. Long, M. Sumption et al., “Frequency dependence of magnetic AC loss in a Roebel cable made of YBCO on Ni-W substrate”. *IEEE Superconductor Science and Technology*, vol. 23 (2010).

[184] M. Majoros, N. Long et al., “Stability, inter-strand contact resistance and AC loss in Roebel cables”. *IEEE Transactions on Applied Superconductivity*, vol. 24 (2014).

[185] E. Pardo and F. Grilli, “Numerical simulation of the angular dependence of magnetization AC loss: coated conductors, Roebel cables and double pancake coils”. *IEEE Superconductor Science and Technology*, vol. 25 (2012).

[186] S. Terzieva, F. Grilli, W. Goldacker, A. Kling et al., “Investigation of the effect of striated strands on the AC losses of 2G Roebel cables”. *IEEE Superconding Science and Technology*, vol. 24 (2011).

[187] Y. Yang, J. Pelegrin, I. Falorio et al., “Magnetization Losses of Roebel Cable Samples With 2G YBCO Coated Conductor Strands”. *IEEE Transactions on Applied Superconductivity*, vol. 26, no. 3 (2016).

[188] B. van Nugteren, Detecting Coupling Currents in HTS Roebel Cables. Master’s thesis, University of Twente, Energy Materials and Systems (2016).

[189] B. Munson, D. Young and A. Okiishi, Fundamentals of Fluid Mechanics. Book, John Wiley and Sons, 4th edition edn. (2002).

[190] K. Pankratov, “How to compute a streamfunction?” Available at http://www-pord.ucsd.edu/ matlab/stream.htm (1994).

[191] C. Bean, “Magnetization of High-Field Superconductors”. *Reviews of Modern Physics*, vol. 36, no. 1, pp. 31–38 (1964).

[192] A. Abrikosov, “The magnetic properties of superconducting alloys”. *Journal of Physics and Chemistry of Solids*, vol. 2, no. 3, pp. 199–208 (1957).

[193] F. Grilli, E. Pardo and A. Stenvall, “Computation of Losses in HTS Under the Action of Varying Magnetic Fields and Currents”. *IEEE Transactions on Applied Superconductivity*, vol. 24, no. 1 (2014).

[194] Feltest, Fuji Pressure Sensitive Film. Available at: http://www.feltest.com.

[195] M. Oomen, AC loss in Superconducting Tapes and Cables. Ph.D. thesis, University of Twente (2000).

[196] E. Brandt, “Superconductors of finite thickness in a perpendicular magnetic field: Strips and slabs”. *Physical Review B*, vol. 54, no. 6, pp. 4246–4263 (1996).

[197] A. Wuis, AC magnetization loss: The role of dimensionality. Master’s thesis, University of Twente (2009).

[198] J. Rabbers, AC loss in superconducting tapes and coils. Ph.D. thesis, University of Twente (2001).

[199] T. Keim and I. Mayergoyz, “Superconducting Filter Coils for High Homogeneity Magnetic Field”. United States Patent: 4,656,447 (1987).

[200] A. Dael, F. Kircher and J. Pagot, “Auto Correction des Harmoniques du champ Magnetique d’un multipole pulse par enroulements supraconducteurs”. *Particle Accelerators*, vol. 4, pp. 145–150, in French (1973).

[201] D. Meyer and R. Flasck, “A new configuration for a dipole magnet for use in high energy physics applications”. *Nuclear Instruments and Methods*, vol. 80, pp. 339–341 (1970).

[202] K. Jaecheol, CATIA V5 Design Fundamentals: A Step by Step Guide. Book, Onsia (2012).

[203] J. Bethune, Engineering Design and Graphics With Solidworks 2016. Book, Peachpit Press Publications (2016).

[204] G. Eremeev, B. Clemens and K. Macha, “Development of a $Nb_3Sn$ cavity vapor diffusion deposition system”. Proceedings of the 16th International Conference on RF Superconductivity, edited by A. Claire (2013).

[205] J. van Nugteren, G. Kirby and G. de Rijk, Canted Cosine-Theta Superconducting Magnet Design. Technical report, CERN, Geneva 23, Geneva, Switzerland (2014).

[206] V. Selvamanickam, M. Gharahcheshmeh, A. Xu et al., “Requirements to achieve high in-field critical current density at 30 K in heavily-doped $(Gd, Y)Ba_2Cu_3O_x$ superconductor tapes”. *IEEE Superconductor Science and Technology*, vol. 28, no. 10 (2015).

[207] M. Marchevski, “Quench detection and protection for HTS accelerator magnets”. Presentation at WAM-HTS3, Lyon, France (2015).

[208] J. Murtomäki, Roebel Strand Max Acceptable Tension. Technical report, CERN (2015).

[209] F. Wiedemann, “Ueber die Wärme-Leitungsfähigkeit der Metalle”. *Annalen der Physik*, vol. 165, no. 8, p. 497–531, in German (1853).

[210] Lakeshore, High Temperature (HT) Cernox RTDs.
Available at: www.lakeshore.com.

[211] J. Järvelä, A. Stenvall and R. Mikkonen, “Common rectifier diodes in temperature measurement applications below 50 K”. *Journal of Physics: Conference Series*, vol. 234 (2010).

[212] A. Collaboration, ATLAS Technical Design Report. Technical report, CERN (1997).

[213] V. Al’tov, V. Bliznyuk, V. Lykhin and A. Sverdlov, $Nb_3Sn$ Multifilamentary Wires and Tapes for High-Field Magnetic Systems. Book, Springer US (1997).

[214] M. Eisterer, “Magnetic properties and critical currents of $MgB_2$”. *Superconductor Science and Technology*, vol. 20, no. 12, pp. 47–73 (2007).

[215] V. Ferrando, P. Orgiani, A. Pogrebnyakov et al., “High upper critical field and irreversibility field in MgB2 coated-conductor fibers”. *Applied Physics Letters*, vol. 87, no. 25 (2005).

[216] F. Hunte, H. Song and J. Schwartz, “Fiber Bragg Optical Sensors for YBCO Applications”. Proceedings of the 9th international particle accelerator conference, pp. 3675–3677 (2009).

[217] A. Chiuchiolo et al., “Fiber Bragg Grating Cryosensors for Superconducting Accelerator Magnets”. *IEEE Photonics Journal*, vol. 6, no. 6, pp. 1–10 (2014).

[218] W. Chan, G. Flanagan and J. Schwartz, “Spatial and temporal resolution requirements for quench detection in (RE)$Ba_2Cu_3O_x$ magnets using Rayleigh-scattering-based fiber optic distributed sensing”. *Superconductor Science and Technology*, vol. 26, no. 10 (2013).

[219] J. van Oort, Critical Current Degradation in $Nb_3Sn$ Superconductors in Accelerator Magnets. Ph.D. thesis, University of Twente (2000).

[220] M. Marchevsky, Y.-Y. Xie and V. Selvamanickam, “Quench detection method for 2G HTS wire”. Eucas Conference Proceedings, Applied Superconductivity, IEEE Transactions on (2009).

[221] T. Ogitsu, A. Devred, K. Kim et al., “Quench Antenna for Superconducting Particle Accelerator Magnets”. *IEEE Transactions on Magnetics*, vol. 30, no. 4, pp. 2273–2276 (1994).

[222] M. Wilson. Private communication during his visit at CERN (2015).

[223] K. Broekens, Quench Detection Study for a HTS Model Dipole Magnet. Master’s thesis, University of Delft, Department of Precision and Microsystems Engineering (2016).

[224] J. van Nugteren, AC losses in Toroidal Coil Systems Constructed with YBCO Tapes. Technical report, University of Twente (2009).

[225] E. Popov, Mechanics of Materials. Book, Prentice Hall (1976).

[226] E. Hearn, Mechanics of Materials, vol. 19 of *International Series on Materials Science and Technology*. Book, Pergamon, 2nd edn. (1985).

[227] K. Miettinen, Nonlinear Multiobjective Optimization. Book, Springer (1999).

[228] L. Cooley, A. Ghosh and R. Scanlan, “Costs of high-field superconducting strands for particle accelerator magnets”. *Superconductor Science and Technology*, vol. 18, no. 4, p. R51 (2005).

[229] B. Bellesia, N. Catalan Lasheras and E. Todesco, “Magnet (re)Training”. Proceedings of Chamonix 2009 workshop on LHC Performance, edited by C. Carli, pp. 264–270, CERN (2009).

[230] G. Mulder. Private communication during visit at Philips healthcare, Best, Netherlands (2011).

[231] L. Bottura, “A Practical fit for the Critical Surface of Nb-Ti”. *IEEE Transactions on Applied Superconductivity*, vol. 10, no. 1, pp. 1054–1057 (2000).

[232] T. Boutboul, S. Le Naour and D. Leroy, “Critical Current Density in Superconducting Nb-Ti Strands in the 100 mT to 11 T Applied Field Range”. *IEEE Transactions on Applied Superconductivity*, vol. 16, no. 2, pp. 1184–1187 (2006).

[233] M. S. Lubell, “Empirical scaling formulas for critical current and critical field for commercial Nb-Ti.” *IEEE Transactions on Magnetics*, vol. MAG-19, no. 3 Pt 1, pp. 754–757 (1982).

[234] A. Godeke, Performance Boundaries in $Nb_3Sn$ Superconductors. Ph.D. thesis, Twente University (2005).

[235] J. Fleiter and A. Ballarino, Parameterization of the critical surface of REBCO conductors from Fujikura. Technical report, CERN (2014).

# List of Figures

# List of Tables

# Nomenclature

## List of Abbreviations

| | |
|---|---|
| AMG | Algebraic Multi-Grid. |
| BHTS-1 | Cable geometry with early Bruker tapes, see Table 2.1 on Page 30. |
| BHTS-2 | Cable geometry with Bruker tapes, see Table 2.1 on Page 30. |
| BiCGSTAB | Stabilized Biconjugent Gradient method. |
| BSCCO | Abbreviation of $Bi_2Sr_2Ca_{n-1}Cu_nO_{2n+4+x}$, a high temperature superconducting compound, see Section 1.3 on Page 7. |
| CERN | European Organization for Nuclear Research located in Geneva, Switzerland. |
| CICC | Cable-In-Conduit Conductor, a cable type developed for use in nuclear fusion reactors. |
| CUDA | Nvidia's GPU parallel programming and computing platform. |
| CUDI | Code developed at CERN in collaboration with the University of Twente to perform transient electro-magnetic and thermal analysis on Rutherford type cables. |
| DAE | Differential Algebraic Equation. |
| EuCARD1 | European project for developing technology for high energy particle colliders. |
| EuCARD2 | Continuation of EuCARD1 and the framework in which Feather-M2 is developed. |
| FCC | Future Circular Collider. |
| Feather-M0 | High Temperature Superconducting demonstrator racetrack coil. |
| Feather-M2 | High Temperature Superconducting demonstrator insert-magnet that has an Aligned Block layout and a 40 mm free aperture. |
| FM0 | Feather-M0, High Temperature Superconducting demonstrator racetrack coil. |
| FM2 | Feather-M2, High Temperature Superconducting demonstrator insert-magnet that has an Aligned Block layout and a 40 mm free aperture. |
| FMM | Fast Multipole Method. |

| | |
|---|---|
| GMRES | Generalized Minimal Residual method. |
| GPU | Graphics Processing Unit. |
| HTS | High Temperature Superconductor. |
| ICED | Inductively Coupled Energy Dissipator Ring. |
| ITER | International Thermonuclear Experimental Reactor, a tokamak nuclear fusion reactor under construction in Cadarache in France. |
| JackPot-AC | A code developed at the University of Twente in order to perform transient electro-magnetic analysis on cable-in-conduit conductors. |
| KIT | Karlsrühe Institute of Technology. |
| LHC | Large Hadron Collider, a particle accelerator at CERN. |
| LTS | Low Temperature Superconductor. |
| LU | Decomposition of a matrix into an upper and lower triangular part. |
| MLFMM | Multi-Level Fast Multipole Method. |
| MQE | Minimum Quench Energy. |
| MUMPS | MUltifrontal Massively Parallel sparse direct Solver. |
| ReBCO | Rare Earth (commonly Ytrium or Gadelinium) Barium Copper Oxide, a high temperature superconducting compound with chemical composition $YBa_2Cu_3O_{7-x}$ that is only available as thin film inside a coated conductor tape, see Section 1.3 on Page 7. |
| SP-1 | Cable geometry with SuperPower tapes, see Table 2.1 on Page 30. |
| Sun-Ox-1 | Cable geometry with Sunam tapes, see Table 2.1 on Page 30. |

## List of Symbols

| | |
|---|---|
| $\alpha_0$ | Operating magnetic field angle. |
| $\boldsymbol{A}_{\text{tdprepre}}$ | Matrix used for pre-pre-conditioner in the transient solver, see Equation 3.70 on Page 121. |
| $\boldsymbol{M}_{sc}$ | Strand contact matrix, see Equation 3.4 on Page 95. |
| $\ell, n, t$ | Coordinates inside the coil windings or cable: $\ell$ is the longitudinal direction, $n$ the normal direction and $t$ the transverse direction. |
| $\ell_1$ | Interpolation array of $\ell$ coordinates used to define elevation of a strand in the Roebel cable, see Equation 3.2 on Page 92. |

| | |
|---|---|
| $\ell_2$ | Interpolation array of $\ell$ coordinates used to define elevation of a strand in the Roebel cable, see Equation 3.2 on Page 92. |
| $\ell_{\text{edge}}$ | Interpolation array of $\ell$ coordinates defining the edge of a strand in a Roebel cable, see Equation 3.1 on Page 92. |
| $\ell_{\text{surf}}$ | Coordinates defining the surface of the tape in the longitudinal direction, see Section 3.2.1 on Page 92. |
| $\ell_{n,p,i,j}$ | Matrix containing the $\ell$ position of the nodes in a Roebel cable unit cell, see Section 3.2.1 on Page 92. |
| $\ell_{n,Q}$ | Array containing the $\ell$ position of the nodes in a Roebel cable unit cell, see Section 3.2.1 on Page 92. |
| $\mu_r$ | Permeability for inductance calculation 1 if in non-magnetic medium, see Equation 3.43 on Page 110. |
| $\phi_{\text{in}}$ | Aperture diameter, see Figure 2.27 on Page 53. |
| $\phi_{\text{out}}$ | Outer diameter, see Figure 2.27 on Page 53. |
| $\theta$ | Magnetic field angle. |
| $\vec{D}_{el,c,p,i,j}$ | Direction vector of a longitudinal element, in unit cell with index $c$, in tape section with index $p$, at coordinate $i$ and $j$ in the grid, see Equation 3.6 on Page 96. |
| $\vec{D}_{et,c,p,i,j}$ | Direction vector of a transverse element, in unit cell with index $c$, in tape section with index $p$, at coordinate $i$ and $j$ in the grid, see Equation 3.5 on Page 96. |
| $\vec{L}_{el,c,p,i,j}$ | Orientation vector pointing along the tape in the $\ell$ direction, for a longitudinal element in unit cell indexed with $c$, for a tape section indexed with $p$ and located at $i$ and $j$ in the grid, see Equation 3.13 on Page 97. |
| $\vec{L}_{el,c,R}$ | Orientation vector pointing along the tape in the $\ell$ direction, for a longitudinal element in unit cell indexed with $c$, with group index $R$, see Equation 3.13 on Page 97. |
| $\vec{L}_{et,c,p,i,j}$ | Orientation vector pointing along the tape in the $\ell$ direction, for a transverse element in unit cell indexed with $c$, for a tape section indexed with $p$ and located at $i$ and $j$ in the grid, see Equation 3.13 on Page 97. |
| $\vec{L}_{et,c,P}$ | Orientation vector pointing along the tape in the $\ell$ direction, for a transverse element in unit cell indexed with $c$, with group index $P$, see Equation 3.13 on Page 97. |
| $\vec{N}_{el,c,p,i,j}$ | Orientation vector pointing in the face normal $n$ direction, for a longitudinal element in unit cell indexed with $c$, for a tape section indexed with $p$ and located at $i$ and $j$ in the grid, see Equation 3.13 on Page 97. |

$\vec{N}_{el,c,R}$ Orientation vector pointing in the face normal $n$ direction, for a longitudinal element in unit cell indexed with $c$, with group index $R$, see Equation 3.13 on Page 97.

$\vec{N}_{et,c,p,i,j}$ Orientation vector pointing in the face normal $n$ direction, for a transverse element in unit cell indexed with $c$, for a tape section indexed with $p$ and located at $i$ and $j$ in the grid, see Equation 3.13 on Page 97.

$\vec{N}_{et,c,P}$ Orientation vector pointing in the face normal $n$ direction, for a transverse element in unit cell indexed with $c$, with group index $P$, see Equation 3.13 on Page 97.

$\vec{T}_{el,c,p,i,j}$ Orientation vector pointing across the tape in the $t$ direction, for a longitudinal element in unit cell indexed with $c$, for a tape section indexed with $p$ and located at $i$ and $j$ in the grid, see Equation 3.13 on Page 97.

$\vec{T}_{el,c,R}$ Orientation vector pointing across the tape in the $t$ direction, for a longitudinal element in unit cell indexed with $c$, with group index $R$, see Equation 3.13 on Page 97.

$\vec{T}_{et,c,p,i,j}$ Orientation vector pointing across the tape in the $t$ direction, for a transverse element in unit cell indexed with $c$, for a tape section indexed with $p$ and located at $i$ and $j$ in the grid, see Equation 3.13 on Page 97.

$\vec{T}_{et,c,P}$ Orientation vector pointing across the tape in the $t$ direction, for a transverse element in unit cell indexed with $c$, with group index $P$, see Equation 3.13 on Page 97.

$\vec{X}_{\ell,i}$ Coil coordinate system longitudinal direction vector, see Section 2.3.4 on Page 46.

$\vec{X}_{c,n,i}$ Cable coordinate system normal vector at origin $i$, see Section 2.3.4 on Page 46.

$\vec{X}_{c,t,i}$ Cable coordinate system transverse vector at origin $i$, see Section 2.3.4 on Page 46.

$\vec{X}_{el,c,p,i,j}$ Position vector of a longitudinal element, in unit cell with index $c$, in tape section with index $p$, at coordinate $i$ and $j$ in the grid, see Equation 3.6 on Page 96.

$\vec{X}_{et,c,p,i,j}$ Position vector of a transverse element, in unit cell with index $c$, in tape section with index $p$, at coordinate $i$ and $j$ in the grid, see Equation 3.5 on Page 96.

$\vec{X}_i$ Position vector defining the origins of the coil coordinate system, see Section 2.3.4 on Page 46.

$\vec{X}'_i$ Transformed Cartesian coordinate at origin $i$, see Section 2.3.4 on Page 46.

| | |
|---|---|
| $\vec{X}_{n,c,p,i,j}$ | Position vector of a node, in unit cell with index $c$, in tape section with index $p$, at coordinate $i$ and $j$ in the grid, see Equation 3.5 on Page 96. |
| $\vec{X}_{n,c,Q}$ | Position vector of a node with group index $Q$, in unit cell with index $c$, see Section 3.2.1 on Page 92. |
| $\vec{X}_{n,i}$ | Coil coordinate system normal direction vector, see Section 2.3.4 on Page 46. |
| $\vec{X}_{t,i}$ | Coil coordinate system transverse direction vector, see Section 2.3.4 on Page 46. |
| $a$ | Helper variable for vector potential calculation, see Equation 3.38 on Page 105. |
| $A_{\text{end}}$ | Coil end angle, see Figure 2.26 on Page 53. |
| $a_{\text{loc}}$ | Feather-M2 winding shear angle as function of axial coordinate $z$, see Equation 2.6 on Page 49. |
| $A_{\text{rot1}}$ | Central shear angle, see Figure 2.26 on Page 53. |
| $A_{\text{rot2}}$ | Wing shear angle, see Figure 2.26 on Page 53. |
| $a_{\text{crot},i}$ | Cable coordinate system rotation angle at origin $i$, see Section 2.3.4 on Page 46. |
| $B$ | Magnetic field. |
| $b$ | Helper variable for vector potential calculation, see Equation 3.38 on Page 105. |
| $B_0$ | Operating magnetic field. |
| $B_{c1}$ | Lower critical field of a superconductor, see Section 1.2 on Page 4. |
| $B_{c2}$ | Upper critical field of a superconductor, see Section 1.2 on Page 4. |
| $B_c$ | Critical field of a superconductor, see Section 1.2 on Page 4. |
| $c$ | Helper variable for vector potential calculation, see Equation 3.38 on Page 105. |
| $C_{p,sp}$ | Heat capacity matrix, see Equation 3.56 on Page 115. |
| $d_{\text{cable}}$ | Thickness of the Roebel cable, see Table 2.6 on Page 54. |
| $d_{\text{insu}}$ | Thickness of the cable insulation layer, see Table 2.6 on Page 54. |
| $d_{\text{rap}}$ | Spacing between aperture and coil, see Figure 2.27 on Page 53. |
| $d_q$ | Diameter of a contact elemement, see Equation 3.43 on Page 110. |

| | |
|---|---|
| $E_{\text{beam}}$ | Beam energy. |
| $E_{\text{mqe}}$ | Minimum Quench Energy. |
| $E_{high}$ | Higher energy limit during MQE search, see Section 2.4.2 on Page 64. |
| $E_{low}$ | Lower energy limit during MQE search, see Section 2.4.2 on Page 64. |
| $f_{\text{circ}}$ | Function calculating the deviation of a circle with respect to a straight line as function of the radius and distance, see Equation 2.2 on Page 47. |
| $G_{ij}$ | Conductance matrix used in the electro-magnetic and if present thermal systems of equations of the network model, see Equation 3.28 on Page 102 and Equation 3.56 on Page 115 respectively. The construction of the matrix is explained in Section 3.3.7 on Page 110. |
| $h_{\text{req1}}$ | Central deck flaring height, see Figure 2.26 on Page 53. |
| $h_{\text{req2}}$ | Wing deck flaring height, see Figure 2.26 on Page 53. |
| $I_0$ | Operating current. |
| $I_{\text{bg},i}$ | Function for calculating the currents resulting from a time changing background field. The function is used in the electro-magnetic and if present thermal systems of equations of the network model, see Equation 3.28 on Page 102 and Equation 3.56 on Page 115 respectively. Further explanation can be found in Section 3.3.4 on Page 105. |
| $I_{\text{nc}}$ | Part of the current that flows inside the matrix, see Section 3.3.8 on Page 111. |
| $I_{\text{res},q}$ | Residual currents used in the electro-magnetic and if present thermal systems of equations of the network model, see Equation 3.28 on Page 102 and Equation 3.56 on Page 115 respectively. |
| $I_{\text{sc}}$ | Part of the current that flows inside the superconductor, see Section 3.3.8 on Page 111. |
| $I_{c,\text{I}}$ | Critical current criterion assuming no current redistribution, see Section 2.3.6 on Page 57. |
| $I_{c,\text{III}}$ | Critical current criterion assuming full current redistribution, see Section 2.3.6 on Page 57. |
| $I_{c,\text{II}}$ | Critical current criterion assuming current redistributions inside the tapes, but not between the tapes, see Section 2.3.6 on Page 57. |
| $I_c$ | Critical current of a tape, cable or coil. |
| $I_{G,sj}$ | Power matrix for the contact conductance elements, see Equation 3.61 on Page 116. |

| | |
|---|---|
| $I_q$ | Array with currents through all elements used in the electro-magnetic and if present thermal systems of equations of the network model, see Equation 3.28 on Page 102 and Equation 3.56 on Page 115 respectively. |
| $I_{s,i}$ | Array with external source currents at nodes used in the electro-magnetic and if present thermal systems of equations of the network model, see Equation 3.28 on Page 102 and Equation 3.56 on Page 115 respectively. External sources are further explained in Section 3.3.9 on Page 113. |
| $J_{cel,p,i,j}$ | Critical current density in the longitudinal elements of strand $p$ at transverse index $i$ and longitudinal index $j$, see Section 2.3.6 on Page 57. |
| $J_c$ | Critical current density of a superconductor, see Section 1.2 on Page 4. |
| $J_e$ | Engineering current density of a superconducting wire or cable, see Section 1.3 on Page 7. |
| $k_{1,i}$ | The first node a contact element indexed with $i$ is connected to, see Section 3.2.1 on Page 92. |
| $k_1$ | Helper variable for vector potential calculation, see Equation 3.36 on Page 105. |
| $k_{2,i}$ | The second node a contact element indexed with $i$ is connected to, see Section 3.2.1 on Page 92. |
| $k_2$ | Helper variable for vector potential calculation, see Equation 3.36 on Page 105. |
| $K_{\text{cool},sp}$ | Cooling matrix, see Equation 3.56 on Page 115. |
| $K_{sp}$ | Heat transfer matrix, see Equation 3.56 on Page 115. |
| $L_0$ | Straight section length, see Figure 2.26 on Page 53 and Figure 2.25 on Page 53. |
| $L_{12,el,c,p,i,j}$ | Length of the longitudinal element, in unit cell indexed with $c$, in tape section $p$, at location $i$ and $j$ in the grid, see Equation 3.10 on Page 97. |
| $L_{12,el,c,R}$ | Length of the longitudinal element, in unit cell indexed with $c$, with group index $P$, see Equation 3.10 on Page 97. |
| $L_{12,et,c,p,i,j}$ | Length of the transverse element, in unit cell indexed with $c$, in tape section $p$, at location $i$ and $j$ in the grid, see Equation 3.10 on Page 97. |
| $L_{12,et,c,P}$ | Length of the transverse element, in unit cell indexed with $c$, with group index $P$, see Equation 3.10 on Page 97. |
| $L_3$ | Enforced coil length, see Figure 2.25 on Page 53. |
| $L_{\text{ca}}$ | Total cable length, see Table 2.6 on Page 54. |

$L_{\text{con}}$ Self-inductance of a wire element, see see Equation 3.44 on Page 110.

$L_{\text{co}}$ Total coil length, see Table 2.6 on Page 54.

$L_{\text{cr}}$ Length of a cross-over in the Roebel cable, see Section 3.2.1 on Page 92.

$L_{\text{rib}}$ Self-inductance of a ribbon element, see Equation 3.43 on Page 110.

$L_{\text{self}}$ Coil self-inductance, see Table 2.6 on Page 54.

$L_{\text{str}}$ Length of a straight section in the Roebel cable, see Section 3.2.1 on Page 92.

$L_{\text{yoke}}$ Yoke length, see Table 2.6 on Page 54.

$L_i$ Longitudinal $\ell$ coordinate of node $i$ in the coil windings, see Section 2.3.4 on Page 46.

$L_{qr}$ Self-inductance matrix used in the electro-magnetic and if present thermal systems of equations of the network model, see Equation 3.28 on Page 102 and Equation 3.56 on Page 115 respectively. The construction of the matrix is explained in Section 3.3.4 on Page 105.

$L_w$ Straight section width, see Figure 2.25 on Page 53.

$M$ Magnetization.

$M_{\text{dPdI},sp}$ Linearisation of the power with the current for the superconducting elements, see Equation 3.70 on Page 121.

$M_{\text{dPdT},sp}$ Linearisation of the power with the temperature for the superconducting elements, see Equation 3.70 on Page 121.

$M_{\text{fr2}}$ Coil mutual inductance with Fresca2, see Table 2.6 on Page 54.

$M_{\text{kcl},ir}$ Kirchhoff's current law connectivity matrix used in the electro-magnetic and if present thermal systems of equations of the network model, see Equation 3.28 on Page 102 and Equation 3.56 on Page 115 respectively. The construction of the matrix is explained in Section 3.3.3 on Page 104.

$M_{\text{kvl},qj}$ Kirchhoff's Voltage law connectivity matrix used in the electro-magnetic and if present thermal systems of equations of the network model, see Equation 3.28 on Page 102 and Equation 3.56 on Page 115 respectively. The construction of the matrix is explained in Section 3.3.3 on Page 104.

$M_{\text{S2T},qr}$ Source to target mutual inductance matrix, calculated form the S2T step in the MLFMM, used in the electro-magnetic and if present thermal systems of equations of the network model, see Equation 3.28 on Page 102 and Equation 3.56 on Page 115 respectively. The construction of the matrix is explained in Section 3.3.4 on Page 105.

| | |
|---|---|
| $m_{el,1,c,p,i,j}$ | First connection node of a longitudinal element, in unit cell indexed with $c$, in tape section $p$, at location $i$ and $j$ in the grid, see Equation 3.9 on Page 97. |
| $m_{el,1,c,R}$ | First connection node of a longitudinal element, in unit cell indexed with $c$, with group index $R$, see Equation 3.9 on Page 97. |
| $m_{el,2,c,p,i,j}$ | Second connection node of a longitudinal element, in unit cell indexed with $c$, in tape section $p$, at location $i$ and $j$ in the grid, see Equation 3.9 on Page 97. |
| $m_{el,2,c,R}$ | Second connection node of a longitudinal element, in unit cell indexed with $c$, with group index $R$, see Equation 3.9 on Page 97. |
| $m_{et,1,c,p,i,j}$ | First connection node of a transverse element, in unit cell indexed with $c$, in tape section $p$, at location $i$ and $j$ in the grid, see Equation 3.9 on Page 97. |
| $m_{et,1,c,P}$ | First connection node of a transverse element, in unit cell indexed with $c$, with group index $P$, see Equation 3.9 on Page 97. |
| $m_{et,2,c,p,i,j}$ | Second connection node of a transverse element, in unit cell indexed with $c$, in tape section $p$, at location $i$ and $j$ in the grid, see Equation 3.9 on Page 97. |
| $m_{et,2,c,P}$ | Second connection node of a transverse element, in unit cell indexed with $c$, with group index $P$, see Equation 3.9 on Page 97. |
| $M_{ij}$ | System Mutual inductance matrix, see Section 2.4.3 on Page 66. |
| $n_1$ | Interpolation array of $n$ coordinates used to define elevation of a strand in the Roebel cable, see Equation 3.2 on Page 92. |
| $n_2$ | Interpolation array of $n$ coordinates used to define elevation of a strand in the Roebel cable, see Equation 3.2 on Page 92. |
| $n_{\text{surf}}$ | Elevation of the surface of a single tape in the Roebel cable, see Equation 3.3 on Page 93. |
| $n_{\text{turn1}}$ | Central deck number of turns, see Figure 2.26 on Page 53. |
| $n_{\text{turn2}}$ | Wing deck number of turns, see Figure 2.26 on Page 53. |
| $N_{el,l}$ | Number of longitudinal elements in each tape section in the longitudinal direction, see Section 3.2.1 on Page 92. |
| $N_{el,t}$ | Number of longitudinal elements in each tape section in the transverse direction, see Section 3.2.1 on Page 92. |
| $N_{et,l}$ | Number of transverse elements in each tape section in the longitudinal direction, see Section 3.2.1 on Page 92. |

| | |
|---|---|
| $N_{et,t}$ | Number of transverse elements in each tape section in the transverse direction, see Section 3.2.1 on Page 92. |
| $n_{n,p,i,j}$ | Matrix containing the $n$ position of the nodes in a Roebel cable unit cell, see Section 3.2.1 on Page 92. |
| $n_{n,Q}$ | Array containing the $n$ position of the nodes in a Roebel cable unit cell, see Section 3.2.1 on Page 92. |
| $N_{nl}$ | Number of nodes in a tape section in the longitudinal direction, see Section 3.2.1 on Page 92. |
| $N_{nt}$ | Number of nodes in a tape section in the transverse direction, see Section 3.2.1 on Page 92. |
| $N_{nu}$ | Number of nodes in the unit cell, see Section 3.2.1 on Page 92. |
| $N_{uec}$ | Number of contact elements in each unit cell, see Section 3.2.1 on Page 92. |
| $N_{uel}$ | Number of longitudinal elements in each unit cell, see Section 3.2.1 on Page 92. |
| $N_{uet}$ | Number of transverse elements in each unit cell, see Section 3.2.1 on Page 92. |
| $N_u$ | Number of unit cells in the modeled cable, where each twist pitch contains $N_s$ unit cells, see Section 3.2.1 on Page 92. |
| $P$ | Group index numbering the transverse elements in a unit cell recombining indexes $p$, $i$ and $j$, see Section 3.2.1 on Page 92. |
| $P_{\mathrm{nl},s}$ | Non-linear power dissipation function for the superconducting elements, calculates the power at the nodes as function of the current, the temperature, the magnetic field and the magnetic field angle at the elements, see Equation 3.56 on Page 115. |
| $p_{\mathrm{twist}}$ | Shear angle factor, see Table 2.6 on Page 54. |
| $P_{G,s}$ | Power dissipation function for the conductance (contact) elements, calculates the power at the nodes as function of the voltages at the nodes, see Equation 3.56 on Page 115. |
| $P_{R,s}$ | Power dissipation function for the normal conducting elements, calculates the power at the nodes as function of the current through the elements, see Equation 3.56 on Page 115. |
| $P_{s,s}$ | Source power at nodes, see Equation 3.56 on Page 115. |
| $Q$ | Group index numbering the nodes in a unit cell recombining indexes $p$, $i$ and $j$, see Section 3.2.1 on Page 92. |

| | |
|---|---|
| $R$ | Group index numbering the longitudinal elements in a unit cell recombining indexes $p$, $i$ and $j$, see Section 3.2.1 on Page 92. |
| $R_{\text{easy}}$ | Easy-way bend radius, see Figure 2.25 on Page 53. |
| $R_{\text{hard}}$ | Hard-way bend radius, see Figure 2.25 on Page 53. |
| $R_{\text{mid}}$ | Medium coil bend radius, see Figure 2.25 on Page 53. |
| $R_{\text{nl},qr}$ | Effective resistance for superconducting elements, see Equation 3.70 on Page 121. |
| $R_{\text{yoke1}}$ | Yoke inner radius, see Figure 2.27 on Page 53. |
| $R_{\text{yoke2}}$ | Yoke outer radius, see Figure 2.27 on Page 53. |
| $R_{qr}$ | Resistance matrix used in the electro-magnetic and if present thermal systems of equations of the network model, see Equation 3.28 on Page 102 and Equation 3.56 on Page 115 respectively. The construction of the matrix is explained in Section 3.3.7 on Page 110. |
| $R_r$ | Radius of the accelerator ring. |
| $T$ | Temperature. |
| $T_{\text{bath}}$ | Temperature of coolant, see Equation 3.56 on Page 115. |
| $t_{\text{cj}}$ | Time stepping constant controlled by the solver, see Equation 3.69 on Page 121 and see Equation 3.70 on Page 121. |
| $t_{\text{edge}}$ | Interpolation array of $t$ coordinates defining the edge of a strand in the Roebel cable, see Equation 3.1 on Page 92. |
| $t_{\text{surf}}$ | Coordinates defining the surface of the tape in the transverse direction, see Section 3.2.1 on Page 92. |
| $T_{cs}$ | Current sharing temperature, see Section 1.8 on Page 20. |
| $T_c$ | Critical temperature of a superconductor, see Section 1.2 on Page 4. |
| $t_{n,p,i,j}$ | Matrix containing the $t$ position of the nodes in a Roebel cable unit cell, see Section 3.2.1 on Page 92. |
| $t_{n,Q}$ | Array containing the $t$ position of the nodes in a Roebel cable unit cell, see Section 3.2.1 on Page 92. |
| $T_p$ | Temperatures at all nodes, see Equation 3.56 on Page 115. |
| $V_{\text{bg},q}$ | Function for calculating the Voltages resulting from a time changing background field. The function is used in the electro-magnetic and if present thermal systems of equations of the network model, see Equation 3.28 on Page 102 and Equation 3.56 on Page 115 respectively. Further explanation can be found in Section 3.3.4 on Page 105. |

$V_{\text{mlfmm},q}$ Function calculating the inductive Voltages from the time derivative of the currents using the MLFMM. The function is used in the electro-magnetic and if present thermal systems of equations of the network model, see Equation 3.28 on Page 102 and Equation 3.56 on Page 115 respectively. Further explanation can be found in Section 3.3.4 on Page 105.

$V_{\text{nl},q}$ Function for calculating the non-linear voltages over the superconducting elements as used in the electro-magnetic and if present thermal systems of equations of the network model, see Equation 3.28 on Page 102 and Equation 3.56 on Page 115 respectively. The function is explained in Section 3.3.8 on Page 111.

$V_{\text{nzp}}$ Normal zone propagation velocity.

$V_{\text{res},i}$ Residual voltages used in the electro-magnetic and if present thermal systems of equations of the network model, see Equation 3.28 on Page 102 and Equation 3.56 on Page 115 respectively.

$V_i$ Array with Voltages at all nodes used in the electro-magnetic and if present thermal systems of equations of the network model, see Equation 3.28 on Page 102 and Equation 3.56 on Page 115 respectively.

$V_{R,sr}$ Power matrix for the contact resistance elements, see Equation 3.62 on Page 116.

$V_{s,q}$ Array with external source voltage at over elements used in the electro-magnetic and if present thermal systems of equations of the network model, see Equation 3.28 on Page 102 and Equation 3.56 on Page 115 respectively. External sources are further explained in Section 3.3.9 on Page 113.

$W_{12,el,c,p,i,j}$ Width of the longitudinal element, in unit cell indexed with $c$, in tape section $p$, at location $i$ and $j$ in the grid, see Equation 3.12 on Page 97.

$W_{12,el,c,R}$ Width of the longitudinal element, in unit cell indexed with $c$, with group index $P$, see Equation 3.12 on Page 97.

$W_{12,et,c,p,i,j}$ Width of the transverse element, in unit cell indexed with $c$, in tape section $p$, at location $i$ and $j$ in the grid, see Equation 3.11 on Page 97.

$W_{12,et,c,P}$ Width of the transverse element, in unit cell indexed with $c$, with group index $P$, see Equation 3.11 on Page 97.

$w_{\text{cable}}$ Width of the cable, see Figure 2.25 on Page 53.

$x, y, z$ Cartesian coordinates, sometimes grouped into a vector $\vec{X}$.

$x_{\text{top}}$ Feather-M2 top profile $x$ coordinate as function of axial coordinate $z$, see Equation 2.5 on Page 49.

| | |
|---|---|
| $x_{n,c,Q}$ | Coordinate in $x$ of the node with group index $Q$, in unit cell with index $c$, see Section 3.2.1 on Page 92. |
| $y_{\text{cen1}}$ | Central deck y-position, see Figure 2.26 on Page 53. |
| $y_{\text{cen2}}$ | Wing deck y-position, see Figure 2.26 on Page 53. |
| $y_{\text{side}}$ | Feather-M2 side profile $y$ coordinate as function of axial coordinate $z$, see Equation 2.4 on Page 48. |
| $y_{n,c,Q}$ | Coordinate in $y$ of the node with group index $Q$, in unit cell with index $c$, see Section 3.2.1 on Page 92. |
| $z_{n,c,Q}$ | Coordinate in $z$ of the node with group index $Q$, in unit cell with index $c$, see Section 3.2.1 on Page 92. |